Synthesis and Characterization of Ruthenium Complexes with (N^N)(P^P) and $(N^P)_2$ Donor Sets

Xinwei Yang

A Thesis Submitted For The Degree Of Doctor Of Philosophy Of The

Australian National University

Australian National University

Canberra, July 2016

Declaration

The work described in this thesis is my own unless stated otherwise. I have not submitted this material for any other degree or qualification. Any contribution from others has been acknowledged appropriately.

Xinwei Yang
(Signature)

Canberra, July 2016

Acknowledgement

During my time for PhD programme at ANU, I would like to thank sincerely the chair of my supervisory panel, Prof. Mark Humphrey. He provided me with an opportunity to do my PhD at ANU and gave me lots of guidance, advice, unlimited support and encouragement during my time in Australia. He is an excellent supervisor with great patience and a strong sense of responsibility.

I would like to thank the members of my supervisory panel, Assoc. Prof. Marie Cifuentes, Prof. Rob Stranger, Dr. Simon Petrie for their support and professional advice. Thanks again to Assoc. Prof. Marie Cifuentes for her considerate care and support in life during my very early days.

I also received a wide range of excellent technical and professional support within RSC. Thus, I would like to express my acknowledgements to Mrs. Anitha Jeyasingham for providing the large amount of mass spectrometry data; to Mr. Chris Blake and Ms. Peta Simmonds for their professional and efficient support in all aspects of NMR spectroscopy and great patience on training; to Paul Gugger and Dr. Peter Simpson for outstanding technical and synthetic support in the chemical laboratory; to Dr. Bandar Babgi for his great support in helping me prepare for the PhD programme; to Dr. Guillaume Grelaud for teaching me cyclic voltammetry and synthesizing the dppf ligand; to Dr. Mahbod Morshedi for great help and advice in laboratory work, especially on CV and the spectroelectrochemistry; to Dr. Genmiao Wang and Dr. Adam Barlow for training me in the use of lasers; and special thanks to Dr. Graeme Moxey for professional advice and the crystallography work which underpins my project.

I am very grateful to be a part of the research group. Thanks to the past and present group members for their friendship given to me: Dr. Adam Barlow, Dr. Areej Merchi, Dr. Bandar Babgi, Dr. Erandi Kulasekera, Dr. Fazira Ilyanaa Abdul Razak, Dr. Guillaume Grelaud, Dr. Huajian Zhao, Dr. Junhong Fu, Mr. Kaili Zhang, Dr. Mahbod Morshedi, Ms. Noor Aisyah Ahmad Shah, Mr. Mark Jennaway, Dr. Nicholas Ripoche, Mr. Paul Gugger, Dr. Peter Simpson, Dr. Torsten Schwich, Mr. Vivek Gupta, Dr. Xiao Zhang, Mr. Amedee Triadon, Mr. Anthony Nolan, Ms. Aradhana

Dissaanyake, Mr. Cristobal Quintana, Mr. Dick Dexter, Dr. Genmiao Wang, Mr. George Laffan, Dr. Graeme Moxey, Ms. Ling Zhang, Mr. Mahesh Kodikara and Ms. Suzy Streatfield.

During my stay in Australia, I experienced laughter and tears. There are many people, even some strangers providing good advice and helping hands. I would like to acknowledge my friends for the friendship built by frank hearts and the kindness from the nice people here. Foremost, special thanks should be given to my wonderful family for the great love, great support and great understanding. I am so proud of you and always cheer myself up when thinking of you.

The time I spent here will never vanish in my mind and always encourage me to be brave and confident in front of the difficulties in the future.

Abstract

Since the discovery of nonlinear effects, both the theory and measurement techniques have been developed significantly, especially since the invention of the laser. However, structure-NLO property relationships for organometallics as well as their NLO mechanisms are far less explored than those of organic molecules and inorganic salts. The greater flexibility and exceptionally large NLO responses of organometallic compounds attracts chemists to this field.

Modification of coordinated co-ligands in organometallic systems has influence on the NLO merit by introducing new electronic charge-transfer transitions, oxidation state and coordination sphere of the metal centers. In this work, the donor sets of the ruthenium complexes were modified from the most investigated $(P\hat{}P)_2$ to $(N\hat{}N)(P\hat{}P)$ and $(N\hat{}P)_2$ and a series of ruthenium complexes were synthesized and characterized.

In Chapter 2, the study of the $Ru(N\hat{}N)(P\hat{}P)$ complexes is detailed. Three bidentate diphosphine ligands (dppe, dppb and dppf) and one diimine ligand (^{t}Bu-bpy) were selected for this study as the diphosphine and diimine ligands, respectively. Ruthenium halide and mono-alkynyl complexes were obtained successfully. Their optical, electrochemical and spectroelectrochemical properties were examined and are discussed. The formation of η^3- and η^1-butenynyl complexes was confirmed by single-crystal X-ray diffraction. Attempts towards bis-alkynyl complexes were made, but no conclusive evidence could be obtained to confirm the successful synthesis of this species.

In Chapter 3, the focus of the work is the study of ruthenium complexes with a $(N\hat{}P)_2$ donor set. Two iminophosphine ligands, 2-(diphenylphosphino)pyridine (PPh_2py) and 8-(diphenylphosphino)quinoline (PPh_2qn), were selected for this study. The *cis*-$RuCl_2(N\hat{}P)$ complexes and the corresponding dimers were synthesized and characterized. Their optical and electrochemical properties were measured and are discussed.

In Chapter 4, the quadratic and cubic nonlinear optical properties of organometallic complexes were explored by hyper-Rayleigh scattering (HRS) and frequency-depentdent Z-scan techniques, respectively. The first hyperpolarizabilities of the ruthenium halide and mono-alkynyl complexes described in Chapter 2 were determined by HRS measurements. The second hyperpolarizabilities of some organometallic complexes synthesized by the Humphrey group and the collaborators were measured by the Z-scan technique.

Table of Contents

Abbreviations

$\boldsymbol{\alpha}$	Linear polarizability
β	TPA coefficient
$\boldsymbol{\beta}$	Second-order hyperpolarizability
β_0	Intrinsic hyperpolarizability
$\boldsymbol{\gamma}$	Third-order hyperplarizability
γ_{imag}	Imaginary component of the second hyperplarizablity
γ_{real}	Real component of the second hyperplarizablity
δ	Chemical shift
ε	Extinction coefficient
ε_0	Permittivity of free space
λ	Wavenumber/ wavelength
$\Delta\Phi_0$	On-axis peak nonlinear phase shift with sample at focus
$\Delta T(Z)$	Normalized transmittance of the sample at the position
$\boldsymbol{\mu}$	Dipole moment
$\boldsymbol{\mu_0}$	Static dipole moment
$\boldsymbol{\mu_{eg}}$	Transition dipole moment
$\boldsymbol{\mu_e}$	Excited state dipole moment
$\boldsymbol{\mu_g}$	Ground state dipole moment
σ	Linear absorption cross-section
σ_2	Two-photon absorption cross-section
σ^2	Mean squared error
Γ_L	Third-order susceptibility of solution in EFISH
χ	Susceptibility coefficient
ω	Frequency
A	Ampere
APT	Attached proton test
bpy	2,2'-Bipyridine
^{t}Bu	*tert*-Butyl
^{t}Bu-bpy	4,4'-di-*tert*-butyl-2,2'-bipyridine
C	Coulomb
cm	Centimeter
COSY	Correlation spectroscopy

d	Doublet
D	Electric displacement
$D(\omega)$	Dispersion factor
DπA	Donor-π-acceptor
DC	Direct current
DCM	Dichloromethane
dd	Doublet of doublets
DFWM	Degenerate four-wave mixing
DMA	N,N'-Dimethylacetamide
dppb	1,2-Bis(diphenylphosphino)benzene
dppe	1,2-Bis(diphenylphosphino)ethane
dppf	1,1'-Bis(diphenylphosphino)ferrocene
DTE	Dithienylethene
E	Electric field
$E_{1/2}$	Half-wave potential
EFISH	Electric field induced second harmonic generation
erg	Potential energy
ESI MS	Electrospray ionisation mass spectrometry
esu	Electrostatic unit
Fc	Ferrocene
GM	Goeppert-Mayer Unit
g	Gram
HMBC	Heteronuclear multiple bond correlation
HSQC	Heteronuclear single quantum coherence
HR	High-resolution
HRS	Hyper-Rayleigh scattering
HV	High voltage
i	Electric current
I_0	On-axis peak irradiance at focus
I_ω	Fundamental beam intensity
$I_{2\omega}$	Hyper-Rayleigh scattering intensity
ILCT	Intra-ligand charge transfer
J	Coupling constant
J	Joule

kg	Kilogram
l	Path length of the scattered light
L^A	Electron-acceptor ligand(s)
L^D	Electron-rich ligand(s)
LMCT	Ligand-to-metal charge transfer
m	Meter
m-	*meta*-
m/z	Mass-to-charge ratio
mCPBA	*meta*-Chloroperoxybenzoic acid
MeOH	Methanol
MLCT	Metal-to-ligand charge transfer
mm	Millimeter
n_2	Third-order nonlinear refractive index
N_c	Number density of the chromophore
N_s	Number density of the solvent
ND	Neutral density
NLA	Nonlinear absorption
NLO	Nonlinear optical
NLR	Nonlinear refraction
nm	Nanometer
NMR	Nuclear magnetic resonance
p-	*para*-
$\boldsymbol{P}$	Nonlinear polarization
PMT	Photomultiplier tube
PPh_2py	2-(Diphenylphosphino)pyridine
PPh_2qn	8-(Diphenylphosphino)quinoline
ppm	Parts per million
PyP	1-(2-Diphenylphosphinoethyl)pyrazole
s	Singlet
S	Transmittance of the aperture with on sample
SHG	Second harmonic generation
SI	System international
T_p	Normalized peak transmittance
T_v	Normalized valley transmittance

THF	Tetrahydrofuran
THG	Third harmonic generation
TPA	Two-photon absorption
V	Volt
w_0	Focal spot size
Z_0	Rayleigh range

Chapter 1 - An Introduction to the Nonlinear Optics of Organometallic Complexes

1.1 INTRODUCTION TO NONLINEAR OPTICS

Nonlinear optical (NLO) effects are caused by the interaction of an applied electromagnetic field with molecules or materials, and were first discovered by John Kerr in 1875 [1]. These kinds of optical phenomena are related to the polarizability of a molecule or bulk materials with emission of new electromagnetic fields that differ in physical properties (e.g. frequency, phase) from the incident fields.

Historically, the Kerr effect was the earliest known NLO effect. It is an electro-optic effect [2]. Kerr's experimental set-up consisted of an upright horseshoe electromagnet, a light source and two Nicol prisms. The details can be found in the literature [1]. In Kerr's first attempt, he found that the polarization state of plane-polarized light can be changed when reflected from a magnetic surface. In his second attempt, the reflections from a magnetic 'mirror' with the orientation of the magnetization lying in the plane of the 'mirror' was addressed with the development of the experimental set-up, which gave rise to the quality control of magnetic storage media. Another electro-optic effect called the Pockels effect was discovered in 1906. This is similar to the Kerr effect, but the Pockels effect is proportional to the electric field while the Kerr effect is proportional to the square of the electric field [2, 3]. All-optical NLO effects were not discovered until the advent of the laser. Second-harmonic generation (SHG) was first observed in single-crystal quartz by Franken and coworkers in 1961 [2, 4, 5]. Parametric amplification was observed in $LiNbO_3$ in 1965. Subsequently, more and more NLO effects, *e.g.* two-photon absorption (TPA) [2, 6, 7], degenerate four-wave mixing (DFWM) [2, 8], third-harmonic generation (THG) [2], were discovered [9, 10].

In general, NLO phenomena are characterized as second-order, third-order or higher order in nature. One second-order NLO phenomenon of interest is the electro-optic or Pockels effect. It finds applications in the development of active optical interconnects and switches, which can be used in data processing and communication systems [2, 3]. Third-order effects include the Kerr effect, optical bistability, optical phased conjugation, photorefractivity, and third-harmonic generation (THG) [2]. The ultimate target applications of third-order NLO

phenomena include all-optical computing and signal processing, higher density optical data storage and high-frequency optical communications. The optical limiting process can be employed for the protection of sensors and eyes from laser light [11].

NLO materials should have the ability to interact with electromagnetic fields and responsed via modifications in frequency, phase, amplitude, polarization, path, *etc*. The ideal NLO materials for device application should have not only fast responses and high hyperpolarizabilities, but also necessary secondary properties such as thermal and/or mechanical stability, high transparency, *etc* [11]. So far, a variety of materials have been investigated for their NLO properties. Inorganic salts such as $LiNbO_3$ and KH_2PO_4 or glasses have been intensively studied and are more advanced toward commercial application [12–16]. During the 1980s, organic materials showed potential as a better choice for NLO applications [17]. First of all, compared with the present inorganic materials, lots of organic compounds exhibit extremely high and fast nonlinearities. Their NLO properties can be custom-tailored depending on the desired application, due to the versatility of organic synthesis. Finally, the chromophores can be incorporated into macroscopic structures such as Langmuir-Blodgett films and polymers. The focus of some research shifted to the optimization of thermal and chemical stability and optical loss. Organic materials can be divided into several types: traditional DπA chromophores, octupolar molecules, charged organic compounds, multichromophore systems, other unconventional organic chromophores, and organometallic compounds.

The field of organometallics for nonlinear optics is relatively less explored than organics for nonlinear optics, although organometallic compounds show greater potential in this field [17]. Organometallics show very strong absorption bands *e.g.* metal-to-ligand charge transfer (MLCT), ligand-to-metal charge transfer (LMCT) or intra-ligand charge transfer (ILCT) in the UV-Vis region, which are related to high transition dipole moments and low transition energies. Furthermore, such complexes enjoy higher structural diversity in the metal centers, ligands, coordination pattern, *etc*, while in some cases the involvement of the metal atom improves the stability of the unstable organic fragment.

NLO materials can be classified as second-order, third-order, or higher-order materials. Second-order materials are used in applications at present, while there is still a long way to go to turn third-order materials into real applications since theory and mechanism of processes are not well understood.

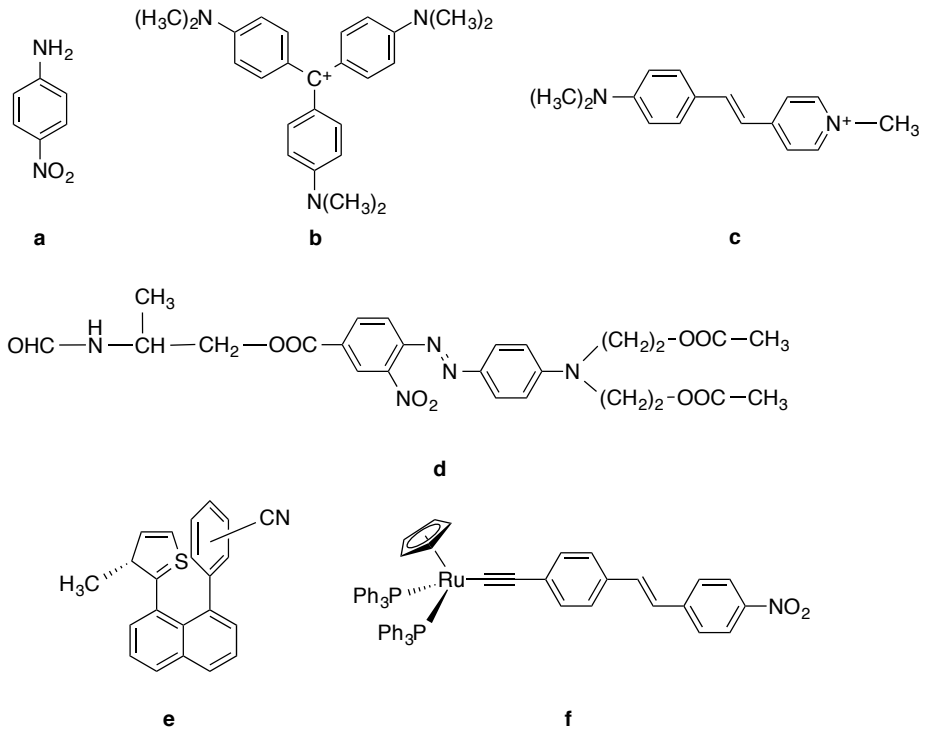

Figure 1.1 Examples of organic materials: **a.** traditional DπA chromophores, **b.** octupolar molecules, **c.** charged organic compounds, **d.** multichromophores, **e.** other unconventional organic chromophore, **f.** organometallic compound.

1.2 BRIEF DESCRIPTION OF NONLINEAR OPTICAL THEORY

Optical nonlinearities are manifested during the interaction of strong electromagnetic fields with matter. A brief theoretical explanation of nonlinear polarizability from both a microscopic and macroscopic view is as follows.

1.2.1 Microscopic view of nonlinear polarizability [2]

Light has an electric field ***E*** that interacts with the charges in materials, distorting the electron density distribution. The first moment of the electron distribution is

called the dipole moment $\boldsymbol{\mu}$, which is the most important quantity with respect to the optical properties. As light travels through a material, its electric field interacts with other electric fields within the material, producing a force. Figure 1.2 exemplifies the instantaneous displacement (polarization). The polarization of the material is assumed to be a linear function of the applied field. However, in reality, the induced polarization produces an internal electric field that can modify the applied field and the secondary polarization. This interrelationship is the origin of the nonlinear polarization $\boldsymbol{P}$.

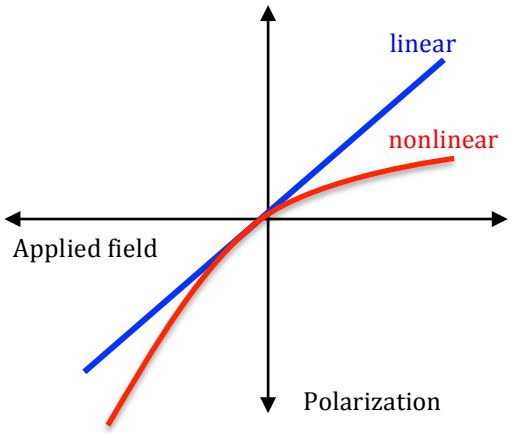

Figure 1.2 Plots of induced polarization vs. applied field for both linear and nonlinear materials.

The application of an electric field associated with a light wave that is a symmetric field to the anharmonic potential leads to an asymmetric polarization response. The polarization wave can be deconvoluted into a DC polarization component and polarization components at the fundamental and second-harmonic frequencies, based on Fourier analysis. The mathematical formula of the nonlinear polarization remains unknown because the NLO process is complex, but a common approximation of polarizability is expansion as a Taylor series:

$$\boldsymbol{\mu} = \boldsymbol{\mu_0} + \boldsymbol{\alpha E} + \boldsymbol{\beta E^2} + \boldsymbol{\gamma E^3} + \ldots \qquad \text{(Equation 1.1)}$$

where $\boldsymbol{\mu_0}$ is the static dipole in the absence of the applied field. The tensorial α, β and γ quantities defined by the equation above are the linear polarizability, the second-order/quadratic hyperpolarizability/first hyperpolarizability, and the third-order/cubic hyperpolarizability/second hyperpolarizability respectively, and they are characteristic properties of a medium that depend on the detailed electronic and molecular structure of the medium. Both $\boldsymbol{\mu}$ and $\boldsymbol{E}$ are vectors. The

equation has limitations. Firstly, it is only an approximation with increasing field strength. Secondly, it is not applicable when the strength of the electric field approaches the strength of the atomic fields than bind electric charges (10^8-10^9 V/cm): fortunately, most nonlinear effects are observed at an electric field of 10^3-10^4 V/cm. Thirdly, the expansion is not valid at or near a resonance frequency. The terms beyond $\alpha\boldsymbol{E}$ are not linear with respect to $\boldsymbol{E}$. Since $\alpha >> \beta, \gamma$, it approximates a linear response at a small field, while nonlinear effects become more significant with increasing field strength.

1.2.2 Macroscopic view of nonlinear polarizability [2]

It is important to understand how the polarizability changes in the evolution from an isolated atom to a molecule, a group of atoms or molecules, an extended array, and ultimately the bulk material. The macroscopic description of nonlinear polarizability in the bulk materials can be expressed by an analogous expression to the equation for the microscopic description, as shown below.

$$\boldsymbol{P}=\varepsilon_0(\chi^{(1)}\boldsymbol{E} + \chi^{(2)}\boldsymbol{E}^2 + \chi^{(3)}\boldsymbol{E}^3 + \ldots) \quad \text{in the MKS system} \quad \text{(Equation 1.2)}$$

$$\boldsymbol{P}= \chi^{(1)}\boldsymbol{E} + \chi^{(2)}\boldsymbol{E}^2 + \chi^{(3)}\boldsymbol{E}^3 + \ldots \quad \text{in the cgs system} \quad \text{(Equation 1.3)}$$

Here, ε_0 denotes the permittivity of free space. Susceptibility coefficients $\chi^{(i)}$ are tensors of order i+1 (*e.g.*, $\chi^{(2)}$ has tensor elements $\chi^{(2)}_{ijk}$).

To some degree, the NLO properties rely on the delocalized electrons of the materials. If the electronic coupling between local clusters of atoms is relatively weak, the macroscopic property can be treated as a sum of the microscopic contributions. For example, the usual way to treat the optical properties of systems containing organic molecules is in terms of the oriented gas model. By following this procedure of transforming tensor properties from one coordinate system to another using matrices of orientational cosines, the macroscopic expressions of the nonlinear susceptibilities are derived. If the coupling is strong, a band structure approach should be used. Nonlocal polarization must be considered in long conjugated chain compounds, semiconductors, or small clusters that are spatially separated, but electronically coupled via resonance tunneling or similar

phenomena. The intermediate situation is of considerable interest since semiconductor clusters have shown unusual NLO behavior. Generally, as polarization dimensions increase, there is a transition from atomic or molecular linear and nonlinear polarizabilities to bulk susceptibilities at some point.

There are several different systems of units used to describe NLO properties [18]. The two most common unit systems are the SI (System International, or MKS) system and Gaussian (or cgs) unit system. The introduction and convertion between the two systems is detailed in the appendix.

1.3 MEASUREMENTS OF NONLINEAR OPTICAL PROPERTIES

Measurements of second- and third-order NLO properties can be performed with a variety of techniques. A short description of the techniques is given in this section; more details can be found in reference [19]. It is worth noting that comparison of measurement results of third-order nonlinearity should be restricted to data from the same laboratory. This is contributed by the use of varying measurement standards and definitions of the measured quantities (e.g., $\chi^{(3)}$) [18-20]. There are several possible different difinitions of $\chi^{(3)}$, and it will be very helpful if well-known standard $\chi^{(3)}$ or γ values used or determined in a given series of experiments (e.g., fused silica or solvents such as chloroform) exist. However, trends observed for the compounds in a single set of experimental results are relatively reliable.

1.3.1 Measurements for Second-order NLO Materials

Many techniques have been developed for measurements of the second-order NLO properties. The specific technique used depends on the form of the material and which kind of method should be adopted in the measurements. For single crystals, the options are varied, such as the phase-matched and parametric fluorescence methods, the powder method and the Maker fringe method. In some cases, the material of interest only exists in the form of thin films. Thin film reflectance and poling (polymer films) are suitable for NLO measurements. The above are all used for assessing bulk materials, but it is sometimes more convenient and appropriate to characterize the individual molecules rather than the bulk materials, especially

for organic materials. Relative methods for such characterization include electric field-induced second-harmonic generation (EFISH), hyper-Rayleigh scattering (HRS) and solvatochromatic measurements.

1.3.1.1 Electric Field-Induced Second-Harmonic Generation

A convenient way of screening a new material is to make it as a solution. The solute molecules with different dipole moments in the solution have very random arrangement. From a macroscopic view, the molecules have no dipole contribution to the whole system, which means there is no macroscopic $\chi^{(2)}$ in the solution. And the solution can be regarded as centrosymmetric. However, due to the instinct dipole moments of the molecules, the symmetry can be broken by applying an external electric field to the solution, since all the solute molecules have the same displacement in this case. This process produces an electric field-induced second-harmonic signal through the molecular second hyperpolarizability γ of the material, and EFISH is a third-order nonlinear process.

In EFISH experiments, the fundamental is polarized along the direction of the applied DC field. The generated second-harmonic will be also polarized along this direction due to the symmetry properties of an isotropic medium. A series of parameters are involved in the calculation. However, the solution dielectric constant ε can be measured using a capacitance bridge; the refractive index n can be obtained by measuring the angular deviation of a laser beam passing through a solution-filled hollow glass prism; Γ_L, the EFISH third-order macroscopic susceptibility of the solution, which is related to the microscopic second hyperpolarizability, is determined by a nearly identical experimental set-up to the wedge Maker-fringe method. The main difference is the details of the EFISH cell. The cell geometry is shown below in Figure 1.3.

The cell consists of two thin glass pieces, cut at small angles and placed together to form a small wedge space for the solution. The solution area is adequately covered by a pair of plane electrodes placed on each side of the wedge windows. High voltage pulses of 1-10 kV are applied to the cell with durations in the range of a few microseconds or milliseconds, which is also used to make sure there is no

current flow in the solution. The second-harmonic pulses are detected with photomultiplier tubes (PMTs), and the signals are averaged in a boxcar integrator. With the acquirement of Γ_L, the pertinent microscopic quantities can be obtained through three equations demonstrated in the literature [6].

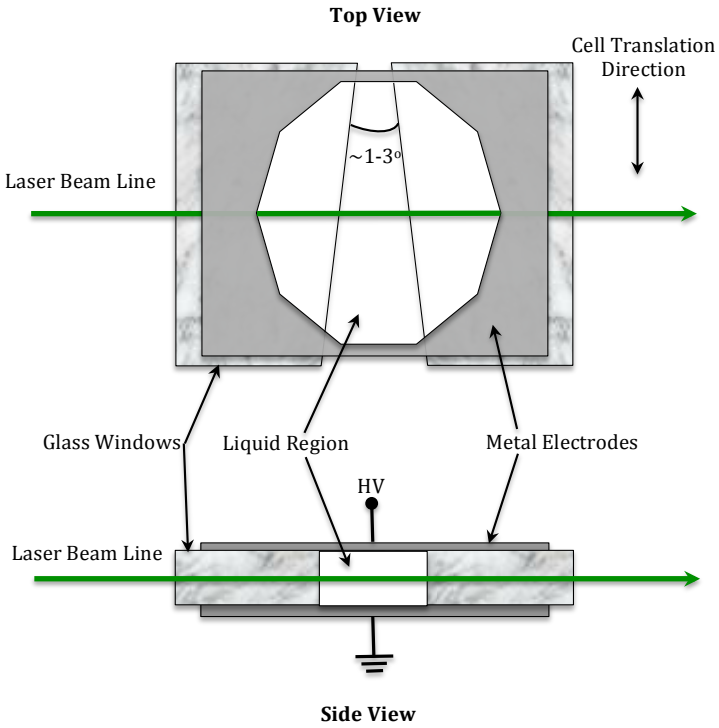

Figure 1.3 Design of an EFISH wedge-shaped liquid cell configured with plane parallel electrodes.

The widely adopted EFISH method has some limitations, although it is well established for characterizing the first hyperpolarizability of organic molecules. First of all, the molecules must possess a permanent dipole moment and must not ionize in solution. It causes some potentially interesting materials to be unable to be analysed. Furthermore, its complexity, such as specialized cells, Maker fringe analysis, *etc.*, makes it challenging for screening some materials.

1.3.1.2 Hyper-Rayleigh Scattering

Hyper-Rayleigh scattering (HRS) offers a method that alleviates some drawbacks of EFISH. Light is scattered at a frequency of 2ω when the sample is irradiated by light at a frequency of ω; this is a parametric frequency conversion process without the involvement of two-photon fluorescence.

The advantages of this technique are obvious. Firstly, it has no DC applied field requirement. Secondly, it offers a way of characterizing the non-vector part of β. Thirdly, it is unnecessary to measure γ or μ, since the second-harmonic scattered light is proportional to β^2. Finally, calibration can be via the internal solvent. Thus, it can be used for nonpolar (*e.g.,* octupolar) and ionic samples with no external field. However, it also has disadvantages. It requires sensitive detection and high fundamental intensity, since the scattered second harmonic is weak. The light intensity should not be so high that it results in self-focusing, stimulated Raman or Brillouin scattering, or even dielectric breakdown in the liquid.

The theory and experimental requirements of HRS will be detailed in Chapter 4 with practical data analysis.

1.3.2 Measurements for Third-order NLO Materials

The third-order susceptibility is an important parameter in nonlinear optics, which leads to a variety of phenomena. Once understood, these phenomena can in turn be used to measure the NLO parameters. The techniques developed include degenerate four-wave mixing, nearly degenerate three-wave mixing, Z-scan, optical Kerr gate and ellipse rotation, interferometric methods, beam self-bending, and third harmonic generation. Some of the popular methods are introduced briefly in this section.

1.3.2.1 Degenerate Four-Wave Mixing

Four-wave mixing refers to the interaction of four waves in a nonlinear medium via the third-order polarization. In this process, three waves out of four are coherent and they are incident on the nonlinear medium. The fourth wave (the phase conjugate) is then generated. This is a widely accepted method for characterizing third-order nonlinear materials using a combination of polarizations for four beams. It can be used for the measurements of isotropic materials.

The theory of degenerate four-wave mixing (DFWM) is very complicated and a detailed explanation can be found in reference [19]. Figure 1.4 shows a typical experimental setup for DFWM illustrating the backward geometry.

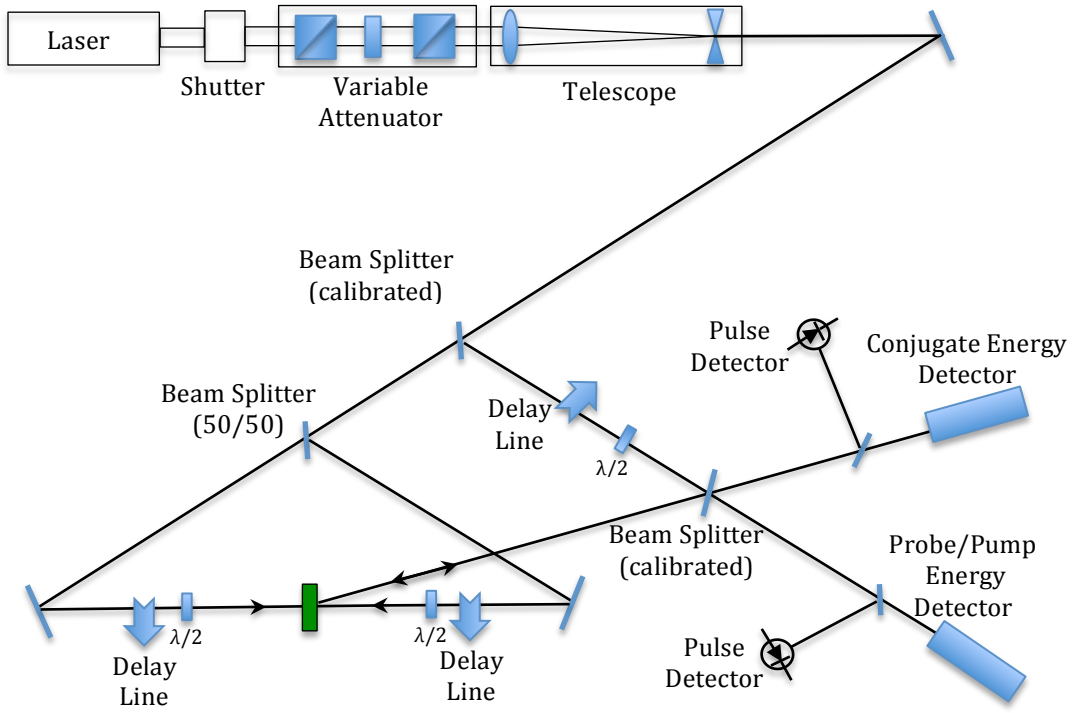

Figure 1.4 Schematic diagram of a DFWM experiment.

All of the interacting beams are derived from the same laser. The path lengths of the beams should not be more than the coherence length of the laser to ensure the beams coherently interact in the sample to generate the phase conjugate beam. Normally the laser is operated at its maximum output to provide a more stable operation. The beam is then attenuated to desired power or energy for the experiment. Telescopes and lenses are used to adjust the beam size for the required range of intensities. The first beam splitter splits the beam into two beams. The smaller fraction is picked off to serve as the probe beam. Most of the beam passing through the splitter is then separated by a 50/50 beam splitter into two beams that are directed by beam steering optics to serve as the counterpropagating pump beams into the sample. The probe beam is directed at a desired angle by the second beam splitter with respect to the forward pump beam into the sample. The second beam splitter also serves to transmit the generated conjugate beam to the corresponding detector. The polarization for each individual beam can be achieved by half-wave plates and/or polarizers. An optical delay line

is set up for time-resolved studies on each beam line. All beam splitters are calibrated to ensure that the energy or power measurements can be translated into the actual beam energy/power used in theoretical analysis.

The technique of DFWM has several advantages. First of all, the phase conjugate beam is distinguished readily by spatial separation from the interacting beams. Secondly, the detected signal is independent from the laser intensity, and can be easily checked for verification. Thirdly, various forms of the samples are acceptable for measurements and all the independent $\chi^{(3)}_{ijkl}$ can be obtained in one single experimental setup for isotropic materials. Finally, the time dependence of the nonlinearity can be studied at the same time. The disadvantages of this technique are obvious. Only the modulus of $\chi^{(3)}$ can be measured, which means the technique needs supplemental measurement to extract the real and imaginary parts of $\chi^{(3)}$. The alignment sensitivity of the three incident beams on the sample is another downside of DFWM.

1.3.2.2 Z-scan

A sensitive self-focusing measurement technique that involves focusing the laser beam through a thin sample and detecting the light transmitted by a small aperture in the far field was developed by Stryland and his coworkers in 1989. Since the sample is scanned along the *z*-direction through the focus of the lens, this measurement technique was named Z-scan.

Compared with DFWM, the simplicity of Z-scan is apparent. As a single-beam technique, there is no difficulty on aligning the beam except keeping the beam centered on the aperture. Furthermore, the data analysis is quick and simple. Most importantly, both the real and imaginary parts of $\chi^{(3)}$ can be obtained through Z-scan measurement. Fourthly, the technique is also of high sensitivity, capable of resolving a phase distortion in samples of high optical quality. Finally, it can be modified to study nonlinearities on different time scales as well as higher-order contributions.

Quite a number of the parameters used in the operation of Z-scan involved in Chapter 4 are closely related to the theory and experimental technique. In order to clearly expain the data obtained from Z-scan measurement, the theory and experimental description of this technique will be detailed in Chapter 4 with practical data analysis, due to the complexity and the strong link between the theoretical and practical measurement.

1.3.2.3 Optical Kerr Gate and Ellipse Rotation

The optical Kerr effect appears in a third-order isotropic medium under polarized optical radiation. The birefringence is induced by the intense light beam and it can lead to two interesting phenomena, induced linear birefringence and ellipse rotation. The two phenomena are collectively regarded as the optical Kerr effect. The goal of the methods discussed in this section is to measure the light intensity passed through a nonlinear material and a final polarizer, which results from a transmitted light of a known polarization state. The nonlinear susceptibility is obtained by inversion of the formulas given in Table 6, Chapter 6 of reference [19]. Although the measurement techniques are straightforward, neither can determine all the tensor components of $\chi^{(3)}$. As a result, optical Kerr gate and ellipse rotation are required to fully characterize the material.

A typical setup for an optical Kerr effect experiment, as shown in Figure 1.5, comprises of two different frequencies, namely the pump and the probe, an attenuator, half-wave plates and polarizers, the analyzer and the detectors. The pump and probe are aligned collinearly through the sample by an appropriate beam splitter; the attenuator controls the incident tunable pump intensity; the desired polarization of each incident beam on the sample is achieved using half-wave plates and polarizers in the pump and probe paths; the analyzer is set to be crossed to the incident probe polarization; three detectors are used for measuring the energies of the pump and the probe and the final transmitted probe energy.

Ellipse rotation is a single-beam experiment technique. The composition of the setup is similar to that of optical Kerr gate. The output beam is directed to another

birefringent element identical to the input birefringent element. In the experiment, the samples are required to have a very small intrinsic birefringence.

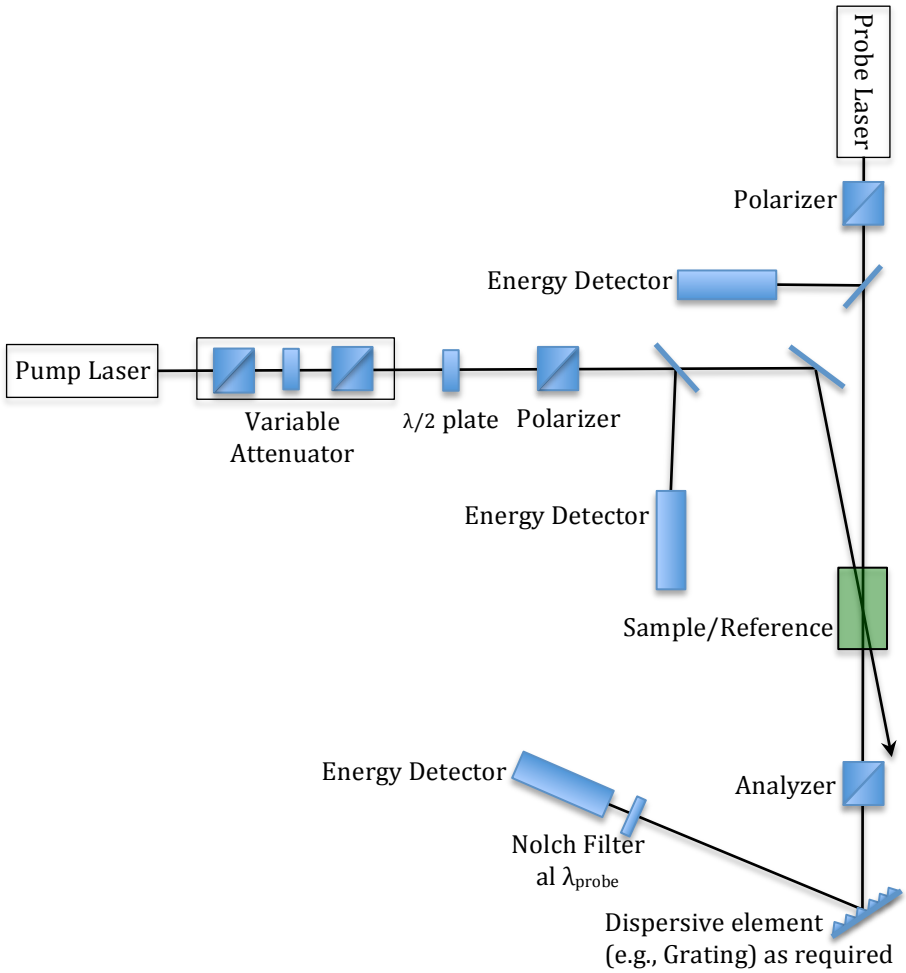

Figure 1.5 Schematic diagram of an optical Kerr gate experiment.

Generally speaking, the simplicity of these experiments is between DFWM and Z-scan. The data analysis is simple, and the experiments are time resolved and invole non-degenerate frequency measurements. Both the real and imaginary parts of $\chi^{(3)}$ can be measured, which is the greatest utility.

1.4 STRUCTURE-PROPERTY RELATIONSHIPS BETWEEN ORGANOMETALLIC COMPLEXES AND NONLINEAR OPTICS

NLO processes are extremely complicated, but what prevents the realization of these technologies is a lack of understanding of structure-property relationships in NLO materials. A bridge between theoretical models for nonlinear polarizability and real NLO materials should be established by chemists [2, 11, 21-27]. The

relationship between the chemical structure of organometallic complexes and the NLO properties will be discussed in this section. However, only metal alkynyl complexes, metallocenyl complexes, and pyridyl-, polypyridyl-complexes are included below since they are closely related to this work.

1.4.1 General Introduction

Investigations on NLO materials were initially focused on purely inorganic and organic systems [21, 28]. The inorganic single crystals (e.g. KH_2PO_4, $LiNbO_3$) have become popular owing to the transparency in the UV region, high structure perfection, and relatively high laser damage threshold. And the bridging hydrogen bonds (such as O-H··· and N-H···O) within KH_2PO_4 crystals were suggested playing a crucial role in optical nonlinearities [29, 30]. Then the inorganic semiconductors, such as gallium arsenide (GaAs) and indium antimonide (InSb), exhibited large response in nonlinear optics [31]. Both of the inorganic salts and semiconductors have been advanced in commercial applications as modulators, Q-switches and harmonic generators of high-powerful lasers *etc.* [32-34]. Later, organic systems were investigated as an alternative to purely inorganic species due to the fast and large nonlinear response, greater synthetic flexibility, intrinsic tailorability [21, 35, 36]. The early-studied organic crystal, urea, has been developed as the reference substance in SHG measurement [37, 38]. The origin of the nonlinearity of the urea crystal is the C-N bond in the conjugated system of bonds $O \Leftarrow C \leftarrow N - H$ [39]. More organic compounds showed excellent NLO response [21]. For example, 2-methyl-4-nitroaniline, exhibited large values of $\chi^{(2)}$ due to the presence of an electron-donating and electron-accepting groups on the benzene ring [40]. A series studies suggested the presence of electron push-pull groups on benzene and stilbene systems was in favor of strong second-order optical nonlinearities. In third-order nonlinearity studies, conjugated organic polymer systems have been of interest, and polydiacetylene is the most significant [41]. The delocalized π-electron backbone is responsible for the NLO activity.

More interest has been shifted to organometallic and coordination compounds. The molecules exhibiting highly active quadratic NLO responses are usually of the

donor-π-bridge-acceptor *(D-π-A)* type. In the case of dipolar organometallic compounds, the metal centres act as donors, as acceptors, or even as the bridge.

The first organometallic compounds in the NLO field to be studied were metal carbonyls [42]. However, the weak quadratic nonlinearities of the metal carbonyls forced researchers to shift the focus to other types of complexes. Metallocene derivatives of higher NLO properties were then reported [43]. The metallocenes interact with a conjugated π-system both through the cyclopentadienyl group and the metal-based orbitals to achieve the coupling of the metal orbital with the π-system, which enables such complexes to possess better NLO performance. Typical examples are ferrocenyl and ruthenocenyl compounds. The third major family that has been investigated as quadratic NLO materials is the metal alkynyl compound class [44]; highlights of this family will be described in Chapter 2.

For cubic NLO active materials, there are no clear structural requirements so far due to the lack of broad wavelength studies, large measurement errors and the low sensitivity of the cubic nonlinearity to the properties of the applied electromagnetic fields [6, 45, 46]. Metallocenes were the first organometallic compounds measured for cubic NLO study, but metal alkynyl complexes have now attracted the most extensive investigation among the organometallics.

1.4.2 Modification of π-delocalizable systems

An advantage of organometallic compounds as potential NLO materials is the great potential for structural modification to tune the electron distribution that is closely associated with the NLO effects.

The π-conjugated systems can be modified by increasing the π-bridge length. This modification is effective in improving the NLO properties for both quadratic and cubic NLO materials. An excellent example for quadratic nonlinearity is shown in Figure 1.6 [6, 47, 48]. In these complexes, the metal atom serves as the donor group connected by a π-linker. The insertion of a 4-C_6H_4-(*E*)-CH=CH group results in an impressive six-fold increase in the quadratic hyperpolarizability. An example for cubic nonlinearity is shown in Figure 1.7 [49]. The hexyloxy groups aim to improve

the solubility of the molecule for NLO characterization. With the increase of the number of phenyl rings, the values of γ and σ_2 indeed increase as expected, but the increase is not significant after three phenyl rings, which may be due to out-of-plane rotation.

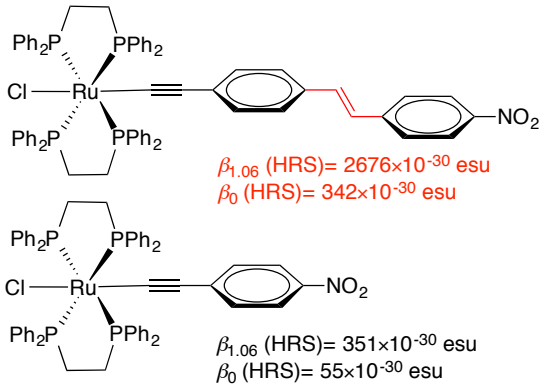

Figure 1.6 Example of the effect of extending π-bridge length on quadratic nonlinearity.

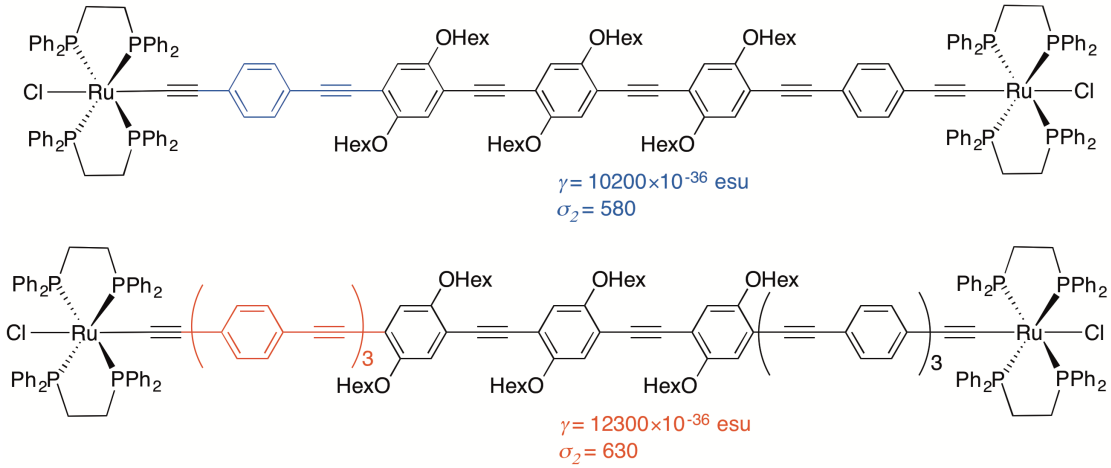

Figure 1.7 Example of the effect of extending π-bridge length on cubic nonlinearity.

The *D*-π-*A* type is the basic structural model for quadratic NLO nonlinearity; when the push-pull process is enhanced, the second-order response may increase. As is shown in Figure 1.8, the asymmetric porphyrins on the left show relatively low second-order response, $\beta_{1.06}$ (HRS) = 118 and 92 × 10^{-30} esu [50, 51]. When the push-pull process is enhanced by changing the position of the nitro group, the response increases to 1501 and 4933 × 10^{-30} esu, respectively, for which a strong coupling between the donor and acceptor substituents occurs. The electron withdrawing ability of the nitro group is much improved in the new structure of the molecules.

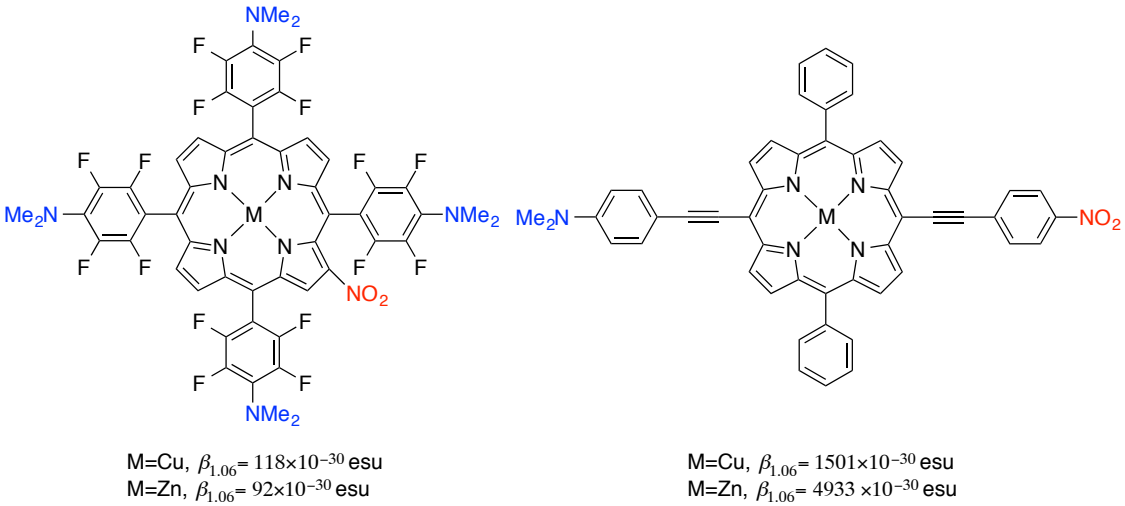

Figure 1.8 Example of enhancing the push-pull process for the quadratic nonlinearity.

A study from Thompson and co-workers [52] revealed that a change in position of the alkene substituents on the benzene ring from *m*- to *p*- can result in a great increase of the third-order susceptibility. In the *p*-Zr dimer, shown in Figure 1.9, the π-conjugated bridge allows for easier movement of electrons, which reduces the energy of transition between the ground and excited states.

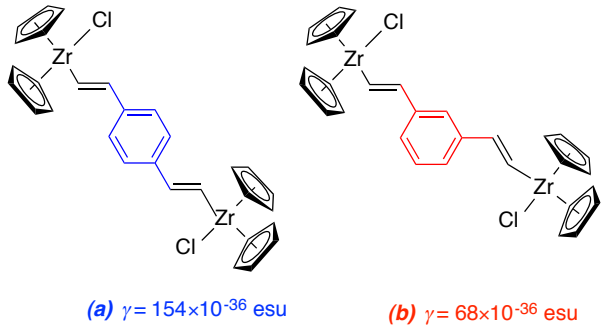

Figure 1.9 (a) *para*-Zr dimer, (b) *meta*-Zr dimer.

1.4.3 Modification of metal centre and co-ligands

Electronic tuning of organometallic compounds can involve changing the metal centre itself. The larger the metal atom is, the more dispersed the electron density is, which may result in a more polarizable metal centre. With this in mind, complexes that differ in their metal atoms (from the same group of the periodic table) have been studied [44, 53-55]. For alkynyl complexes of Fe, Ru and Os, there is a clear trend that the quadratic nonlinearity β increases in the order Fe < Ru < Os. On the other hand, no obvious trend could be seen for the cubic nonlinearity. Another example is shown in Figure 1.10. In these alkynyl organometallic complexes, the NLO responses vary with different ligated metal centres. The trend is Au < Ni < Ru

for the second-order hyperpolarizability, while it is Au < Ni < Ru for the third-order hyperpolarizability.

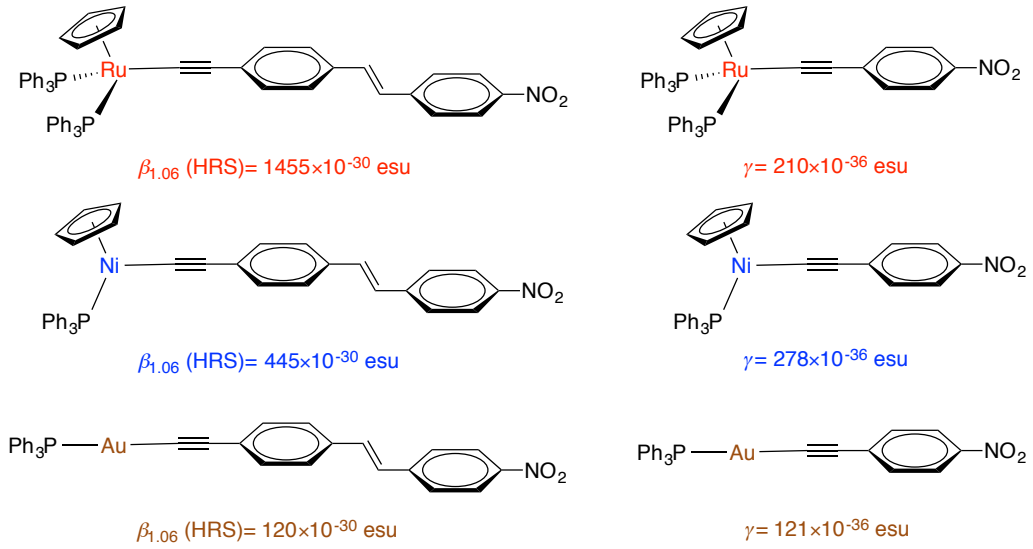

Figure 1.10 Examples of different metal atoms for both quadratic and cubic nonlinearity.

The ligands around the metal atoms have different affinities for withdrawing or donating electrons. So a change of the ligand set can induce a change of NLO behavior. As shown in Figure 1.11, the ligand PMe_3 is more electron donating than PPh_3 and the γ value is correspondingly larger.

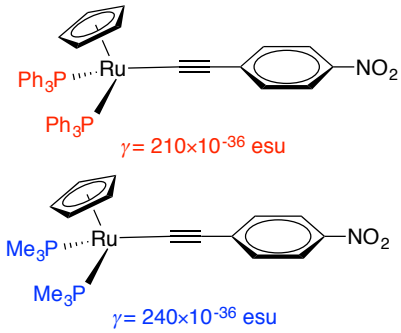

Figure 1.11 The influence on cubic nonlinearity resulting from different donating ligands.

The ligands can be either monodentate or polydentate. Nonchelated pyridyl and chelated bipyridyl complexes were synthesized and their second-order hyperpolarizabilities compared [56]; the β value of the former is relatively large compared to the latter. This can be attributed to a larger π-delocalization in the molecule of the latter which may decrease the strength of MLCT.

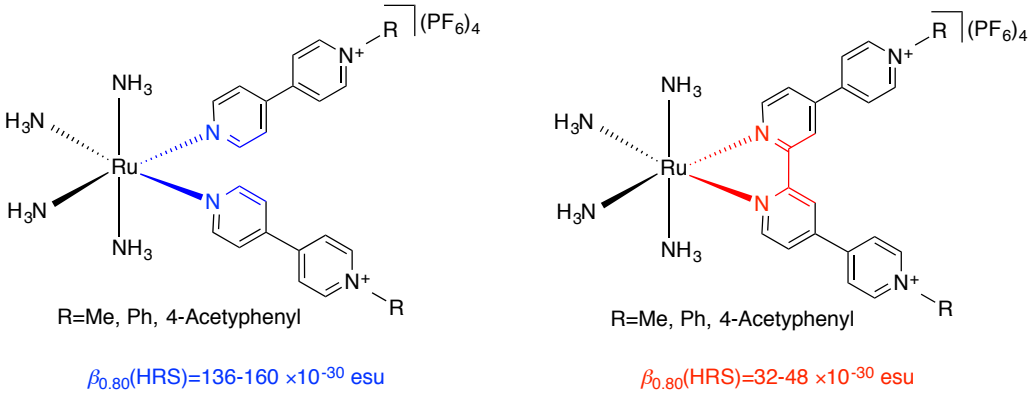

$\beta_{0.80}$(HRS)=136-160 ×10^{-30} esu

$\beta_{0.80}$(HRS)=32-48 ×10^{-30} esu

Figure 1.12 The influence on quadratic nonlinearity of chelated and nonchelated ligands.

1.4.4 Dentritic effect

A newly explored structural modification of organometallic complexes is hyperbranching in dendrimers [57, 58]. The two charged NLO chromophores developed by Le Bozec and coworkers are shown in Figure 1.13. The zero-generation dendrimer exhibits a $\beta_{1.91}$(HRS) value of 380 × 10^{-30} esu in CH_2Cl_2. Which increases to 1900 × 10^{-30} esu on proceeding to the first-generation dendrimer [59-62]. A second example of a dendritic effect is shown in Figure 1.14 [57, 58]. It can be concluded from two aspects that he dentritic effect is beneficial to the NLO properties. On one hand, the more ruthenium centres the molecule has, the better NLO response it may have. On the other hand, the dramatically large π-conjugated chain/area is significantly helpful on improving the NLO performance.

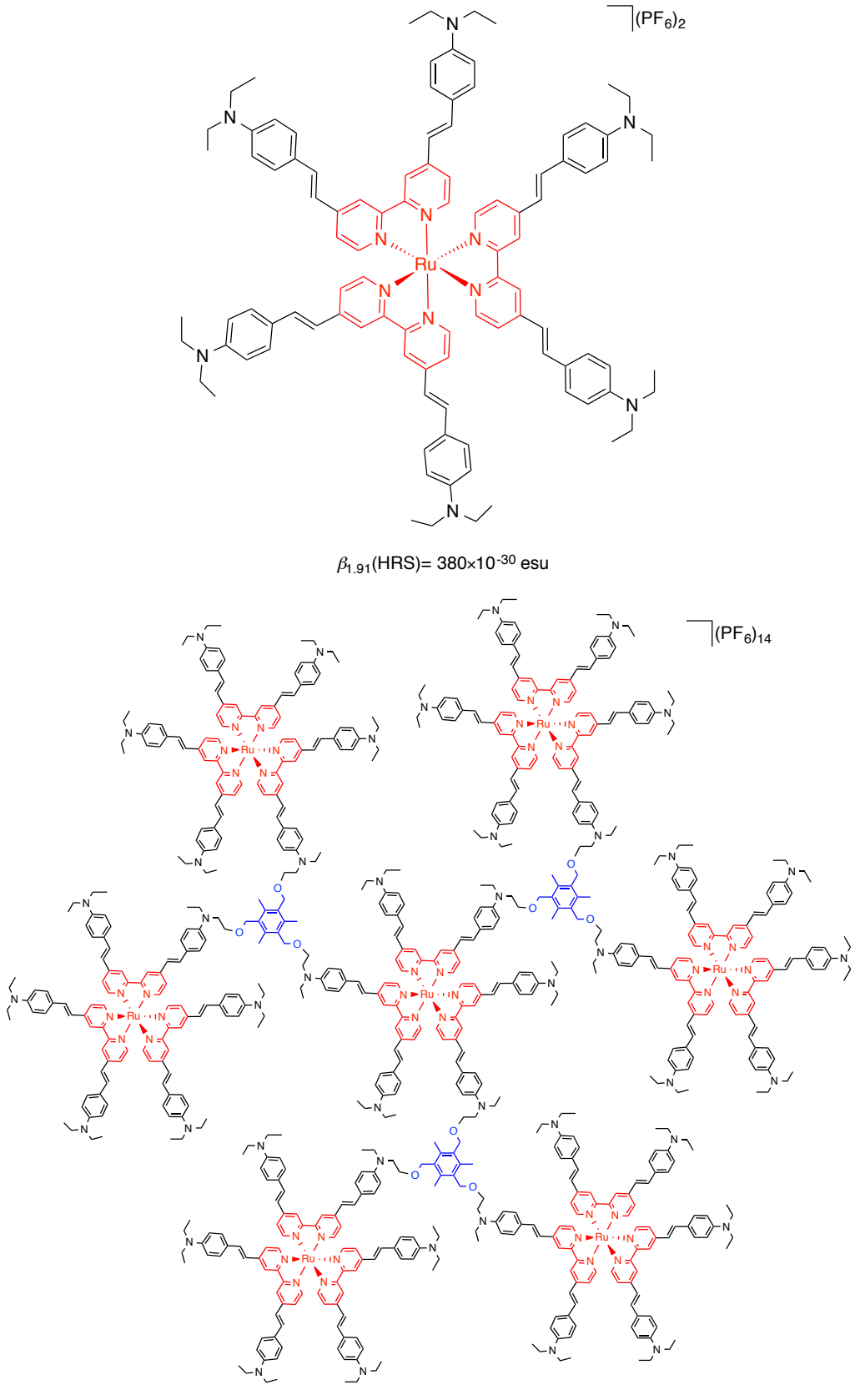

Figure 1.13 The dendritic effect on quadratic nonlinearity.

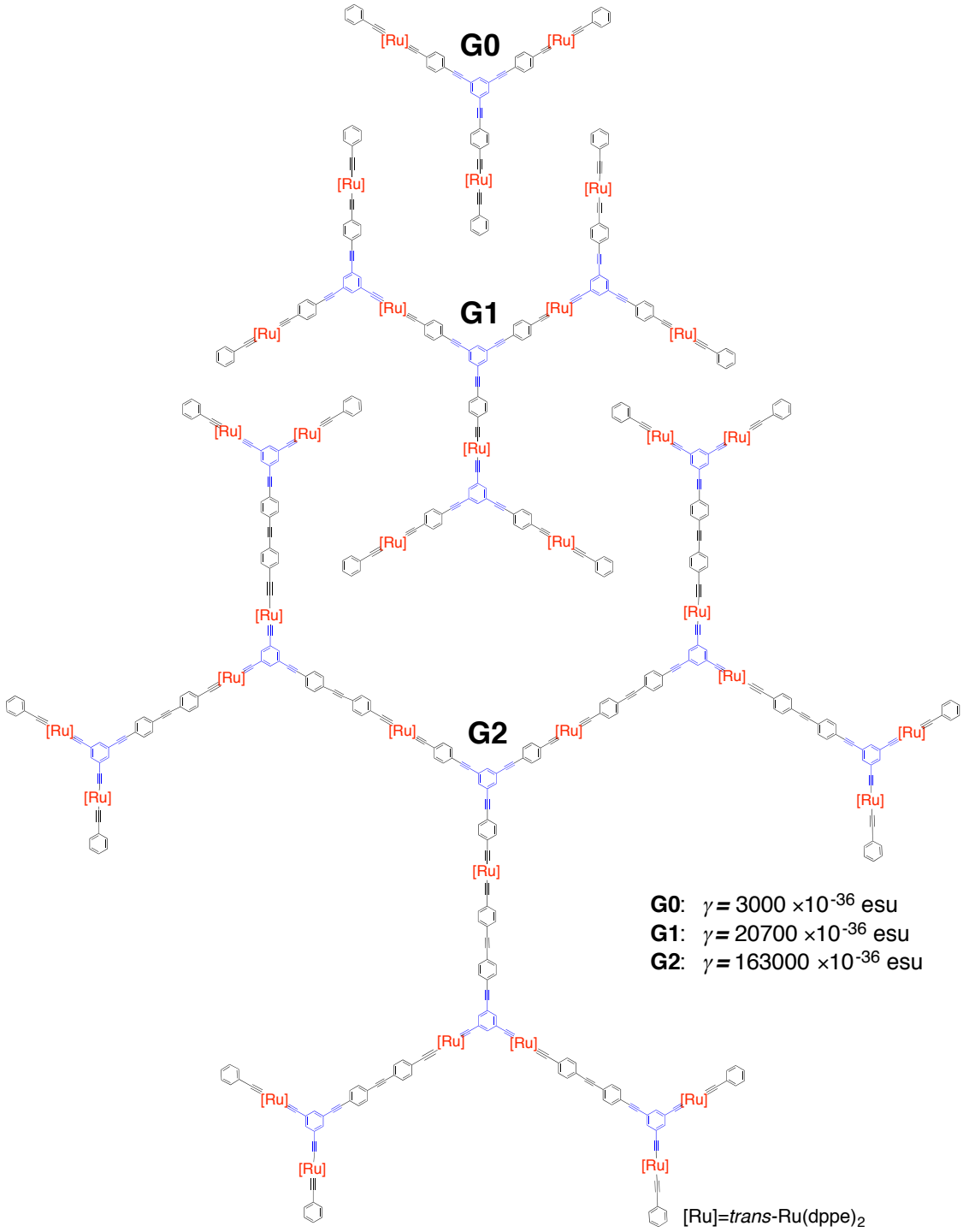

Figure 1.14 The dendritic effect on cubic nonlinearity.

1.5 CONCLUSION

Since the discovery of nonlinear effects, both the theory and measurement techniques have been developed significantly, especially since the invention of the laser. However, due to the extreme complexity of nonlinear optics, there is still a great gap between the theoretical models and real materials. A lot of effort from

chemists has been poured into this field. However, structure-NLO property relationships for organometallics as well as their NLO mechanisms are far less explored than those of organic molecules and inorganic salts. The greater flexibility and exceptionally large NLO responses of organometallic compounds attracts chemists to this field. The most intensive studies of organometallics have focused on ferrocenyl and metal alkynyl compounds, especially ruthenium complexes. In this work, the donor sets of the ruthenium complexes were modified from the most investigated $(P\hat{}P)_2$ to $(N\hat{}N)(P\hat{}P)$ and $(N\hat{}P)_2$ and a series of ruthenium alkynyl complexes were synthesized. Specifically, ruthenium alkynyl complexes with a $(N\hat{}N)(P\hat{}P)$ donor set are described in Chapter 2 in detail and those with a $(N\hat{}P)_2$ donor set are discussed in Chapter 3. A series of NLO studies are summarized in Chapter 4.

1.6 REFERENCE

1. Weinberger, P., *Phil. Mag. Lett.,* **2008**, 1.
2. Marder, S.; Sohn, J.; Stucky, G.; Eds, *Materials for Nonlinear Optics, Chemical Perspectives.* American Chemical Society: Washington DC, **1991**.
3. Stegeman, G. I., *NATO ASI Ser., Ser. B*, **1998**, 369, 1.
4. Franken, P. A.; Hill, A. E.; Peters, C. W.; Weinreich, G., *Phys. Rev. Lett.,* **1961**, 7, 118.
5. Long, N., *Angew. Chem. Int. Ed.,* **1995**, 34, 21.
6. Morrall, J. P.; Dalton, G. T.; Humphrey, M. G.; Samoc, M., *Adv. Organomet. Chem.*, **2007**, 55, 61.
7. Marder, S. R., *Chem. Commun.,* **2006**, 131.
8. Strohkendl, F.; Dalton, L. R.; Hellwarth, R. W.; Sarkas, H. W.; Kafaafi, Z. H., *J. Opt. Soc. Am. B*, **1997**, 14, 92.
9. Samoc, M.; Morrall, J. P.; Dalton, G. T.; Cifuentes, M. P.; Humphrey, M. G., *Angew. Chem. Int. Ed.,* **2007**, 46, 731.
10. He, G.; Tan, L.; Zheng, Q.; Prasad, P. N., *Chem. Rev.*, **2008**, 108, 1245.
11. Karna, S. P.; Yeates, A. T., *Nonlinear Optical Materials Theory and Modeling*. American Chemical Society: Washington DC, **1996**.
12. Wickleder, M. S., *Chem. Rev.,* **2002**, 102, 2011.
13. Becker, P., *Adv. Mater.*, **1998**, 10, 979.

14. Chen, C.; Wang, Y.; Wu, B.; Wu, K.; Zeng, W.; Yu, L., *Nature*, **1995**, 373, 322.
15. Boyd, C. D.; Buehler, E.; Storz, F. G., *Appl. Phys. Lett.,* **1971**, 18, 301.
16. Pritula, I. M.; Kostenyukova, E. I.; Bezkrovnaya, O. N.; Kolybaeva, M. I.; Sofronov, D. S.; Dolzhenkova, E. F.; Kanaev, A.; Tsurikov, V., *Opt. Mater.,* **2016**, 57, 217.
17. Verbiest, T.; Houbrechts, S.; Kauranen, M.; Clays, K.; Persoons, A., *J. Mater. Chem.,* **1997**, 7, 2175.
18. Boyd R.W., *Nonlinear Optics*, Academic Press: Boston, **2008**.
19. Sutherland, R. L., *Handbook of Nonlinear Optics*, Marcel Dekker Inc.: New York, **1996**.
20. Whittall, I. R.; McDonagh, A. M.; Humphrey, M. G., *Adv. Organomet. Chem.,* **1998**, 42, 291.
21. Long, N. J., *Angew. Chem. Int. Ed. Engl.,* **1995**, 34, 21.
22. Liu, J.; Gao, W.; Kityk, I.; Liu, X.; Zhen, Z., *Dyes and pigments*, **2015**, 122, 74.
23. Andrews, J. H.; Guzan, K. A., *Encyclopedia of Polymer Science and Technology (4th Edition*), **2014**, 9, 123.
24. Zhong, R.; Xu, H.; Li, Z.; Su, Z., *J. Phys. Chem. Lett.,* **2015**, 6, 612.
25. Nayar, C. R.; Ravikumar, R., *J. Coord. Chem.,* **2014**, 67, 1.
26. Suresh, S.; Arivuoli, D., *Rev. Adv. Mater. Sci*., **2012**, 30, 243.
27. Mitsopoulou, C. A., *Coord. Chem. Rev.*, **2010**, 254, 1448.
28. Boyd, G. D.; Miller, R. C.; Nassau, K.; Bond, W. L., *Appl. Phys. Lett.*, **1964**, 5, 234.
29. Xue, D.; Zhang, S., *J. Phys. Chem.,* **1996**, 57, 1321.
30. Xue, D.; Zhang, S., *Chem. Phys. Lett.,* **1999**, 301, 449.
31. Ashkin, A.; Boyd, G. D.; Dziezik, J. M.; Smith, R. G.; Ballman, A. A.; Nassan, K., *Appl. Phys. Lett.,* **1966**, 9, 72.
32. Glass, A. M., *MRS Bull.*, **1988**, 13, 16.
33. Fan, Y.; Eckhardt, R. C.; Byer, R. L.; Route, R. K.; Fiegelson, R. S., *Appl. Phys. Lett.,* **1984**, 45, 313.
34. Zaitseva, N.; Carmen, L. J., *Prog. Cryst. Growth Charact. Mater.*, **2001**, 43, 1.
35. Baumert, J. C.; Twieg, R. J.; Bjorklund, G. C.; Logan, J. A.; Dirk, C. W., *Appl. Phys. Let.,* **1987**, 51, 1484.
36. Dehu, C.; Meyers, F.; Bredas, J. L., *J. Am. Chem. Soc.,* **1993**, 115, 6198.
37. Ishida, T.; Osaka, H.; Nogami, T.; Yamazaki, R.; Yasui, M.; Iwasaki, F., *Synthetic Met.,* **1993**, 55, 2013.

38. Perrin, M.; Thozet, A.; Lecocq, S.; Perrin, R.; Lamartine, R., *New Opt. Mater.,* **1983**, 0400, 176.
39. Xue, D.; Zhang, S., *J. Phys. Chem. A,* **1997**, 101, 5547.
40. Levine, B. F.; Bethea, C. G.; Thurmond, C. D.; Lyneh, R. T.; Bernstein, J. L., *J. Appl. Phys.*, **1979**, 50, 2523.
41. Sauteret, C.; Hermann, J. P.; Frey, R.; Pradere, F.; Ducuing, J.; Baughman, L. H.; Chance, R. R., *Phys. Rev. Lett.,* **1976**, 36, 956.
42. Roth, G.; Fischer, H.; Meyer-Friedrichsen, T.; Heck, J.; Houbrechts, S.; Persoons, A., *Organometallics*, **1998**, 17, 1511.
43. Barlow, S.; Marder, S. R., *Chem. Commun*., **2000**, 1555.
44. Hurst, S.; Cifuentes, M. P.; Morrall, J. P.; Lucas, N. T.; Whittall, I. R.; Humphrey, M. G.; Asselberghs, I.; Persoons, A.; Samoc, M.; Luther-Davies, B.; Willis, A. C., *Organometallics*, **2001**, 20, 4664.
45. Samoc, M.; Morrall, J. P.; Dalton, G. T.; Cifuentes, M. P.; Humphrey, M. G., *Angew. Chem. Int. Ed*., **2007**, 46, 731.
46. Humphrey, M. G.; Cifuentes, M. P.; Samoc, M., *Top. Organomet. Chem*., **2010**, 28, 57.
47. Powell C. E.; Humphrey, M. G., *Coord. Chem. Rev*., **2004**, 248, 725.
48. Cifuentes, M. P.; Humphrey, M. G*., J. Organomet. Chem*., **2004**, 689, 3968.
49. Dalton, G. T.; Cifuentes, M. P.; Watson, L. A.; Petrie, S.; Stranger, R.; Samoc, M.; Humphrey, M. G., *Inorg. Chem*., **2009**, 48, 6534.
50. Sen, A.; Ray, P. C.; Das, K.; Krishnan, V., *J. Phys. Chem*., **1996**, 100, 19611.
51. LeCours, S. M.; Guan, H. W.; DiWagno, S. G.; Therien, M. J., *J. Am. Chem. Soc.*, **1996**, 118, 1497.
52. Myers, L. K.; Ho, D. M.; Thompson, M. E.; Langhoff, C., *Polyhedron,* **1995**, 14, 57.
53. Hurst, S.; Humphrey, M. G.; Isoshima, T.; Wostyn, K.; Asselberghs, I.; Clays, K.; Persoons, A.; Samoc, M.; Luther-Davies, B., *Organometallics*, **2002**, 21, 2024.
54. Whittall, I. R.; Cifuentes, M. P.; Humphrey, M. G., *Organometallics,* **1997**, 16, 2631.
55. Garcia, M. H.; Robalo, M. P.; Dias, A. R.; Duarte, T.; Wenseleers, W.; Aerts, G.; Goovaerts, E.; Cifuentes, M. P.; Hurst, S.; Humphrey, M. G.; Samoc, M.; Luther-Davies, B., *Organometallics*, **2002**, 21, 2107.
56. Coe, B. J.; Harris, J. A.; Jones, L. A.; Brunschwig, B. S.; Song, K.; Clays, K.; Garin J.; Orduna, J.; Coles, S. J.; Hursthouse, M. B., *J. Am. Chem. Soc*., **2005**, 127, 4845.

57. McDonagh, A. M.; Humphrey, M. G.; Samoc, M.; Luther-Davies, B., *Organometallics*, **1999**, 18, 5195.

58. Green, K. A.; Simpson, P. V.; Corkery, T. C.; Cifuentes, M. P.; Samoc, M.; Humphrey, M. G., *Macromol. Rapid Commun.*, **2012**, 33, 573.

59. Le Bouder, T.; Maury, O. Le Bozec, H.; Ledoux, I.; Zyss, J., *Chem. Commun.*, **2001**, 2430.

60. Le Bozec, H.; Le Bouder, T.; Maury, O.; Bondon, A.; Ledoux, I.; Deveau, S.; Zyss, J., *Adv. Mater.*, **2001**, 13, 1677.

61. Le Bozec, H.; Le Bouder, T.; Maury, O.; Ledoux, I.; Zyss, J., *J. Opt. A Pure Appl. Opt. 4*, **2002**, S189.

62. Le Bouder, T.; Maury, O.; Bondon, A.; Costuas, K.; Amouyal, E.; Ledoux, I.; Zyss, J., *J. Am. Chem. Soc.*, **2003**, 125, 12284.

Chapter 2 – Synthesis and Characterization of Ruthenium Complexes with (N^N)(P^P) Donor Sets

2.1 INTRODUCTION

2.1.1 Common ligand sets of ruthenium complexes for NLO studies

Modification of the coordinated co-ligands in organometallic complexes can introduce new electronic charge-transfer transitions between the metal atoms and the ligands, and sometimes change the oxidation state of the metal centers, which in turn can influence the NLO merit [1-5]. Some ligand sets have been intensively studied due to the excellent NLO response when they are coordinated to ruthenium atoms.

Ruthenium Ammine Complexes

NLO studies of ruthenium ammine complexes were mainly undertaken by Coe and coworkers [6-11]. The early complexes with the composition *trans*-$[Ru(NH_3)_4(L^D)]^{2+}$ (L^D = an electron-rich ligand), as shown in Figure 2.1, are electron-rich and air-stable in the Ru^{II} forms. The combination with an electron-acceptor ligand (L^A) gives rise to species with significant quadratic NLO response. Later, two-dimensional systems were developed: (1) the *cis*-$[Ru(NH_3)_4]^{2+}$ centre in combination with two L^A ligands resulted in two-dimensional systems, and the presence of the L^A ligands afforded complexes with multiple MLCT bands, the energies of which can be tuned by modifying the substituents of the L^A ligands; the NLO merits can be increased by extending the π-conjugation of the L^A ligands; (2) a two-dimensional system was also achieved by pyrazinyl-centred (L^A) Ru^{II} ammine complexes. The visible MLCT absorption gains in intensity on increasing the number of metal atoms, but the energy remains constant.

Ruthenium η^5-Cyclopentadienyl Complexes

Since the report by Green *et al.* [12] revealing good SHG efficiencies for ferrocenyl derivatives, the interest in organometallics for developing new NLO materials has increased considerably. Ruthenium η^5-cyclopentadienyl half-sandwich complexes exhibit excellent NLO response [4, 13-19], leading to higher β values than compounds with the usual organic donor groups (NR_2, NH_2, *etc.*). Some typical chemical

structures of this type are shown in Figure 2.1. They are strongly asymmetric systems obtained by combining a π-conjugated chain with electron donor and/or acceptor groups. The metal centres can behave as either donor or acceptor group by simply varying the metal oxidation state.

Ruthenium Diimine Complexes

Octupolar molecules have zero net ground-state dipole moments, but substantial NLO response can be generated by large dipole moment change, accompanying intra-ligand charge transfer (ILCT) excitations. The first such transition metal complex for NLO studies was $[Ru(bpy)_3]^{2+}$ in D_3 symmetry, reported by Zyss and his coworkers [20] in 1993. The metal centre is engaged in σ-bonding with the bipyridine ligand, which results in low energy MLCT, and hence the molecule is promising for NLO applications. Following this work, a vast field of research based on Ru^{II} and polypyridyl ligands, specifically Ru^{II} tris-chelate bipyridine complexes as shown in Figure 2.1, with applications ranging from anti-tumoral activity [21] to optical properties [22-29], was gradually developed.

The ruthenium 4,4'-disubstituted-2,2'-bipyridine complexes have synthetic flexibility that allows fine-tuning of the optical properties by simple modification of the π-conjugated backbone [30]. The substituted derivatives can be electron-donating (*e.g.* styryl) groups [23-26] or electron-withdrawing (*e.g.* pyridinium) groups [27, 28]. The dithienylethene (DTE) group can be used to control donor-acceptor interactions in Ru^{II} tris-chelate bipyridine complexs, and has been used in switches [29]. The ruthenium tris(bipyridine) core can be incorporated in a dendritic structure [25, 26], exhibiting excellent quadratic NLO performance.

Ruthenium Bidentate Diphosphine Complexes

1,2-Bis(diphenylphosphino)ethane and bis(diphenylphosphino)methane (dppe and dppm, respectively) are widely investigated electron donating and bidentate diphosphine ligands for NLO studies [31-40]. The ruthenium σ-alkynyl complexes with (P^P) donor sets, as shown in Figure 2.1, are the most favourable class of second-order NLO chromophores, mainly developed by Humphrey and his

coworkers [32-38]. In such complexes, the almost linear M-C≡C-R structures allow good coupling between the metal d-orbitals and the π^* system of the σ-alkynyl bridge, resulting in strong low-energy MLCT excitations to enhance the NLO properties. Based on the Ru(C≡CR)(P^P)$_2$ structure, various organometallic complexes exhibiting excellent NLO response were developed, *e.g.* a cubic NLO switch with a DTE bridge [32], Ru alkynyl dendritic species [33-37], heterobimetallic complexes [38-40], *etc.*.

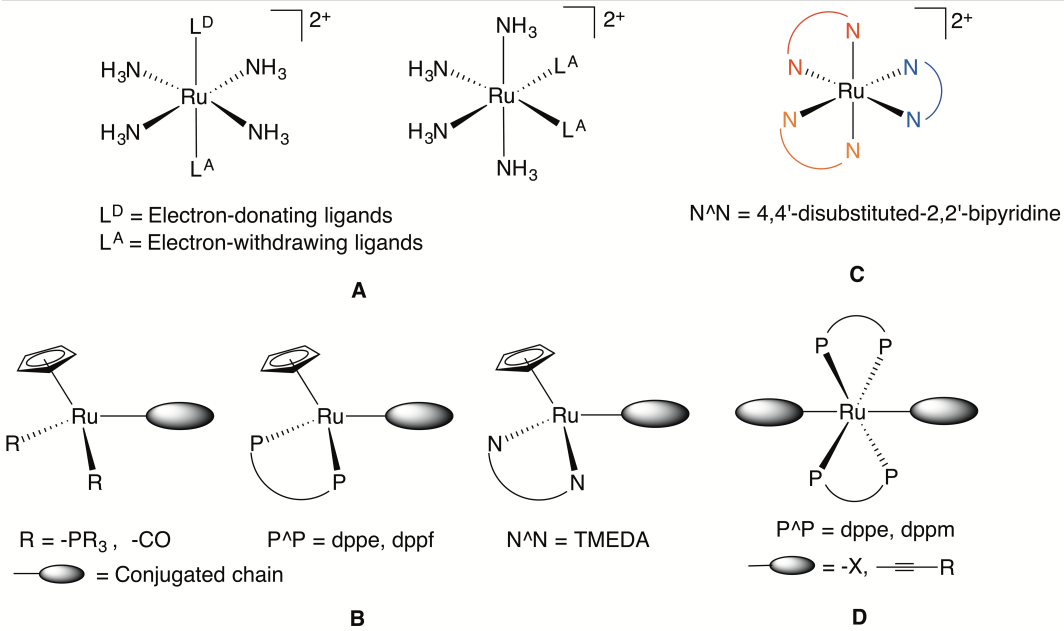

Figure 2.1. Ruthenium ammine complexes (**A**), typical ruthenium η^5-cyclopentadienyl complexes (**B**), ruthenium(II) tris-chelate N^N complexes (**C**) and ruthenium(II) (P^P)$_2$ complexes (**D**) for NLO studies.

2.1.2 Alkynyl ruthenium complexes

The study of transition metal σ-alkynyl complexes has been an intense area of research since the mid-1980's [41]. The carbon-rich "rigid-rod" alkynyl species have promising electronic and structural properties including NLO effects [42-43], luminescence and photoconductivity [44-45] and electronic communication [46].

Group 8 metal alkynyl complexes, especially the ruthenium complexes, are one of the most promising classes of organometallic complexes with regard to their NLO merits [32-38]. This is in part due to their ease of preparation and high stability. More importantly, σ-alkynyl complexes have significant π-electron conjugation in a linear structure. The NLO response can be enhanced by optimizing the π-

conjugated system. The alkynyl ligand and the auxiliary ligands share a role in determining the ease of oxidation at the metal centre, which is another important factor impacting the NLO merit.

2.1.3 Ligand options

Changing the co-ligands in organometallic systems has been shown to influence NLO merit. The aim of the research described in this Chapter is to investigate the effect on reactivity and properties resulting from changing the donor set around the ruthenium atom from $(P\hat{}P)_2$ to $(N\hat{}N)(P\hat{}P)$.

4,4'-Disubstituted-2,2'-bipyridines are diimine (N^N) ligands with synthetic flexibility, allowing fine tuning of the optical properties by modification of the π-conjugated backbone [30]; they are excellent building blocks for the construction of either octahedral [22] or pseudo-tetrahedral octupolar complexes [47]. In these complexes, the metal atom may play two important roles: 1) as a powerful template to gather ligands in the octupolar arrangement, and 2) as a Lewis acid to induce strong ILCT transitions. 4,4'-Di-*tert*-butyl-2,2'-bipyridine (^{t}Bu-bpy) was selected as the diimine ligand, because the ^{t}Bu- group improves the solubility of the ruthenium complexes.

For diphosphine (P^P) ligand options, three candidate bidentate ligands were considered: dppe, dppb and dppf. In order to make a comparison with previous studies, the dppe ligand, having an extensive background in coordination chemistry, is an excellent choice. The dppb ligand has two types of aromatic groups attached to the phosphorus atoms: the bridging *o*-phenylene group and phenyl groups, and from the structural perspective it is expected to have a smaller bite when chelating with metal atoms due to the rigid backbone. There are also some reports of phosphorescence from transition metal complexes bearing the dppb ligand [48-50]. The dppf ligand, acting mainly as a κ^2-mode diphosphine ligand despite high coordinative versatility [51], is a well-known ferrocene-based molecule. The ferrocene group is a well-documented redox-active centre [52-53], and a promising approach to construct active molecular circuits is to develop ferrocene-based systems. Thus far, several multistate redox-active architectures

containing the ferrocene group have been synthesized [54-55], and the dppf ligand has been employed in multistate switching molecules with a combination of $Ru^{II/III}$ and $Fe^{II/III}$ redox-active centres for NLO, as shown in Figure 2.2.

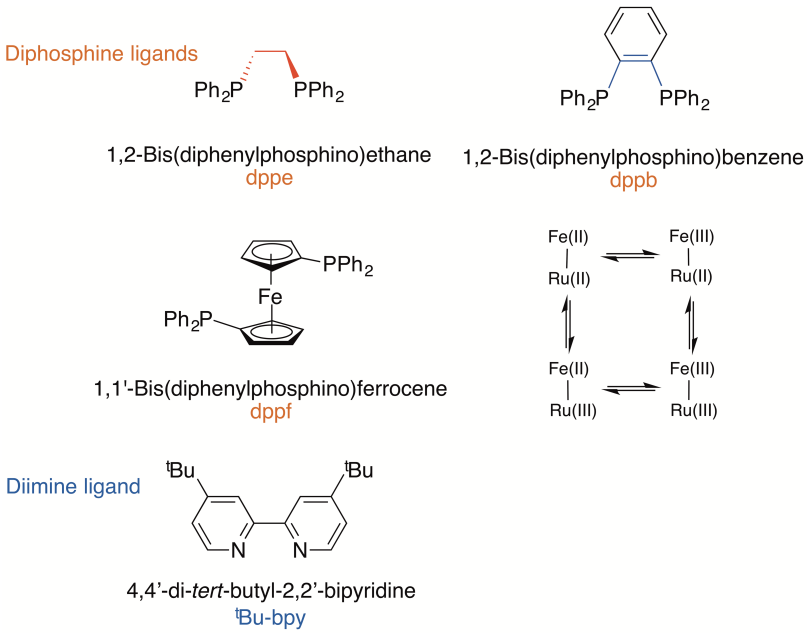

Figure 2.2. Chemical structures of selected ligands for Ru(N^N)(P^P) complexes.

2.1.4 Conclusion

To our knowledge, there is no report of ruthenium complexes bearing a diimine-diphosphine donor set for NLO study. A series of Ru(N^N)(P^P) complexes have therefore been synthesized and characterized in this Chapter. Three bidentate diphosphine ligands (dppe, dppb and dppf) and one diimine ligand (^{t}Bu-bpy) were used in this study.

2.2 SYNTHESIS AND CHARACTERIZATION

2.2.1 Synthesis of $RuCl_2$(N^N)(P^P)

The synthesis of $RuCl_2$(N^N)(P^P) complexes is the basis of this project. Since the ^{t}Bu-bpy ligand has stronger coordinating ability than the diphosphine ligands, the synthetic strategy of the Ru(N^N)(P^P) core is to introduce the diimine ligand first, and then attach the diphosphine ligand, as shown in Scheme 2.1. The starting materials $RuCl_2(PPh_3)_3$ [56] and $RuCl_2(^t$Bu-bpy$)(PPh_3)_2$ [57] were prepared through

literature methods. $RuCl_2(^tBu\text{-}bpy)(PPh_3)_2$ reacted with different diphosphine ligands in refluxing $CHCl_3$ for more than three hours, leading to the desired products in good yields. The two doublets in each ^{31}P-NMR spectrum suggested all products are *cis*-isomers.

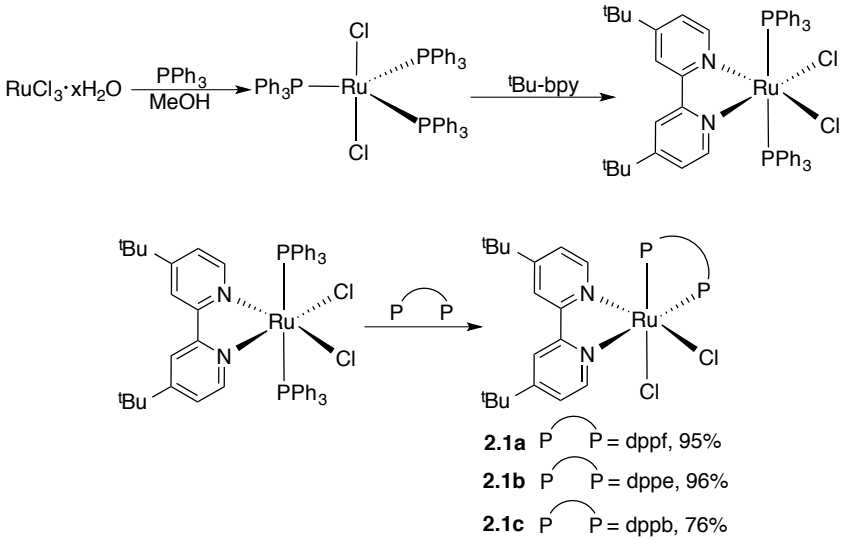

Scheme 2.1 Synthesis of *cis*-$RuCl_2$(N^N)(P^P) complexes.

2.2.2 Synthesis of mono-alkynyl complexes

An efficient, stepwise approach to ruthenium mono-alkynyl compounds is provided via the intermediacy of vinylidene complexes. The isolated vinylidene species are then deprotonated by Et_3N [41]. The syntheses towards the mono-alkynyl Ru(N^N)(P^P) complexes, using the classical method, are displayed in Scheme 2.2. The vinylidene salts of the Ru(N^N)(P^P) series were found to be easily oxidized, as shown in Scheme 2.3. The structure of one oxidized vinylidene complex **2.3a** was confirmed by X-ray study. Unlike the other $Ru(P^P)_2$ compounds [32-38], the ruthenium atom was coordinated by mixed ligands in this project, one P^P ligand and one N^N ligand, which differ in the electron withdrawing ability. Obviously, ^{t}Bu-bpy ligand has better performance on this aspect and enhances the δ^+ property of C_β atom in the vinylidene arm, which makes the attack from the oxidant (e. g. oxygen) more easily. As a result, the isolation of vinylidene species was not pursued, but rather they were immediately reacted with base, and the mono-alkynyl products were obtained successfully. The yields of the products varied during the purification procedure, because pads of basic

alumina needed for chromatographic purification also decomposed the products to different extents.

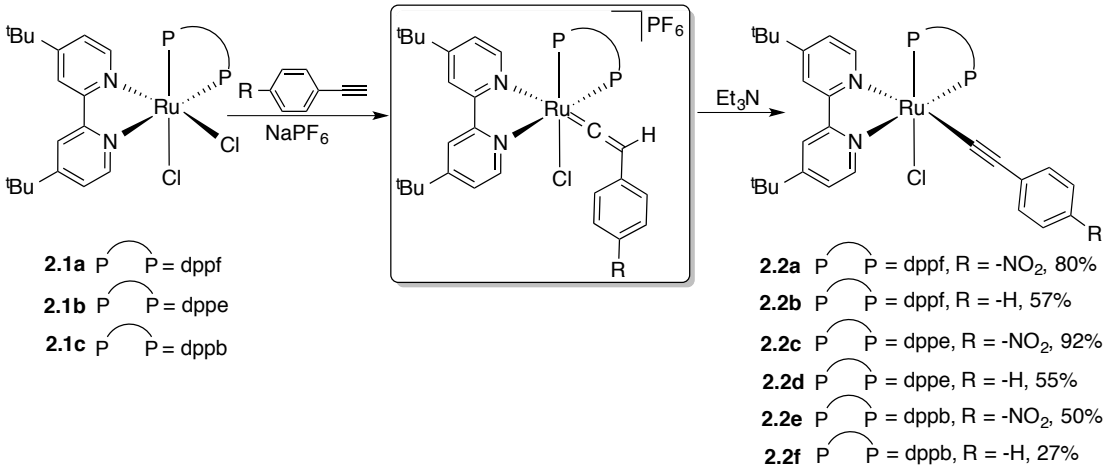

Scheme 2.2 Synthesis of ruthenium mono-alkynyl complexes.

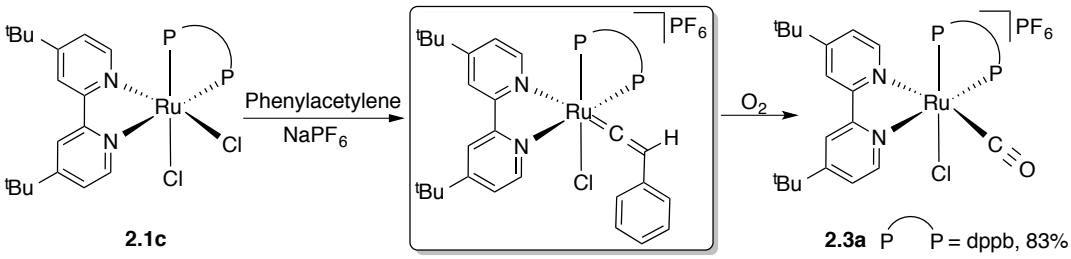

Scheme 2.3 Oxidation of a vinylidene complex.

2.2.3 Synthesis of η^3-butenynyl complexes

In the presence of both Et_3N and $NaPF_6$, reaction of dichloro complexes or chloro-ligated five-coordinate cations with excessive alkynyl ligand (ca. 3 equiv.) can lead to the formation of bis-alkynyl species [41]. However, this does not occur to these Ru(N^N)(P^P) complexes. The outcome of the reactions is shown in Scheme 2.4. Using either ruthenium halides or mono-alkynyl complexes as the starting materials, and carrying out the reactions at room temperature or in refluxing CH_2Cl_2, the products were η^3-butenynyl species resulting from alkyne coupling.

The first ruthenium precedent of this kind was reported by Jia *et al.* [58] in 1989 and a possible mechanism was suggested. During the past 27 years, more investigations have been reported [59-63]. The most similar synthetic route to that described in this Chapter was from Lynam [62] and Low [63]. Mechanistic studies were carried out with the aid of isotopic labeling [62] and DFT methods [63]. The

proposed mechanism, based on the previous reports and the observations in this Chapter, is shown in Scheme 2.5.

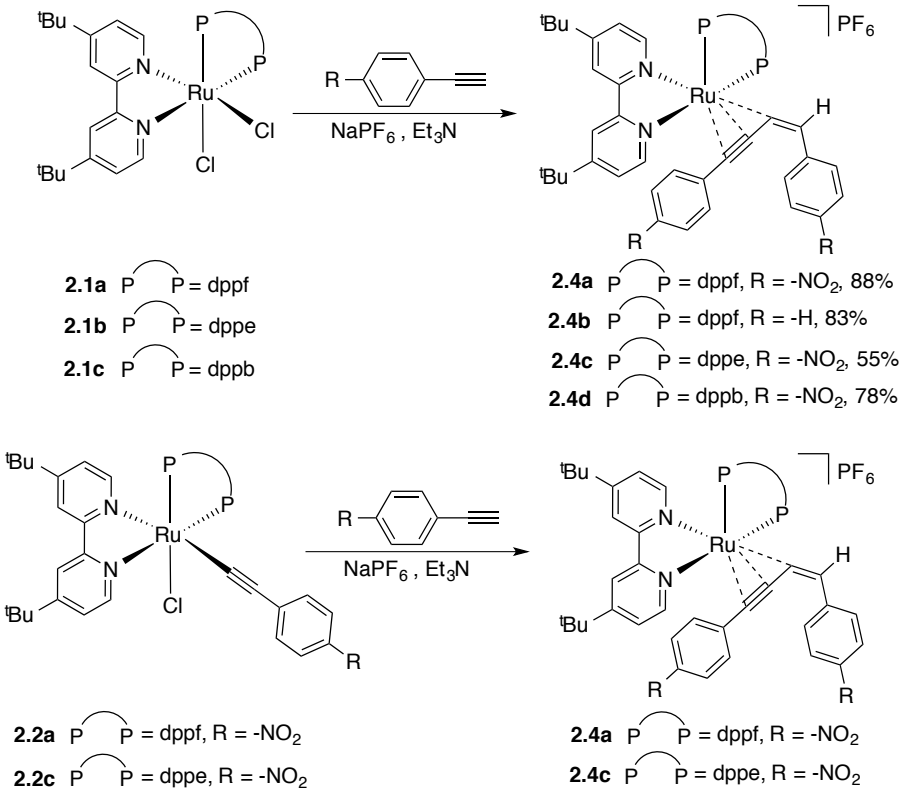

Scheme 2.4 Synthesis of ruthenium η^3-butenynyl complexes.

Based on the experimental result that the mono-alkynyl complexes leads to the formation of the η^3-butenynyl species, the reaction of *cis*-$RuCl_2$(N^N)(P^P) and HC≡C-4-C_6H_4-R (R= -H, -NO_2) with $NaPF_6$ is presumed to firstly result in the formation of the vinylidene species, and then the mono-alkynyl complexes. Subsequent reaction of mono-alkynyl complexes with HC≡C-4-C_6H_4-R (R = -H, -NO_2) may then be envisaged to result in the formation of intermediates **A** [62]. Formation of **A1** or **A2** depends on steric factors. In **A** species, on one hand, the C_α of alkynyl group is δ^-, while the C_α in the vinylidene arm is δ^+; on the other hand, the two carbon atoms are very close to each other. Thus the bonding between the C_αs tends to be formed, as shown in intermediates **B**. The proton could shift from one arm to the other end along the newly-formed conjugated C_4 chain, and **B3** is the one that is assumed to be the most stable form, since it could provide more space to the bulky diphosphine ligand, compared with the other two **B** species. The C-C bond formation in this step could be slow and fragile, and require long time and high energy. In order to achieve a relatively stable state, the molecule is assumed to transform to a lower energy transition state, the **C** species, and then

finally **D** species [63]. The procedure forming **D** species from intermediates **C** may be slow and proton shifts could occur much more frequently, as shown in Scheme 2.5.

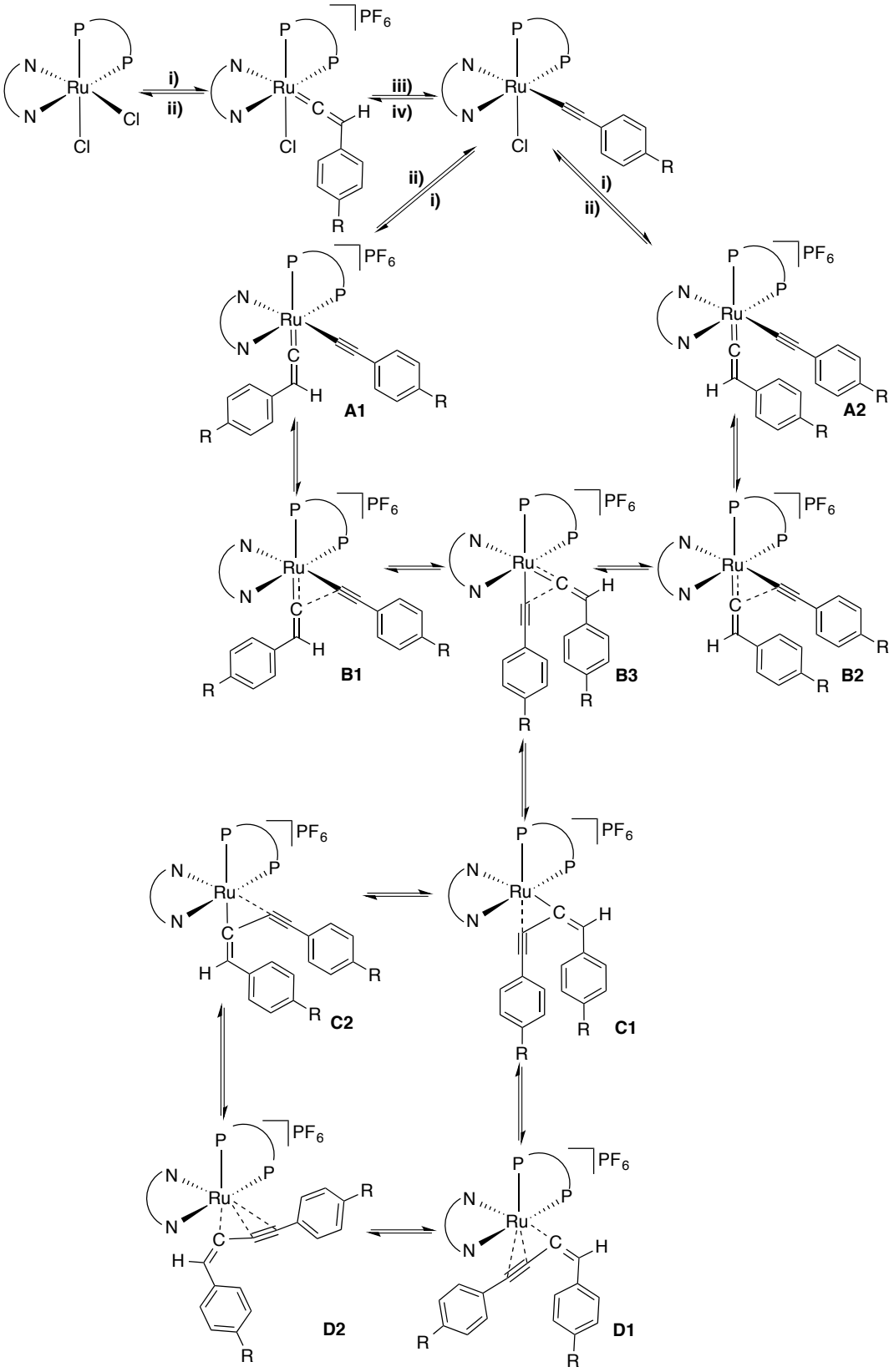

Scheme 2.5 Proposed mechanism for the formation of ruthenium η^3-butenynyl complexes, where: i) + HC≡C-4-C_6H_4-R, PF_6^-, -Cl; ii) - HC≡C-4-C_6H_4-R, PF_6^-, +Cl; iii) –H, PF_6^-; iv) + H, PF_6^- (R = -H, -NO_2).

The alkyne-coupling complexes can be used as catalysts in the dimerization of terminal alkynes, firstly disclosed by Jia [58] and then confirmed by Caulton [61]. No other applications have been suggested or investigated so far.

2.2.4 Synthesis of η^1-coordinated complexes

The dppe-ligated ruthenium η^3-butenynyl complex can convert to a η^1- butenynyl complex in the presence of excess ^{n}Bu$_4$NCl, as shown in Scheme 2.6. The structure was confirmed by a single-crystal X-ray study. In the structure, the chlorine atom from ^{n}Bu$_4$NCl has formed a new bond with ruthenium, and cleaved of two Ru-C bonds replacing the η^3-coordination with a η^1-binding mode.

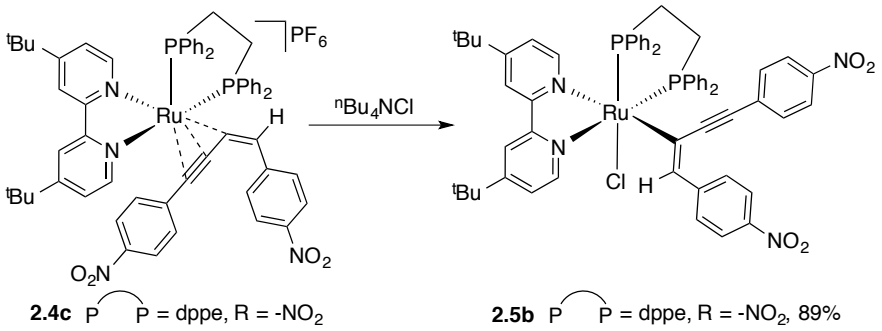

Scheme 2.6 Synthesis of ruthenium η^1-butenynyl complexes.

The first η^1-ligated complex **2.5a** confirmed by X-ray study (Figure 2.3), was obtained from the attempted purification of *cis*-[Ru(C$_4$HPh$_2$)(dppf)(^{t}Bu-bpy)]PF$_6$ (**2.4b**) when passing a solution of the complex through a short pad of basic Al$_2$O$_3$. Crystals of **2.4b** and **2.5a** crystallized from the eluent. Further investigation revealed that this complex **2.5a** cannot be synthesized through the reaction with ^{n}Bu$_4$NCl in a similar fashion to the synthesis of **2.5b**. This is attributed to the bulky dppf ligand. The reactions of **2.4d** and **2.4a** with excess ^{n}Bu$_4$NCl were carried out under the same conditions affording **2.5c** and **2.5d**, respectively. The ^{31}P-NMR data are summarized in Table 2.1. The signals of **2.5b** and **2.5c** are shifted significantly downfield and have larger coupling constants than those of the analogous η^3-bound complexes. A molecular ion of [Ru(C=CH(4-C$_6$H$_4$-NO$_2$)C≡C(4-C$_6$H$_4$-NO$_2$))Cl(dppb)(^{t}Bu-bpy)] was found in the mass spectrum (HR ESI MS ([M – Cl]$^+$, 100): calcd for C$_{64}$H$_{57}$O$_4$N$_4$P$_2$^{102}Ru 1109.2899, found 1109.2891), consistent with

the product of the reaction of the dppb-containing complex being the η^1-complex. In contrast, the ^{31}P-NMR data of the dppf complex **2.5d** does not follow the same trend as those of the dppe and dppb analogues, which indicated the reaction pathway and outcome may vary.

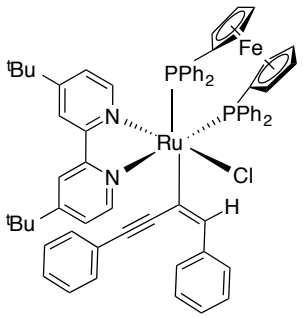

2.5a

Figure 2.3 Chemical structure of *cis*-[Ru(C=CHPh)C≡CPh]Cl(dppf)(^{t}Bu-bpy)].

Table 2.1 Chemical shifts in positive range of ^{31}P-NMR spectra.

Complex No.	δ/ppm	Complex No.	δ /ppm	Complex No.	δ /ppm
2.1b	61.7 (J = 21 Hz)	**2.1c**	70.0 (J = 23 Hz)	**2.1a**	36.0 (J = 30 Hz)
	70.0 (J = 22 Hz)		73.4 (J = 23 Hz)		43.0 (J = 29 Hz)
2.4c	63.8 (J = 13 Hz)	**2.4d**	68.1 (J = 19 Hz)	**2.4a**	34.7 (J = 26 Hz)
	69.4 (J = 13 Hz)		74.6 (J = 19 Hz)		42.6 (J = 25 Hz)
2.5b	65.1 (J = 23 Hz)	**2.5c**	73.9 (J = 32 Hz)	**2.5d**	14.9 (J = 16 Hz)
	78.5 (J = 23 Hz)		84.8 (J = 32 Hz)		43.4 (J = 16 Hz)

Note: **2.5c** = *cis*-[Ru(C=CH(4-$C_6H_4NO_2$)C≡C(4-$C_6H_4NO_2$))Cl(dppb)(^{t}Bu-bpy)]

2.5d = *cis*-[Ru(C=CH(4-$C_6H_4NO_2$)C≡C(4-$C_6H_4NO_2$))Cl(dppf)(^{t}Bu-bpy)]

2.2.5 Attempted formation of a C_8 ligand

The η^3-butenynyl ligands can be regarded as C_4 ligands. Complexes of C_8 ligands were pursued through the reactions with (4-nitrophenyl)butadiyne, as shown in Scheme 2.7.

Different diphosphine ligands resulted in different products. The reaction of **2.1b** afforded a mixture, yielding 54 % of the mono-alkynyl complex **2.6b** and 25 % of a secondary product **2.7a**. Although it also resulted in a mixture, the selectivity of the reaction with **2.1c** was higher, yielding **2.6c** in 87 % yield; in this case, the yield of the secondary product was too small to be isolated. The dppf-containing complex afforded two main products under the same conditions, with ^{31}P-NMR signals at δ 12. 7 (d, J_{PP} = 29 Hz) and 43.4 (d, J_{PP} = 29 Hz) (**2.6a**), and δ 19.9 (d, J_{PP} = 30 Hz) and 45.7 (d, J_{PP} = 28 Hz) (**2.6a***). Mass spectrometry confirmed the

existence of the dppf analogus, but the solubilities of the two compounds were very similar and they could not be separated by precipitation or chromatography. The longer the mixture was left on the plug, the greater the amount of **2.6a***. The decrease in **2.6a** and the increase in **2.6a*** occurred simultaneously as the reaction proceeded, eventually affording only **2.6a*** which did not match the expected molecular weight for a dppf-containing **2.6** analogous. Because there are no symmetry elements in the molecule, which leads to extremely complicated NMR spectra, the chemical structure of **2.6a*** remains unknown, but two points can be confirmed: 1) **2.6a** corresponds to signals at δ 12. 7 (d, J_{PP} = 29 Hz), 43.4 (d, J_{PP} = 29 Hz) (**2.6a**) in the ^{31}P-NMR spectrum, and is the dppf-containing analogous of **2.6**; 2) **2.6a*** is a neutral molecule, and is thus neither a "**2.6**" species nor an analogue of the aforementioned secondary species.

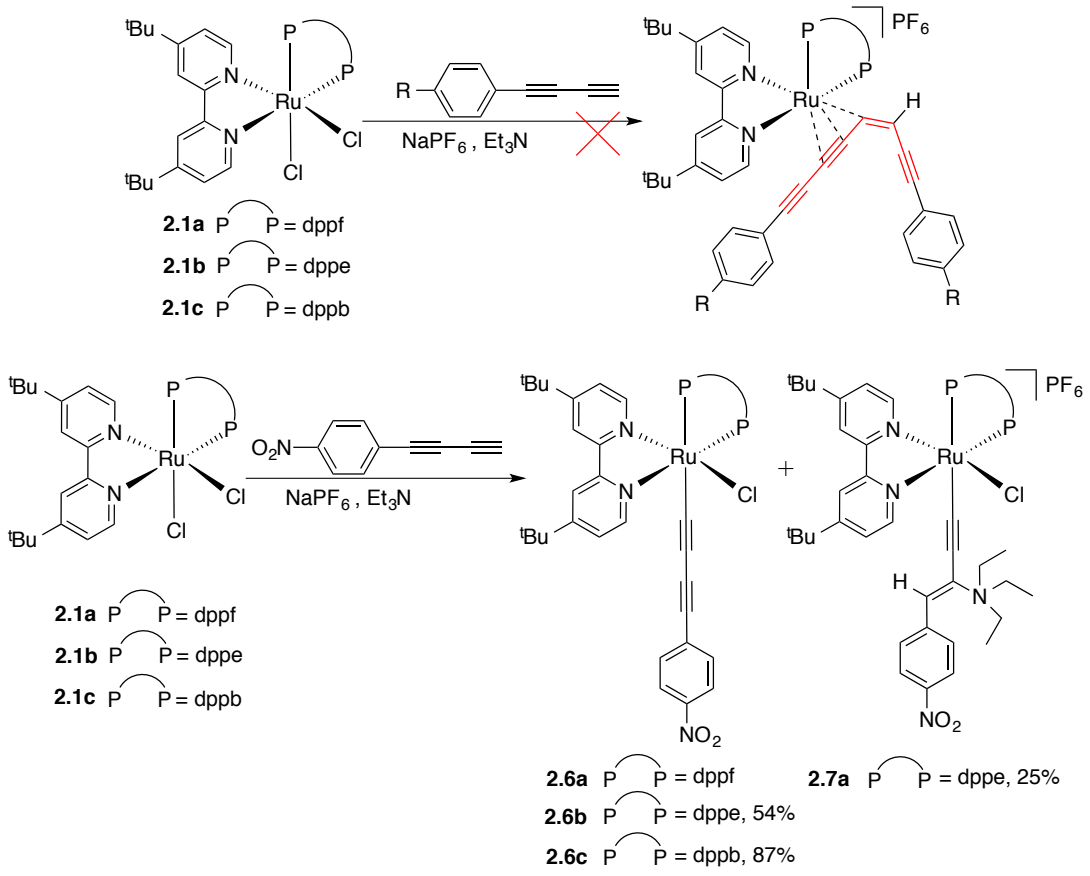

Scheme 2.7 Reactions with 4-nitrophenylbutadiyne.

The formation of the (vinylammonio)alkynyl complex **2.7a** via the intermediacy of the cationic butatrienylidene *cis*-[Ru(C=C=C=CH(NEt$_3$))(^{t}Bu-bpy)(dppe)]$^+$ is shown in Figure 2.4. Both C$_\alpha$ and C$_\gamma$ are electrophilic, but due to steric effects, C$_\gamma$ is more easily attacked by the lone pair of electrons of the nitrogen atom.

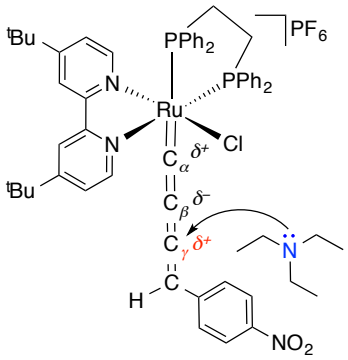

Figure 2.4 Chemical structure of *cis*-[Ru(C=C=C=CH(4-$C_6H_4NO_2$))(^{t}Bu-bpy)(dppe)]PF_6 and Et_3N.

Another (vinylammonio)alkynyl complex was obtained in THF/Et_3N (1:1) by Bruce and his coworkers [64]. They conducted a CV study of this species, and further reaction of their (vinylammonio)alkynyl cation with 4 equiv. I_2 at room temperature resulted in migration of the alkynyl group to the cyclopentadienyl group to give [RuI(dppe){η-$C_5H_4C{\equiv}CC(Et_3N){=}CHFc$}]$I_3$, as shown in Scheme 2.8. So far, there is no report on the spectroelectrochemistry or NLO studies.

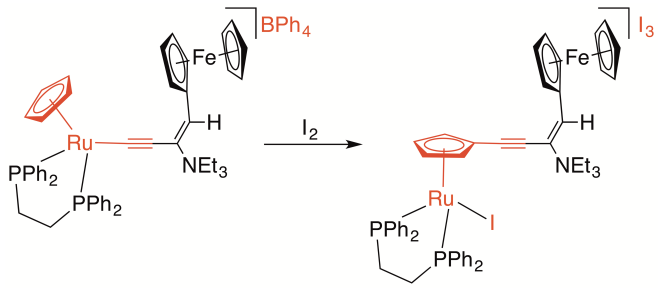

Scheme 2.8 Migration of the alkynyl group to the Ru-C_5 ring [64].

The reaction of **2.1b** with diisopropylamine, a secondary amine replacing the role of Et_3N, was attempted. The main product was **2.6b**, consistent with the result employing Et_3N.

2.2.6 Attempted syntheses of bis-alkynyl complexes

Several attempts to synthesize Ru(N^N)(P^P) bis-alkynyl complexes were made, summarized below.

2.2.6.1 Order of introduction of ligands

The successful order of introduction of ligands for the synthesis of mono-alkynyl complexes was firstly the diphosphine, and subsequently the alkynyl ligand, but further addition of alkyne failed to afford bis-alkynyl complexes. The synthetic strategy was therefore modified, the order of ligand introduction being adjusted to alkynyl groups first, followed by diphosphine ligand. Mono-alkynyl complexes were successfully synthesized using this strategy, as shown in Scheme 2.9. Attempts to prepare bis-alkynyl complexes using this second synthetic strategy were therefore conducted, as described in this section below.

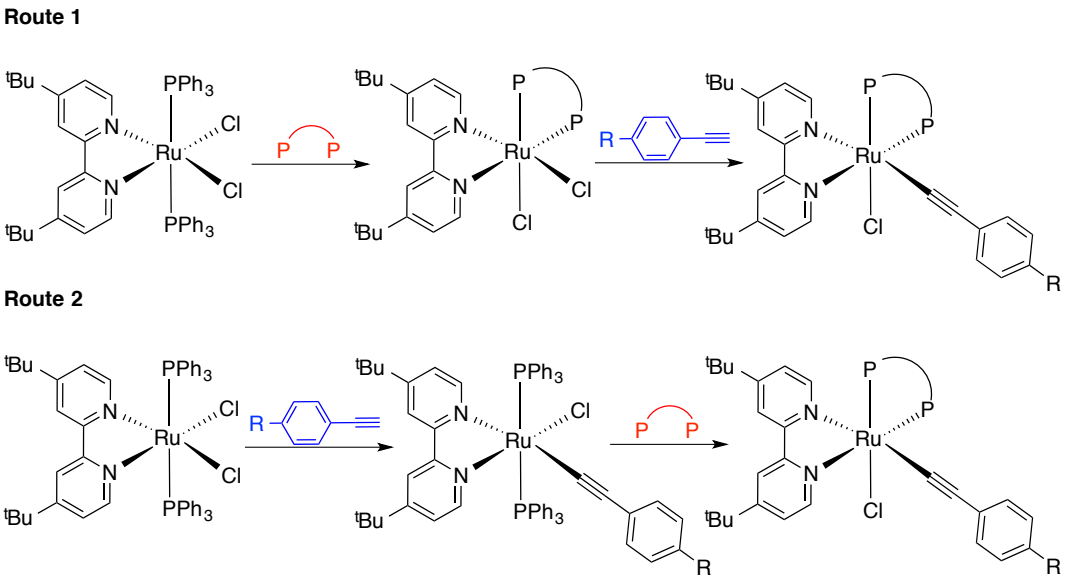

Scheme 2.9 Synthetic routes to mono-alkynyl complexes.

Reaction with lithium alkynyl complex

The reaction with lithium alkynyl complex is shown in Scheme 2.10. The molecular ratio of $RuCl_2(^tBu\text{-}bpy)(PPh_3)_2$ was taken as 1.0 equiv.. The molecular ratio of ^nBuLi was up to 3.78 equiv. and it was 3.01 equiv. for phenylacetylene. The reaction ended up with a mixture of mono- and bis-alkynyl complexes of a ratio ca. 4:1, concluded from the ^{31}P-NMR study, shown in Figure 2.5. The solubility of bis-alkynyl complex was slightly higher than that of mono-product in THF or CH_2Cl_2, but quite close to each other, which caused the difficulties in separation. But the stabilities varied. The bis-alkynyl complex $Ru(C{\equiv}CPh)_2(^tBu\text{-}bpy)(PPh_3)_2$ could decompose in $CDCl_3$ in the air.

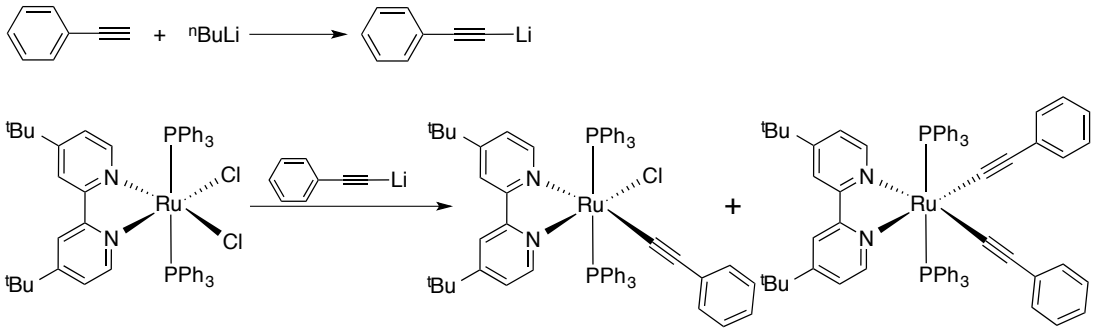

Scheme 2.10 Reaction of $RuCl_2(^tBu\text{-}bpy)(PPh_3)_2$ with lithium alkynyl complex.

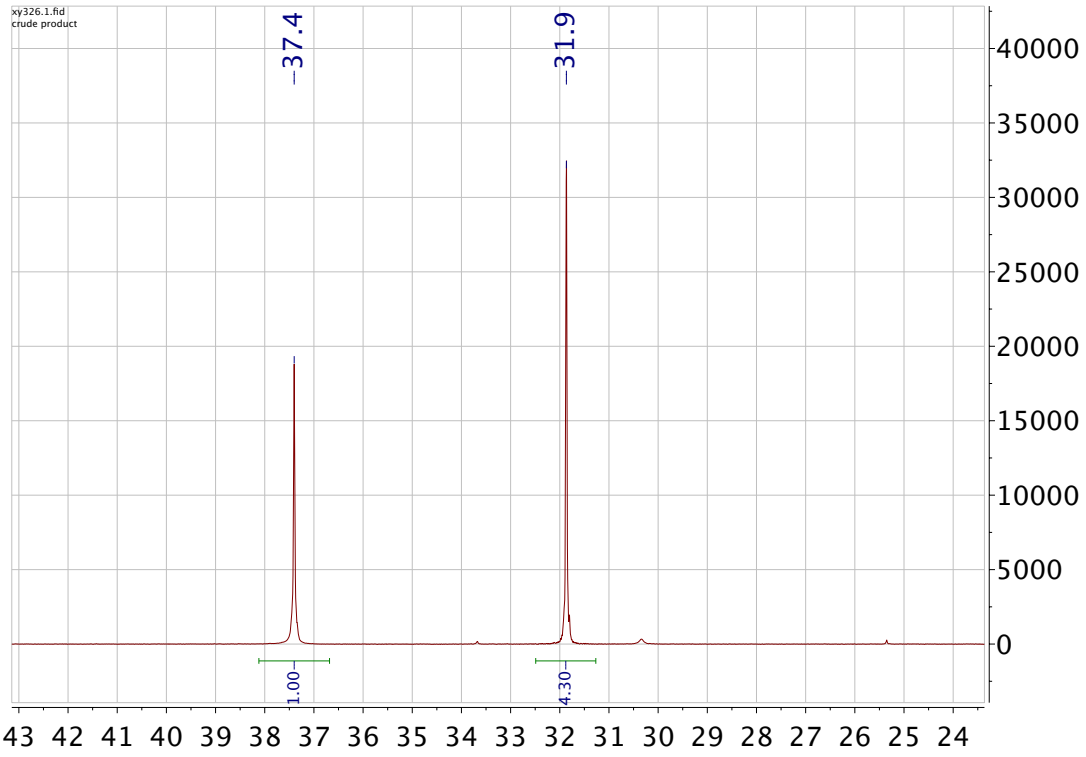

Figure 2.5 ^{31}P-NMR spectrum of the reaction products of $RuCl_2(^tBu\text{-}bpy)(PPh_3)_2$ with Li-C≡CPh.

The precipitate from petrol spirit, was taken as the starting material for the next step, as shown in Scheme 2.11. The experimental conditions were the same as the syntheses of Ru(N^N)(P^P) cores in Route 1. The result is shown in Figure 2.6. ^{31}P-NMR spectra confirmed the existence of **2.2b** as the leading product. The secondary product at δ 35.4 (d) and 42.1 (d), corresponded the peaks at 1127.2866 as $C_{68}H_{63}N_2P_2FeRu$ in mass spectrum, which is a possibility of capping a proton for the target bis-alkynyl complex $C_{68}H_{62}N_2P_2FeRu$. However, the chemical shift of the product moved upfield compared with that of mono-alkynyl complex, which is opposite to the trend that bis-alkynyl complexes move downfield usually. So, the secondary product could not be concluded as the target product.

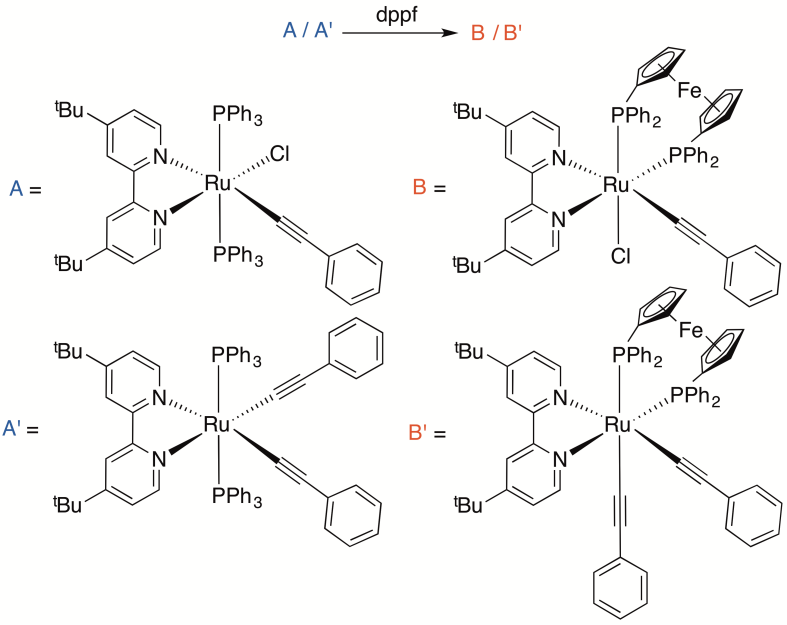

Scheme 2.11 Expected reactions of ruthenium acetylides with the dppf ligand.

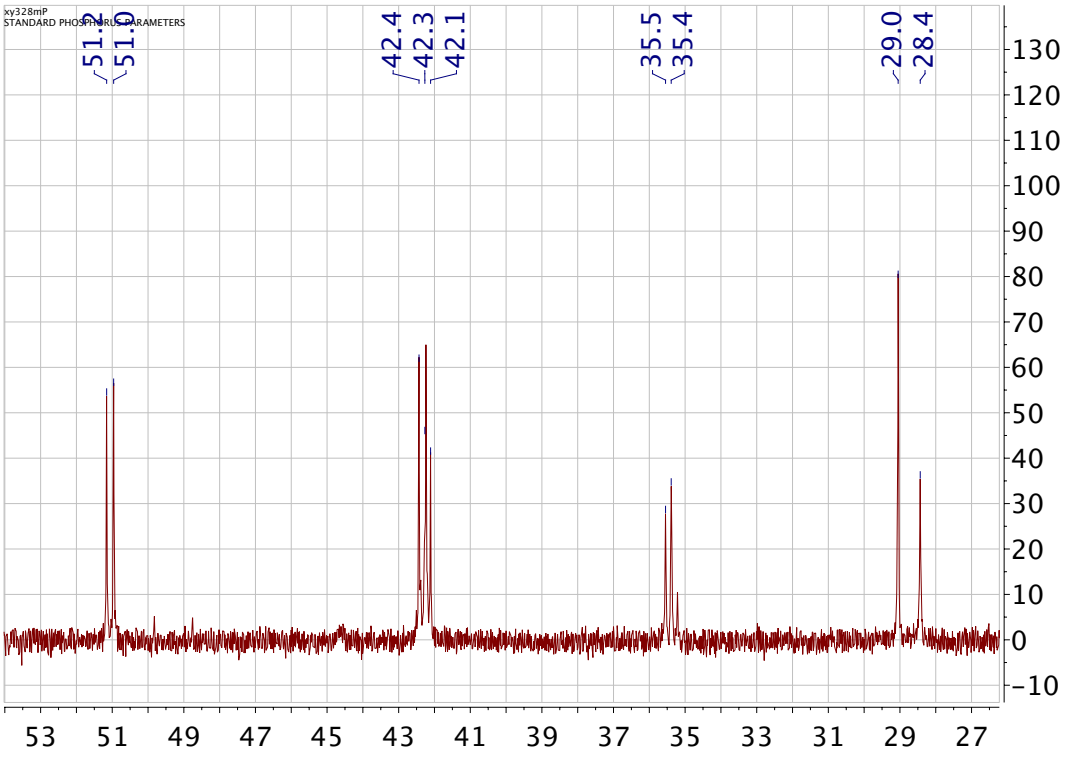

Figure 2.6 ^{31}P-NMR spectra of the product reaction of ruthenium acetylides with the dppf ligand.

Reaction with arylalkynes in the presence of halide abstracting agents

The same synthetic method as employed for the synthesis of the Ru(N^N)(P^P) mono-alkynyl complexes was used to prepare the Ru(^{t}Bu-bpy)(PPh_3)$_2$ alkynyl

complexes, as shown in Scheme 2.12. Ru(C≡CPh)Cl(^{t}Bu-bpy)(PPh_3)$_2$ was obtained pure, while Ru(C≡CPh)$_2$(^{t}Bu-bpy)(PPh_3)$_2$ was formed, but could not be purified.

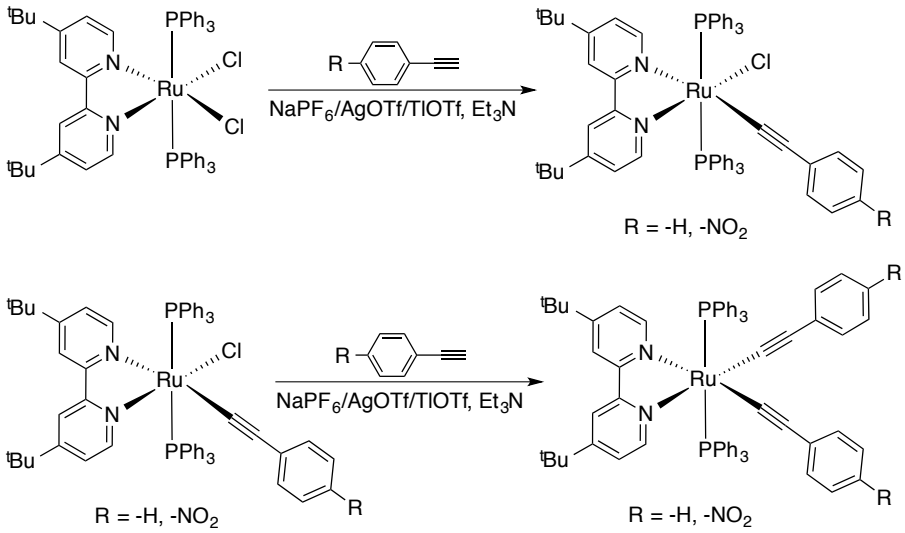

Scheme 2.12 Syntheses of the Ru(^{t}Bu-bpy)(PPh_3)$_2$ alkynyl complexes.

A common impurity resonating at δ 56.0 (s) in the ^{31}P-NMR spectrum was formed with both phenylacetylene and 4-nitrophenylacetylene as the starting material. The impurity was presumed to be connected in some way to the presence of $NaPF_6$. As a result, reactions of $RuCl_2$(^{t}Bu-bpy)(PPh_3)$_2$ with $NaPF_6$ only were conducted at room temperature and in refluxing CH_2Cl_2, as shown in Scheme 2.13. The dominant product was proved to be the species resonating at δ 56.0 (s); its chemical structure was determined by crystallography, and shown to be a ruthenium dimer bridged by three chlorine atoms.

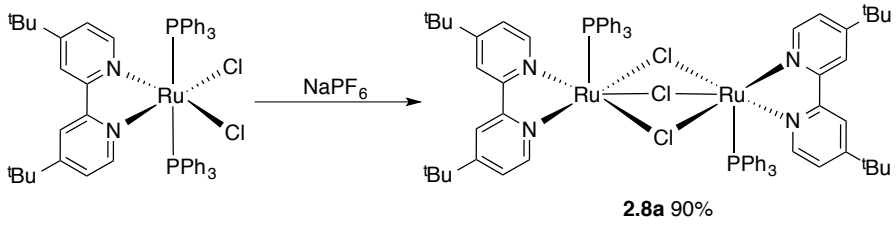

Scheme 2.13 Determination of the impurity from several reactions.

Another impurity was generated during the purification. A yellow band appeared on the top of the short pad of basic alumina as the eluent CH_2Cl_2/Et_3N (10:1) was passed through, overlapping with the band of Ru(C≡CPh)Cl(^{t}Bu-bpy)(PPh_3)$_2$. The impurity formed bright yellow crystals from CH_2Cl_2/n-hexane at -19^{o}C. An X-ray structural study confirmed the chemical structure as that shown in Figure 2.7.

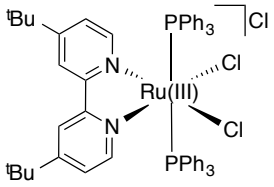

2.8b

Figure 2.7 The chemical structure of the impurity from the short pad of alumina.

A more-logical synthesis of **2.8b** was attempted, based on a report from Batista and James [65, 66] in which $[RuCl_2(bpy)(PPh_3)_2]Cl{\cdot}4H_2O$, a similar complex, was synthesized successfully in hexane from $RuCl_3(PPh_3)_2(DMA){\cdot}DMA$ (bpy = 2,2'-bipyridine, DMA = *N,N'*-dimethylacetamide). However, as shown in Scheme 2.14, no target product $[RuCl_2(^tBu\text{-}bpy)(PPh_3)_2]Cl$ was isolated. The reaction carried out in hexane led to a Ru(III) species, in which the oxidation state was unchanged. In the polar solvent MeOH, the product was a chloride salt of an Ru(II) species with two ^{t}Bu-bpy ligands.

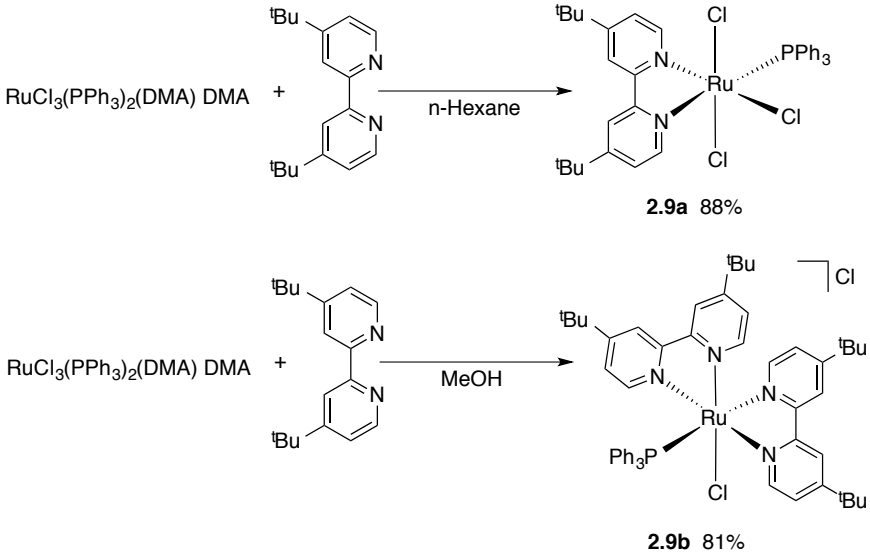

Scheme 2.14 Reactions of $RuCl_3(PPh_3)_2(DMA){\cdot}DMA$ with ^{t}Bu-bpy in different solvents.

2.2.6.2 Attempts to prepare trans-bis(alkynyl) isomers

The alkynyl and vinylidene ligands in *cis*-isomers couple to form the η^3-butenynyl complexes. In contrast, the two alkynyl ligands in *trans*-isomers should hopefully not couple, so attempts to prepare *trans*-isomers were made.

The first attempt was to convert *cis*-$RuCl_2(^t$Bu-bpy)(dppf) to its *trans*-isomer. *Cis*-$RuCl_2(^t$Bu-bpy)(dppf) was stirred in toluene for three days, but proved unreactive.

Since the polarity of the reaction solvent may influence the product, and *cis*-isomers were synthesized in polar solvents, the same synthetic procedure was conducted except the solvent was replaced by nonpolar toluene. However, this still afforded the *cis*-isomer.

Another synthetic route to the *trans*-isomer was explored based on de Araujo's report [67] (Scheme 2.15). In de Araujo's work, a Schlenk flask containing a degassed CH_2Cl_2 solution of $RuCl_2(PPh_3)_3$ and dppf was stirred for five minutes. The reaction was protected from exposure to light and 2,2'-bipyridine was added. The mixture was stirred for additional two minutes. In this work, the described procedure was adopted. But the secondary ligand was the ^{t}Bu-bpy ligand. Finally, the resultant *trans*-isomer was detected by ^{31}P-NMR (a singlet at δ 41.7). The whole procedure, including the determination was carried out in the absence of light.

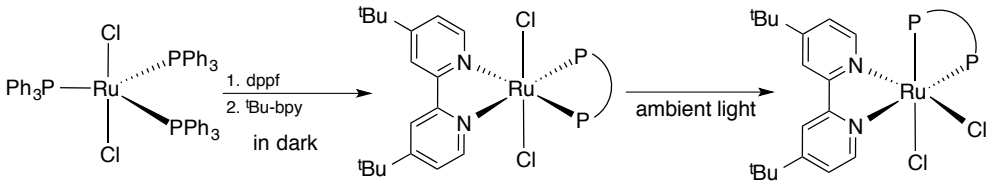

Scheme 2.15 Synthesis of *trans*-$RuCl_2$(^{t}Bu-bpy)(dppf).

However, the *trans*-isomer (the kinetic isomer) readily isomerized when exposed to ambient light, leading to the formation of the *cis*-isomer (the thermodynamic isomer). The well-sealed $CDCl_3$ solution of the freshly-made *trans*-isomer was monitored by ^{31}P-NMR study. Then the solution was exposed under the ambient light for 15 minutes and monitored. The ratio of the *cis*-isomer increased as the exposure time increased. The solution containing both *trans*- and *cis*-isomer was detected for the second time. The procedure was repeated until the ratio of the two isomers remained unchanged. Subsequently, a conversion curve could be drawn and it is shown in Figure 2.8, with the ratio of the two isomers expressed as the concentration in integration ratio of *trans*- and *cis*-isomers and time in minutes. The amount of *trans*-isomer drops quickly. Plotting the natural logarithm of concentration versus time gave a straight line, which indicates that the reaction is a first-order reaction (i.e. if the concentration of the *trans*-isomer doubled, the rate of production of *cis*-isomer would also double).

In order to try and avoid the production of *cis*-isomer, the synthesis of mono-alkynyl complex in toluene was carried out in the dark, but proceeded without isolation of the *trans*-isomer, as shown in Scheme 2.16, and affording the *cis*-, mono-alkynyl complex.

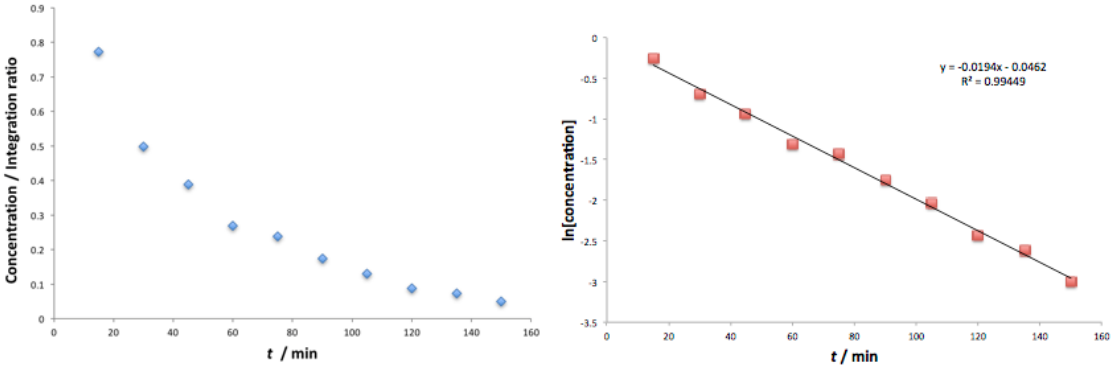

Figure 2.8 Conversion from the *trans*-isomer to the *cis*-isomer: the plots of concentration versus time (left) and ln[concentration] versus time (right).

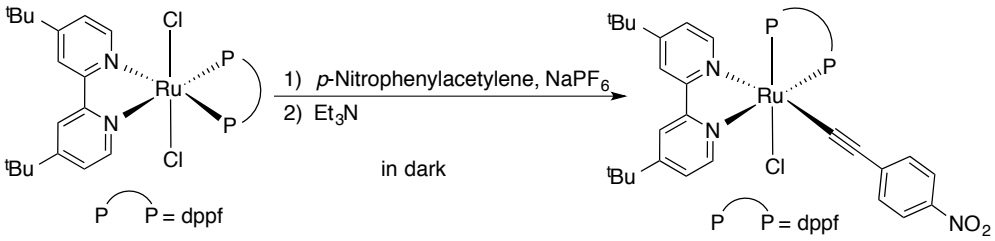

Scheme 2.16 Reaction of *trans*-$RuCl_2$(^{t}Bu-bpy)(dppf) with *p*-nitrophenylacetylene.

2.2.6.3 Reactions of a η^1-butenynyl complex with 4-nitrophenylacetylene

This reaction shown in Scheme 2.17 was conducted in chlorinated solvents. The target complex was *cis*-[Ru(C=CH-4-$C_6H_4NO_2$C≡C-4-$C_6H_4NO_2$)(C≡C-4-$C_6H_4NO_2$)(dppe)(^{t}Bu-bpy)]. However, the molecular weight of the cations detected by MS study at 1061.2900 matched that of the η^3-butenynyl ruthenium cation $C_{60}H_{57}N_4O_4P_2{}^{102}Ru$, and there was no further peak icon detected beyond 1061, which doubted the existence of the target complex. Besides, the chemical shifts of ^{31}P-NMR spectrum showed no difference from the already confirmed complex **2.4c**. In a word, the attempt afforded the η^3-butenynyl species, confirmed by MS and ^{31}P-NMR studies.

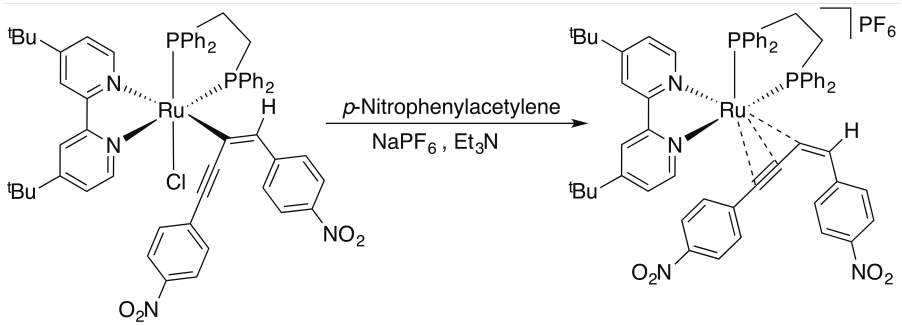

Scheme 2.17 Reaction of η^1-butynenyl complex with 4-nitrophenylacetylene.

2.2.6.4 Reactions with lithium alkynyl compound

One well-established synthesis of transition metal σ-alkynyl complexes is from the interaction of either an alkali metal alkynyl R-C≡C-M (M = Li, Na, *etc.*) with a transition metal halide L_nMX (X = Cl, Br, I). This is a displacement reaction, in which the alkynyl anion acts as a nucleophile, and the metal centre as an electrophilic substrate [41]. Furthermore, this can avoid the formation of the vinylidene complexes that contribute to the formation of the η^3-butenynyl coupling species. As a result, the reactions of *cis*-$RuCl_2$(N^N)(P^P) with PhC≡CH and ^{n}BuLi were carried out, targeting the formation of bis-alkynyl complexes.

As shown in Scheme 2.18, excess ^{n}BuLi (3.0 equiv., taking *cis*-$RuCl_2$(N^N)(P^P) as 1.0 equiv.) reacted with excess phenylacetylene (3.2 equiv.) in distilled THF at -78°C to form Ph-C≡C-Li. The solution was then transferred to a flask containg *cis*-$RuCl_2$(N^N)(P^P), but neither of the expected products, *cis*- or *trans*-isomers, were obtained.

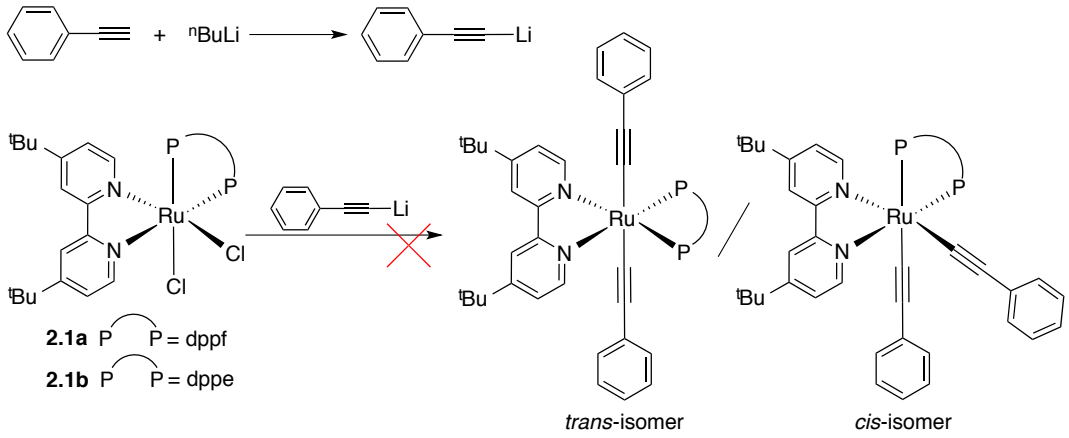

Scheme 2.18 Reactions of *cis*-$RuCl_2$(N^N)(P^P) with lithium alkynyl complex.

For *cis*-$RuCl_2$(^{t}Bu-bpy)(dppf), the freshly-obtained product was analyzed by NMR, as shown in Figure 2.9. The major product resonates at δ 14.7 (d, J_{PP} = 22 Hz) and 43.6 (d, J_{PP} = 22 Hz), and is accompanied by a complex resonating at δ 22.8 (d, J_{PP} = 22 Hz) and 47.8 (d, J_{PP} = 22 Hz). There was no trace of the starting material, but the mono-alkynyl complex **2.2b** was detected. The crude product was separated into two parts. The first part was purified by chromatography through a pad of basic alumina, revealing that the majority of material had converted to **2.2b**, as confirmed by a ^{31}P-NMR study. Crystallization was attempted on the other part, but NMR studies revealed replacement of the major product by **2.2b** in non-chlorinated solvents in the absence of light (Figure 2.9).

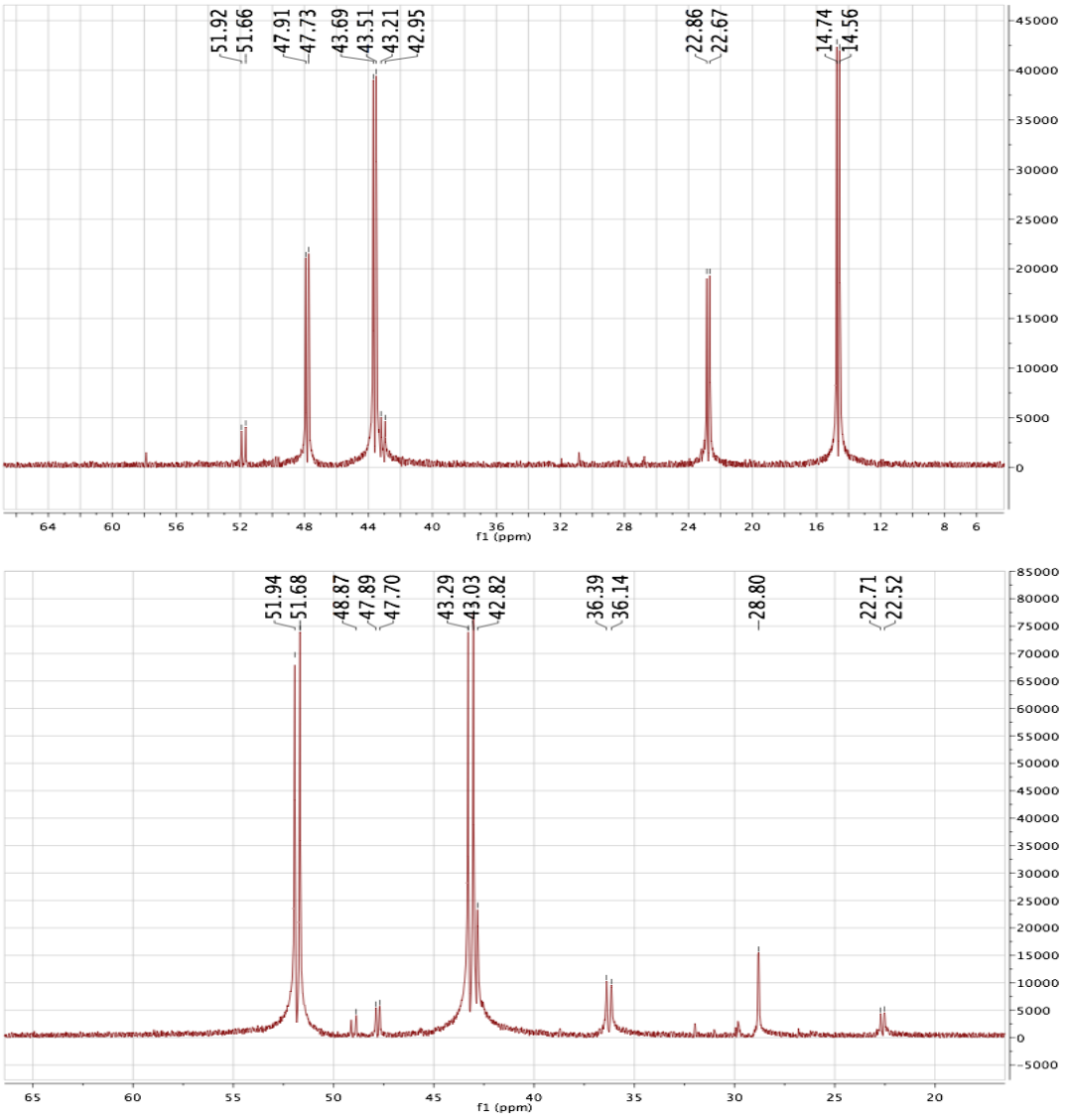

Figure 2.9 ^{31}P-NMR study of the product from *cis*-$RuCl_2$(^{t}Bu-bpy)(dppf): freshly-obtained product (above) and product following attempted crystalization (below).

Studies with *cis*-$RuCl_2$(^{t}Bu-bpy)(dppe) were more complicated than the related studies with the dppf complexes because more impurities had appeared at the end of the reaction. One of the impurities crystalized from CH_2Cl_2/n-hexane, as shown in Figure 2.10. It was proposed that the addition of MeI used to quench the ^{n}BuLi reaction lead to the formation of the iodo product from **2.2d**. Reaction with ^{n}Bu$_4$NI, which has a non-coordinating cation, was attempted to prove this idea (Scheme 2.19). Excessive ^{n}Bu$_4$NI was added to a THF solution of **2.2d** with stirring for 24 h. An HR ESI mass spectrum confirmed the existence of *cis*-Ru(C≡CPh)I(^{t}Bu-bpy)(dppe): ([M + H]$^+$) calcd 997.1851, found 997.1852 for $C_{52}H_{54}N_2P_2{}^{127}I^{102}Ru$, supporting the suggestion of the iodine atom from MeI replacing the chlorine atom in **2.2d** to form *cis*-Ru(C≡CPh)I(^{t}Bu-bpy)(dppe).

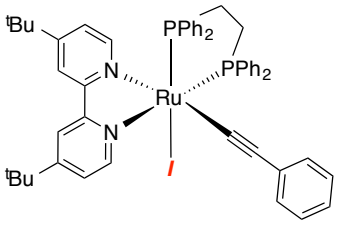

Figure 2.10 Chemical structure of *cis*-Ru(C≡CPh)I(^{t}Bu-bpy)(dppe) (**2.2d***).

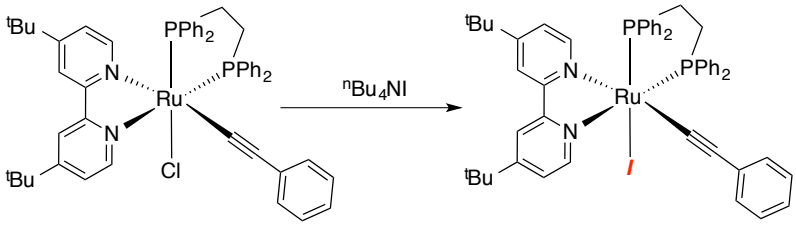

Scheme 2.19 Reaction of **2.2d** with ^{n}Bu$_4$NI.

Overall, none of the attempts at preparing bis-alkynyl complexes were successful in affording the desired product.

2.2.7 Investigation on an oxidized phosphine complex

The complex **2.3a** was exposed to air as a solid for nearly two years at room temperature. After this period, the existence of two complexes, **2.3a-1** and **2.3a-2**, was confirmed by crystallography, as shown in Figure 2.11. They crystallized from CH_2Cl_2/n-hexane. A series of investigation were conducted.

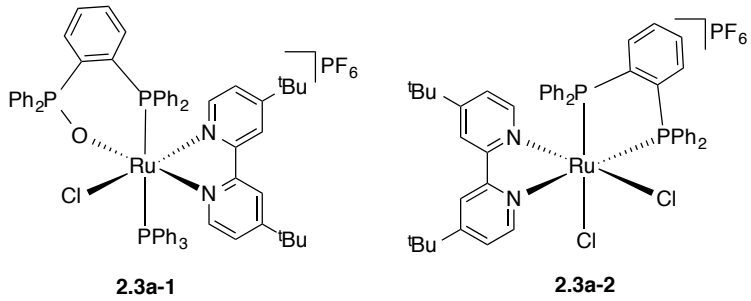

Figure 2.11 Crystallized impurities from **2.3a** over two years.

2.2.7.1 Investigation based on Van't Hoff Rule

The molecules of **2.3a** were surrounded by other molecules and experience strong packing forces in the solid state, having little mobility when the oxidation occurring. By contrast, the molecules in solution are surrounded by solvent and have greater freedom of motion. The investigation described in this section is a qualitative attempt, aiming to get some sort of ideas of the upper bounds for a solution reaction.

The Van't Hoff Rule indicates that the speed of chemical reactions is increased twofold or more for each rise of 10 °C in temperature (very approximately). Based on this approximation, the oxidation of **2.3a**, which required 730 days (two years) at 25 °C, could in principle occur in three days at 105 °C. Toluene, with a boiling point at 110.6 °C, was selected as the reaction solvent. The crystals of **2.3a** were placed in refluxing toluene for three days. The pale suspension gradually became a light brownish yellow solution under aeration. A sample was taken to dryness and examined by MS and ^{31}P-NMR spectroscopy. The result is shown in Figure 2.12.

The majority of the product was **2.3a**, and the other peaks indicated that reaction had indeed happened. However, none of the likely target products were observed in the MS spectra. It may be concluded that: 1) the complexes **2.3a-1** and **2.3a-2** are not thermally stable; 2) any traces of **2.3a-1** and **2.3a-2** are insufficient to be detected.

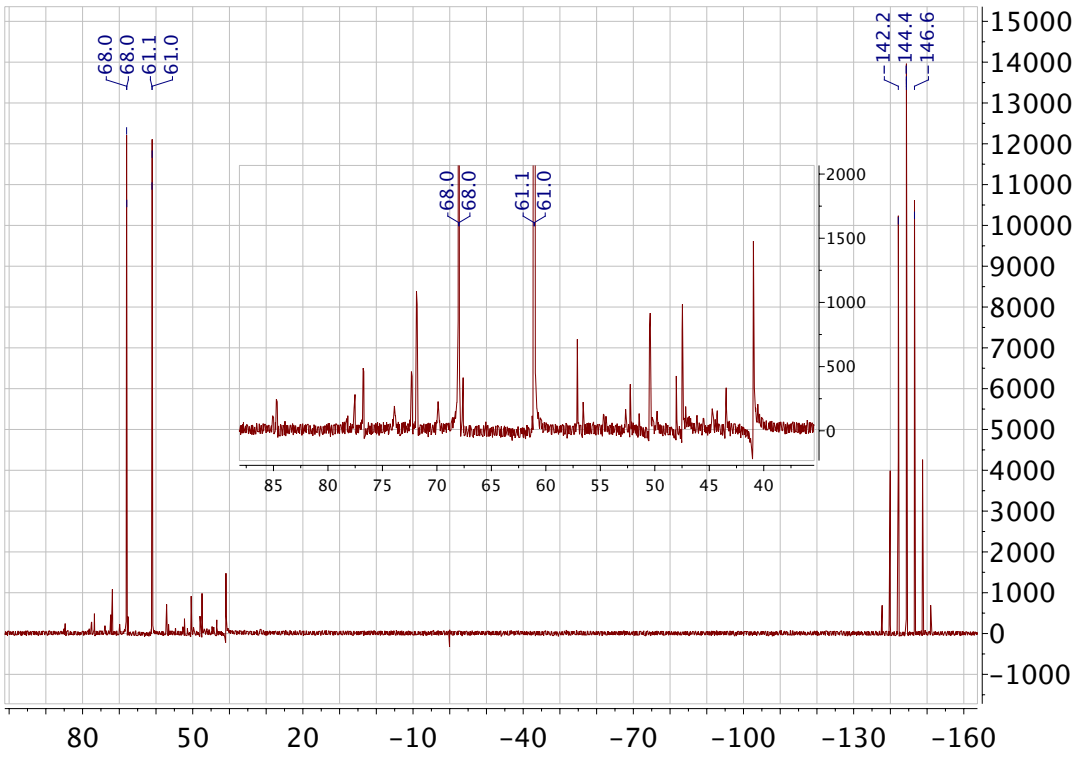

Figure 2.12 Experimental investigation results based on Van't Hoff Rule.

2.2.7.2 Investigation on a secondary possibility

A secondary possible source of **2.3a-1** is shown in Scheme 2.20. Because of the synthesis employed, the sample of the complex **2.1c** may have contained a trace of PPh_3. The formation of intermediate **2.3a-1*** could then occur in the presence of $NaPF_6$. Subsequently, **2.3a-1*** may be oxidized to **2.3a-1**.

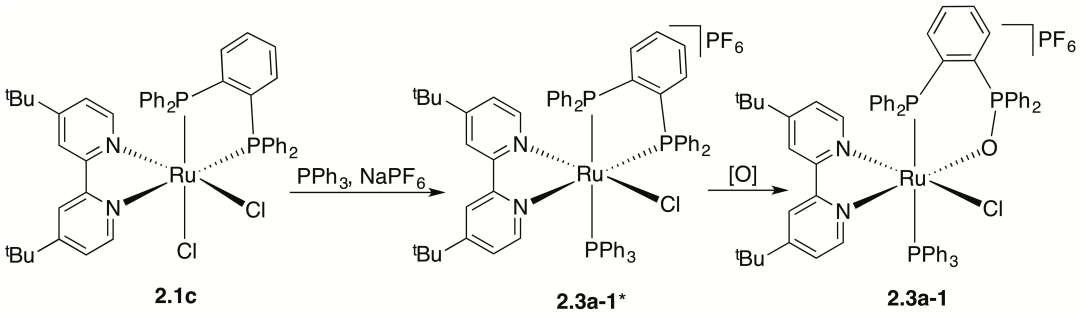

Scheme 2.20 A secondary possible source of **2.3a-1**.

The reaction of **2.1c** (16.9 mg, 1.0 equiv.) with PPh_3 (1.1 equiv.) and $NaPF_6$ (1.1 equiv.) was performed in distilled CH_2Cl_2 at room temperature for 45 h. The crude product was dissolved in the minimum amount of CH_2Cl_2 and then precipitated from ca. 20 mL petrol. The orange precipitate analyzed by ^{31}P-NMR spectroscopy

and MS studies. The HR ESI mass spectrum showed a match for [M+] corresponding to **2.3a-1***: calcd for $C_{66}H_{63}N_2P_3{}^{35}Cl^{102}Ru$ 1113.2936, found 1113.2927. The ^{31}P-NMR spectrum is shown in Figure 2.13. The starting material **2.1c** reacted completely. Four phosphorus resonances at δ -144 (sept), 16 – 18 (dd), 59 – 60 (dd) and 60 (m) ppm, can be recognized with significant integrals, in accordance with the chemical structure of target product **2.3a-1***. The oxidation of **2.3a-1*** was attempted using two methods.

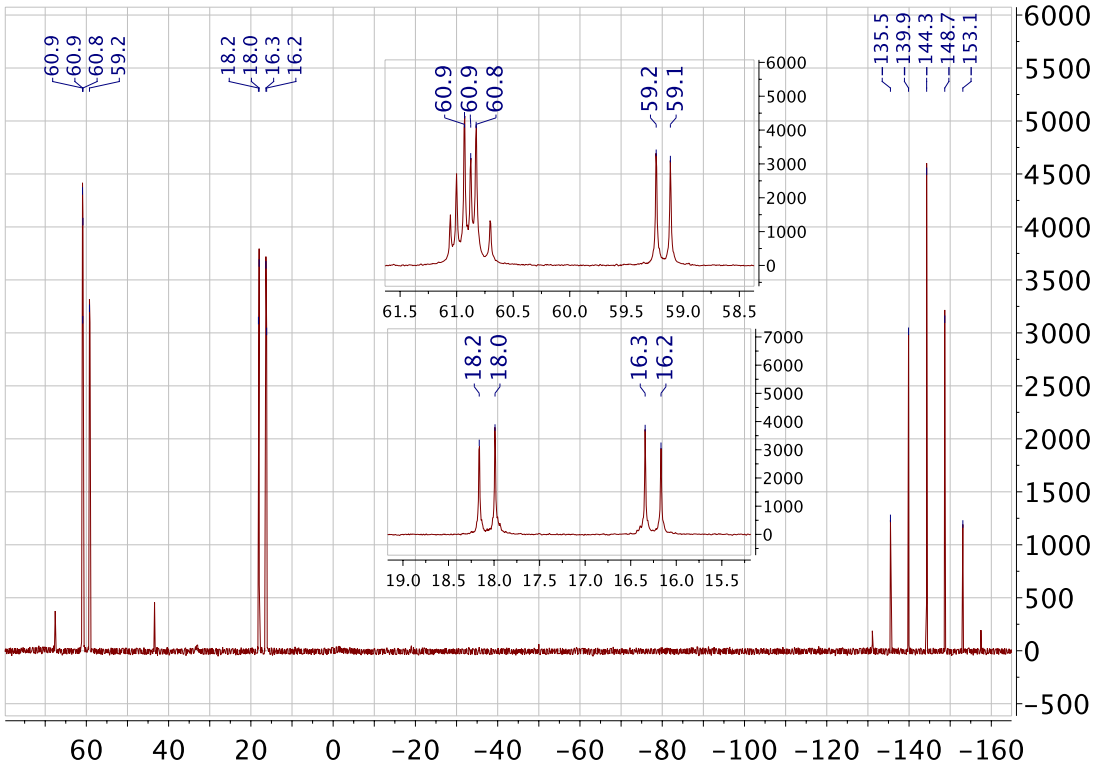

Figure 2.13 ^{31}P-NMR spectrum of **2.3a-1***.

Method A: Sparging air into a toluene solution

Toluene solutions of **2.3a-1*** were sparged with air for three days at room temperature and 65 ^{o}C. The results showed no obvious difference. Although a trace of **2.3a-1** was found in the mass spectrum, it could not be regarded as solid evidence for the formation of **2.3a-1**, because the signal corresponding to **2.3a-1** was too weak to support that the majority of **2.3a-1** came from a trace reaction shown in Scheme 2.20.

Method B: Reaction with mCPBA

A stronger oxidant mCPBA (*meta*-chloroperoxybenzoic acid) was reacted with **2.3a-1*** in CH_2Cl_2 at room temperature for 24 h, leading to a dominant product resonating at δ 30.5 (s) in ^{31}P-NMR spectrum. No trace of **2.3a-1** could be found from mass spectrometry.

2.2.7.3 Investigation on 2.3a-2

A toluene solution of **2.1c** and $^{n}Bu_4NPF_6$ (1.05 equiv.) was heated to 65 ^{o}C with aeration for three days. The hoped-for reaction is shown in Scheme 2.21.

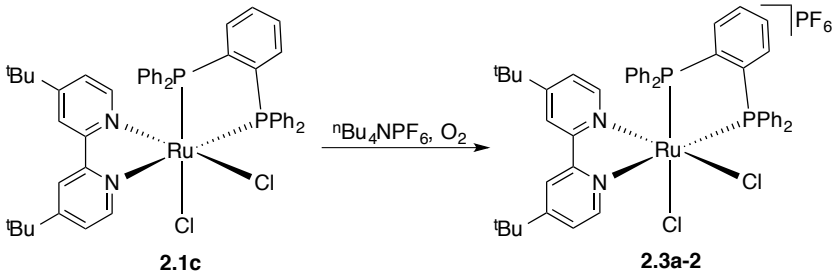

Scheme 2.21 Anticipated reaction of **2.1c** with oxygen and $^{n}Bu_4NPF_6$.

The mass spectrum cannot distinguish between these compounds, since **2.3a-2** has the same ligand environment as **2.1c**. The ^{31}P-NMR spectrum is shown in Figure 2.14. There are no broad signals. Instead, sharp signals resonating at δ 65.0 (s), 65.3 (s), 69.1 (d) and 74.5 (d) ppm, indicated the formation of new complexes. The other two doublets on the ^{31}P-NMR spectrum (at δ 69.6 (d) and 73.0 (d) ppm) are from the starting material **2.1c**. There are seemingly no signals from the target complex **2.3a-2**, since it is a Ru(III) species and paramagnetic. Curiously, no signals from PF_6 or its oxidized species were detected.

Separation was attempted using thin-layer chromatography. The material in the yellow first band afforded a mass spectrum with the exact molecular weight of RuCl(^{t}Bu-bpy)(dppb) + MeCN, and showed no signals in its ^{31}P-NMR spectrum. This may be the target compound **2.3a-2**. The second band proved to be an inseparable mixture.

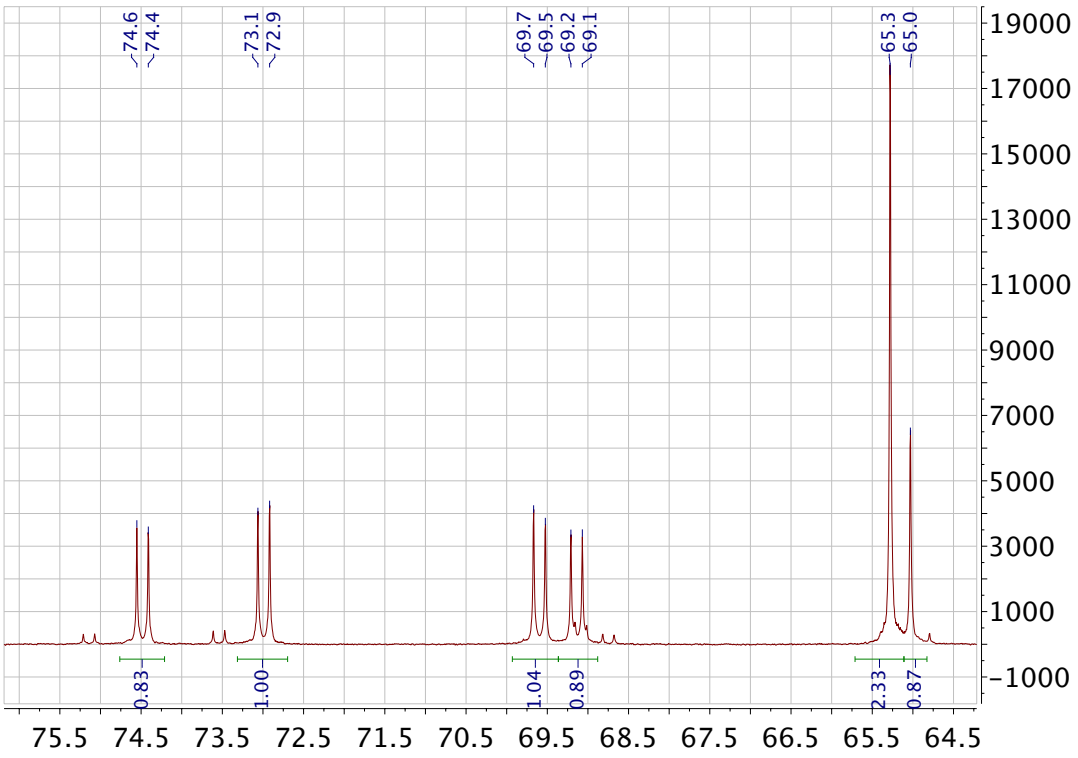

Figure 2.14 ^{31}P-NMR spectrum from the reaction of **2.1c** with oxygen and $^{n}Bu_4NPF_6$.

2.2.8 NMR analysis

The structures of all stable and purified complexes in this Chapter were assigned from 1D-NMR (^{1}H-, ^{13}C-, ^{31}P-NMR and DEPT or APT) and 2D-NMR (gHSQC, gHMBC and gCOSY) spectra. All the complexes, except **2.8a**, have no symmetry elements.

Only complexes **2.8a** and **2.9b** show a singlet in the positive range of their ^{31}P-NMR spectra: **2.8a** is a dimer with two symmetric phosphorus nuclei, while there is only one phosphorus nucleus in **2.9b**. All the complexes with Ru(N^N)(P^P) cores proved to be *cis*-isomers, showing two doublets in their ^{31}P-NMR spectra. The complex **2.5b** has the most downfield chemical shifts at δ 65.1 (d, 1P, J_{PP} = 23 Hz), 78.5 (d, 1P, J_{PP} = 23 Hz) ppm. Compared with Ru halide complexes, the signals from the corresponding mono-alkynyl complexes are more downfield, except those from **2.6b** and **2.6c**. The data are tabulated in Table 2.2. One phosphorus nucleus is *trans* to the –C≡C group and the other to the ^{t}Bu-bpy ligand in **2.6b**, **2.6c** and **2.7a**, while one phosphorus nucleus is *trans* to –Cl and the other to the ^{t}Bu-bpy ligand in the other mono-alkynyl complexes, which may explain the differing chemical shifts behavior.

Table 2.2 Chemical shifts in positive range of ^{31}P-NMR spectra.

Complex No.	δ/ppm	Complex No.	δ /ppm	Complex No.	δ /ppm
2.1b	61.7 (J = 22 Hz)	**2.1c**	70.0 (J = 23 Hz)	**2.1a**	36.0 (J = 30 Hz)
	70.0 (J = 22 Hz)		73.4 (J = 23 Hz)		43.0 (J = 30 Hz)
2.2c	64.7 (J = 17 Hz)	**2.2e**	75.2 (J = 23 Hz)	**2.2a**	41.7 (J = 31 Hz)
	74.5 (J = 17 Hz)		77.1 (J = 23 Hz)		50.1 (J = 31 Hz)
2.6b	43.6 (J = 12 Hz)	**2.6c**	49.9 (J = 14 Hz)		
	66.9 (J = 12 Hz)		73.5 (J = 14 Hz)		
2.7a	45.0 (J = 12 Hz)				
	70.3 (J = 12 Hz)				

Three types of carbons are found in the complexes: primary, tertiary and quaternary. The only primary carbons are those of the ^{t}Bu-bpy ligands, and can be easily recognized as the dominant peaks upfield in the ^{13}C-NMR spectra. Based on the information provided by DEPT or APT studies, the other two types can be separated clearly. All quaternary carbons connected to phosphorus atoms exhibit coupling with chemical shifts ranging from δ 134 – 147 ppm. In several cases, it is difficult to reliably extract coupling constants because of the complexity of the ^{13}C-NMR spectra in this region. For the dppf complexes, the signals of the dppf carbons lie in the range δ 70 – 85 ppm. For the dppe complexes, there are two doublets in the range δ 25 – 29 ppm with coupling constants J_{PP} = 10 – 15 Hz. For the dppb complexes, the carbon signals are difficult to assign because they appear within the Ph-C region.

In the ^{1}H-NMR studies, the two dominant singlets are from ^{t}Bu-Hs. For the dppf complexes, the signals from the Fc-Hs are found in the range δ 3.0 – 6.6 ppm and are all singlets. In the ^{1}H-NMR spectra of **2.1a** and **2.2a**, eight peaks are found, showing different chemical environments for each proton, while some signals from the Fc-Hs overlap in spectra of the other dppf complexes. The assignments of the Fc-Hs were achieved with the aid of gCOSY. For the dppe complexes, unlike Ru(dppe)$_2$ complexes, the signals from the four protons attached to secondary carbons, exhibit multiple peaks in the range δ 2.4 – 3.5 ppm. For the dppb complexes, consistent with the ^{13}C-NMR spectra, the four protons from the dppb ligands are difficult to assign.

2.3 X-RAY STRUCTURAL STUDIES

A series of crystal structures were obtained from the X-ray diffraction measurements, the results from which are discussed in this section.

The molecular geometry and atom labeling of the ruthenium halides are shown in Figure 2.15 and selected bond information is listed in Table 2.3. From the structure of *cis*-$RuCl_2$(dppe)(^{t}Bu-bpy), it is obvious that the bite angle of the bipyridine group is much smaller than that of the dppe ligand. The bite angles of the bipyridine group are similar among the three *cis*-Ru(N^N)(P^P) complexes. The bite angle of the dppf group is 96.69(8)^o, which is significantly larger than the other two ligands (dppe and dppb groups). Due to the large size of the dppf group, the Cl(1)-Ru-Cl(2) bond angle of *cis*-$RuCl_2$(dppf)(^{t}Bu-bpy) is also slightly smaller than Cl(1)-Ru-Cl(2) bond angles of the other two complexes. However, a significant difference between *cis*-$RuCl_2$(dppe)(^{t}Bu-bpy) and *cis*-$RuCl_2$(dppb)(^{t}Bu-bpy) is the backbones: as expected, the coordinated dppb ligand has a rigid backbone, while the backbone is flexible in the dppe complex. The bond length of Ru-P in **2.1c** is slightly shorter, which may be influenced by the π-conjugated backbone.

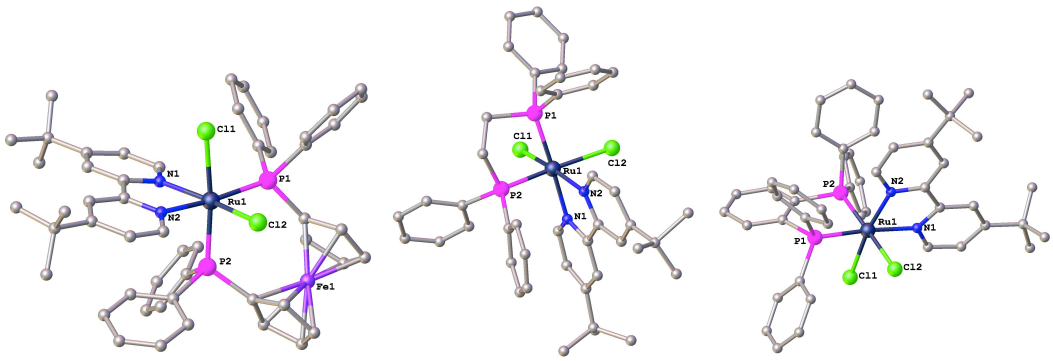

Figure 2.15 Molecular geometry and atomic labeling scheme for *cis*-$RuCl_2$(dppf)(^{t}Bu-bpy) **(2.1a)** (left), *cis*-$RuCl_2$(dppe)(^{t}Bu-bpy) (**2.1b**) (middle), and *cis*-$RuCl_2$(dppb)(^{t}Bu-bpy) (**2.1c**) (right). Hydrogen atoms have been omitted for clarity.

Table 2.3 Selected bond lengths (Å) and angles (°) for *cis*-$RuCl_2$(dppf)(^{t}Bu-bpy) (**2.1a**), *cis*-$RuCl_2$(dppe)(^{t}Bu-bpy) (**2.1b**), and *cis*-$RuCl_2$(dppb)(^{t}Bu-bpy) (**2.1c**).

Complexes	**2.1a**	**2.1b**	**2.1c**
Bond Lengths			
Ru-Cl(1)	2.498(2)	2.4188(10)	2.4310(15)
Ru-Cl(2)	2.428(2)	2.4921(10)	2.4664(16)
Ru-P(1)	2.345(2)	2.3045(10)	2.2824(15)
Ru-P(2)	2.295 (2)	2.2574(11)	2.2434(15)
Ru-N(1)	2.106(6)	2.103(3)	2.117(5)
Ru-N(2)	2.095(7)	2.083(3)	2.074(4)
Bond Angles			
Cl(2)-Ru-Cl(1)	90.36(8)	92.28(3)	92.40(5)
P(1)-Ru-Cl(1)	90.59(8)	83.59(3)	83.90(5)
P(1)-Ru-Cl(2)	87.63(7)	96.45(3)	92.30(5)
P(2)-Ru-Cl(1)	172.71(8)	91.83(3)	90.59(5)
P(2)-Ru-Cl(2)	90.33(8)	175.86(4)	175.30(5)
P(2)-Ru-P(1)	96.69(8)	84.46(3)	84.41(5)
N(1)-Ru-Cl(1)	84.4(2)	93.98(10)	92.75(14)
N(1)-Ru-Cl(2)	166.5(2)	84.56(9)	84.51(14)
N(1)-Ru-P(1)	104.8(2)	177.39(11)	175.28(13)
N(1)-Ru-P(2)	93.3(2)	94.71(9)	98.97(14)
N(2)-Ru-Cl(1)	82.44(19)	170.98(8)	170.39(13)
N(2)-Ru-Cl(2)	90.0(2)	84.73(9)	84.56(13)
N(2)-Ru-P(1)	172.6(2)	105.18(9)	105.29(13)
N(2)-Ru-P(2)	90.3(2)	91.14(9)	93.05(13)
N(2)-Ru-N(1)	77.0(3)	77.29(13)	77.91(18)

Information on the crystal structures of the mono-alkynyl complexes **2.2a**, **2.2b**, **2.2c**, **2.2e** and **2.2d*** is provided in Figure 2.16 and Table 2.4. The mono-alkynyl complexes retain the cis-geometry of the ruthenium halides. The halogen atoms which were *trans* to the ^{t}Bu-bpy ligands in $RuCl_2$(N^N)(P^P) complexes were replaced by an alkynyl groups in each complex. As expected, the bond lengths of the Ru-C bonds are smaller than those of Ru-Cl bonds. Generally, most of the structural details follow the same trend as those of the Ru(N^N)(P^P) cores in the structures discussed above. What is notable is that the bond angle of Cl-Ru-C in **2.2e** is much larger than those in the other three complexes. The reason may be due to the unique rigid and aromatic structure of the dppb ligand. Different from the other four mono-alkynyl complexes, the halogen atom in the complex **2.2d*** is iodine, which is much larger than the chlorine atom. Thus, the bond length of Ru-I is significantly longer than that of Ru-Cl, and the angle of C-Ru-I is increased to 95.6°.

The dppe-containing complexes **2.6a** and **2.7a** are also octahedral *cis*-isomers, as shown in Figure 2.17. Unlike **2.2c**, the alkynyl group in these complexes is *trans* to

one of the phosphorus atoms, while it is *cis* to all the phosphorus atoms in **2.2c**. The existence of the butadiynyl group is confirmed from the bond length information in Table 2.5. Incorporation of the Et_3N in **2.7a** is also confirmed. The C(3)=C(4) bond lengths and angles are consistent with a C=C bond.

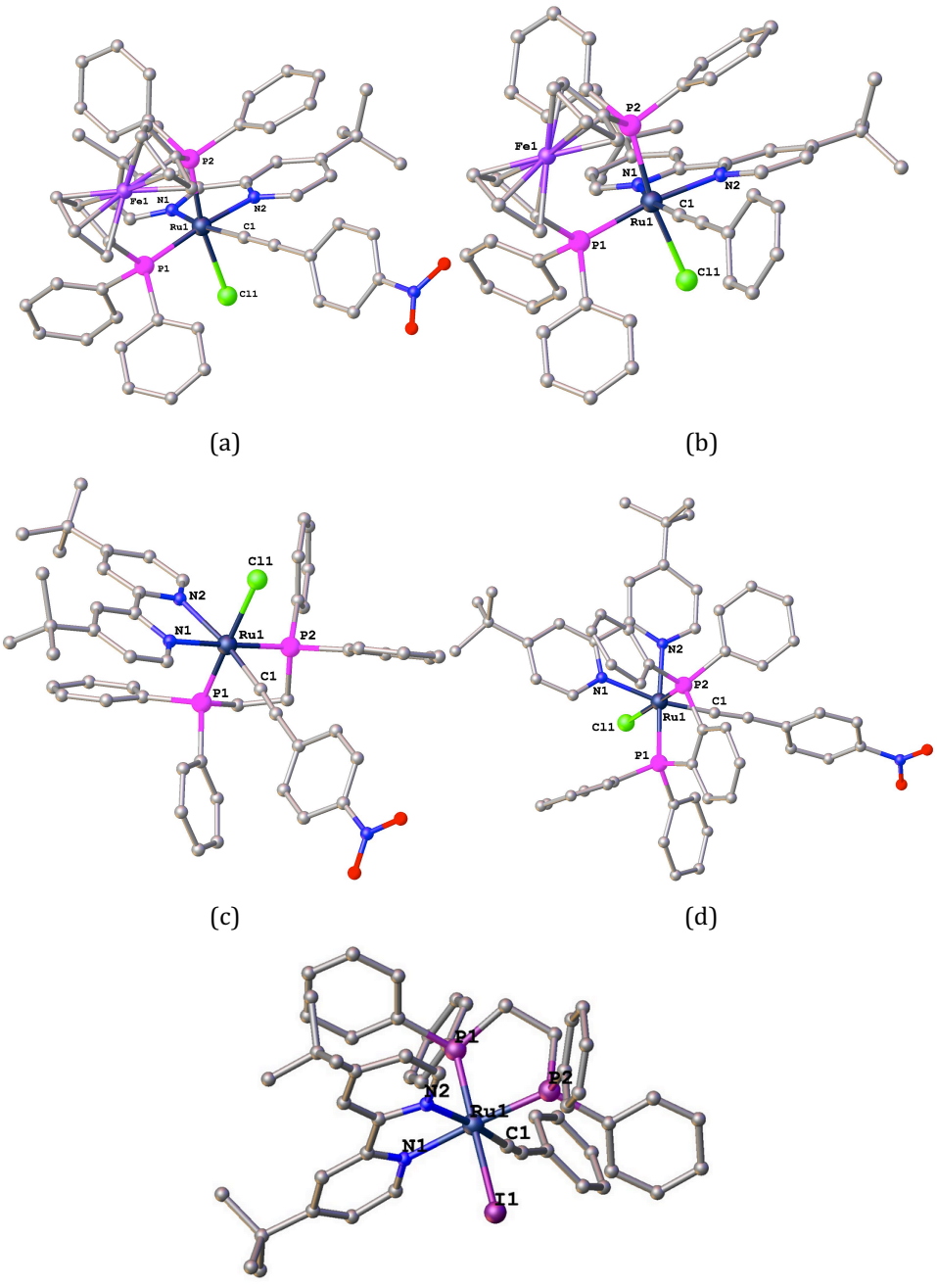

Figure 2.16 Molecular geometry and atomic labeling scheme for *cis*-Ru(C≡C-4-$C_6H_4NO_2$)Cl(dppf)(^{t}Bu-bpy) (**2.2a**) (a), *cis*-Ru(C≡CPh)Cl(dppf)(^{t}Bu-bpy) (**2.2b**) (b), *cis*-Ru(C≡C(4-$C_6H_4NO_2$))Cl(dppe)(^{t}Bu-bpy) (**2.2c**) (c), *cis*-Ru(C≡C(4-$C_6H_4NO_2$))Cl(dppb)(^{t}Bu-bpy) (**2.2e**) (d) and *cis*-Ru(C≡CPh)Cl(dppe)(^{t}Bu-bpy)I (**2.2d***) (e). Hydrogen atoms have been omitted for clarity.

Table 2.4 Selected bond lengths (Å) and angles (°) for *cis*-Ru(C≡C-4-$C_6H_4NO_2$)Cl(dppf)(^{t}Bu-bpy) (**2.2a**), *cis*-Ru(C≡CPh)Cl(dppf)(^{t}Bu-bpy) (**2.2b**), *cis*-Ru(C≡C(4-$C_6H_4NO_2$))Cl(dppe)(^{t}Bu-bpy) (**2.2c**) and *cis*-Ru(C≡C(4-$C_6H_4NO_2$))Cl(dppb)(^{t}Bu-bpy) (**2.2e**) and *cis*-Ru(C≡CPh)(dppe)(^{t}Bu-bpy)I (**2.2d***).

Complexes	**2.2a**	**2.2b**	**2.2c**	**2.2e**	**2.2d***
Bond Lengths					
Ru-P(1)	2.341(3)	2.335(2)	2.2640(16)	2.269(2)	2.263(3)
Ru-P(2)	2.302(3)	2.272(2)	2.2823(15)	2.2315(19)	2.276(3)
Ru-X(1)	2.481(3)	2.488(2)	2.4801(16)	2.5516(15)	2.7792(12)
Ru-N(2)	2.127(9)	2.125(6)	2.176(5)	2.145(6)	2.158(9)
Ru-N(1)	2.195(8)	2.165(7)	2.128(4)	2.170(6)	2.105(8)
Ru-C(1)	2.014(11)	2.022(10)	2.028(7)	2.003(8)	2.139(10)
Bond Angles					
P(2)-Ru-P(1)	97.81(11)	96.51(8)	84.59(5)	85.22(7)	85.44(10)
X(1)-Ru-P(1)	89.10(10)	91.52(7)	176.81(5)	91.92(6)	175.58(8)
X(1)-Ru-P(2)	170.57(9)	171.78(8)	92.70(5)	174.74(7)	92.87(7)
N(2)-Ru-P(1)	172.6(3)	172.39(18)	88.80(14)	177.04(17)	88.9(2)
N(2)-Ru-P(2)	89.5(3)	91.04(18)	104.93(13)	94.87(16)	105.6(2)
N(2)-Ru-X(1)	83.8(3)	80.90(17)	90.28(14)	88.22(16)	87.6(2)
N(1)-Ru-P(1)	101.7(2)	103.71(19)	97.86(13)	106.85(18)	96.8(2)
N(1)-Ru-P(2)	98.2(2)	94.81(18)	177.41(13)	95.44(17)	177.2(2)
N(1)-Ru-X(1)	86.6(2)	84.91(18)	84.88(13)	81.15(16)	85.0(2)
N(1)-Ru-N(2)	75.7(3)	76.5(3)	76.04(17)	76.1(2)	76.2(3)
C(1)-Ru-P(1)	93.0(3)	88.3(2)	91.62(18)	85.1(2)	88.3(3)
C(1)-Ru-P(2)	84.7(3)	87.7(2)	86.59(16)	85.7(2)	83.8(3)
C(1)-Ru-X(1)	88.6(3)	90.9(2)	89.89(18)	98.5(2)	95.6(3)
C(1)-Ru-N(2)	89.1(4)	91.1(3)	168.5(2)	91.9(3)	169.9(4)
C(1)-Ru-N(1)	164.5(4)	167.3(3)	92.5(2)	168.0(3)	94.6(3)

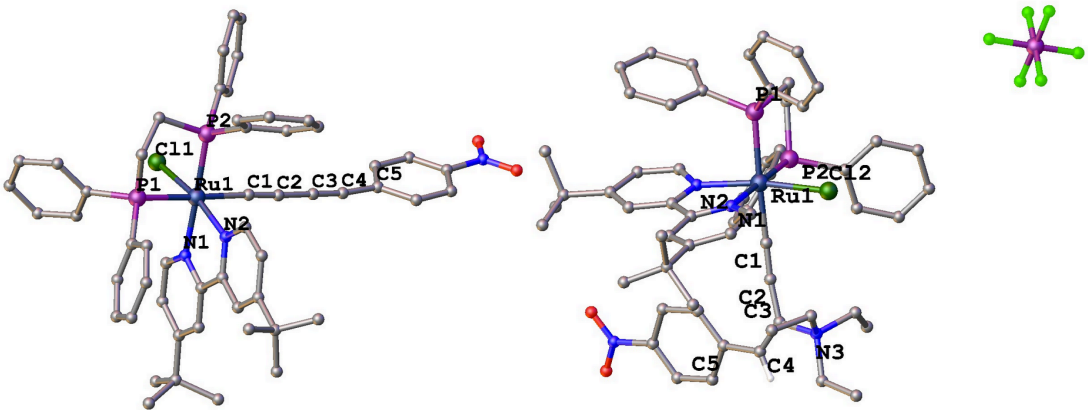

Figure 2.17 Molecular geometry and atomic labeling scheme for *cis*-Ru(C≡CC≡C-4-$C_6H_4NO_2$)Cl(dppe)(^{t}Bu-bpy) (**2.6b**) (left) and *cis*-[Ru(C≡CC(NEt_3)=CH-4-$C_6H_4NO_2$)Cl(dppe)(^{t}Bu-bpy)]PF_6 (**2.7a**) (right). Hydrogen atoms except C=CH have been omitted for clarity.

Table 2.5 Selected bond lengths (Å) and angles (°) for *cis*-Ru(C≡CC≡C-4-$C_6H_4NO_2$)Cl(dppe)(^{t}Bu-bpy) (**2.6b**) and *cis*-[Ru(C≡CC(NEt$_3$)=CH-4-$C_6H_4NO_2$)Cl(dppe)(^{t}Bu-bpy)]PF_6 (**2.7a**).

Complexes	2.7a	2.6b	Complexes	2.7a	2.6b
Bond Lengths					
Ru-C(1)	2.027(6)	2.044(4)	C(3)-C(4)	1.342(8)	1.204(5)
C(1)-C(2)	1.194(9)	1.189(5)	C(4)-C(5)	1.467(9)	
C(2)-C(3)	1.412(5)	1.399(5)	C(3)-N(3)	1.530(8)	
Bond Angles					
Ru-C(1)-C(2)	173.8(5)	176.5(3)	C(3)-C(4)-C(5)	126.4(6)	173.3(4)
C(1)-C(2)-C(3)	171.0(6)	177.4(4)	C(2)-C(3)-N(3)	112.0(5)	
C(2)-C(3)-C(4)	128.1(6)	179.5(4)	N(3)-C(3)-C(4)	119.9(5)	

The structures of the η^3-butenynyl complexes were confirmed by X-ray diffraction, the structural information being provided in Figure 2.18 and Table 2.6. Each ruthenium atom is within bonding distance of seven atoms. The complexes are formally Ru(II) species with one PF_6^- anion in the vicinity of the ruthenium-containing cation. The chelating dppf and butyl-containing ^{t}Bu-bpy ligands occupy two *cis*-disposed positions each. The η^3-butenynyl ligands exhibite *E*-stereochemistry and occupy the remaining coordination sites at the ruthenium centres. Ru, C(1), C(2) and C(3) are approximately in a plane. Notable is the much smaller bite angle of the ^{t}Bu-bpy ligand compared to aforementioned structures, in the present cases affording more space for the η^3-coupling ligands.

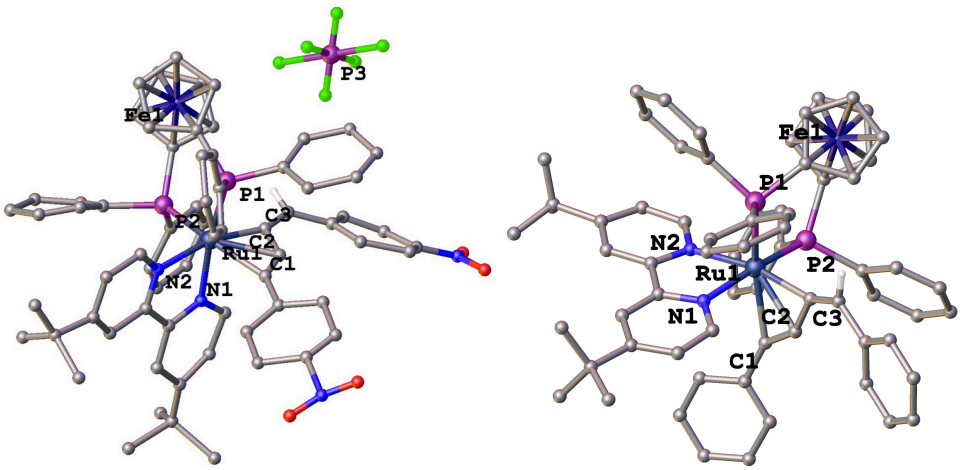

Figure 2.18 Molecular geometry and atomic labeling scheme for *cis*-[Ru(C$_4$H(4-$C_6H_4NO_2$)$_2$)(dppf)(^{t}Bu-bpy)]PF_6 (**2.4a**) (left) *and cis*-[Ru(C$_4$HPh$_2$)(dppf)(^{t}Bu-bpy)]PF_6 (**2.4b**) (right). PF_6 anion in **2.4b** and hydrogen atoms except C=CH have been omitted for clarity.

Table 2.6 Selected bond lengths (Å) and angles (°) for *cis*-[Ru(C$_4$H(4-$C_6H_4NO_2$)$_2$)(dppf)(^{t}Bu-bpy)]PF_6 (**2.4a**) and *cis*-[Ru(C$_4$HPh)$_2$)(dppf)(^{t}Bu-bpy)]PF_6 (**2.4b**).

Complexes	2.4a	2.4b	Complexes	2.4a	2.4b
Bond Lengths					
Ru-P(1)	2.371(4)	2.352(3)	Ru-C(1)	2.290(14)	2.296(10)
Ru-P(2)	2.376(4)	2.374(2)	Ru-C(2)	2.171(15)	2.212(11)
Ru-N(1)	2.126(11)	2.130(7)	Ru-C(3)	2.091(13)	2.100(9)
Ru-N(2)	2.140(12)	2.157(7)			
Bond Angles					
P(2)-Ru-P(1)	99.09(13)	99.73(9)	C(2)-Ru-P(2)	133.7(4)	131.6(3)
N(1)-Ru-P(1)	169.2(3)	168.6(2)	C(2)-Ru-N(1)	87.4(5)	86.4(4)
N(1)-Ru-P(2)	91.6(3)	91.3(2)	C(2)-Ru-N(2)	128.2(5)	130.6(4)
N(2)-Ru-P(1)	100.9(3)	100.0(2)	C(2)-Ru-C(1)	31.6(5)	32.7(4)
N(2)-Ru-P(2)	96.2(3)	95.2(2)	C(3)-Ru-P(1)	90.8(4)	92.2(2)
N(2)-Ru-N(1)	76.5(4)	76.3(3)	C(3)-Ru-P(2)	95.6(4)	93.3(3)
C(1)-Ru-P(1)	86.4(4)	88.6(3)	C(3)-Ru-N(1)	89.3(5)	89.6(3)
C(1)-Ru-P(2)	164.4(4)	162.6(3)	C(3)-Ru-N(2)	161.8(5)	163.7(3)
C(1)-Ru-N(1)	83.5(4)	81.4(3)	C(3)-Ru-C(1)	69.6(5)	71.0(4)
C(1)-Ru-N(2)	97.0(5)	98.4(3)	C(3)-Ru-C(2)	38.1(5)	38.4(4)
C(2)-Ru-P(1)	86.0(4)	88.1(3)			

The molecular geometry of the η^1-coordinated complexes **2.5a** and **2.5b** is confirmed in Figure 2.19. The molecules are all neutral species in contrast to the η^3-butenynyl complexes. The cleavage of the two Ru-C bonds and introduction of chlorine atoms on proceeding from η^3- to η^1-coordination results in the geometry at ruthenium reverting to pseudo-octahedral. The -C=CHRC≡CR ligands retain *E*-stereochemistry. Despite similarities, there is a key difference between the two complexes. In **2.5a**, the chlorine atom is *cis*-disposed with respect to the dppf ligand, while it is *trans*-disposed to one phosphorus atom and *cis* to the other phosphorus atom of the dppe ligand in **2.5b**. Since the chlorine atom is electron-withdrawing, the relative location of the chlorine atom and the dppe ligand may explain the significant signal move downfield in the ^{31}P-NMR study of **2.5b**. The C-Ru-Cl angle in **2.5a** is smaller than that in **2.5b**, presumably a result of accommodating the larger dppf ligand.

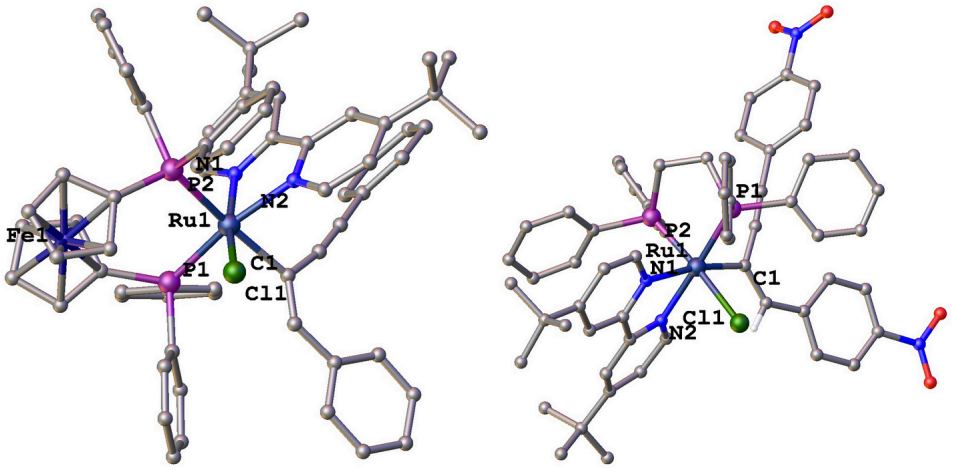

Figure 2.19 Molecular geometry and atomic labeling scheme for *cis*-Ru(C=CHPhC≡CPh)Cl(dppf)(^{t}Bu-bpy) (**2.5a**) (left) and *cis*-Ru(C=CH(4-$C_6H_4NO_2$)C≡C(4-$C_6H_4NO_2$))Cl(dppe)(^{t}Bu-bpy) (**2.5b**) (right). Hydrogen atoms except C=CH have been omitted for clarity.

Table 2.7 Selected bond lengths (Å) and angles (°) for *cis*-Ru(C=CHPhC≡CPh)Cl(dppf)(^{t}Bu-bpy) (**2.5a**) and *cis*-Ru(C=CH(4-$C_6H_4NO_2$)C≡C(4-$C_6H_4NO_2$))Cl(dppe)(^{t}Bu-bpy).

Complexes	2.5a	2.5b	Complexes	2.5a	2.5b
Bond Lengths					
Ru-P(1)	2.3316(19)	2.297(3)	Ru-N(2)	2.124(5)	2.139(8)
Ru-P(2)	2.4535(18)	2.251(3)	Ru-N(1)	2.072(5)	2.184(8)
Ru-Cl(1)	2.4364(17)	2.497(3)	Ru-C(1)	2.153(7)	2.103(9)
Bond Angles					
P(2)-Ru-P(1)	100.36(6)	85.84(10)	N(1)-Ru-Cl(1)	167.52(15)	84.6(2)
Cl(1)-Ru-P(1)	93.18(6)	94.52(9)	N(1)-Ru-N(2)	78.2(2)	76.3(3)
Cl(1)-Ru-P(2)	82.06(6)	172.31(10)	C(1)-Ru-P(1)	86.95(17)	87.2(3)
N(2)-Ru-P(1)	168.76(15)	177.4(2)	C(1)-Ru-P(2)	168.00(16)	98.0(3)
N(2)-Ru-P(2)	90.78(15)	93.1(2)	C(1)-Ru-Cl(1)	88.09(17)	89.7(3)
N(2)-Ru-Cl(1)	89.78(15)	86.2(2)	C(1)-Ru-N(2)	82.3(2)	95.4(3)
N(1)-Ru-P(1)	99.26(15)	101.3(2)	C(1)-Ru-N(1)	93.5(2)	170.1(3)
N(1)-Ru-P(2)	94.63(15)	87.8(2)			

Figure 2.20 displays the molecular geometries obtained by X-ray crystallography of the complexes **2.8a**, **2.8b**, **2.9a** and **2.9b**. **2.8a** is a dimer bridged by three chlorine atoms. Each ruthenium atom is coordinated with one ^{t}Bu-bpy ligand and one PPh_3. Each of the two nitrogen atoms, two phosphorus atoms and two chlorine atoms at the ruthenium centre of the Ru(III) complex **2.8b** are equivalent, and so **2.8b** has the highest symmetry of the complexes studied. The complex **2.9a**, in which the ruthenium atom is coordinated by one ^{t}Bu-bpy ligand and one PPh_3, is effectively the monomer of **2.8a**. It is a Ru(III) complex as is **2.8b**, but unlike **2.8b**, it is a neutral molecule, not in a salt form comprised by the anion and cation; The complex **2.9b** is a chloride salt of a Ru(II) cation with octahedral geometry at the

metal. There are no symmetry elements: ruthenium atom is coordinated by two ^{t}Bu-bpy ligands and one PPh_3, and each of the atoms, except the ^{t}butyl groups in the ^{t}Bu-bpy ligands, exhibits different signals in the NMR spectra.

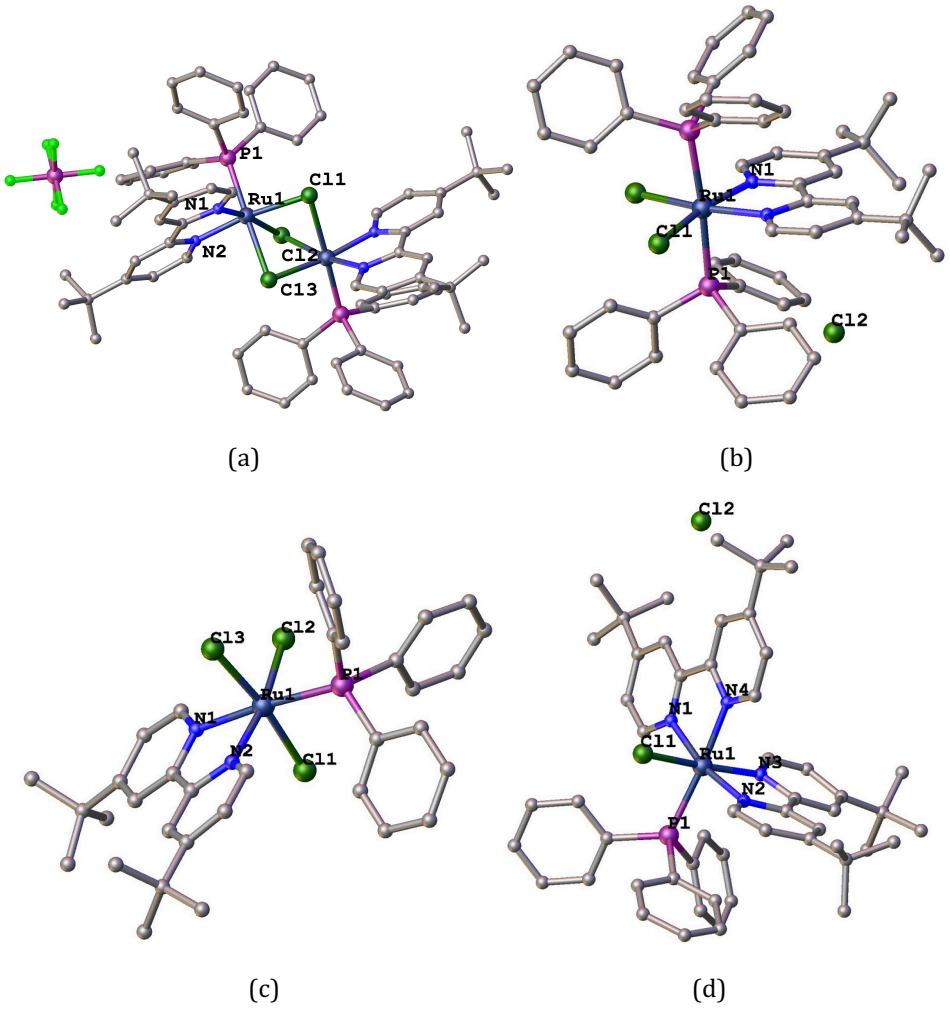

Figure 2.20 Molecular geometry and atomic labeling scheme for $[Ru_2(\mu\text{-}Cl)_3(PPh_3)_2(^{t}Bu\text{-}bpy)_2]PF_6$ (**2.8a**) (a), $[RuCl_2(PPh_3)_2(^{t}Bu\text{-}bpy)]Cl$ (**2.8b**) (b), $RuCl_3(PPh_3)(^{t}Bu\text{-}bpy)$ (**2.9a**) (c) and $[RuCl(PPh_3)(^{t}Bu\text{-}bpy)_2]Cl$ (**2.9b**) (d). Hydrogen atoms have been omitted for clarity.

The molecular geometry of the complexes **2.3a**, **2.3a-1** and **2.3a-2**, related to the oxidation of the vinylidene complex, are shown in Figure 2.21. All of the three complexes possess six-coordinate octahedral geometries at ruthenium and all have PF_6^- counter-ions. The vinylidene ligand has reacted to form a C≡O ligand in **2.3a**. **2.3a-1** has three phosphorus atoms coordinated to ruthenium, and confirms insertion of one oxygen atom between the ruthenium atom and the dppb ligand. Complex **2.3a-2** has a ruthenium core exactly the same as **2.1c**, except that the oxidation state of Ru is +3.

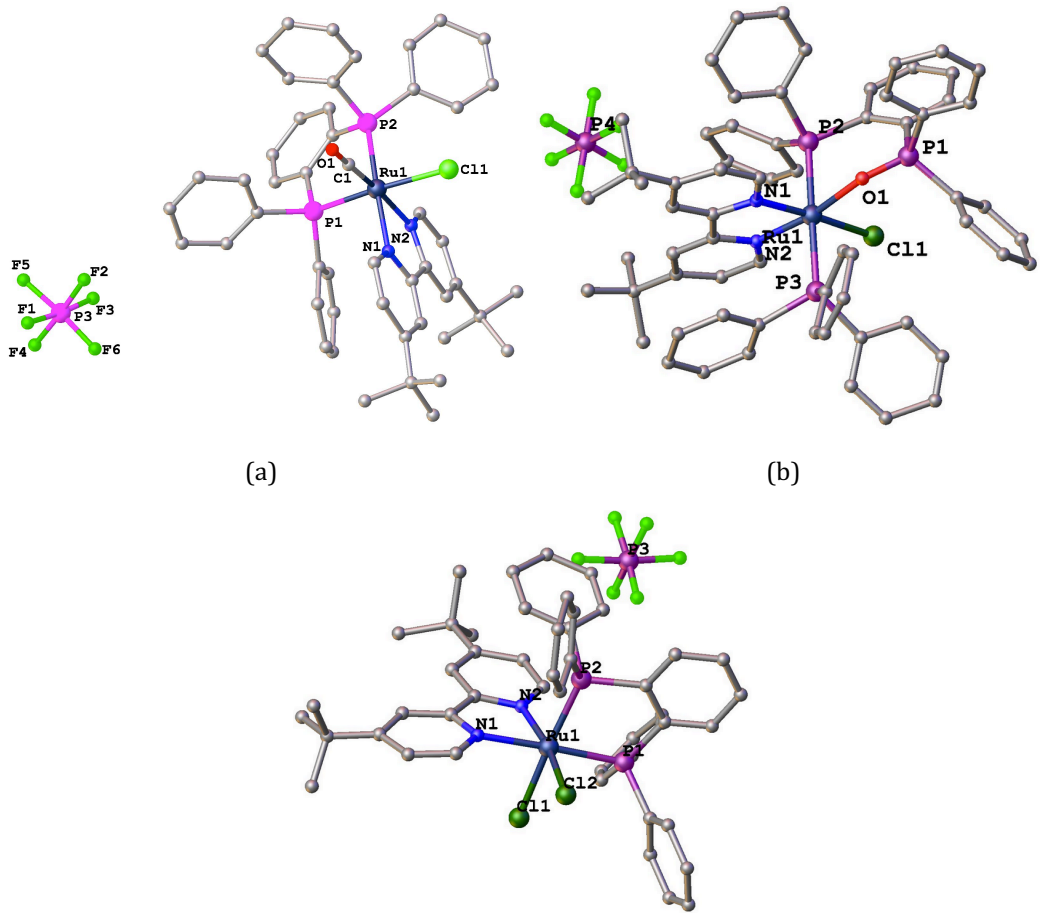

Figure 2.21 Molecular geometry and atomic labeling scheme for *cis*-[Ru(C≡O)Cl(dppb)(ᵗBu-bpy)]PF_6 **(2.3a) (a)**, [RuCl(ᵗBu-bpy)(O-dppb)(PPh_3)]PF_6 (**2.3a-1**) (b) and *cis*-[$RuCl_2$(dppb)(ᵗBu-bpy)]PF_6 (**2.3a-2**) (c). Hydrogen atoms have been omitted for clarity.

2.4 LINEAR OPTICAL STUDIES

Linear optical studies were conducted on a UV-Vis spectrometer in CH_2Cl_2 using a quartz cell at 298 K. The UV-Vis absorption spectra are displayed below.

The spectra of *cis*-$RuCl_2$(dppf)(ᵗBu-bpy) (**2.1a**), *cis*-$RuCl_2$(dppe)(ᵗBu-bpy) (**2.1b**) and *cis*-$RuCl_2$(dppb)(ᵗBu-bpy) (**2.1c**) are shown in Figure 2.22. All the spectra are similar, with weaker broad absorption in the visible region and stronger absorption in the UV region. The bands in the lower energy region are tentatively assigned as MLCT transitions from the ruthenium centre to the ᵗBu-bpy ligand. The intense bands at higher energy are proposed to be intra-ligand π-π^* transitions between the diphosphine ligands and the ᵗBu-bpy ligand. **2.1a** and **2.1c** have slightly larger molar extinction coefficient than **2.1b**.

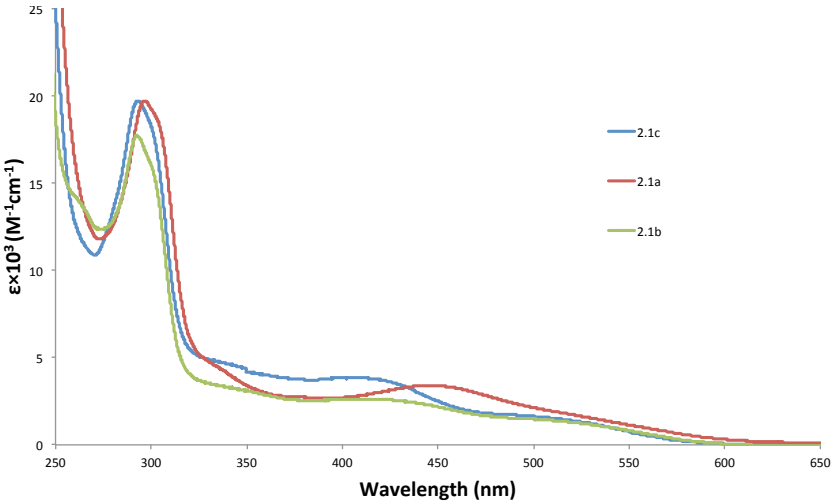

Figure 2.22 UV-Vis absorption spectra (CH_2Cl_2, 298 K) for *cis*-$RuCl_2$(N^N)(P^P) complexes.

The spectra of *cis*-Ru(C≡C-4-$C_6H_4NO_2$)Cl(dppf)(^{t}Bu-bpy) (**2.2a**), *cis*-Ru(C≡CPh)Cl(dppf)(^{t}Bu-bpy) (**2.2b**), *cis*-Ru(C≡C-4-$C_6H_4NO_2$)Cl(dppe)(^{t}Bu-bpy) (**2.2c**) and *cis*-Ru(C≡C-4-$C_6H_4NO_2$)Cl(dppb)(^{t}Bu-bpy) (**2.2e**) are displayed in Figure 2.23. The complex **2.2b** has the highest intensity band in the high-energy region with weak absorption in the visible region. The mono-alkynyl complexes with a nitro group show the same trend as **2.2b**, exhibiting an intense peak around 300 nm, but show differences in the visible region as their spectra contain relatively intense broad bands. Generally, the absorption intensities are similar to those of the *cis*-$RuCl_2$(N^N)(P^P) complexes. The bands in the UV region are attributed to intra-ligand π-π^* transitions from the diphosphine ligands to the ^{t}Bu-bpy ligand. The introduction of nitro group in **2.2a**, **2.2c** and **2.2e** induces broad bands in the UV-Vis spectra, because it enhances the MLCT from the ruthenium atoms and alkynyl ligands to the nitro groups as well as ILCT. In **2.2b**, the weak absorption in the visible region is induced by MLCT (from the ruthenium atom to the ^{t}Bu-bpy ligand) and LLCT (from the alkynyl group to the ^{t}Bu-bpy ligand).

Figure 2.24 shows the UV-Vis absorption spectra of the ruthenium dppf complexes *cis*-$RuCl_2$(dppf)(^{t}Bu-bpy) (**2.1a**), *cis*-Ru(C≡C-4-$C_6H_4NO_2$)Cl(dppf)(^{t}Bu-bpy) (**2.2a**) and *cis*-Ru(C≡CPh)Cl(dppf)(^{t}Bu-bpy) (**2.2b**). The complexes **2.1a** and **2.2b** are similar, while the significant absorption in the low-energy region induced by the nitro group distinguishes **2.2a** from the other two. Both the absorption intensities of **2.2a** and **2.2b** are stronger than those of **2.1a**.

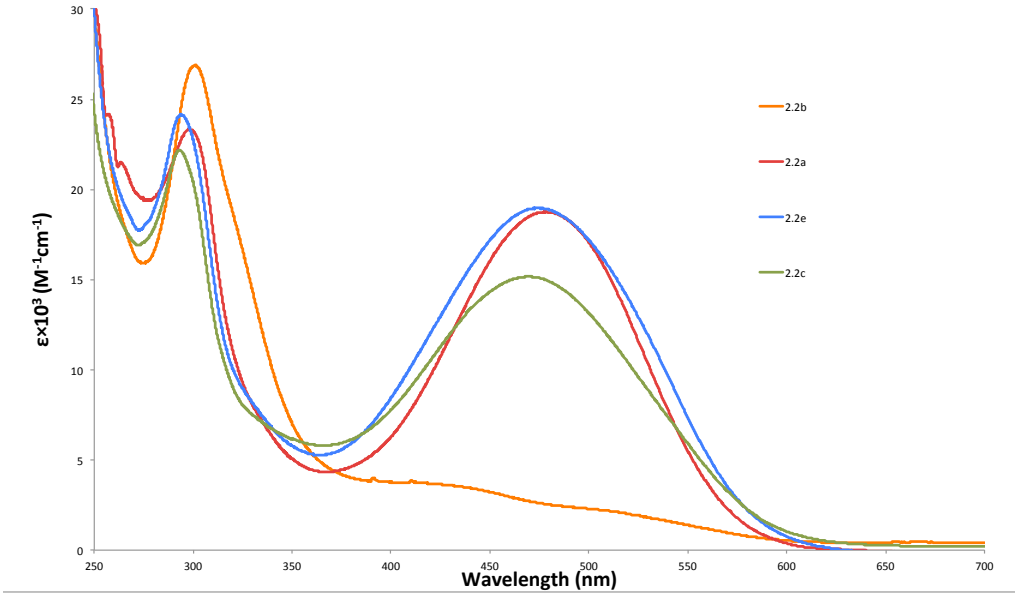

Figure 2.23 UV-Vis absorption spectra (CH_2Cl_2, 298 K) of *cis*-Ru(C≡C-4-C_6H_4R)Cl(N^N)(P^P), (R = -H, -NO_2) complexes.

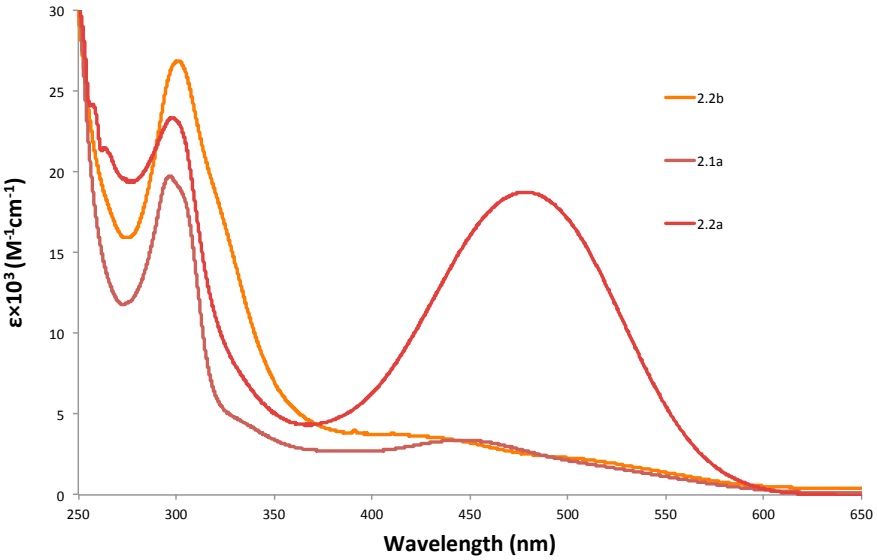

Figure 2.24 UV-Vis absorption spectra (CH_2Cl_2, 298 K) of Ru(dppf)(^{t}Bu-bpy) complexes.

The complexes *cis*-Ru(C≡C-4-$C_6H_4NO_2$)Cl(dppe)(^{t}Bu-bpy) (**2.2c**), *cis*-Ru(C≡C-4-$C_6H_4NO_2$)Cl(dppb)(^{t}Bu-bpy) (**2.2e**), *cis*-Ru(C≡CC≡C-4-$C_6H_4NO_2$)Cl(dppe)(^{t}Bu-bpy) (**2.6b**) and *cis*-Ru(C≡CC≡C-4-$C_6H_4NO_2$)Cl(dppb)(^{t}Bu-bpy) (**2.6c**) differ in the number of C≡C bonds and co-ligands. The UV-Vis spectra of **2.2c**, **2.2e**, **2.6b** and **2.6c** are collected in Figure 2.25. The dppe and dppb complexes follow the same trend. Compared with **2.2c** and **2.2e**, the absorption intensities of **2.6b** and **2.6c** are significantly stronger, and a blue shift is seen for the bands attributed to the MLCT involving the nitro group. The explanation is as follow: 1) in **2.6b** and **2.6c**,

the π-conjugated chain is increased by one more C≡C bond. Since the absorption in the visible region is mainly contributed by the MLCT from Ru(C≡C-R)Cl to the nitro group, a longer π-conjugated chain may enhance the charge transfer. 2) The absorption in the high-energy region is dominated by the intra-ligand π-π^* transitions from the diphosphine ligands to the ^{t}Bu-bpy ligand. The Cl is *trans* to a phosphorus atom in **2.2c** and **2.2e**, while a π-electron-rich and electron-donating ligand, the C≡CC≡C-R ligand, is *trans* to the phosphorus atom at the same position in **2.6b** and **2.6c**. The replacement of Cl by the C≡CC≡C-R ligand may influence the transition.

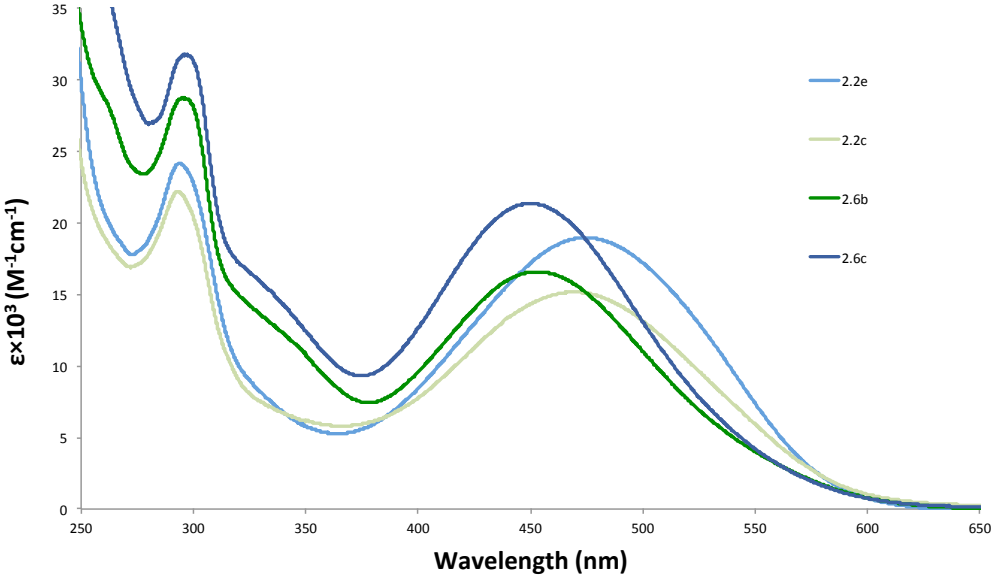

Figure 2.25 UV-Vis absorption spectra (CH_2Cl_2, 298 K) of ruthenium mono-alkynyl complexes.

The UV-Vis absorption spectra of *cis*-[Ru(C_4H(4-$C_6H_4NO_2$)$_2$)(dppf)(^{t}Bu-bpy)]PF_6 (**2.4a**), *cis*-[Ru(C_4HPh_2)(dppf)(^{t}Bu-bpy)]PF_6 (**2.4b**), *cis*-[Ru(C_4HPh_2)(dppe)(^{t}Bu-bpy)]PF_6 (**2.4c**) and *cis*-[Ru(C_4H(4-$C_6H_4NO_2$)$_2$)(dppb)(^{t}Bu-bpy)]PF_6 (**2.4d**) are shown in Figure 2.26. There are three absorption peaks in the spectra of each complex except **2.4b** which lacks nitro groups. The intense absorptions in the UV region are assigned as intra-ligand π-π^* transitions from the diphosphine ligands to the ^{t}Bu-bpy ligand, consistent with the other Ru(N^N)(P^P) complexes. Both MLCT and ILCT transitions contribute to the absorption in the visible region, but their individual contributions cannot be deconvoluted.

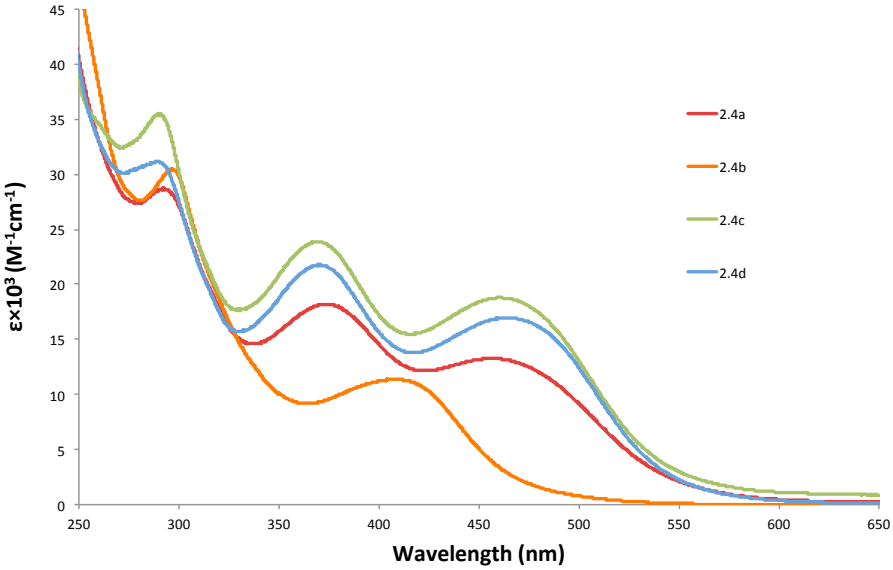

Figure 2.26 UV-Vis absorption spectra (CH_2Cl_2, 298 K) of ruthenium η^3-butenynyl complexes.

2.5 ELECTROCHEMICAL STUDIES

The electrochemical behavior of the Ru(N^N)(P^P) complexes was investigated by means of cyclic and square-wave/differential pulse voltammetry in distilled CH_2Cl_2 with 0.1 M $^nBu_4NPF_6$ as the supporting electrolyte. Under the same conditions, the ferrocene/ferrocenium (FcH/FcH^*) oxidations are one-electron, reversible redox processes at 100 mV/s scan rate.

The electrochemical data of the $RuCl_2$(N^N)(P^P) complexes are tabulated in Table 2.8. All the complexes exhibit reversible processes. **2.1a** undergoes two redox processes, the peak at 0.69 V being assigned as the $Fe^{II/III}$ redox couple based on previous reports [52, 53, 67]. The electron-withdrawing ferrocenium decreases the electron density at the ruthenium centre, making the ruthenium oxidation more difficult. Thus, the oxidation potential of **2.1a** at 1.11 V is much higher than those of **2.1b** and **2.1c** at 0.68 and 0.70 V, respectively. This also shows that **2.1a** has the potential to be developed as a multi-stated switch. Both the complexes **2.1b** and **2.1c** possess one redox active center. The half-wave potential ($E_{1/2}$) of **2.1c** is more anodic than that of **2.1b**, indicating that the dppb ligand withdraws more electron density from the ruthenium centre and makes the oxidation more difficult. Thus, the dppb ligand is more capable of stabilizing the ruthenium centre than the dppe ligand.

Table 2.8 Electrochemical data of $RuCl_2$(N^N)(P^P) complexes (E in volts, I in μA).

Compound No.	Peak No.	E_c	E_a	ΔE	$E_{1/2}$	I_c	I_a	I_a / I_c
2.1a	1	0.76	0.61	0.15	0.69	1.74	1.67	0.96
	2	1.18	1.04	0.14	1.11	1.00	0.99	0.99
2.1b	1	0.72	0.63	0.096	0.68	2.80	2.81	1.00
2.1c	1	0.74	0.67	0.076	0.70	2.16	2.18	1.00

Note: **2.1a** = *cis*-$RuCl_2$(dppf)(^{t}Bu-bpy) **2.1b** = *cis*-$RuCl_2$(dppe)(^{t}Bu-bpy) **2.1c** = *cis*-$RuCl_2$(dppb)(^{t}Bu-bpy)

With the introduction of the alkynyl group, the complexes have different behaviours. The electrochemical data of the Ru(C≡C-R)Cl(N^N)(P^P) complexes are summarized in Table 2.9. Generally, the Ru(C≡C-R)Cl(N^N)(P^P) complexes can be catalogued as two types: nitro complexes and non-nitro complexes. All the nitro groups in the nitro-containing complexes except **2.2c** and **2.2e** exhibit quasi-reversible processes, with $E_{1/2}$ ranging from -1.11 to -0.92 V. Each of the complexes **2.2c**, **2.2e**, **2.6b**, **2.6c** and **2.7a** has one reversible redox wave, with no obvious difference on the values of the half-wave potential with that of the corresponding $RuCl_2$(^{t}Bu-bpy)(P^P). Unlike the other analogues, the complex **2.2a** bearing the dppf ligand has no reversible processes. In contrast, complex **2.7a** shows significant stability with a shift of the $Ru^{II/III}$ redox potential to higher value at 0.84 V.

The non-nitro complexes **2.2b**, **2.2d** and **2.2f** exhibit complicated processes in their electrochemical studies, so a combination of cyclic and square-wave (SQWV) voltammetry or differential pulse (DPV) voltammetry was conducted. The results of **2.2b** and **2.2d** are shown in Figure 2.27. Both of them have irreversible waves around 0.60 and 1.05 V. The expected redox wave in **2.2b** induced by the $Fe^{II/III}$ redox couple could not be observed. Thus, it seems clear that chemical reactions occur during the oxidation of the non-nitro complexes **2.2b**, **2.2d** and **2.2f**.

To the date, the redox behaviour of the ruthenium η^3- or η^1-butenynyl complexes have not been reported. In this Chapter, the electrochemical studies on such complexes were conducted and the data is summarized in Table 2.10. The complex **2.4b** displayed similar redox behaviour to **2.2b** but at higher potentials. The oxidation of other nitro complexes becomes more difficult as well, and no reversible redox waves could be observed. The two nitro groups in each complex show two quasi-reversible processes ranging from -0.78 to -0.91 V, which could be

distinguished by square-wave voltammetry studies, as shown in Figure 2.28. In the complex **2.4c**, the peak at 0.56 V is the redox wave from the reference chemical, the FcH/FcH* redox couple, and the other peaks represent the redox behaviour of **2.4c**. The area under the peak at ca. 1.3 V is smaller than that of the reference peak that corresponding to a one-electron reversible redox process. It indicates that there is no simple one-electron $Ru^{II/III}$ redox process occurring in **2.4c**. The other nitro complexes show the same trend.

Table 2.9 Electrochemical data of Ru(C≡CR)Cl(N^N)(P^P) complexes (E in volts, I in μA).

Compound No.	Peak No.	E_c	E_a	ΔE	$E_{1/2}$	I_c	I_a	I_a / I_c
2.2a	1	-1.01	-1.20	0.18	-1.11	2.29	2.29	1.0
	2	0.76	0.71	0.054	-	2.11	0.62	0.29
	3	1.17	1.05	0.12	-	2.36	2.21	0.94
	4							
2.2b	1	0.60	0.52	0.080	-	1.68	0.75	0.45
	2	1.03	0.96	0.068	1.00	1.42	1.39	0.98
	3	1.16	1.07	0.098	-	38.0	15.5	0.41
2.2c	1	-1.20	-1.00	0.20	-	0.80	0.47	0.59
	2	0.70	0.63	0.076	0.67	0.39	0.38	0.97
2.2d	1	0.63		0.11	-	0.53	0.33	0.62
	2	1.11		0.22	-	0.44	0.33	0.75
2.2e	1	-1.16	-1.01	0.15	-	0.47	0.42	0.89
	2	0.72	0.67	0.056	0.70	0.39	0.39	1.0
2.2f	1	0.77		0.084	-	0.71	0.66	0.93
	2	1.37		0.12	-	0.35	0.26	0.74
	3	1.71		-	-	0.89	0.26	0.29
2.3a	1	-1.37		-	-	-10.4	-9.06	0.87
	2	-1.18		-	-			
2.6b	1	-0.87	-1.01	0.13	-0.94	0.86	0.85	0.99
	2	0.69	0.64	0.054	0.67	0.89	0.86	0.97
2.6c	1	-0.97	-0.87	0.10	-0.92	0.56	0.56	1.0
	2	0.71	0.67	0.038	0.69	0.57	0.56	0.98
2.7a	1	-0.87	-0.96	0.084	-0.92	1.38	1.37	0.99
	2	0.87	0.80	0.068	0.84	1.37	1.37	1.0

Note: **2.2a** = *cis*-Ru(C≡C-4-$C_6H_4NO_2$)Cl(dppf)(^{t}Bu-bpy) **2.2b** = *cis*-Ru(C≡CPh)Cl(dppf)(^{t}Bu-bpy)

2.2c = *cis*-Ru(C≡C-4-$C_6H_4NO_2$)Cl(dppe)(^{t}Bu-bpy) **2.2d** = *cis*-Ru(C≡CPh)Cl(dppe)(^{t}Bu-bpy)

2.2e = *cis*-Ru(C≡C-4-$C_6H_4NO_2$)Cl(dppb)(^{t}Bu-bpy) **2.2f** = *cis*-Ru(C≡CPh)Cl(dppb)(^{t}Bu-bpy)

2.3a = *cis-[Ru(C≡O)Cl(dppb)(^{t}Bu-bpy)]* PF_6 **2.6b** = *cis*-Ru(C≡CC≡C-4-$C_6H_4NO_2$)Cl(dppe)(^{t}Bu-bpy)

2.2c = *cis*-Ru(C≡CC≡C-4-$C_6H_4NO_2$)Cl(dppb)(^{t}Bu-bpy)

2.7a = *cis-[Ru(C≡CC(NEt$_3$)=CH-4-$C_6H_4NO_2$)Cl(dppe)(^{t}Bu-bpy)]*PF_6

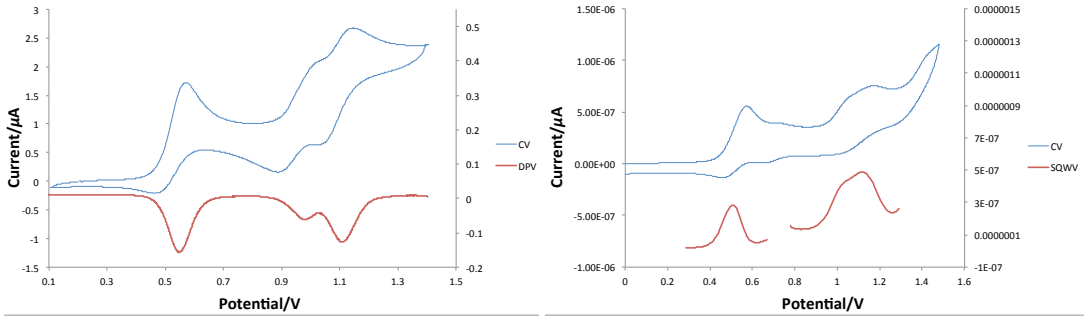

Figure 2.27 Electrochemical studies of the complexes **2.2b** (left) and **2.2d** (right).

Table 2.10 Electrochemical data of ruthenium η^3- and η^1-butenynyl coupling complex (E in volts, I in μA).

Compound No.	Peak No.	E_c	E_a	ΔE	$E_{1/2}$	I_c	I_a	I_a / I_c
2.4a	1	-0.71	-0.85	0.14	-0.78	4.58	4.47	0.98
	2	1.08	1.01	0.076	1.04	4.04	3.95	0.98
2.4b	1	1.04	0.98	0.060	-	1.23	0.97	0.79
	2	1.37	1.27	0.098	-	1.35	0.29	0.21
	3	1.56	1.48	0.078	1.52	1.74	1.69	0.97
2.4c	1	-0.91		-	-	1.16	1.13	0.97
	2	-0.83		-	-	1.16	1.13	0.97
	3	1.35	1.26	0.086	-	0.86	0.65	0.76
2.4d	1	-0.86		-	-	1.21	1.21	1.0
	2	-0.78		-	-	1.21	1.21	1.0
	3	1.38	1.28	0.096	-	0.92	0.79	0.86
2.5b	1	-0.85		-	-	1.02	1.02	1.0
	2	-0.78		-	-			
	3	1.22	1.01	0.21	-	0.51	0.20	0.39
	4	1.33	1.27	0.066	-	3.70	2.40	0.65

Note: **2.4a** = *cis*-[Ru(C$_4$H(4-C$_6$H$_4$NO$_2$)$_2$)(dppf)(ᵗBu-bpy)]PF$_6$ **2.4b** = *cis*-[Ru(C$_4$HPh$_2$)(dppf)(ᵗBu-bpy)]PF$_6$

2.4c = *cis*-[Ru(C$_4$H(4-C$_6$H$_4$NO$_2$)$_2$)(dppe)(ᵗBu-bpy)]PF$_6$ **2.4d** = *cis*-[Ru(C$_4$H(4-C$_6$H$_4$NO$_2$)$_2$)(dppb)(ᵗBu-bpy)]PF$_6$

2.5b = *cis*-[Ru(C=CH(4-C$_6$H$_4$NO$_2$)C≡C(4-C$_6$H$_4$NO$_2$))Cl(dppe)(ᵗBu-bpy)]

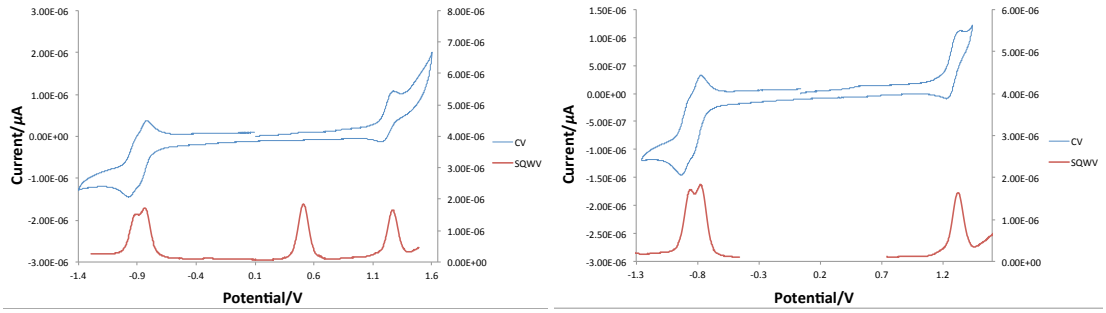

Figure 2.28 Electrochemical studies of the complexes **2.4c** (left) and **2.4b** (right).

The redox data of the Ru(PPh$_3$)$_n$(ᵗBu-bpy)$_n$ complexes are tabulated in Table 2.11. The complex **2.8a** bearing two ruthenium centres has two one-electron reversible Ru$^{II/III}$ redox processes, one at 0.83 V and the other at 1.59 V. The first ruthenium oxidation makes the second Ru^{II}-oxidation much more difficult. The Ru(III)

complex **2.9a** has two one-electron irreversible redox processes, as shown in Figure 2.29, assigned as $Ru^{III/IV}$ and ^{t}Bu-bpy/^{t}Bu-bpy^{+} redox couples. The Ru(II) complex **2.9b** has a dominant wave around 1.06 V with a shoulder towards higher oxidation potential, assign as $Ru^{II/III}$ redox processes. Compared with the FcH/FcH* redox process (the signal at 0.56 V in the SQWV study shown in Figure 2.29), it proves not to be a one-electron redox process. The process occurring in the cathodic region is regarded as corresponding to the ^{t}Bu-bpy/^{t}Bu-bpy^{+} couple.

Table 2.11 Electrochemical data of $Ru(PPh_3)_n(^{t}Bu\text{-}bpy)_n$ complexes (n = 1, 2) (E in volts, I in μA).

Compound No.	Peak No.	E_c	E_a	ΔE	$E_{1/2}$	I_c	I_a	I_a / I_c
2.8a	1	0.87	0.79	0.074	0.83	1.62	1.62	1.0
	2	1.63	1.55	0.080	1.59	2.10	1.93	0.92
2.9a	1	1.51	1.40	0.11	-	5.35	2.59	0.48
	2	-0.11	-0.017	0.092	-	3.02	1.40	0.46
2.9b	1	1.09	1.03	0.058	1.06	0.69	0.68	0.99

Note: **2.8a** = $[Ru_2(\mu\text{-}Cl_3)(PPh_3)_2(^{t}Bu\text{-}bpy)_2]PF_6$ **2.9a** = $RuCl_3(PPh_3)(^{t}Bu\text{-}bpy)$ **2.9b** = $[RuCl(PPh_3)(^{t}Bu\text{-}bpy)_2]Cl$

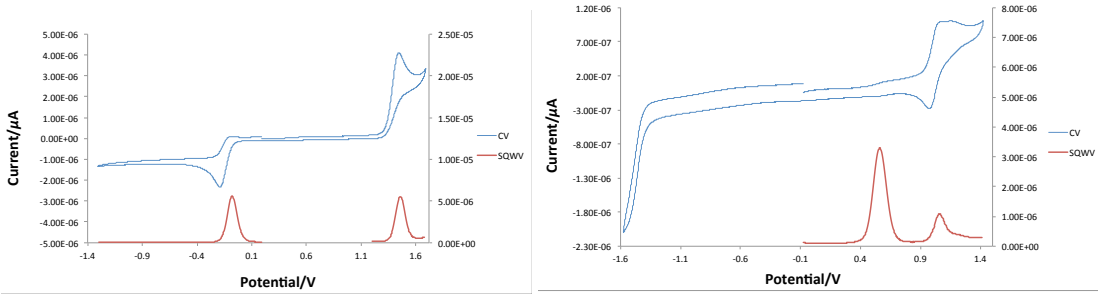

Figure 2.29 Electrochemical studies of the complexes **2.9a** (left) and **2.9b** (right).

2.6 SPECTROELECTROCHEMICAL STUDIES

Combining electrochemistry with various spectroscopic techniques provides the possibility to probe into the effect of electron transfer upon the bonding and the structure of the complexes. Herein, the UV-Vis spectroelectrochemical measurements were conducted for the complexes **2.1a**, **2.1b**, **2.1c**, **2.2c**, **2.2e**, **2.6b** and **2.7a** which exhibited reversible redox processes in cyclic voltammetry studies. The data collected between -15 - 30 ^{o}C in CH_2Cl_2 using an OTTLE cell are summarized in Table 2.12.

Table 2.12 UV-Vis-NIR spectroelectrochemical data for the Ru(N^N)(P^P) complexes (λ_{max} in nm, ε in $M^{-1}\,cm^{-1}$).

Complexes	[M] λ_{max} [ε 10^3]	$[M]^+$ λ_{max} [ε 10^3]	$[M]^{2+}$ λ_{max} [ε 10^3]
2.1a	296 [19.7]	295 [15.4]	301 [21.8]
cis-$RuCl_2$(dppf)(^{t}Bu-bpy)	445 [3.40]	309 [13.7]	363 [5.81]
		377 [3.55]	
		580 [0.832]	
2.1b	293 [17.7]	307 [12.1]	
cis-$RuCl_2$(dppe)(^{t}Bu-bpy)		340 [3.45]	
		560 [1.13]	
2.1c	293 [19.7]	313 [13.8]	
cis-$RuCl_2$(dppb)(^{t}Bu-bpy)	408 [3.85]^{sh}	342 [4.63]	
		580 [1.19]	
2.2c	293 [22.2]	394 [10.9]	
cis-Ru(C≡C-4-$C_6H_4NO_2$)Cl(dppe)(^{t}Bu-bpy)	469 [15.2]	738 [0.844]	
2.2e	294 [24.2]	295 [21.0]	
cis-Ru(C≡C-4-$C_6H_4NO_2$)Cl(dppb)(^{t}Bu-bpy)	474 [19.0]	451 [10.0]	
		738 [2.79]	
2.6b	295 [28.7]	298 [19.0]	
cis-Ru(C≡CC≡C-4-$C_6H_4NO_2$)Cl(dppe)(^{t}Bu-bpy)	452 [16.6]	374 [15.7]	
		496 [3.86]	
		784 [4.97]	
2.7a	296 [33.9]	301 [23.7]	
cis-[Ru(C≡CC(NEt_3)=CH-4-$C_6H_4NO_2$)Cl (dppe)(^{t}Bu-bpy)]PF_6	439 [12.1]	308 [23.9]	
		363 [15.1]	
		597 [2.61]	

Figure 2.30 shows the spectroelectrochemical behaviour of the first oxidation induced by the dppf ligand in **2.1a**. The intra-ligand π-π^* transitions band in the UV region split into two sharp peaks at 295 and 309 nm with decreased intensities. A blue shift in the MLCT band in the visible region to the near UV region at 376 nm was observed. The first oxidation proved to be irreversible, and there were no isosbestic points in the spectra of the second oxidation from Ru^{II} to Ru^{III}. Although it showed two reversible waves in the cyclic voltammetry study, the result of the spectroelectrochemistry study suggested that the complex **2.1a** was not a possible candidate for multiple states switching applications. The analogous complexes **2.1b** and **2.1c** to **2.1a** have similar spectra plots with little significance difference. The plots are shown in Figure 2.31 and 2.32. The intra-ligand π-π^* transitions band in the UV region did not split into two sharp peaks as **2.1a** did, but red-shifted to 307 and 313 nm in **2.1b** and **2.1c**, respectively, with a shoulder at a higher-energy wavelength.

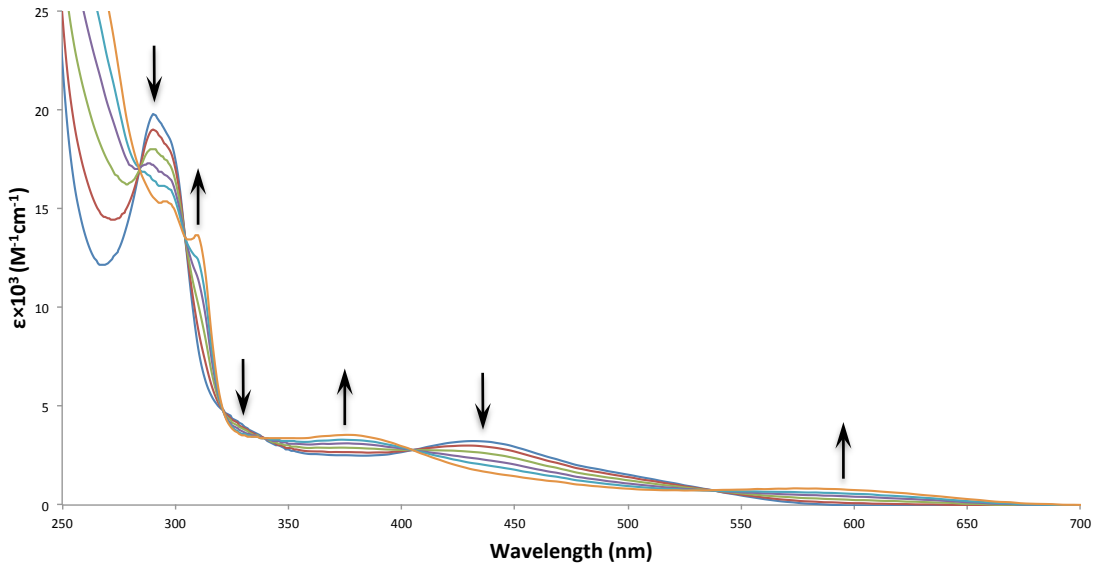

Figure 2.30 UV-Vis-NIR spectroelectrochemical plot of **2.1a** at 0.7 V [243 – 258 K, 1st oxidation].

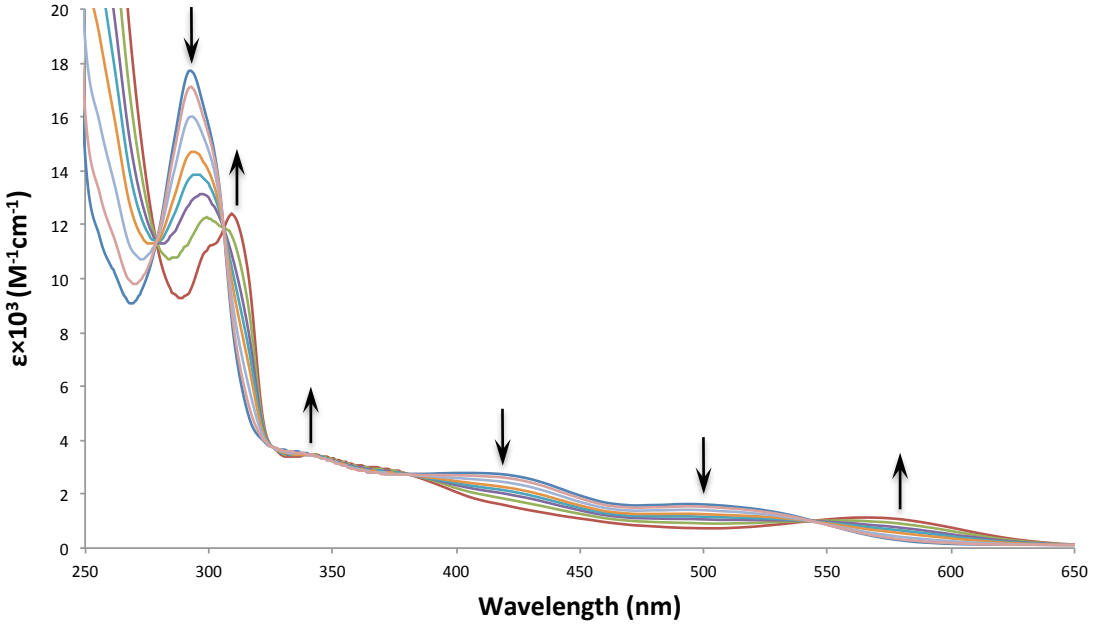

Figure 2.31 UV-Vis-NIR spectroelectrochemical plot of **2.1b** at 0.8 V [243 – 258 K].

The spectroelectrochemical plots of the mono-alkynyl complexes **2.2c** and **2.2e** are shown in Figure 2.33 and 2.34. The intensities of the intra-ligand π-π^* transitions band in the UV region decrease, and a blue-shift is observed in the MLCT absorptions associated with the nitro groups in each complex. However, the complexes **2.2c** and **2.2e** do show difference. Firstly, the intra-ligand π-π^* transitions band in the UV region of **2.2e** changes to a peak of weaker intensity at 295 nm with a closely-located shoulder, while the analogous band in the UV region of **2.2c** disappears. Secondly, compared with **2.2e**, the MLCT band in the visible

region of **2.2c** experiences a greater blue shift of 75 nm with stronger absorption. Finally, **2.2e** has a more distinct new band forming at 738 nm. The oxidations of the complexes **2.2c** and **2.2e** were irreversible processes, with 37 -52 % and 46 – 58 % recovery rates, respectively.

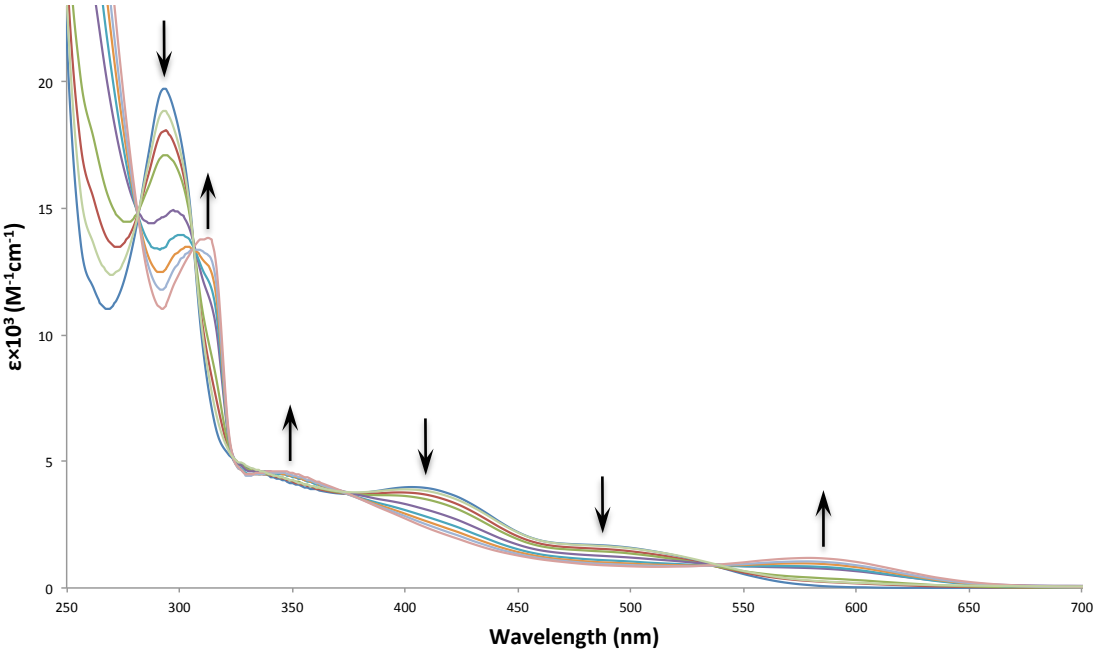

Figure 2.32 UV-Vis-NIR spectroelectrochemical plot of **2.1c** [243 – 258 K].

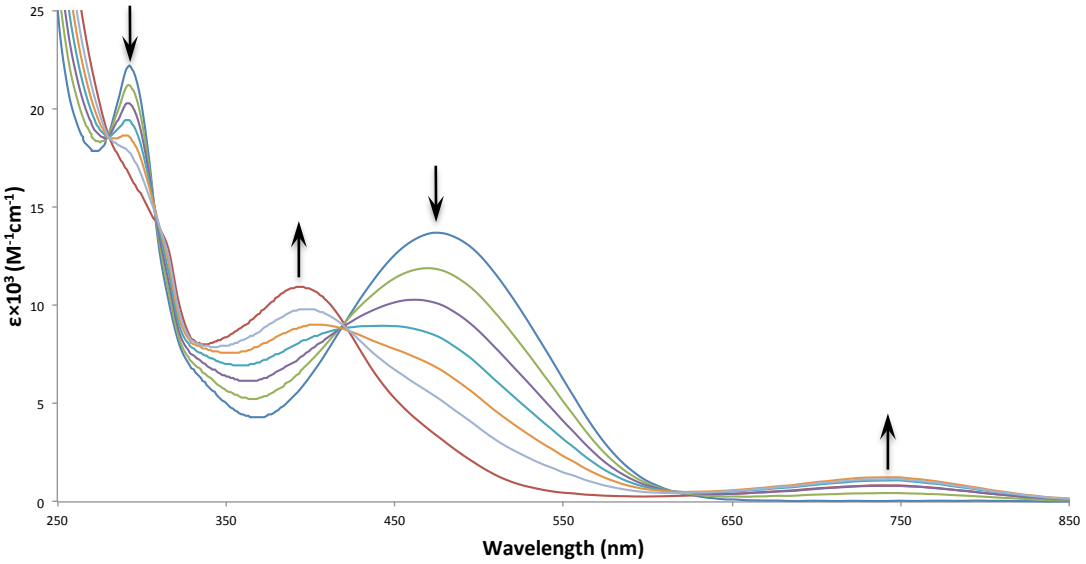

Figure 2.33 UV-Vis-NIR spectroelectrochemical plot of **2.2c** [298.15 K].

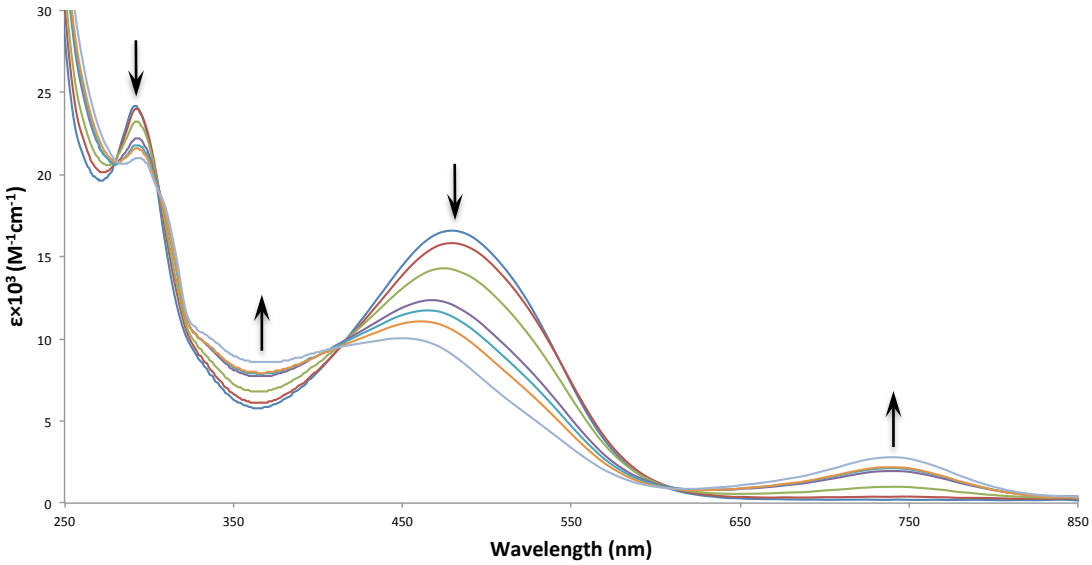

Figure 2.34 UV-Vis-NIR spectroelectrochemical plot of **2.2e** at 0.6 V [243 – 258 K].

Similarly, the complex **2.6b** displayed an irreversible oxidation with a recovery rate of 46 – 80 %. The plot is shown in Figure 2.35. A significant new absorption band formed at 784 nm with an intensity of 4.97×10^3 M^{-1} cm^{-1}. A secondary peak developed at 496 nm on the shoulder of the peak at 374 nm. The broad absorption at 374 nm was formed by contribution from the blue shifted MLCT band associated with the nitro group and the development of a former shoulder around 330 nm into a distinct band located at 343 nm.

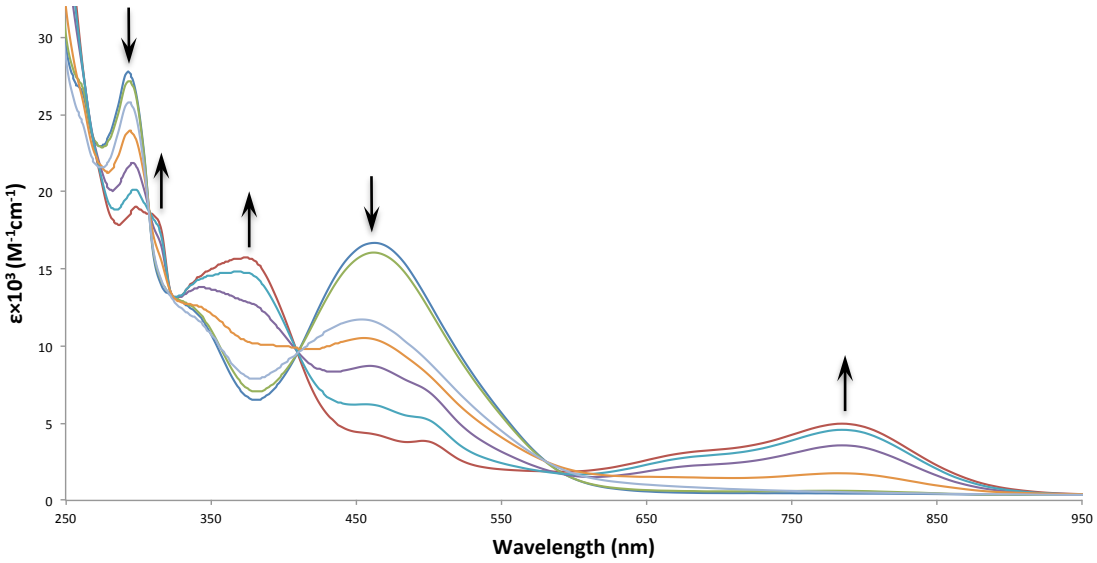

Figure 2.35 UV-Vis-NIR spectroelectrochemical plot of **2.6b** at 0.9 V [243 – 258 K].

Figure 2.36 demonstrates the reversible oxidation of the complex **2.7a**. There are five isosbestic points in the plot. Two significant absorption peaks with similar intensities of 23.7 and 23.9 × 10^3 M^{-1} cm^{-1} are apparent, one at 301 nm from the weakened former intra-ligand π-π^* transitions band, and the other at 308 nm was a development of a former shoulder around 320 nm into a distinct peak. The blue-shift of the MLCT band was 76 nm, showing no difference with the other dppe-containing complexes, but the absorption became more intense. Unlike **2.6b**, no significant new absorption band could be detected between 600 and 850 nm.

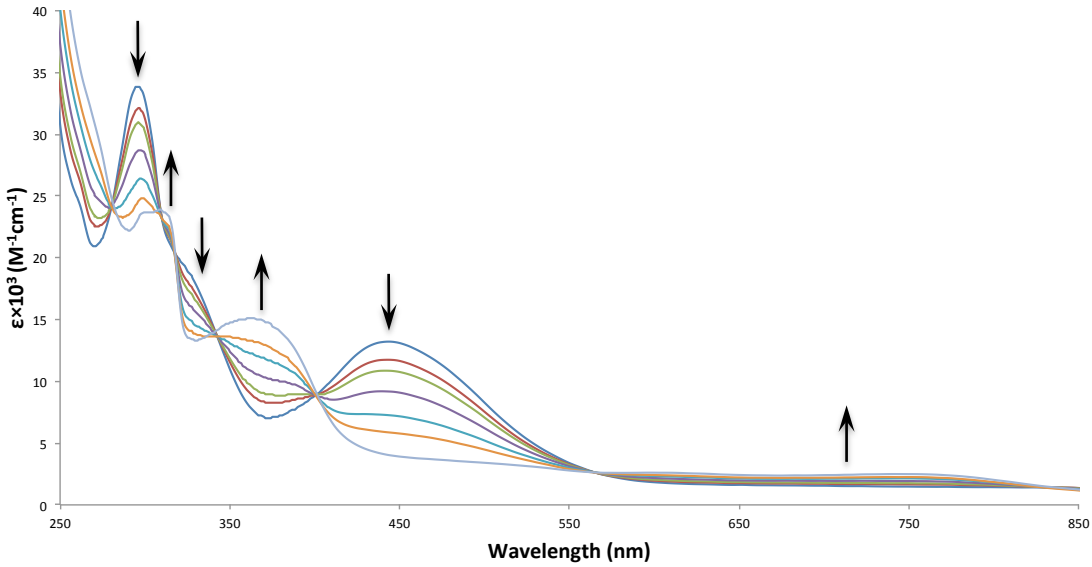

Figure 2.36 UV-Vis-NIR spectroelectrochemical plot of **2.7a** at 1.0 V [243 – 258 K].

2.7 EXPERIMENTAL SECTION

General. Reactions were performed under a nitrogen atmosphere with the use of standard Schlenk techniques, with no precautions to exclude air during workup. The starting materials $RuCl_3(PPh_3)_3$ [56], $RuCl_2(PPh_3)_2(^tBu\text{-}bpy)$ [57] and $RuCl_3(PPh_3)_2(DMA)\cdot DMA$ [65] were synthesized as described in the literature. The ligands, 1,2-bis(diphenylphosphino)benzene (dppb) [68, 69], 1,1'-bis(diphenylphosphino)ferrocene [70, 71] and (4-nitrophenyl)butadiyne [72, 73] were prepared based on literature procedures. All commercially available materials were used as received. Petrol refers to a fraction of petroleum with a boiling range of 60 -80 °C. Reagent grade solvent CH_2Cl_2 (Merck) was dried by distilling over calcium hydride and stored under N_2, THF (Merck) over sodium/benzophenone, and toluene (Merck) over sodium and stored under N_2. All other solvents were

used as received. High-resolution electrospray ionization mass spectra (HR ESI MS) were obtained using a VG Quattro II triple quadrupole instrument; peaks are reported as *m/z* (assignment, relative intensity). Microanalyses were carried out by the Microanalysis Service Unit, Research School of Chemistry, Australian National University and Elemental Analysis Service Unit, Science Centre, London Metropolitan University. UV-Vis spectra were recorded as CH_2Cl_2 solutions in 1 cm quartz cells using a Cary 5 spectrophotometer; bands are reported in the form frequency (cm^{-1}) [extinction coefficient, 10^3 M^{-1} cm^{-1}]. Infrared spectra were recorded on KBr discs or NaCl plates using a Perkin Elmer Spectrum One FT-IR spectrometer. NMR spectra were recorded using a Varian MR-400 FT-NMR or Bruker Avance 800 MHz NMR spectrometer and are referenced to residual $CHCl_3$ (7.26 ppm (^{1}H, 400 MHz/800 MHz) or $CDCl_3$ 77.16 ppm (^{13}C, 100 MHz/201 MHz). Cyclic voltammetry measurements were recorded using an e-corder 401 potentiostat system from eDaq Pty Ltd. Measurements were carried out at room temperature using Pt disc working-, Pt wire auxiliary- and Ag/AgCl reference electrodes, such that the ferrocene/ferrocenium redox couple was located at 0.56 V (CH_2Cl_2) (i_{pc}/i_{pa} = 1, ΔE_p 0.09 V). Scan rates were typically 100 mV s^{-1}. Electrochemical solutions contained 0.1 M $^nBu_4NPF_6$ and ca. 10^{-3} M complex in dried and distilled CH_2Cl_2. Solutions were purged and maintained under a nitrogen atmosphere. Spectroelectrochemistry spectra were recorded using a Perkin Elmer Lambda 950 UV-Vis-NIR spectrophotometer. Data for the oxidized species obtained by electrogeneration using a μAutolab III potentiostat were recorded by a Cary 5 spectrophotometer at temperatures ranging from -15 to -30 °C in an optically-transparent thin-layer electrochemical (OTTLE) cell (0.5 mm) with a Pt grid working-, a Pt auxiliary- and an Ag/AgCl reference electrode. The oxidation potential was set ca. 0.1 V beyond $E_{1/2}$ measured using cyclic voltammetry to ensure complete oxidation. The reversibility of the processes was tested by applying a sufficiently negative potential to reduce the oxidized species, and observing the reappearance of the spectrum for the remaining 'neutral' species.

Synthesis of cis-[$RuCl_2$(dppf)(^{t}Bu-bpy)] (**2.1a**)

$RuCl_2(PPh_3)_2(^tBu\text{-}bpy)$ (0.925 g, 0.958 mmol) was dissolved in $CHCl_3$ (60 mL), dppf (0.558 g, 1.007 mmol) was added, and the solution was refluxed for 4 h. The

solution was allowed to cool and the volume was reduced to ca. 2 mL. A mixture of diethyl ether and n-hexane (150 mL, V_{ether}:$V_{n\text{-}hexane}$ = 3:2) was added and the resulting precipitate collected and washed with diethyl ether and n-hexane to give an orange solid identified as **2.1a** (0.905 g, 0.910 mmol, 95%). A red single crystal suitable for X-ray study was obtained from concentrated $CDCl_3$ at room temperature. HR ESI MS ([M + MeCN - Cl]$^+$, 100): calcd 1000.1953, found 1000.1954. Microanalysis for $C_{52}H_{52}Cl_2FeN_2P_2Ru$: Calcd C, 62.79; H, 5.27; N, 2.82. Found C, 62.99; H, 5.32; N, 3.27. UV-Vis (CH_2Cl_2): 22490 [3.40], 33750 [19.7]. IR (KBr): 3584 (w), 3053 (m), 2965 (m), 1615 (m), 1481 (m), 1432 (m) cm^{-1}. ^{1}H-NMR ($CDCl_3$, 399 MHz): δ 1.24 (s, 9H, ^{t}Bu-H), 1.33 (s, 9H, ^{t}Bu-H), 3.40 (s, 1H, $H_{41/42}$/$H_{43/44}$), 4.12 (s, 1H, $H_{45/46}$/$H_{47/48}$), 4.22 (s, 1H, $H_{47/48}$/$H_{45/46}$), 4.30 (s, 1H, $H_{47/48}$/$H_{45/46}$), 4.46 (s, 1H, $H_{45/46}$/$H_{47/48}$), 4.55 (s, 1H, $H_{43/44}$/$H_{41/42}$), 4.94 (s, 1H, $H_{43/44}$/$H_{41/42}$), 6.13 (s, 1H, $H_{41/42}$/$H_{43/44}$), 6.45 (d, 1H, J_{HH} = 4.8 Hz, $H_{7/8}$), 6.70 – 8.55 (m, 20H, Ar-H), 6.97 (m, overlap, 1H, $H_{7/8}$), 7.64 (s, 1H, $H_{3/4}$), 7.73(s, 1H, $H_{3/4}$), 8.10 (d, 1H, J_{HH} = 6.4 Hz, $H_{9/10}$), 9.27 (dd, 1H, J_{HH} = 5.6 Hz, J_{HH} = 2.4 Hz, $H_{9/10}$). ^{13}C-NMR ($CDCl_3$, 100 MHz): δ 30.4 ($C_{13/14}$), 30.6 ($C_{13/14}$), 34.7 ($C_{11/12}$), 34.9 ($C_{11/12}$), 70.3 (J_{CP} = 5 Hz, $C_{45/46}$/$C_{47/48}$), 70.4 (J_{CP} = 5 Hz, $C_{47/48}$/$C_{45/46}$), 71.1 (J_{CP} = 5 Hz, $C_{47/48}$/$C_{45/46}$), 73.3 (J_{CP} = 8 Hz, $C_{44/45}$/$C_{41/42}$), 73.7 (J_{CP} = 5 Hz, $C_{45/46}$/$C_{47/48}$), 75.6 (J_{CP} = 5 Hz, $C_{41/42}$/$C_{44/45}$), 77.4 (J_{CP} = 5 Hz, $C_{45/46}$/$C_{47/48}$), 78.7 (J_{CP} = 11 Hz, $C_{41/42}$/$C_{44/45}$), 80.9 (J_{CP} = 49 Hz, C_{39}/C_{40}), 84.2 (J_{CP} = 44 Hz, C_{39}/C_{40}), 117.5 ($C_{3/4}$), 118.4 ($C_{3/4}$), 120.4 ($C_{7/8}$), 122.6 ($C_{7/8}$), 126.1 - 137.2 (Ar-C), 134.6 (J_{CP} = 41 Hz, $C_{15/16/17/18}$), 136.7 (J_{CP} = 42 Hz, $C_{15/16/17/18}$), 138.1 (J_{CP} = 45 Hz, $C_{15/16/17/18}$), 140.7 (J_{CP} = 32 Hz, $C_{15/16/17/18}$), 151.4 ($C_{9/10}$), 155.9 ($C_{1/2}$), 157.9 ($C_{9/10}$), 159.0 ($C_{5/6}$), 159.4 ($C_{5/6}$), 159.7 ($C_{1/2}$). ^{31}P-NMR ($CDCl_3$, 162 MHz): δ 36.0 (d, 1P, J_{PP} = 30 Hz), 43.0 (d, 1P, J_{PP} = 30 Hz).

Synthesis of cis-[$RuCl_2$(dppe)(^{t}Bu-bpy)] (**2.1b**)

$RuCl_2(PPh_3)_2$(^{t}Bu-bpy) (0.973 g, 1.008 mmol) was dissolved in $CHCl_3$ (60 mL) and dppe (0.421 g, 1.057 mmol) was added. The solution was stirred and refluxed under N_2 for 3 h and the volume was then reduced to ca. 2 mL. Petroleum spirit (200 mL) was added to precipitate the complex, which was filtered and washed with petroleum spirit. The product was dried under vacuum, yield 0.812 g (0.968 mmol, 96%). A red single crystal for X-ray study was obtained from

CH_2Cl_2/petroleum spirit at 5 °C. HR ESI MS ([M + MeCN - Cl]$^+$, 100): calcd 844.2690, found 844.2690. Microanalysis for $C_{44}H_{48}Cl_2N_2P_2Ru$: Calcd C, 63.00; H, 5.77; N, 3.34. Found C, 62.67; H, 6.11; N, 3.02. UV-Vis (CH_2Cl_2): 34130 [17.7]. IR (KBr): 3051 (m), 2963 (m), 2870 (w), 1613 (m), 1482 (m), 1434 (m) cm^{-1}. ^{1}H-NMR ($CDCl_3$, 399 MHz): δ 1.24 (s, 9H, ^{t}Bu-H), 1.43 (s, 9H, ^{t}Bu-H), 2.42 (s, 1H, $H_{39/40}$), 2.52 (d, J_{HH} = 2.8 Hz, 1H, $H_{39/40}$), 2.78 (s, 1H, $H_{39/40}$), 3.17 (s, 1H, $H_{39/40}$), 6.23 (dd, 1H, J_{HH} = 6.0 Hz, J_{HH} = 2.0 Hz, $H_{7/8}$), 6.50 - 8.21 (m, 20H, Ar-H), 7.16 (m, overlapped, 1H, $H_{9/10}$), 7.23 (dd, 1H, J_{HH} = 5.2 Hz, J_{HH} = 1.6 Hz, $H_{7/8}$), 7.30 (d, 1H, J_{HH} = 2.0 Hz, $H_{3/4}$), 7.36 (d, 1H, J_{HH} = 1.2 Hz, $H_{3/4}$), 9.70 (d, 1H, J_{HH} = 6.0 Hz, $H_{9/10}$). ^{13}C-NMR ($CDCl_3$, 100 MHz): δ 25.0 (J_{CP} = 30 Hz, J_{CP} = 11 Hz, $C_{39/40}$), 27.7 (J_{CP} = 34 Hz, J_{CP} = 14 Hz, $C_{39/40}$), 30.4 ($C_{13/14}$), 30.7 ($C_{13/14}$), 34.6 ($C_{11/12}$), 35.2 ($C_{11/12}$), 118.0 ($C_{3/4}$), 118.9 ($C_{3/4}$), 120.9 ($C_{7/8}$), 122.7 ($C_{7/8}$), 127.4 - 134.0 (Ar-C), 134.8 (J_{CP} = 38 Hz, $C_{15/16/17/18}$), 135.2 (J_{CP} = 40 Hz, $C_{15/16/17/18}$), 136.9 (J_{CP} = 44 Hz, $C_{15/16/17/18}$), 137.2 (J_{CP} = 36 Hz, $C_{15/16/17/18}$), 151.8 ($C_{9/10}$), 156.1 ($C_{9/10}$), 156.4 ($C_{1/2}$), 158.7 ($C_{1/2}$/$C_{5/6}$), 160.5 ($C_{5/6}$). ^{31}P-NMR ($CDCl_3$, 162 MHz): δ 61.7 (d, 1P, J_{PP} = 22 Hz), 70.0 (d, 1P, J_{PP} = 21 Hz).

Synthesis of cis-[$RuCl_2$(dppb)(^{t}Bu-bpy)] (**2.1c**)

$RuCl_2(PPh_3)_2$(^{t}Bu-bpy) (0.772 g, 0.799 mmol) was dissolved in $CHCl_3$ (60 mL) and dppb (0.382 g, 0.855 mmol) was added. The solution was stirred and refluxed under N_2 for 20 h, and after that the volume was reduced to ca. 2 mL. Petroleum spirit (150 mL) was added to precipitate the complex, which was filtered and washed. The red product was dried under vacuum. The yield of the synthese is ca. 76% (0.539 g, 0.607 mmol). A red single crystal for X-ray diffraction was obtained from THF/n-hexane at -19 °C. HR ESI MS ([M + MeCN - Cl]$^+$,100): calcd 894.2259, found 894.2261. Microanalysis for $C_{48}H_{48}Cl_2N_2P_2Ru$: Calcd C, 65.01; H, 5.46; N, 3.16. Found C, 64.83; H, 5.49; N, 3.31. UV-Vis (CH_2Cl_2): 34120 [19.7]. IR (KBr): 3051 (m), 2964 (m), 2870 (w), 1614 (m), 1481 (m), 1432 (m) cm^{-1}. ^{1}H-NMR ($CDCl_3$, 400 MHz): δ 1.19 (s, 9H, ^{t}Bu-H, $H_{13/14}$), 1.41 (s, 9H, ^{t}Bu-H, $H_{13/14}$), 5.73 (dd, 1H, J = 5.0 Hz, J = 2.0 Hz, $H_{7/8}$), 6.09 (d, 1H, J = 6.0 Hz, $H_{9/10}$), 6.20-8.50 (m, 24H, Ar-H), 7.38 (d, 1H, J = 5.6 Hz, $H_{7/8}$), 7.71 (s, 1H, $H_{3/4}$), 7.96 (s, 1H, $H_{3/4}$), 9.76 (dd, 1H, J = 6.0 Hz, J = 2.8 Hz, $H_{9/10}$). ^{13}C-NMR ($CDCl_3$, 100 MHz): δ 30.4 ($C_{13/14}$), 30.6 ($C_{13/14}$), 34.5 ($C_{11/12}$), 35.2 ($C_{11/12}$), 117.8 ($C_{3/4}$), 118.3 ($C_{3/4}$), 120.3 ($C_{7/8}$), 122.3 ($C_{7/8}$), 126.0 - 140.0 (Ar-C), 135.2 (J_{CP} = 45 Hz, C_{39}/C_{40}), 137.5 (J_{CP} = 37 Hz, C_{39}/C_{40}), 144.2 (J_{CP} = 31 Hz,

$C_{15/16/17/18}$), 144.7 (J_{CP} = 30 Hz, $C_{15/16/17/18}$), 145.3 (J_{CP} = 33 Hz, $C_{15/16/17/18}$), 145.8 (J_{CP} = 33 Hz, $C_{15/16/17/18}$), 151.2 ($C_{9/10}$), 154.9 ($C_{9/10}$), 156.3 ($C_{1/2}$), 158.3 ($C_{1/2}$), 158.3 ($C_{5/6}$), 160.3 ($C_{5/6}$). ^{31}P-NMR ($CDCl_3$, 162 MHz): δ 70.0 (d, 1P, J_{PP} = 23 Hz), 73.4 (d, 1P, J_{PP} = 23 Hz).

Synthesis of cis-[Ru(C≡C-4-$C_6H_4NO_2$)Cl(dppf)(^{t}Bu-bpy)] (**2.2a**)

$NaPF_6$ (0.018 g, 0.105 mmol) was added to a solution of **2.1a** (0.101 g, 0.100 mmol) and 4-nitrophenylacetylene (0.024 g, 0.162 mmol) in CH_2Cl_2 (20 mL) and the resulting solution was stirred at room temperature overnight. n-Pentane (ca. 20 mL) was added and a light yellow was obtained and filtered out under N_2. Et_3N (0.1 mL, 0.72 mmol) was added into the solution. The red solution was stirred for one hour. The solvent was reduced to ca. 2 mL, and n-pentane (ca. 100 mL) was added to precipitate the product. The solid was collected and then dissolved in a minimum amount of CH_2Cl_2. The solution was passed through a pad of basic alumina. Elution with CH_2Cl_2/Et_3N (100/1) gave a red solution that was taken to dryness on a rotary evaporator, affording **2.2a** as a red powder (0.089 g, 0.081 mmol, 80 %). A red single crystal for X-ray study was obtained from CH_2Cl_2/n-pentane at room temperature. HR ESI MS ([M + MeCN - Cl]$^+$, 100): calcd 1111.2506, found 1111.2507. Microanalysis for $C_{60}H_{56}ClFeN_3O_2P_2Ru$: Calcd C, 65.19; H, 5.11; N, 3.80. Found C, 65.55; H, 5.49; N, 3.56. UV-Vis (CH_2Cl_2): 20690 [18.2], 33550 [23.5]. IR (KBr): 2045 cm^{-1} ν(*C*≡*C*). ^{1}H-NMR ($CDCl_3$, 399 MHz): δ 1.28 (d, 9H, J = 1.6 Hz, ^{t}Bu-H), 1.31 (d, 9H, J = 1.6 Hz, ^{t}Bu-H), 3.36 (s, 1H, $H_{41/42}$/$H_{43/44}$), 4.06 (s, 1H, $H_{45/46}$ /$H_{47/48}$), 4.16 (s, 1H, $H_{43,44,47,48}$/$H_{41,42,45,46}$), 4.20 (s, 1H, $H_{43,44,47,48}$/$H_{41,42,45,46}$), 4.25 (s, 1H, $H_{43,44,47,48}$/$H_{41,42,45,46}$), 4.90 (s, 2H, $H_{43,44,47,48}$/$H_{41,42,45,46}$), 4.38 (s, 1H, $H_{45/46}$/$H_{47/48}$), 6.25 (s, 1H, $H_{41/42}$/$H_{43/44}$), 6.70 (d, J = 6.0 Hz, 1H, H_7/H_8), 6.80 - 8.60 (m, 25H, Ph-H, H_7/H_8), 7.73 (s, 1H, H_3/H_4), 7.75 (s, 1H, H_3/H_4), 8.15 (d, J = 6.8 Hz, 1H, H_9/H_{10}), 9.39 (m, 1H, H_9/H_{10}). ^{13}C-NMR ($CDCl_3$, 100 MHz): δ 30.4 ($C_{13/14}$), 30.6 ($C_{13/14}$), 34.9 ($C_{11/12}$), 70.2 (J_{CP} = 5 Hz, $C_{43,44,47,48}$/$C_{41,42,45,46}$), 71.3 (J_{CP} = 5 Hz, $C_{43,44,47,48}$/$C_{41,42,45,46}$), 73.5 (J_{CP} = 8 Hz, $C_{43,44,47,48}$/$C_{41,42,45,46}$), 70.7 (J_{CP} = 6 Hz, $C_{45/46}$/ $C_{47/48}$), 74.2 (J_{CP} = 6 Hz, $C_{45/46}$/$C_{47/48}$), 75.8 - 77.0 (m, overlapped, $C_{41/42}$, $C_{43/44/47/48}$/$C_{43/44}$, $C_{41/42/45/46}$), 80.9 (J_{CP} = 54 Hz, C_{39}/C_{40}), 84.5 (J_{CP} = 40 Hz, C_{40}/C_{39}); 117.0-161.0 (Ph-C & ^{t}Bu-bpy-C), 118.0 (C_4/C_3), 118.4 (C_3/C_4), 120.9

(C_7/C_8), 123.2 (C_8/C_7), 124.0 (C_9/C_{10}), 159.6 (C_5/C_6), 160.4 (C_5/C_6). ^{31}P-NMR ($CDCl_3$, 162 MHz): δ 41.7 (d, 1P, J_{PP} = 31 Hz), 50.1 (d, 1P, J_{PP} = 31 Hz).

Synthesis of cis-[Ru(C≡CPh)Cl(dppf)(^{t}Bu-bpy)] (**2.2b**)

$NaPF_6$ (0.029 g, 0.173 mmol) was added to a solution of **2.1a** (0.164 g, 0.164 mmol) and phenylacetylene (0.03 mL, 0.273 mmol) in CH_2Cl_2 (20 mL) and the resulting solution was stirred at room temperature for 21 h. Deoxygenated n-pentane (ca. 20 mL) was added and the white precipitate was filtered, which gave a clear yellow solution. Et_3N (0.1 mL, 0.72 mmol) was added into the stirring solution. The red solution was kept stirring for another 1 h. The solvent was reduced to ca. 2 mL, then n-pentane was added to precipitate the product, which was filtered and extracted with CH_2Cl_2. The extracted residue was purified on a pad of basic alumina. Elution with CH_2Cl_2/Et_3N (100/1) gave a red solution from which the solvent was removed completely, affording the complex **2.2b** (0.099 g, 0.093 mmol, 57%). A red single crystal for X-ray diffraction was obtained from CH_2Cl_2/n-hexane at 5 ^{o}C. HR ESI MS ([M + MeCN - Cl]$^+$, 100): calcd 1066.2655, found 1066.2653. Microanalysis for $C_{60}H_{57}ClFeN_2P_2Ru$: Calcd C, 67.96; H, 5.42; N, 2.64. Found C, 67.87; H, 5.66; N, 2,71. UV-Vis (CH_2Cl_2): 33270 [26.9]. IR (KBr): 2065 cm^{-1} ν (*C*≡*C*). ^{1}H-NMR ($CDCl_3$, 399 MHz): δ 1.26 (s, 9H, ^{t}Bu-H), 1.30 (s, 9H, ^{t}Bu-H), 3.28 (s, 1H, $H_{41/42}/H_{43/44}$), 3.99 (s, 1H, $H_{45/46}/H_{47/48}$), 4.12 (s, 2H, $H_{43/44/47/48}/H_{41/42/45/46}$), 4.21 (s, 1H, $H_{47/48}/H_{45/46}$), 4.35 (s, 1H, $H_{45/46}/H_{47/48}$), 4.90 (s, 1H, $H_{43/44}/H_{41/42}$), 6.64 (s, 1H, $H_{41/42}/H_{43/44}$), 6.65 (m, overlap, 1H, H_7/H_8), 6.80 - 8.70 (m, 26H, H_8/H_7, Ph-H), 7.71 (s, 1H, H_3/H_4), 7.74 (s, 1H, H_3/H_4), 7.92 (d, 1H, *J* = 5.5 Hz, H_9/H_{10}), 9.60 (dd, 1H, *J* = 6.0 Hz, *J* = 3.0 Hz, H_9/H_{10}). ^{13}C-NMR ($CDCl_3$, 100 MHz): δ 30.4 ($C_{13/14}$), 30.6 ($C_{13/14}$), 34.8 ($C_{11/12}$), 69.7 (J_{CP} = 5 Hz, $C_{41/42/45/46}/C_{43/44/47/48}$), 70.3 ($J_{CP}$ = 6 Hz, $C_{45/46}/C_{47/48}$), 70.8 (J_{CP} = 5 Hz, $C_{47/48}/C_{45/46}$), 73.3 (J_{CP} = 8 Hz, $C_{41/42}/C_{43/44}$), 74.2 (J_{CP} = 6 Hz, $C_{45/46}/C_{47/48}$), 75.8 (J_{CP} = 5 Hz, $C_{41/42}/C_{43/44}$), 77.1 (J_{CP} = 7 Hz, $C_{41/42/45/46}/C_{43/44/47/48}$), 77.7 ($J_{CP}$ = 11 Hz, $C_{41/42}/C_{43/44}$), 81.5 (J_{CP} = 54 Hz, C_{39}/C_{40}), 85.3 (J_{CP} = 47 Hz, C_{39}/C_{40}), 114.9 (C_{50}), 117.6 ($C_{3/4}$), 118.2 ($C_{4/3}$), 120.7 ($C_{7/8}$), 122.9 ($C_{7/8}$), 123.3 - 142.0 (Ph-C), 131.0 (C_{51}), 135.0 (J_{CP} = 37 Hz, $C_{15/16/17/18}$), 137.7 (J_{CP} = 45 Hz, $C_{15/16/17/18}$), 138.3 (J_{CP} = 47 Hz, $C_{15/16/17/18}$), 141.2 (J_{CP} = 31 Hz, $C_{15/16/17/18}$), 152.6 ($C_{9/10}$), 154.5 ($C_{9/10}$), 155.3

($C_{1/2}$), 157.2 ($C_{1/2}$), 159.0 ($C_{5/6}$), 159.8 ($C_{5/6}$). ^{31}P-NMR ($CDCl_3$, 162 MHz): δ 42.9 (d, 1P, J_{PP} = 32 Hz), 51.7 (d, 1P, J_{PP} = 32 Hz).

Synthesis of cis-[Ru(C≡C-4-$C_6H_4NO_2$)Cl(dppe)(^{t}Bu-bpy)] (**2.2c**)

To a solution of **2.1b** (0.103 g, 0.123 mmol) and 4-nitrophenylacetylene (0.020 g, 0.135 mmol) in CH_2Cl_2 (20 mL) was added $NaPF_6$ (0.023 g, 0.135 mmol) and the resulting solution was stirred at room temperature for 44 h. Deoxygenated n-pentane (ca. 20 mL) was added and the precipitate was filtered off, which gave a clear orange solution. Et_3N (0.1 mL, 0.72 mmol) was added into the solution. The solution was kept stirring for a further 1 h. The volume was reduced to ca. 2 mL, and then n-pentane (ca. 100 mL) was added to precipitate the product, which was filtered and extracted with CH_2Cl_2. The extracted residue was purified on a pad of basic alumina. Elution with $V_{acetone}/V_{n\text{-}hexane}$ (3/7) gave a red solution. Reduction in volume of the solvent on a rotary evaporator afforded a red powder (0.107 g, 0.113 mmol, 92%). The solvent system CH_2Cl_2/n-pentane offered a red single crystal for X-ray diffraction at -19 ^{o}C. HR ESI MS ([M - Cl]$^+$, 100): calcd 914.2578, found 914.2580. Microanalysis for $C_{52}H_{52}ClN_3O_2P_2Ru{\cdot}0.5CH_2Cl_2$: Calcd C, 63.57; H, 5.39; N, 4.24. Found C, 63.44; H, 5.46; N, 3.95. UV-Vis (CH_2Cl_2): 21210 [15.2], 34120 [22.2]. IR (KBr): 2049cm^{-1} ν(*C*≡*C*). ^{1}H-NMR ($CDCl_3$, 399 MHz): δ 1.27 (s, 9H, ^{t}Bu-H), 1.42 (s, 9H, ^{t}Bu-H), 2.45 - 3.00 (m, 4H, $H_{39/40}$), 6.42 (dd, 1H, J_{HH} = 5.8 Hz, J_{HH} = 1.8 Hz, $H_{7/8}$), 6.56 - 8.33 (m, 25H, Ar-H), 7.23 (m, overlapped, 1H, $H_{9/10}$), 7.81 (d, 1H, J_{HH} = 1.6 Hz, $H_{3/4}$), 7.86 (d, 1H, J_{HH} = 9.2 Hz, $H_{7/8}$), 7.97 (s, 1H, $H_{3/4}$), 9.80 (dd, 1H, J_{HH} = 6.0 Hz, J_{HH} = 2.8 Hz, $H_{9/10}$). ^{13}C-NMR ($CDCl_3$, 100 MHz): δ 25.4 (J_{CP} = 31 Hz, J_{CP} = 11 Hz, $C_{39/40}$), 28.4 (J_{CP} = 36 Hz, J_{CP} = 12 Hz, $C_{39/40}$), 30.5 ($C_{13/14}$), 30.7 ($C_{13/14}$), 34.9 ($C_{11/12}$), 35.3 ($C_{11/12}$), 116.8 (C_{42}), 118.5 ($C_{3/4}$), 118.9 ($C_{3/4}$), 121.5 ($C_{7/8}$), 123.2 ($C_{7/8}$), 123.2 - 133.4 (Ar-C), 135.5 (J_{CP} = 11 Hz, $C_{15/16/17/18}$), 135.9 (J_{CP} = 20 Hz, $C_{15/16/17/18}$), 136.9 (C_{43}), 137.3 (J_{CP} = 14 Hz, $C_{15/16/17/18}$), 137.8 (J_{CP} = 8 Hz, $C_{15/16/17/18}$), 146.6 (C_{41}), 153.2 ($C_{9/10}$), 156.1 ($C_{1/2}$), 156.5 ($C_{1/2}$), 160.1 ($C_{5/6}$), 160.8 ($C_{5/6}$). ^{31}P-NMR ($CDCl_3$, 162 MHz): δ 64.7 (d, 1P, J_{PP} = 17 Hz), 74.5 (d, 1P, J_{PP} = 17 Hz).

Synthesis of cis-[Ru(C≡CPh)Cl(dppe)(^{t}Bu-bpy)] (**2.2d**)

To a solution of **2.1b** (0.037 g, 0.044 mmol) and phenylacetylene (5 μL, 0.046 mmol) in CH_2Cl_2 (10 mL) was added $NaPF_6$ (0.008 g, 0.047 mmol) and the resulting solution was stirred at room temperature for 67 h. Et_3N (0.01 mL, 0.072 mmol) was added to the solution. The solution was kept stirring for 5 min, and then taken to dryness. The red solid was dissolved in ca. 1 mL acetone. The acetone solution was titrated into stirring distilled water. The precipitate was filtered off and redissolved by CH_2Cl_2. $MgSO_4$ was added to dry the CH_2Cl_2 solution, after which it was filtered and the solvent removed. The crude product was concentrated in the minimum amount of CH_2Cl_2 (ca. 0.5 mL), and then 30 mL mixed solvent ($V_{Diethyl\ ether}$ /$V_{petroleum\ spirit}$ = 1:1) was added to precipitate the impurity which was then filtered off. The filtrate was concentrated and the final product was precipitated from petroleum spirit as a red powder (0.022 g, 0.024 mmol, 55%). HR ESI MS ([M – Cl + MeCN]$^+$, 100): calcd 910.2993, found 910.2996. UV-Vis (CH_2Cl_2): 33990 [20.2]. IR (KBr): 2070 cm^{-1} ν (*C*≡*C*). ^{1}H-NMR ($CDCl_3$, 399 MHz): δ 1.27 (s, 9H, ^{t}Bu-H), 1.40 (s, 9H, ^{t}Bu-H), 2.30 - 3.00 (m, 4H, $H_{39/40}$), 6.39 (dd, 1H, J_{HH} = 6.0 Hz, J_{HH} = 2.0 Hz, $H_{7/8}$), 6.61 - 8.42 (m, 25H, Ar-H), 6.76 (d, 2H, J_{HH} = 7.6 Hz, H_{44}/H_{48}), 7.20 (m, overlap, 1H, $H_{9/10}$), 7.33 (m, 1H, $H_{7/8}$), 7.80 (s, 1H, $H_{3/4}$), 7.93 (s, 1H, $H_{3/4}$), 9.91 (dd, 1H, J_{HH} = 5.8 Hz, J_{HH} = 2.6 Hz, $H_{9/10}$). ^{13}C-NMR ($CDCl_3$, 100 MHz): δ 25.6 (J_{CP} = 32 Hz, J_{CP} = 11 Hz, $C_{39/40}$), 28.7 (J_{CP} = 36 Hz, J_{CP} = 12 Hz, $C_{39/40}$), 30.6 ($C_{13/14}$), 30.7 ($C_{13/14}$), 34.9 ($C_{11/12}$), 35.2 ($C_{11/12}$), 114.4 (C_{42}), 118.1($C_{3/4}$), 118.6 ($C_{3/4}$), 121.3 ($C_{7/8}$), 122.9 - 134.4 (Ar-C), 123.0 ($C_{7/8}$), 136.2 (J_{CP} = 43 Hz, $C_{15/16/17/18}$), 136.6 (J_{CP} = 33 Hz, $C_{15/16/17/18}$), 137.8 (J_{CP} = 47 Hz, $C_{15/16/17/18}$), 138.5 (J_{CP} = 32 Hz, $C_{15/16/17/18}$), 153.1 ($C_{9/10}$), 153.4 ($C_{9/10}$), 156.0 ($C_{1/2}$), 156.7 ($C_{1/2}$), 159.4 ($C_{5/6}$), 160.0 ($C_{5/6}$), C_{41} not observed. ^{31}P-NMR ($CDCl_3$, 162 MHz): δ 67.2 (d, 1P, J_{PP} = 20 Hz), 76.7 (d, 1P, J_{PP} = 20 Hz).

Synthesis of cis-[Ru(C≡C-4-$C_6H_4NO_2$)Cl(dppb)(^{t}Bu-bpy)] (**2.2e**)

To a solution of **2.1c** (0.117 g, 0.132 mmol) and 4-nitrophenylacetylene (0.022 g, 0.148 mmol) in CH_2Cl_2 (20 mL) was added $NaPF_6$ (0.025 g, 0.154 mmol) and the resulting solution was stirred at room temperature for 20 h. Deoxygenate n-pentane (ca. 20 mL) was added to lower the polarity of the solution. The white precipitate was filtered, which gave a clear yellow solution. Et_3N (0.1 mL, 0.72 mmol) was added into the solution. The red solution was stirred for 1 h. The volume was reduced to ca. 2 mL, and then n-pentane was added to precipitate the

product, which was filtered and extracted with CH_2Cl_2. The extracted residue was purified on a pad of alumina. Elution with $V_{acetone}/V_{n\text{-}hexane}$ (3/7) gave a red solution. Reduction in volume of the solvent on a rotary evaporator afforded a red powder (0.066 g, 0.066 mmol, 50%). A red single crystal was obtained from CH_2Cl_2/n-pentane at -19 ^oC. HR ESI MS ([M - Cl]$^+$, 100): calcd 962.2578, found 962.2574. Microanalysis for $C_{56}H_{52}ClN_3O_2P_2Ru \cdot 0.75CH_2Cl_2$: Calcd C, 64.23; H, 5.08; N, 3.96. Found C, 64.48; H, 5.12; N, 4.27. UV-Vis (CH_2Cl_2): 21090 [19.0]; 34050 [24.2]. IR (KBr): 2049 cm^{-1} ν (*C*≡*C*). ^{1}H-NMR ($CDCl_3$, 399 MHz): δ 1.26 (s, 9H, ^{t}Bu-H, $H_{13/14}$), 1.42 (s, 9H, ^{t}Bu-H, $H_{13/14}$), 6.08 (d, 1H, J_{HH} = 5.2 Hz, $H_{7/8}$), 6.20 (d, 1H, J_{HH} = 5.6 Hz, $H_{9/10}$), 6.37 - 8.51 (m, 30H, Ar-H), 6.85 (d, 2H, J_{HH} = 8.4 Hz, H_{49}), 7.4 (overlapped, $H_{7/8}$), 7.85 (s, 1H, $H_{3/4}$), 7.90 (d, 2H, J_{HH} = 8.8 Hz, H_{48}), 8.01 (s, 1H, $H_{3/4}$), 9.85 (dd, 1H, J_{HH} = 5.6 Hz, J_{HH} = 2.4 Hz, $H_{9/10}$). ^{13}C-NMR ($CDCl_3$, 100 MHz): δ 30.5 ($C_{13/14}$), 30.6 ($C_{13/14}$), 34.7 ($C_{11/12}$), 35.2 ($C_{11/12}$), 118.3 (C_3/C_4), 121.0 ($C_{7/8}$), 123.0 ($C_{7/8}$), 123.4 (C_{48}), 127.0 - 137.7 (Ar-C), 130.5 (C_{49}), 142.6 (C_{50}), 144.6 - 145.7 (J_{CP} uncertain, $C_{15}/C_{16}/C_{17}/C_{18}$), 149.6 ($J_{CP}$ = 23 Hz, $C_{39/40}$), 149.8 (J_{CP} = 23 Hz, $C_{39/40}$), 152.1 ($C_{9/10}$), 152.6 ($C_{9/10}$), 155.9 ($C_{1/2}$), 155.9 ($C_{1/2}$), 159.6($C_{5/6}$), 160.6 ($C_{5/6}$), C_{45}, C_{46} not observed. ^{31}P-NMR ($CDCl_3$, 162 MHz): δ 75.2 (d, 1P, J_{PP} = 23Hz), 77.1 (d, 1P, J_{PP} = 23Hz).

Synthesis of cis-[Ru(C≡CPh)Cl(dppb)(^{t}Bu-bpy)] (**2.2f**)

To a solution of **2.1c** (0.204 g, 0.230 mmol) and phenylacetylene (30 μL, 0.273 mmol) in CH_2Cl_2 (20 mL) was added $NaPF_6$ (0.047g, 0.281 mmol) and the resulting solution was stirred at room temperature for 11 h. Deoxygenated n-pentane (ca. 20 mL) was added to lower the polarity of the solution. The white precipitate was removed by filtration. Et_3N (0.1 mL, 0.72 mmol) was added to the solution. The solution turned red in seconds and was kept stirring for another two min, and then taken to dryness. The red solid was dissolved in ca. 1 mL acetone. The acetone solution was dropped into stirring distilled water and then the precipitation was filtrated and dissovled in CH_2Cl_2. $MgSO_4$ was added to dry the solution, and then the solution was filtered and the solvent was removed from the filtrate. The crude product was dissolved in the minimum amount of CH_2Cl_2 (ca. 0.5 mL), and then ca. 60 mL of a mixed solvent ($V_{Diethyl\ ether}/V_{petroleum\ spirit}$ =1:1) was added to precipitate the impurity which was filtered off. The filtrate was concentrated and the final

product was precipitated from petroleum spirit as a red powder (0.060 g, 0.063 mmol, 27%). HR ESI MS ([M – Cl + MeCN]$^+$, 100): calcd 958.2993, found 958.2992. UV-Vis (CH_2Cl_2): 33950 [18.6]. IR (KBr): 2070 cm^{-1} ν ($C\equiv C$). ^{1}H-NMR ($CDCl_3$, 800 MHz): δ 1.23 (s, 9H, ^{t}Bu-H, $H_{13/14}$), 1.39 (s, 9H, ^{t}Bu-H, $H_{13/14}$), 6.00 (d, 1H, J_{HH} = 5.5 Hz, $H_{7/8}$), 6.12 (d, 1H, J_{HH} = 6.5 Hz, $H_{9/10}$), 6.33 - 8.65 (m, 29H, Ar-H, H_{49}, $H_{7/8}$), 6.89 (overlapped, H_{49}), 6.95 (d, 2H, J_{HH} = 7.0 Hz, H_{48}), 7.35 (overlapped, $H_{7/8}$), 7.80 (s, 1H, $H_{3/4}$), 7.96 (s, 1H, $H_{3/4}$), 10.04 (d, 1H, J_{HH} = 5.5 Hz, $H_{9/10}$). ^{13}C-NMR ($CDCl_3$, 201 MHz): δ 30.5 ($C_{13/14}$), 30.6 ($C_{13/14}$), 34.7 ($C_{11/12}$), 35.2 ($C_{11/12}$), 115.9 (C_{47}), 118.1 ($C_{3/4}$), 118.2 ($C_{3/4}$), 120.8 ($C_{7/8}$), 122.8 ($C_{7/8}$), 122.9 (C_{49}), 127.0 - 137.9 (Ar-C), 130.6 (C_{48}), 136.8 (J_{CP} = 42 Hz, $C_{39/40}$), 138.7 (J_{CP} = 36 Hz, $C_{39/40}$), 145.2 (J_{CP} = 30 Hz, C_{15}/C_{16}/C_{17}/C_{18}), 145.4 (J_{CP} = 21 Hz, C_{15}/C_{16}/C_{17}/C_{18}), 145.6 (J_{CP} = 21 Hz, C_{15}/C_{16}/C_{17}/C_{18}), 145.8 (J_{CP} = 33 Hz, C_{15}/C_{16}/C_{17}/C_{18}), 152.2 ($C_{9/10}$), 153.0 ($C_{9/10}$), 156.0 ($C_{1/2}$), 156.2 ($C_{1/2}$), 159.0 ($C_{5/6}$), 160.1 ($C_{5/6}$). ^{31}P-NMR ($CDCl_3$, 324 MHz): δ 76.4 (d, 1P, J_{PP} = 24 Hz), 77.9 (d, 1P, J_{PP} = 24 Hz).

Synthesis of cis-[Ru(C≡O)Cl(dppb)(^{t}Bu-bpy)]PF_6 (**2.3a**)

To a solution of **2.1c** (0.282 g, 0.319 mmol) and phenylacetylene (0.18 mL, 1.64 mmol) in CH_2Cl_2 (40 mL) was added $NaPF_6$ (0.061g, 0.366 mmol) and the resulting solution was stirred at room temperature for 20 h. n-Pentane (ca. 30 mL) was added and then the precipitate was filtered off, giving a clear yellow solution. The volume was reduced to ca. 2 mL, and then n-pentane was added to precipitate the product, which was collected by filtration and extracted with CH_2Cl_2. The extracted residue was purified on a pad of basic alumina. Elution with CH_2Cl_2/Et_3N (100/1) gave a bright yellow solution. Reduction in volume of the solvent on a rotary evaporator afforded a yellow powder (0.272 g, 0.266 mmol, 83%). A yellow single crystal was obtained at -19 ^{o}C from CH_2Cl_2/n-hexane. HR ESI MS ([M + MeCN - Cl]$^+$,100): calcd 879.2081, found 879.2068. Microanalysis for $C_{49}H_{48}ClF_6N_2OP_3Ru{\cdot}CH_2Cl_2$: Calcd C, 54.14; H, 4.54; N, 2.53. Found C, 53.89; H, 4.68; N, 2.45. UV-Vis (CH_2Cl_2): 31730 [12.8], 32830 [11.4]. IR (KBr): 837 cm^{-1} ν (*P-F*), 1993 cm^{-1} ν ($C\equiv O$). ^{1}H-NMR ($CDCl_3$, 800 MHz): δ 1.27 (s, 9H, ^{t}Bu-H, H_{13}/H_{14}), 1.44 (s, 9H, ^{t}Bu-H, H_{13}/H_{14}), 6.40 - 8.06 (m, 25H, Ar-H, $H_{7/8}$), 6.47 (d, 1H, *J* = 6.0 Hz, $H_{7/8}$), 6.68 (d, 1H, *J* = 6.0 Hz, $H_{9/10}$), 7.88 (s, 1H, $H_{3/4}$), 8.07 (s, overlapped, $H_{3/4}$), 8.67 (d, 1H, *J* = 5.5 Hz, $H_{9/10}$). ^{13}C-NMR ($CDCl_3$, 201 MHz): δ 30.2 ($C_{13/14}$), 30.4 ($C_{13/14}$), 35.5

($C_{11/12}$), 35.8 ($C_{11/12}$), 120.5 ($C_{3/4}$), 120.8 ($C_{3/4}$), 130.0 ($C_{7/8}$), 124.9 ($C_{7/8}$), 127.5 - 135.8 (Ar-C), 140.3 (J_{CP} = 30 Hz, $C_{15}/C_{16}/C_{17}/C_{18}$), 140.5 ($J_{CP}$ = 30 Hz, $C_{15}/C_{16}/C_{17}/C_{18}$), 141.6 ($J_{CP}$ = 30 Hz, $C_{15}/C_{16}/C_{17}/C_{18}$), 141.9 ($J_{CP}$ = 30 Hz, $C_{15}/C_{16}/C_{17}/C_{18}$), 151.5 ($C_{9/10}$), 151.8 ($C_{9/10}$), 155.0 ($C_{1/2}$), 155.2 ($C_{1/2}$), 164.6 ($C_{5/6}$), 165.7 ($C_{5/6}$), C_{45} not observed. ^{31}P-NMR ($CDCl_3$, 324 MHz): δ 62.0 (d, 1P, J_{PP} = 16 Hz), 68.9 (d, 1P, J_{PP} = 16 Hz), -143.4 (septet, 1P, J_{PF} = 716 Hz, PF_6^-).

Synthesis of cis-[Ru(C_4H(4-$C_6H_4NO_2$)$_2$)(dppf)(^{t}Bu-bpy)]PF_6 (**2.4a**)

Method A: $NaPF_6$ (0.031 g, 0.184 mmol) was added to a solution of **2.1a** (0.061 g, 0.061 mmol) and 4-nitrophenylacetylene (0.025 g, 0.168 mmol) in CH_2Cl_2 (20 mL) with 5 drops of Et_3N and the solution was stirred and refluxed for 17 h. The volume of the solution was reduced after it cooled down to room temperature. The red solid was dissolved in ca. 2 mL acetone. The solution was dropped into stirring distilled water. The precipitate was collected by filtration and extracted with CH_2Cl_2. $MgSO_4$ was added to the extract. After that, the solution was filtered and the solvent was removed from the filtrate. n-Pentane was added to precipitate the product which was filtered out and collected (0.072 g, 0.053 mmol, 88%).

Method B: $NaPF_6$ (0.022 g, 0.130 mmol) was added to a solution of **2.2a** (0.011 g, 0.009 mmol) and 4-nitrophenylacetylene (0.002 g, 0.011 mmol) in CH_2Cl_2 (30 mL) with 5 drops of Et_3N and the solution was stirred at room temperature for 43 h. The volume of the solution was reduced. The red solid was dissolved in ca. 2 mL acetone. The solution was dropped into stirring distilled water. The precipitate was collected by filtration and extracted with CH_2Cl_2. $MgSO_4$ was added to the extract. After that, the solution was filtered and the solvent was removed from the filtrate. n-Pentane was added to precipitate the product which was filtered out and collected (0.011 g, 0.008 mmol, 88%).

A concentrated $CDCl_3$ solution at room temperature gave a red single crystal for X-ray study. HR ESI MS ($[M]^+$, 100): calcd 1217.2561, found 1217.2589. Microanalysis for $C_{68}H_{61}F_6FeN_4O_4P_3Ru$: Calcd C, 59.96; H, 4.51; N, 4.11. Found C, 59.61; H, 4.50; N, 4.21. UV-Vis (CH_2Cl_2): 21900 [13.3], 26770 [18.2], 34220 [28.7]. IR (NaCl/Nujol): 1614 (s, w), 1584 (s, m), 1514 (s, m), 1336 (s, s), 1260 (s, w),

1162 (s, w), 1107 (s, m), 1090 (s, m), 1027 (s, w), 840 (s, s) cm^{-1}. ^{1}H-NMR ($CDCl_3$, 399 MHz): δ 1.29 (s, 9H, $H_{13/14}$), 1.49 (s, 9H, $H_{13/14}$), 3.72 (s, 1H, $H_{41/42}$/$H_{43/44}$), 4.42 (s, 3H, $H_{45/46}$, $H_{43/44}$, $H_{47/48}$/$H_{47/48}$, $H_{41/42}$, $H_{45/46}$), 4.60 (s, 1H, $H_{47/48}$/$H_{45/46}$), 4.70 (s, 1H, $H_{43/44}$/$H_{41/42}$), 4.93 (s, 1H, $H_{45/46}$/$H_{47/48}$), 5.57 (s, 1H, $H_{41/42}$/$H_{43/44}$), 6.70 - 7.60 (29H, Ph-H, C=C-H), 6.95 (s, 1H, H_9/H_{10}), 9.12 (d, 1H, J = 6.0 Hz, $H_{9/10}$), 8.05 (d, 1H, J = 3.1 Hz, $H_{7/8}$), 8.17 (d, 1H, J = 5.0 Hz, $H_{7/8}$), 8.08 (s, 1H, $H_{3/4}$), 8.14 (s, 1H, $H_{3/4}$). ^{13}C-NMR ($CDCl_3$, 100 MHz): δ 30.3 ($C_{13/14}$), 30.5 ($C_{13/14}$), 35.5 ($C_{11/12}$), 35.8 ($C_{11/12}$), 65.1 (C_{52}), 71.7 (J_{CP} = 5 Hz, $C_{45/46}$, $C_{43/44}$, $C_{47/48}$/$C_{47/48}$, $C_{41/42}$, $C_{45/46}$), 72.3 (J_{CP} = 4 Hz, $C_{45/46}$, $C_{43/44}$, $C_{47/48}$/$C_{47/48}$, $C_{41/42}$, $C_{45/46}$), 75.3 (J_{CP} = 2 Hz, $C_{45/46}$, $C_{43/44}$, $C_{47/48}$/$C_{47/48}$, $C_{41/42}$, $C_{45/46}$), 74.2 (J_{CP} = 15 Hz, $C_{43/44}$/$C_{41/42}$), 75.0 (J_{CP} = 8 Hz, $C_{45/46}$/$C_{47/48}$), 75.1 (J_{CP} = 7 Hz, $C_{47/48}$/$C_{45/46}$), 75.5 (J_{CP} = 3 Hz, $C_{41/42}$/$C_{43/44}$), 76.2 (J_{CP} = 15 Hz, $C_{41/42}$/$C_{43/44}$), 79.4 (J_{CP} = 51 Hz, C_{39}/C_{40}), 110.0 - 136.0 (Ph-C), 119.0, 120.9 (C_7/C_8), 124.3 ($C_{3/4}$), 124.6 ($C_{3/4}$), 130.4 (J_{CP} = 45 Hz, C_{15}/C_{16}/C_{17}/C_{18}), 131.6 (J_{CP} = 36 Hz, C_{15}/C_{16}/C_{17}/C_{18}), 133.2 (J_{CP} = 39 Hz, C_{15}/C_{16}/C_{17}/C_{18}), 135.4 (J_{CP} = 40 Hz, C_{15}/C_{16}/C_{17}/C_{18}), 143.1 ($C_{51/53}$), 159.3 ($C_{51/53}$), 145.9 ($C_{49/56}$), 146.8 ($C_{49/56}$), 149.5 ($C_{9/10}$), 157.6 ($C_{9/10}$), 155.2 ($C_{1/2}$), 156.0 ($C_{1/2}$), 164.4 ($C_{5/6}$), 163.4 ($C_{5/6}$), Some of the carbon peaks are overlapped. ^{31}P-NMR ($CDCl_3$, 162 MHz): δ 34.7 (d, 1P, J_{PP} = 25 Hz), 42.6 (d, 1P, J_{PP} = 25 Hz), -143.5 (sept, 1P, J_{PF} = 713 Hz, PF_6^-).

Synthesis of cis-[Ru(C_4HPh_2)(dppf)(^{t}Bu-bpy)]PF_6 (**2.4b**)

To a solution of **2.1a** (0.065 g, 0.065 mmol) and phenylacetylene (0.02 mL, 0.18 mmol) in CH_2Cl_2 (20 mL) with 5 drops of Et_3N was added $NaPF_6$ (0.033 g, 0.196 mmol) and the solution was stirred and refluxed for 17 h. The volume of the solution was reduced after it cooled down to room temperature. The yellow solid was dissolved in ca. 2 mL acetone. The solution was dropped into stirring distilled water, and then the precipitate was collected by filtration and extracted with CH_2Cl_2. $MgSO_4$ was added to the extract. After that, the mixture was filtered, and the filtrate solvent was reduced to ca. 3 mL. n-Pentane (ca. 100 mL) was added to precipitate the product which was collected (0.061 g, 0.054 mmol, 83%). The solvent system of THF/n-hexane gave an orange single crystal for X-ray study at -19 °C. HR ESI MS ($[M]^+$, 100): calcd 1127.2859, found 1127.2861. Microanalysis for $C_{68}H_{63}F_6FeN_2P_3Ru{\cdot}0.5CH_2Cl_2$: Calcd C, 62.59; H, 4.91; N, 2.13. Found C, 62.85; H, 5.21; N, 2.08. UV-Vis (CH_2Cl_2): 24510 [11.4], 33710 [30.5]. IR (NaCl/Nujol): 3053

(s, m), 1614 (s, m), 1592 (s, w), 1541 (s, w), 1481 (s, s), 1436 (s, s), 1410 (s, m), 1306 (s, w), 1256 (s, m), 1163 (s, m), 1088 (s, m), 1027 (s, m), 839 (s,s) cm^{-1}. ^{1}H-NMR ($CDCl_3$, 399 MHz): δ 1.28 (s, 9H, $H_{13/14}$), 1.50 (s, 9H, $H_{13/14}$), 3.69 (s, 1H, $H_{41/42}$/$H_{43/44}$), 4.36 (s, 1H, $H_{47/48}$/$H_{45/46}$), 4.39 (s, 2H, $H_{45/46}$, $H_{47/48}$), 4.53 (s, 1H, $H_{43/44}$/$H_{41/42}$), 4.67 (s, 1H, $H_{43/44}$/$H_{41/42}$), 4.86 (s, 1H, $H_{45/46}$/$H_{47/48}$), 5.72 (s, 1H, $H_{41/42}$/$H_{43/44}$), 6.40 - 7.60 (m, 33H, Ph-H, C=C-H, H_7, H_8, $H_{9/10}$), 6.85 (m, $H_{7/8}$), 7.07 (m, $H_{9/10}$), 7.35 (m, $H_{7/8}$), 7.92 (s, 1H, $H_{3/4}$), 8.11 (d, 1H, J = 2.0 Hz, $H_{3/4}$), 9.12 (d, 1H, J = 6.4 Hz, $H_{9/10}$). ^{13}C-NMR ($CDCl_3$, 100 MHz): δ 30.4 ($C_{13/14}$), 30.5 ($C_{13/14}$), 35.3 ($C_{11/12}$), 35.7 ($C_{11/12}$), 59.5 (C_{52}), 71.5 (J_{CP} = 4 Hz, $C_{45/46}$), 72.1 (J_{CP} = 5 Hz, $C_{47/48}$), 74.2 (J_{CP} = 15 Hz, $C_{43/44}$/$C_{41/42}$), 74.6 (J_{CP} = 10 Hz, $C_{45/46}$/$C_{47/48}$), 74.7 (J_{CP} = 8 Hz, $C_{43/44}$/$C_{41/42}$), 75.2 (J_{CP} = 2 Hz, $C_{47/48}$/$C_{45/46}$), 75.3 (J_{CP} = 3 Hz, $C_{41/42}$/$C_{43/44}$), 76.3 (J_{CP} = 15 Hz, $C_{41/42}$/$C_{43/44}$), 77.4 (overlapped, $C_{39/40}$), 79.8 (J_{CP} = 50 Hz, $C_{39/40}$), 118.0 ($C_{3/4}$), 120.0 ($C_{3/4}$), 123.4 ($C_{7/8}$), 124.9 ($C_{7/8}$), 125.0 - 140.0 (Ph-C), 128.6 ($C_{50/55}$), 138.0 ($C_{50/55}$), 130.6 (J_{CP} = 44 Hz, C_{15}/C_{16}/C_{17}/C_{18}), 133.1 (J_{CP} = 35 Hz, C_{15}/C_{16}/C_{17}/C_{18}), 134.0 (J_{CP} = 38 Hz, C_{15}/C_{16}/C_{17}/C_{18}), 136.4 (J_{CP} = 44 Hz, C_{15}/C_{16}/C_{17}/C_{18}), 155.1 ($C_{1/2}$), 156.4 ($C_{1/2}$), 162.4 ($C_{5/6}$), 163.5 ($C_{5/6}$), Some of the carbon peaks are overlapped or failed to be assigned. ^{31}P-NMR ($CDCl_3$, 162 MHz): δ 37.0 (d, 1P, J_{PP} = 27 Hz), 43.0 (d, 1P, J_{PP} = 27 Hz), -143.6 (sept, 1P, J_{PF} = 713 Hz, PF_6^-).

Synthesis of cis-[Ru(C_4H(4-$C_6H_4NO_2$)$_2$)(dppe)(^{t}Bu-bpy)]PF_6 (**2.4c**)

To a solution of **2.1b** (0.159 g, 0.190 mmol) and 4-nitrophenylacetylene (0.089 g, 0.603 mmol) in CH_2Cl_2 (20 mL) with 5 drops of Et_3N was added $NaPF_6$ (0.115 g, 0.685 mmol), and the resulting solution was stirred and refluxed for 16 h. The solvent was removed after the solution had cooled down to room temperature. The residue was extracted with ca. 2 mL acetone. The solution was dropped into stirring distilled water, and then the precipitate was collected by filtration and dissolved in CH_2Cl_2. $MgSO_4$ was added to the solution, after then the mixture was filtered and the filtrate was reduced to ca. 3 mL. Diethyl ether (ca. 60 mL) was added to precipitate the product. The dissolution/precipitation was repeated 3 times, and the dark red solid was collected (0.126 g, 0.104 mmol, 55%). HR ESI MS ($[M]^+$, 100): calcd 1061.2899, found 1061.2893. Microanalysis for $C_{60}H_{57}F_6N_4O_4P_3Ru$: Calcd C, 59.75; H, 4.76; N, 4.65. Found C, 59.67; H, 4.61; N, 4.75.

UV-Vis (CH_2Cl_2): 21700 [18.8], 27130 [23.9], 34510 [35.5]. IR (KBr): 837 (s) cm^{-1} ν (*P-F*), 1106 (s), 1338 (s), 1585 (s), 1612 (s), 2924 (m), 2963 (m) cm^{-1}. ^{1}H-NMR ($CDCl_3$, 399 MHz): δ 1.33 (s, 9H, ^{t}Bu-H), 1.37 (s, 9H, ^{t}Bu-H), 2.60 - 3.70 (m, 4H, $H_{39/40}$), 6.18 (s, 1H, H_{48}), 6.48 - 8.14 (m, 34H, Ar-H, H_3, H_4, H_7, H_8, H_9, H_{10}), 7.44 (overlapped, $H_{3/4}$), 7.62 (overlapped, $H_{9/10}$), 7.98 (d, J_{HH} = 2.0 Hz, overlapped, $H_{9/10}$), 8.05 (d, J_{HH} = 9.2 Hz, overlapped, $H_{7/8}$), 8.08 (s, overlapped, $H_{3/4}$), 8.12 (d, J_{HH} = 9.2 Hz, overlapped, $H_{7/8}$). ^{13}C-NMR ($CDCl_3$, 100 MHz): δ 26.7 (J_{CP} = 34 Hz, J_{CP} = 12 Hz, $C_{39/40}$), 28.4 (J_{CP} = 34 Hz, J_{CP} = 11 Hz, $C_{39/40}$), 30.4 ($C_{13/14}$), 30.5 ($C_{13/14}$), 35.4 ($C_{11/12}$), 35.7 ($C_{11/12}$), 119.1($C_{3/4}$), 120.2 ($C_{9/10}$), 123.9 ($C_{7/8}$), 124.1 - 154.6 (Ph-C), 124.4 ($C_{7/8}$), 125.8 (C_{50}), 128.7 (C_{48}), 130.9 (J_{CP} = 42 Hz, $C_{15/16/17/18}$), 131.6 (J_{CP} = 36 Hz, $C_{15/16/17/18}$), 134.2 (J_{CP} = 54 Hz, $C_{15/16/17/18}$), 145.7 (C_{49}), 154.9 ($C_{1/2}$), 155.3 ($C_{1/2}$), 158.8 (C_{47}), 162.8 ($C_{5/6}$), 163.6 ($C_{5/6}$). Some of the carbon peaks could not be assigned. ^{31}P-NMR ($CDCl_3$, 162 MHz): δ 63.8 (d, 1P, J_{PP} = 13 Hz), 69.4 (d, 1P, J_{PP} = 13 Hz), -143.5 (sept, 1P, J_{PF} = 713 Hz, PF_6^-).

Synthesis of cis-[Ru(C$_4$H(4-C$_6$H$_4$NO$_2$)$_2$)(dppb)(^{t}Bu-bpy)]PF$_6$ (**2.4d**)

To a solution of **2.1c** (0.013 g, 0.014 mmol) and 4-nitrophenylacetylene (0.007 g, 0.048 mmol) in CH_2Cl_2 (30 mL) with 5 drops of Et_3N was added $NaPF_6$ (0.018 g, 0.11 mmol) and the solution was stirred and refluxed for 18 h. The volume of the solution was reduced after it had cooled down to room temperature. The resulting red solid was dissolved in ca. 1 mL acetone. The solution was dropped into stirring distilled water, and then the precipitate was collected by filtration and redissolved in CH_2Cl_2. $MgSO_4$ was added to the solution, the mixture was filtered, and the solvent volume of the filtrate was reduced. Diethyl ether (ca. 100 mL) was added to precipitate the product, which was dried and collected (0.014 g, 0.011 mmol, 78%). HR ESI MS ([M]$^+$, 100): calcd 1109.2899, found 1109.2897. Microanalysis for $C_{64}H_{57}F_6N_4O_4P_3Ru$: Calcd C, 61.29; H, 4.58; N, 4.47. Found C, 61.45; H, 4.44; N, 4.64. UV-Vis (CH_2Cl_2): 21570 [17.0], 27030 [21.8], 34550 [31.2]. IR (KBr): 839 (s) cm^{-1} ν (*P-F*), 1334 (s), 1513 (m), 1584 (m), 2926 (w), 2959 (w) cm^{-1}. ^{1}H-NMR ($CDCl_3$, 800 MHz): δ 1.35 (s, 9H, ^{t}Bu-H), 1.36 (s, 9H, ^{t}Bu-H), 5.69 (s, 1H, H_{52}), 6.64 - 8.07 (m, 31H, Ar-H, H_3, H_4, $H_{9/10}$), 6.71 (d, J = 5.0 Hz, 1H, $H_{7/8}$), 7.01 (d, J = 8.5 Hz, 2H, H_{55}), 7.12 (d, J = 8.5 Hz, 2H, H_{54}), 7.23 (d, J = 5.5 Hz, 1H, $H_{9/10}$), 7.38 (d, J = 5.5 Hz, 1H, $H_{7/8}$), 7.90 ($H_{9/10}$), 7.91 ($H_{3/4}$), 7.92 ($H_{3/4}$). ^{13}C-NMR ($CDCl_3$, 201 MHz): δ 30.4

($C_{13/14}$), 30.5 ($C_{13/14}$), 35.5 ($C_{11/12}$), 35.7 ($C_{11/12}$), 119.3 ($C_{3/4}$), 120.3 ($C_{3/4}$), 123.5 ($C_{7/8}$), 124.2 - 142.7 (Ph-C), 124.5 ($C_{7/8}$), 126.0 (C_{54}), 128.0 (C_{52}), 131.1 (C_{55}), 140.0 - 142.6 ($C_{15/16/17/18}$), 145.7 (C_{56}), 147.0 (C_{53}), 149.1 ($C_{9/10}$), 153.6 ($C_{9/10}$), 154.4 ($C_{1/2}$), 155.0 ($C_{1/2}$), 163.2 ($C_{5/6}$), 163.7 ($C_{5/6}$), C_{45}, C_{48}, C_{49}, C_{50}, and C_{51} could not be assigned. ^{31}P-NMR ($CDCl_3$, 324 MHz): δ 68.1 (d, 1P, J_{PP} = 20 Hz), 74.6 (d, 1P, J_{PP} = 20 Hz), -144.1 (sept, 1P, J_{PF} = 713 Hz, PF_6^-).

Synthesis of cis-[Ru(C=CH(4-$C_6H_4NO_2$)C≡C(4-$C_6H_4NO_2$))Cl(dppe)(^{t}Bu-bpy)] (**2.5b**)

^{n}Bu$_4$NCl (0.005 g, 0.018 mmol) was added to a THF (ca. 30 mL) solution of **2.4c** (0.017 g, 0.0138 mmol) at room temperature. The solution was stirred for 1 h and then taken to dryness under vacuum. The mixture was redissolved in $CHCl_3$ and the solution was filtered. The filtrate was concentrated and the product was precipitated by addition to n-pentane (ca. 30 mL), and collected (0.013 g, 0.0123 mmol, 89%). The solvent system CH_2Cl_2/diethyl ether afforded a dark red single crystal for X-ray diffraction at -19 °C. HR ESI MS ([M - Cl]$^+$, 100): calcd for $C_{60}H_{57}N_4O_4P_2{}^{102}Ru$ 1061.2899, found 1061.2899. Microanalysis for $C_{60}H_{57}ClN_4O_4P_2Ru{\cdot}0.75CH_2Cl_2$: Calcd C, 62.89; H, 5.08; N, 4.83. Found C, 63.04; H, 5.41; N, 4.89. UV-Vis (CH_2Cl_2): 21730 [17.1], 26750 [19.7], 33770 [29.1]. IR (KBr): 2017 cm^{-1} ν (*C*≡*C*). ^{1}H-NMR ($CDCl_3$, 800 MHz): δ 1.21 (s, 9H, ^{t}Bu-H), 1.45 (s, 9H, ^{t}Bu-H), 2.50 - 3.25 (m, 4H, $H_{39/40}$), 6.03 (d, *J* = 9.0 Hz, 2H, H_{43}), 6.20 - 8.24 (m, 28H, Ar-H, $H_{3/4}$, $H_{7/8}$), 6.38 (d, *J* = 6.5 Hz, 1H, $H_{7/8}$), 7.50 (d, *J* = 6.5 Hz, 1H, $H_{9/10}$), 7.54 (s, 1H, $H_{3/4}$), 7.59 (overlapped, $H_{7/8}$), 7.89 (overlapped, $H_{3/4}$), 8.38 (s, 1H, H_{48}), 9.87 (d, *J* = 5.5 Hz, $H_{9/10}$). ^{13}C-NMR ($CDCl_3$, 201 MHz): δ 25.2 (J_{CP} = 30 Hz, J_{CP} = 12 Hz, $C_{39/40}$), 26.4 (J_{CP} = 30 Hz, J_{CP} = 12 Hz, $C_{39/40}$), 30.5 ($C_{13/14}$), 30.7 ($C_{13/14}$), 34.8 ($C_{11/12}$), 35.3 ($C_{11/12}$), 104.5 (C_{45}), 118.8 ($C_{3/4}$), 119.2 ($C_{3/4}$), 121.6 ($C_{7/8}$), 122.3 ($C_{7/8}$), 123.3 - 146.2 (Ph-C), 127.5 (C_{50}), 135.7 (J_{CP} = 39 Hz, $C_{15/16/17/18}$), 137.5 (J_{CP} = 39 Hz, $C_{15/16/17/18}$), 138.0 (J_{CP} = 42 Hz, $C_{15/16/17/18}$), 145.7 (*J* = 12 Hz, C_{48}), 152.4 (*J* = 18 Hz, $C_{9/10}$), 153.2 ($C_{9/10}$), 155.9 ($C_{1/2}$), 157.2 ($C_{1/2}$), 159.7 ($C_{5/6}$), 160.9 ($C_{5/6}$), C_{41}, C_{44}, C_{46}, C_{47}, C_{49} and C_{52} could be assigned. ^{31}P-NMR ($CDCl_3$, 324 MHz): δ 65.1 (d, 1P, J_{PP} = 24 Hz), 78.5 (d, 1P, J_{PP} = 24 Hz).

Synthesis of cis-Ru(C≡CC≡C-4-$C_6H_4NO_2$)Cl(dppe)(^{t}Bu-bpy) (**2.6b**)

To a solution of **2.1b** (0.016 g, 0.0191 mmol) and 4-nitrophenylbutadiyne (0.010 g, 0.058 mmol) in CH_2Cl_2 (20 mL) with 5 drops of Et_3N was added $NaPF_6$ (0.010 g, 0.062 mmol). The solution was stirred at room temperature for 17 h and then concentrated and purified on a pad of basic alumina. Elution with CH_2Cl_2/Et_3N (100/1) gave a red solution. Reduction in volume of the solvent on a rotary evaporator afforded a red powder. Reprecipitation from n-pentane (20 mL) and filtration afforded the product (0.010 g, 0.0102 mmol, 54 %). The red single crystal for X-ray study was obtained from CH_2Cl_2/n-hexane at room temperature. HR ESI MS ($[M]^+$, 100): calcd for $C_{54}H_{52}{}^{35}ClN_3O_2P_2{}^{102}Ru$ 973.2267, found 973.2268. Microanalysis for $C_{54}H_{52}ClN_3O_2P_2Ru$: Calcd C, 66.62; H, 5.38; N, 4.32. Found C, 66.40; H, 5.20; N, 4.44. UV-Vis (CH_2Cl_2): 21680 [16.2], 33540 [27.2]. IR (KBr): 2012 cm^{-1} ν ($C\equiv C$), 2146 cm^{-1} ν ($C\equiv C$). ^{1}H-NMR ($CDCl_3$, 399 MHz): 1.23 (s, 9H, ^{t}Bu-H, $H_{13/14}$), 1.47 (s, 9H, ^{t}Bu-H, $H_{13/14}$), 2.40 - 3.40 (m, 4H, H_{39}/H_{40}), 6.08 (d, 1H, J_{HH} = 4.4 Hz, $H_{7/8}$), 6.44 - 8.20 (m, 25H, Ar-H), 7.14 (m, $H_{9/10}$), 7.53 (m, $H_{7/8}$), 7.68 (s, 1H, $H_{3/4}$), 7.96 (s, 1H, $H_{3/4}$), 9.98 (dd, 1H, J_{HH} = 6.0 Hz, J_{HH} = 2.4 Hz, $H_{9/10}$). ^{13}C-NMR ($CDCl_3$, 100 MHz): δ 26.0 (J_{CP} = 11 Hz, $C_{39/40}$), 26.8 (J_{CP} = 11 Hz, $C_{39/40}$), 30.6 ($C_{13/14}$), 30.8 ($C_{13/14}$), 34.7 ($C_{11/12}$), 35.3 ($C_{11/12}$), 63.4 (C_{43}/C_{44}), 90.0 (J = 28 Hz, C_{42}), 117.8 ($C_{7/8}$), 118.7 ($C_{7/8}$), 121.2 ($C_{3/4}$), 122.7 ($C_{3/4}$), 123.4 - 132.4 (Ar-C), 134.0 (C_{45}), 134.6 (J_{CP} = 23 Hz, $C_{15/16/17/18}$), 135.3 (J_{CP} = 30 Hz, $C_{15/16/17/18}$), 136.7 (J_{CP} = 18 Hz, $C_{15/16/17/18}$), 137.1 (J_{CP} = 26 Hz, $C_{15/16/17/18}$), 151.7 ($C_{9/10}$), 155.7 ($C_{9/10}$, $C_{1/2}$), 157.9 ($C_{1/2}$), 158.2 ($C_{5/6}$), 160.2 ($C_{5/6}$), C_{41} not observed. ^{31}P-NMR ($CDCl_3$, 162 MHz): δ 43.6 (d, 1P, J_{PP} = 12 Hz), 66.9 (d, 1P, J_{PP} = 12 Hz).

Synthesis of cis-Ru(C≡CC≡C-4-$C_6H_4NO_2$)Cl(dppb)(^{t}Bu-bpy) (**2.6c**)

To a solution of **2.1c** (0.119 g, 0.135 mmol) and 4-nitrophenylbutadiyne (0.029 g, 0.172 mmol) in THF (30 mL) was added $NaPF_6$ (0.029 g, 0.175 mmol). The solution was stirred at room temperature for 17 h, and then 0.2 mL Et_3N was added. The resulting solution was concentrated after a further 5 min stirring, and then purified on a pad of basic alumina. Elution with CH_2Cl_2/petroleum spirit/Et_3N (100/100/1) gave a red solution. The eluent was taken to dryness under the rotavapor. A CH_2Cl_2 extract of the dark red powder was precipitated from n-pentane (30 mL) and collected by filtration (0.120 g, 0.117 mmol, 87 %). HR ESI MS ($[M]^+$, 100): calcd for $C_{58}H_{52}{}^{35}ClN_3O_2P_2{}^{102}Ru$ 1021.2267, found 1021.2277. UV-

Vis (CH_2Cl_2): 22200 [21.4], 33700 [31.8]. IR (KBr): 2015 cm^{-1} ν (*C*≡*C*), 2147 cm^{-1} ν (*C*≡*C*). ^{1}H-NMR (800 MHz): δ 1.21 (s, 9H, ^{t}Bu-H, $H_{13/14}$), 1.43 (s, 9H, ^{t}Bu-H, $H_{13/14}$), 5.75 (d, 1H, J_{HH} = 8.0 Hz, $H_{7/8}$), 6.17 - 8.10 (m, 28H, Ar-H), 6.19 (J_{HH} = 9.5 Hz, $H_{9/10}$), 7.41 (d, 1H, J_{HH} = 5.5 Hz, $H_{7/8}$), 7.67 (s, 1H, $H_{3/4}$), 7.91 (s, 1H, $H_{3/4}$), 9.86 (d, 1H, J_{HH} = 5.0 Hz, $H_{9/10}$). ^{13}C-NMR ($CDCl_3$, 201 MHz): δ 30.6 ($C_{13/14}$), 30.8 ($C_{13/14}$), 34.6 ($C_{11/12}$), 35.2 ($C_{11/12}$), 117.6 (C_3/C_4), 118.2 (C_3/C_4), 120.7 ($C_{7/8}$), 122.5 ($C_{7/8}$), 123.4 - 137.0 (Ar-C), 134.1 (C_{52}), 144.1 - 144.8 (C_{15}/C_{16}/C_{17}/C_{18}), 145.1 (C_{49}), 146.1 (J_{CP} = 21 Hz, $C_{39/40}$), 146.7 (J_{CP} = 18 Hz, $C_{39/40}$), 154.7 ($C_{9/10}$), 155.5 ($C_{1/2}$), 157.6 ($C_{1/2}$), 158.0 ($C_{5/6}$), 160.0 ($C_{5/6}$), C_{45}, one of $C_{9/10}$ not observed, C_{46}, C_{47}, C_{48} could not be assigned. ^{31}P-NMR ($CDCl_3$, 324 MHz): δ 49.9 (d, 1P, J_{PP} = 16 Hz), 73.5 (d, 1P, J_{PP} = 16 Hz).

Synthesis of cis-[Ru(C≡CC(NEt$_3$)=CH-4-C$_6$H$_4$NO$_2$)Cl(dppe)(^{t}Bu-bpy)]PF$_6$ (**2.7a**)

To a solution of **2.1b** (0.149 g, 0.166 mmol) and 4-nitrophenylbutadiyne (0.067g, 0.394 mmol) in CH_2Cl_2 (20 mL) with 5 drops of Et_3N was added $NaPF_6$ (0.088 g, 0.526 mmol). The solution was stirred at room temperature for 17 h and then concentrated. The extracted residue was purified on a pad of basic alumina. Elution with CH_2Cl_2/Et_3N (100/1) and then ethyl acetate/Et_3N (100/1) gave an orange band that was collected and reduced in on a rotary evaporator to afford an orange powder (0.050 g, 0.041 mmol, 25 %). The red single crystal for X-ray study was obtained from CH_2Cl_2/diethyl ether at room temperature. HR ESI MS ($[M]^+$, 100): calcd for $C_{60}H_{68}O_2N_4P_2{}^{35}Cl^{102}Ru$ 1075.3550, found 1075.3552. Microanalysis for $C_{60}H_{68}ClF_6N_4O_2P_3Ru$: Calcd C, 59.04; H, 5.62; N, 4.59. Found C, 58.88; H, 5.51; N, 4.64. UV-Vis (CH_2Cl_2): 22770 [12.1], 33750 [33.9]. IR (KBr): 840 (s) cm^{-1} ν (*P-F*), 2034 (m) cm^{-1}, 2152 (w) cm^{-1} ν (*C*≡*C*). ^{1}H-NMR ($CDCl_3$, 399 MHz): δ 1.02 (t, 9H, J_{HH} = 6.8 Hz, H_{50}), 1.28 (s, 9H, ^{t}Bu-H, $H_{13/14}$), 1.43 (s, 9H, ^{t}Bu-H, $H_{13/14}$), 2.60 - 3.50 (m, 10H, H_{39}, H_{40}, H_{49}), 6.24 (d, 1H, J_{HH} = 6.0 Hz, $H_{7/8}$), 6.47 - 8.05 (m, 20H, Ar-H), 6.56 (s, 1H, H_{44}), 7.11 (s, $H_{9/10}$), 7.51 (d, 1H, J_{HH} = 6.0 Hz, $H_{7/8}$), 7.70 (H_{47}), 7.87 (s, 1H, $H_{3/4}$), 8.08 (s, 1H, $H_{3/4}$), 8.16 (d, 1H, J_{HH} = 8.4 Hz, H_{46}), 9.92 (d, 1H, J_{HH} = 5.6 Hz, $H_{9/10}$). ^{13}C-NMR ($CDCl_3$, 100 MHz): δ 8.2 (C_{50}), 26.8 (J = 27 Hz, J = 13 Hz, $C_{39/40}$), 27.9 (J = 29 Hz, J = 16 Hz, $C_{39/40}$), 30.4 ($C_{13/14}$), 30.6 ($C_{13/14}$), 35.0 ($C_{11/12}$), 35.4 ($C_{11/12}$), 52.7 (C_{49}), 99.2 (J = 26 Hz, C_{42}), 123.2 - 140.7 (Ar-C), 127.3 (C_{43}), 129.6 (C_{45}, C_{46}), 133.2 (J_{CP} = 30 Hz, $C_{15/16/17/18}$), 134.9 (J_{CP} = 31 Hz, $C_{15/16/17/18}$), 135.9 (J_{CP}

= 39 Hz, $C_{15/16/17/18}$), 137.8 (J_{CP} = 46 Hz, $C_{15/16/17/18}$), 146.6 (C_{48}), 151.2 ($C_{9/10}$), 155.9 ($C_{1/2}$), 156.1 ($C_{9/10}$), 157.7 ($C_{1/2}$), 159.9($C_{5/6}$), 161.4 ($C_{5/6}$), C_{41} not observed. ^{31}P-NMR ($CDCl_3$, 162 MHz): δ 45.0 (d, 1P, J_{PP} = 12Hz), 70.3 (d, 1P, J_{PP} = 12Hz), -143.6 (sept, 1P, J_{PF} = 713Hz, PF_6^-).

Synthesis of $[Ru_2(\mu\text{-}Cl)_3(PPh_3)_2(^tBu\text{-}bpy)_2]PF_6$ (**2.8a**)

To a solution of $RuCl_2(PPh_3)_3(^tBu\text{-}bpy)$ (0.007 g, 0.008 mmol) in CH_2Cl_2 (20 mL) was added $NaPF_6$ (0.010 g, 0.060 mmol) and the resulting solution was stirred refluxed for 17 h, after which the solution was allowed to cool to room temperature. A CH_2Cl_2 extract was washed with water to remove excessive $NaPF_6$. The CH_2Cl_2 layer was collected and dried by $MgSO_4$, which was then removed by filtration. The filtrate was reduced to ca. 1 mL. n-Hexane was added, affording the product as an orange solid that was washed by n-hexane (0.005 g, 0.003 mmol, 90 %). Red single crystals for X-ray diffraction were obtained from CH_2Cl_2/diethyl ether at room temperature and CH_2Cl_2/n-hexane at -19 ^oC, respectively. HR ESI MS ($[M]^+$, 100): calcd for $C_{72}H_{78}N_4P_2{}^{35}Cl_3{}^{102}Ru_2$: 1369.2854, found 1369.2850; calcd for $C_{72}H_{78}N_4P_2{}^{35}Cl_2{}^{37}Cl{}^{102}Ru_2$: 1371.2825, found 1371.2821. Microanalysis for $C_{72}H_{78}Cl_3F_6N_4P_3Ru_2$: Calcd C, 57.09; H, 5.19; N, 3.70. Found C, 57.22; H, 5.12; N, 3.61. UV-Vis (CH_2Cl_2): 20640 [10.4], 30020 [12.3], 33690 [44.6]. IR (KBr): 1481 (m), 1614 (w), 2960 (m), 3059 (w) cm^{-1}, 838 cm^{-1} ν (*P-F*). ^{1}H-NMR ($CDCl_3$, 399 MHz): δ 1.59 (s, 9H, ^{t}Bu-H, $H_{13/14}$), 1.69 (s, 9H, ^{t}Bu-H, $H_{13/14}$), 7.10 (d, 1H, J_{HH} = 5.6 Hz, $H_{7/8}$), 7.26 (m, 6H, H_{17}), 7.31 (d, 1H, J_{HH} = 4.0 Hz, $H_{7/8}$), 7.41 (m, 3H, H_{18}), 7.51 (m, 6H, H_{16}), 8.07 (s, 1H, $H_{3/4}$), 8.10 (s, 1H, $H_{3/4}$), 8.74 (d, 1H, J_{HH} = 4.8 Hz, $H_{9/10}$), 8.95 (d, 1H, J_{HH} = 4.8 Hz, $H_{9/10}$). ^{13}C-NMR ($CDCl_3$, 100 MHz): δ 30.6 ($C_{13/14}$), 30.7 ($C_{13/14}$), 35.2 ($C_{11/12}$), 35.3 ($C_{11/12}$), 118.3 ($C_{3/4}$), 118.5 ($C_{3/4}$), 122.7 ($C_{7/8}$), 123.0 ($C_{7/8}$), 127.8 (J_{CP} = 9.9 Hz, C_{17}), 129.2 (C_{18}), 133.2 (J_{CP} = 10 Hz, C_{16}), 133.5 (J_{CP} = 44 Hz, C_{15}), 154.4 ($C_{9/10}$), 154.5 ($C_{9/10}$), 159.0 ($C_{1/2}$), 159.4 ($C_{1/2}$), 160.1 ($C_{5/6}$), 160.2 ($C_{5/6}$). ^{31}P-NMR ($CDCl_3$, 162 MHz): δ 56.0 (s, 2P, -PPh_3), -146.0 (sept, 1P, J_{PF} = 712 Hz, PF_6^-).

Synthesis of $RuCl_3(PPh_3)(^tBu\text{-}bpy)$ (**2.9a**)

$RuCl_3(PPh_3)_2(DMA)\cdot DMA$ (0.165 g, 0.182 mmol) and ^{t}Bu-bpy (0.286 g, 1.06 mmol) were suspended in n-hexane (20 mL) and the solvent refluxed for 18 h. The resulting orange suspension was allowed to cool to room temperature and the product was collected by filtration and washed with diethyl ether (0.1181 g, 0.160 mmol, 88 %). An orange single crystal for X-ray study was obtained from CH_2Cl_2/n-hexane at -20 ^{o}C. HR ESI MS ($[M + Na]^+$, 100): calcd for $C_{36}H_{39}N_2NaP^{35}Cl_3{}^{102}Ru$: 760.0858, found 760.0848; calcd for $C_{36}H_{39}N_2NaP^{35}Cl_2{}^{37}Cl^{102}Ru$: 762.0828, found 762.0830. Microanalysis for $C_{36}H_{39}Cl_3N_2PRu$: Calcd C, 58.58; H, 5.33; N, 3.80. Found C, 58.51; H, 5.46; N, 3.74. UV-Vis (CH_2Cl_2): 25280 [4.62], 34480 [14.5]. IR (KBr): 695 (s), 745 (s), 1091 (m), 1434 (s), 1604 (s), 1966 (w), 2965 (m), 3057 (m) cm^{-1}.

Synthesis of [RuCl(PPh$_3$)(^{t}Bu-bpy)$_2$]Cl (**2.9b**)

$RuCl_3(PPh_3)_2(DMA)\cdot DMA$ (0.093 g, 0.103 mmol) and ^{t}Bu-bpy (0.136g, 0.508 mmol) were suspended in distilled MeOH (20 mL) and the solvent refluxed for 24 h. The red solution was allowed to cool to room temperature and then concentrated. The product was precipitated by addition of diethyl ether (50 mL), and then collected by filtration, and washed with diethyl ether (0.081 g, 0.083 mmol, 81 %). The solvent system CH_2Cl_2/diethyl ether afforded a red single crystal for X-ray diffraction at room temperature. HR ESI MS ($[M]^+$, 100): calcd for $C_{54}H_{63}N_4P^{35}Cl^{102}Ru$: 935.3522, found 935.3521; calcd for $C_{54}H_{63}N_4P^{37}Cl^{102}Ru$: 937.3493, found 937.3494. UV-Vis (CH_2Cl_2): 21680 [6.93], 34160 [35.6]. IR (KBr): 698 (m), 1481 (m), 1613 (m), 2854 (m), 2924(s), 2958 (s), 3310 (br) cm^{-1}. ^{1}H-NMR ($CDCl_3$, 399 MHz): δ 1.37 (s, 9H, ^{t}Bu-H, H_7), 1.42 (s, 9H, ^{t}Bu-H, H_7), 1.49 (s, 18H, ^{t}Bu-H, H_7), 6.94 (d, 1H, *J* = 6.0 Hz, H_4), 6.99 (d, 1H, *J* = 5.6 Hz, H_5), 7.05 (d, 1H, *J* = 6.0 Hz, H_4), 7.13 - 7.17 (m, 7H, H_9, H_5), 7.26 - 7.30 (m, 8H, H_{10}, $2H_4$), 8.22 (s, 1H, H_2), 8.28 (s, 1H, H_2), 8.51 (s, 1H, H_2), 8.53 (s, 1H, H_2), 9.03 (d, 1H, *J* = 6.0 Hz, H_5), 9.09 (d, 1H, *J* = 6.4 Hz, H_5). ^{13}C-NMR ($CDCl_3$, 100 MHz): δ 30.5 (C_7), 30.6 (C_7), 30.7 (C_7), 30.8 (C_7), 35.4 (C_6), 35.5 (C_6), 35.6 (C_6), 119.7 (C_2), 120.0 (C_2), 120.7 (C_2), 120.9 (C_2), 123.3 (C_4), 123.6 (C_4), 124.3 (C_4), 124.6 (C_4), 128.1 (C_9), 128.2 (C_9), 129.6 (C_{11}), 132.1 (J_{CP} = 40 Hz, C_8), 133.6 (C_{10}), 133.7 (C_{10}), 148.6 (C_5), 150.9 (C_5), 153.3 (C_5), 156.7 (C_5), 156.3 (C_1), 156.6 (C_1), 158.1 (C_1), 158.8 (C_1), 161.3 (C_1), 161.6 (C_1), 161.8 (C_1), 162.1 (C_1). ^{31}P-NMR ($CDCl_3$, 162 MHz): δ 45.1 (s).

Attempted synthesis of cis-[RuCl(dppb)(^{t}Bu-bpy)(PPh_3)]PF_6 (**2.3a-1***)

To a solution of **2.1c** (0.017 g, 0.019mmol) and triphenylphosphine (0.006 g, 0.021 mmol) in CH_2Cl_2 (15 mL) was added $NaPF_6$ (0.003 g, 0.020 mmol). The solution was stirred at room temperature for 45 h and then concentrated to ca. 1 mL. Precipitation from petrol spirit (30 mL) and filtration afforded the final orange powder. HR ESI MS: calcd for $C_{66}H_{63}N_2P_3{}^{35}Cl^{102}Ru$ 1113.2936, found 1113.2927. ^{31}P-NMR ($CDCl_3$, 162 MHz): δ 17.2 (dd, 2P, J_{PP} = 300 Hz, J_{PP} = 16 Hz), 59.1 (d, 1P, J_{PP} = 16 Hz), 60.9 (m, 3P), -144.3 (d, 2P, J_{PP} = 712 Hz, PF_6^-).

Attempted synthesis of cis-[$RuCl_2$(dppb)(^{t}Bu-bpy)]PF_6 (**2.3a-2**)

^{n}Bu_4NPF_6 (0.012 g, 0.031 mmol) was added to a toluene (60 mL) solution of **2.1c** (0.026 g, 0.029 mmol, in crystal form). The solution was stirred and sparged with air at 65°C for 68.5 h and then taken to dryness under vacuum. The thin-layer chromatography was adopted and the developing solvent was a mixture of CH_2Cl_2 and Et_3N (100:1). The first band (R_f = 0.8) was collected and studied. HR ESI MS: calcd for $C_{50}H_{51}N_3P_2{}^{35}Cl^{102}Ru$ 892.2291, found 892.2290; calcd for $C_{50}H_{51}N_3P_2{}^{37}Cl^{102}Ru$ 894.2261, found 894.2268. No NMR spectra obtained.

Synthesis of cis-[Ru(C=CH(4-$C_6H_4NO_2$)C≡C(4-$C_6H_4NO_2$))Cl(dppb)(^{t}Bu-bpy)] (**2.5c**)

^{n}Bu_4NCl (0.015 g, 0.052 mmol) was added to a THF (3 mL) solution of **2.4d** (0.010 g, 0.008 mmol) at room temperature. The solution was stirred for 1 h and then taken to dryness under vacuum. The solid sample was sent to analysis immediately. HR ESI MS ([M - Cl]$^+$, 100): calcd for $C_{64}H_{57}N_4O_4P_2{}^{102}Ru$ 1109.2899, found 1109.2891. ^{31}P-NMR ($CDCl_3$, 162 MHz): δ 73.9 (d, 1P, J_{PP} = 32 Hz), 84.8 (d, 1P, J_{PP} = 32 Hz).

Attempted synthesis of cis-[Ru(C=CH(4-$C_6H_4NO_2$)C≡C(4-$C_6H_4NO_2$))Cl(dppf)(^{t}Bu-bpy)] (**2.5d**)

^{n}Bu_4NCl (0.014 g, 0.050 mmol) was added to a THF (3 mL) solution of **2.4a** (0.006 g, 0.004 mmol) at room temperature. The solution was stirred for 1 h and then

taken to dryness under vacuum. The solid sample was sent to analysis immediately. HR ESI MS: calcd for $C_{68}H_{62}FeN_4O_4P_2{}^{35}Cl^{102}Ru$ 1253.2328, found 1253.2336. ^{31}P-NMR ($CDCl_3$, 162 MHz): δ 14.9 (d, 1P, J_{PP} = 16 Hz), 43.4 (d, 1P, J_{PP} = 16 Hz).

Attempted synthesis of cis-[Ru(C≡CC≡C-4-$C_6H_4NO_2$)Cl(dppf)(^{t}Bu-bpy)] (**2.6a** and **2.6a***)

To a solution of **2.1a** (0.455 g, 0.457 mmol) and 4-nitrophenylbutadiyne (0.091 g, 0.531 mmol) in THF (50 mL) with 5 drops of Et_3N was added $NaPF_6$ (0.086 g, 0.510 mmol). The solution was stirred at room temperature for 5 h and then concentrated and purified on a pad of basic alumina. Elution with CH_2Cl_2/petrol spirit/Et_3N (50/75/1) with gave a red solution. Reduction in volume of the solvent on a rotary evaporator afforded a red powder. Reprecipitation from n-pentane (20 mL) and filtration afforded the final product. HR ESI MS: found 1306.2994, found 1265.2701. ^{31}P-NMR ($CDCl_3$, 162 MHz): δ 12.7 (d, 1P, J_{PP} = 29 Hz), 43.4 (d, 1P, J_{PP} = 29 Hz) (**2.6a**); δ 19.9 (d, 1P, J_{PP} = 30 Hz), 45.7 (d, 1P, J_{PP} = 28 Hz) (**2.6a***).

Synthesis of Ru(C≡C-C_6H_5)Cl(PPh_3)$_2$(^{t}Bu-bpy) and Ru(C≡C-C_6H_5)$_2$(PPh_3)$_2$(^{t}Bu-bpy) (Scheme 2.10)

To a solution of phenylacetylene (0.095 mL, 0.865 mmol) was slowly added ^{n}BuLi (0.5 mL, 0.800 mmol, in 1.6 mol/L n-hexane solution) in THF (ca. 50 mL). The solution was stirred at -78^{o}C for 25 min and then transferred to a solution of $RuCl_2(PPh_3)_2(^t$Bu-bpy) (0.278 g, 0.288 mmol) in THF (ca. 50 mL). The reaction was kept at -78^{o}C for another 2 h under stirring, then warmed up slowly to room temperature. The solution was stirred at room temperature for 20 h. The solvent was reduced to ca. 2 mL, then 100 mL diethyl ether was added. The precipitation was filtered by celite and the filtration was concentrated to ca. 2 mL. n-Pentane (ca. 30 mL) was added to precipitate the product, which was filtered and collected, affording a mixture of Ru(C≡C-C_6H_5)Cl(PPh_3)$_2$(^{t}Bu-bpy) and Ru(C≡C-C_6H_5)$_2$(PPh_3)$_2$(^{t}Bu-bpy). HR ESI MS: calcd for $C_{72}H_{68}N_3P_2{}^{102}Ru$ 1138.3932, found 1138.3934 ([Ru(C≡C-C_6H_5)$_2$(PPh_3)$_2$(^{t}Bu-bpy) + MeCN + H]$^+$). ^{31}P-NMR ($CDCl_3$, 162

MHz): δ 31.9 (s) (Ru(C≡C-C_6H_5)Cl(PPh_3)$_2$(^{t}Bu-bpy)); δ 37.4 (s) (Ru(C≡C-C_6H_5)$_2$(PPh_3)$_2$(^{t}Bu-bpy)).

Attempted synthesis of Ru(C≡C-C_6H_5)Cl(dppf)(^{t}Bu-bpy) and Ru(C≡C-C_6H_5)$_2$(dppf)(^{t}Bu-bpy) (Scheme 2.11)

To a flask containing a mixture of Ru(C≡C-C_6H_5)Cl(PPh_3)$_2$(^{t}Bu-bpy) and Ru(C≡C-C_6H_5)$_2$(PPh_3)$_2$(^{t}Bu-bpy) (0.018 g, ca. 0.0171 mmol) and dppf (0.013 g, 0.0235 mmol) was added $CHCl_3$ (ca. 15 mL). The solution was refluxing and stirred for 4 h. After cooled down to room temperature, the solution was concentrated to ca. 2 mL. Diethyl ether (ca. 30 mL) was added to precipitate the product. The solid was dried and collected. HR ESI MS: calcd for $C_{60}H_{57}FeN_2P_2{}^{102}Ru$ 1025.2390, found 1025.2385 ([Ru(C≡C-C_6H_5)Cl(PPh_3)$_2$(^{t}Bu-bpy) - Cl]$^+$); calcd for $C_{68}H_{63}FeN_2P_2{}^{102}Ru$ 1127.2859, found 1127.2860 ([Ru(C≡C-C_6H_5)$_2$(dppf)(^{t}Bu-bpy) + H]$^+$). ^{31}P-NMR ($CDCl_3$, 162 MHz): δ 28.4 (s), 29.0 (s), 35.4 (d, J_{PP} = 16 Hz), 42.3 (m), 51.1 (d, J_{PP} = 32 Hz).

Attempted synthesis of trans-[Ru(C≡C-4-$C_6H_4NO_2$)Cl(dppf)(^{t}Bu-bpy)] (Scheme 2.16)

To a solution of $RuCl_2(PPh_3)_3$ (0.091 g, 0.095 mmol) was added dppf (0.053 g, 0.095 mmol) in CH_2Cl_2 (ca. 15 mL). The solution was stirred at room temperature for 6 min and then quickly added ^{t}Bu-bpy (0.026 g, 0.095 mmol). The solution was taken to dryness after 2 min. Then to the flask was added nitrophenylacetylene (0.016 g, 0.107 mmol), toluene (ca. 50 mL) and $NaPF_6$ (0.018 g, 0.107 mmol) in order. After the solution was stirred at room temperature for 67.5 h, 4 drops of Et_3N was added. The solution was kept stirring for further 1.5 h. Then the solution was taken to dryness. The crude product washed by petrol spirit was sent to ^{31}P-NMR study. The whole procedure was carried out in dark. ^{31}P-NMR ($CDCl_3$, 162 MHz): δ 21.3 (s), 25.3 (s), 29.7 (s), 36.0 (d, J_{PP} = 29 Hz), 41.7 (d, J_{PP} = 31 Hz), 42.7 (d, J_{PP} = 29 Hz), 50.1 (d, J_{PP} = 31 Hz).

Attempted synthesis of cis-[Ru(C=CH-4-$C_6H_4NO_2$C≡C-4-$C_6H_4NO_2$)(C≡C-4-$C_6H_4NO_2$)(dppe)(^{t}Bu-bpy)] (Scheme 2.17)

To a solution of **2.5b** (0.010 g, 0.009 mmol) and nitrophenylacetylene (0.002 g, 0.014 mmol) was added $NaPF_6$ (0.009 g, 0.056 mmol) in CH_2Cl_2 (ca. 15 mL). After the solution was stirred at room temperature for 16.5 h, 3 drops of Et_3N was added. The solution was kept stirring for further 0.5 h. Then the solution was taken to dryness. The red crude product was sent to analysis. HR ESI MS: calcd for $C_{60}H_{57}N_4O_4P_4{}^{102}Ru$ 1061.2899, found 1061.2900 ([Ru(C_4H(4-$C_6H_4NO_2$)$_2$)(dppe)(^{t}Bu-bpy)]$^+$). ^{31}P-NMR ($CDCl_3$, 162 MHz): δ 33.3 (s), 63.8 (d, J_{PP} = 13 Hz), 69.4 (d, J_{PP} = 13 Hz), 97.8 (s).

To a solution of **2.5b** (0.062 g, 0.057 mmol) and nitrophenylacetylene (0.012 g, 0.080 mmol) was added AgOTf (0.016 g, 0.062 mmol) in CH_2Cl_2 (ca. 20 mL). 5 drops of Et_3N was added subsequently. After the solution was stirred at room temperature for 21.5 h, the solution was taken to dryness. The crude product was red powder.

Attempted synthesis of Ru(C≡C-C_6H_5)$_2$(dppf)(^{t}Bu-bpy) (Scheme 2.18)

To a solution of phenylacetylene (0.350 mL, 3.19 mmol) was slowly added ^{n}BuLi (1.20 mL, 3.00 mmol, in 2.5 mol/L n-hexane solution) in THF (ca. 60 mL). The solution was stirred at -78^{o}C for 20 min and then transferred to a solution of **2.1a** (0.972 g, 0.977 mmol) in THF (ca. 100 mL). The reaction was kept at -78^{o}C for another 3 h under stirring, then warmed up slowly to room temperature. The solution was stirred at room temperature for 20 h. The solvent was reduced to ca. 10 mL, then 150 mL diethyl ether was added. The precipitation was filtered and collected as the crude product. The crude product was analysized by ^{31}P-NMR. ^{31}P-NMR ($CDCl_3$, 122 MHz): δ 14.7 (d, J_{PP} = 22 Hz), 22.8 (d, J_{PP} = 22 Hz), 43.6 (d, J_{PP} = 22 Hz), 47.8 (d, J_{PP} = 22 Hz).

The crude product was separated into two parts. One part was purified on a pad of basic alumina. Elution with CH_2Cl_2/Et_3N (100/1) gave a red solution. The eluent was taken to dryness under the rotavapor. The product was analysized by ^{31}P-NMR. ^{31}P-NMR ($CDCl_3$, 122 MHz): δ 43.2 (d, J_{PP} = 32 Hz), 51.8 (d, J_{PP} = 32 Hz). The other part was purified by crystallization in THF/n-hexane in dark. There were no crystals with good quality after a long period, but the solid was collect and sent to

^{31}P-NMR study. ^{31}P-NMR ($CDCl_3$, 122 MHz): δ 43.2 (d, J_{PP} = 32 Hz), 51.8 (d, J_{PP} = 32 Hz).

Attempted synthesis of Ru(C≡C-C_6H_5)$_2$(dppe)(^{t}Bu-bpy) (Scheme 2.18)

To a solution of phenylacetylene (0.080 mL, 0.728 mmol) was slowly added ^{n}BuLi (0.250 mL, 0.625 mmol, in 2.5 mol/L n-hexane solution) in THF (ca. 20 mL). The solution was stirred at -78^{o}C for 40 min and then transferred to a solution of **2.1b** (0.179 g, 0.214 mmol) in THF (ca. 35 mL). The reaction was kept at -78^{o}C for another 2 h under stirring, then warmed up slowly to room temperature. The solution was stirred at room temperature for 17 h. After that, MeI (0.15 mL, 2.41 mmol) was added to quench the reaction. The solvent was reduced to ca. 2 mL, then 60 mL diethyl ether was added. The precipitation was filtered and collected as the crude product. The crude product was analysized by ^{31}P-NMR. ^{31}P-NMR ($CDCl_3$, 162 MHz): δ 52.2 (d, J_{PP} = 15 Hz), 63.3 (d, J_{PP} = 15 Hz), 65.1 (d, J_{PP} = 25 Hz), 71.1 (d, J_{PP} = 25 Hz). The filtration was taken to dryness and purified on a pad of basic alumina. The secondary elution with ethyl acetate/Et_3N (100/1) gave a red solution. The eluent was taken to dryness under the rotavapor, affording a product as red powder. The powder was attempted to be purified by crystallization in CH_2Cl_2/n-hexane. Red crystals were obtained and proved to be *cis*-[Ru(C≡C-C_6H_5)(dppe)I(^{t}Bu-bpy)].

Attempted synthesis of cis-[Ru(C≡C-C_6H_5)(dppe)I(^{t}Bu-bpy)] (Scheme 2.19)

To a flask containing **2.2d** (0.028 g, 0.031 mmol) and ^{t}BuNI (0.013 g, 0.036 mmol) was added THF (ca. 15 mL). The solution was stirred at room temperature for 25 h. The solution was taken to dryness, affording the crude product as red solid. The crude product was sent to MS and ^{31}P-NMR study. HR ESI MS: calcd for $C_{52}H_{54}N_2P_2{}^{127}I^{102}Ru$ 997.1851, found 997.1852 ([Ru(C≡C-C_6H_5)(dppe)I(^{t}Bu-bpy) + H]$^+$). ^{31}P-NMR ($CDCl_3$, 162 MHz): δ 67.2 (d, J_{PP} = 20 Hz), 76.7 (d, J_{PP} = 20 Hz) (**2.2d**); δ 69.6 (d, J_{PP} = 18 Hz), 78.6 (d, J_{PP} = 18 Hz).

2.8 REFERENCE

1. Di Bella, S., *Chem. Soc. Rev.*, **2001**, 30, 355.
2. Cadierno, V.; Conejero, S.; Gamasa, M. P.; Gimeno, J.; Asselberghs, I.; Houbrechts, S.; Clays, K.; Persoons, A.; Borge, J.; Garcia-Granda, S., *Organometallics*, **1999**, 18, 582.
3. Houbrechts, S.; Clays, K.; Persoons, A.; Cadierno, V.; Gamasa, M. P.; Gimeno, J., *Organometallics*, **1996**, 15, 5266.
4. Powell, C. E.; Cifuentes, M. P.; McDonagh, A. M.; Hurst, S. K.; Lucas, N. T.; Delfs, C. D.; Stranger, R.; Humphrey, M. G.; Houbrechts, S.; Asselberghs, I.; Persoons, A.; Hockless, D. C. R., *Inorg. Chim. Acta*, **2003**, 352, 9.
5. Garcia, M. H.; Rabalo, M. P.; Dias, A. R.; Duarte, M. T.; Wenseleers, W.; Aerts, G.; Goovaerts, E.; Cifuentes, M. P.; Hurst, S.; Humphrey, M. G.; Samoc, M.; Luther-Davies, B., *Organometallics*, **2002**, 21, 2107.
6. Coe, B. J.; Jones, L. A.; Harris, J. A.; Sanderson, E. E.; Brunschwig, B. S.; Asselberghs, I.; Clays, K.; Persoons, A., *Dalton Trans.,* **2003**, 11, 2335.
7. Coe, B. J.; Harris, J. A.; Brunschwig, B. S., *Dalton Trans.,* **2003**, 12, 2384.
8. Coe, B. J.; Harries, J. L.; Helliwell, M.; Brunschwig, B. S.; Harris, J. A.; Asselberghs, I.; Hung, S.; Clays, K.; Horton, P. N.; Hursthouse, M. B., *Inorg. Chem.*, **2006**, 45, 1215.
9. Coe, B. J.; Fielden J.; Foxon, S. P.; Asselberghs, I.; Brunschwig, B. S., *Inorg. Chem.*, **2010**, 49, 10718.
10. Coe, B. J.; Foxon, S. P.; Harper, E. C.; Helliwell, M.; Raftery, J.; Swanson, C. A.; Brunschwig, B. S.; Clays, K.; Franz, E.; Garin, J.; Orduna, J.; Horton, P. N.; Hursthouse, M. B., *J. Am. Chem. Soc.,* **2010**, 132, 1706.
11. Boubekeur-Lecaque, L.; Coe, B. J.; Harris, J. A.; Helliwell, M.; Asselberghs, I.; Clays, K.; Foerier, S.; Verbiest, T., *Inorg. Chem.*, **2011**, 50, 12886.
12. Green, M. L. H.; Marder, S. R.; Thompson, M. E.; Bandy, J. A.; Bloor, D.; Kolinsky, P. V.; Jones, R. J., *Nature*, **1987**, 330, 360.
13. Powell, C. E.; Humphrey, M. G., *Coord. Chem. Soc.,* **2004**, 248, 725.
14. Cifuentes, M. P.; Driver, J.; Humphrey, M. G.; Asselberghs, I.; Persoons, A.; Samoc, M.; Luther-Davies, B., *J. Organomet. Chem.,* **2000**, 607, 72.

15. Babgi, B. A.; Al-Hindawi, A.; Moxey, G. J.; Razak, F. I. A.; Cifuentes, M. P.; Kulasekera, E.; Stranger, R.; Teshome, A.; Asselberghs, I.; Clays, K., *J. Organomet. Chem.,* **2013**, 730, 108.
16. Fonum, T. N.; Green, K. A.; Randles, M. D.; Cifuentes, M. P.; Willis, A. C.; Teshome, A.; Asselberghs, I.; Clays, K., *J. Organomet. Chem.,* **2008**, 693, 1605.
17. Trujillo, A.; Veillard, R.; Argouarch, G.; Roisnel, T.; Singh, A.; Ledoux, I.; Paul, F., *Dalton Trans.,* **2012**, 41, 7454.
18. Silva, T. J. L.; Menes, P. J.; Garcia, M. H.; Robalo, M. P.; Ramalho, J. P. P.; Carvalho, A. J. P.; Buchert, M.; Wittenburg, C.; Heck, J., *Eur. J. Inorg. Chem.*, **2013**, 3506.
19. Garcia, M. H.; Florindo, F.;Peidade, M. F. M.; Duarte, M. T.; Robalo, M. P.; Goovaerts, E.; Wenseleers, W., *J. Organomet. Chem.,* **2009**, 694, 433.
20. Zyss, J.; Dhenaut, C.; Chau Van, T.; Ledoux, I., *Chem. Phys. Lett.,* **1993**, 206, 409.
21. Erkkila, K. E.; Odom, D. T.; Barton, J. K., *Chem. Rev.*, **1999**, 99, 2777.
22. Dhenaut, C.; Ledoux, I.; Samuel, I. D. W.; Zyss, J.; Bourgault, M.; Le Bozec, H., *Nature*, **1995**, 374, 339.
23. Maury, O.; Viau, L.; Senechal, K.; Corre, B.; Guegan, J.; Renouard, T.; Ledoux, I.; Zyss, J.; Le Bozec, H., *Chem. Eur. J.,* **2004**, 10, 4454.
24. Zuniga, C.; Crivelli, I.; Loeb, B., *Polyhedron*, **2015**, 85, 511.
25. Le Bouder, T.; Maury, O.; Bondon, A.; Costuas, K.; Amouyal, E.; Ledoux, I.; Zyss, J.; Le Bozec, H., *J. Am. Chem. Soc.,* **2003**, 125, 12284.
26. Ledoux-Rak, I.; Zyss, J.; Le Bouder, T.; Maury, O.; Bondon, A.; Le Bozec, H., *J. Lumin.,* **2005**, 111, 307.
27. Coe, B. J.; Harris, J. A.; Brunschwig, B. S.; Asselberghs, I.; Clays, K.; Garin, J.; Orduna, J., *J. Am. Chem. Soc.,* **2005**, 127, 13399.
28. Coe, B. J.; Fielden, J.; Foxon, S. P.; Brunschwig, B. S.; Asselberghs, I.; Clays, K.; Samoc, A.; Samoc, M., *J. Am. Chem. Soc.,* **2010**, 132, 3496.
29. Ordronneau, L.; Nitadori, H.; Ledoux, I.; Singh, A.; Williams, J. A. G.; Akita, M.; Guerchais, V.; Le Bozec, H., *Inorg. Chem.*, **2012**, 51, 5627.
30. Maury, O.; Guegan, J.; Renouard, T.; Hilton, A.; Dupau, P.; Sandon, N.; Toupet, L.; Le Bozec, H., *New J. Chem.*, **2001**, 25, 1553.
31. Nisic, F.; Colombo, A.; Dragonetti, C.; Garoni, E.; Marinotto, D.; Righetto, S.; De Angelis, F.; Lobello, M. G.; Salvatori, P.; Biagini, P.; Melchiorre, F., *Organometallics*, **2015**, 34, 94.

32. Green, K. A.; Cifuentes, M. P.; Corkery, T. C.; Samoc, M.; Humphrey, M. G., *Angew. Chem. Int. Ed.*, **2009**, 48, 7876.

33. McDonagh, A. M.; Humphrey, M. G.; Samoc, M.; Luther-Davies, B.; Houbrechts, S.; Wada, T.; Sababe, H.; Persoons, A., *J. Am. Chem. Soc.,* **1999**, 121, 1405.

34. Cifuentes, M. P.; Powell, C. E.; Humphrey, M. G.; Heath, G. A.; Samoc, M.; Luther-Davies, B., *J. Phys. Chem. A*, **2001**, 105, 9625.

35. Hurst, S. K.; Lucas, N. T.; Humphrey, M. G.; Isoshima, T.; Wostyn, K.; Asselberghs, I.; Clays, K.; Persoons, A.; Samoc, M.; Luther-Davies, B., *Inorg. Chim. Acta*, **2003**, 350, 62.

36. Cifuentes, M. P.; Powell, C. E.; Morrall, J. P.; McDonagh, A. M.; Lucas, N. T.; Humphrey, M. G.; Samoc, M.; Houbrechts, S.; Asselberghs, I.; Clays, K.; Persoons, A.; Isoshima, T., *J. Am. Chem. Soc.,* **2006**, 128, 10819.

37. Green, K. A.; Simpson, P. V.; Corkery, T. C.; Cifuentes, M. P.; Samoc, M.; Humphrey, M. G., *Macromol. Rapid Commun.*, **2012**, 33, 573.

38. Merhi, A.; Grelaud, G.; Green, K. A.; Minh, N. H.; Reynolds, M.; Ledoux, I.; Barlow, A.; Wang, G.; Cifuentes, M. P.; Humphrey, M. G.; Paul, F.; Paul-Roth, C. O., *Dalton Trans.,* **2015**, 44, 7748.

39. Bharate, B. G.; Jadhav, A. N.; Chavan, S. S., *Polyhedron*, **2012**, 33, 179.

40. Chavan, S. S.; Bharate, B. G., *Inorg. Chim. Acta*, **2013**, 394, 598.

41. Long, N. J.; Williams, C. K., *Angew, Chem. Int. Ed.*, **2003**, 42, 2586.

42. Long, N. J., *Angew, Chem. Int. Ed.*, **1995**, 34, 21.

43. Barlow, S.; O'Hare, D., *Chem. Rev.*, **1997**, 97, 637.

44. Lewis, J.; Khan, M. S.; Kakkar, A. K.; Johnson, B. F. G.; Marder, T. B.; Fyfe, H. B.; Wittmann, F.; Friend, R. H.; Day, A. E., *J. Organomet. Chem.,* **1992**, 425, 165.

45. Chawdhury, N.; Kohler, A.; Friend, R. H.; Younus, M.; Long, N. J.; Raithby, P. R.; Lewis, J., *Macromolecules,* **1998**, 31, 722.

46. Paul, F.; Lapinte, C., *Coord. Chem. Rev.*, **1998**, 178-180, 431.

47. Renouard, T.; Le Bozec, H.; Ledoux, I.; Zyss, J., *Chem. Commun.*, **1999**, 871.

48. Xue, W.; Chan, M. C.; Su, Z.; Cheung, K.; Liu, S.; Che, C., *Organometallics*, **1998**, 17, 1622.

49. Pawlowski, V.; Kunkely, H.; Lenartz, C.; Bohn, K.; Vogler, A., *Eur. J. Inorg. Chem.,* **2004**, 4242.

50. Osawa, M.; Kawata, I.; Igawa, S.; Tsuboyama, A.; Hashizume, D.; Hoshino, M., *Eur. J. Inorg. Chem.,* **2009**, 4242.

51. Bandoli, G.; Domella, A., *Coord. Chem. Rev.,* **2000**, 209, 161.

52. Sixt, T.; Fiedler, J.; Kaim, W., *Inorg. Chem. Commun.*, **2000**, 3, 80.

53. Therrien, B.; Vieille-Petit, L.; Jeanneret-Gris, J.; Stepnicka, P.; Suss-Fink, G., *J. Organomet. Chem.,* **2004**, 689, 2456.

54. Goretzki, G.; Davies, E. S.; Argent, S. P.; Warren, J. E.; Blake, A. J.; Champness, N. R., *Inorg. Chem.*, **2009**, 48, 10264.

55. Li, Z.; Liu, Y.; Mertens, S. F. L.; Pobelov, I. V.; Wandlowski, T., *J. Am. Chem. Soc.,* **2010**, 132, 8187.

56. Hallman, P. S.; Stephenson, T. A.; Wilkinson, G., *Inorg. Synth.*, **1970**, 12, 237.

57. Batista, A. A.; Santiago, M. O.; Donnici, C. L.; Moreira, I. S.; Healy, P. C.; Berners-Price, S. J.; Queiroz, S. L., *Polyhedron*, **2001**, 20, 2123.

58. Jia, G.; Rhelngold, A. L., Meek, D. W., *Organometallics,* **1989**, 8, 1378.

59. Albertin, G.; Antoniutti, S.; Bordignon, E.; Cazzaro, F.; Ianelli, S.; Pelizzi, G., *Organometallics,* **1995**, 14, 4114.

60. Field, L. D.; Magill, A. M.; Jensen, P., *Organometallics,* **2008**, 27, 6539.

61. Lee, J.; Caulton, K. G., *J. Organomet. Chem.,* **2008**, 693, 1664.

62. Lynam, J. M.; Nixon, T. D.; Whitwood, A. C., *J. Organomet. Chem.,* **2008**, 693, 3103.

63. Eaves, S. G.; Yufit, D. S.; Skelton, B. W.; Lynam, J. M.; Low, P. J., *Dalton Trans.,* **2015**, 44, 21016.

64. Bruce, M. I.; de Montigny, F.; Jevric, M.; Lapinte, C.; Skelton, B. W.; Smith, M. E.; White, A. H., *J. Organomet. Chem.,* **2004**, 689, 2860.

65. Mudalige, D. C.; Ma, E. S. F.; Rettig, S. J.; Patrick, B. O.; James, B. R., *Can. J. Chem.,* **2014**, 92, 716.

66. Batista, A. A.; Polato, E. A.; Queiroz, S. L.; Nascimento, O. R.; James, B. R.; Rettig, S. J., *Inorg. Chim. Acta*, **1995**, 230, 111.

67. Gallatti, T. F.; Bogado, A. L.; von Poelhsitz, G.; Ellena, J.; Castellano, E. E.; Batista, A. A.; de Araujo, M. P., *J. Organomet. Chem.,* **2007**, 692, 5447.

68. Zhang, F.; Wang, L.; Chang, S.; Huang, K.; Chi, Y.; Hung, W.; Chen, C.; Lee, G.; Chou, P., *Dalton Trans.,* **2013**, 42, 7111.

69. Reed, R. W.; Santarsiero, B.; Cavell, R. G., *Inorg. Chem.*, **1996**, 35, 4292.

70. Bishop, J. J.; Davision, A.; Katcher, M. L.; Lichtenberg, D. W.; Merrill, R. E., *J. Organomet. Chem.,* **1971**, 27, 241.

71. Casellato, U.; Ajo, D.; Valle, G.; Corain, B.; Longato, B.; Graziani, R., *J. Chem. Cryst.*, **1988**, 18, 583.

72. Graham, E. M.; Miskowski, V. M.; Perry, J. W.; Coulter, D. R.; Stiegman, A. E.; Schaefer, W. P.; Marsh, R. E., *J. Am. Chem. Soc.,* **1989**, 111, 8771.

73. Eastmond, R.; Johnson, T. R.; Walton, D. R. W., *Tetrahedron*, **1972**, 28, 4601.

Chapter 3 – Synthesis and Characterization of Ruthenium Complexes with $(N\hat{}P)_2$ Donor Sets

3.1 INTRODUCTION

Ruthenium(II) polypyridine complexes have been studied intensively for their potential application in energy conversion, luminescent sensing, biotechnology, *etc* [1-7]. Due to the σ-donating and π-accepting abilities of phosphine ligands to control the electronic structure of the ruthenium center, ruthenium(II) phosphine complexes are also well documented [8-13]. Control over the spectroscopic and electrochemical properties of ruthenium complexes can be achieved by changing the number and position of donor sets. Thus, conducting studies on mixed-ligand ruthenium complexes are worthwhile. The diimine-diphosphine (N^N)(P^P) donor set has been detailed in Chapter 2. A study of the iminophosphine $(N^P)_2$ donor set is described in this Chapter.

Two iminophosphine ligands, namely 2-(diphenylphosphino)pyridine and 8-(diphenylphosphino)quinoline, were selected for this study, as shown in Figure 3.1. The heterobifunctional ligands, having both imine and phosphine moieties can act as unsymmetrical bidentate ligands. The π-acceptor phosphorus atom can stabilize a low oxidation state of the metal atom, while the σ-donor nitrogen is helpful to stabilize a higher oxidation state and make the metal atom more susceptible to an oxidative addition reaction. The Cu^{I} complexes based on the PPh_2qn ligand exhibit higher electro- and photochemical stability than those complexes with traditional diimine or diphosphine ligands [14].

2-(diphenylphosphino)pyridine
PPh_2py

8-(diphenylphosphino)quinoline
PPh_2qn

Figure 3.1 Chemical structures of the N^P ligands used in this study.

The concept of hemilability was first mentioned by Jeffrey and Rauchfuss, referring to the labile coordination of ligands bearing soft and hard donor atoms [15]. The two N^P ligands herein represent an important class of hemilabile ligands which can bind to transition metals with medium strength. Due to the dynamic chelating ability, organometallics containing such hemilabile ligands can provide potential sites for reversible binding to metal centres, which makes the hemilabile metal

complexes extremely important in catalysis and various organic transformations [16-18].

PPh_2py is among the most widely studied hemilabile N^P ligands, and is one of the most useful ligands in coordination chemistry, with four different possible coordination modes as shown in Figure 3.2: N-monodentate [19], P-monodentate [20, 21], N^P bridge [22-25] and N^P chelate mode [26, 27]. In its chelating coordination mode, it forms strained four-membered rings, which are relatively unstable and play a crucial role in chemical- and bio-catalysis [28, 29]. The catalysis studies of PPh_2py organometallics are numerous. Additionally, the half sandwich organometallic complexes with PPh_2py have potential applications as chemotherapeutics [30].

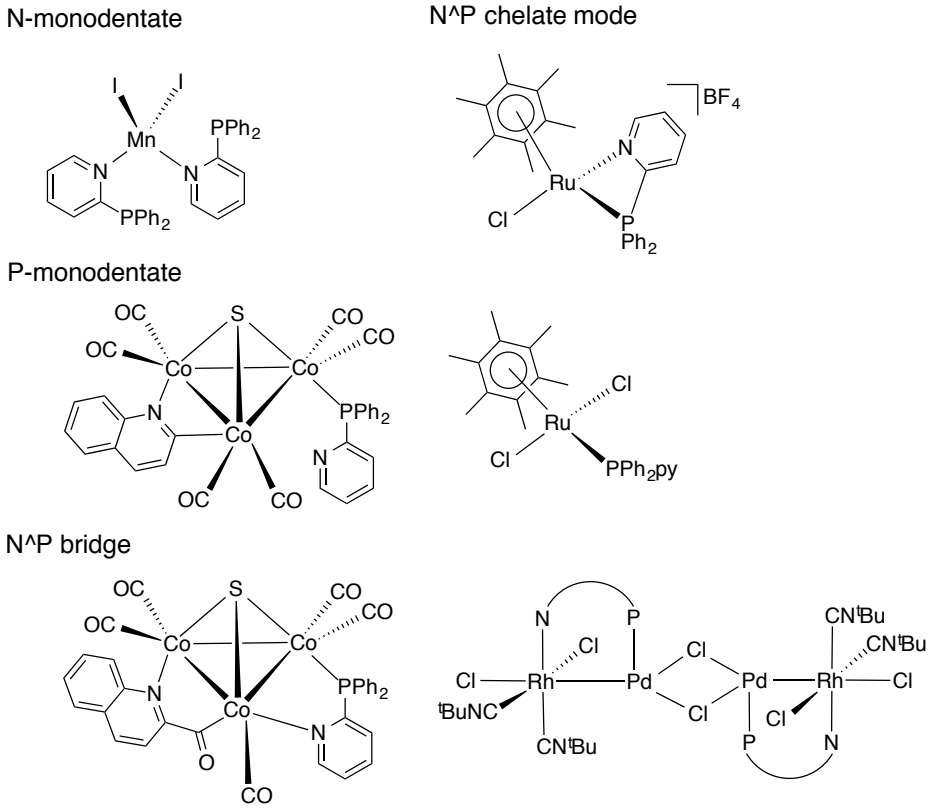

Figure 3.2 Possible coordination modes of the PPh_2py ligand.

Compared with the PPh_2py ligand, there have been much fewer investigations of the PPh_2qn ligand. Unlike the former, the PPh_2qn ligand can form a planar five-membered chelating ring with the metal atom which may further stabilize unusual oxidation states and /or coordination geometries, owing to the steric requirements

and the electronic differentiation of the phosphine and quinolyl donor groups [31]. So far, research on the PPh_2qn ligand coordinating with Cu^I [32-35],Zn^{II} [35, 36], Ru^{II} [37, 38], Pd^{II} [39, 40] and Ir^{III} [41, 42] has been reported widely, and some complexes with the PPh_2qn ligand coordinating with Ni^I [43] and Au^I [44] have been synthesized. Similar to the PPh_2py ligand, research on organometallics bearing the PPh_2qn ligand mainly focuses on catalysis.

There are no reports of the NLO properties of ruthenium complexes with $(N^P)_2$ donor set. In this work, a series of such complexes were synthesized and characterized, including linear absorption and electrochemical studies. The NLO properties of these complexes will be examined in the near future following reestablishment of a local femtosecond Z-scan capability.

3.2 SYNTHESIS AND CHARACTERIZATION

3.2.1 Solvent effect on the synthesis of *cis*-$[RuCl_2(PPh_2py)_2]$

The complex *cis,cis,cis*-$[RuCl_2(PPh_2py)_2]$, as shown in Figure 3.3, has been synthesized by Faraone and his co-workers through a two-step reaction from $[Ru(C_8H_{12})Cl_2]_n$ in a total yield of 32 % [45]. The Messerle group has synthesized *trans,cis,cis*-$[RuCl_2(PyP)_2]$ (PyP = 1-(2-diphenylphosphinoethyl)pyrazole) successfully from $RuCl_2(PPh_3)_3$ in chlorinated solvent, then *cis,cis,cis*-$[RuCl_2(PyP)_2]$ through stirring *trans,cis,cis*-$[RuCl_2(PyP)_2]$ in EtOH overnight [46]. A similar experimental procedure to Messerle's synthesis was used in this work. To a Schlenk flask with $RuCl_2(PPh_3)_3$ and more than two equiv. PPh_2py ligand was added distilled CH_2Cl_2. The brown solution gradually became yellow after stirring for two hours. In contrast to Messerle's result, the dominant product in this study is *cis,cis,cis*-$[RuCl_2(PPh_2py)_2]$, which may be a result of steric effects due to insufficient space for two PPh_2py ligands sited in the same plane; compared with Faraone's method, this synthetic route saves time and results in a much higher yield of 82 %.

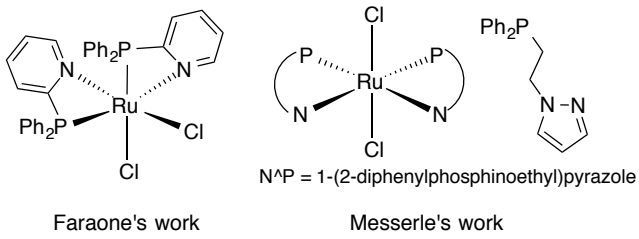

Figure 3.3 Chemical structures of *cis,cis,cis*-[$RuCl_2(PPh_2py)_2$] (left) and *trans,cis,cis*-[$RuCl_2(PyP)_2$] (right)

The influence on the reaction outcome of different solvents employed in the synthesis of *cis*-[$RuCl_2(PPh_2py)_2$] (**3.1a**) is shown in Scheme 3.1. In non-polar solvents, *e.g.* toluene, the main product is the *cis*-isomer. As the solvent polarity is increased, *e.g.* in THF, **3.1a***, confirmed by MS and a single-crystal X-ray study, appears as a minor product. In polar solvents, *e.g.* MeOH, **3.1a*** replaces **3.1a** as the dominant product. The structure of **3.1a*** reveals that two of the three PPh_3 ligands have been replaced by two bidentated PPh_2py ligands, with one PPh_3 ligand remaining; one Cl atom is no longer in the coordination sphere, but present as a chloride counter-ion.

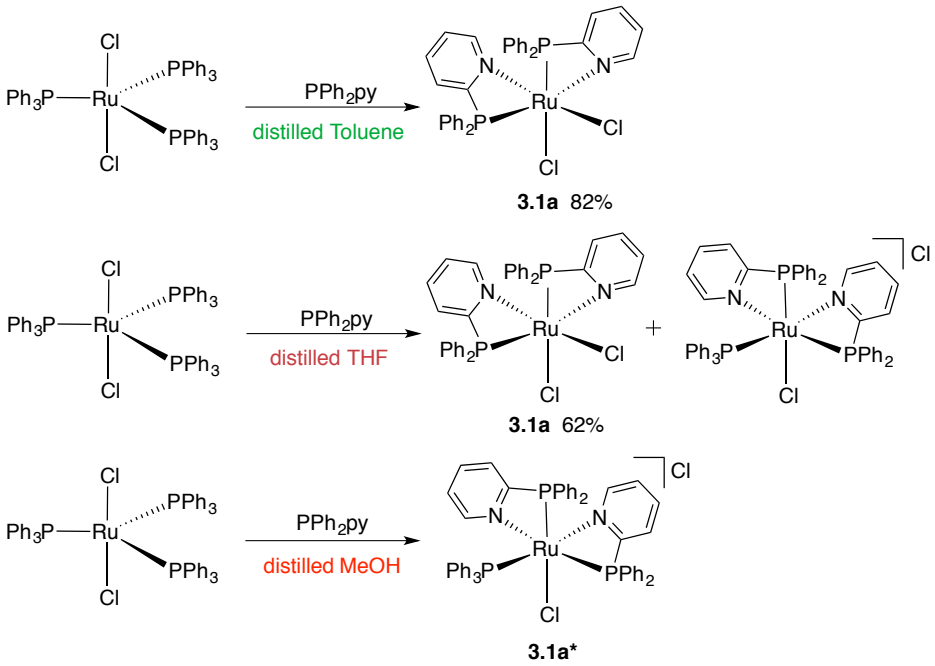

Scheme 3.1 Varying synthetic outcome in different solvents.

3.1a* is stable in the crystalline form, while decomposition is observed in deuterated solvent as shown in Figure 3.4. Initially, three different phosphorus atoms can be observed at δ -28.5, -11.1 and 38.9 ppm, which are assigned as the phosphorus nuclei in PPh_2py, PPh_3 and PPh_2py, respectively. All the resonances

are doublets of doublets. The coupling constant between PPh_3 and PPh_2py is ca. 30 Hz, while the coupling between the two PPh_2py ligands is much stronger (coupling constant ca. 300 Hz). After three days, some of the **3.1a*** converts to **3.1a** and other complexes of uncertain composition.

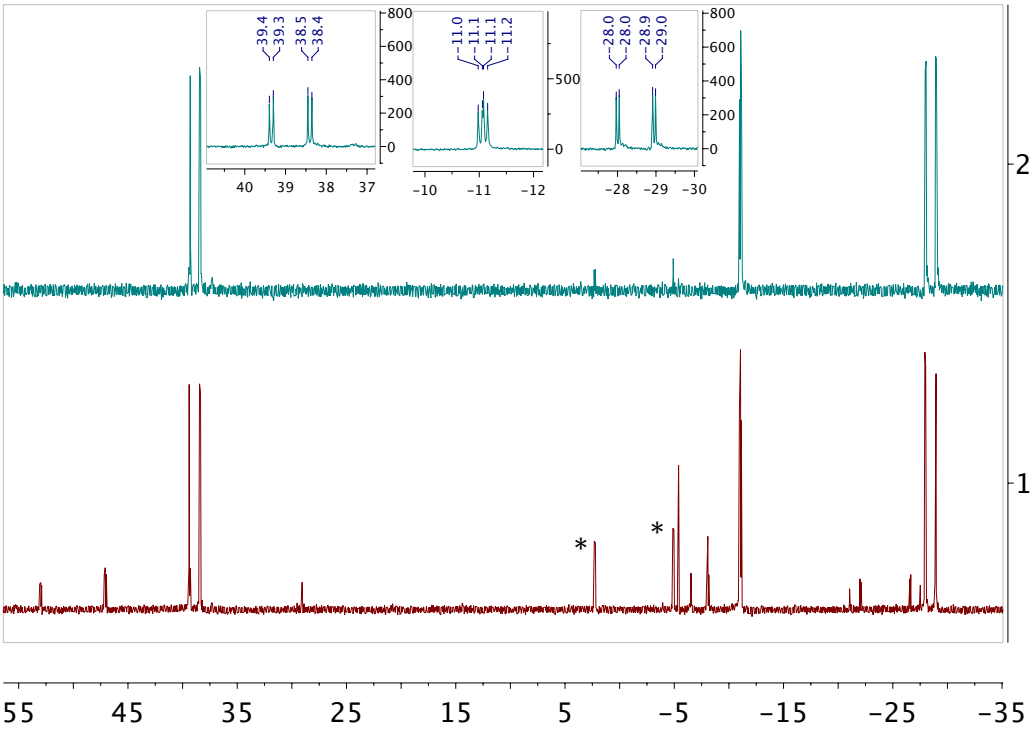

Figure 3.4 NMR spectra of **3.1a*** in $CDCl_3$: after solution preparation (above) and three days later (below). The peaks with * are assigned to **3.1a.**

3.2.2 Attempts to form *mono*-alkynyl complexes

Attempts to form mono-alkynyl complexes were made, the results being shown in Scheme 3.2. In the presence of phenylacetylene, $NaPF_6$ and Et_3N, no alkynyl or η^3-coupling products were synthesized. Instead, the dimer *cis*-$[Ru_2(\mu\text{-}Cl_2)(PPh_2py)_4](PF_6)_2$ (**3.2a**), confirmed by a single-crystal X-ray diffraction study, was the dominant product. A secondary product **3.2a***, as shown in the scheme, was crystallized from CH_2Cl_2/*n*-hexane. In **3.2a***, one of the previous Ru-N bonds has been cleaved and replaced by a Ru-C bond from insertion of a C=CHPh group. Further investigations were conducted.

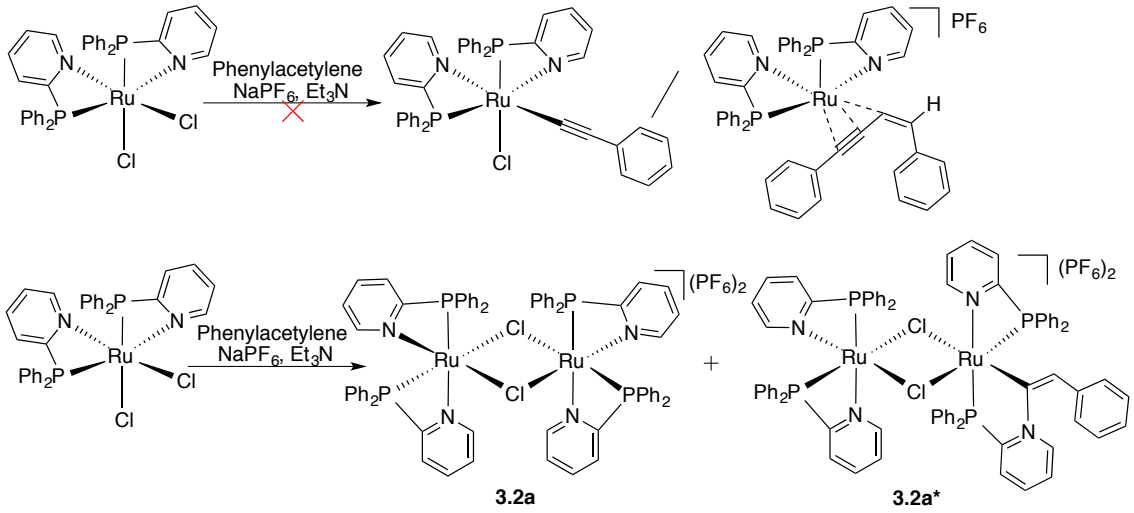

Scheme 3.2 Expected (above) and actual (below) synthetic results of the reactions making mono-alkynyl complexes .

The complex **3.2a** was also synthesized in the presence of $NaPF_6$ only, in a 71 % yield and with less impurities. **3.2a*** could not be made from **3.2a** as shown in Scheme 3.3, which suggests competition occurs between the formation of **3.2a** and **3.2a*** in the presence of phenylacetylene when **3.1a** is used as the precursor.

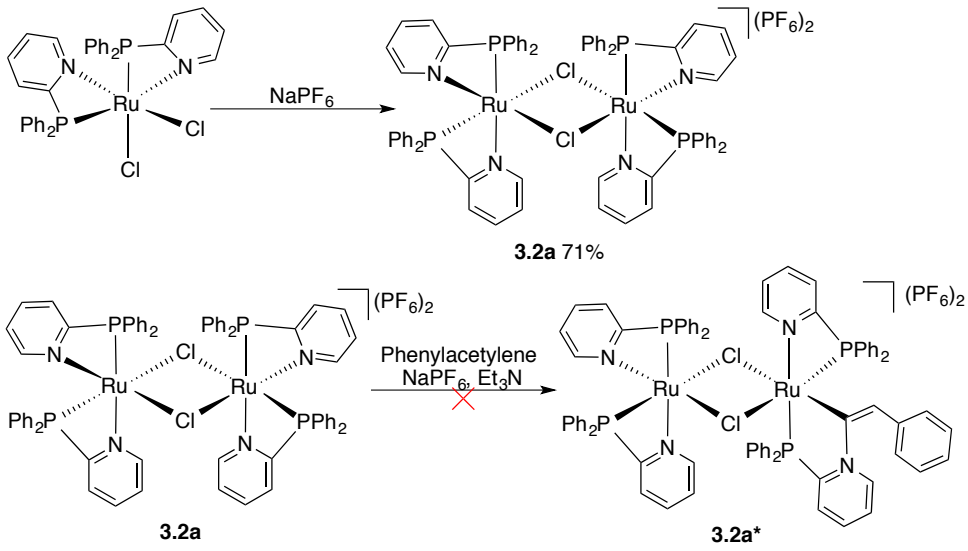

Scheme 3.3 Further investigations of ruthenium PPh_2py complexes.

3.2.3 Synthesis of PPh_2qn complexes

The synthesis of ruthenium PPh_2qn complexes followed the same strategy as that of PPh_2py series, as shown in Scheme 3.4. The complex **3.1b** was obtained from $RuCl_2(PPh_3)_3$ and excess iminophosphine ligand in distilled THF. **3.2b** was

synthesized easily in the presence of $NaPF_6$ in good yield. Similarly, no mono-alkynyl or bis-alkynyl complexes were detected in the presence of the alkyne reagent in a further attempt, which was consistent with the results of the PPh_2py reactions. However, no product analogous to **3.2a*** was observed in the MS spectra from the PPh_2qn reactions. Overall, the selectivity of the PPh_2qn reactions is better than that of the PPh_2py reactions, which can possibly be attributed to the more stable five-membered chelate ring formed by the N^P ligand and the ruthenium atom.

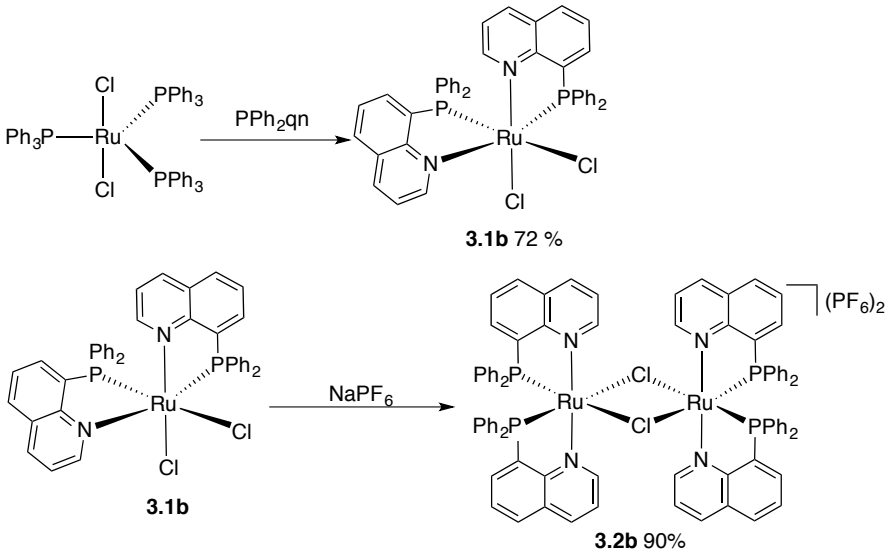

Scheme 3.4 Synthesis of PPh_2qn ruthenium complexes.

3.2.4 NMR analysis

The structures of all stable complexes in this Chapter were assigned from 1D-NMR (^{1}H-, ^{13}C-, ^{31}P-NMR and APT) and 2D-NMR (gHSQC, gHMBC and gCOSY) spectra, except **3.2a** because of insufficient solubility to obtain useful APT or ^{13}C-NMR spectra. There are no symmetry elements in **3.1a**, **3.1b** or **3.2a**, while the four N^P ligands are in the same chemical environment in **3.2b**.

3.1a, **3.1b** and **3.2a** show a doublet of doublets in their ^{31}P-NMR spectra, suggesting *cis*-isomers. The two phosphorus nuclei in each N^P ligand couple with each other, with a coupling constant of ca. 30 Hz. For **3.2b**, there is one singlet in the ^{31}P-NMR spectra at δ 64.0 ppm which corresponds to the PPh_2qn ligand, and a septet signal from the PF_6 at δ -144.2 ppm (J_{PF} = 706 Hz), which is in good agreement with the structure.

The two types of carbons in the complexes, tertiary and quaternary, can be recognized easily based on the information provided by APT studies. All quaternary carbons connected to phosphorus atoms exhibit coupling in **3.1b** and **3.2b**, with chemical shifts ranging from δ 132.9 – 133.5 and 130.7 – 131.9 ppm respectively. Because of the complexity of the ^{13}C-NMR spectra in this region, it is difficult to reliably extract coupling constants. The ^{13}C-NMR spectrum of **3.1a** is similar; the chemical shifts of the Ph-Cs connected to the phosphorus atoms range from δ 129.7 – 130.3 ppm, and again have uncertain coupling constants. The two quaternary Py-Cs have large downfield chemical shifts (δ 172.8 and 174.4 ppm) and large coupling constants (ca. 53 and 48 Hz, respectively).

In the ^{1}H-NMR studies, all the complexes in this work have no signals upfield (< δ 5.0 ppm). The protons attached to the tertiary carbon atoms next to the nitrogen atoms have the greatest downfield chemical shift in **3.1a**, **3.1b** and **3.2b**.

3.3 X-RAY STRUCTURAL STUDIES

Single crystal structure determinations have been made for the complexes **3.1a**, **3.1a***, **3.1b**, **3.2a**, **3.2a*** and **3.2b**. Crystal data and plots of each molecule with the atom labeling are summarized below.

Figure 3.5 and Table 3.1 show the data and plots of **3.1a** and **3.1b**. Both of them are *cis*-octahedral isomers and six-coordinate. The PPh_2py ligand forms a four-membered ring with the ruthenium atom and with a N-Ru-P angle of ca. 70^{o}, while it forms a five-membered ring in **3.1b** with a wider N-Ru-P angle of ca. 82^{o}. The four-membered ring forces the two chloride atoms closer to each other than those in **3.1b**. The crystal data of **3.1a*** is listed in Table 3.1. The ruthenium centre is six-coordinate with two PPh_2py ligands, one PPh_3 ligand and one chlorine atom. The phosphorus atoms from the PPh_2py ligands are *cis*-disposed, and the phosphorus atom from the PPh_3 ligand is trans to the chloride atom, and cis to the other two phosphorus atoms.

The complex **3.2a**, the dimer of **3.1a** as shown in Figure 3.7, is a charged ruthenium complex with two PF_6 groups. The related information on bond lengths and angles is tabulated in Table 3.3. There is no difference in bond lengths between **3.1a** and **3.2a**, while the angles vary. The smaller angle between the two chlorine atoms induced by the bridging function, is reduced to 83.66(9)^o in **3.2a,** which provides more space for the two PPh_2py ligands. The values of the N-Ru-Cl angles are increased as well.

A single crystal structure determination has been made for **3.2a***, the result being summarized in Figure 3.8 and Table 3.4. The complex is a charged species with four PPh_2py ligands. What is notable here is the insertion of a C=CHPh group into one of the former Ru-N bonds. The angles of N(1)-Ru-C(1), C(2)-C(1)-Ru and C(1)-C(2)-C(3) are all around 120^o, and the bond length of C(1)-C(2) is within the reasonable range of the C=C bond.

Figure 3.9 and Table 3.5 exhibit the result of the X-ray study of complex **3.2b,** a +2 charged diruthenium complex. The crystal of **3.2b** belongs to the monoclinic crystal system with a Cc space group. The four phosphorus atoms are in the same chemical environment, showing one singlet in the ^{31}P-NMR study. Compared with **3.1b**, the two chlorine atoms are closer with an angle of Cl-Ru-Cl at 79.12(8)^o, much smaller than that of **3.1b** (92.157(15)^o). The phosphorus atom in **3.2b** is *cis* to one chlorine atom and *trans* to the other chlorine atom. The two chlorine and the two phosphorus atoms are in the same plane, while one phosphorus atom is perpendicular to the corresponding plane in **3.1b**. Similarly, the nitrogen atoms in **3.2b** are *cis* to the phosphorus and chlorine atoms. The bond data of **3.2b** within the PPh_2qn ligands has no obvious differences to that of **3.1b**.

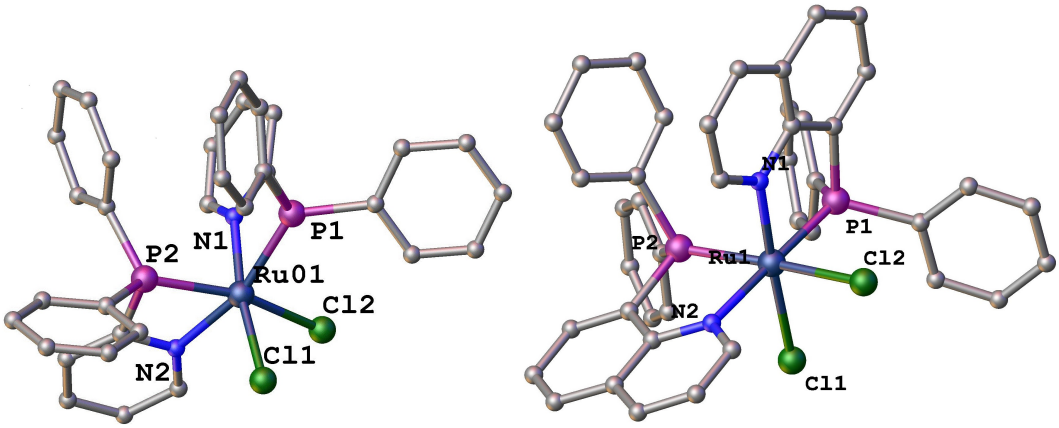

Figure 3.5 Molecular geometry and atomic labeling scheme for *cis*-[$RuCl_2(PPh_2py)_2$] (**3.1a**) (left) and *cis*-[$RuCl_2(PPh_2qn)_2$] (**3.1b**) (right). Hydrogen atoms have been omitted for clarity.

Table 3.1 Selected bond lengths (Å) and angles (°) for for *cis*-[$RuCl_2(PPh_2py)_2$] (**3.1a**) and *cis*-[$RuCl_2(PPh_2qn)_2$] (**3.1b**).

Complexes	**3.1a**	**3.1b**	**Complexes**	**3.1a**	**3.1b**
Bond Lengths					
Ru-P(1)	2.249(4)	2.2392(5)	Ru-N(2)	2.114(13)	2.1884(15)
Ru-P(2)	2.243(4)	2.2512(4)	Ru-N(1)	2.137(12)	2.0822(15)
Ru-Cl(1)	2.463(4)	2.4488(4)	Ru-Cl(2)	2.454(4)	2.4750(4)
Bond Angles					
P(2)-Ru-P(1)	100.74(15)	100.684(16)	N(1)-Ru-Cl(1)	88.6(3)	176.66(4)
Cl(1)-Ru-P(1)	157.13(14)	96.226(16)	N(1)-Ru-N(2)	98.7(5)	95.31(6)
Cl(1)-Ru-P(2)	99.97(14)	91.163(16)	Cl(2)-Ru-P(1)	97.24(15)	87.010(16)
N(2)-Ru-P(1)	91.4(3)	177.50(4)	Cl(2)-Ru-P(2)	99.52(15)	171.242(16)
N(2)-Ru-P(2)	70.5(4)	81.48(4)	Cl(2)-Ru-Cl(1)	88.76(14)	92.157(15)
N(2)-Ru-Cl(1)	86.5(3)	84.93(4)	Cl(2)-Ru-N(2)	168.0(3)	90.74(4)
N(1)-Ru-P(1)	69.2(3)	83.41(5)	Cl(2)-Ru-N(1)	92.3(4)	84.51(4)
N(1)-Ru-P(2)	165.5(4)	92.16(4)			

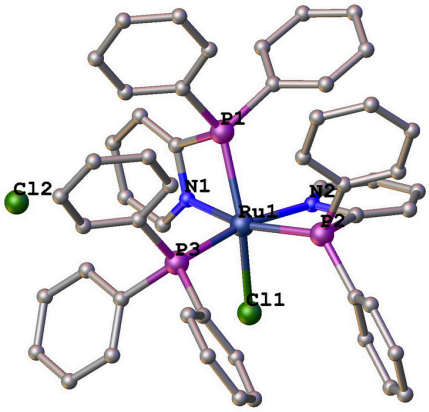

Figure 3.6 Molecular geometry and atomic labeling scheme for *cis*-[$RuCl(PPh_2py)_2(PPh_3)$]Cl (**3.1a***). Hydrogen atoms have been omitted for clarity.

Table 3.2 Selected bond lengths (Å) and angles (°) for for *cis*-[RuCl(PPh_2py)$_2$(PPh_3)]Cl (**3.1a***).

Bond Lengths			
Ru-P(1)	2.3175(15)	Ru-N(2)	2.123(4)
Ru-P(2)	2.3143(15)	Ru-N(1)	2.126(4)
Ru-Cl(1)	2.4210(15)	Ru-P(3)	2.3342(14)
Bond Angles			
P(2)-Ru-P(1)	104.21(4)	N(1)-Ru-Cl(1)	88.64(11)
Cl(1)-Ru-P(1)	155.30(4)	N(1)-Ru-N(2)	92.51(16)
Cl(1)-Ru-P(2)	95.04(4)	P(3)-Ru-P(1)	102.10(4)
N(2)-Ru-P(1)	88.33(11)	P(3)-Ru-P(2)	101.97(5)
N(2)-Ru-P(2)	68.73(12)	P(3)-Ru-Cl(1)	88.61(4)
N(2)-Ru-Cl(1)	84.34(11)	P(3)-Ru-N(2)	167.69(12)
N(1)-Ru-P(1)	68.11(11)	P(3)-Ru-N(1)	97.41(12)
N(1)-Ru-P(2)	160.34(12)		

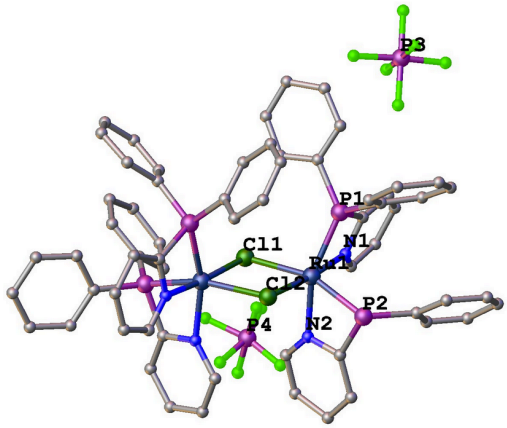

Figure 3.7 Molecular geometry and atomic labeling scheme for *cis*-[$Ru_2(\mu$-Cl)$_2$(PPh_2py)$_4$](PF_6)$_2$ (**3.2a**). Hydrogen atoms have been omitted for clarity.

Table 3.3 Selected bond lengths (Å) and angles (°) for for *cis*-[$RuCl_2(PPh_2py)_2$] (**3.1a**) and *cis*-[$Ru_2(\mu$-Cl)$_2$(PPh_2py)$_4$](PF_6)$_2$ (**3.2a**).

Complexes	**3.1a**	**3.2a**	**Complexes**	**3.1a**	**3.2a**
Bond Lengths					
Ru-P(1)	2.249(4)	2.317(4)	Ru-N(2)	2.114(13)	2.131(12)
Ru-P(2)	2.243(4)	2.255(4)	Ru-N(1)	2.137(12)	2.076(9)
Ru-Cl(1)	2.463(4)	2.246(3)	Ru-Cl(2)	2.454(4)	2.445(3)
Bond Angles					
P(2)-Ru-P(1)	100.74(15)	98.75(15)	N(1)-Ru-Cl(1)	88.6(3)	92.7(3)
Cl(1)-Ru-P(1)	157.13(14)	102.49(12)	N(1)-Ru-N(2)	98.7(5)	92.5(5)
Cl(1)-Ru-P(2)	99.97(14)	158.71(15)	Cl(2)-Ru-P(1)	97.24(15)	108.16(12)
N(2)-Ru-P(1)	91.4(3)	157.6(3)	Cl(2)-Ru-P(2)	99.52(15)	91.15(11)
N(2)-Ru-P(2)	70.5(4)	68.7(3)	Cl(2)-Ru-Cl(1)	88.76(14)	83.66(9)
N(2)-Ru-Cl(1)	86.5(3)	90.7(3)	Cl(2)-Ru-N(2)	168.0(3)	91.1(3)
N(1)-Ru-P(1)	69.2(3)	69.1(4)	Cl(2)-Ru-N(1)	92.3(4)	174.9(3)
N(1)-Ru-P(2)	165.5(4)	93.5(3)			

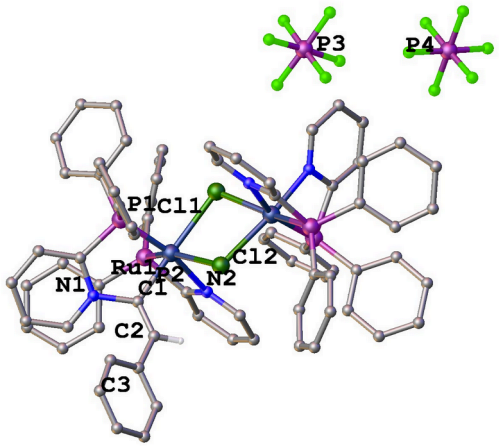

Figure 3.8 Molecular geometry and atomic labeling scheme for *cis*-[$Ru_2(\mu$-$Cl)_2(C{=}CHPhPPh_2py)(PPh_2py)_3](PF_6)_2$ (**3.2a***). Hydrogen atoms except C=CH have been omitted for clarity.

Table 3.4 Selected bond lengths (Å) and angles (°) for for *cis*-[$Ru_2(\mu$-$Cl)_2(C{=}CHPhPPh_2py)(PPh_2py)_3](PF_6)_2$ (**3.2a***).

Bond Lengths			
Ru-P(1)	2.2250(18)	Ru-N(2)	2.158(6)
Ru-P(2)	2.2673(18)	Ru-C(1)	2.027(7)
Ru-Cl(1)	2.5415(17)	Ru-Cl(2)	2.4749(17)
C(1)-C(2)	1.346(10)	C(2)-C(3)	1.475(10)
C(1)-N(1)	1.488(9)		
Bond Angles			
P(2)-Ru-P(1)	99.05(7)	C(1)-Ru-Cl(1)	91.2(2)
Cl(1)-Ru-P(1)	104.96(6)	C(1)-Ru-N(2)	89.7(3)
Cl(1)-Ru-P(2)	155.96(6)	Cl(2)-Ru-P(1)	94.75(6)
N(2)-Ru-P(1)	1165.43(16)	Cl(2)-Ru-P(2)	100.56(6)
N(2)-Ru-P(2)	68.75(16)	Cl(2)-Ru-Cl(1)	78.85(5)
N(2)-Ru-Cl(1)	87.31(16)	Cl(2)-Ru-N(2)	95.35(16)
C(1)-Ru-P(1)	82.4(2)	Cl(2)-Ru-C(1)	168.6(2)
C(1)-Ru-P(2)	90.8(2)	N(1)-C(1)-Ru	116.8(5)
C(2)-C(1)-Ru	123.8(6)	C(1)-C(2)-C(3)	132.7(7)

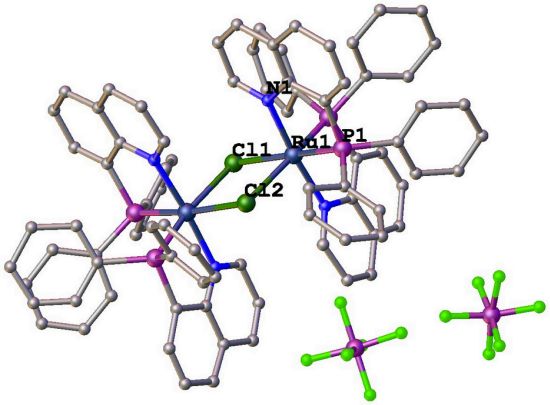

Figure 3.9 Molecular geometry and atomic labeling scheme for $[Ru_2(\mu\text{-}Cl)_2(PPh_2qn)_4](PF_6)_2$ (**3.2b**). Hydrogen atoms have been omitted for clarity.

Table 3.5 Selected bond lengths (Å) and angles (°) for for $[Ru_2(\mu\text{-}Cl)_2(PPh_2qn)_4](PF_6)_2$ (**3.2b**).

Complexes	**3.2b**
Bond Lengths	
Ru-P(1)	2.250(2)
Ru-Cl(1)	2.505(3)
Ru-Cl(2)	2.507(7)
Ru-N(1)	2.109(9)
Bond Angles	
Cl(1)-Ru-Cl(2)	79.12(8)
Cl(1)-Ru-P(1)	174.06(9)
Cl(2)-Ru-P(1)	95.71(9)
N(1)-Ru-Cl(1)	93.9(3)
N(1)-Ru-Cl(2)	92.6(3)
N(1)-Ru-P(1)	83.3(3)

3.4 LINEAR OPTICAL STUDIES

Linear optical studies were conducted on a UV-Vis spectrometer in CH_2Cl_2 using a quartz cell. The spectra are displayed in Figure 3.10. All the complexes have intense absorption bands in the higher-energy region which are dominated by intra-ligand π-π^* transitions, and moderately intense lower-energy absorption bands assigned to metal-to-ligand charge transfer (MLCT). The shoulder absorption of **3.1a** at ca. 430 nm corresponds to MLCT.

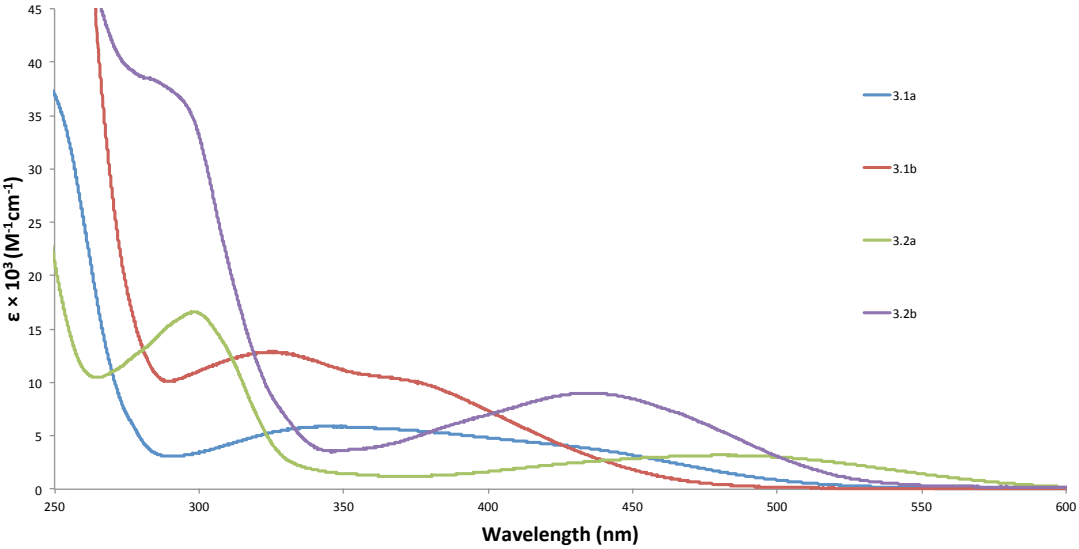

Figure 3.10 UV-Vis absorption spectra (CH_2Cl_2, 298 K) for ruthenium $(N\hat{}P)_2$ complexes.

The PPh_2qn complexes have weaker MLCT bands and stronger ILCT bands than the PPh_2py complexes. The absorption strength of the dimers is doubled that of the mono-ruthenium complexes, consistent with doubling the number of ruthenium centres. A blue shift can be observed in the spectra of the dimers, compared to the

mono-ruthenium complexes, 1630 cm^{-1} for the PPh_2py complexes and 2180 cm^{-1} for the PPh_2qn complexes. The broad absorption band of **3.1b** at 480 nm and the blue shift in proceeding to **3.2b** explain the difference in colour between the two complexes.

3.5 ELECTROCHEMICAL STUDIES

The redox behavior of the ruthenium $(N^P)_2$ complexes has been investigated by cyclic voltammetry and square-wave voltammetry with 0.1 M $^nBu_4NPF_6$ as the supporting electrolyte. The electrochemical data are tabulated in Table 3.6. All complexes undergo one oxidation process in the potential region from 0.70 to 1.50 V, assigned to a $Ru^{II/III}$ redox couple. **3.1a**, **3.1b** and **3.2b** display reversible waves with the half-wave potential ($E_{1/2}$) at +0.70, +0.71 and +1.47 V vs ferrocene/ferrocenium (FcH/FcH^+), respectively. The oxidation potentials of the complexes bearing PPh_2qn ligands are more positive than those of the PPh_2py series, 0.01 V higher than **3.1a** and 0.17 V higher than **3.2**, which suggests that the PPh_2qn ligand is a better π-acceptor than the PPh_2py ligand. The big gap in oxidation potentials between the two dimers indicates that geometry can strongly affect redox behavior.

Table 3.6 Electrochemical data of ruthenium $(N^P)_2$ complexes (E in volts, I in μA).

Compound No.	Peak No.	E_c	E_a	ΔE	$E_{1/2}$	I_c	I_a	I_a / I_c
3.1a	1	0.74	0.67	0.070	0.70	1.62	1.64	1.0
3.2b	1	1.30		-	-	0.80	0.56	0.70
3.1b	1	0.75	0.68	0.074	0.71	1.01	1.01	1.0
3.2b	1	1.50	1.45	0.058	1.47	0.98	0.96	1.0

3.6 EXPERIMENTAL SECTION

General. Reactions were performed under a nitrogen atmosphere with the use of standard Schlenk techniques with no precautions to exclude air during workup. $RuCl_2(PPh_3)_3$ and 8-(diphenylphosphino)quinoline were synthesized as described in the literature [47]. All commercially available materials were used as received. Petrol refers to a fraction of petroleum with a boiling range of 60 -80 ^oC. Reagent grade solvents CH_2Cl_2 (Merck) was dried by distilling over calcium hydride, THF

(Merck) over sodium/benzophenone, and toluene (Merck) over sodium and stored under N_2. All other solvents were used as received. High-resolution electrospray ionization mass spectra (HR ESI MS) were obtained using a VG Quattro II triple quadrupole instrument; peaks are reported as *m/z* (assignment, relative intensity). Microanalyses were carried out by the Elemental Analysis Service Unit, Science Centre, London Metropolitan University. UV-Vis spectra were recorded as CH_2Cl_2 solutions in 1 cm quartz cells using a Cary 5 spectrophotometer; bands are reported in the form frequency (cm^{-1}) [extinction coefficient, 10^3 M^{-1} cm^{-1}]. Infrared spectra were recorded on KBr discs using a Perkin Elmer Spectrum One FT-IR spectrometer. NMR spectra were recorded using a Bruker Avance 800 MHz NMR spectrometer and are referenced to residual $CHCl_3$ (7.26 ppm (^1H, 800 MHz), $CDCl_3$ 77.16 ppm (^{13}C, 201 MHz), residual CH_2Cl_2 (5.32 ppm (^1H, 800 MHz), CD_2Cl_2 53.5 ppm (^{13}C, 201 MHz), or residual acetone (2.05 ppm (^1H, 800 MHz), $(CD_3)_2CO$ 29.8 ppm (^{13}C, 201 MHz). Cyclic voltammetry measurements were recorded using an e-corder and EA161 potentiostat from eDaq Pty Ltd. Measurements were carried out at room temperature using Pt disc working-, Pt wire auxiliary- and Ag/AgCl reference electrodes, such that the ferrocene/ferrocenium redox couple was located at 0.46 V (CH_2Cl_2) (i_{pc}/i_{pa} = 1, ΔE_p 0.09 V). Scan rates were typically 100 mV s^{-1}. Electrochemical solutions contained 0.1 M $^nBu_4NPF_6$ and ca 10^{-3} M complex in dried and distilled CH_2Cl_2. Solutions were purged and maintained under a nitrogen atmosphere. Electronic spectra were recorded using a Cary 5 spectrophotometer.

Synthesis of cis-[$RuCl_2(PPh_2py)_2$] (**3.1a**)

To a solution of $RuCl_2(PPh_3)_3$ (0.509 g, 0. 530 mmol) in 40 mL toluene was added the ligand diphenyl-2-pyridylphosphine (0.361 g, 1.369 mmol). The solution was stirred at room temperature for 2 h, filtered, and the product was washed with 10 mL toluene and then 30 mL diethyl ether, yielding the product as a yellow powder at (0.3046 g, 82%). The orange crystal for X-ray study was obtained from CH_2Cl_2/*n*-hexane at room temperature. HR ESI MS ($[M - Cl + MeCN]^+$): calcd for $C_{36}H_{31}N_3P_2{}^{35}Cl^{102}Ru$ 704.0725, found 704.0726; ($[M - Cl]^+$): calcd for $C_{34}H_{28}N_2P_2{}^{35}Cl^{102}Ru$ 663.0460, found 663.0460. UV-Vis (CH_2Cl_2): 29120 [5.89]. IR (KBr): 1099 (s), 1434 (m), 1594 (s), 3391 (br) cm^{-1}. ^1H-NMR (CD_2Cl_2, 800 MHz): δ

6.43 - 8.06 (m, 22H, Ar-H, H_3, H_8), 6.80 (t, 1H, *J* = 6.0 Hz, $H_{4/9}$), 7.02 (dd, 1H, *J* = 7.5 Hz, *J* = 3.0 Hz, $H_{2/7}$), 7.29 (dd, 1H, *J* = 7.5 Hz, *J* = 4.0 Hz, $H_{2/7}$), 7.43 (m, overlap, $H_{3/8}$), 7.50 (d, 1H, *J* = 5.0 Hz, $H_{5/10}$), 7.55 (t, 1H, *J* = 6.5 Hz, $H_{4/9}$), 7.88 (m, overlap, $H_{3/8}$), 9.14 (d, 1H, *J* = 4.5 Hz, $H_{5/10}$). ^{13}C-NMR (CD_2Cl_2, 201 MHz): δ 125.6 ($C_{2/7}$), 126.2 ($C_{2/7}$), 126.4 ($C_{4/9}$), 127.4 ($C_{4/9}$), 128.5-135.9 (Ar-C), 137.6 ($C_{3/8}$), 151.7 (*J* = 14 Hz, $C_{5/10}$), 152.8 (*J* = 13 Hz, $C_{5/10}$), 172.8 (J_{CP} = 53 Hz, $C_{1/6}$), 174.4 (J_{CP} = 48 Hz, $C_{1/6}$). ^{31}P-NMR (CD_2Cl_2, 324 MHz): δ 1.7 (d, 1P, J_{PP} = 32 Hz), -5.6 (d, 1P, J_{PP} = 32 Hz).

Synthesis of cis-[$RuCl_2(PPh_2qn)_2$] (**3.1b**)

To a solution of $RuCl_2(PPh_3)_3$ (0.189 g, 0.197 mmol) in 30 mL THF was added excess ligand 8-(diphenylphosphino)quinoline (0.155 g, 0.493 mmol). The solution was stirred under N_2 at room temperature for 3 h and then concentrated under reduced pressure. A red powder was precipitated following addition to diethyl ether, collected by filtration, and washed with diethyl ether. The product was collected and dried under vacuum, yield 0.113 g (72%). A red single crystal suitable for X-ray study was obtained from CH_2Cl_2/*n*-pentane at room temperature. HR ESI MS ([M - Cl]$^+$): calcd for $C_{42}H_{32}N_2P_2{}^{35}Cl^{102}Ru$ 763.0773, found 763.0778. Microanalysis for $C_{42}H_{32}N_2P_2Cl_2Ru{\cdot}0.75CH_2Cl_2$: Calcd C, 59.54; H, 3.92; N, 3.25. Found C, 59.69; H, 4.28; N, 3.38. UV-Vis (CH_2Cl_2): 20900 [3.19], 33540 [16.59]. IR (KBr): 692 (s), 1091 (m), 1433 (m), 2921 (s) cm^{-1}. ^{1}H-NMR ($CDCl_3$, 800 MHz): δ 6.17 (t, 2H, *J* = 8.5 Hz, Ar-H), 6.36 (t, 1H, *J* = 5.5 Hz, $H_{2/19}$), 6.54 (t, 2H, *J* = 7.0 Hz, $H_{12/16/29/33}$), 6.75 (t, 2H, *J* = 7.0 Hz, $H_{12/16/29/33}$), 6.83 (t, 1H, *J* = 7.5 Hz, $H_{13/17/30/34}$), 6.97 (t, 1H, *J* = 7.0 Hz, $H_{13/17/30/34}$), 7.01 (t, 2H, *J* = 6.5 Hz, Ar-H), 7.25 (overlapped, Ar-H), 7.34 (m, 4H, $H_{5/22}$, Ar-H), 7.55 (m, 1H, $H_{1/18}$), 7.58 (m, 3H, $H_{3/20}$/$H_{4/21}$, Ar-H), 7.71 (m, 3H, $H_{2/19}$, $H_{3/20}$, $H_{4/21}$), 7.79 (d, 1H, *J* = 8.0 Hz, $H_{6/23}$), 8.06 (d, 1H, *J* = 8.0 Hz, $H_{6/23}$), 8.39 (m, 4H, $H_{3/20}$, $H_{5/22}$, Ar-H), 10.83 (s, 1H, $H_{1/18}$). ^{13}C-NMR ($CDCl_3$, 201 MHz): δ 121.0 ($C_{2/19}$), 123.4 ($C_{2/19}$), 127.1-128.0 (Ph-C), 128.5 ($C_{13/17/30/34}$), 128.6 ($C_{13/17/30/34}$), 129.3 ($C_{9/26}$), 129.6-129.9 (Ph-C), 130.0 ($C_{9/26}$), 131.0 ($C_{6/23}$), 131.1 ($C_{6/23}$), 131.5-131.9 (Ph-C), 132.9-133.5 ($C_{7,}$ C_{10}, C_{14}, C_{24}, C_{27}, C_{31}), 134.4 ($C_{3/20}$), 134.5-134.6 (Ph-C), 135.6 ($C_{8/25}$), 136.3-136.4 (Ph-C), 136.7 ($C_{5/22}$), 136.7 ($C_{5/22}$), 137.1 (Ph-C), 138.1 ($C_{8/25}$), 156.0 ($C_{1/18}$), 156.1($C_{1/18}$). ^{31}P-NMR ($CDCl_3$, 324 MHz): δ 53.9 (d, 1P, *J* = 32 Hz), 62.2 (d, 1P, *J* = 32 Hz).

Synthesis of cis-[$Ru_2(\mu\text{-}Cl)_2(PPh_2py)_4$]($PF_6$)$_2$ (**3.2a**)

To a solution of **3.1a** (0.040 g, 0.057 mmol) in 6 mL CH_2Cl_2 was added $NaPF_6$ (0.023 g, 0.137 mmol). The solution was stirred under N_2 at room temperature for 15 h and passed through a pad of Celite. The yellow product suitable for X-ray study crystallized from CH_2Cl_2/*n*-hexane, yield 0.033 g (71%). HR ESI MS ($[M]^{2+}$): calcd for $C_{34}H_{28}N_2P_2{}^{35}Cl^{102}Ru$ 663.0460, found 663.0460, ($[M + MeCN]^{2+}$): calcd for $C_{36}H_{31}N_3P_2{}^{35}Cl^{102}Ru$ 704.0725, found 704.0732. Microanalysis for $C_{68}H_{56}N_4P_6Cl_2F_{12}Ru_2$: Calcd C, 50.54; H, 3.49; N, 3.47. Found C, 50.43; H, 3.47; N, 3.49. UV-Vis (CH_2Cl_2): 30750 [12.9]. IR (KBr): 837 (s) ν(*P-F*), 1095 (w), 1435 (w), 2850 (w), 2918 (m) cm^{-1}. ^{1}H-NMR (CD_2Cl_2, 800 MHz): δ 6.00 (t, 2H, *J* = 8.0 Hz), 6.63 (dd, 1H, *J* = 7.5 Hz, *J* = 3.4 Hz), 6.81 (t, 2H, *J* = 6.5 Hz), 6.90 (t, 2H, *J* = 7.0 Hz), 6.94 (t, 1H, *J* = 6.0 Hz), 7.05 (t, 1H, *J* = 6.0 Hz), 7.14 (t, 1H, *J* = 7.5 Hz), 7.17 (d, 1H, *J* = 5.5 Hz), 7.20 (t, 1H, *J* = 7.0 Hz), 7.27 (dd, 1H, *J* = 7.5 Hz, *J* = 4.0 Hz), 7.9-7.32 (m, 2H), 7.43 (t, 1H, *J* = 7.5 Hz), 7.47 (t, 2H, *J* = 7.5 Hz), 7.54 (m, 2H), 7.63-7.67 (m, 3H), 7.75-7.78 (m, 2H), 7.83-7.86 (m, 2H), 8.87 (d, 1H, *J* = 5.0 Hz). ^{31}P-NMR (CD_2Cl_2, 324 MHz): δ 0.5 (d, 1P, J_{PP} = 32 Hz), -16.2 (d, 1P, J_{PP} = 32 Hz), -143.8 (septet, 1P, J_{PF} = 712 Hz).

Synthesis of [$Ru_2(\mu\text{-}Cl)_2(PPh_2qn)_4$]($PF_6$)$_2$ (**3.2b**)

To a solution of **3.1b** (0.012 g, 0.015 mmol) in 15 mL CH_2Cl_2 was added $NaPF_6$ (0.007 g, 0.044 mmol). The solution was stirred under N_2 at room temperature for 17 h and then passed through a pad of Celite. The bright yellow product suitable for X-ray study crystallized from CH_2Cl_2/*n*-pentane, yield 0.019 g (90%). HR ESI MS ($[M]^{2+}$): calcd for $C_{42}H_{32}N_2P_2{}^{35}Cl^{102}Ru$ 763.0733, found 763.0780. Microanalysis for $C_{84}H_{64}N_4P_6Cl_2F_{12}Ru_2$: Calcd C, 55.55; H, 3.55; N, 3.08. Found C, 55.54; H, 3.61; N, 3.14. UV-Vis (CH_2Cl_2): 23080 [9.02]. IR (KBr): 841 (s) ν(*P-F*), 1591 (m), 3435 (m) cm^{-1}. ^{1}H-NMR (Acetone-d_6, 800 MHz): δ 5.79 (m, 2H, $H_{15/11}$), 6.44 (t, 2H, *J* = 7.5 Hz, $H_{16/12}$), 6.82 (m, 2H, $H_{11/15}$), 6.87 (t, 1H, *J* = 7.5 Hz, $H_{17/13}$), 7.04 (dd, 1H, *J* = 8.5 Hz, *J* = 5.0 Hz, H_2), 7.16 (t, 2H, *J* = 7.5 Hz, $H_{12/16}$), 7.39 (t, 1H, *J* = 7.0 Hz, $H_{13/17}$), 8.09 - 8.12 (m, 2H, H_5, H_6), 8.65 (d, 1H, *J* = 7.5 Hz, H_4), 8.84 (d, 1H, , *J* = 8.0 Hz, H_3), 8.93 (d,

1H, J = 4.0 Hz, H_1). ^{13}C-NMR (Acetone-d_6, 201 MHz): δ 124.1 (C_7), 129.0 (C_5, $C_{12/16}$), 129.1 ($C_{16/12}$), 130.1 ($C_{17/13}$), 130.3 ($C_{15/11}$), 130.4 ($C_{13/17}$), 130.7 – 131.9 (C_7, C_{10}, C_{14}), 131.4 (C_9), 134.3 ($C_{11/15}$), 134.8 (C_4), 140.0 (C_3), 140.7 (C_6), 157.6 (J = 10 Hz, C_8), 158.4 (C_1). ^{31}P-NMR (Acetone-d_6, 324 MHz): δ 64.0 (s, 2P), -144.2 (septet, 1P, J_{PF} = 708 Hz).

Synthesis of cis-[RuCl(PPh$_3$)(PPh$_2$py)$_2$]Cl (**3.1a***)

To a solution of $RuCl_2(PPh_3)_3$ (0.141 g, 0. 145 mmol) in 40 mL MeoH was added the ligand diphenyl-2-pyridylphosphine (0.091 g, 0.346 mmol). The brown suspension was stirred at room temperature for 2 h and turned out to be bright yellow solution gradually. After he solvent was removed, the crude product was redissolved in ca. 1 mL CH_2Cl_2. Then a mixture of CH_2Cl_2 and diethyl ether (20 mL, V_{DCM}:V_{ether} = 1:4), yielding the product as a yellow powder. The orange crystal for X-ray study was obtained from CH_2Cl_2/*n*-hexane at room temperature. HR ESI MS ([M]$^+$, 100): calcd for $C_{52}H_{43}N_2P_3{}^{35}Cl^{102}Ru$ 925.1371, found 925.1365. ^{31}P-NMR ($CDCl_3$, 324 MHz): δ 39.0 (dd, 1P, J_{PP} = 291 Hz, J_{PP} = 32 Hz), -11.1 (m, 1P), -28.5 (dd, 1P, , J_{PP} = 291 Hz, J_{PP} = 32 Hz).

3.7 REFERENCE

1. Juris, A.; Balzani, V.; Barigelletti, F.; Campagna, S.; Belser, P.; von Zelewsky, A., *Coord. Chem. Rev.*, **1988**, 84, 85.
2. Thompson, D. W.; Wishart, J. F.; Brunschwig, B. S.; Sutin, N., *J. Phys. Chem*. A, **2001**, 105, 8117.
3. Ward, M. D.; Barigelletti, F., *Coord. Chem. Rev.*, **2001**, 216, 127.
4. Gao, F. G.; Bard, A. J., *J. Am. Chem. Soc.*, **2000**, 122, 7426.
5. Simon, J. A.; Curry, S. L.; Schmehl, R. H.; Schatz, T. R.; Piotrowiak, P.; Jin, X.; Thummel, R. P., *J. Am. Chem. Soc.*, **1997**, 119, 11012.
6. Tyson, D. S.; Luman, C. R.; Zhou, X.; Castellano, F. N., *Inorg. Chem.,* **2001**, 40, 4063.
7. Gray, H. B.; Winkler, J. R., *Annu. Rev. Biochem.*, **1996**, 65, 537.
8. Schwab. P.; France, M. B.; Ziller, J. W.; Grubbs, R. H., *Angew. Chem. Int. Ed.*, **1995**, 34, 2039.

9. Clavier, H.; Nolan, S. P., *Chem. Eur. J.*, **2007**, 13, 8029.
10. Dutta, D. K.; Deb, B., *Coord. Chem. Rev.*, **2011**, 255, 1686.
11. Bruce, M. I.; Humphrey, M. G.; Patrick, J. M.; White, A. H., *Aust. J. Chem.*, **1983**, 36, 2065.
12. Mellone, I.; Peruzzini, M.; Rosi, L.; Mellmann, D.; Junge, H.; Beller, M.; Gonsalvi, L., *Dalton Trans.*, **2013**, 42, 2495.
13. Kinoshita, T.; Dy, J. T.; Uchida, S.; Kubo, T.; Segawa, H., *Nat. Photonics*, **2013**, 7, 535.
14. Qin, L.; Zhang, Q.; Sun, W.; Wang, J.; Lu, C.; Cheng, Y.; Wang, L., *Dalton Trans.*, **2009**, 43, 9388.
15. Jeffrey, J. C.; Rauchfuss, T. B., *Inorg. Chem.,* **1979**, 18, 2658.
16. Espinet, P.; Soulantica, K., *Coord. Chem. Rev.*, **1999**, 193, 499.
17. Khin, C.; Hashmi, A. S. K.; Rominger, F., *Eur. J. Inorg. Chem.*, **2010**, 7, 1063.
18. Kumar, P.; Singh, A. K.; Sharma, S.; Pandey, D. S., *J. Organomet. Chem.*, **2009**, 693, 3643.
19. Braunstein, P.; Kelly, D. G.; Tiripicchio, A.; Ugozzoli, F., *Bull. Soc. Chim. Fr.*, **1995**, 132, 1083.
20. Arena, C. G.; Rotondo, E.; Faraone, F.; Lanfranchi, M.; Tiripicchio, A., *Organometallics*, **1991**, 10, 3877.
21. Hirsivaara, L.; Haukka, M.; Pursiaine, J., *Inorg. Chem. Commun.,* **2000**, 3, 508.
22. Farr, J. P.; Olmstead, M. M.; Balch, A. L., *J. Am. Chem. Soc.*, **1980**, 102, 6654.
23. Rotondo, E.; Bruno, G.; Nicolo, F.; Lo Schiavo, S.; Piraino, P., *Inorg. Chem.*, **1991**, 30, 1195.
24. Reinhard, G.; Hirle, B.; Schubert, U.; Knorr, M.; Braunstein, P.; DeCian, A.; Fischer, J., *Inorg. Chem.*, **1993**, 32, 1656.
25. Hong, F.; Chen, S.; Tsai, Y.; Chang, Y., *J. Organomet. Chem.*, **2002**, 655, 172.
26. Govindaswamy, P.; Mozharivskyj, Y. A.; Kollipara, M. R., *Polyhedron*, **2004**, 23, 3115.
27. Jain, V. K.; Jakkal, V. S.; Bohra, R., *J. Organomet. Chem.*, **1990**, 389, 417.
28. Kumar, P.; Singh, A. K.; Pandey, R.; Pandey, D. S., *J. Organomet. Chem.*, **2011**, 696, 3454.
29. Breit, B.; Gellrich, U.; Li, T.; Lynam, J. M.; Milner, L. M.; Pridmore, N. E.; Slattery, J. M.; Whitwood, A. C., *Dalton Trans.*, **2014**, 43, 11277.

30. Aliende, C.; Perez-Manrique. M.; Jalon, F. A.; Manzano, B. R.; Rodriguez, A. M.; Cuevas, J. V.; Espino, G.; Matrinez, M. A.; Massaguer, A.; Gonzalez-Bartulos, M.; de Llorens, R.; Moreno, V., *J. Inorg. Biochem.*, **2012**, 117, 171.
31. Hudali, H. A.; Kingston, J. V.; Tayim, H. A., *Inorg. Chem.*, **1979**, 18, 1391.
32. Tsubomura, T.; Takahashi, N.; Saito, K.; Tsukuda, T., *Chem. Lett.*, **2004**, 33, 678.
33. Armaroli, N.; Accorsi, G.; Holler, M.; Moudam, O.; Nierengarten, J. F.; Zhou, Z.; Wegh, R. T.; Welter, R., *Adv. Mater.*, **2006**, 18, 1313.
34. Barbieri, A.; Accorsi, G.; Armaroli, N., *Chem. Commun.*, **2008**, 2185.
35. Tsukuda, T.; Nishigata, C.; Arai, K.; Tsubomura, T., *Polyhedron*, **2009**, 28, 7.
36. Sapochak, L. S.; Benincasa, F. E.; Schofield, R. S.; Baker, J. L.; Riccio, K. C.; Fogarty, D.; Kohlmann, H.; Ferris, K. F.; Burrows, P. E., *J. Am. Chem. Soc.*, **2002**, 124, 6119.
37. Suzuki, T.; Kuchiyama, T.; Kishi, S.; Kaizaki, S.; Kato, M., *Bull. Chem. Soc. Jpn.*, **2002**, 75, 2433.
38. Nakamura, G.; Okamura, M.; Yoshida, M.; Suzuki, T.; Takagi, H. D.; Kondo, M.; Masaoka, S., *Inorg. Chem.*, **2014**, 53, 7214.
39. Suzuki, T., *Bull. Chem. Soc. Jpn*, **2004**, 77, 1869.
40. Aguirre, P. A.; Lagos, C. A.; Moya, S. A.; Zuniga, C.; Vera-Oyarce, C.; Sola, E.; Peris, G.; Bayon, J. C., *Dalton Trans.*, **2007**, 5419.
41. Suzuki, T.; Kotera, M.; Takayama, A.; Kojima, M., *Polyhedron*, **2009**, 28, 2287.
42. Aranda, B.; Aguirre, P.; Moya, S. A.; Bonneau, M.; Williams, G. J.A.; Toupet, L.; Escadeillas, M.; Le Bozec, H.; Guerchais, V., *Polyhedron*, **2015**, 86, 120.
43. Hashimoto, A.; Yamaguchi, H.; Suzuki, T.; Kashiwabara, K.; Kojima, M.; Takagi, H. D., *Eur. J. Inorg. Chem.*, **2010**, 39.
44. Monkowius, U.; Zabel, M.; Fleck, M.; Yersin, H., *Z. Naturforsch. B*, **2009**, 64, 1513.
45. Dormmi, D.; Nicolo, F.; Arena, C. G.; Bruno, G.; Faraone, F.; Gobetto, R., *Inorg. Chim. Acta,* **1994**, 221, 109.
46. Dabb, S. L.; Messerle, B. A.; Smith, M. K.; Willis, A. C., *Inorg. Chem.*, **2008**, 47, 3034.
47. Kwong, F.; Lai, C.; Yu, M.; Tian, Y.; Chan, K., *Tetrahedron*, **2003**, 59, 10295.

Chapter 4 – Nonlinear Optical Measurements for Organometallic Complexes

4.1 INTRODUCTION

As described in Chapter 1, both HRS and Z-scan techniques are used to conduct the NLO studies, HRS for second-order NLO materials, and Z-scan for third-order NLO materials [1].

Second-order optical hyperpolarizabilities in solutions were measured by the traditional method, EFISH for dipolar molecules. In this method, the molecules are oriented in an DC electric field, but it is not suitable for the ionic or octopolar species. On contrary, based on second harmonic scattering, HRS has no requirements for DC electric field [2, 3], which enables HRS to provide the measurement of second-order hyperpolarizabilities of molecules (e.g. octopolar molecules) with no electric dipole moment [4]. Up to date, HRS has been successfully used to study NLO properties of proteins dissolved in isotropic media, charged chromophores, nondipolar chromophores and nanoparticles [5-9]. The second-order hyperpolarizabilities of the complexes synthesized in Chapter 2, which are of octopolar species, were studied by HRS.

The techniques developed for the measurement of the third-order NLO parameters of materials (e.g. DFWM, ellipse rotation, beam-distortion), require much more complicated experimental apparatuses and set-ups than Z-scan [10-12]. Z-scan proposed by Sheik-Bahae, is based on the spatial distortion of a laser beam [12, 13]. This technique is widely used in material characterization because of not only the relatively simplicity, but also higher sensitivity. A variety of organic materials has been characterized by Z-scan, including fullerenes, carbon nanotubes, dyes, chalcones and the derivatives and so on [14-18]. Although a number of organometallic complexes has been studied using Z-scan [19-22], the investigation of such materials is still far from sufficient. Since there was no enough time left for the characterization of the complexes described in Chapter 2 or 3 due to the set-up maintenance, the samples for Z-scan study in this thesis were prepared by the Humphrey group or sent by collaborators. Some of the synthsis of these compounds can be found in the literature [23-25].

The synthsis described in this thesis, was designed to investigate the relationship between the chemical structure and NLO response. Although the Z-scan study for the newly-prepared complexes was unavailable, a better understanding of the interrelationships between the chemical structures and the corresponding optical effects will be obtained with the information obtained from this NLO studies, which will be of help in tailoring future compounds towards desired properties. In addition, a more detailed introduction to the HRS and Z-scan techniques is given. Supplementary plots of NLO data can be found in the Appendix.

4.2 HYPER-RAYLEIGH SCATTERING

4.2.1 Basic Theory of HRS [1,26]

HRS is the scattering of light at frequency 2ω, due to orientational fluctuations of asymmetric molecules in solution, when a liquid sample is irradiated by a light at frequency ω. Unlike ordinary scattering, the intensity of the scattering light only depends on the first hyperpolarizability of the solute molecules and varies quadratically with the incident light intensity.

In a typical measurement, the refractive indices as well as the solvent number densities are assumed to be constant with the solute density for dilute solutions. Then, in the dilute concentration limit, the relationship between the HRS intensity ($I_{2\omega}$) and the intensity of the fundamental beam (I_{ω}) can be expressed as:

$$I_{2\omega} = G(N_c\langle\beta_c^2\rangle + N_s\langle\beta_s^2\rangle)I_{\omega}^2 \qquad \text{(Equation 4.1)}$$

where N_c is the number density of the chromophore, N_s is the number density of the solvent, $\langle\beta_c^2\rangle$ and $\langle\beta_s^2\rangle$ are the orientation averages of the square of the first molecular hyperpolarizability tensor elements of the chromophore and solvent, respectively, and the constant G accounts for the averages over direction cosines, electronic measuring instrument factors and other constants. If there is a linear absorption at the second-harmonic wavelength, the scattered intensity should be corrected by Beer's Law according to:

$$I_{2\omega} = G(N_c\langle\beta_c^2\rangle + N_s\langle\beta_s^2\rangle)I_\omega^2 \times 10^{-\sigma l N_c} \qquad \text{(Equation 4.2)}$$

where σ is the linear absorption cross-section at 2ω (in units of cm^2) for the chromophore and l is the path length of the scattered light (in units of cm).

For donor-acceptor NLO chromophores, the β value is assumed to arise predominantly from charge transfer between the ground state and the excited state. The "intrinsic hyperpolarizability" β_0 and dispersion factor $D(\omega)$ can be calculated through the Oudar-Chemla's Two-Level Model using the measured wavelength dependent β_{HRS} data. The equations are given below.

$$\beta_{HRS}(2\omega) = \beta_0 D(\omega) \qquad \text{(Equation 4.3)}$$

$$D(\omega) = [1 - \left(\frac{\omega^2}{\omega_0^2}\right)]^{-1}[1 - \left(\frac{4\omega^2}{\omega_0^2}\right)]^{-1} \qquad \text{(Equation 4.4)}$$

Herein, ω is the angular frequency of the fundamental beam, and ω_0 is the angular resonance frequency of the charge-transfer transition. It should be noted that the Oudar-Chemla equations make reasonable approximations by neglecting the vibronic structure of the electronic transition, finite linewidths arising from population decay, and dephasing due to the interaction of chromophores with solvent molecules.

4.2.2 Experimental Measurement of HRS

A typical experimental configuration as described by Clays and Persoons in 1992[27] is shown in Figure 4.1. The HRS measurement setup adopted for the studies in this Chapter is nearly the same as the original setup. The pulsed laser beam passed through a half-wave plate and a polarizer acting as a beam attenuator (VBA05-1064, Thorlabs). The half-wave plate was mounted on a rotational stage with a servo motor driver (PRM1MZ8E, Thorlabs). By controlling the rotation of the half-wave plate through a Visual Basic program, the intensity of the incident laser could be varied, and the measurement process automated. A small portion of the incident laser beam was then reflected towards a battery-powered photodiode via a beam splitter. The signal from the photodiode served two purposes. Firstly, it

monitored the intensity of the incident laser beam. Secondly, it provided the trigger signal for the oscilloscope. The majority of the laser beam passed through a high-pass filter and was focused into the sample by a focusing lens. The sample cell was placed in a position where the focal point of the beam was in the middle of the cell.

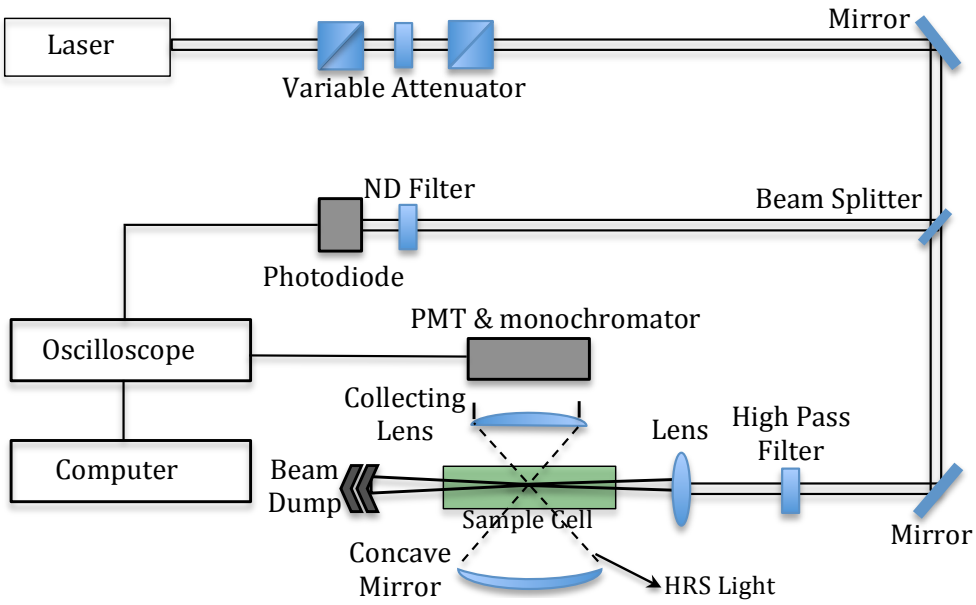

Figure 4.1 Schematic diagram of HRS experimental configuration.

To efficiently collect the scattered HRS light, a camera lens was placed orthogonal to the beam propagation direction. At the other side of the sample cell was a concave mirror reflecting the scattered light back towards the camera lens. The camera lens was used not only to collect all the HRS light, but also to focus the light into the opening slit of a monochromator. The monochromaor (Spex 500M) isolated the second-harmonic frequency, which was detected with a photomultiplier tube (PMT, R269 Hamamatzu). The signals from both the photodiode and PMT were passed to an oscilloscope (TDS2024C, Tektronix) for averaging and displaying. A dedicated computer with a custom Visual Basic program acquired data from the oscilloscope and ran the measurements automatically.

4.2.3 Calculations of HRS

For a given complex, the HRS measurement needed several milligrams of sample. The samples were dissolved in distilled solvent, usually THF. The stock solution

was then diluted into a series of solutions with different concentrations, and the HRS measurements were carried out for each solution. The relationship between the intensities of the incident laser beam and the scattered light for a dilute solution is given by Equation 4.1. Based on this equation, a plot of $I_{2\omega}/I_{\omega}^2$ and the mole concentration of the solute yields a straight line, as shown in Figure 4.2.

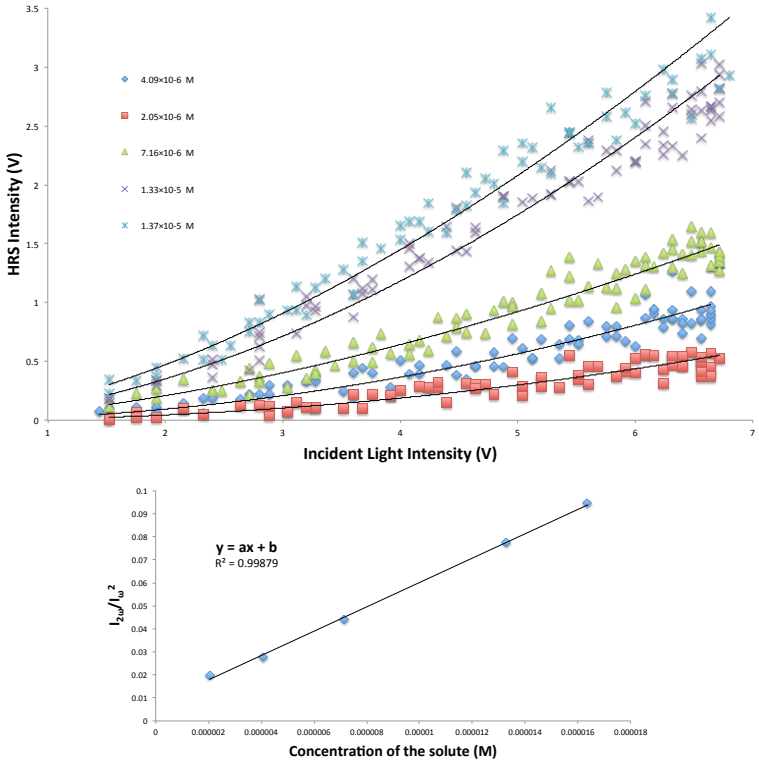

Figure 4.2 Above: HRS signal as a function of incident light intensity that shows the quadratic relationship. Below: Linear relationship between $I_{2\omega}/I_{\omega}^2$ and the mole concentration of the solute.

With the slope of the line as a and the intercept as b, β_c can be worked out from Equation 4.7, since β_s is known:

$$a = G\langle\beta_c^2\rangle \qquad \text{(Equation 4.5)}$$

$$b = GN_s\langle\beta_s^2\rangle \qquad \text{(Equation 4.6)}$$

$$\langle\beta_c\rangle = \sqrt{aN_s\langle\beta_s^2\rangle/b} \qquad \text{(Equation 4.7)}$$

4.3 *Z*-SCAN

The brief theory, experimental measurement and calculations of Z-scan is described in this section due to its complexity.

Z-Scan, developed by Eric van Stryland and Mansoor Sheik-Bahae, is the standard technique for determining the refractive and absorptive NLO properties of materials [13]. The Z-scan technique is performed by translating a sample through the beam waist of a focused beam and then measuring the power transmitted through the sample. Z-scan has many possible configurations, such as EZ-scan [28], White Light Z-scan [29], and Excite-Probe Z-scan [30]. In this Chapter, only the standard "open aperture" (NLA) and "closed aperture" (NLR) Z-scan are adopted and discussed.

At a given wavelength, third-order NLO properties are related to the cubic coefficient γ, which can be divided into its imaginary and real parts as shown in Equation 4.8. The real part of γ is responsible for the nonlinear refractive properties of the molecules, including instantaneous electronic effects such as the Kerr effect, while the imaginary part is related to the nonlinear absorption properties. These parameters can be determined or calculated in the Z-scan experiment.

$$\gamma = \sqrt{\gamma_{real}^2 + \gamma_{imag}^2} \qquad \text{(Equation 4.8)}$$

Figure 4.3 illustrates the Z-scan apparatus described in this Chapter. An intense Gaussian laser beam passed through a variable attenuator. The beam was then spilt by a beam splitter. A fraction of the beam was sent to a photodiode (reference photodiode). The rest of the beam then passed through an aperture that clipped roughly half of the beam intensity. After focus, the beam was sent to a "thin" sample that was translated through the beam waist using a motorized transition stage. The beam after the sample was then split again by another beam splitter. One fraction went to the open-aperture photodiode after a collecting lens. The closed-aperture photodiode behind a pin-hole screen detected the intensity of the beam passing through the iris. It should be noted here that it is only a "thin" sample when the sample thickness L is no more than the Rayleigh range Z_0 for a Guassian beam as seen in Equation 4.9 [31].

$$L \leq Z_0 = \pi w_0^2 / \lambda \qquad \text{(Equation 4.9)}$$

Herein, w_0 is the focal spot size (half-width at the $1/e^2$ maximum in the irradiance).

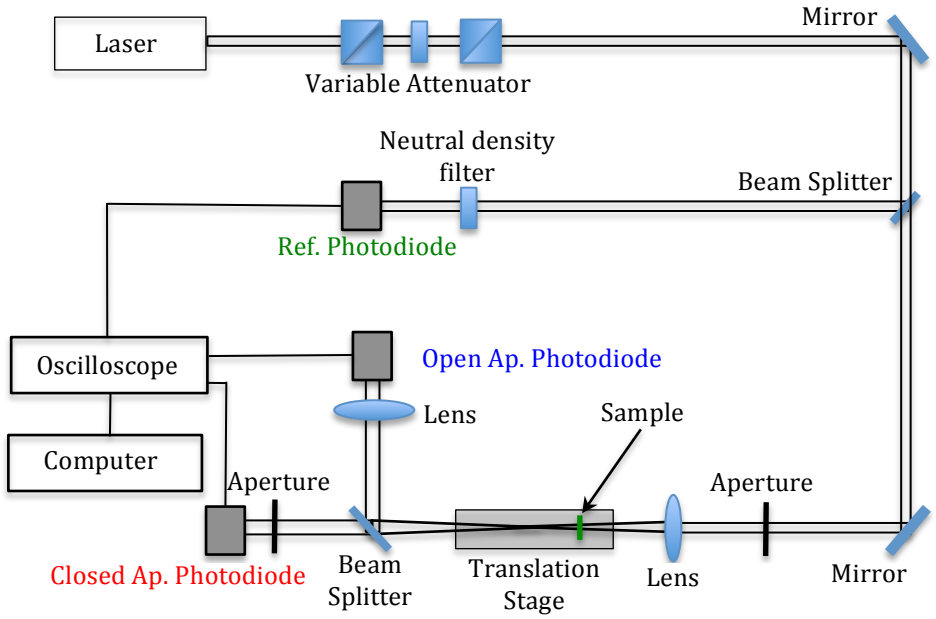

Figure 4.3 Schematic diagram of the Z-scan experimental setup. Ref.: reference, Ap.: aperture.

In this configuration, the closed-aperture detector measures the refractive index change in the sample as a function of the intensity change and has a transmission profile with Z-position as described in Figure 4.4. The open-aperture detector collects all of the light split off by the second beam splitter and measures the absorption change as the intensity increases through the sample, as illustrated in Figure 4.4. In order to remove the distortions from laser fluctuations, the transmittance referred to in this Chapter was normalized, normalization being defined as the transmittance of the sample divided by the transmittance of the sample far from focus (Z >>0). The reference detector was used to normalize the traces by division of the open- and closed-aperture traces by the reference values.

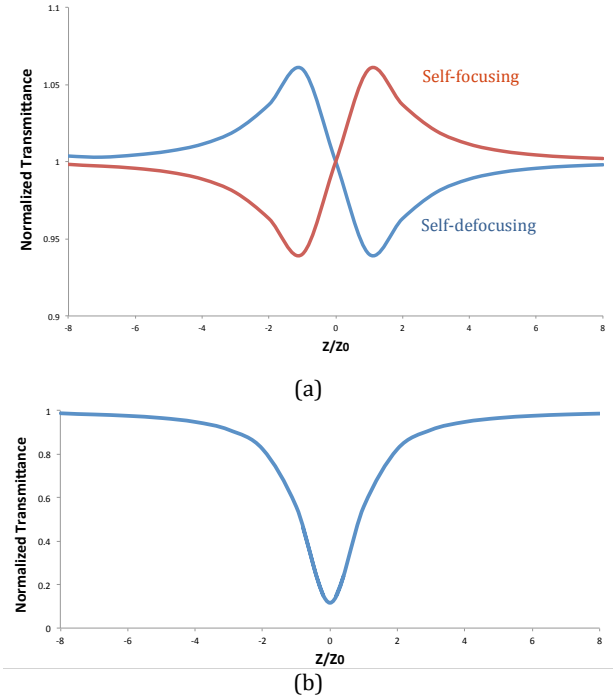

Figure 4.4 (a) Illustration of nonlinear refraction in the Z-scan experiment from closed-aperture studies: Phase shift is positive - Self-focusing; Phase shift is negative - Self-defocusing. (b) Illustration of nonlinear absorption in the Z-scan experiment from open-aperture studies: Two-photon absorption.

Closed Aperture-Nonlinear Refraction As the sample is translated through the focal region of the laser beam, the closed-aperture photodiode records the intensity of the light passing through the second aperture. If the beam experiences any nonlinear phase shift due to the sample, then the fraction of the light falling on the photodiode varies due to the Kerr lens generated in the material by the intense laser beam. In this case, the signal recorded by the detector exhibits a peak and valley as the sample is translated, as seen in Figure 4.4 (a). We define the change in transmittance between the peak and valley in a Z-scan as ΔT_{pv}=T_p-T_v where T_p and T_v are the normalized peak and valley transmittances. For a third-order nonlinear refractive process in the absence of NLA, an empirically determined relation between the induced phase distortion, $\Delta\Phi_0$, and ΔT_{pv} is described in Equation 4.10.

$$\Delta T_{pv} \cong 0.406(1-S)^{0.27}|\Delta\Phi_0|,\ (|\Delta\Phi_0| \leq \pi) \qquad \text{(Equation 4.10)}$$

$$\Delta\Phi_0 = \frac{2\pi}{\lambda} n_2 I_0 L_{eff} \qquad \text{(Equation 4.11)}$$

$$L_{eff} = (1-e^{-\alpha L})/\alpha \qquad \text{(Equation 4.12)}$$

Herein, S is the transmittance of the aperture in the absence of a sample, n_2 is the third-order nonlinear refractive index, α is the linear absorption coefficient, and $\Delta\Phi_0$ and I_0 are the on-axis peak nonlinear phase shift and the irradiance with the sample at focus respectively. The accuracy of this relation is ±3% for $\Delta T_{pv} < 1$. A more precise method based on Gaussian deconvolution is presented by van Stryland and co-workers [13] if additional accuracy is required.

Open Aperture-Nonlinear Absorption As the sample is translated through the focal region of the laser beam, the open-aperture photodiode records the intensity of the total transmitted light after the second beam splitter. Any deviation in the total transmitted intensity is attributed to multi-photon absorption since only the irradiance at the sample is changing as the sample is translated. Furthermore, the nonlinear absorption determined in open-aperture Z-scan is dominated by two-photon absorption (TPA) as it is related to the third-order hyperpolarizability where higher orders are less abundant (e.g. four-photon absorption is a seventh-order effect). The normalized change in transmitted intensity can be approximated by the following equations:

$$\Delta T(Z) \approx \frac{q_0}{2\sqrt{2}} \frac{1}{[1+Z^2/Z_0^2]} \qquad \text{(Equation 4.13)}$$

$$q_0 = \beta I_0 L_{eff} \qquad \text{(Equation 4.14)}$$

Here, Z is the position of the sample with respect to the focal position, Z_0 is the Rayleigh range, ΔT(Z) is the normalized transmittance of the sample at Z, and β is the TPA coefficient. Once the open-aperture data are collected, they can be readily fitted to Equation 4.13 where q_0 is used to generate the curve as shown in Figure 4.4(b) and balance the equation. The TPA coefficient β can then be determined through Equation 4.14. Since the value is proportional to β and the concentration of the active compound in the sample, the TPA cross-section σ_2 can be calculated. This parameter is expressed in Goeppert-Mayer units (GM, 1GM = 10^{-50} cm^4 s $photon^{-1}$ $molecule^{-1}$) for convenience.

Overall, by fitting the theoretical curves based on Equation 4.12 and 4.13 through a custom-written program from Prof. Marek Samoc, the third-order nonlinear refractive index n_2 and TPA coefficient β can be determined. The TPA cross-section

σ_2, the cubic coefficients γ, γ_{real} and γ_{imag} can then be calculated based on a series of complex equations. The parameters associated with the configuration (e.g. I_0, L_{eff}) can be obtained by measuring the reference Si plate and CH_2Cl_2, respectively. More details can be found in references [1,13].

4.4 NLO MEASUREMENTS

4.4.1 HRS Measurements

Experimentally obtained data at 1064 nm by HRS and the two-level corrected values are shown in Table 4.1. Due to different co-ligands, the values of the quadratic NLO parameters of the dichloro-ruthenium compounds have the trend: $\beta_{2.1a} > \beta_{2.1c} > \beta_{2.1b}$. The ruthenium alkynyl compounds with dppf ligands possess the greatest values. Phenyl- and nitrophenylalkynyl ligands were employed. Both have a positive impact on the second-order NLO response compared to the precursor chloro complexes, generally two times larger for the phenylalkynyl compounds compared to the dichloro-ruthenium compounds, and impressively more than ten times larger for the nitrophenylalkynyl compounds because the nitro group is a strong electron acceptor than enhances push-pull process. Notable is the involvement of the nitrophenylbutadiynyl groups as shown in compounds **2.6b** and **2.6c**: the β values are dramatically larger than those of **2.2d** and **2.2f**. This suggests that the longer the π-bridge, the larger the quadratic NLO response.

Table 4.1 Experimental linear optical spectroscopic and quadratic NLO response parameters [a].

No.	Complexes	λ_{max} (nm) (ε, 10^3 $M^{-1}cm^{-1}$)	β_{exp} [b] (10^{-30} esu)	β_0 [c] (10^{-30} esu)
2.1a	*cis*-$RuCl_2$(dppf)(^{t}Bu-bpy)	297 [19.6]	77.7	49
2.1b	*cis*-$RuCl_2$(dppe)(^{t}Bu-bpy)	294 [18.4]	38.0	24
2.1c	*cis*-$RuCl_2$(dppb)(^{t}Bu-bpy)	295 [20.2]	58.7	38
2.2a	*cis*-Ru(C≡C-4-$C_6H_4NO_2$)Cl(dppf)(^{t}Bu-bpy)	478 [17.7]	1097	169
2.2b	*cis*-Ru(C≡CPh)Cl(dppf)(^{t}Bu-bpy)	302 [28.2]	169	105
2.2c	*cis*-Ru(C≡C-4-$C_6H_4NO_2$)Cl(dppe)(^{t}Bu-bpy)	471 [15.7]	666	116
2.2d	*cis*-Ru(C≡CPh)Cl(dppe)(^{t}Bu-bpy)	297 [21.5]	104	66
2.2e	*cis*-Ru(C≡C-4-$C_6H_4NO_2$)Cl(dppb)(^{t}Bu-bpy)	472 [20.5]	535	91
2.2f	*cis*-Ru(C≡CPh)Cl(dppb)(^{t}Bu-bpy)	296 [18.0]	125	80
2.6b	*cis*-Ru(C≡CC≡C-4-$C_6H_4NO_2$)Cl(dppe)(^{t}Bu-bpy)	461 [15.8]	1250	253
2.6c	*cis*-Ru(C≡CC≡C-4-$C_6H_4NO_2$)Cl(dppb)(^{t}Bu-bpy)	457 [22.1]	1386	296

[a] All measurements in THF solvent. All complexes are optically transparent at 1064 nm.

[b] HRS at 1064 nm; values ±15%.

[c] HRS at 1064 nm corrected for resonance enhancement at 532 nm using the two-level model; damping factors not included.

4.4.2 Z-Scan Measurements

The Z-scan measurements were carried out in distilled CH_2Cl_2, following the lab procedure and operation developed by Dr. Genmiao Wang and Dr. Adam Barlow. The samples stated in this section were synthesized by members of the Humphrey group or were obtained from collaborators.

Ruthenium-alkynyl Cruciform Molecules

One structure-NLO property relationship developed in early studies of organic molecules is the observation of an increase in NLO properties on replacing an yne linkage in the π-bridging unit with an *E*-ene linkage [32]. Contemporaneously, metal alkynyl complexes were shown to function as efficient NLO materials [33-16]. Cruciform molecules possessing both features were prepared by Zhiwei Chen from the Jiangnan University lab of the Humphrey group and are shown in Figure 4.5.

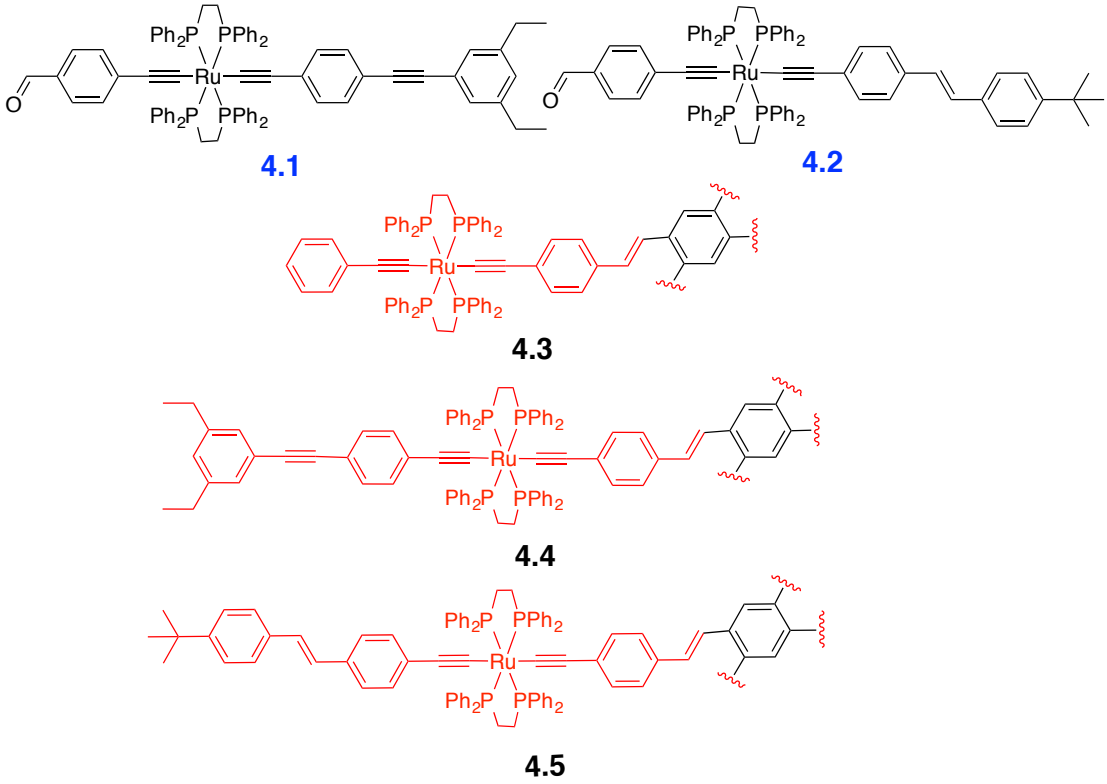

Figure 4.5 Ruthenium alkynyl cruciform molecules measured by Z-scan.

Because it corresponds to a region of optical transparency for all these samples, the third-order optical nonlinearities of the cruciform molecules were assessed at

a benchmark wavelength of 750 nm, which may reduce the effects of resonance enhancement. The data are collected in Table 4.2.

All complexes exhibit positive nonlinear absorption and negative nonlinear refraction as shown in Figure 4.6, which is consistent with the presence of two-photon resonance effects. It is difficult to develop structure-property relationships since the real components of the cubic nonlinearities, in particular, have significant error margins. Nevertheless, some comparisons might usefully be made. While being mindful of variations that result from a difference in measurement wavelength (750 versus 800 nm), the nonlinearity $|\gamma|$ varies little between the two classes of complexes with yne- or *E*-ene-containing π bridges as illustrated by data for complexes **4.1-4.5**.

Table 4.2 Cubic nonlinear optical data for complexes **4.1-4.5**.

Complexes	λ (nm)	γ_{real} (10^{-36} esu)	γ_{imag} (10^{-36} esu)	$\lvert\gamma\rvert$ (10^{-36} esu)	σ_2 (GM)
4.1	800	-5860 ± 770	850 ± 230	5920 ± 800	210 ± 60
	750	-9000 ± 610	1670 ± 410	9150 ± 730	470 ± 110
4.2	800	-14400 ± 1100	3420 ± 520	14800 ± 1200	830 ± 120
	750	-10100 ± 3500	2010 ± 720	10300 ± 3600	570 ± 200
4.3	800	-25000 ± 2000	7070 ± 1900	26000 ± 2800	1720 ± 470
	750	-38200 ± 7800	7370 ± 3100	38900 ± 8400	2090 ± 880
	440	-38200 ± 7800	7370 ± 3100	38900 ± 8400	2090 ± 880
4.4	800	-47000 ± 7100	13500 ± 4000	48900 ± 8200	3280 ± 970
	750	-36000 ± 11000	14200 ± 5800	38700 ± 12000	4020 ± 1600
	393	-36000 ± 11000	14200 ± 5800	38700 ± 12000	4020 ± 1600
4.5	800	-28700 ± 4700	6480 ± 1600	29400 ± 5000	1570 ± 400
	750	-56300 ± 7100	9460 ± 2600	57100 ± 7600	2680 ± 740
	415	-36000 ± 11000	14200 ± 5800	38700 ± 12000	4020 ± 1600

Note: Measurements are referenced to the nonlinear refractive index of silica $n_2 = 3 \times 10^{-16}$ cm^2 W^{-1}.

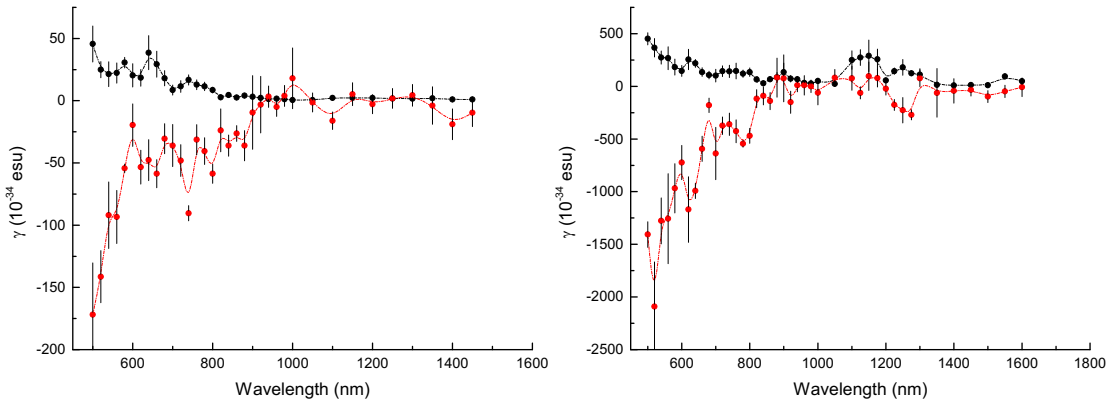

(a) (b)

Figure 4.6 The real (red) and imaginary (black) parts of the cubic hyperpolarizability of **4.1** (a) and **4.4** (b).

The monometallic complexes **4.1** and **4.2** have a common TPA peak at 640 nm, with the ethenyl-linked **4.2** having a larger cross-section. The TPA maxima are at lower energy for **4.2** than **4.1** in the range 740-900 nm, which is consistent with the lower-energy MLCT in the linear absorption spectrum. The monometallic compounds are building blocks for the formation for **4.4** and **4.5**. Addition of the monomer **4.1**/**4.2** to the core to afford **4.4**/**4.5** appreciably changes the TPA spectrum. TPA maxima are shifted to lower energy by around 20-40 nm, and the values of the cross-section at these wavelengths increase seven- to tenfold. A strong response at around 1150 nm also appears, which correlates closely with three times the wavelength of the lowest-energy linear absorption band.

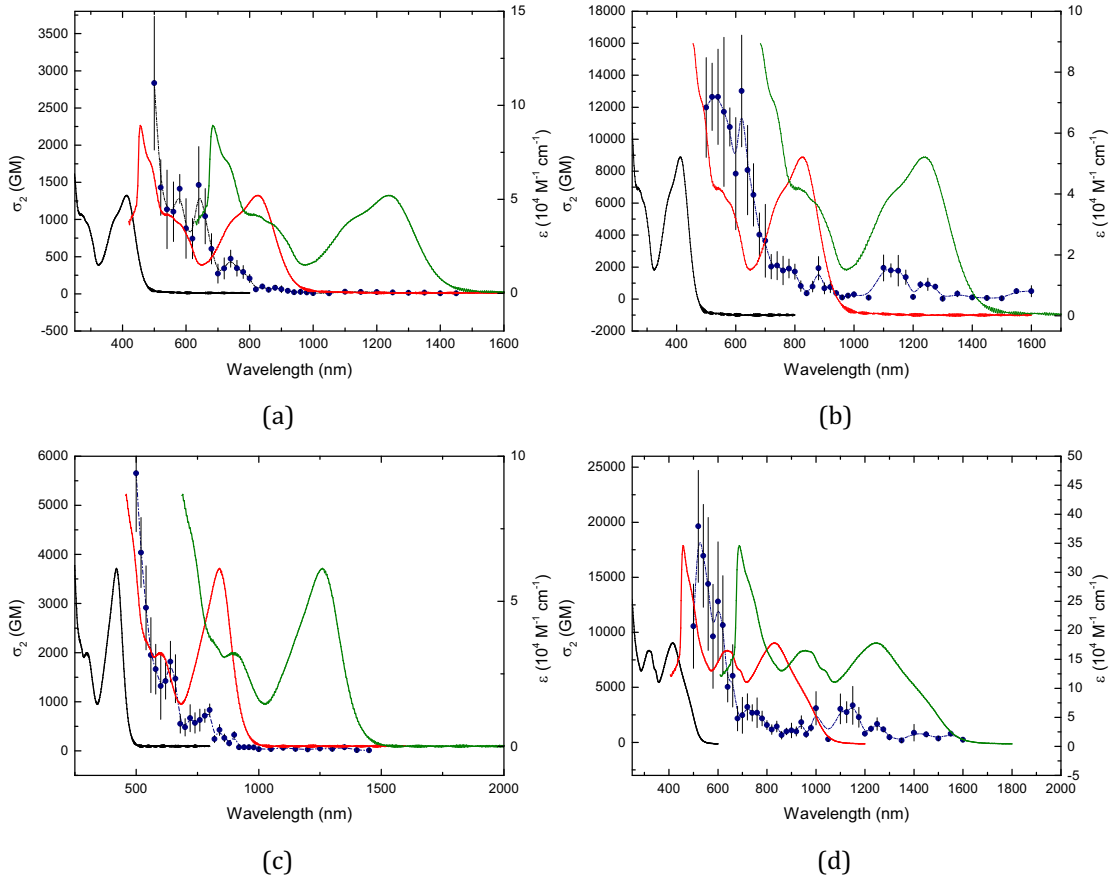

Figure 4.7 σ_2 traces for complexes **4.1** (a), **4.2** (c), **4.4** (b), **4.5** (d) overlaid on the UV-Vis spectrum (black), and plots of the UV-Vis spectrum at twice (red) and three times (green) the wavelength.

Fluorene containing complexes

The red part of the structures as shown in Figure 4.8, a conformationally locked biphenyl and the highly strained 5-membered ring, is a kind of widely used

fluorene functional group in the design of many two-photon absorbing materials and dyes [37-39]. Such molecules bearing the fluorene moiety have large extinction coefficients as well as considerable fluorescent properties. Metal alkynyl complexes featuring the fluorene groups have been synthesized by Floriane Malvolti, and the TPA properties were studied in this work.

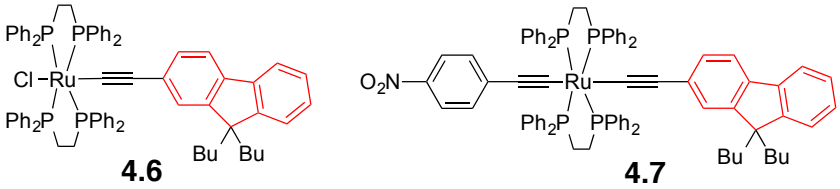

Figure 4.8 Ruthenium alkynyl complexes with a fluorene functional group.

The two complexes listed in Figure 4.8 are types of alkynyl-ruthenium compounds. **4.6** is a mono-alkynyl complex, while **4.7** is a bis-alkynyl complex with a nitrophenylalkynyl electron-withdrawing ligand. The optical data are summarized in Table 4.3 and the diagrams illustrating wavelength dependence of nonlinear absorption are displayed in Figure 4.9.

Table 4.3 Cubic nonlinear optical data for complexes **4.6** and **4.7**.

Complexes	λ (nm)	γ_{real} (10^{-36} esu)	γ_{imag} (10^{-36} esu)	$\lvert\gamma\rvert$ (10^{-36} esu)	σ_2 (GM)
4.6	750	42.0 ± 3.0	13.0 ± 2.0	44.0 ± 3.6	340 ± 60
4.7	800	-310 ± 95	60 ± 13	316 ± 96	1460 ± 330
	750	-670 ± 43	54 ± 8.0	672 ± 44	1720 ± 230

Note: Measurements are referenced to the nonlinear refractive index of silica n_2=3×10^{-16} cm^2W^{-1}.

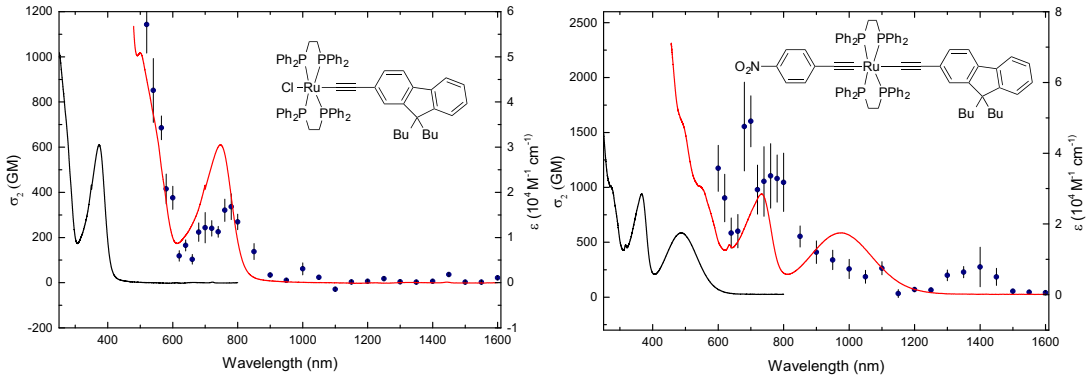

Figure 4.9 Diagrams of TPA cross-sections σ_2 for complexes **4.6** and **4.7** overlaid on the UV-Vis spectrum (black), and plots of the UV-Vis spectrum at twice the wavelength (red).

For both complexes, the values of $|\gamma|$ are mainly contributed by those of γ_{real}. Both of the two complexes have a peak around 750 nm in the TPA cross-section spectra

corresponding to a linear transition at 390 nm. Interestingly, the value of **4.7** is five times of that of **4.6**. The TPA cross-section traces of **4.6** closely follows the linear absorption spectra at two-times the wavelength, while that of **4.7** does not follow the UV-Vis spectrum strictly, which may result from the large errors on measurements. However, we can still conclude that the nitrophenyl moiety is quite favorable for improving the two-photon absorbing performance of the materials.

Isocyanurate and 1, 3, 5-substituted phenyl cored octupolar complexes

Molecules of octupolar geometry in nonlinear optics have been extensively studied. However, the effect of addition of electron-withdrawing groups in such complexes has not been broadly explored, except capping with a strong acceptor such as a nitro-functionalized phenylethynyl ligand. A novel approach is the addition of electron-withdrawing groups to the core in a 1,3,5-trisubstituted arrangement, such as isocyanurate trimers [40, 41]. Organometallic compounds containing the isocyanurate moiety have been synthesized by Romain Veillard as shown in Figure 4.10. **4.8** is the smallest organometallic complex with the isocyanurate moiety and **4.9** is a trimer of **4.8**. Different from **4.8** and **4.9**, **4.10** has a 1,3,5-substituted phenyl core, while there is an isocyanurate core in both **4.8** and **4.9**. Compared with **4.8**, **4.9** and **4.10** are both bis-alkynyl complexes containing peripheral 4-hexylester- functionalized phenylethynyl ligands.

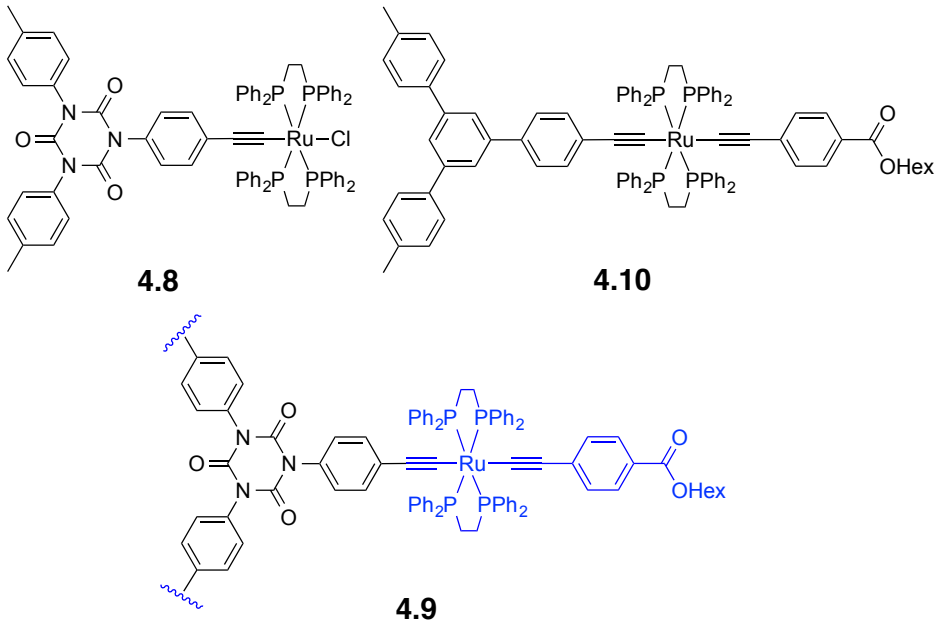

Figure 4.10 Isocyanurate-cored complexes studied by Z-scan.

The TPA cross-sections were measured in the range 500 to 1600 nm and displayed at the twice the wavelength to compare with the corresponding linear absorptions, seen in Figure 4.11 and Table 4.4. All of the three compounds have a peak between 700 and 800 nm and the peaks presumably correspond to the charge-transfer transition from ruthenium to the cores. The TPA cross-section value of **4.9**, up to 684 GM, is three times that of **4.8**, which is in agreement with the results of the corresponding organic compounds measured by Paul and coworkers [40]. However, the result may suggest enlarging the π-delocalisation in a trimer is unhelpful for improving the TPA performance. The TPA cross-section value of **4.10** is much larger than those of the other two complexes due to the electron-withdrawing group and the 1,3,5-substituted phenyl core which has a more efficient conjugation than the isocyanurate core.

Table 4.4 Cubic nonlinear optical data for complexes **4.8**, **4.9** and **4.10**.

Complexes	λ (nm)	γ_{real} (10^{-36} esu)	γ_{imag} (10^{-36} esu)	$\lvert\gamma\rvert$ (10^{-36} esu)	σ_2 (GM)
4.8	700	-12.0 ± 4.0	7.0 ± 0.9	13.9 ± 4.1	236 ± 30
4.9	800	-75.0 ± 16.0	28.0 ± 4.0	8.1 ± 17	684 ± 93
4.10	700	-30.0 ± 20	27.0 ± 5.0	40.4 ± 21	1400 ± 320

Note: Measurements are referenced to the nonlinear refractive index of silica $n_2 = 3 \times 10^{-16}$ cm^2 W^{-1}.

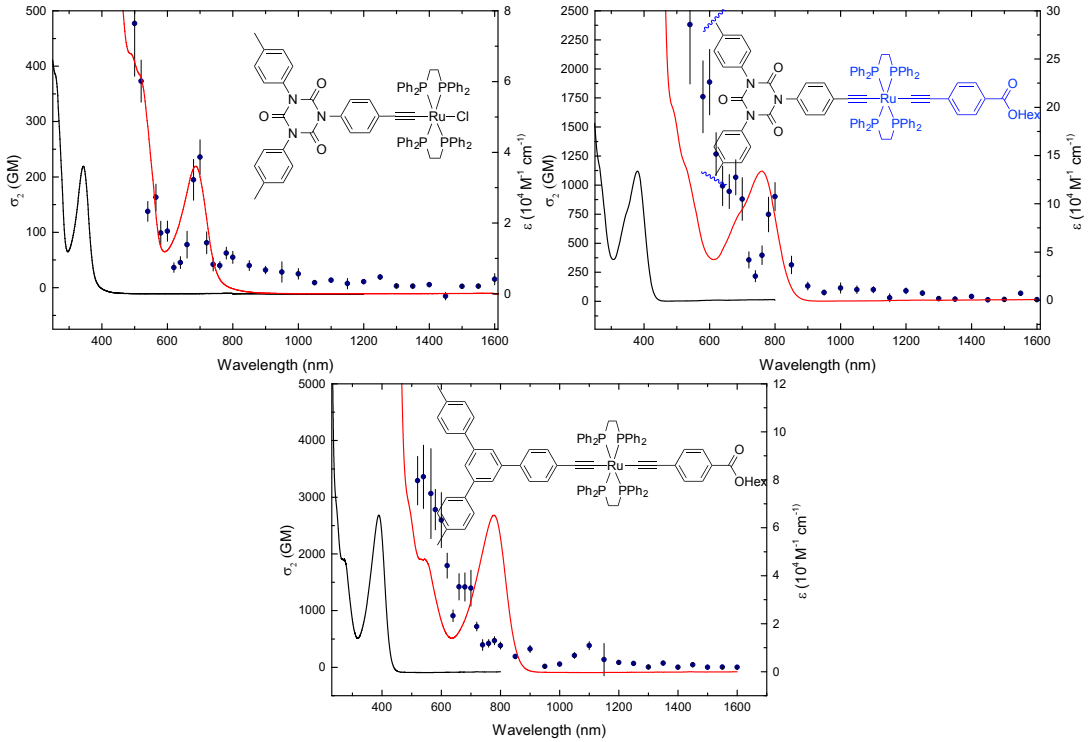

Figure 4.11 Plots of TPA cross-sections σ_2 for complexes **4.8**, **4.9** and **4.10** overlaid on the UV-Vis spectrum (black), and plots of the UV-Vis spectrum at the twice the wavelength (red).

A diiridium complex

A diiridium complex was characterized by Z-scan. The two iridium atoms are in the same plane, each capped by a pentamethylcyclopentadienyl ligand.

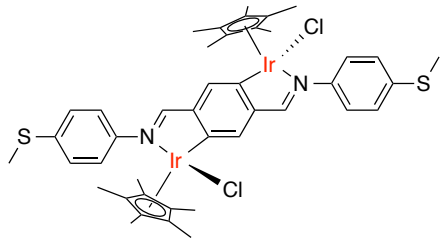

4.11

Figure 4.12 The structure of a diiridium complex

Table 4.5 Cubic nonlinear optical data for complex **4.11**.

Complex	λ (nm)	γ_{real} (10^{-36} esu)	γ_{imag} (10^{-36} esu)	$\lvert\gamma\rvert$ (10^{-36} esu)	σ_2 (GM)
4.11	520	710 ± 140	220 ± 60	743 ± 150	12700 ± 3600
	600	550 ± 110	90 ± 27	557 ± 110	4000 ± 1200
	720	145 ± 13	29.1 ± 3.6	148 ± 13	870 ± 110

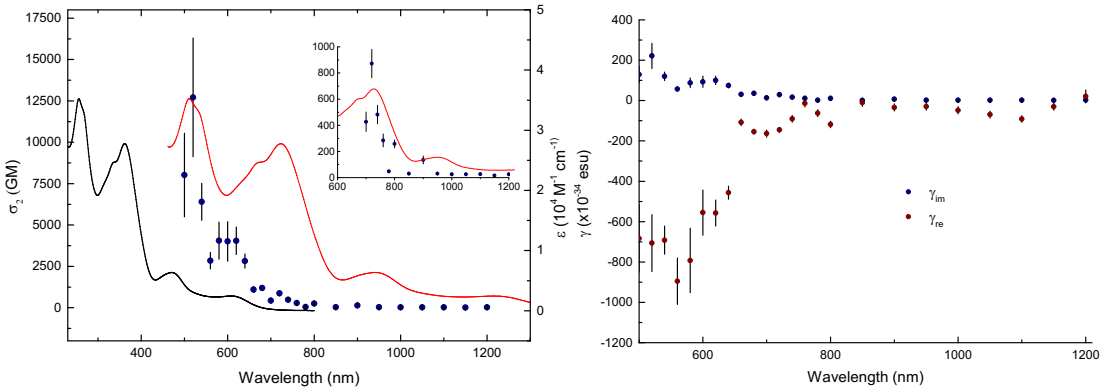

(a) (b)

Figure 4.13 (a) TPA cross-sections plot (blue) overlaid on the UV-Vis spectrum (black) and at the twice the wavelength (red). Insert: the same trace enlarged from 600 to 1200 nm. (b) Second hyperpolarizability (γ) dispersion.

The resultant data are shown in Table 4.5. As shown in Figure 4.13, at all wavelengths, the complex exhibits negative nonlinear refraction and positive nonlinear absorption, which is consistent with the presence of two-photon resonance effects. The overall values of $|\gamma|$ are dominated by the large γ_{real} contributions. Generally, the TPA spectrum is in good agreement with the linear

absorption. It has three peaks at 520, 600 and 720 nm with large values, corresponding with the linear absorption at 250, 360 and 470 nm respectively.

Ruthenium alkynyl phosphine oxides

The N-C bonds in triphenylamine are in a plane, while the P-C bonds in triphenylphosphine and triphenylphosphine oxide are in pyramidal geometry. Guillaume Grelaud synthesized a series of metal alkynyl-substituted triphenylphosphine and triphenylamine complexes. The phosphine series studied by Z-scan are displayed in Figure 4.14. The results of the nonlinear studies are summarized in Table 4.6.

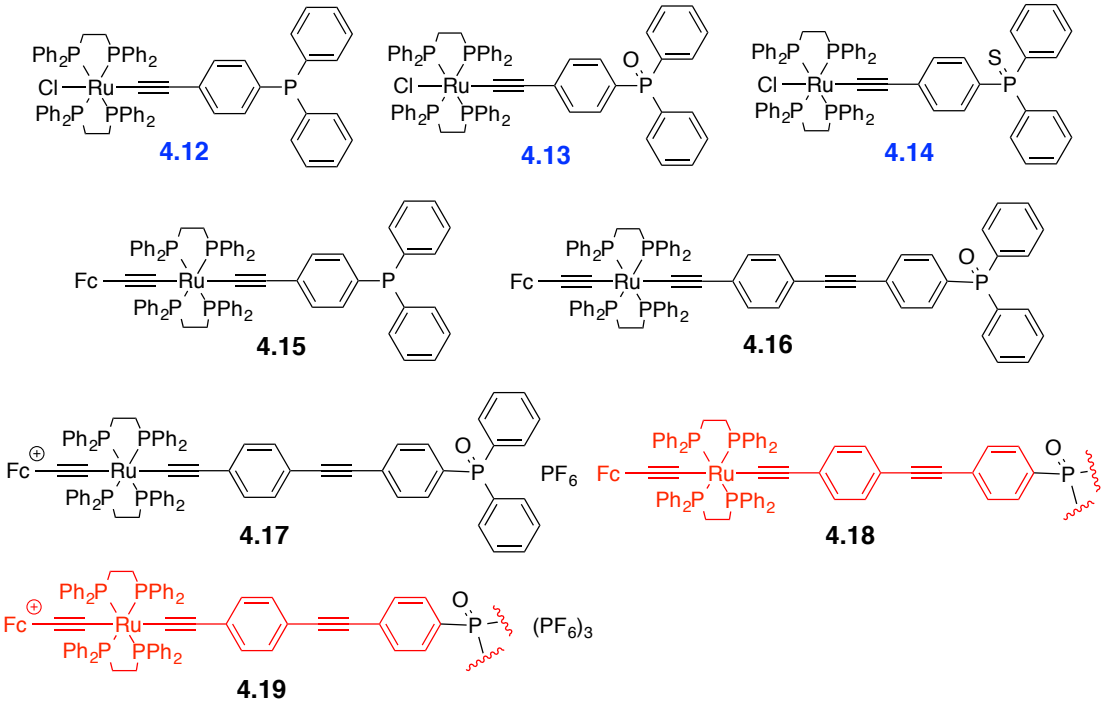

Figure 4.14 Ruthenium alkynyl-functionalized phosphine oxides studied by Z-scan.

The traces of $|\gamma|$ were affected greatly by those of γ_{real}. The existence of large errors limits the analysis of the nonlinear polarizabilities. Even so, a conclusion can be drawn that all the complexes have positive values of γ_{imag} and negative values of γ_{real}, except the two salts, **4.17** and **4.19**, as shown in Figure 4.15.

Several points can be made. Firstly, the maximal value of the TPA cross-section of **4.15** at 620 nm is more than five times that of **4.12**, which may result from the ferrocene ligand, a large π-delocalized system. Secondly, comparison between

4.12, **4.13** and **4.14** suggests that the oxygen and sulfur atoms are favourable for improving the TPA absorption, because the TPA cross-section of **4.12** is much smaller than the other two. Thirdly, the maximal value of **4.16** is 800 GM, more than that of **4.15**, 300 GM, a result suggesting that longer π-bridge chain length affords better nonlinear performance, consistent with previous studies. Fourthly, complex **4.18**, the trimer of **4.16** based on the triphenylphosphine oxide core, has a large response of 2200 GM, while that of **4.16** has 800 GM. The values of the TPA cross-section in these compounds have nearly a linear relationship, which may not be ideal for improving TPA. Finally, the PF_6 salt complexes **4.17** and **4.19** have negative absorption at 580 nm, which differs from the other complexes.

Table 4.6 Cubic nonlinear optical data for complexes **4.12-4.19**.

Complexes	λ (nm)	γ_{real} (10^{-36} esu)	γ_{imag} (10^{-36} esu)	$\lvert\gamma\rvert$ (10^{-36} esu)	σ_2 (GM)
4.12	720	-9 ± 1.6	3.6 ± 0.4	9.7 ± 1.6	109 ± 12
	620	-6 ± 3.5	4 ± 0.8	7.2 ± 3.6	155 ± 35
4.13	720	-20 ± 3.4	7 ± 1	21.2 ± 3.5	212 ± 30
4.14	740	-26.8 ± 4.8	10.2 ± 2.2	28.7 ± 5.3	289 ± 64
4.15	700	-31.1 ± 5	17.1 ± 3	35.3 ± 5.8	543 ± 99
	620	-43.4 ± 4	21.7 ± 3	48.5 ± 5	878 ± 120
4.16	1250	-132 ± 14	35.6 ± 9	137 ± 17	254 ± 90
	800	-82.2 ± 3.4	35.8 ± 4.2	89.7 ± 5.4	869 ± 100
4.17	760	-840 ± 70	156 ± 32	854 ± 77	4190 ± 860
	680	-737 ± 32	2 ± 0.4	737 ± 32	78 ± 13
	580	-1730 ± 540	-303 ± 100	1760 ± 550	-14000 ± 5040
4.18	1250	-197 ± 14	57.3 ± 9.2	205 ± 17	570 ± 92
	800	-226 ± 10	91.7 ± 12	244 ± 15	2230 ± 280
	620	410 ± 72	40 ± 9	412 ± 73	1630 ± 370
4.19	760	-882 ± 76	173 ± 40	899 ± 86	4640 ± 1090
	680	-1880 ± 110	82.9 ± 15	1880 ± 120	2780 ± 510
	580	-2110 ± 270	-287 ± 65	2130 ± 280	-13200 ± 3000

Note: Measurements are referenced to the nonlinear refractive index of silica $n_2 = 3 \times 10^{-16}$ cm^2 W^{-1}.

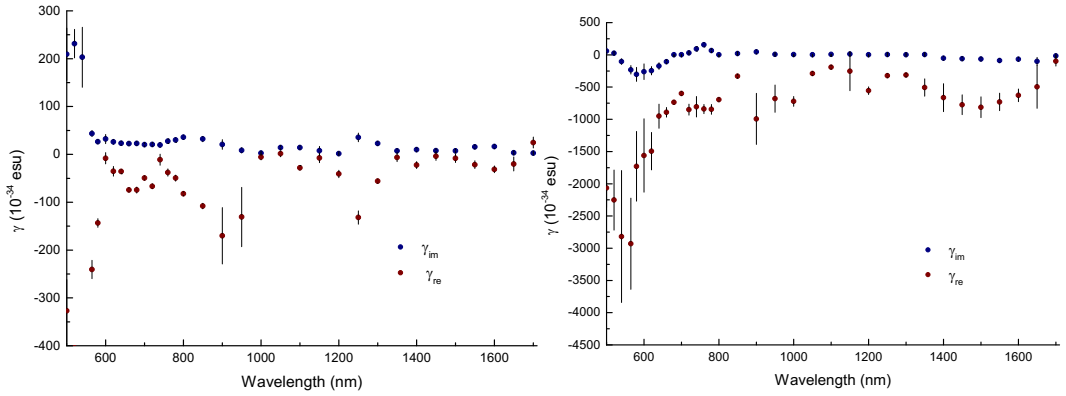

(a) (b)

Figure 4.15 Traces of nonlinear polarizabilities of (a) **4.16** and (b) **4.17**.

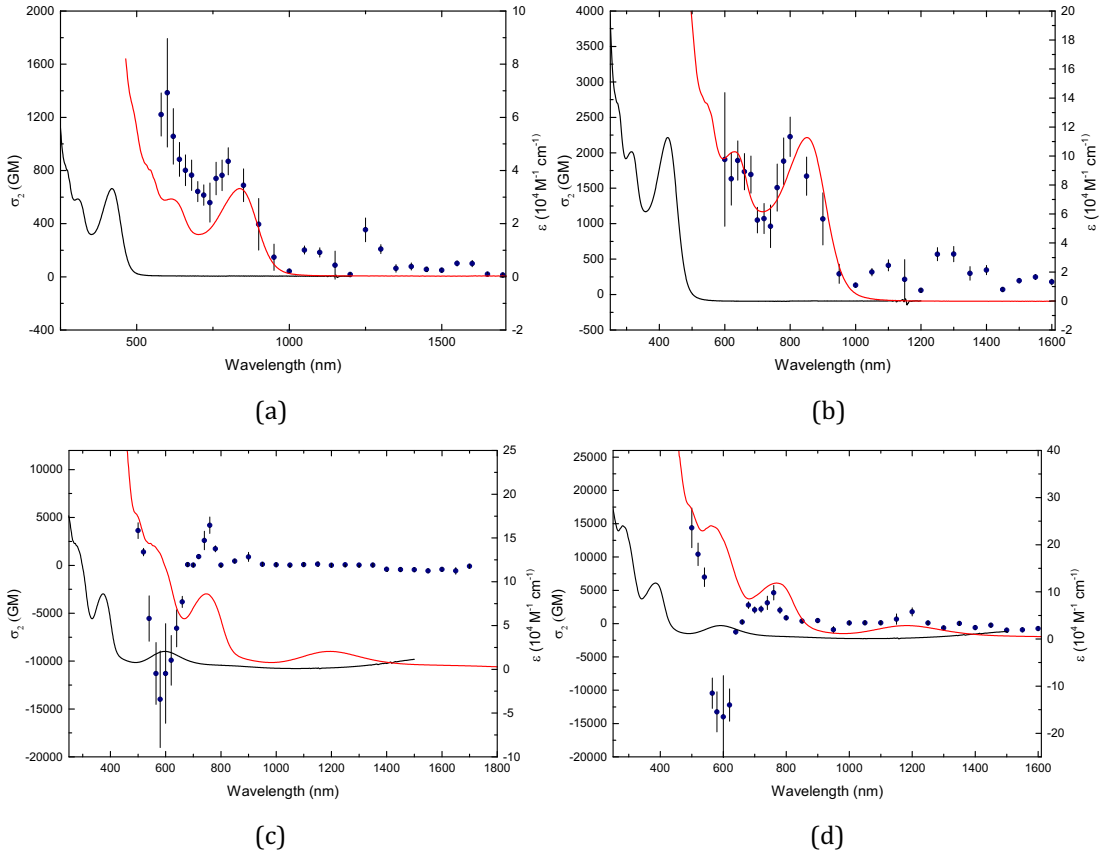

Figure 4.16 TPA cross-section plots (blue) of (a) **4.16**, (b) **4.18**, (c) **4.17** and (d) **4.19** overlaid on the UV-Vis spectrum (black) and at the twice the wavelength (red).

Ruthenium alkynyl dendrimers

Dendritic structures have attracted global interest in nonlinear optics, not only for the fact that hyper-branched structures maintain good solubility on increasing molecular size in contrast to linear molecules, but also because the structures disfavor centrosymmetric crystal packing. There may also be an enhancement known as a "dendritic effect" where the properties can be enhanced to a greater extent than expected on increasing the molecular size [42-44]. Katy Green, Torsten Schwich and others from the Humphrey group have synthesized first- and second-generation ruthenium alkynyl dendrimers and studied the effects of extension of the phenyleneethynylene bridge length and of replacing the phenyl core with nitrogen and boron cores [45, 46]. Dendrimers with different peripheral groups were provided by Bandar Babgi as shown in Figure 4.17.

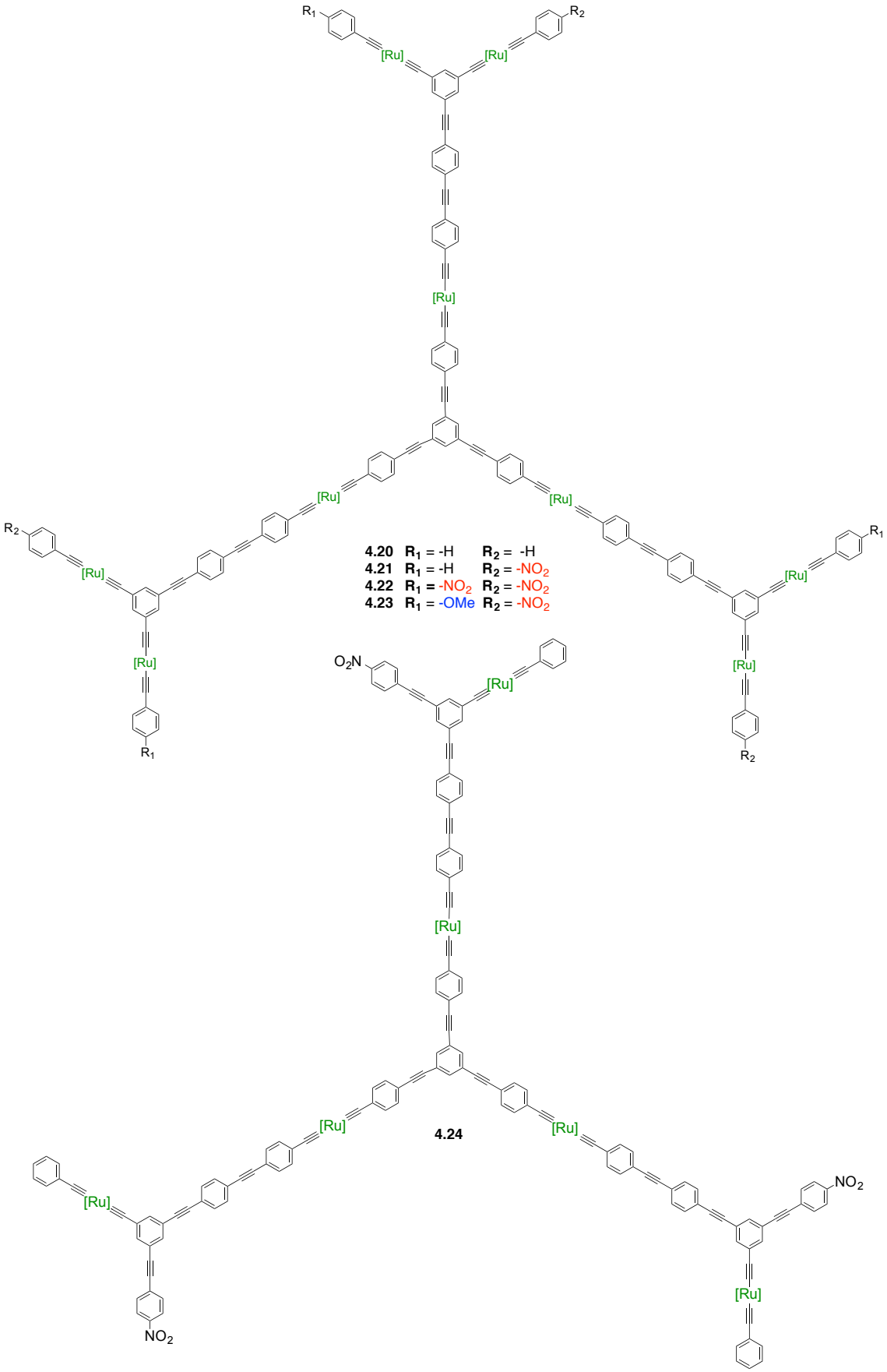

Figure 4.17 Ruthenium alkynyl dendrimers synthesized by Bandar Babgi.

Z-scan data are tabulated in Table 4.7 and displayed in Figure 4.18. The values of $|\gamma|$ are dominated by γ_{real} for all the dendrimers here. **4.22** containing two nitro groups has the largest γ_{real} value, two times that of **4.23**, and is then followed in magnitude by **4.20**, **4.21** and **4.24**. This suggests the electron-withdrawing group has a positive effect on improving the hyperpolarizability. However, the TPA results differ. The TPA spectra of the dendrimers follow the linear absorption and have two peaks around 600 and 750 nm. The maximal TPA cross-sections of **4.20** and **4.23** up to 80000 GM are similar. **4.24** has the worst performance and has fewer ruthenium centres.

Table 4.7 Cubic nonlinear optical data for complexes **4.20-4.24**.

Complexes	λ (nm)	γ_{real} (10^{-36} esu)	γ_{imag} (10^{-36} esu)	$\|\gamma\|$ (10^{-36} esu)	σ_2 (GM)
4.20	1200	132 ± 530	540 ± 170	556 ± 56	5830 ± 1900
	800	-1420 ± 930	820 ± 340	1640 ± 990	20000 ± 8300
	580	-7350 ± 350	1880 ± 260	7590 ± 436	87600 ± 12000
4.21	1150	1700 ± 1300	900 ± 500	1920 ± 1393	10600 ± 6000
	800	-2070 ± 930	900 ± 380	2260 ± 1005	21800 ± 9200
	780	-2960 ± 730	947 ± 330	3110 ± 802	24200 ± 8500
	580	-8810 ± 520	1230 ± 170	8900 ± 546	56600 ± 7700
4.22	950	-2050 ± 300	1150 ± 230	2350 ± 378	19700 ± 4000
	800	-2600 ± 320	576 ± 180	2660 ± 367	14000 ± 4300
	720	10800 ± 640	1320 ± 190	10900 ± 667	39500 ± 5600
	540	-23400 ± 1300	925 ± 140	23400 ± 1327	49400 ± 7300
4.23	1100	-1690 ± 760	1120 ± 400	2020 ± 855	14400 ± 5200
	800	-1720 ± 740	640 ± 260	1840 ± 784	15600 ± 650
	780	-7200 ± 460	1060 ± 160	7280 ± 486	27000 ± 4000
	580	-12300 ± 500	1780 ± 280	12500 ± 571	82200 ± 13000
4.24	1300	-580 ± 200	260 ± 50	636 ± 206	2430 ± 470
	800	-1790 ± 200	580 ± 160	1880 ± 256	14200 ± 4000
	780	-3100 ± 1200	950 ± 170	3240 ± 1212	24200 ± 4400
	640	-7720 ± 620	960 ± 100	7780 ± 628	23550 ± 4600

Note: Measurements are referenced to the nonlinear refractive index of silica $n_2 = 3 \times 10^{-16}$ cm^2 W^{-1}.

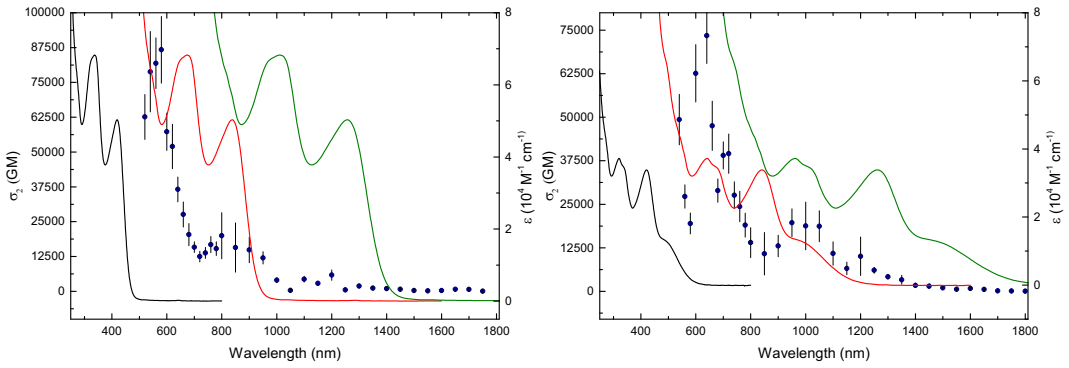

(a) (b)

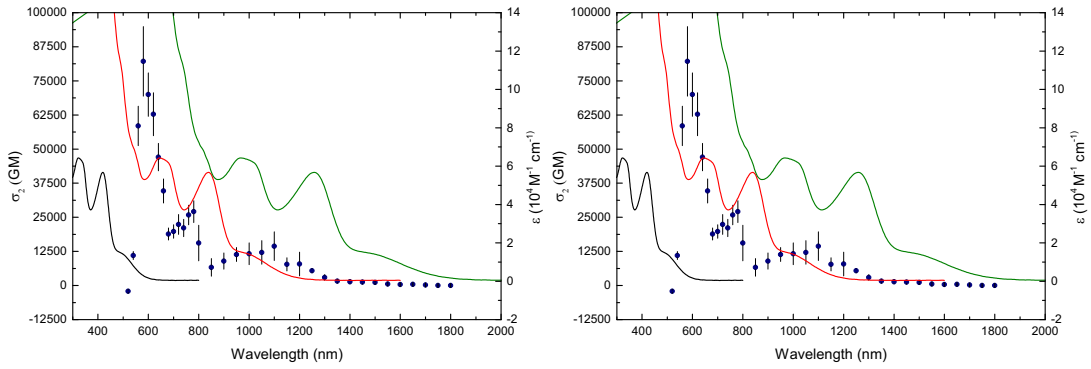

(c) (d)

Figure 4.18 TPA cross-section plots (blue) of (a) **4.20**, (b) **4.22**, (c) **4.23** and (d) **4.24** overlaid on the UV-Vis spectra (black) at twice the wavelength (red) and at triple the wavelength (green).

4.4 EXPERIMENTAL

4.4.1 HRS

Materials: Measurements were conducted on THF solutions of materials placed in a rectangular standard silica cell with Teflon stopper (45×12.5×7.5 mm). THF was distilled over Na and benzophenone. The concentrations of the samples varied but were typically around 10^{-5}-10^{-6} M. The samples were solids and were prepared through the syntheses described in Chapter 2.

Methods and Instrumentation: A pulsed Nd: YAG laser (Spectra-Physics, Nd: YAG GRC-150-30, 1064 nm, 30 Hz) with a maximum pulse energy of 200 mJ was focused into the cell with Teflon stopper containing the sample. The intensity of the incident beam was varied by rotation of a half-wave plate between crossed polarizers. Part of the laser pulse was sampled by a photodiode to measure the vertically polarized incident light intensity. The frequency-doubled light was collected and detected by a photomultiplier. The harmonic scattering and linear scattering were distinguished by appropriate monochromators; gated integrators were used to obtain intensities of the incident and harmonic scattered light. All measurements were performed in distilled THF using *p*-nitroaniline (β = 21.4 × 10^{-30} esu) as a reference.

4.4.2 Z-Scan

Materials: Measurements were conducted on solutions of materials in CH_2Cl_2 placed in 1 mm optical glass cells. CH_2Cl_2 was distilled over CaH_2 and subsequently deoxygenated by sparging under N_2. The concentrations of all samples varied but were typically around 0.10-0.20 % w/w.

Methods and Instrumentation: Spectral-dependence Z-scan experiments were conducted using a laser source consisting of a Quantronix Integra-C3.5F pumping a Quantronix Palitra-FS optical parametric amplifier, tuneable over a wavelength range from 460 nm to 1800 nm, which was confirmed by an Ocean Optics USB2000+ spectrometer or an Ocean Optics NIR-Quest spectrometer (1000-1800 nm). The output delivered 130 fs pulse with a 1 kHz repetition rate. A combination of glass filters and a Thorlabs polarizing filter was used to remove undesired wavelengths and the power was adjusted by applying neutral density filters to obtain nonlinear phase shifts between 0.1 to 1.3 rad. The focal length of the beam in the experiments was either 120 mm or 75 mm, obtained by an appropriate lens. A 120 mm lens gave a Gaussian beam waist of 25-60 mm (depending on the wavelength) and the 75 mm lens gave 25-45 mm beam waist, both of which gave Rayleigh lengths longer than the thickness of the sample. The sample cell travelled along the Z axis on a Thorlabs motorized stage between 0 and 100 mm with a 120 mm lens, or between 5-45 mm with a 75 mm lens. The intensities of the beams were detected by three types of Thorlabs photodiodes: Si based detectors (500-900 nm), InGaAs detectors (900-1300 nm) and amplified InGaAs detectors (1300-2000 nm). The data collected from the detectors were processed by a Tektronix oscilloscope feeding a custom LabVIEW program written by Prof. Marek Samoc, permitting fitting of a theoretical trace. A blank CH_2Cl_2 sample was run at each wavelength as an aid in referencing to a 3 mm fused silica plate; the real and imaginary components of the second hyperpolarizability (γ) of the materials were calculated assuming additivity to these reference samples.

4.5 REFERENCE

1. Sutherland, R. L., *Handbook of Nonlinear Optics*, Marcel Dekker Inc.: New York, **1996**.
2. Terhune, R. W.; Maker, P. D.; Savage, C. M., *Phys. Rev. Lett.,* **1965**, 14, 681.
3. Clays, K.; Persoons, A., *Phys. Rev. Lett.,* **1991**, 66, 2980.
4. Laidlaw, W. M.; Denning, R. G.; Verbiest, T.; Chauchard, E.; Persoons, A., *Nature*, **1993**, 363, 58.
5. Vance, F. W.; Hupp, J. T., *J. Am. Chem. Soc.*, **1999**, 121, 4047.
6. Clays, K.; Hendrickx, E.; Triest, M.; Verbiest, T.; Persoons, A.; Dehu, C.; Bredas, J. L., *Science*, **1993**, 262, 1419.
7. Zhang, Y.; Wang, X.; Fu, D.; Cheng, J.; Shen, Y.; Liu, J.; Lu, Z., *J. Phys. Chem. Solids*, **2001**, 62, 903.
8. Vance, F. W.; Lemon, B. I.; Hupp, J. T., *J. Phys. Chem. B*, **1998**, 102, 10091.
9. Johnson, R. C.; Li, J.; Hupp, J. T.; schatz, G. C., *Chem. Phys. Lett.*, **2002**, 356, 534.
10. Kuciauskas, D.; Porsch, M. J.; Pakalnis, S.; Lott, K. M.; Wright, M. E., *J. Phys. Chem. B*, **2003**, 107, 1559.
11. Sakai, Y.; Ueda, M.; Yahagi, A.; Tanno, N., *Polymer*, **2002**, 43, 3497.
12. Sheik-Bahae, M.; Said, A. A.; Van Stryland, E. W., *Opt. Lett.*, **1989**, 14, 955.
13. Sheik-Bahae, M.; Said, A. A.; Wei, T.; Hagan, D. J.; van Stryland, E. W., *J. Quantum Electron.*, **1990**, 26, 760.
14. Elim, H.I.; Ouyang, J.; He, J.; Goh, S. H.; Tang, S. H.; Ji, W., *Chem. Phys. Lett.*, **2003**, 369, 281.
15. Kost, A. R.; Jensen, J. E.; Loufty, R. O.; Wither, J. C., *Appl. Phys. B*, **2005**, 80, 281.
16. Zidan, M. D.; Allaf, A. W.; Alsous, M. B.; Allahham, A., *Opt. Laser Technol.*, **2014**, 58, 128.
17. Nasseri, F.; Rokhsat, E.; Dorranian, D., *Optik*, **2016**, 127, 6813.
18. Chandra Shekhara Shetty, T.; Raghavendra, S.; Chidan Kumar, C. S.; Dharmaprakash, S. M., *Opt. Laser Technol.*, **2016**, 77, 23.
19. Manjunatha, K. B.; Dileep, R.; Umesh, G.; Ramachandra, B., *Mater. Lett.*, **2013**, 105, 173.
20. Sabari Girisun, T. C.; Dhanuskodi, S.; Vinitha, G., *Mater. Chem. Phys.*, **2011**, 129, 9.

21. Sun, J.; Guo, W.; Wang, X.; Zhang, G.; Sun, X.; Zhu, L.; Ren, Q.; Xu, D., *Opt. Commun.*, **2007**, 280, 183.
22. Zidan, M. D.; Alktaifani, M.; Allahham, A., *Optik*, **2015**, 126, 1491.
23. Chen, Z.; Jeffery, C. J.; Morshedi, M.; Moxey, G. J.; Barlow, A.;Yang, X.; Babgi, B. A.; Dalton, G. T.; Randles, M. D.; Smith, M. K.; Zhang, C.; Samoc, M.; Cifuentes, M. P.; Humphrey, M. G., *ChemPlusChem,* **2015**, 80, 1329.
24. B. A. Babgi, *Toward structure-optical property relationships of ruthenium alkynyl complexes.* Ph.D Thesis, The Australian National University, **2012**.
25. G. Grelaud, *New electrochromic organometallic materials for light modulation.* Ph.D Thesis, The Australian National University, **2012**.
26. Tai O.; Wang, C.; Ma, H.; Jen, A., *J. Chem. Phys.,* **2004**, 121, 6086.
27. Clays K.; Persoons, A., *Rev. Sci. Instrum.,* **1992**, 63, 3285.
28. Xia, T.; Sheik-Bahae, M.; Said, A. A.; Hagan, D. J.; van Stryland, E. W., *J. Nonlinear Opt. Phys.,* **1994**, 3, 489.
29. Balu, M.; Hales, J.; Hagan, D. J.; van Stryland, E. W., *Opt. Express,* **2004**, 12, 3820.
30. Imangholi, B.; Hasselbeck, M. P.; Sheik-Bahae, M., *Opt. Commun.,* **2003**, 227, 337.
31. Kuzyk, M. G.; Dirk, C. W., *Characterization Techniques and Tabulations for Organic Nonlinear Materials*, Marcel Dekker Inc.: New York, **1998**.
32. Cheng, L. T.; Tam, W.; Marder, S. R.; Stiegman, A. E.; Rikken, G.; Spangler, C. W., *J. Phys. Chem.,* **1991**, 95, 10643.
33. Porter, P. L.; Guha, S.; Kang, K.; Frazier, C. C., *Polymer,* **1991**, 32, 1756.
34. Myers, L. K.; Langhoff, C.; Thompson, M. E., *J. Am. Chem. Soc.,* **1992**, 114, 7560.
35. Whittall, I. R.; Humphrey, M. G.; Samoc, M.; Swiatkiewicz, J.; Luther-Davies, B., *Organometallics,* **1995**, 14, 5493.
36. Houbrechts, S.; Clays, K.; Persoons, A.; Cadierno, V.; Gamasa, M. P.; Gimeno, J., *Organometallics,* **1996**, 15, 5266.
37. Malvolti, F.; Rouxel, C.; Mongin, O.; Hapiot, P.; Toupet, L.; Blanchard-Desce, M.; Paul, F., *Dalton Trans.,* **2011**, 40, 6616.
38. Zheng, Q.; He, G. S.; Lu, C.; Prasad, P. N., *J. Mater. Chem.,* **2005**, 15, 3488.
39. Belfield, K. D.; Hagan, D. J.; van Stryland, E. W.; Schafer, K. J.; Negres, R. A., *Org. Lett.,* **1999**, 1, 1575.

40. Argouarch, G.; Veillard, R.; Roisnel, T.; Amar, A.; Meghezzi, H.; Boucekkine, A.; Hugues, V.; Mongin, O.; Blanchard-Desce, M.; Paul, F., *Chem. Eur. J.,* **2012**, 18, 11811.

41. Trujillo, A.; Veillard, R.; Argouarch, G.; Roisnel, T.; Singh, A.; Ledoux, I.; Paul, F., *Dalton Trans.,* **2012**, 41, 7454.

42. Green, K. A.; Cifuentes, M. P.; Samoc, M.; Humphrey, M. G., *Coord. Chem. Rev.,* **2011**, 255, 2025.

43. Humphrey, M. G.; Cifuentes, M. P.; Samoc, M.; Isoshima, T.; Persoons, A., *Spec. Pub. –Roy. Soc. Chem.*, **2003**, 287, 100.

44. Gao, J.; Cai, Y.; Yu, J.; Lin, W.; Wang, Z.; Qian, G., *J. Mater. Chem.,* **2011**, 21, 3197.

45. Green, K. A., *Organometallic Dendrimers and Multi-state Switches for Nonlinear Optics.* Ph.D Thesis, The Australian National University, **2010**.

46. Schwich, T., *Towards Octupolar Ruthenium Acetylide Complexes for Nonlinear Materials,* Ph.D Thesis, The Australian National University, **2011**.

Appendices

A. NMR Spectra

The ordering of the spectra for individual compounds is: ^{1}H-, ^{13}C-, and ^{31}P-NMR. Each compound is annotated using different numbering scheme, which are marked and presented in the ^{1}H spectra. In every case, where a carbon atom has multiple protons bound to it, all of those protons are equivalent, and therefore they are annotated using the number of the carbon atom to which they are bound. Phosphorus atoms within each molecule are not annotated.

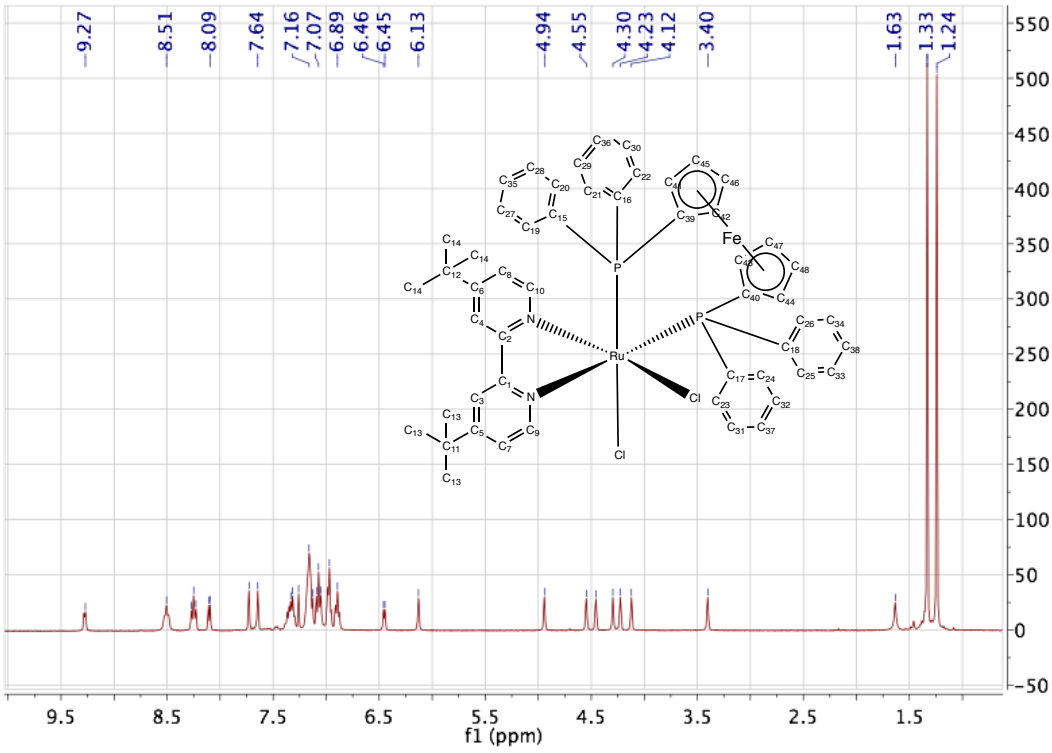

Figure A01 ^{1}H-NMR spectrum of **2.1a** recorded in $CDCl_3$.

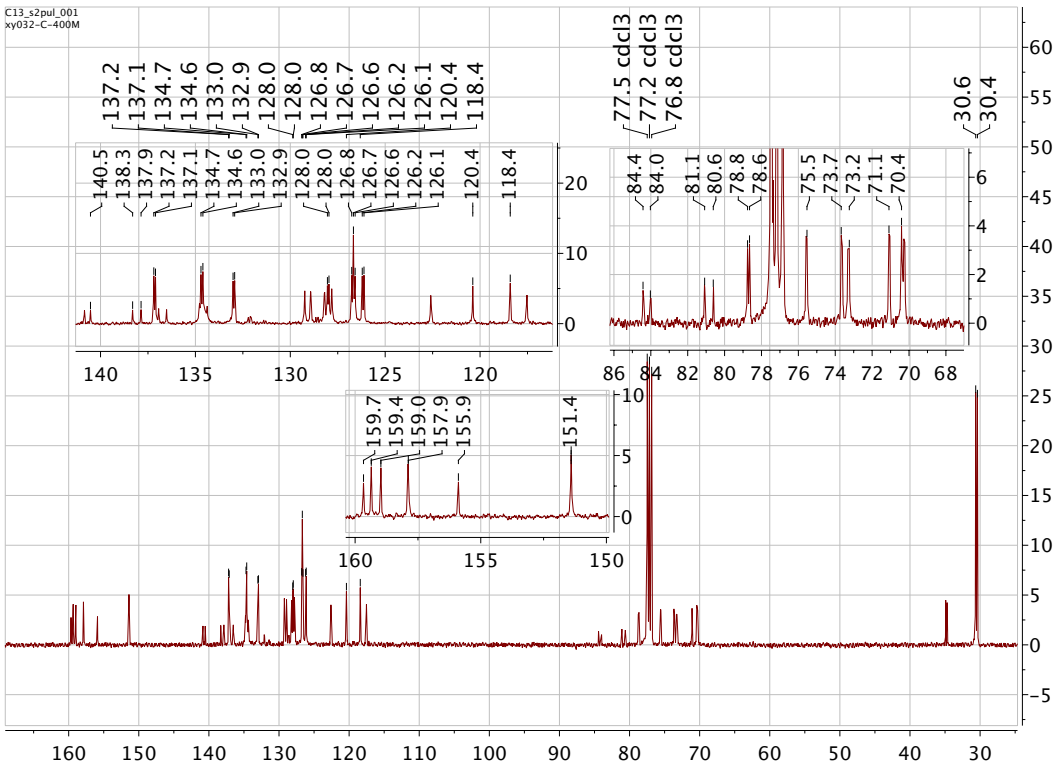

Figure A02 ^{13}C-NMR spectrum of **2.1a** recorded in $CDCl_3$.

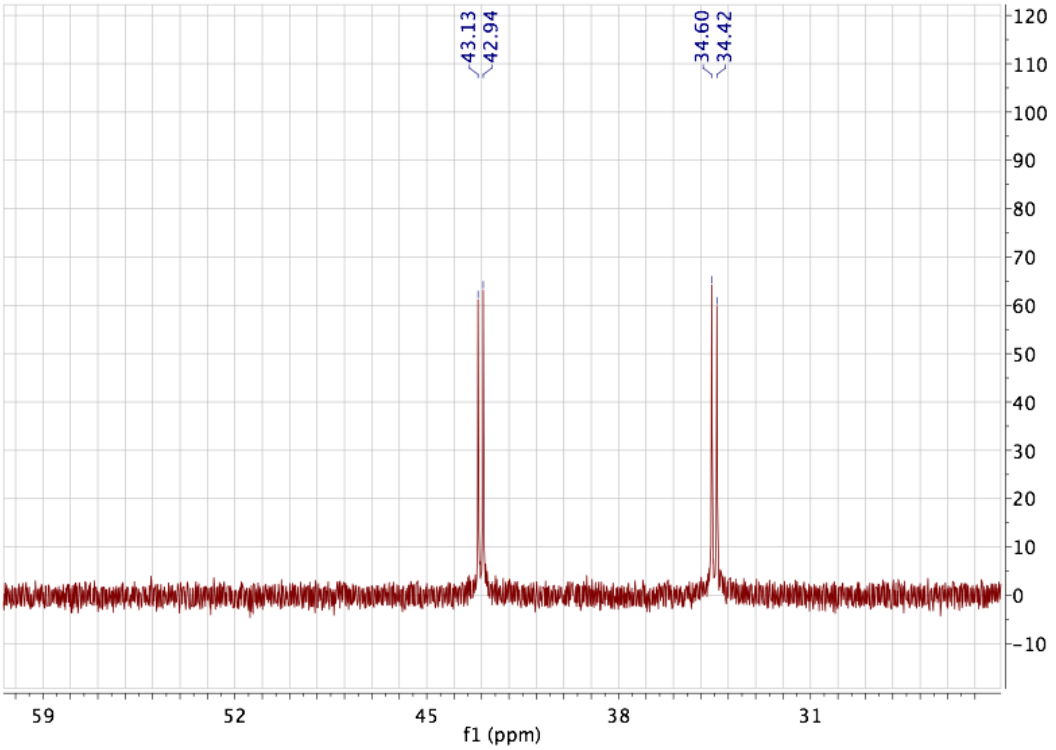

Figure A03 ^{31}P-NMR spectrum of **2.1a** recorded in $CDCl_3$.

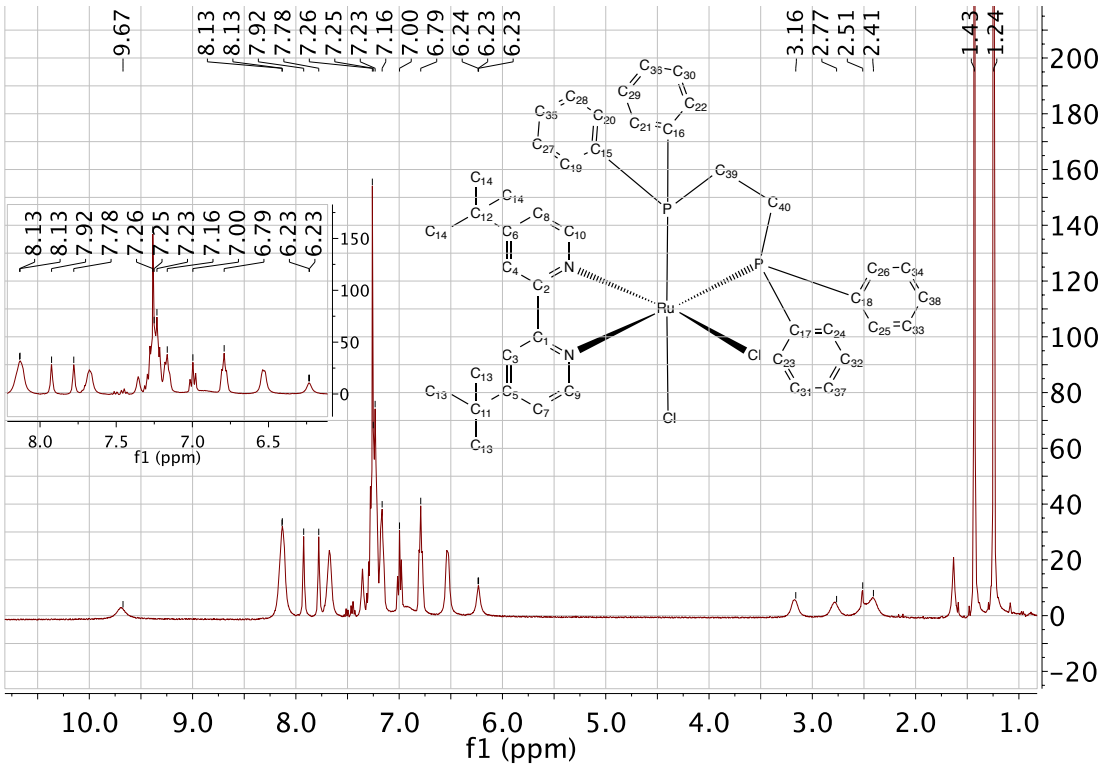

Figure A04 ^{1}H-NMR spectrum of **2.1b** recorded in $CDCl_3$.

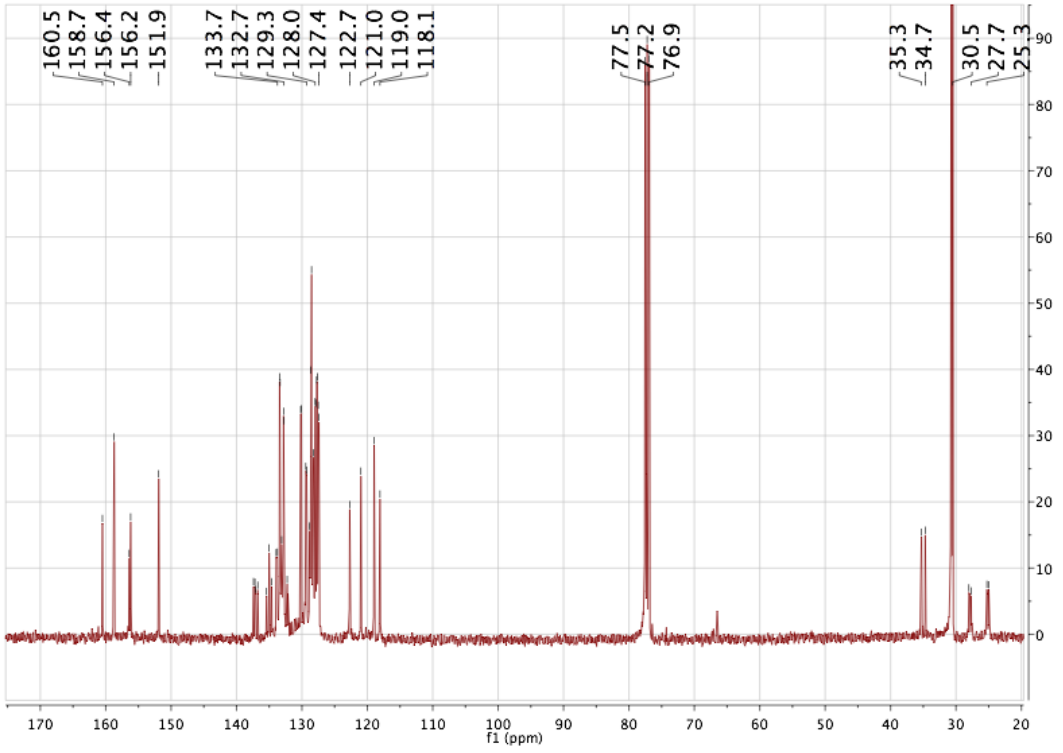

Figure A05 ^{13}C-NMR spectrum of **2.1b** recorded in $CDCl_3$.

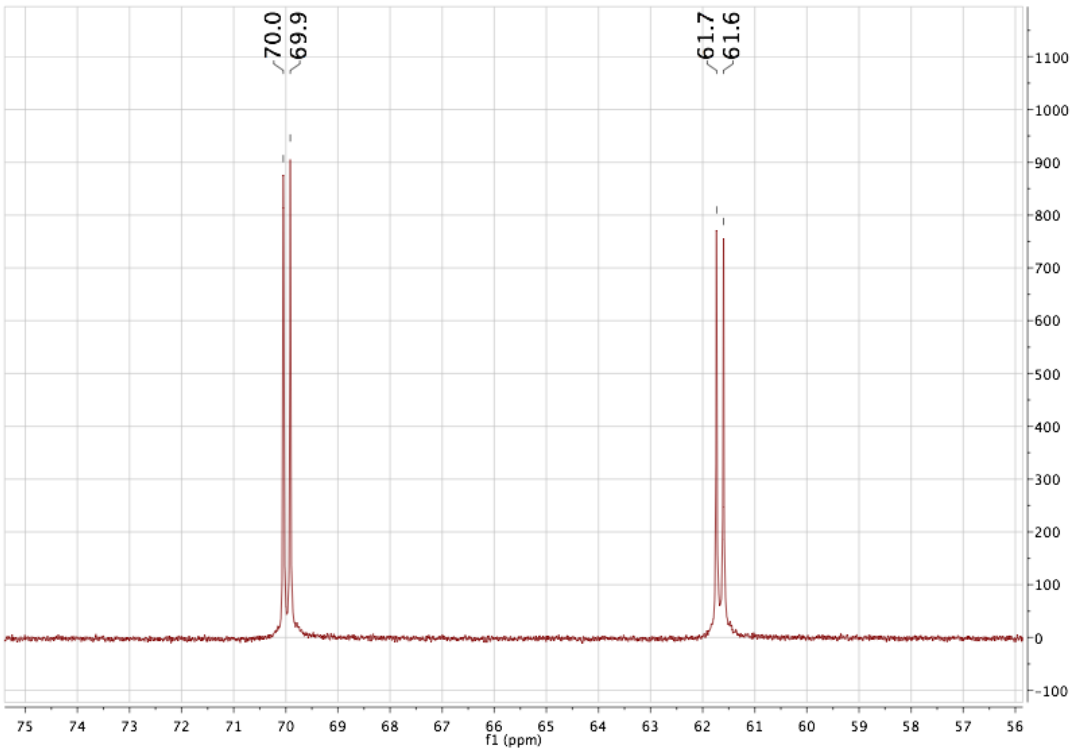

Figure A06 ^{31}P-NMR spectrum of **2.1b** recorded in $CDCl_3$.

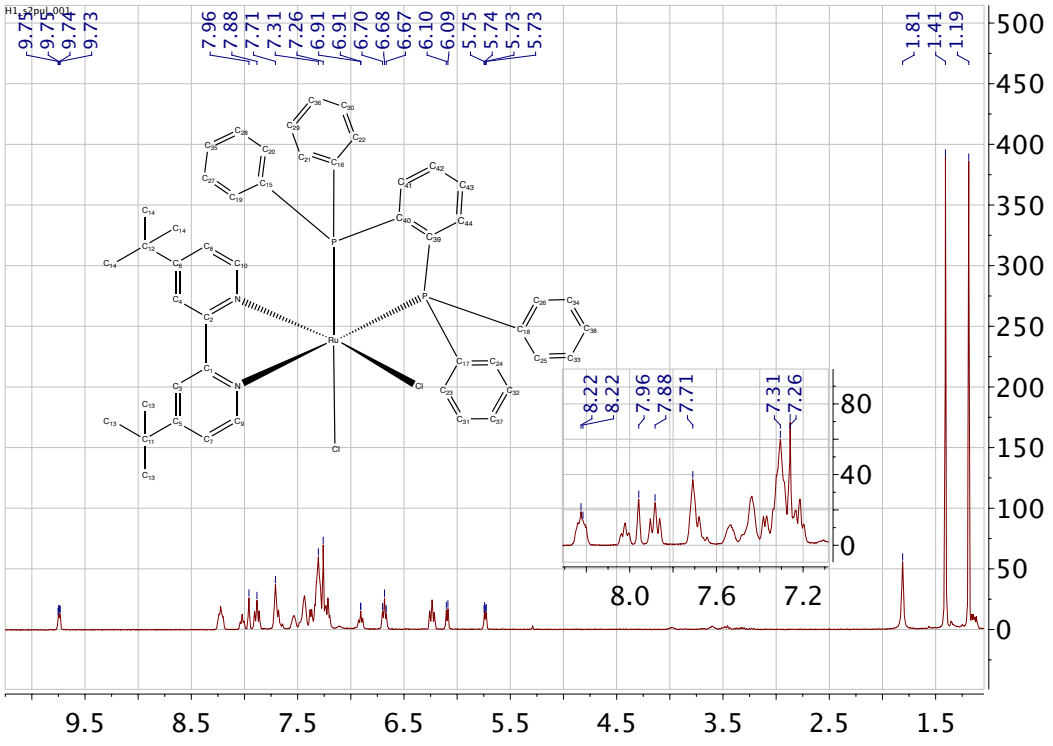

Figure A07 ^{1}H-NMR spectrum of **2.1c** recorded in $CDCl_3$.

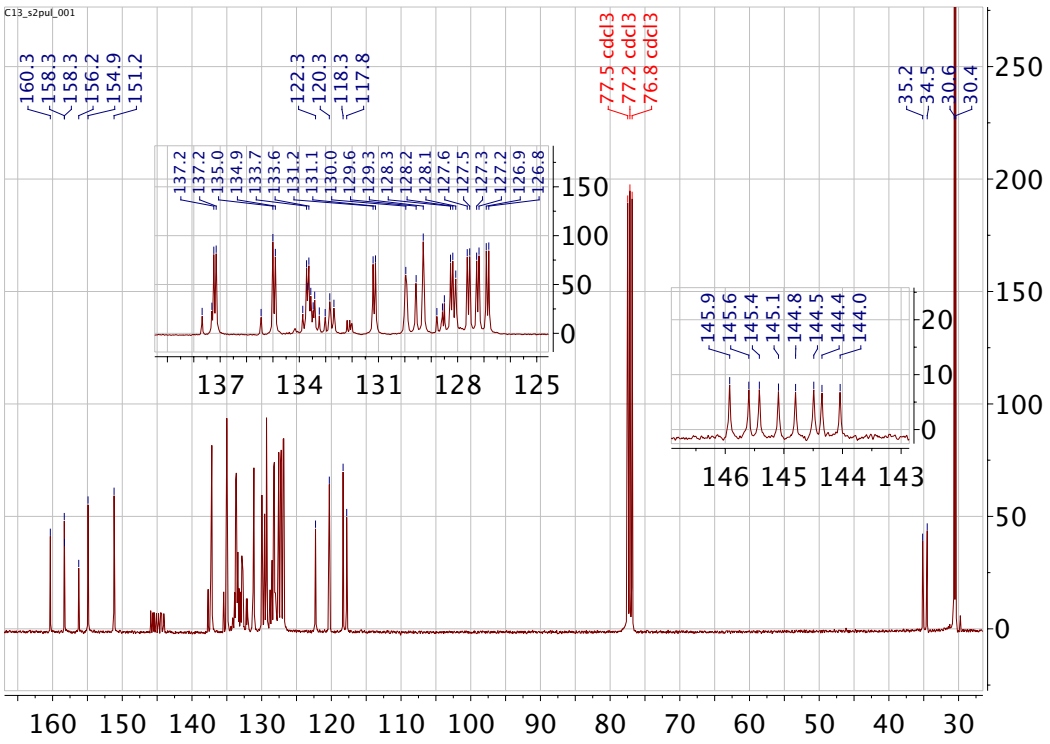

Figure A08 ^{13}C-NMR spectrum of **2.1c** recorded in $CDCl_3$.

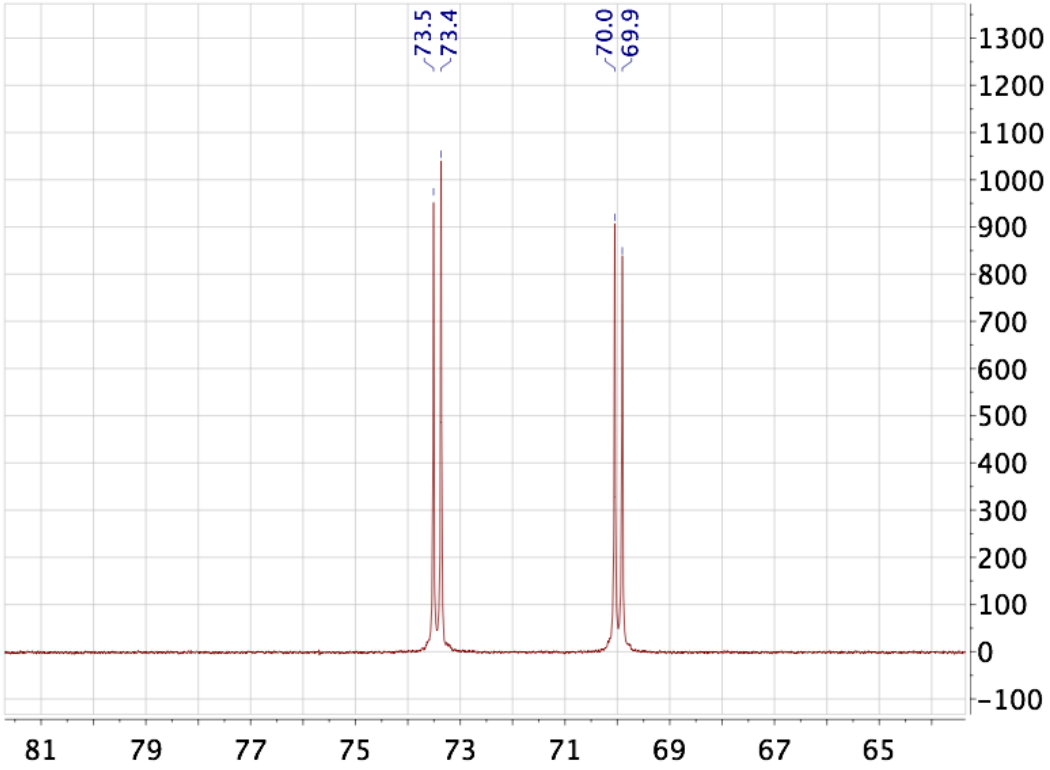

Figure A09 ^{31}P-NMR spectrum of **2.1c** recorded in $CDCl_3$.

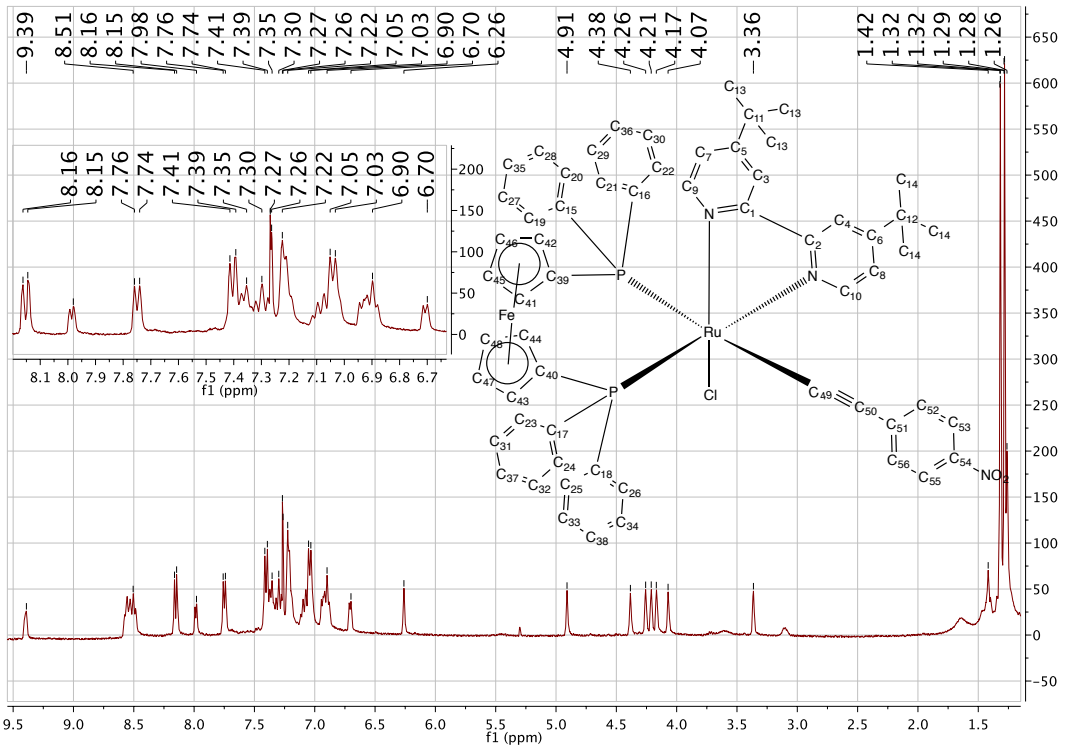

Figure A10 ^{1}H-NMR spectrum of **2.2a** recorded in $CDCl_3$.

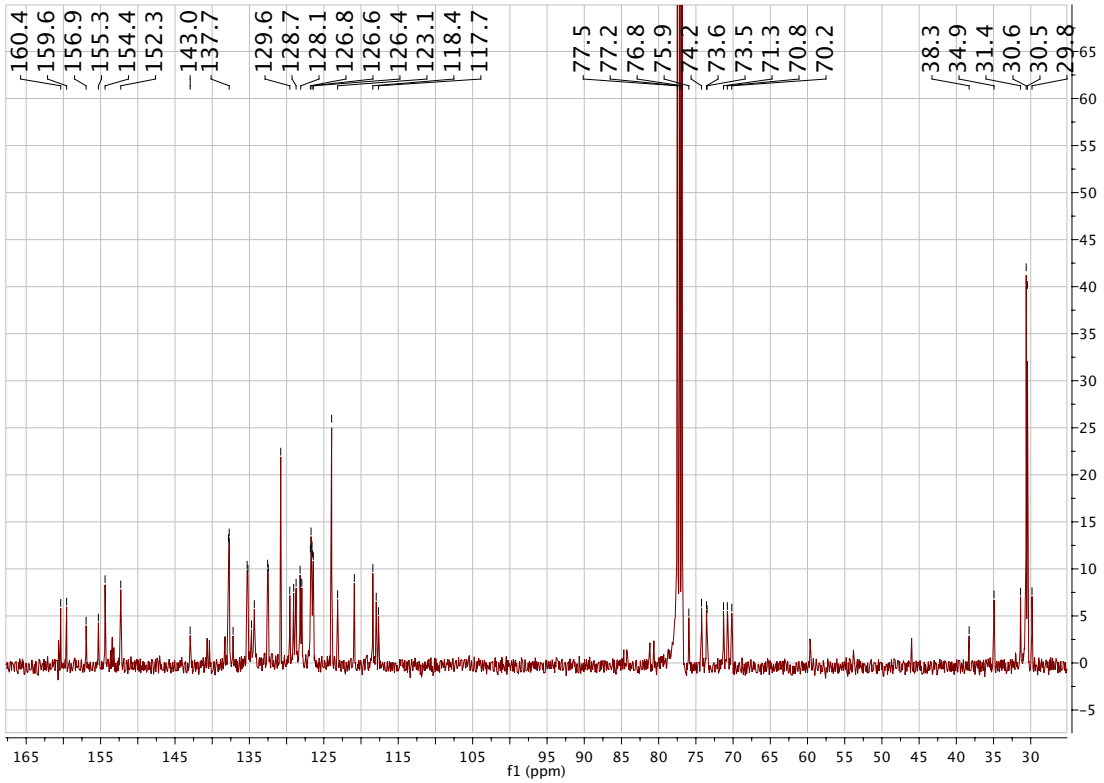

Figure A11 ^{13}C-NMR spectrum of **2.2a** recorded in $CDCl_3$.

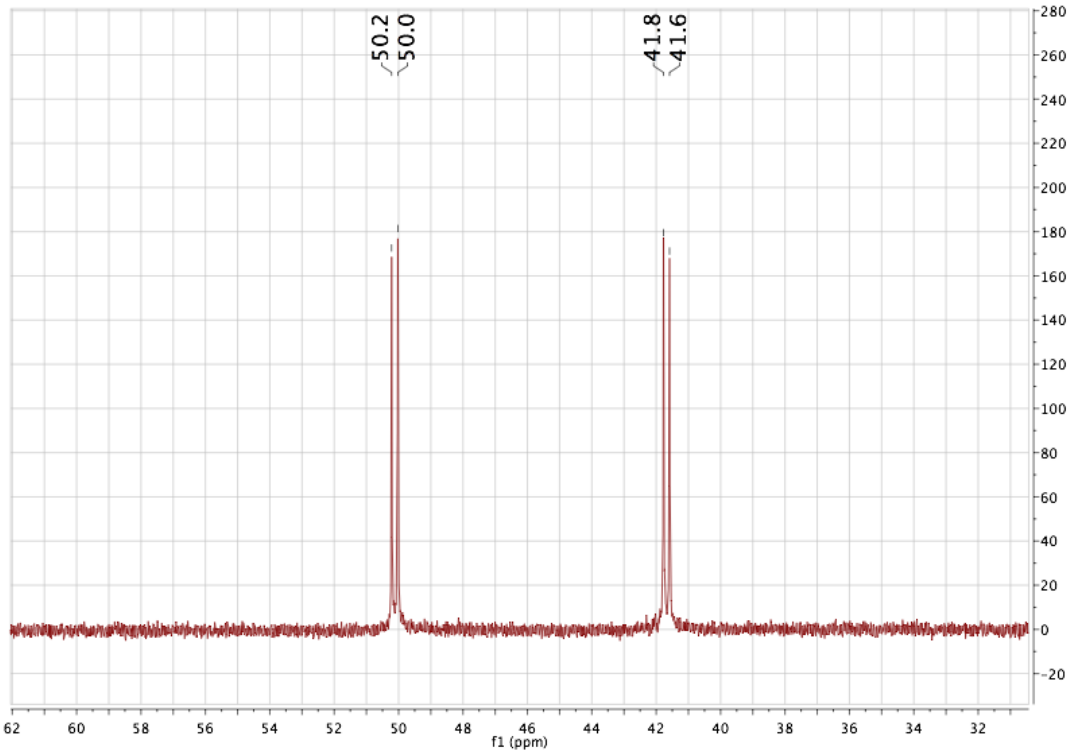

Figure A12 ^{31}P-NMR spectrum of **2.2a** recorded in $CDCl_3$.

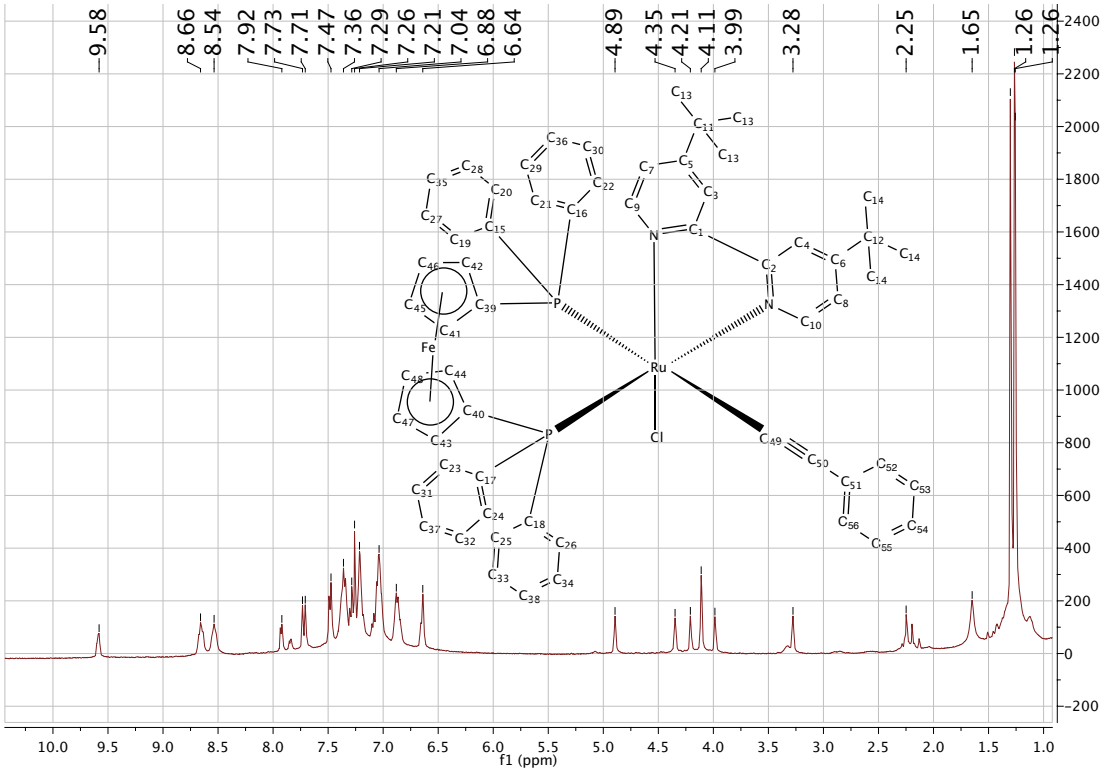

Figure A13 ^{1}H-NMR spectrum of **2.2b** recorded in $CDCl_3$.

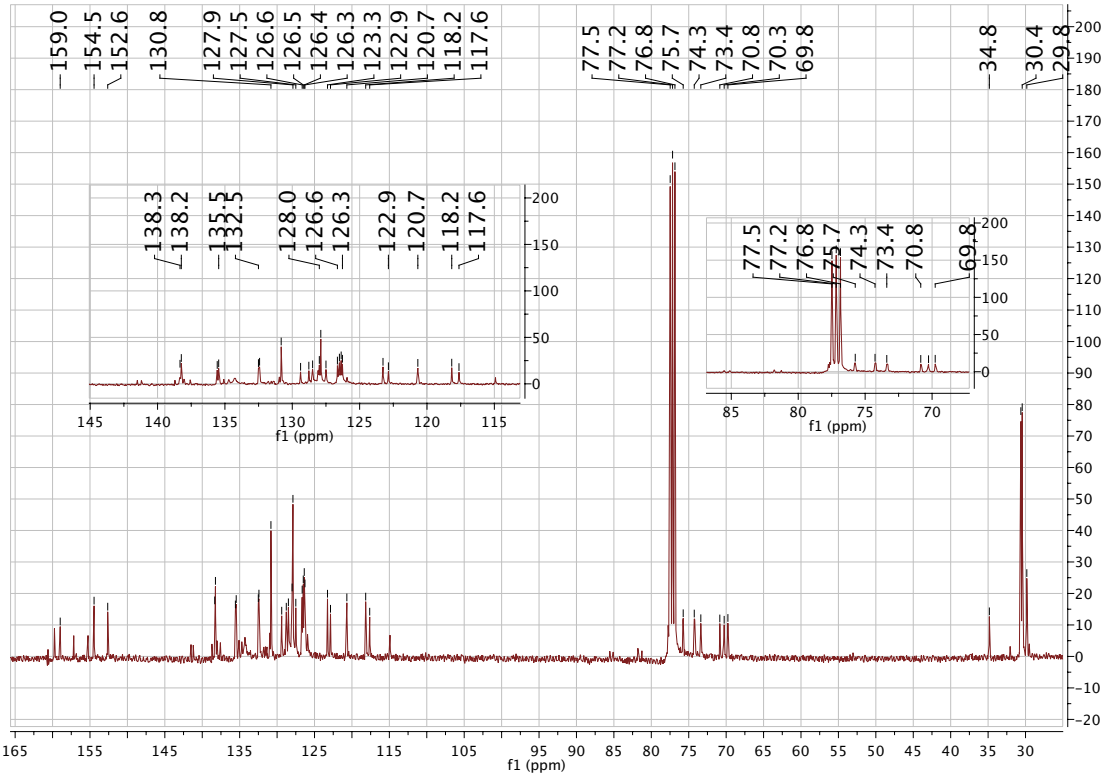

Figure A14 ^{13}C-NMR spectrum of **2.2b** recorded in $CDCl_3$.

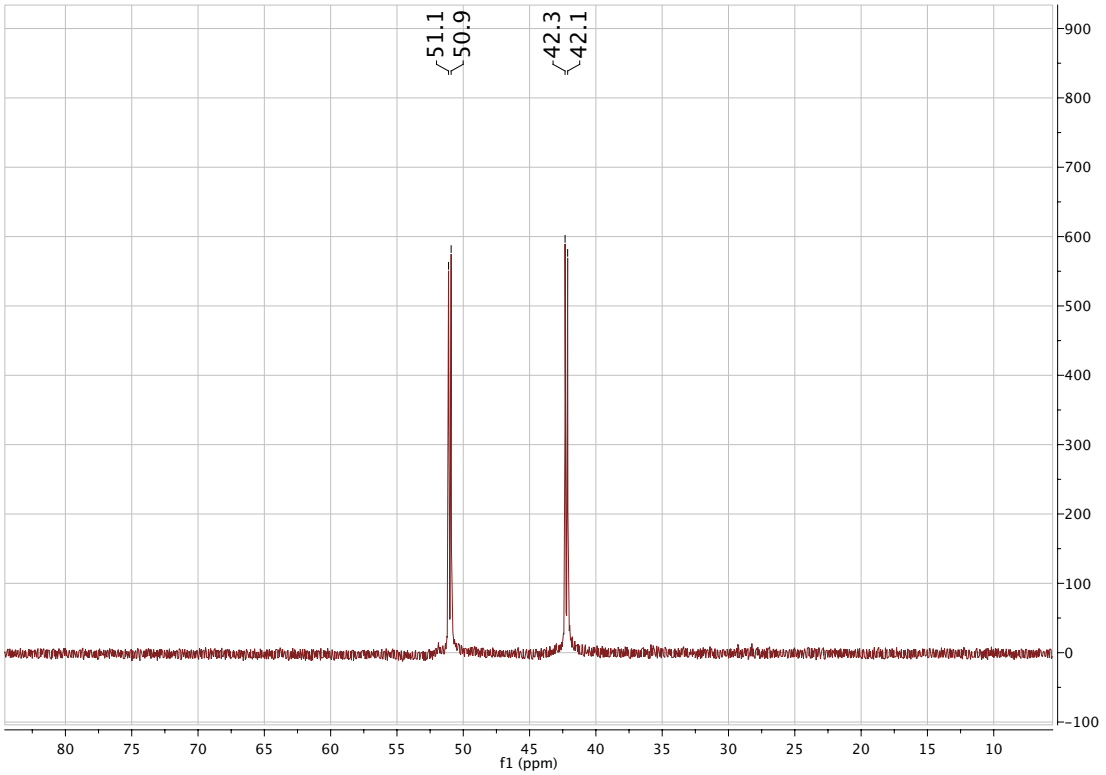

Figure A15 ^{31}P-NMR spectrum of **2.2b** recorded in $CDCl_3$.

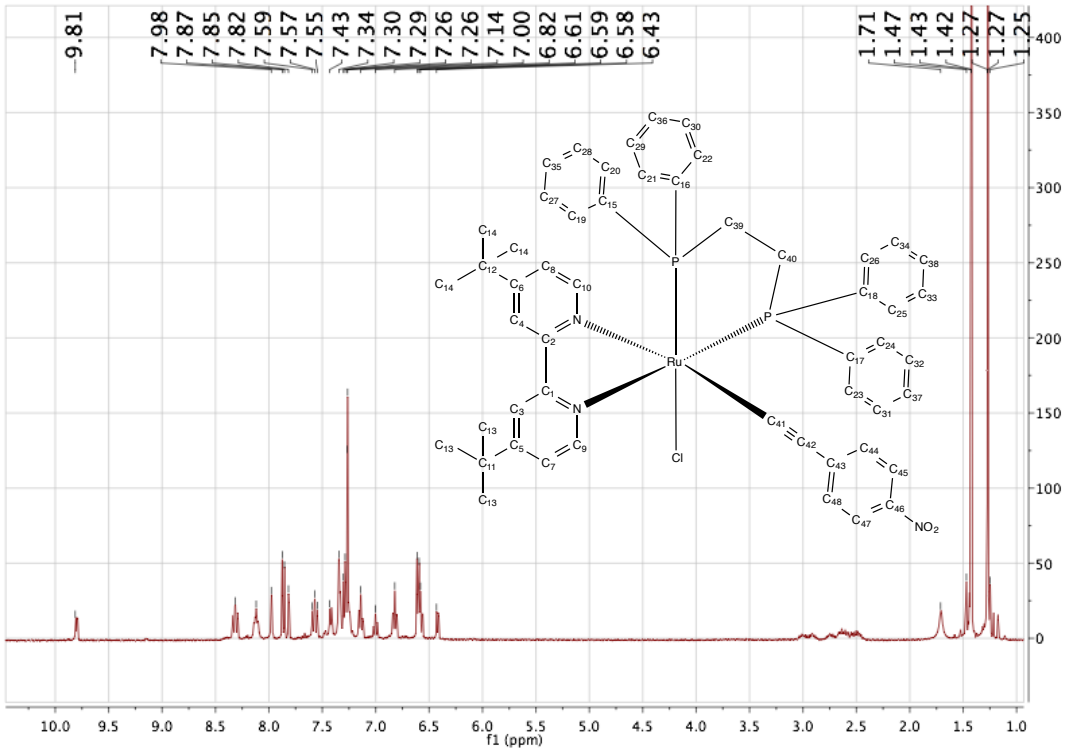

Figure A16 ^{1}H-NMR spectrum of **2.2c** recorded in $CDCl_3$.

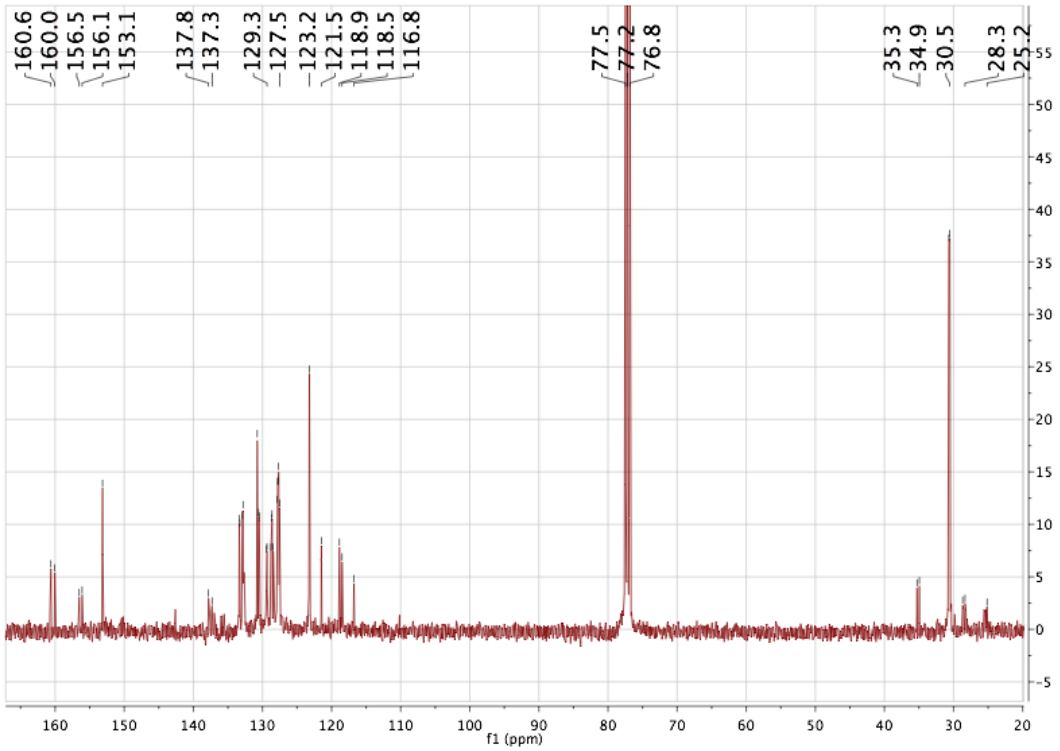

Figure A17 ^{13}C-NMR spectrum of **2.2c** recorded in $CDCl_3$.

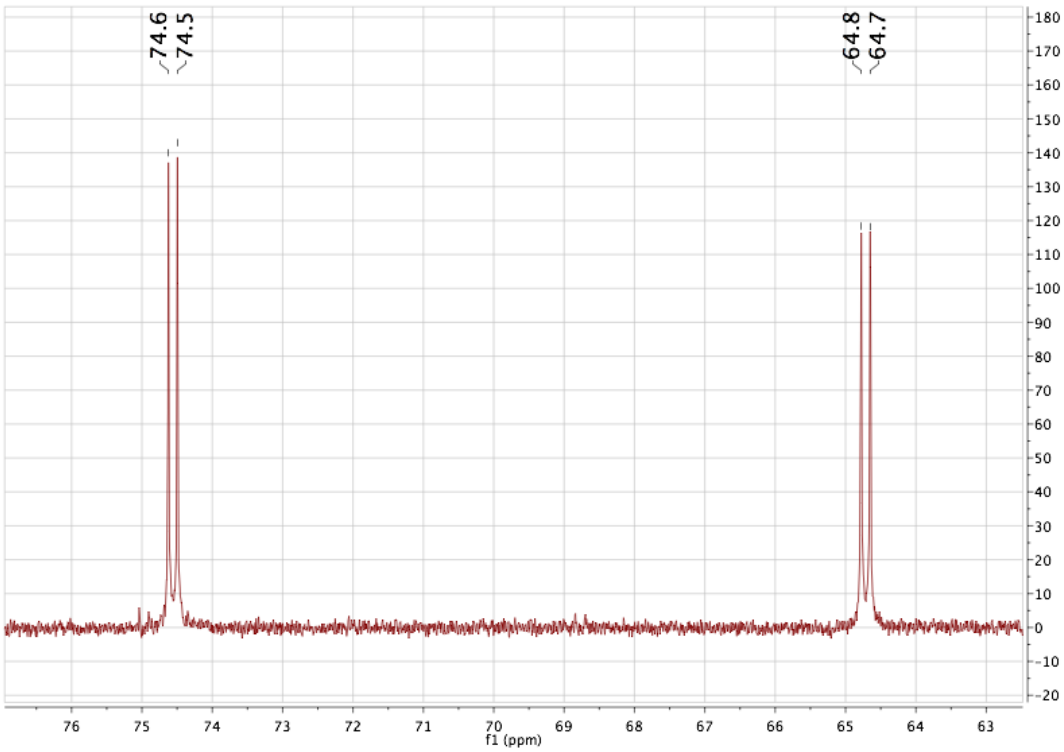

Figure A18 ^{31}P-NMR spectrum of **2.2c** recorded in $CDCl_3$.

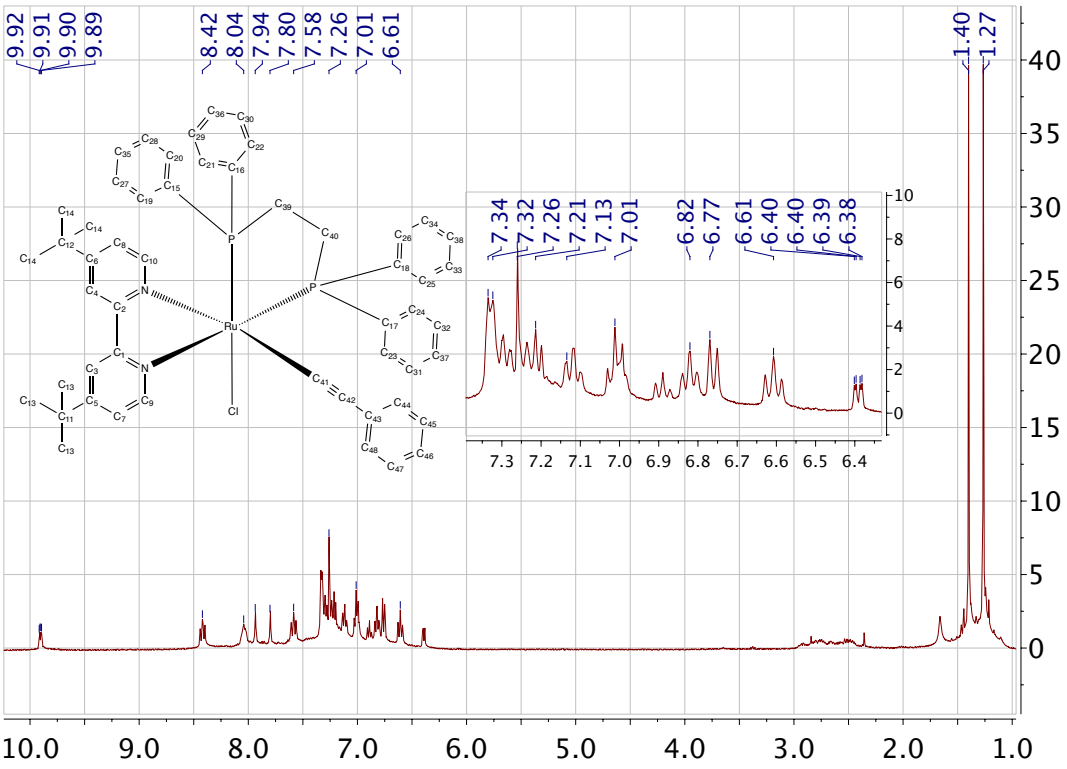

Figure A19 ^{1}H-NMR spectrum of **2.2d** recorded in $CDCl_3$.

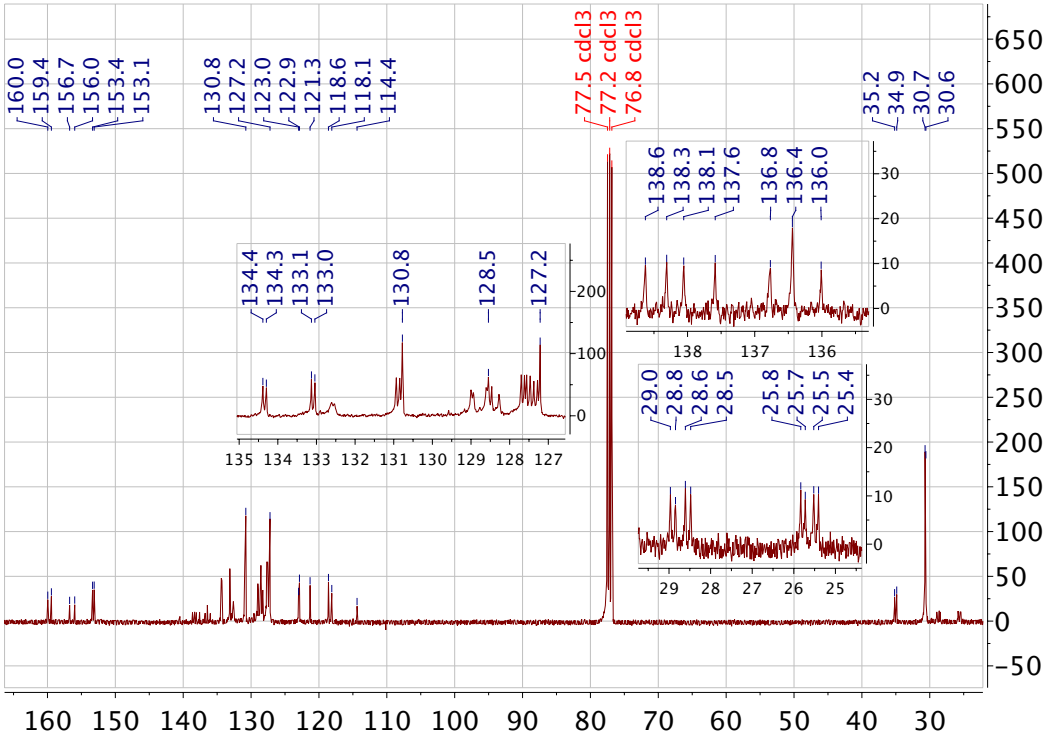

Figure A20 ^{13}C-NMR spectrum of **2.2d** recorded in $CDCl_3$.

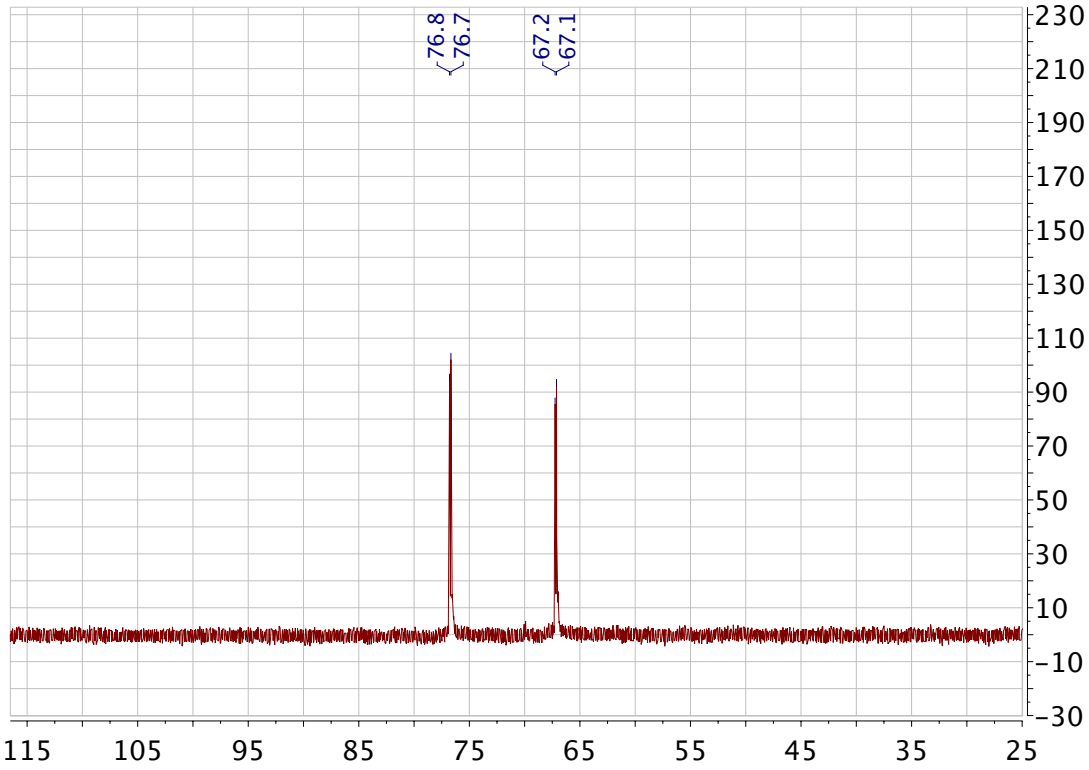

Figure A21 ^{31}P-NMR spectrum of **2.2d** recorded in $CDCl_3$.

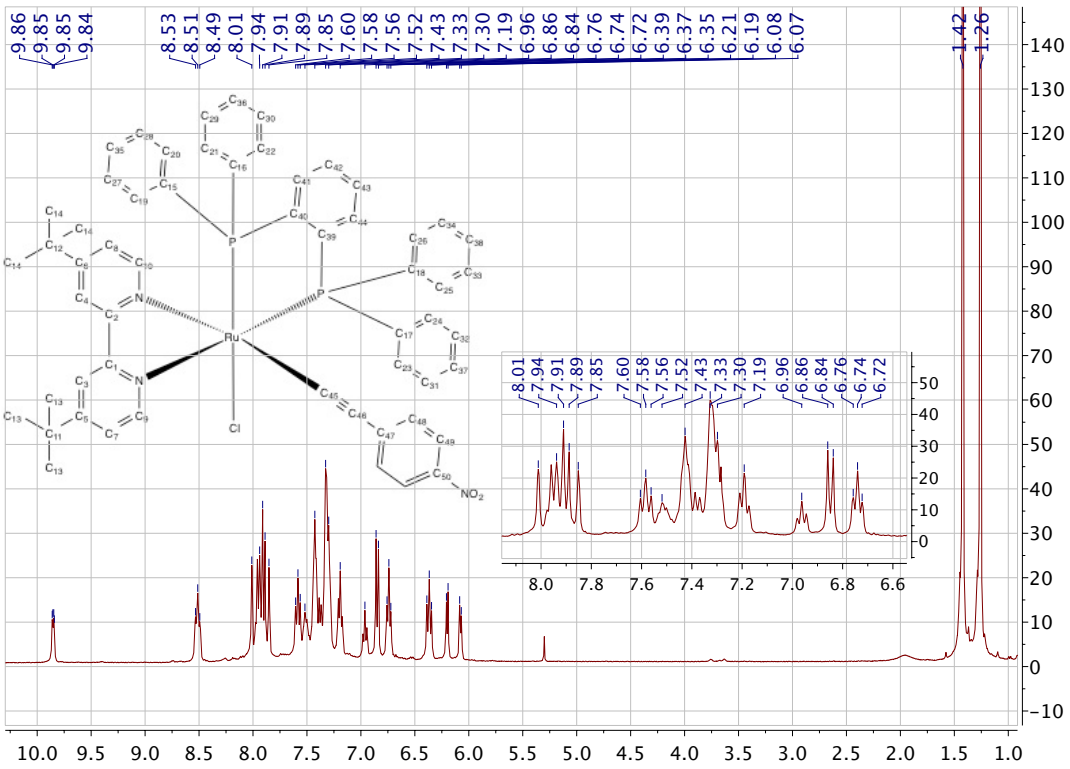

Figure A22 ^{1}H-NMR spectrum of **2.2e** recorded in $CDCl_3$.

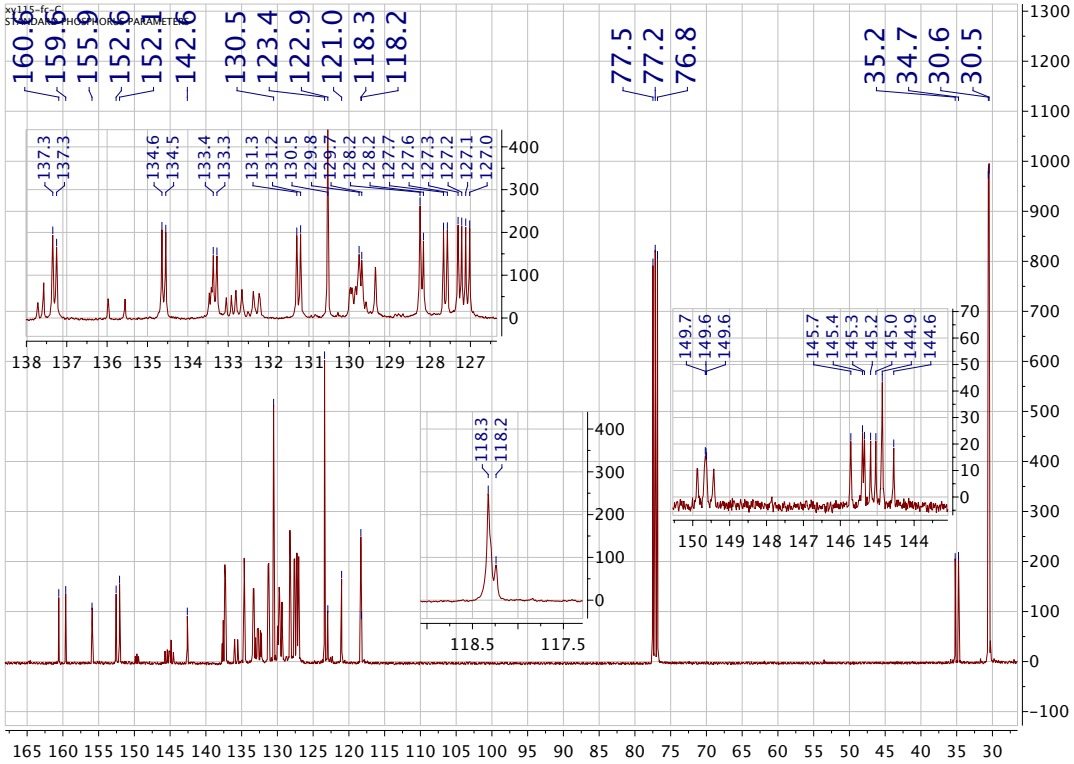

Figure A23 ^{13}C-NMR spectrum of **2.2e** recorded in $CDCl_3$.

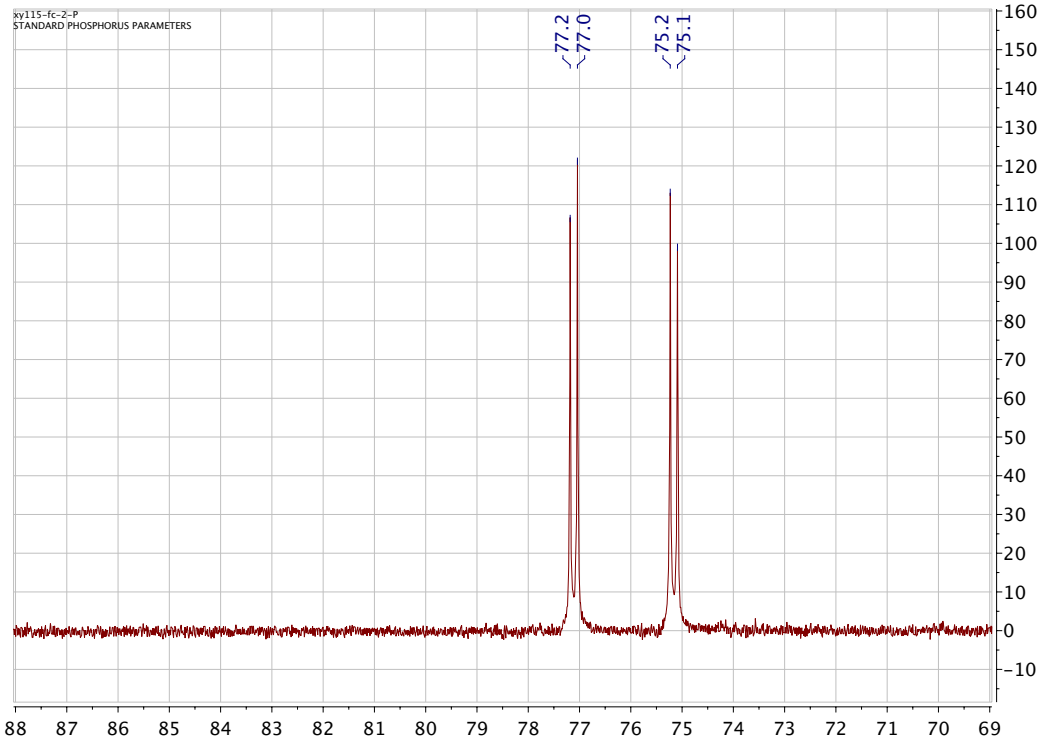

Figure A24 ^{31}P-NMR spectrum of **2.2e** recorded in $CDCl_3$.

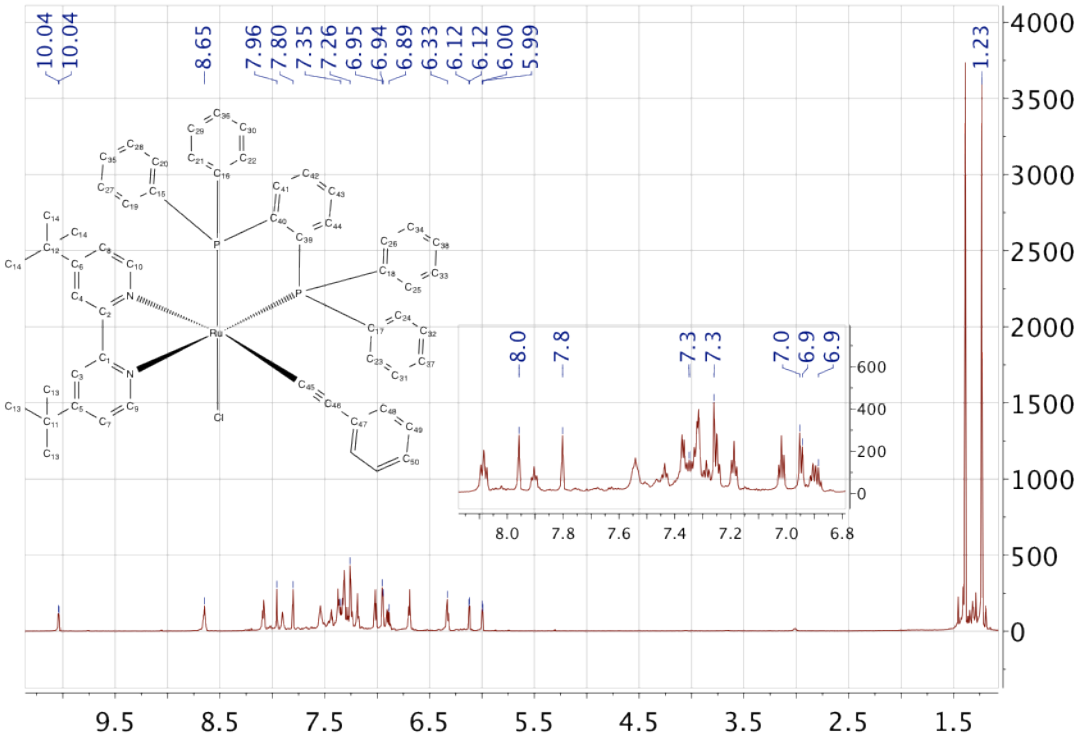

Figure A25 ^{1}H-NMR spectrum of **2.2f** recorded in $CDCl_3$.

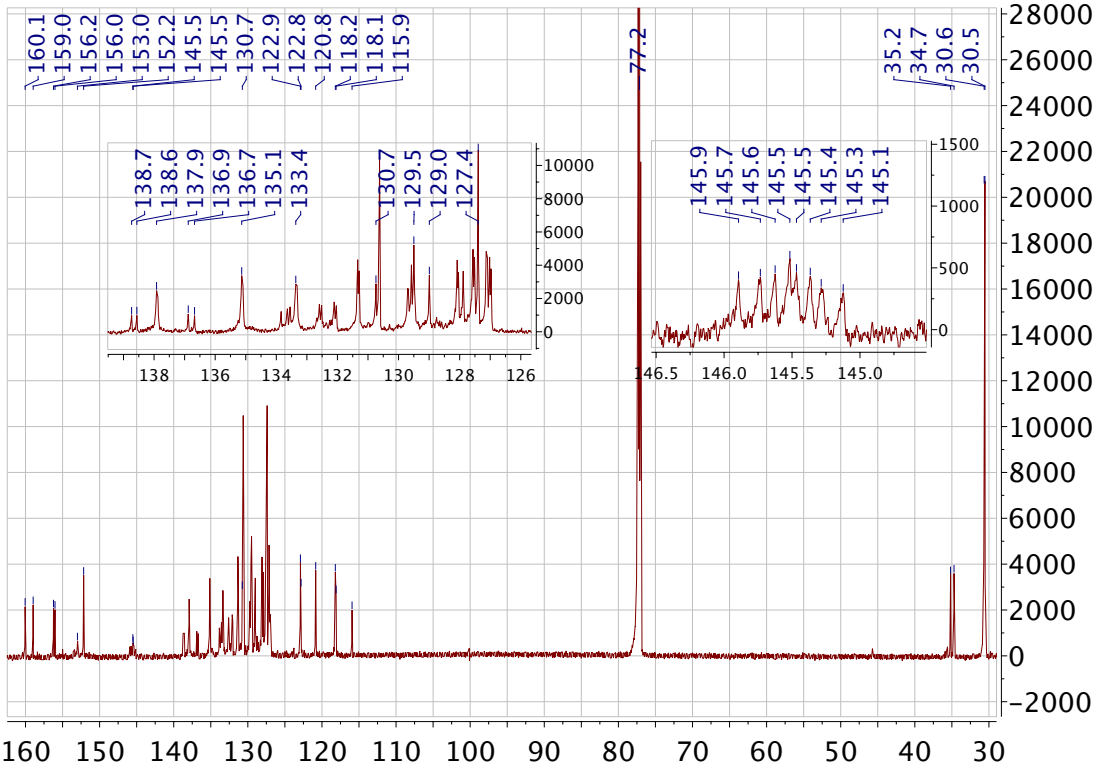

Figure A26 ^{13}C-NMR spectrum of **2.2f** recorded in $CDCl_3$.

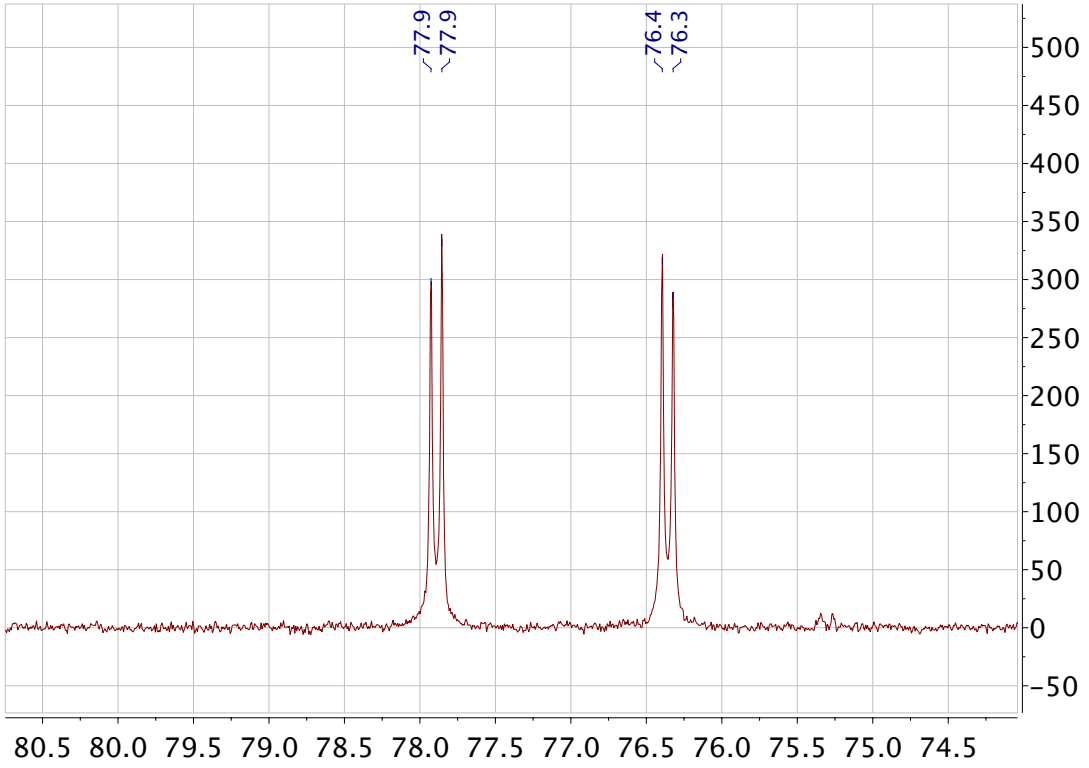

Figure A27 ^{31}P-NMR spectrum of **2.2f** recorded in $CDCl_3$.

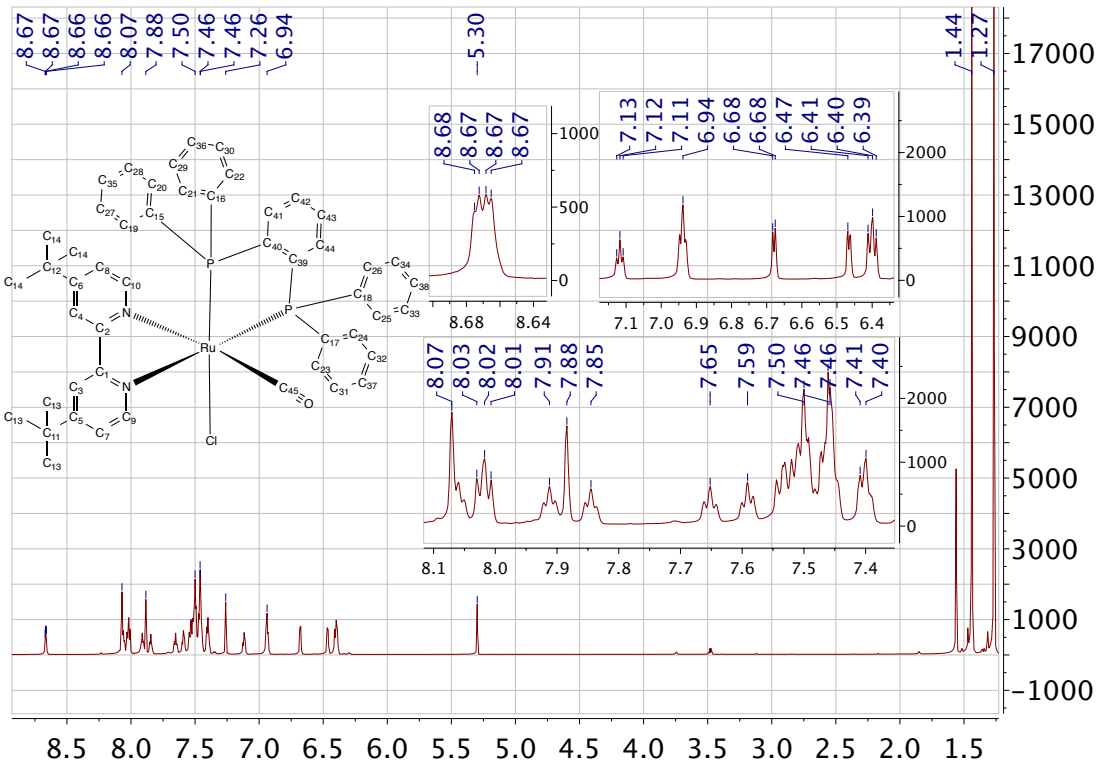

Figure A28 ^{1}H-NMR spectrum of **2.3a** recorded in $CDCl_3$.

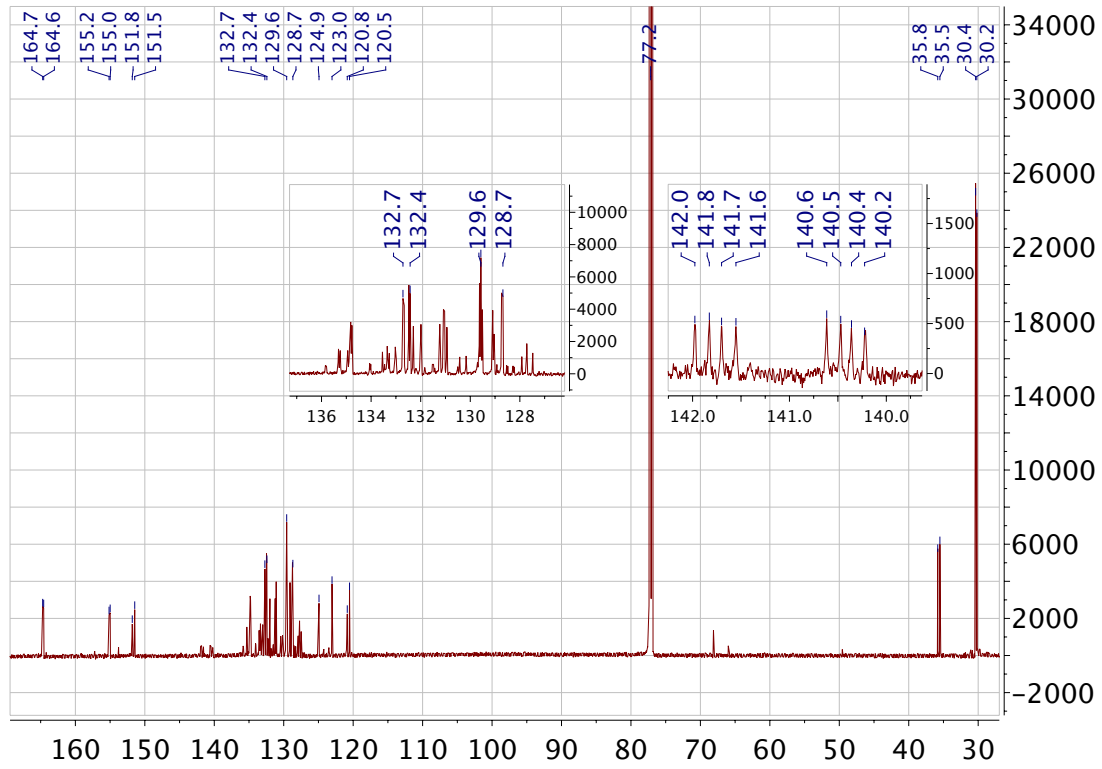

Figure A29 ^{13}C-NMR spectrum of **2.3a** recorded in $CDCl_3$.

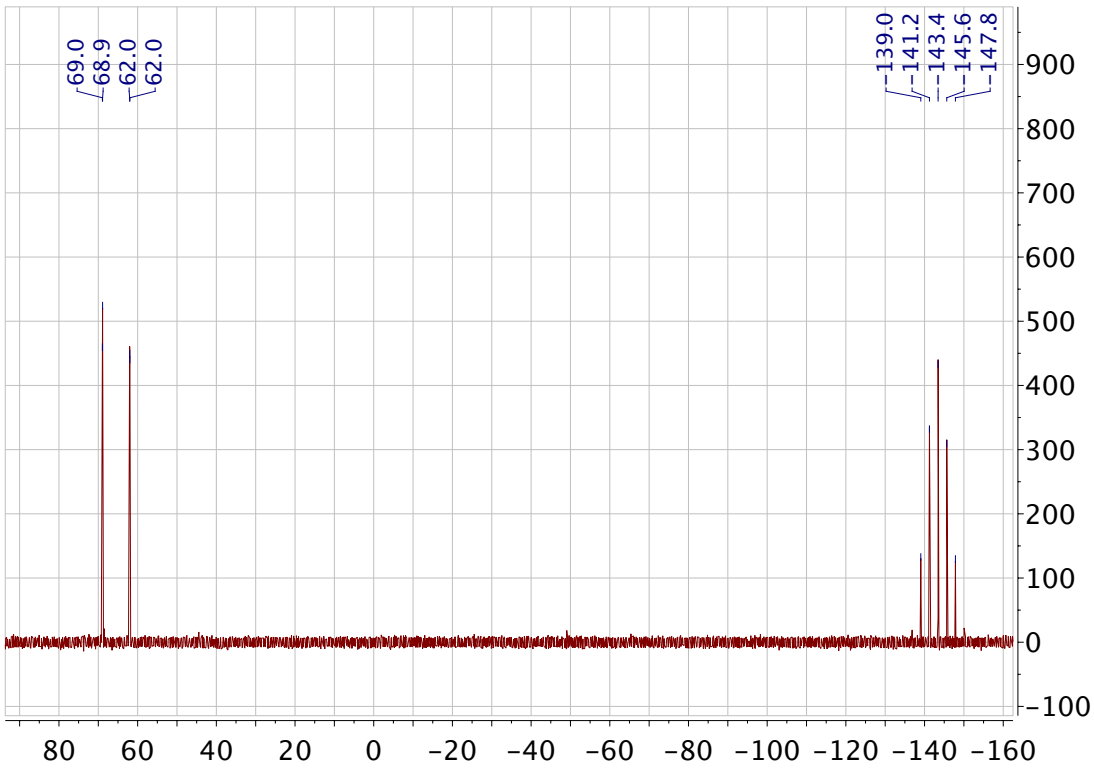

Figure A30 ^{31}P-NMR spectrum of **2.3a** recorded in $CDCl_3$.

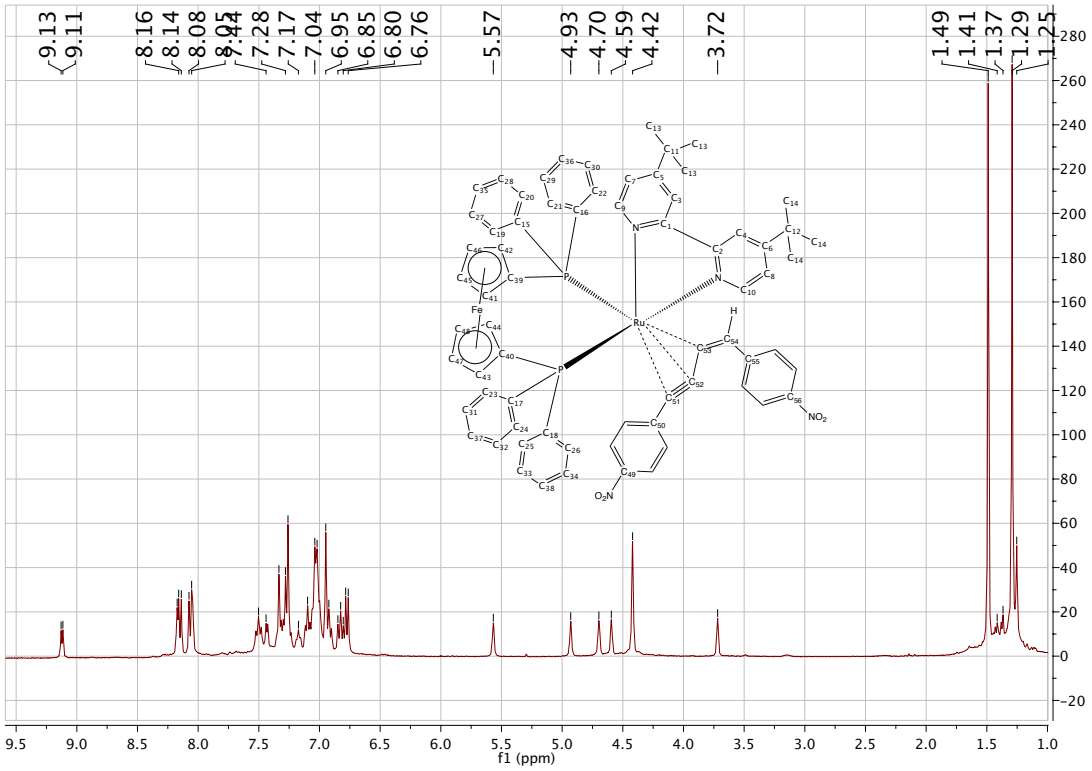

Figure A31 ^{1}H-NMR spectrum of **2.4a** recorded in $CDCl_3$.

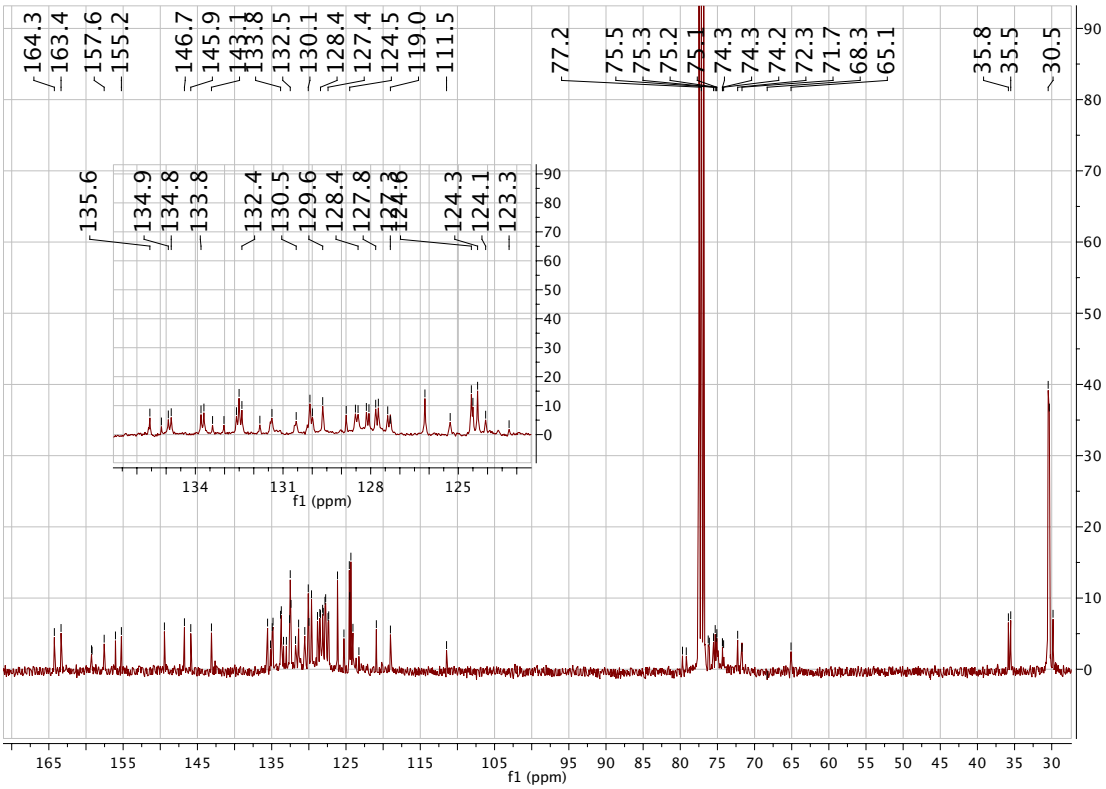

Figure A32 ^{13}C-NMR spectrum of **2.4a** recorded in $CDCl_3$.

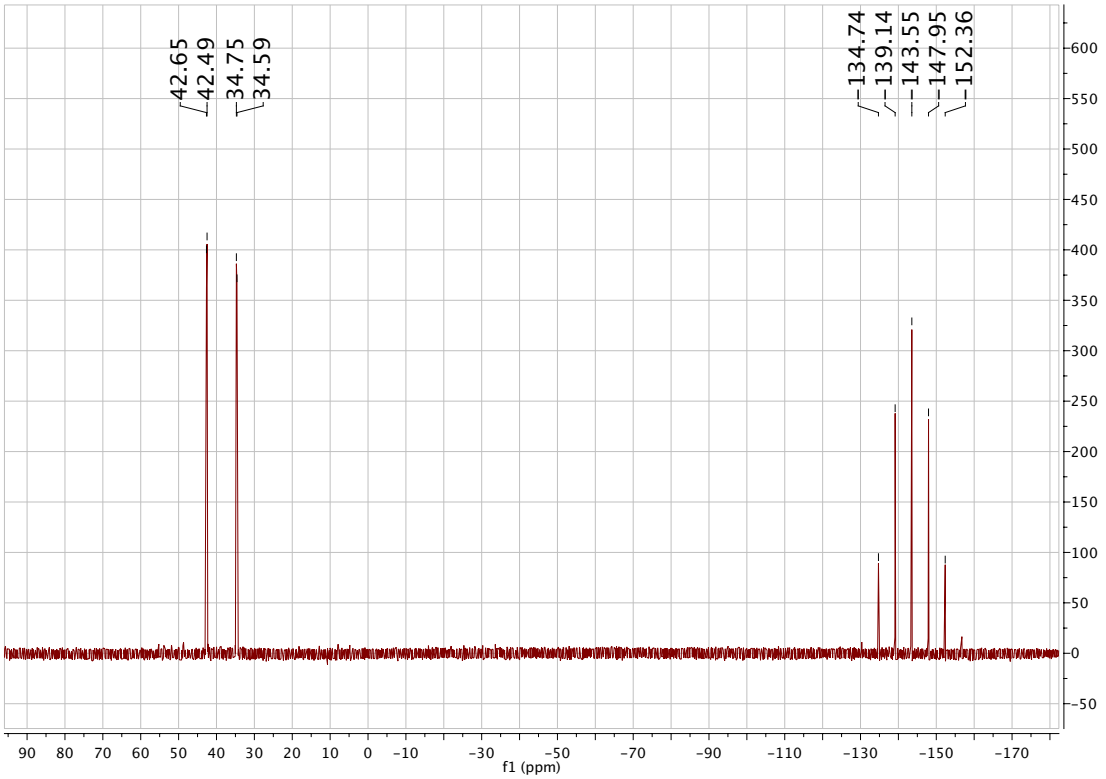

Figure A33 ^{31}P-NMR spectrum of **2.4a** recorded in $CDCl_3$.

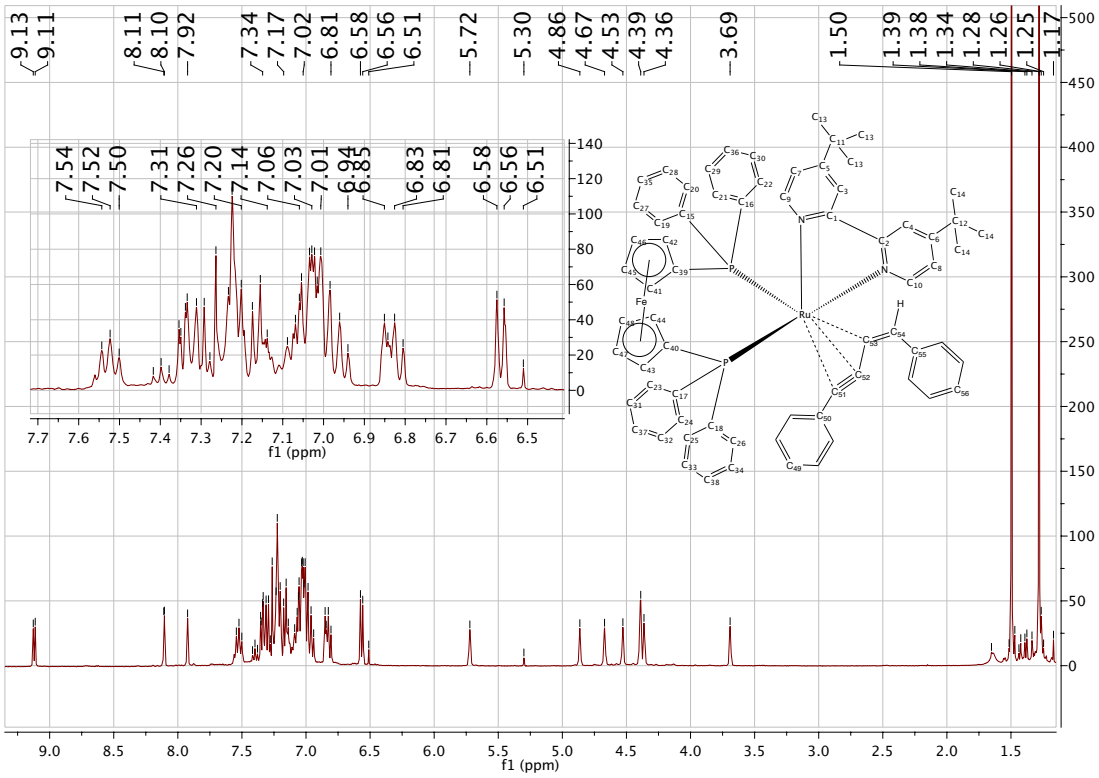

Figure A34 ^{1}H-NMR spectrum of **2.4b** recorded in $CDCl_3$.

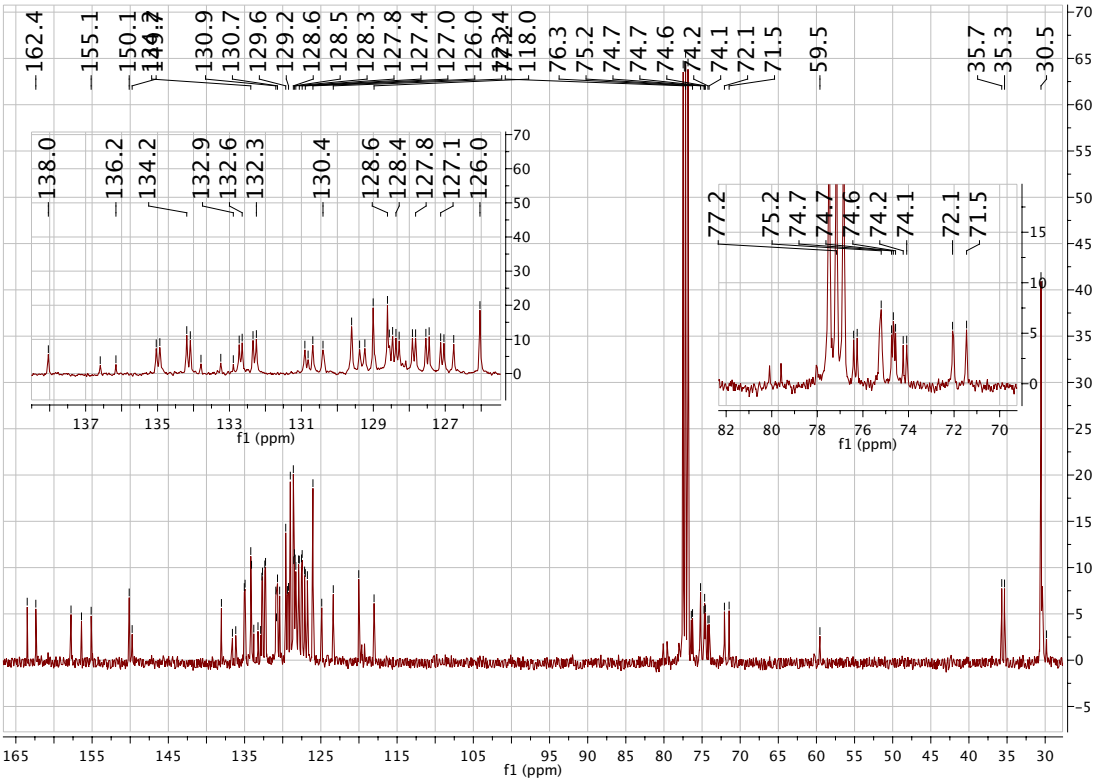

Figure A35 ^{13}C-NMR spectrum of **2.4b** recorded in $CDCl_3$.

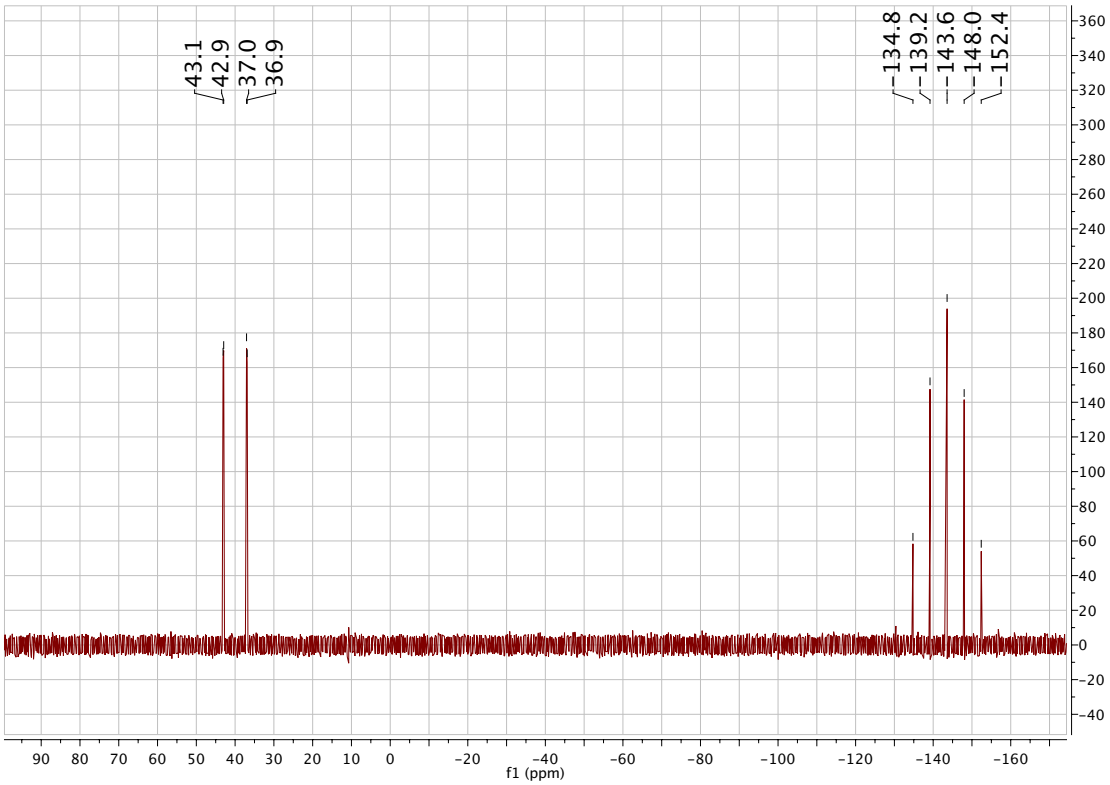

Figure A36 ^{31}P-NMR spectrum of **2.4b** recorded in $CDCl_3$.

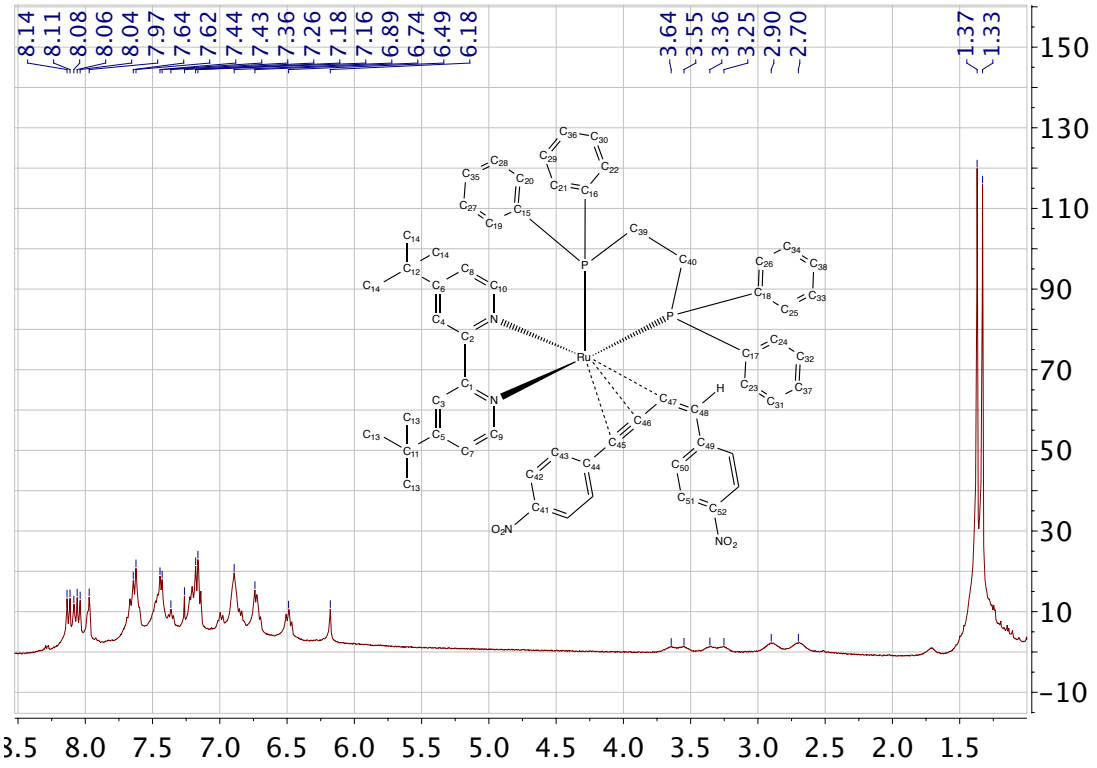

Figure A37. ^{1}H-NMR spectrum of **2.4c** recorded in $CDCl_3$.

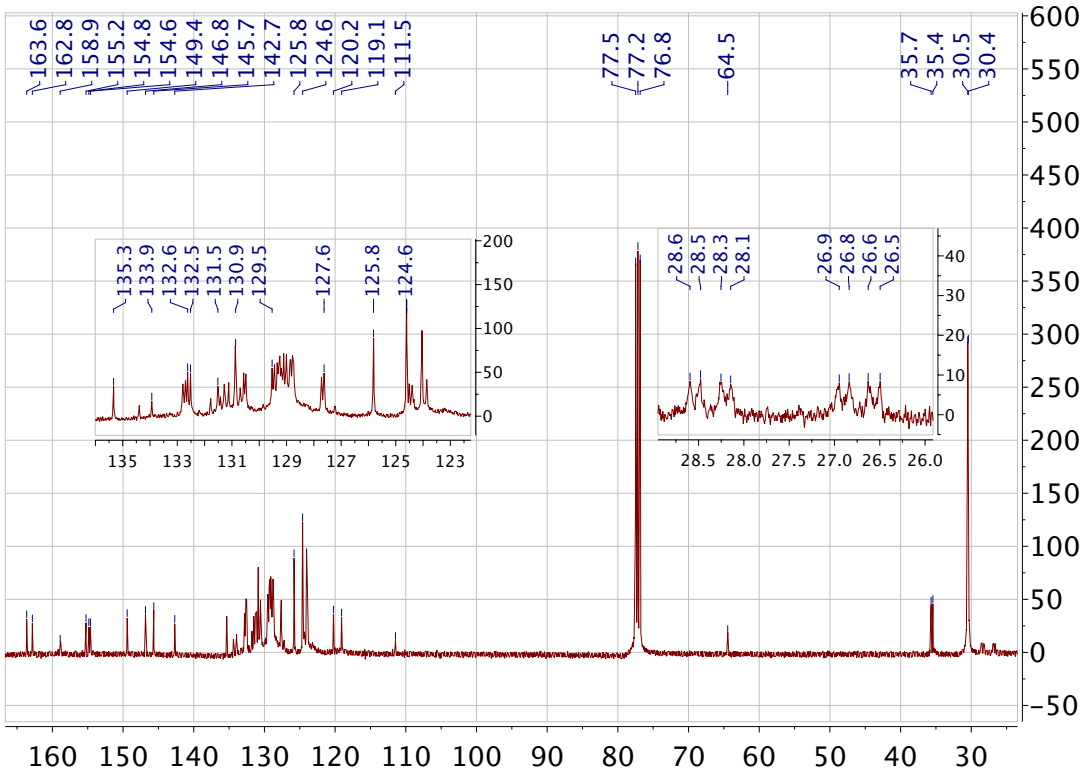

Figure A38 ^{13}C-NMR spectrum of **2.4c** recorded in $CDCl_3$.

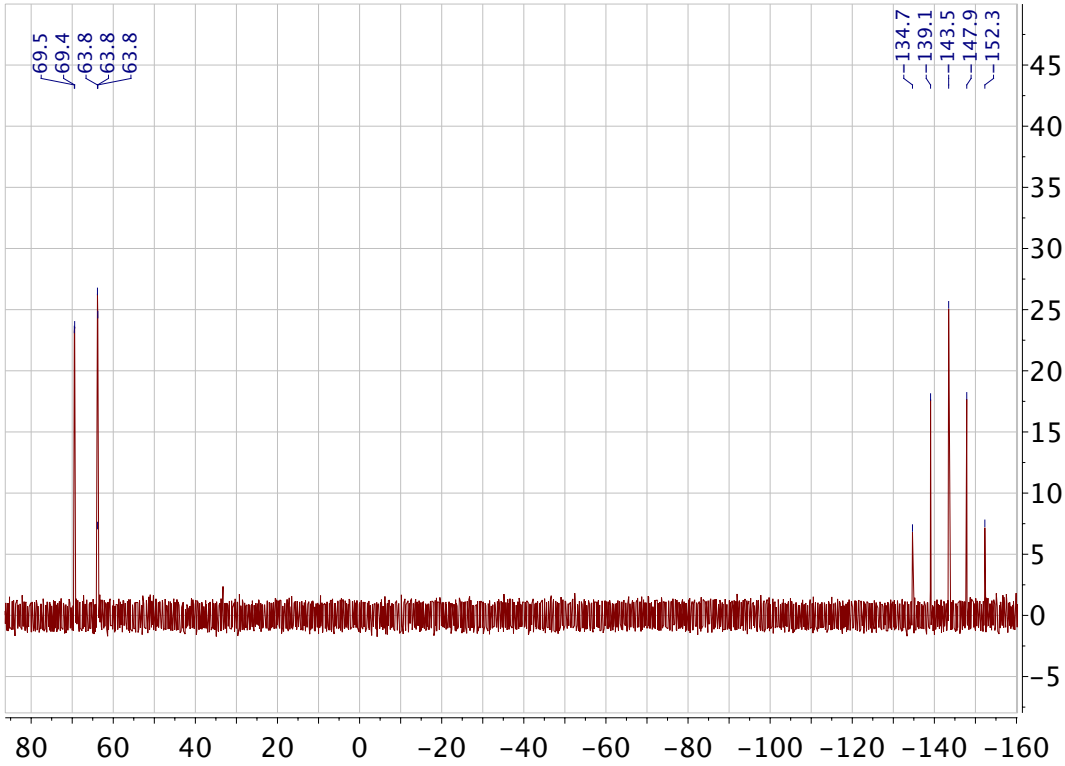

Figure A39 ^{31}P-NMR spectrum of **2.4c** recorded in $CDCl_3$.

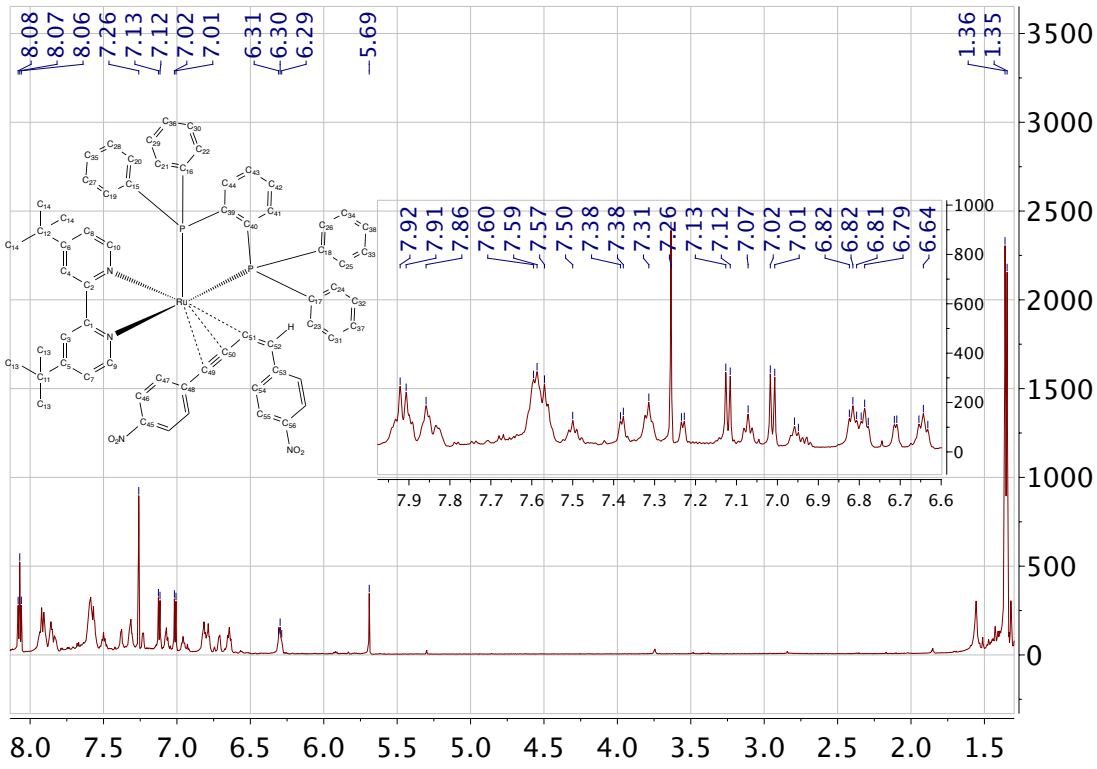

Figure A40 ^{1}H-NMR spectrum of **2.4d** recorded in $CDCl_3$.

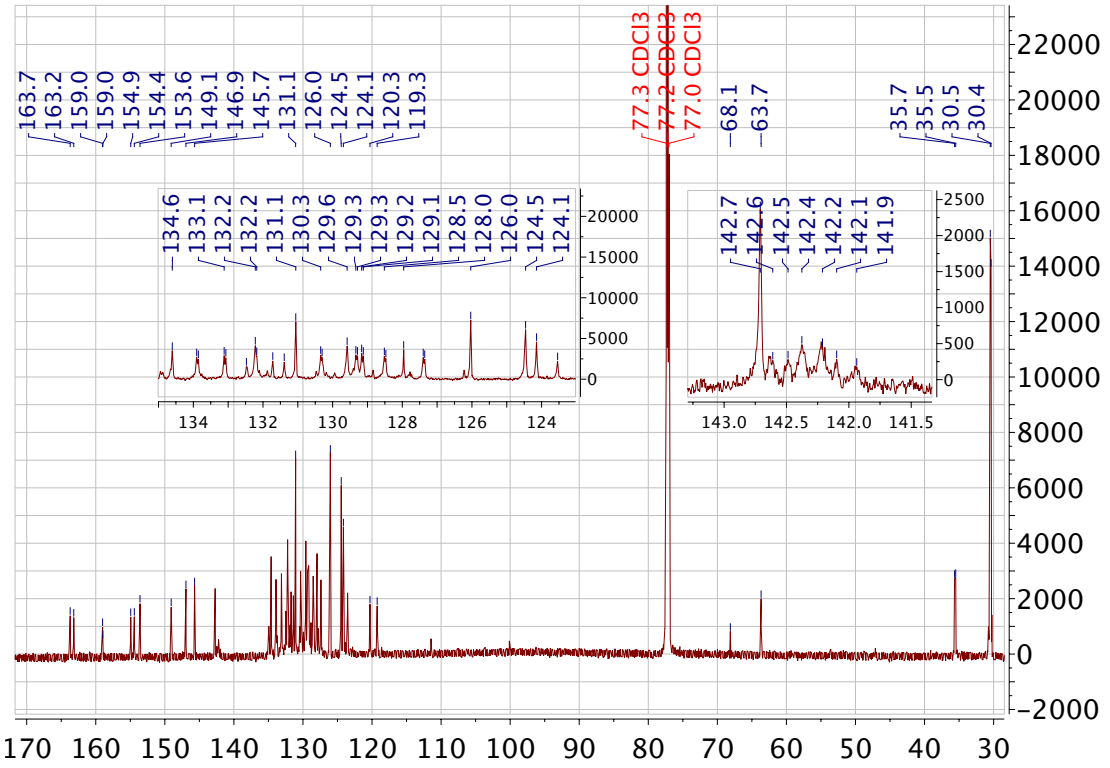

Figure A41 ^{13}C-NMR spectrum of **2.4d** recorded in $CDCl_3$.

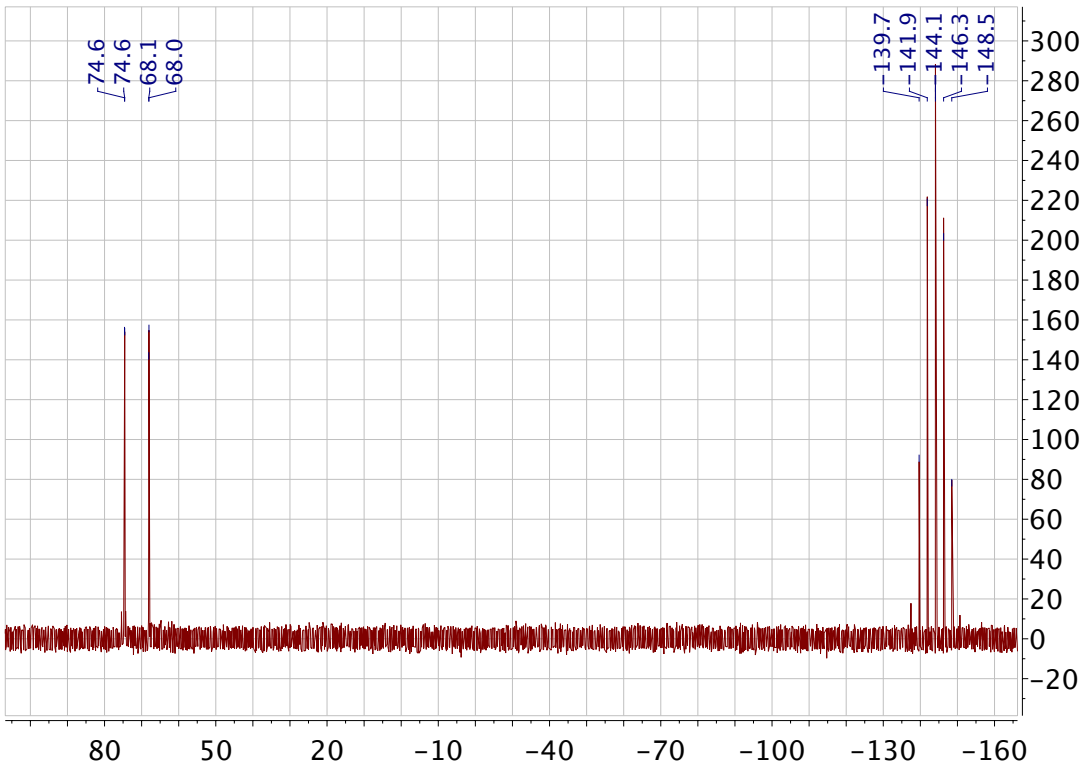

Figure A42 ^{31}P-NMR spectrum of **2.4d** recorded in $CDCl_3$.

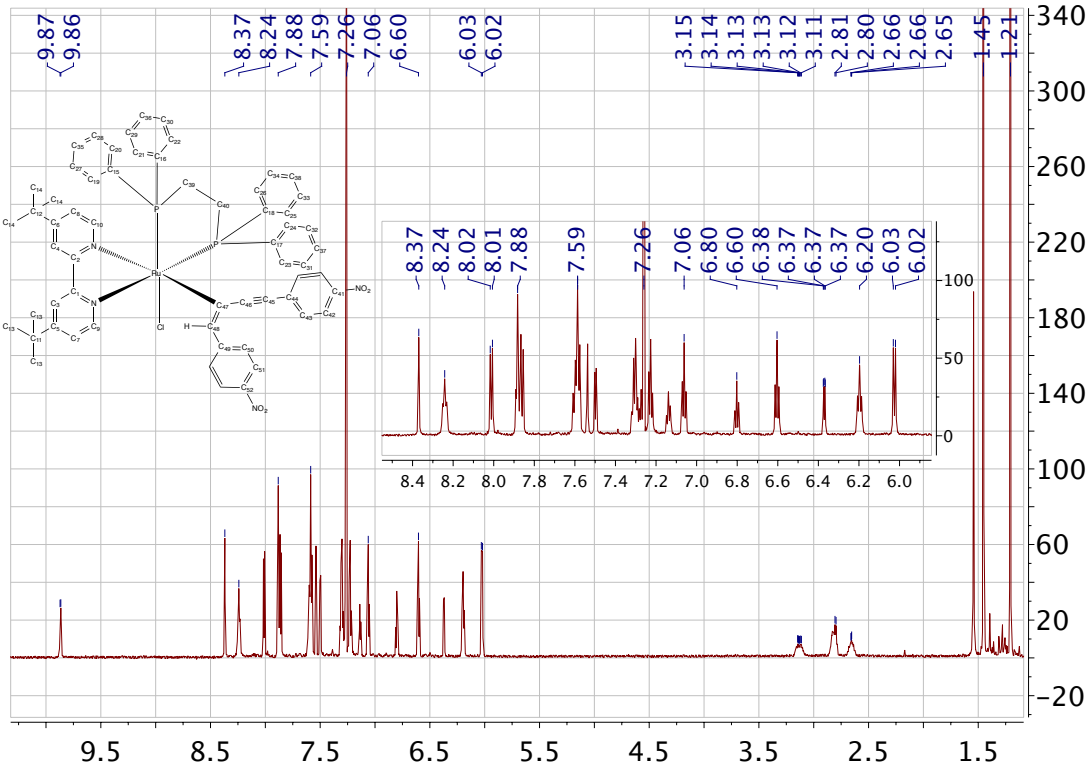

Figure A43 ^{1}H-NMR spectrum of **2.5b** recorded in $CDCl_3$.

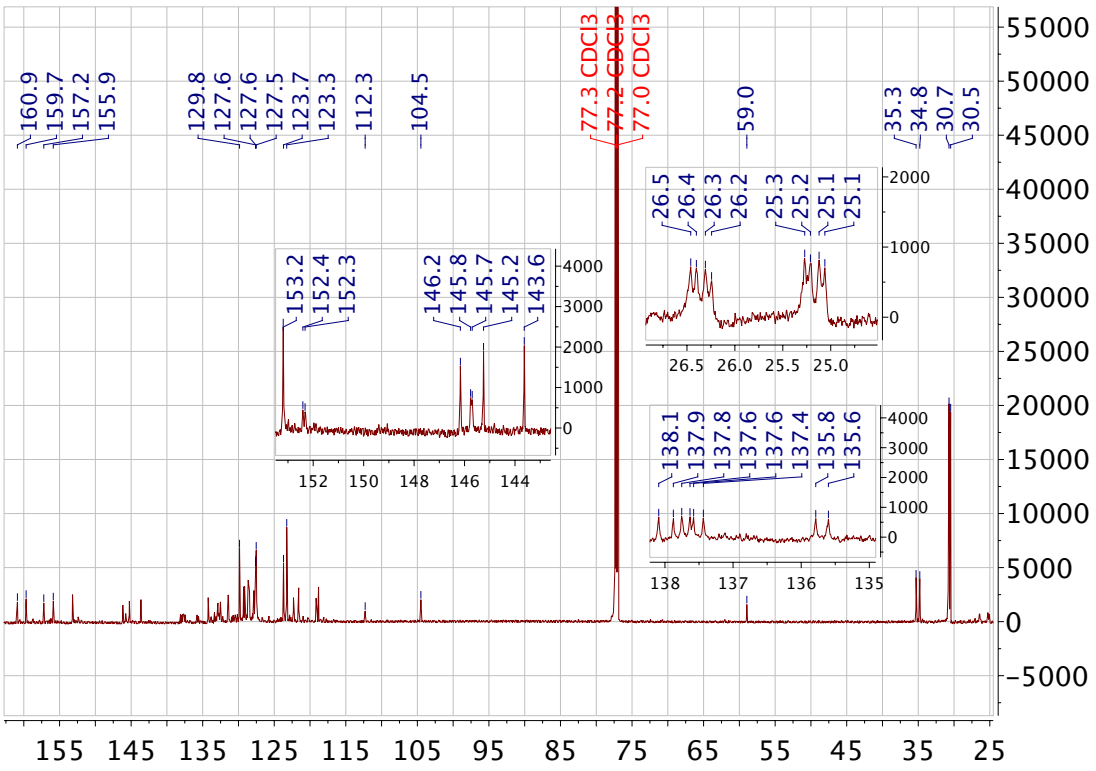

Figure A44 ^{13}C-NMR spectrum of **2.5b** recorded in $CDCl_3$.

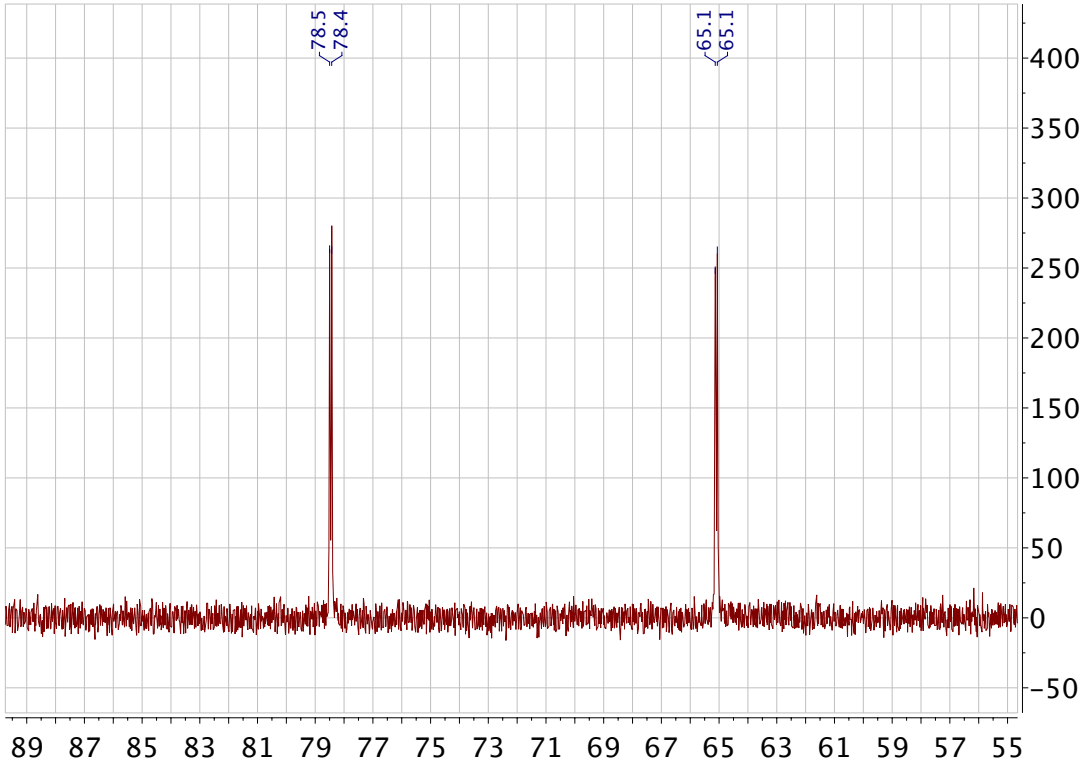

Figure A45 ^{31}P-NMR spectrum of **2.5b** recorded in $CDCl_3$.

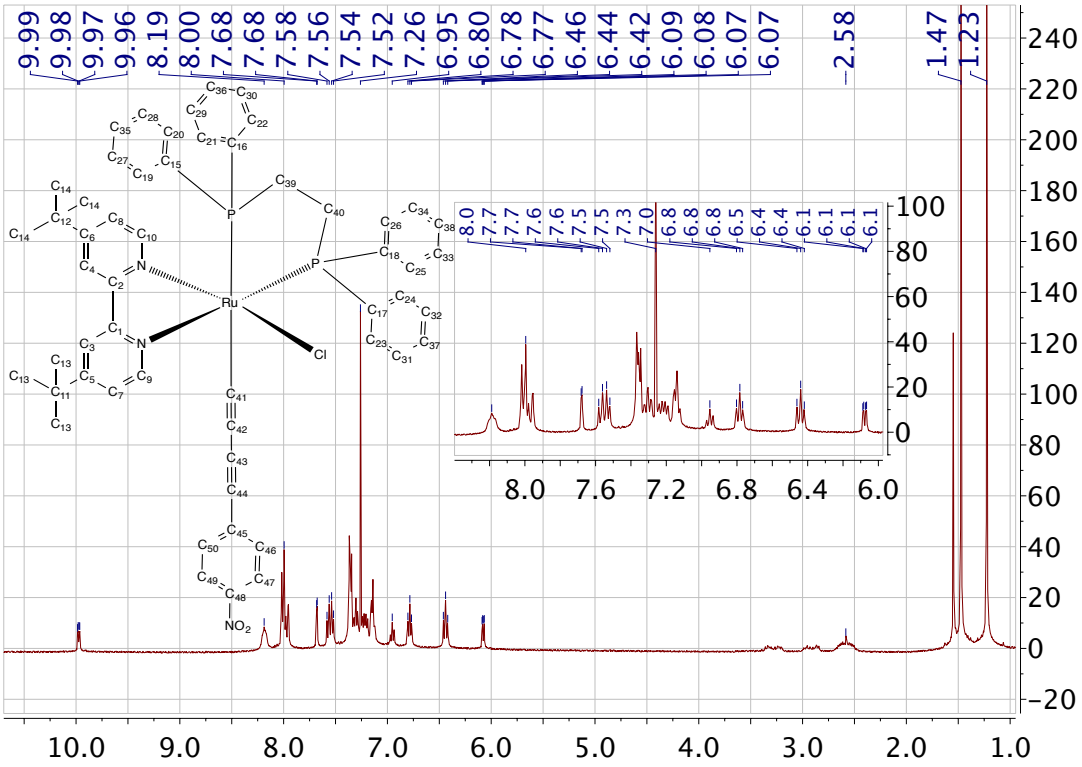

Figure A46 ^{1}H-NMR spectrum of **2.6b** recorded in $CDCl_3$.

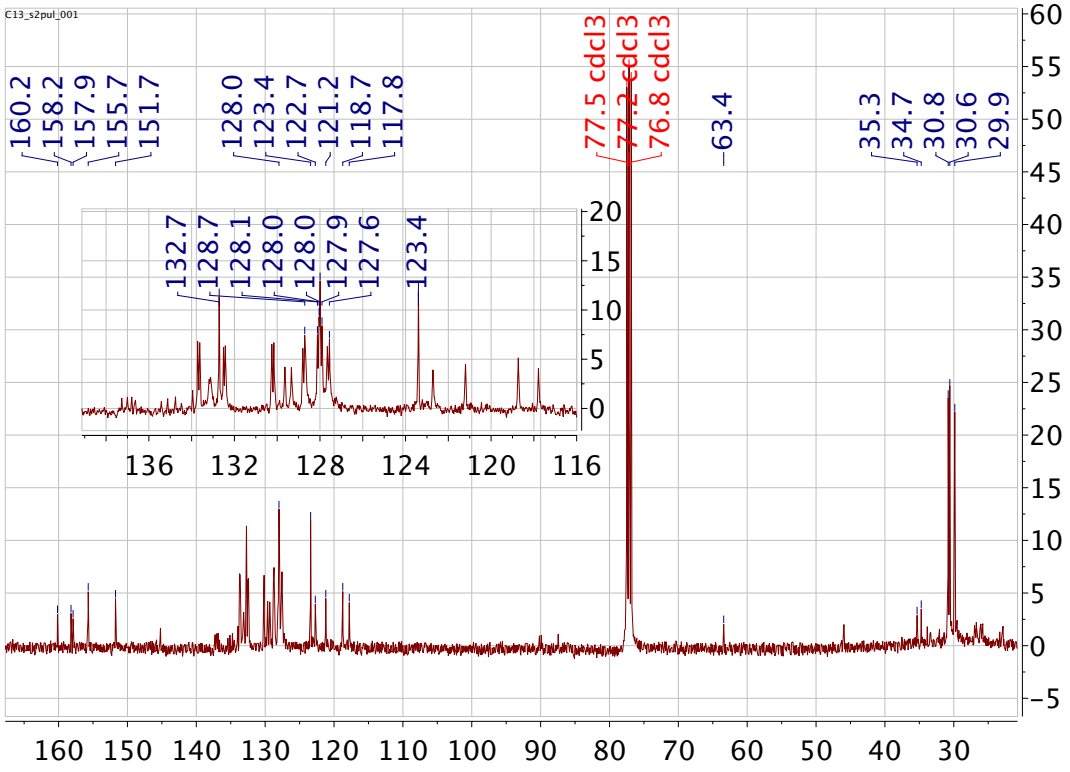

Figure A47 ^{13}C-NMR spectrum of **2.6b** recorded in $CDCl_3$.

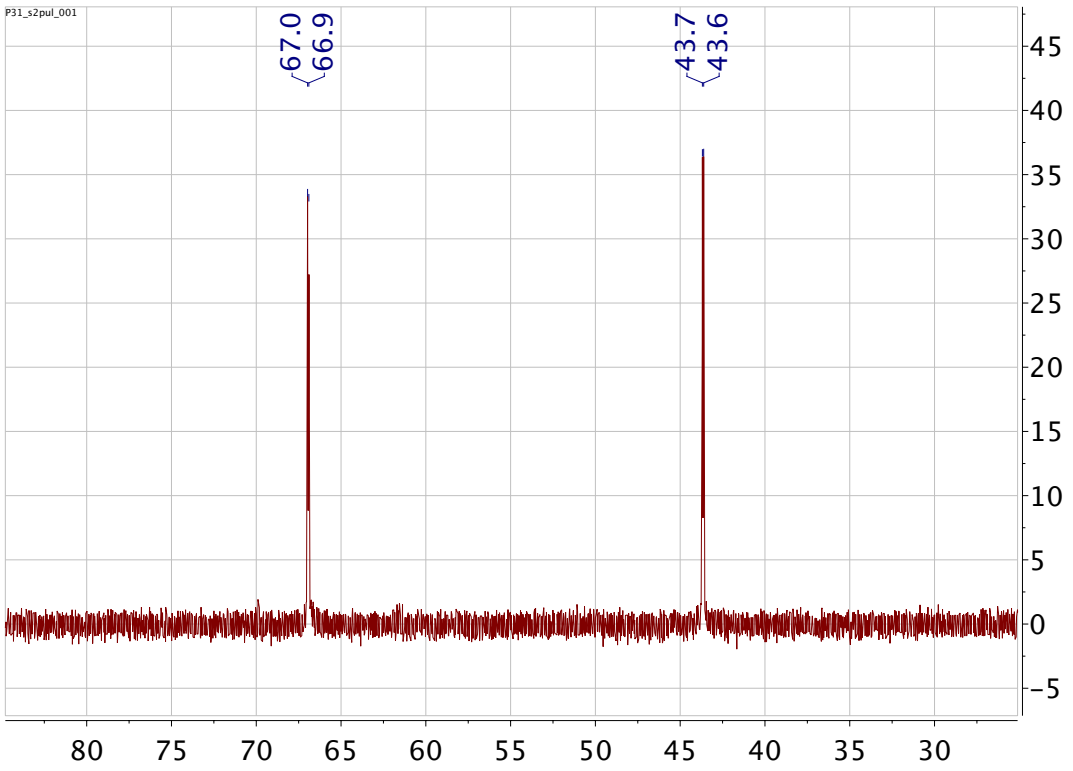

Figure A48 ^{31}P-NMR spectrum of **2.6b** recorded in $CDCl_3$.

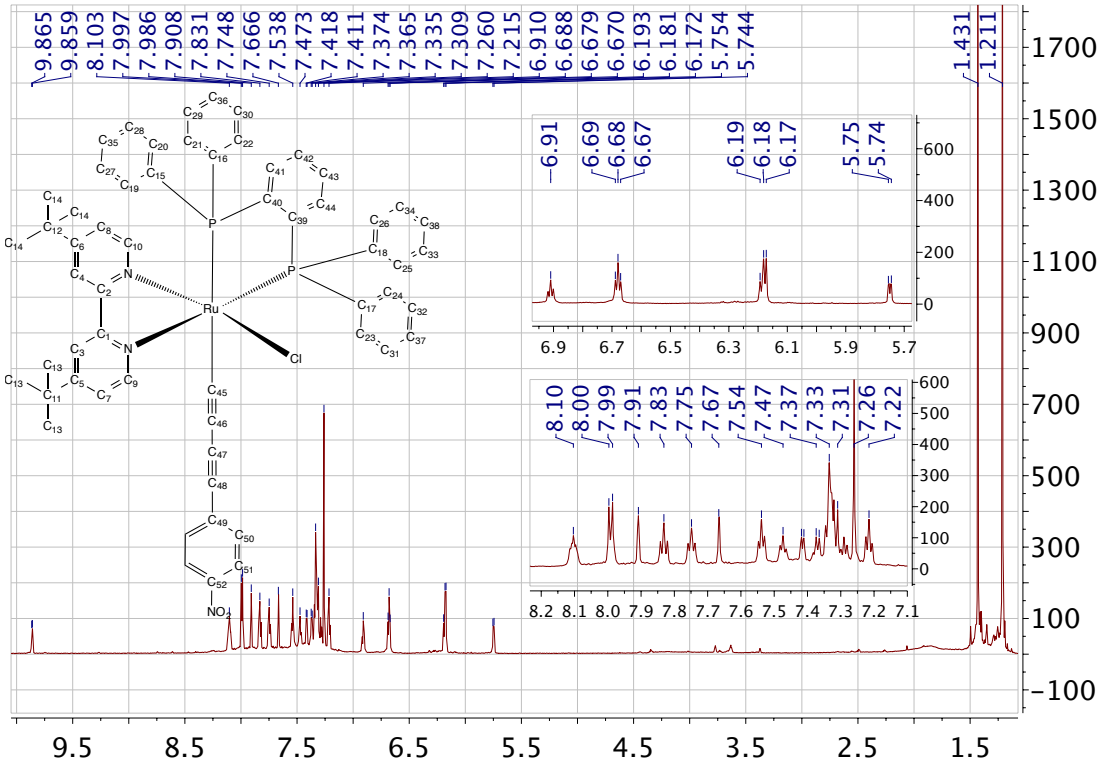

Figure A49 ^{1}H-NMR spectrum of **2.6c** recorded in $CDCl_3$.

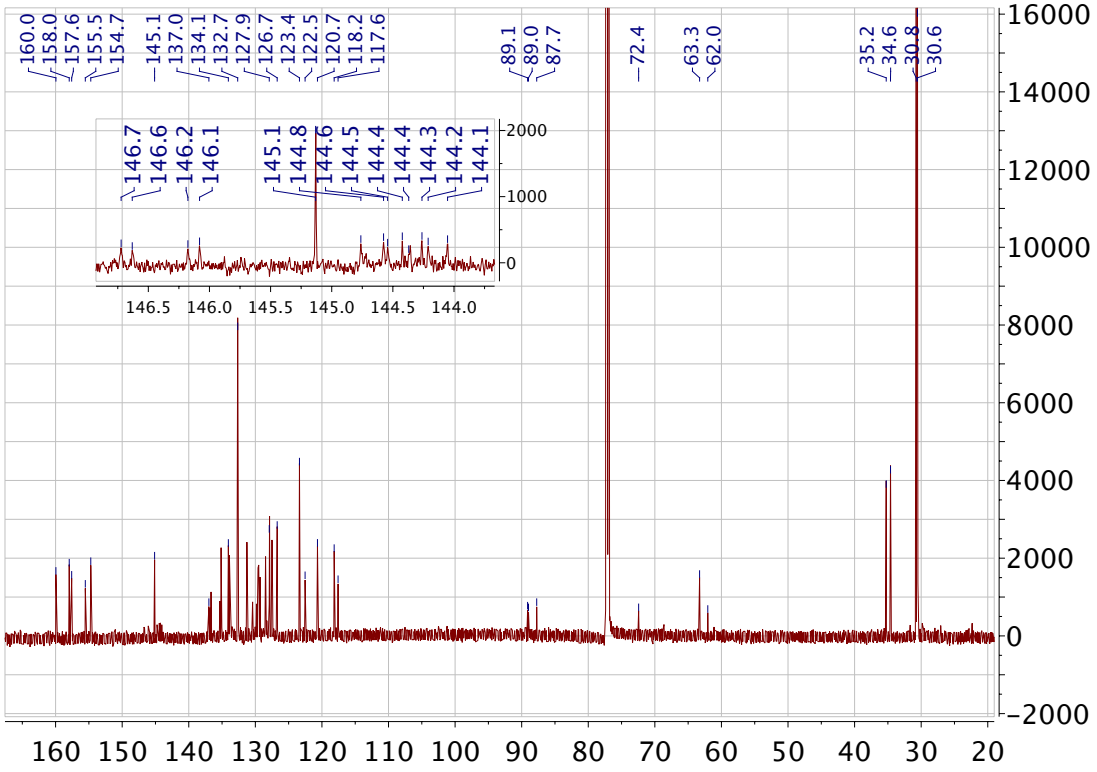

Figure A50 ^{13}C-NMR spectrum of **2.6c** recorded in $CDCl_3$.

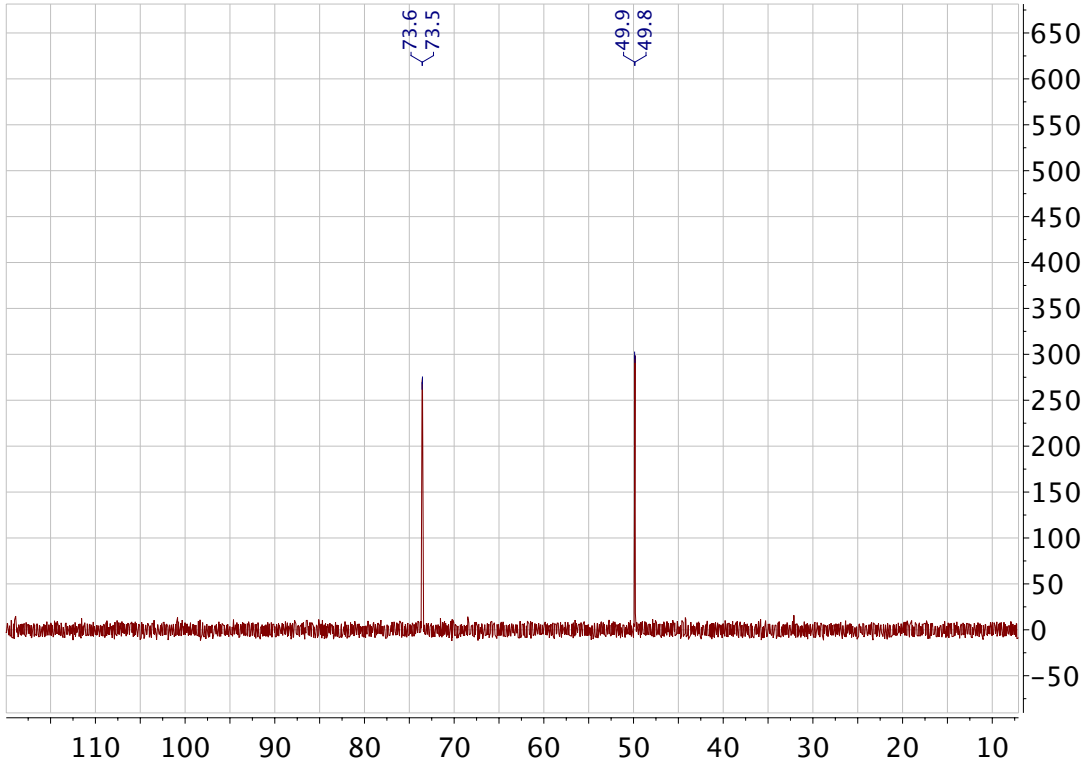

Figure A51 ^{31}P-NMR spectrum of **2.6c** recorded in $CDCl_3$.

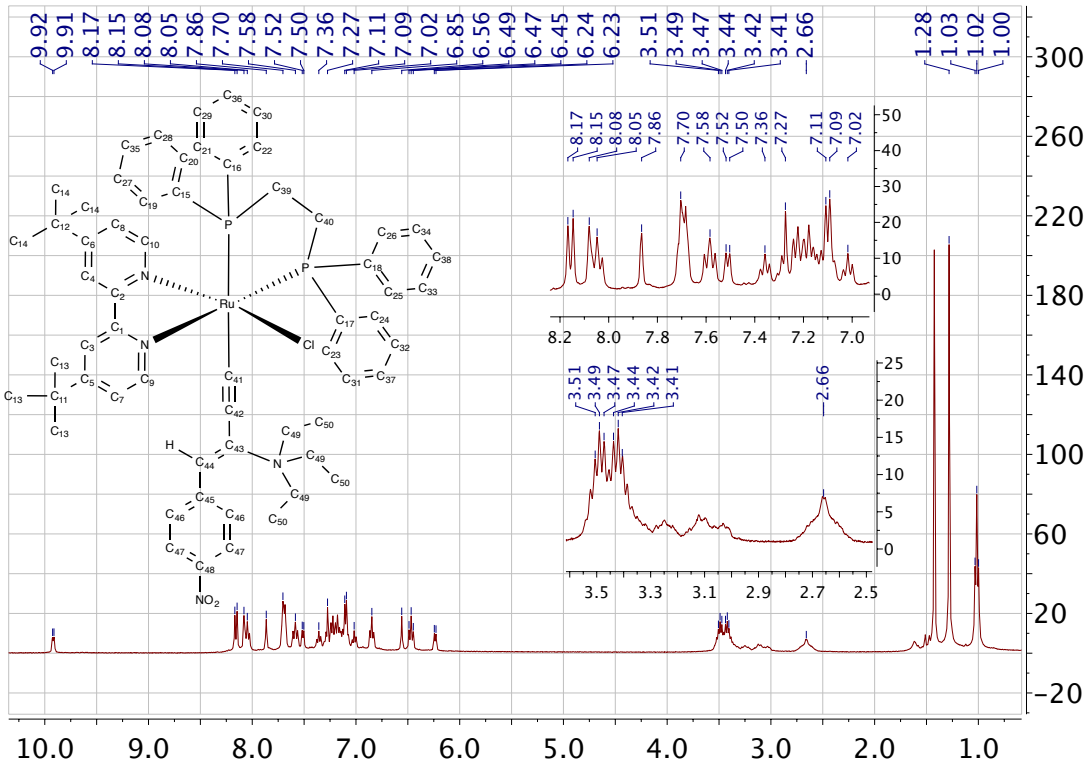

Figure A52 ^{1}H-NMR spectrum of **2.7a** recorded in $CDCl_3$.

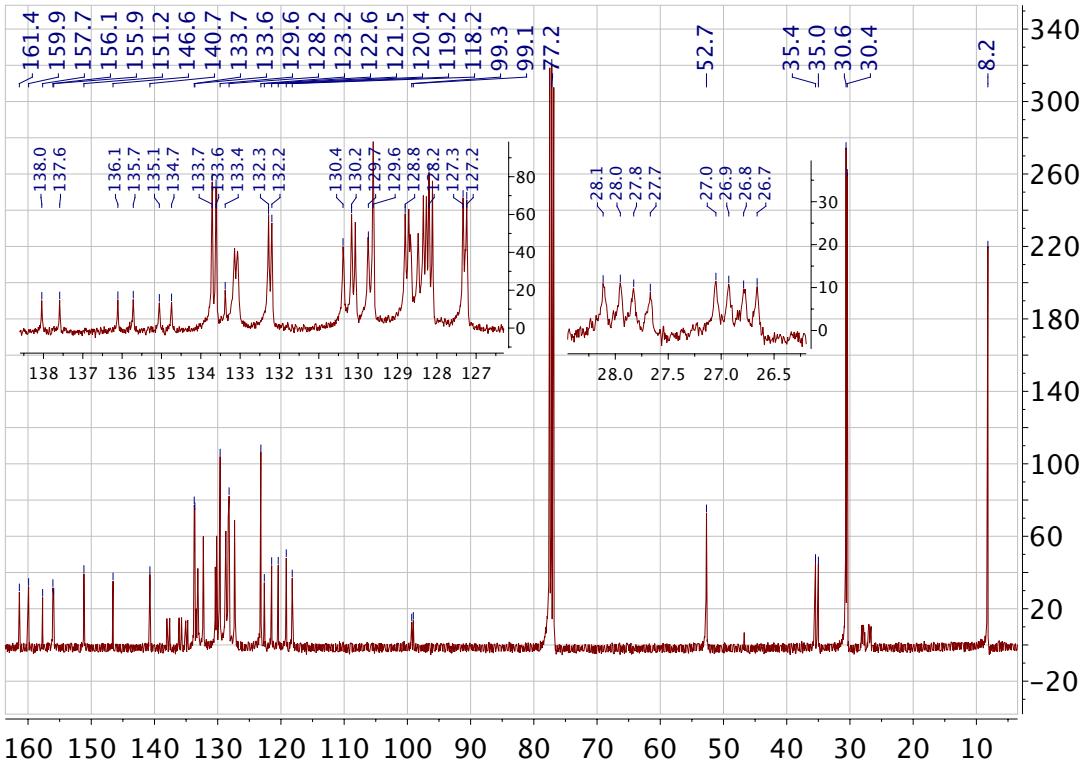

Figure A53 ^{13}C-NMR spectrum of **2.7a** recorded in $CDCl_3$.

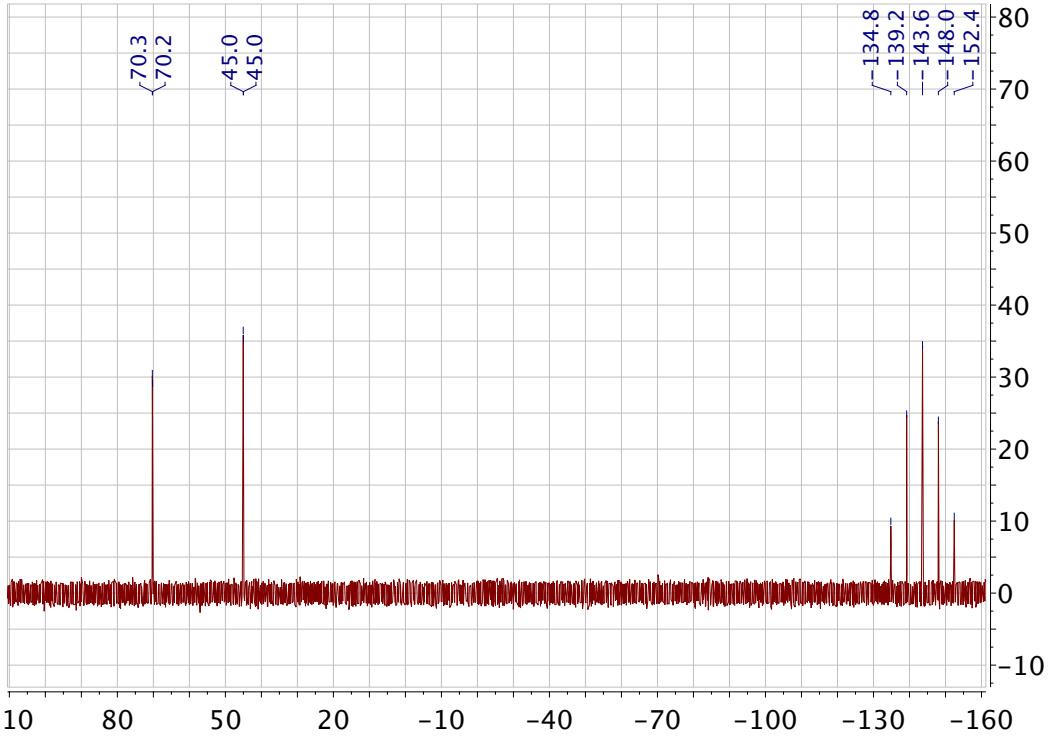

Figure A54 ^{31}P-NMR spectrum of **2.7a** recorded in $CDCl_3$.

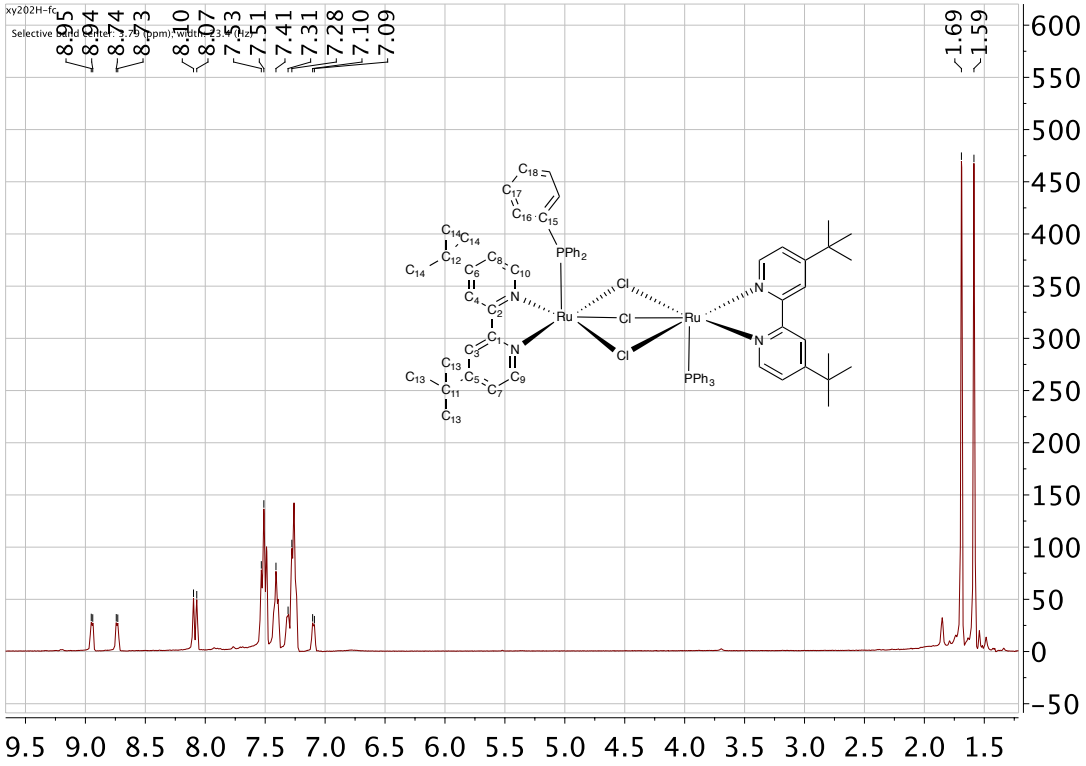

Figure A55 ^{1}H-NMR spectrum of **2.8a** recorded in $CDCl_3$.

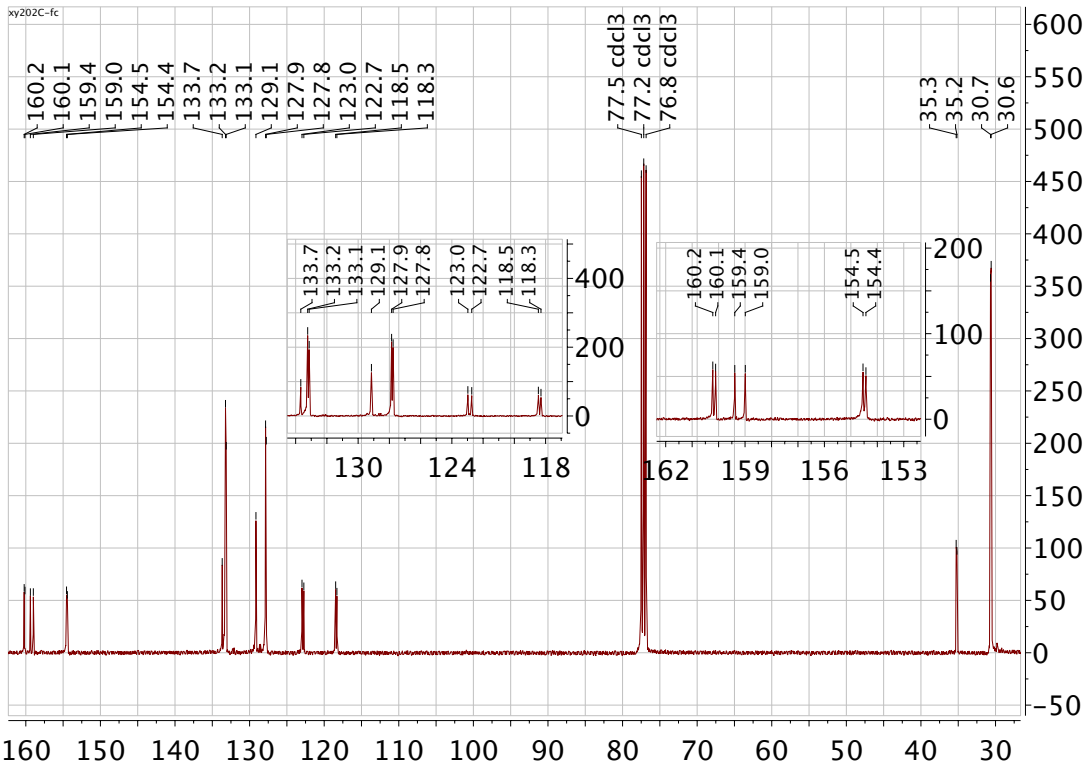

Figure A56 ^{13}C-NMR spectrum of **2.8a** recorded in $CDCl_3$.

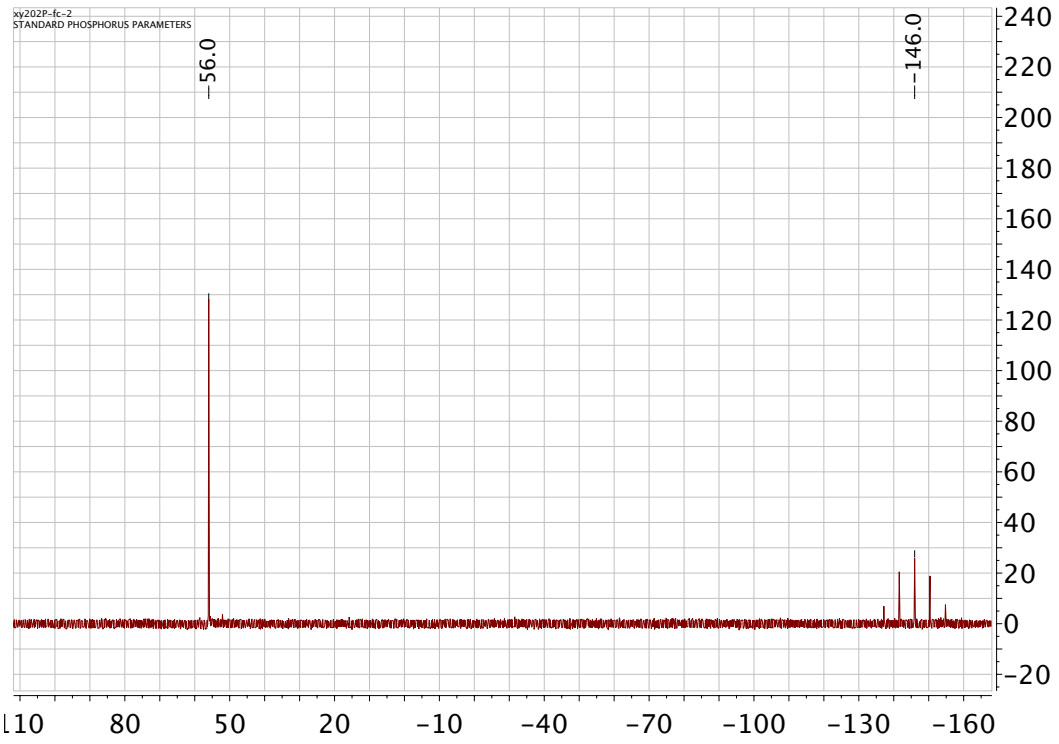

Figure A57 ^{31}P-NMR spectrum of **2.8a** recorded in $CDCl_3$.

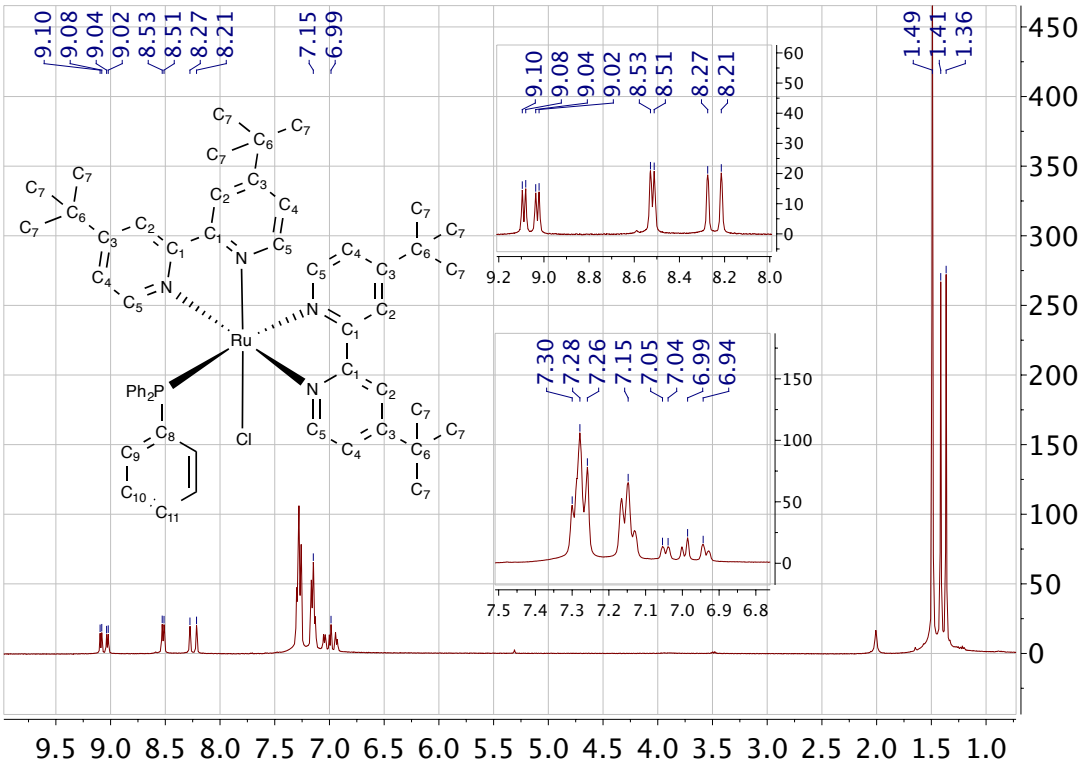

Figure A58 ^{1}H-NMR spectrum of **2.9b** recorded in $CDCl_3$.

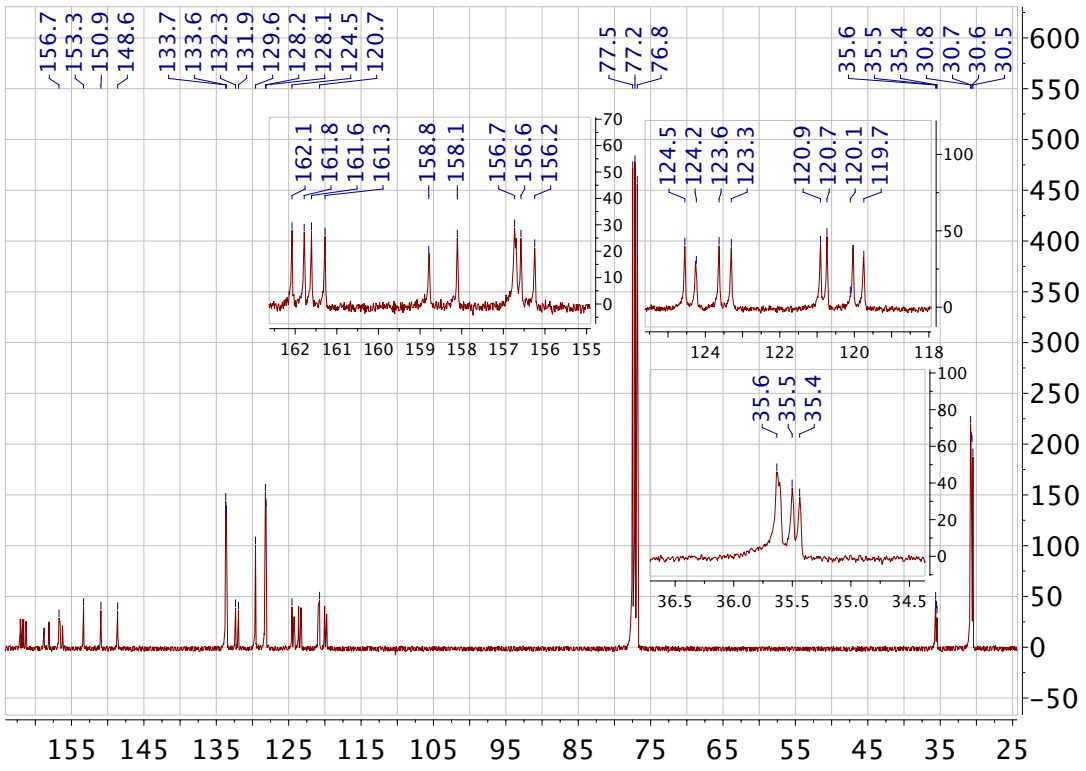

Figure A59 ^{13}C-NMR spectrum of **2.9b** recorded in $CDCl_3$.

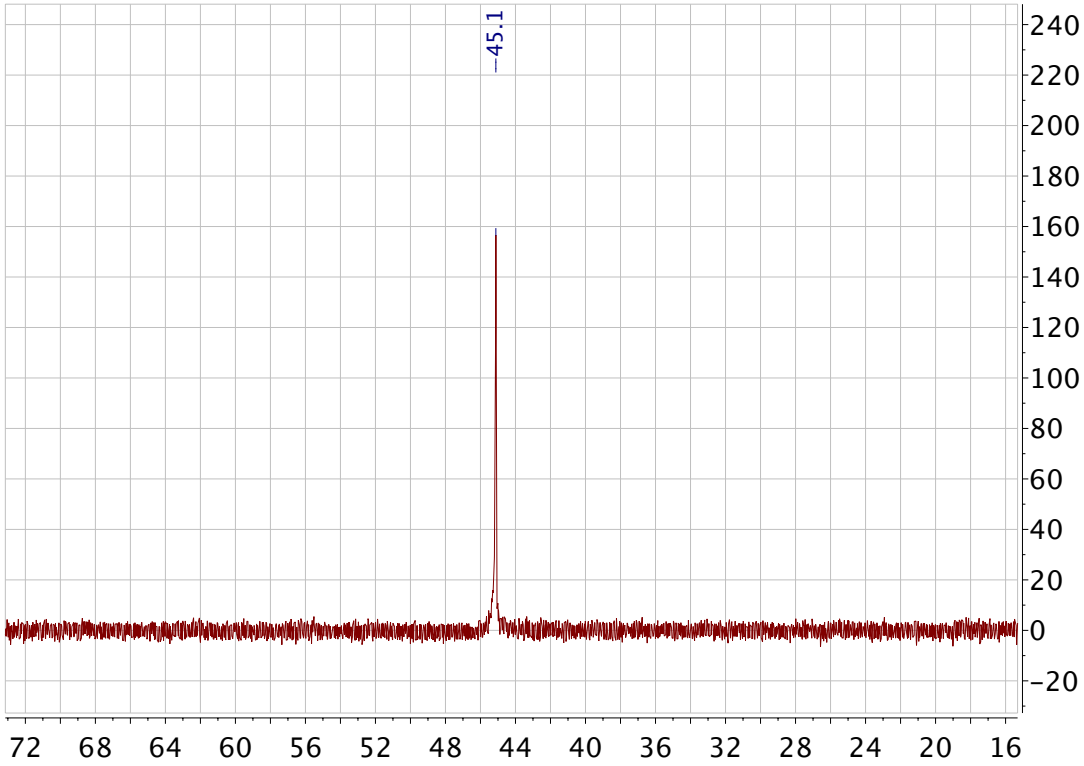

Figure A60 ^{31}P-NMR spectrum of **2.9b** recorded in $CDCl_3$.

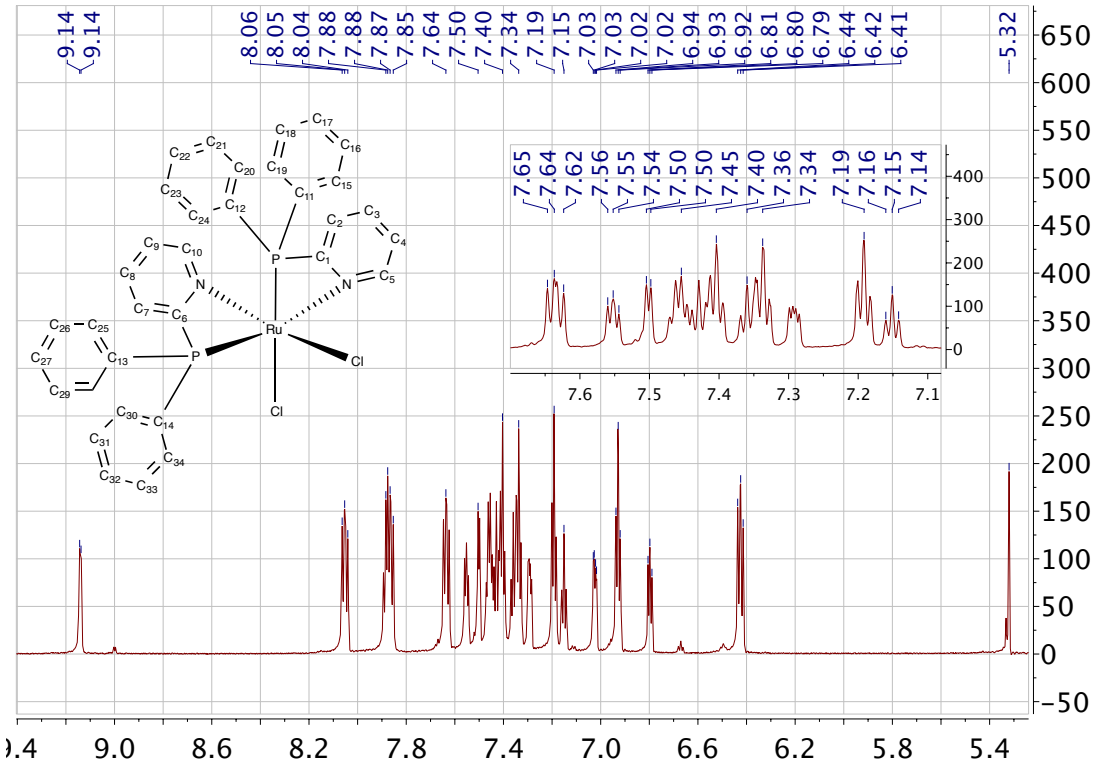

Figure A61 ^{1}H-NMR spectrum of **3.1a** recorded in CD_2Cl_2.

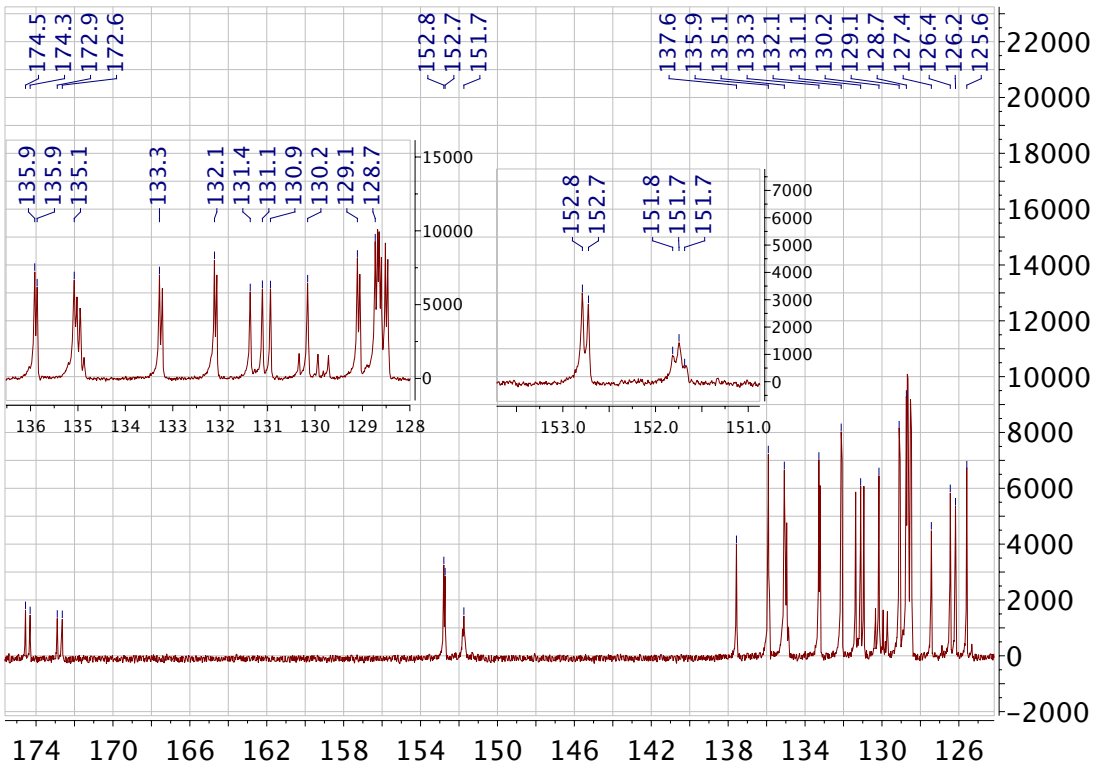

Figure A62 ^{13}C-NMR spectrum of **3.1a** recorded in CD_2Cl_2.

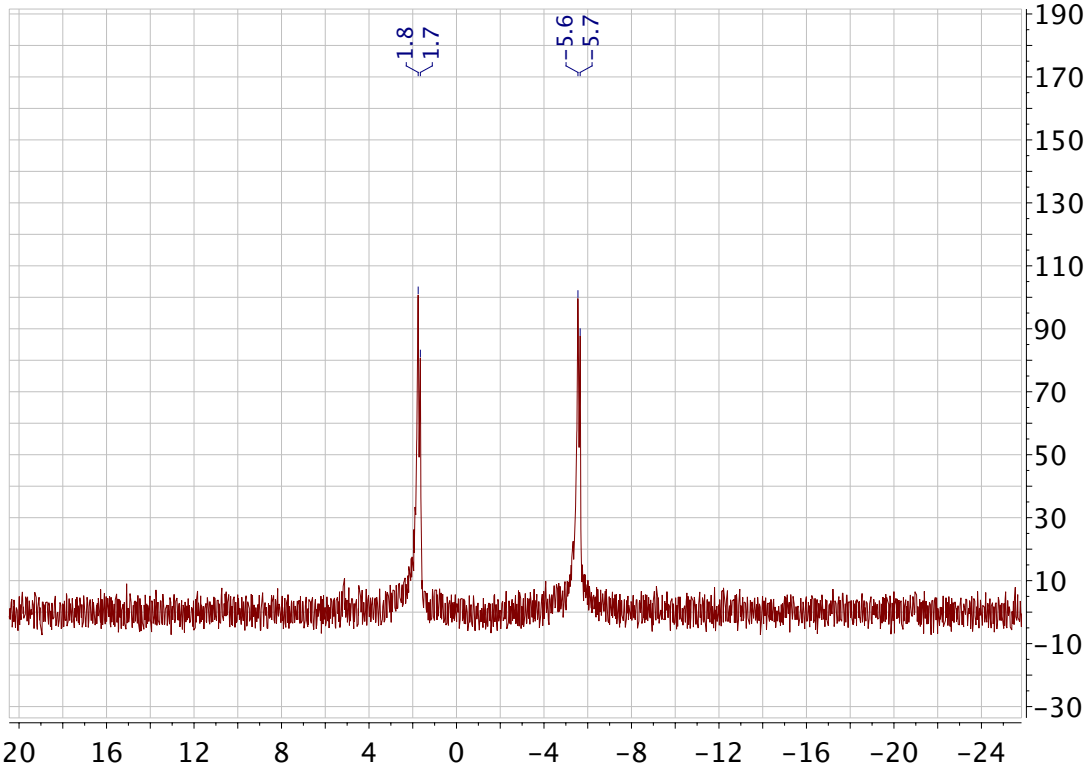

Figure A63 ^{31}P-NMR spectrum of **3.1a** recorded in CD_2Cl_2.

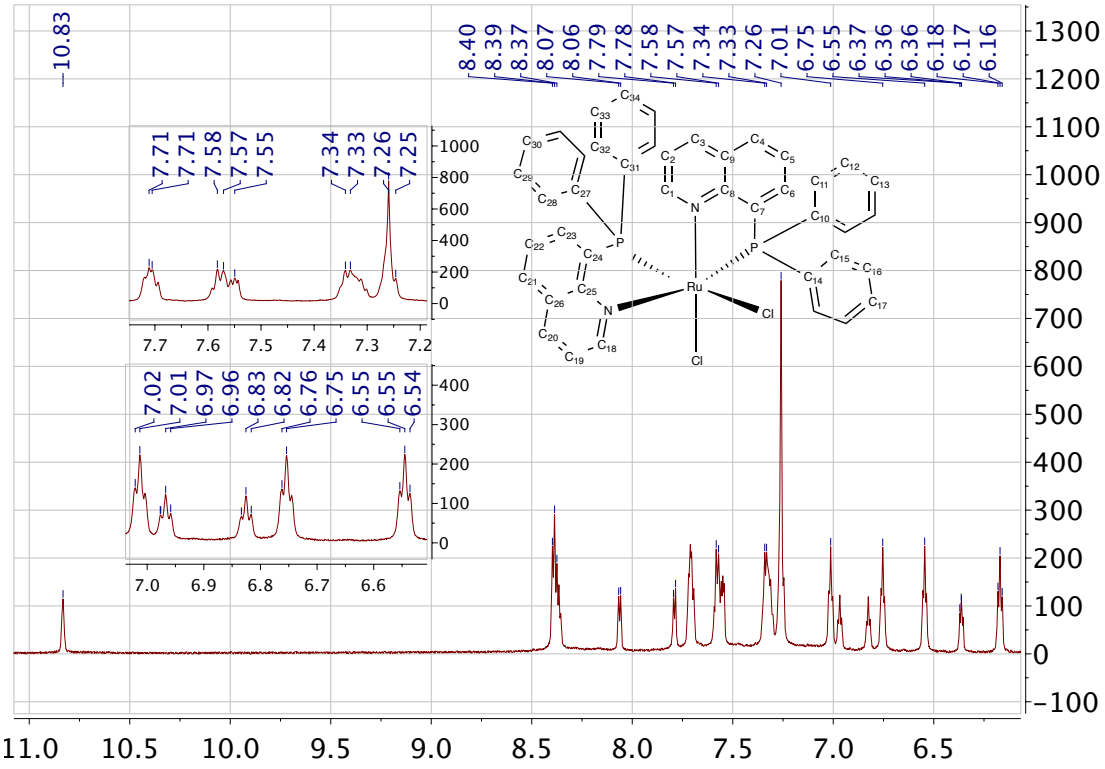

Figure A64 ^{1}H-NMR spectrum of **3.1b** recorded in $CDCl_3$.

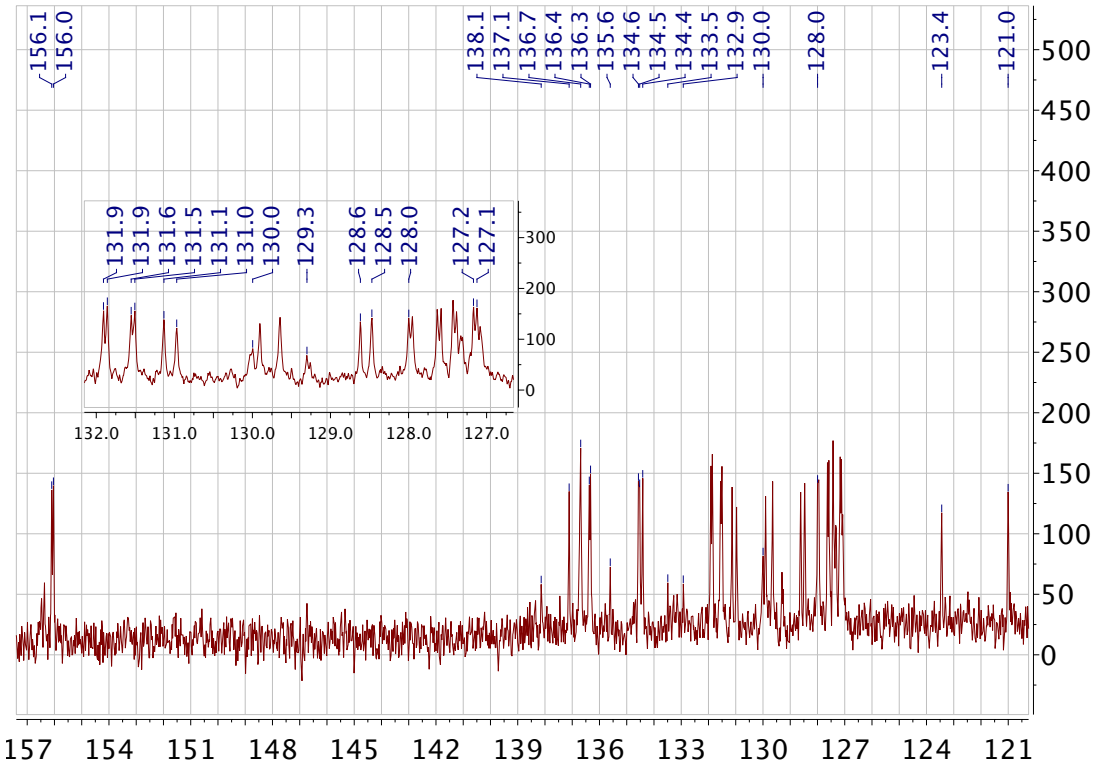

Figure A65 ^{13}C-NMR spectrum of **3.1b** recorded in $CDCl_3$.

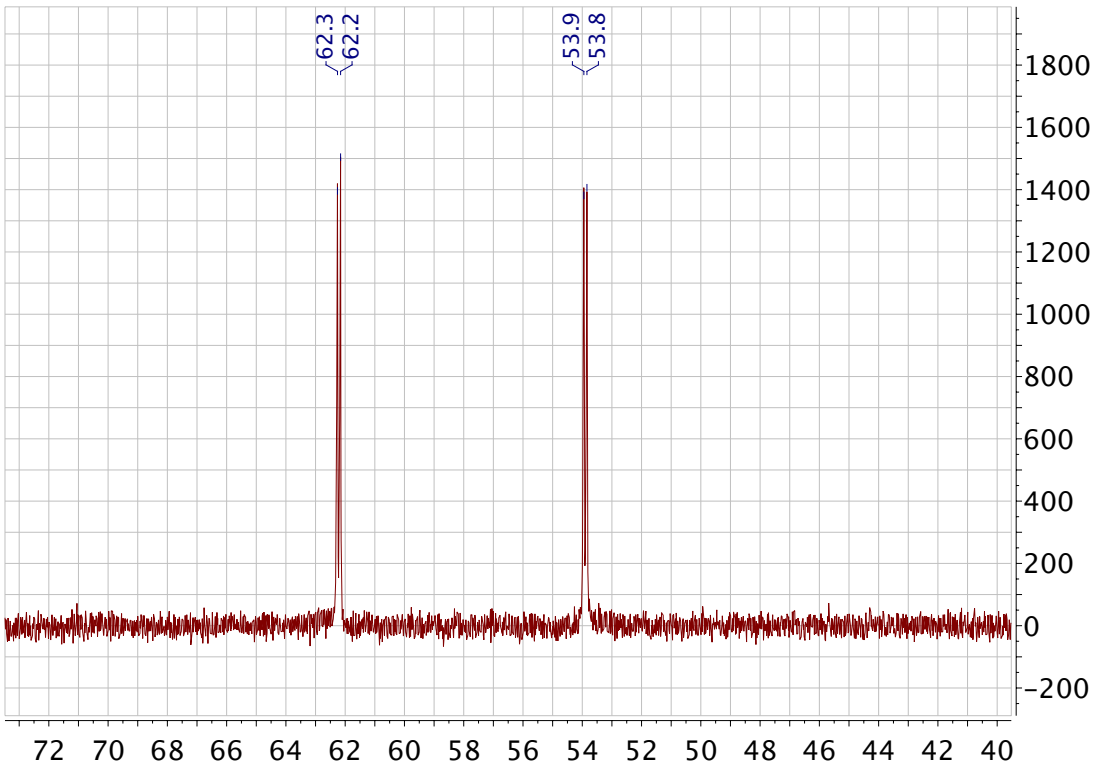

Figure A66 ^{31}P-NMR spectrum of **3.1b** recorded in $CDCl_3$.

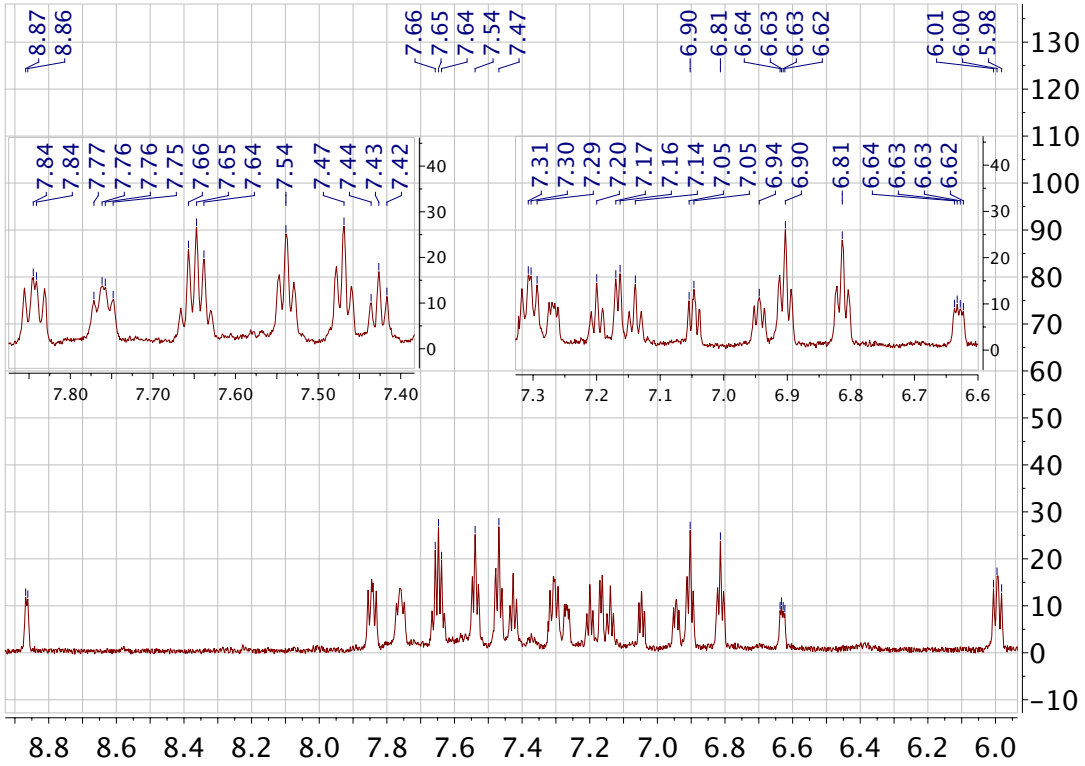

Figure A67 ^{1}H-NMR spectrum of **3.2a** recorded in CD_2Cl_2.

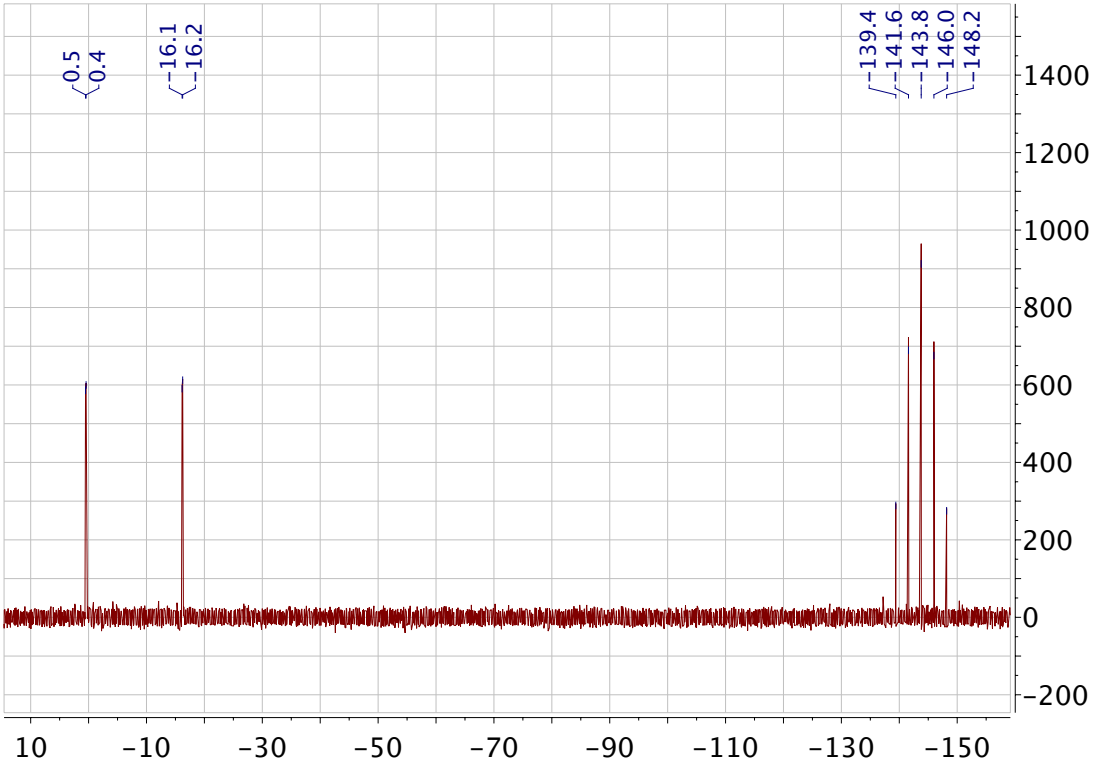

Figure A68 ^{31}P-NMR spectrum of **3.2a** recorded in CD_2Cl_2.

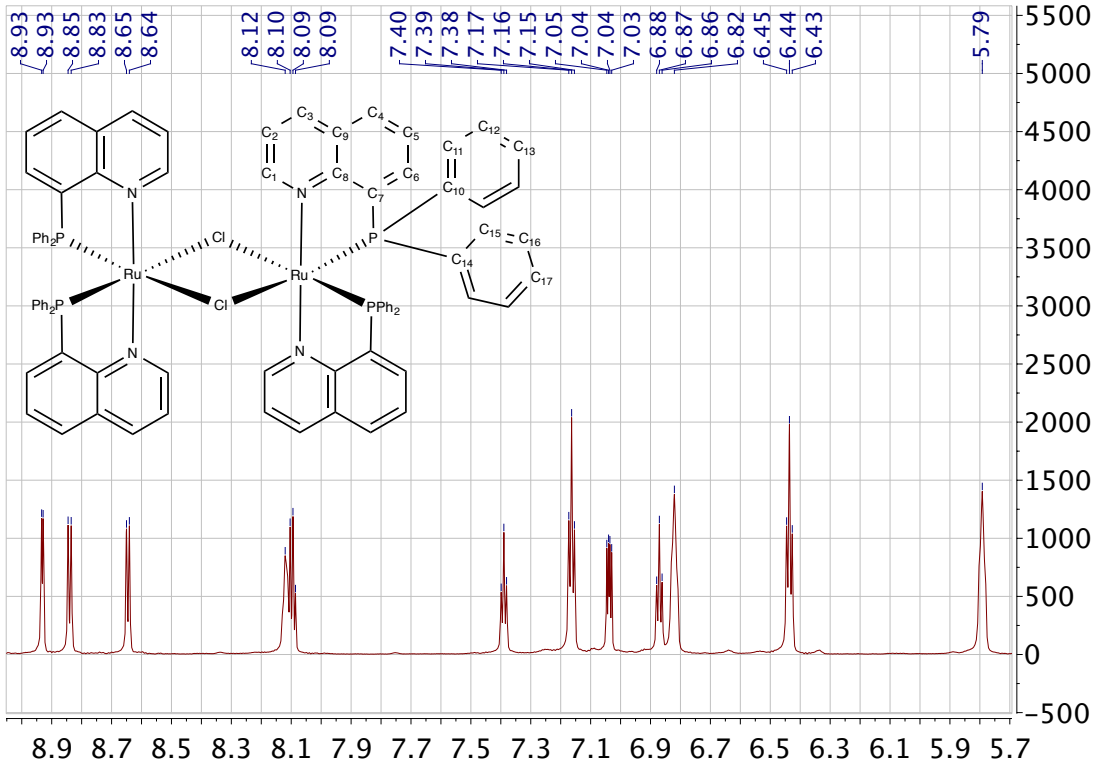

Figure A69 ^{1}H-NMR spectrum of **3.2b** recorded in Acetone-d_6.

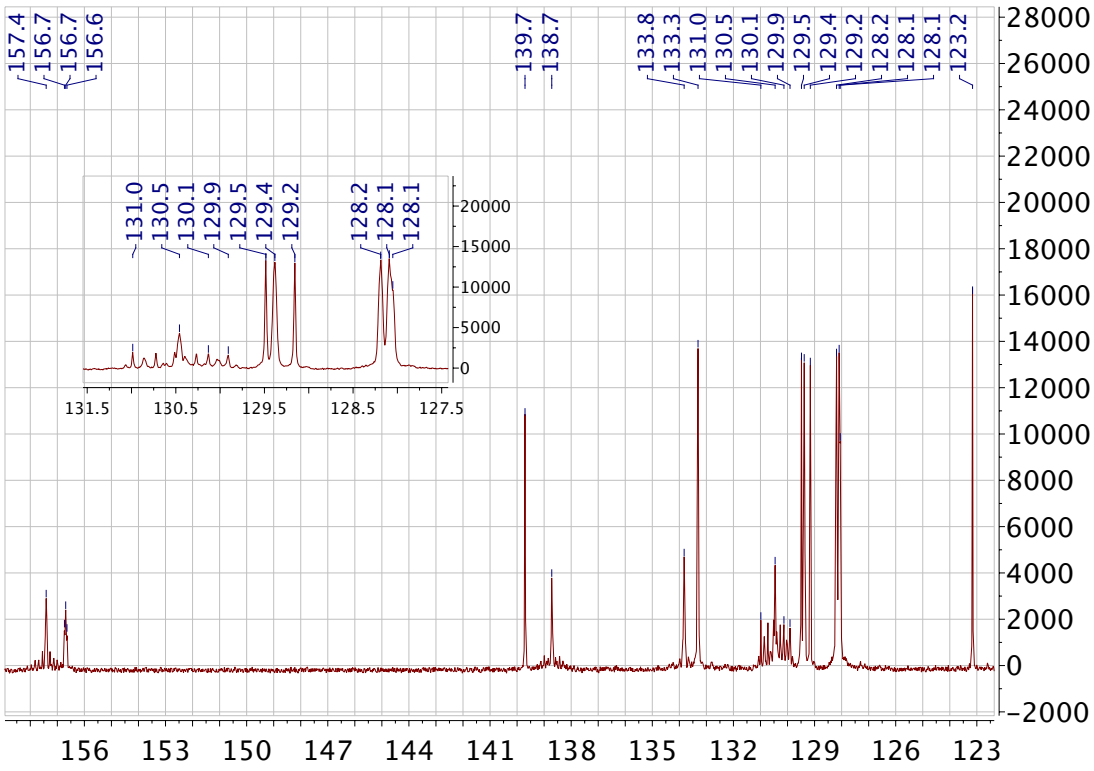

Figure A70 ^{13}C-NMR spectrum of **3.2b** recorded in Acetone-d_6.

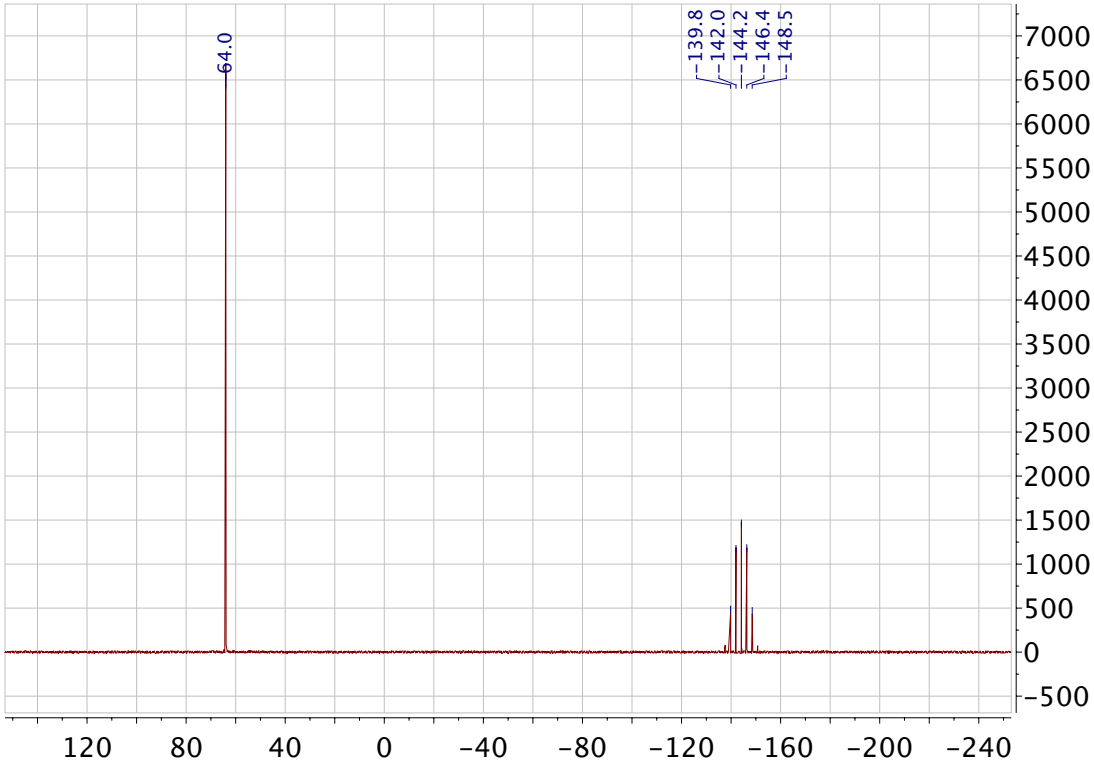

Figure A71 ^{31}P-NMR spectrum of **3.2b** recorded in Acetone-d_6.

B. NLO Data in Chapter 4

Spectral dependent Z-scan data for **4.1**.

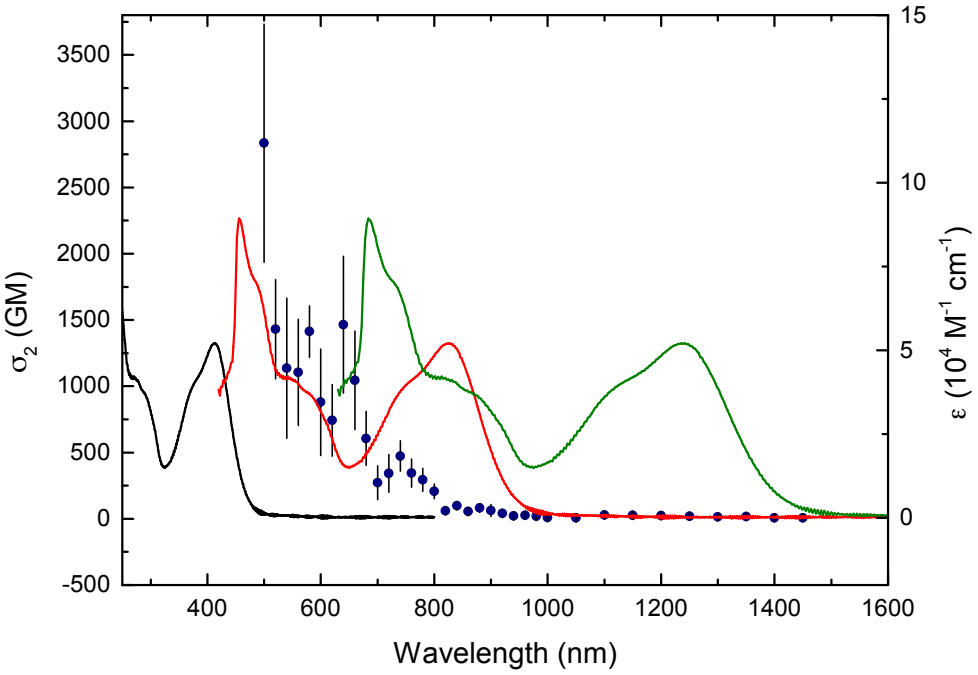

Figure B01 TPA cross-section plot of **4.1** overlaid on the UV-Vis spectrum (black), and plots of the UV-Vis spectrum at twice (red) and three times (green) the wavelengths.

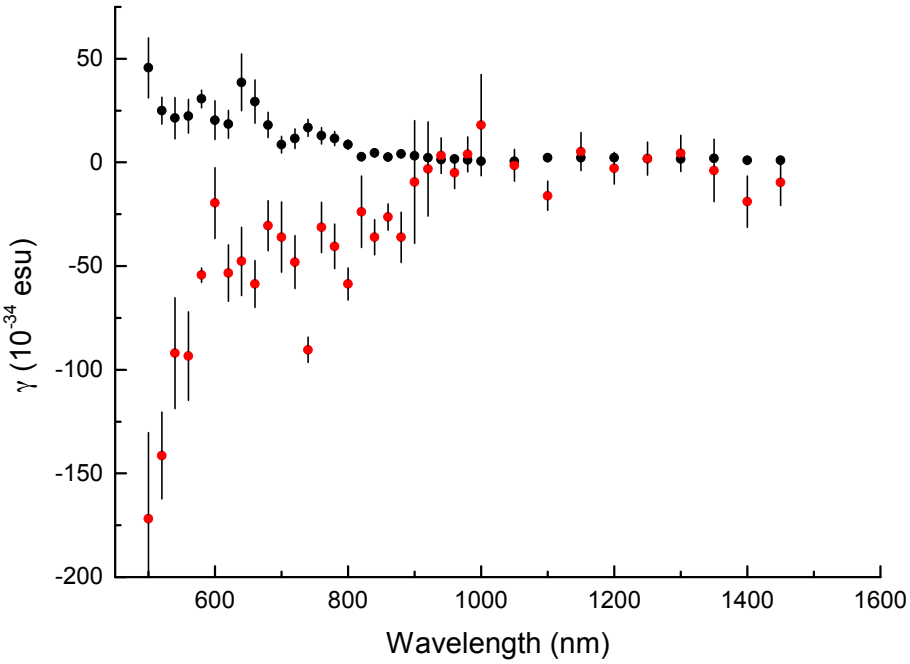

Figure B02 Cubic nonlinear hyperpolarisability γ_{real} (red) and γ_{imag} (blue) traces of **4.1**.

Spectral dependent Z-scan data for **4.2**.

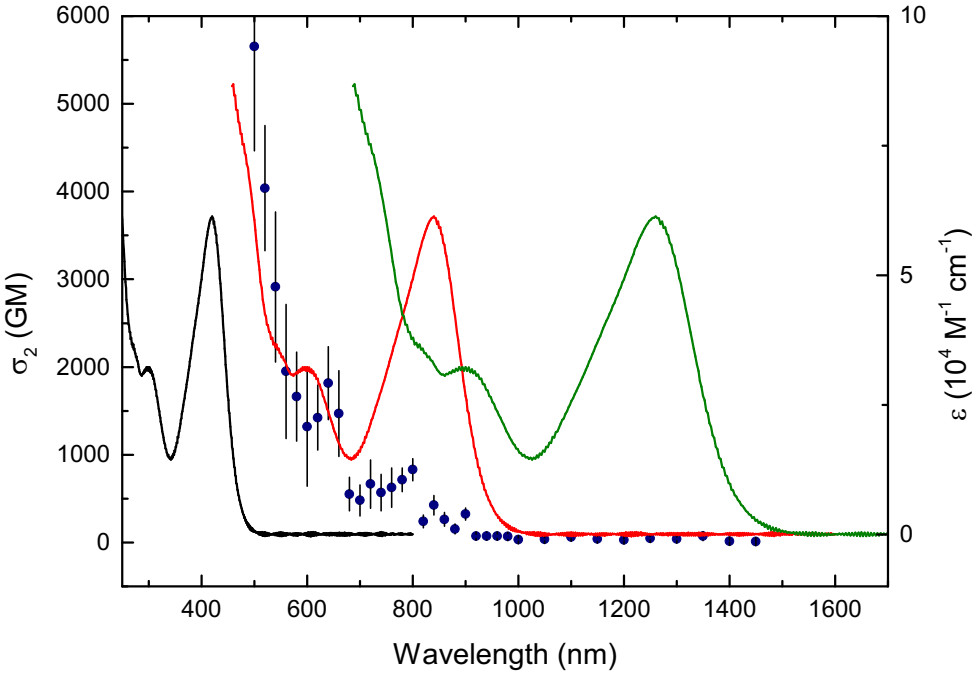

Figure B03 TPA cross-section plot of **4.2** overlaid on the UV-Vis spectrum (black), at twice (red) and three times (green) the wavelengths.

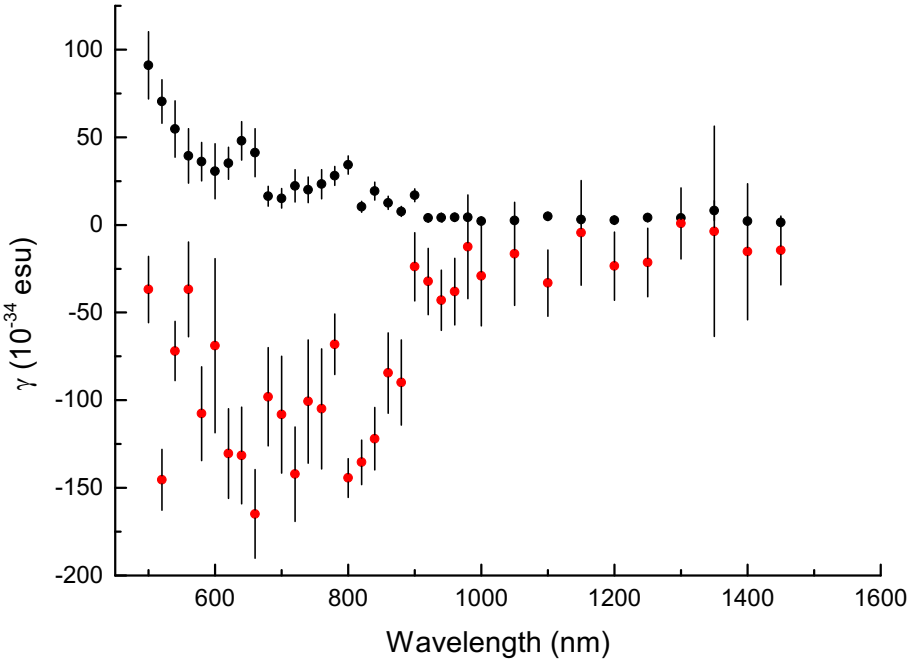

Figure B04 Cubic nonlinear hyperpolarisability γ_{real} (red) and γ_{imag} (blue) traces of **4.2**.

Spectral dependent Z-scan data for **4.3**.

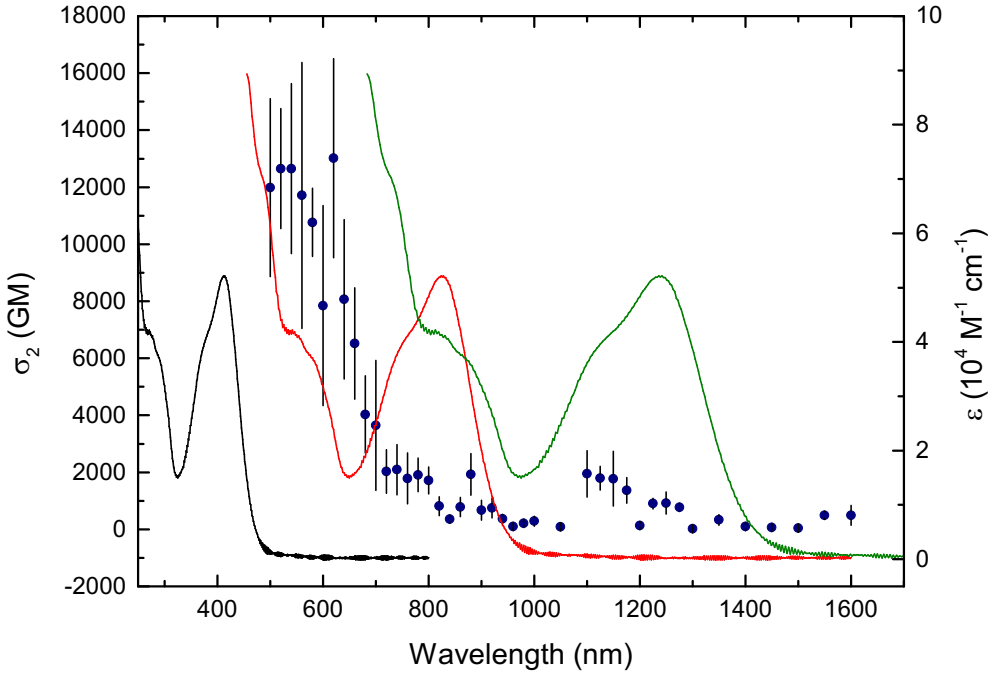

Figure B05 TPA cross-section plot of **4.3** overlaid on the UV-Vis spectrum (black), at twice (red) and three times (green) the wavelengths.

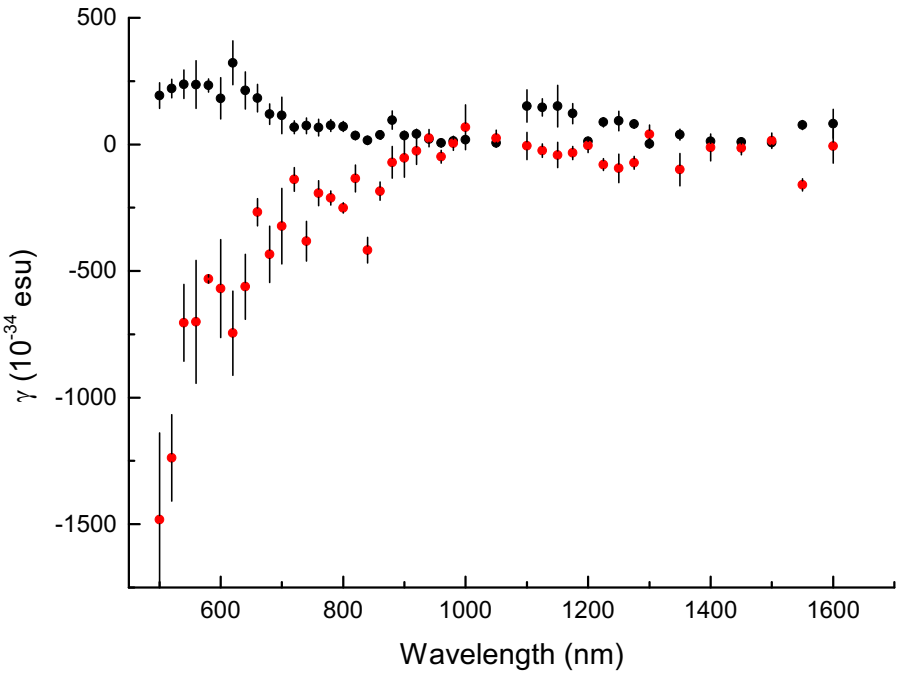

Figure B06 Cubic nonlinear hyperpolarisability γ_{real} (red) and γ_{imag} (blue) traces of **4.3**.

Spectral dependent Z-scan data for **4.4**.

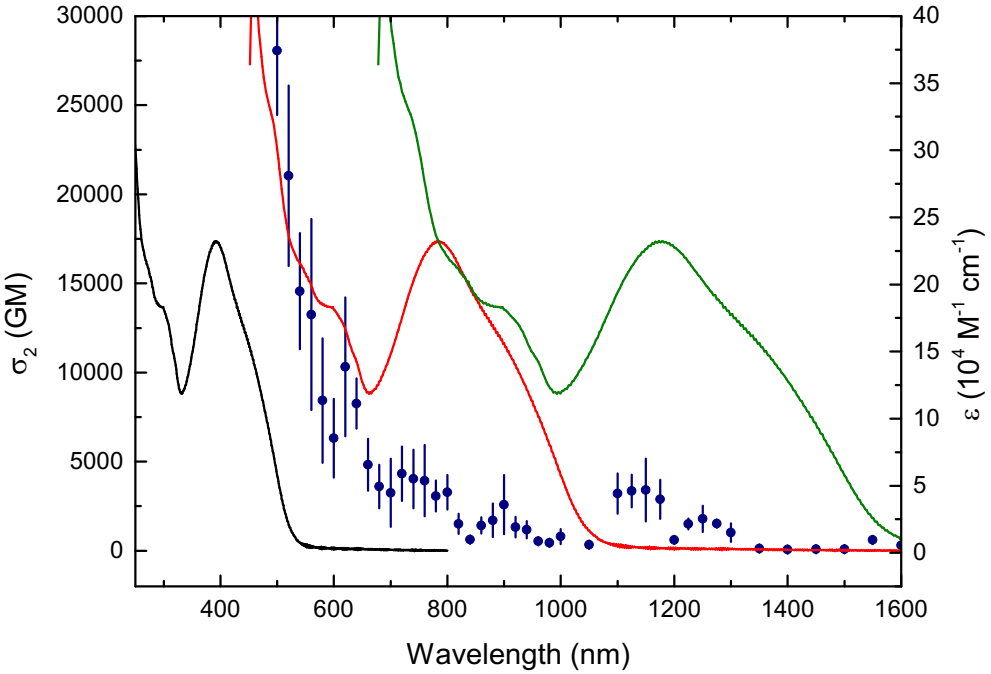

Figure B07 TPA cross-section plot of **4.4** overlaid on the UV-Vis spectrum (black), at twice (red) and three times (green) the wavelengths.

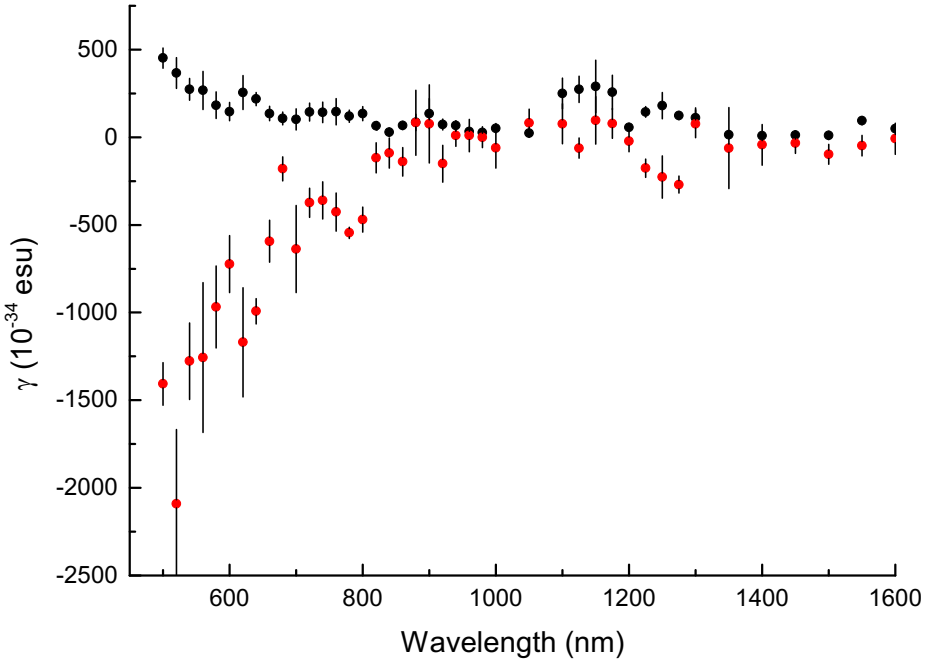

Figure B08 Cubic nonlinear hyperpolarisability γ_{real} (red) and γ_{imag} (blue) traces of **4.4**.

Spectral dependent Z-scan data for **4.5**.

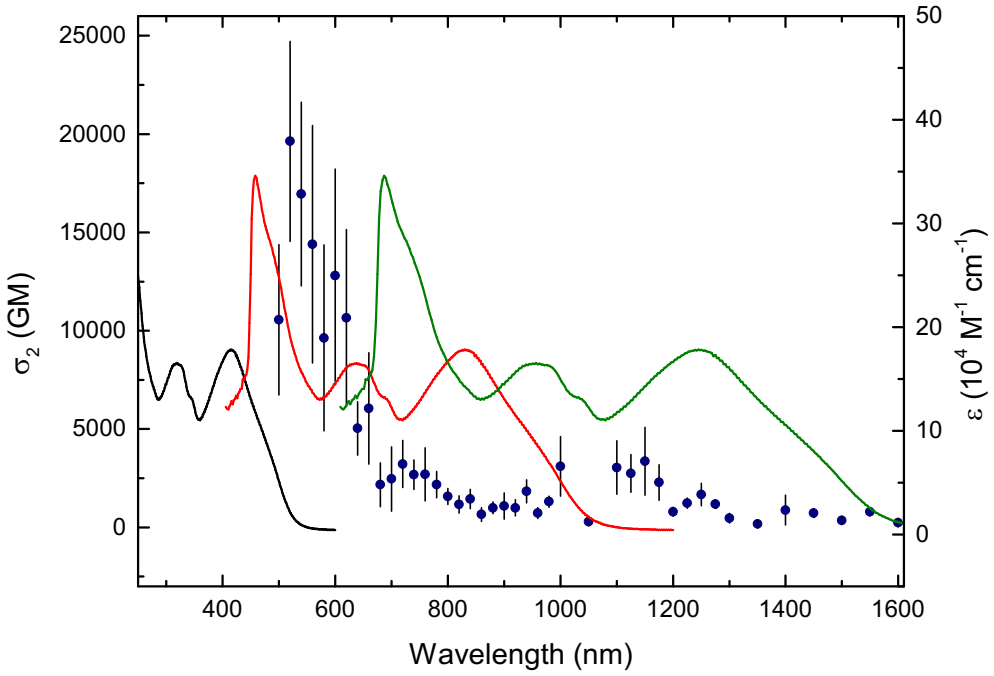

Figure B09 TPA cross-section plot of **4.5** overlaid on the UV-Vis spectrum (black), at twice (red) and three times (green) the wavelengths.

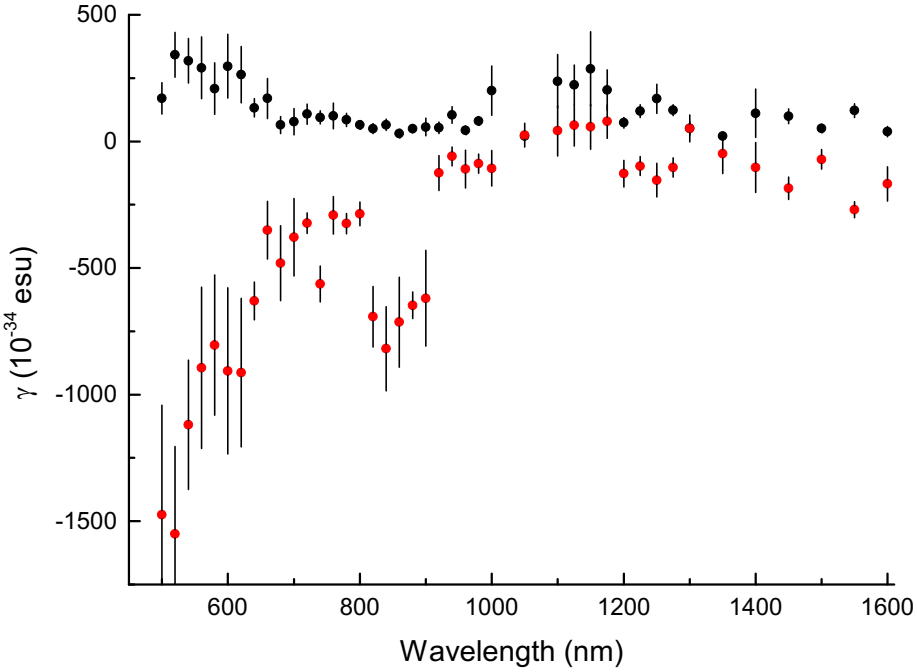

Figure B10 Cubic nonlinear hyperpolarisability γ_{real} (red) and γ_{imag} (blue) traces of **4.5**.

Spectral dependent Z-scan data for **4.6**.

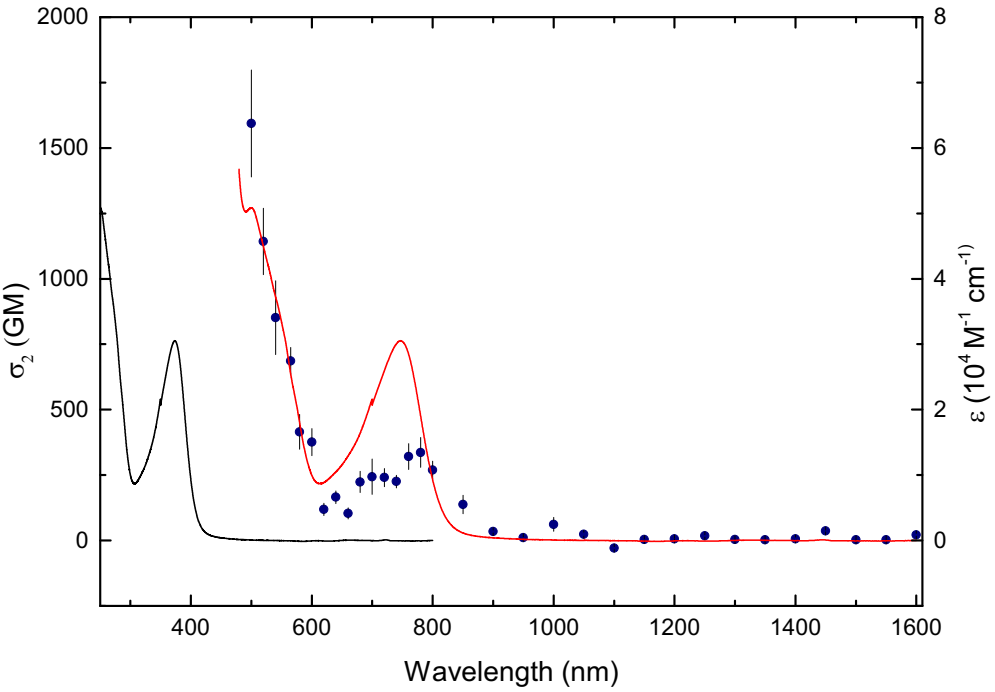

Figure B11 TPA cross-section plot of **4.6** overlaid on the UV-Vis spectrum (black) and at twice (red) the wavelength.

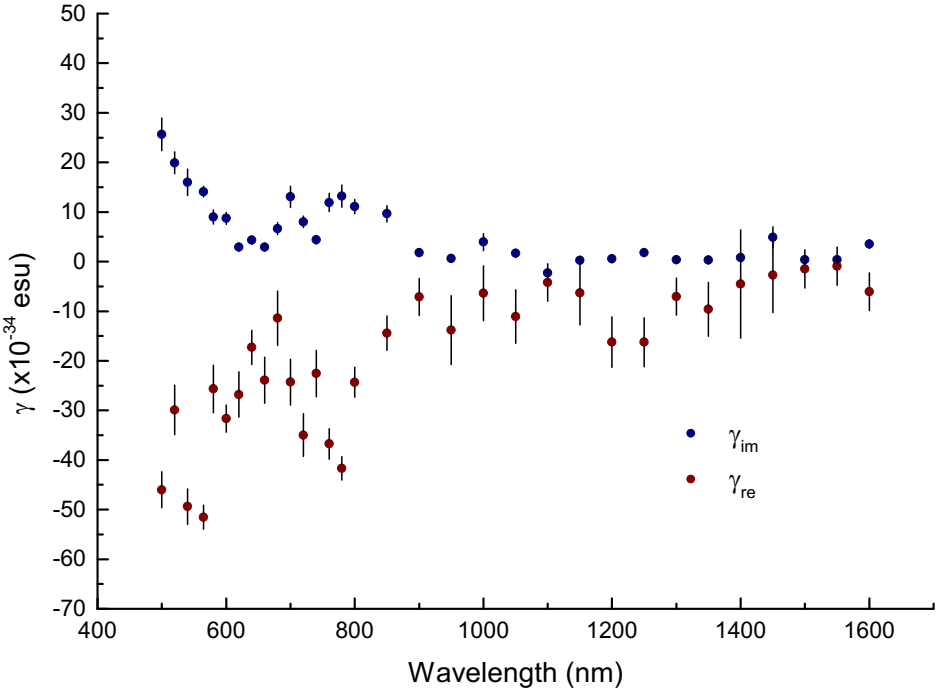

Figure B12 Cubic nonlinear hyperpolarisability γ_{real} (red) and γ_{imag} (blue) traces of **4.6**.

Spectral dependent Z-scan data for **4.7**.

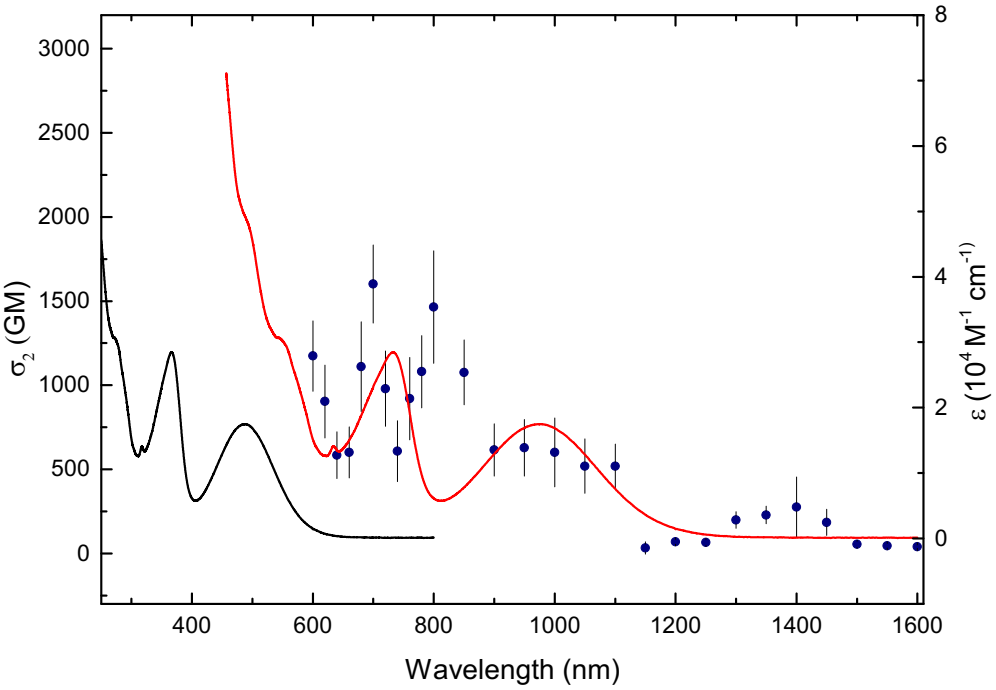

Figure B13 TPA cross-section plot of **4.7** overlaid on the UV-Vis spectrum (black) and at twice (red) the wavelength.

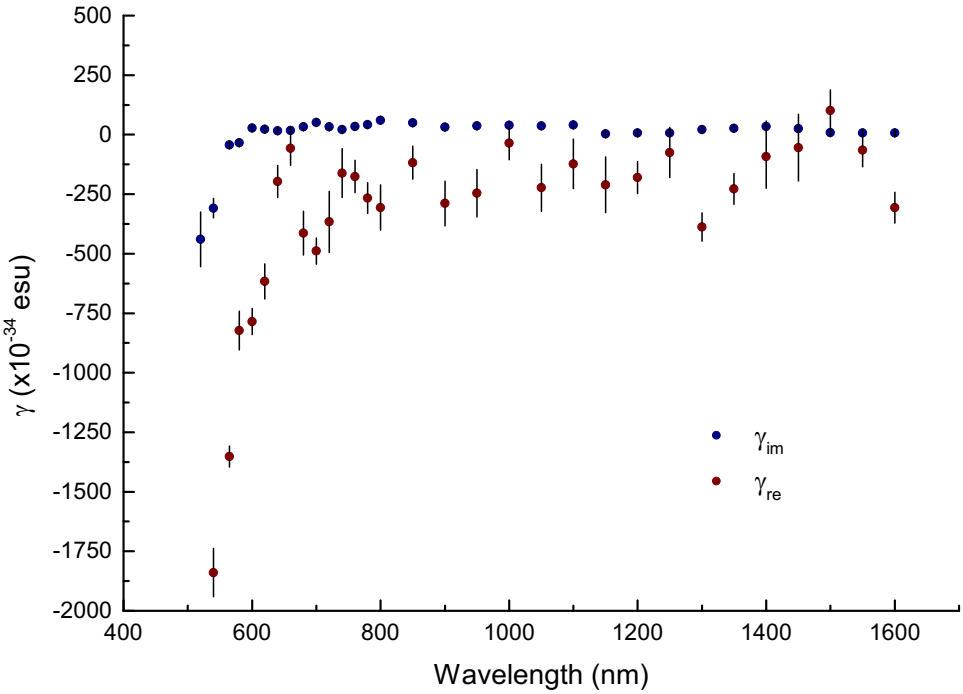

Figure B14 Cubic nonlinear hyperpolarisability γ_{real} (red) and γ_{imag} (blue) traces of **4.7**.

Spectral dependent Z-scan data for **4.8**.

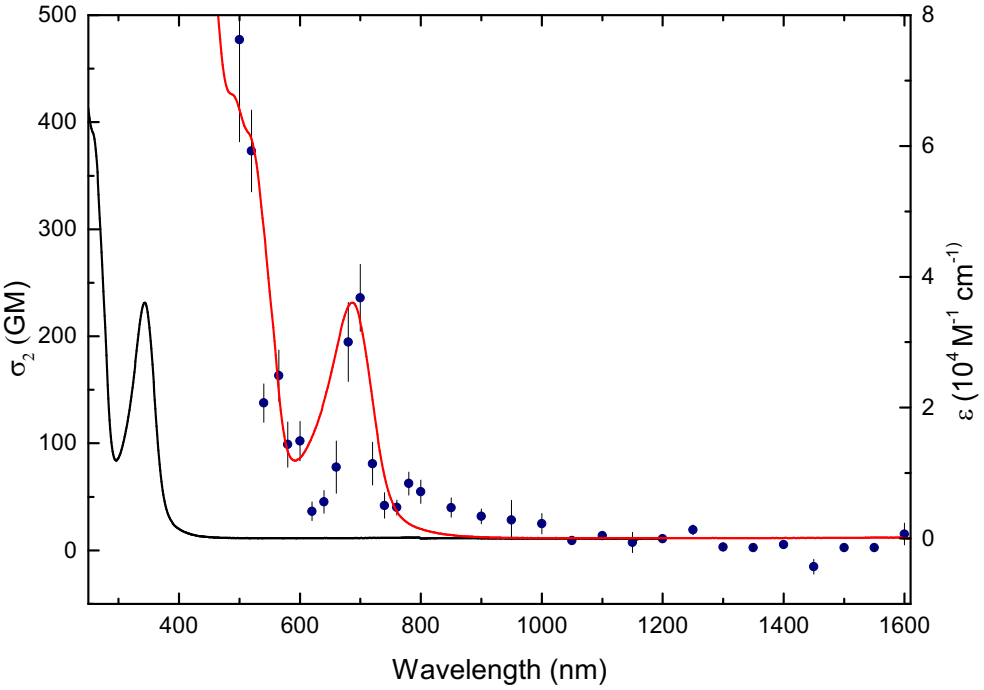

Figure B15 TPA cross-section plot of **4.8** overlaid on the UV-Vis spectrum (black) and at twice (red) the wavelength.

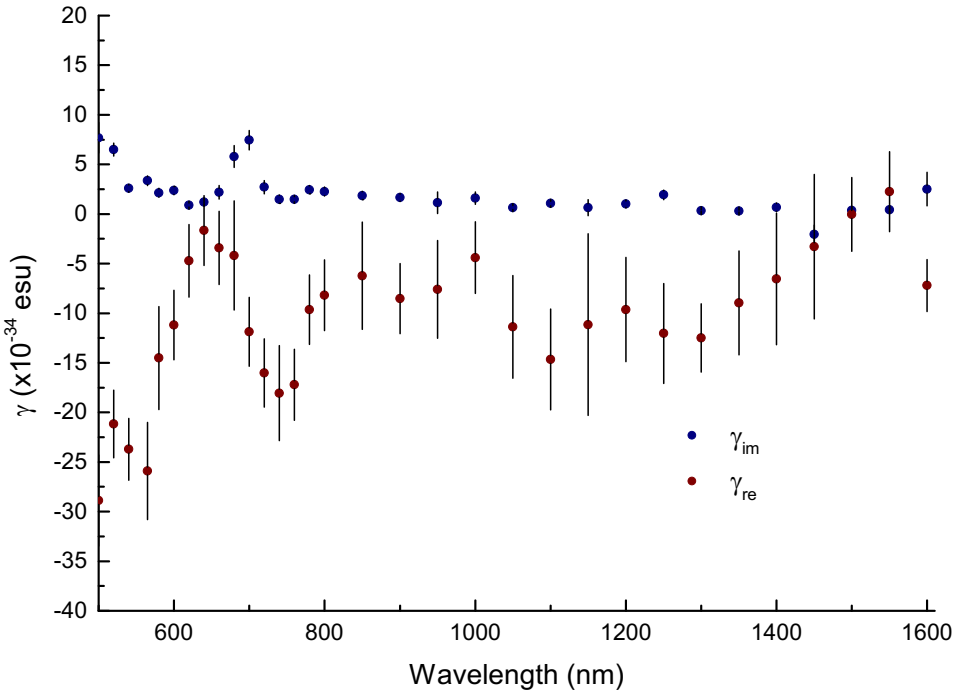

Figure B16. Cubic nonlinear hyperpolarisability γ_{real} (red) and γ_{imag} (blue) traces of **4.8**.

Spectral dependent Z-scan data for **4.9**.

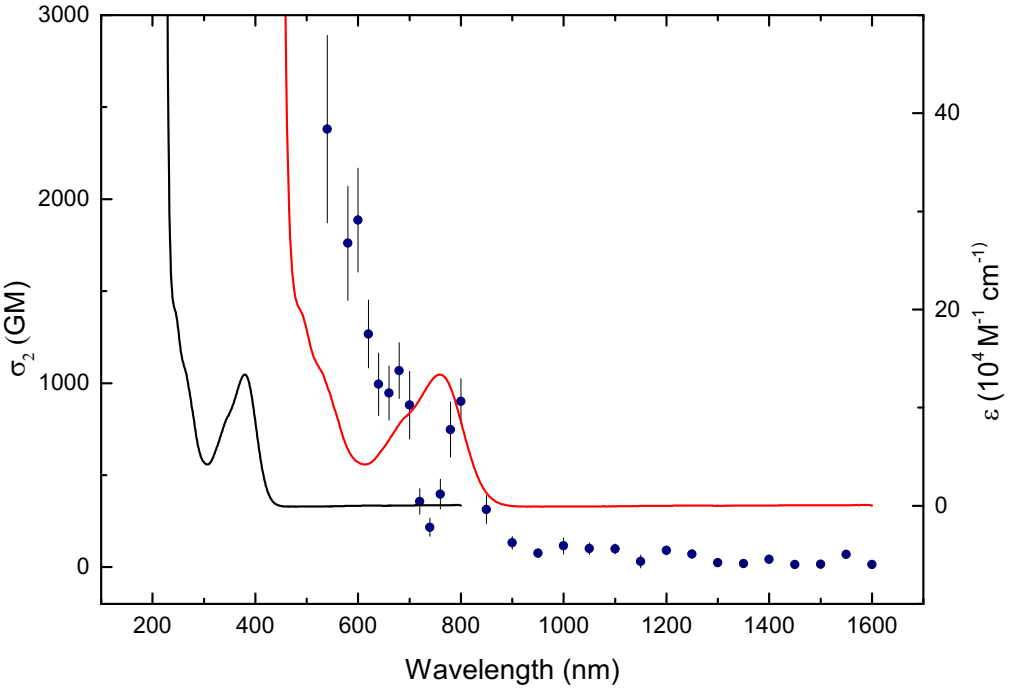

Figure B17 TPA cross-section plot of **4.9** overlaid on the UV-Vis spectrum (black) and at twice (red) the wavelength.

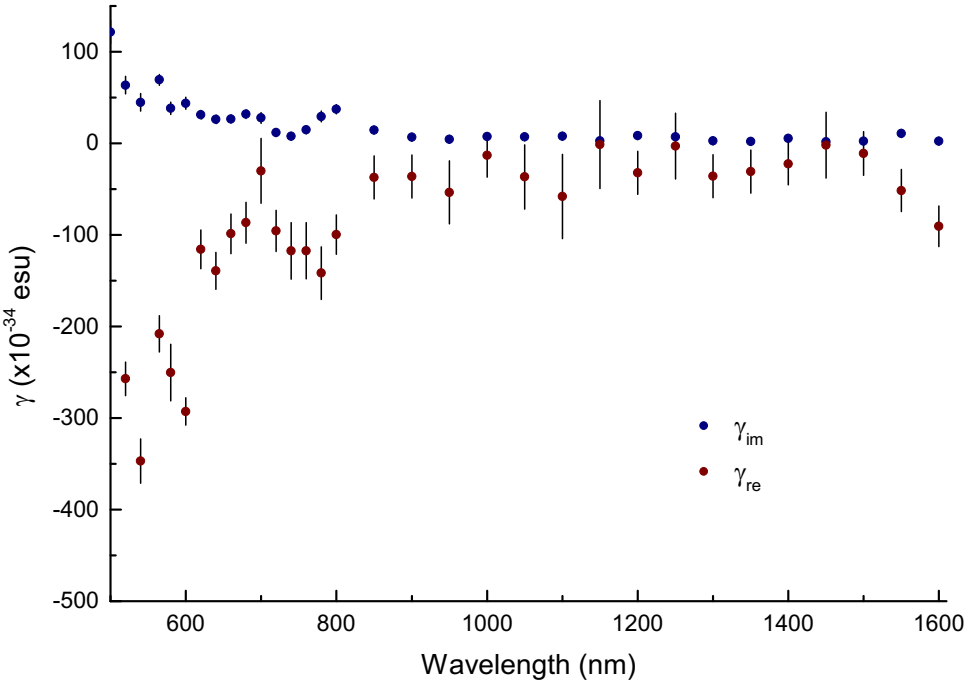

Figure B18 Cubic nonlinear hyperpolarisability γ_{real} (red) and γ_{imag} (blue) traces of **4.9**.

Spectral dependent Z-scan data for **4.10**.

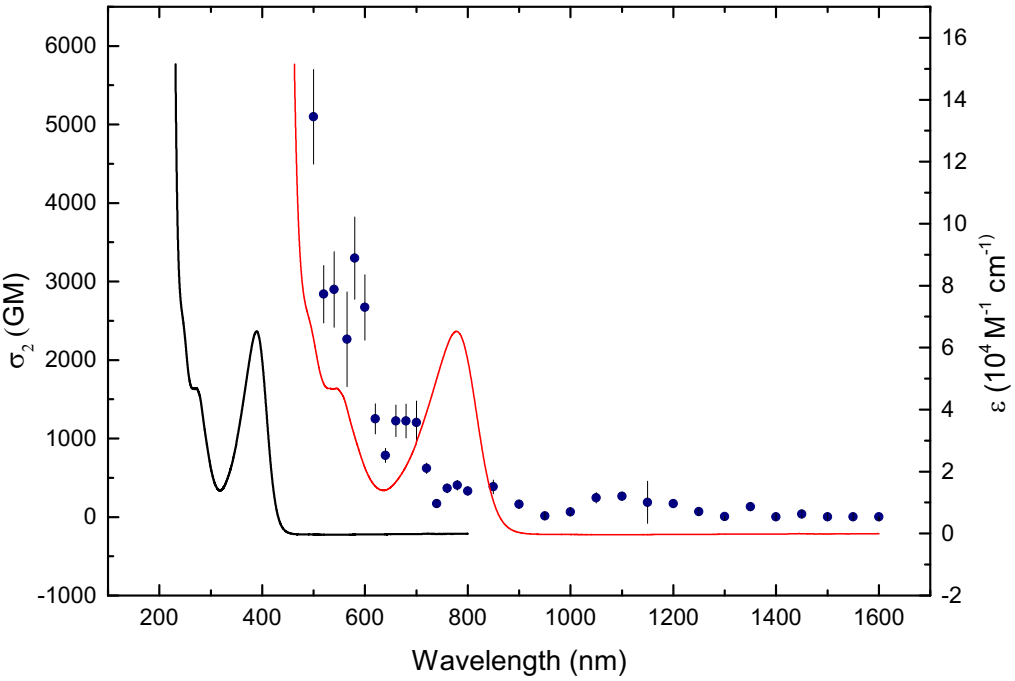

Figure B19 TPA cross-section plot of **4.10** overlaid on the UV-Vis spectrum (black) and at twice (red) the wavelength.

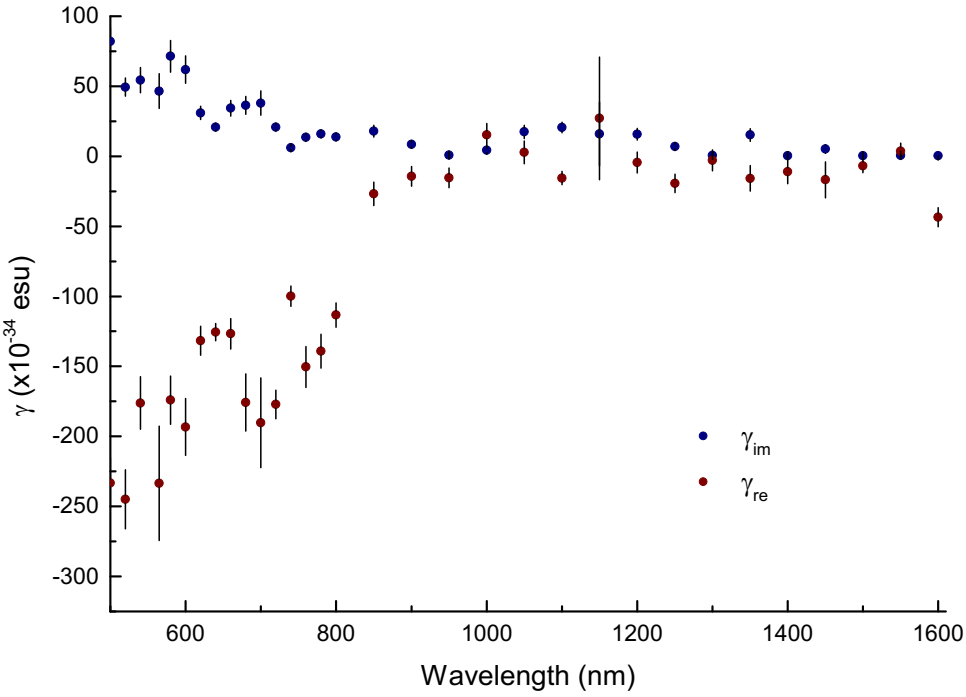

Figure B20 Cubic nonlinear hyperpolarisability γ_{real} (red) and γ_{imag} (blue) traces of **4.10**.

Spectral dependent Z-scan data for **4.11**.

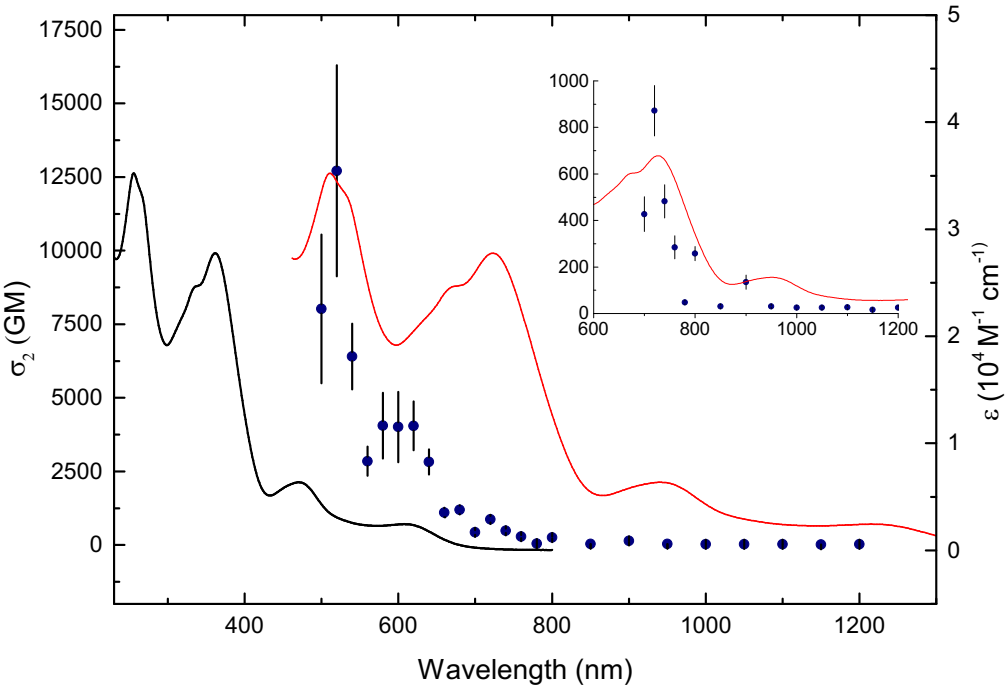

Figure B21 TPA cross-section plot of **4.11** overlaid on the UV-Vis spectrum (black) and at twice (red) the wavelength. Insert: the same trace enlarged from 600 – 1200 nm.

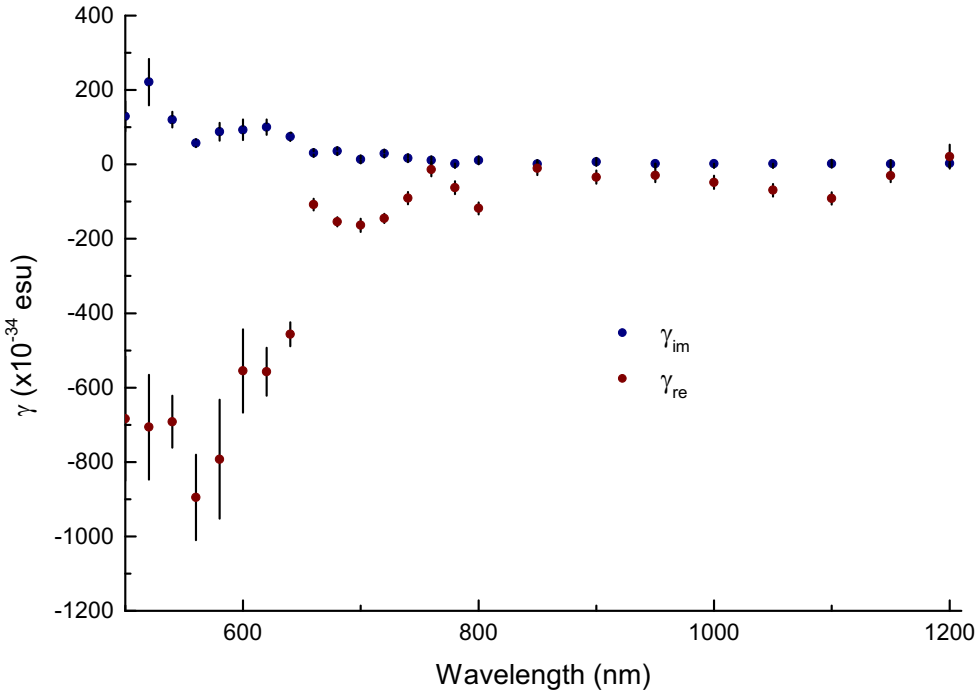

Figure B22 Cubic nonlinear hyperpolarisability γ_{real} (red) and γ_{imag} (blue) traces of **4.11**.

Spectral dependent Z-scan data for **4.12**.

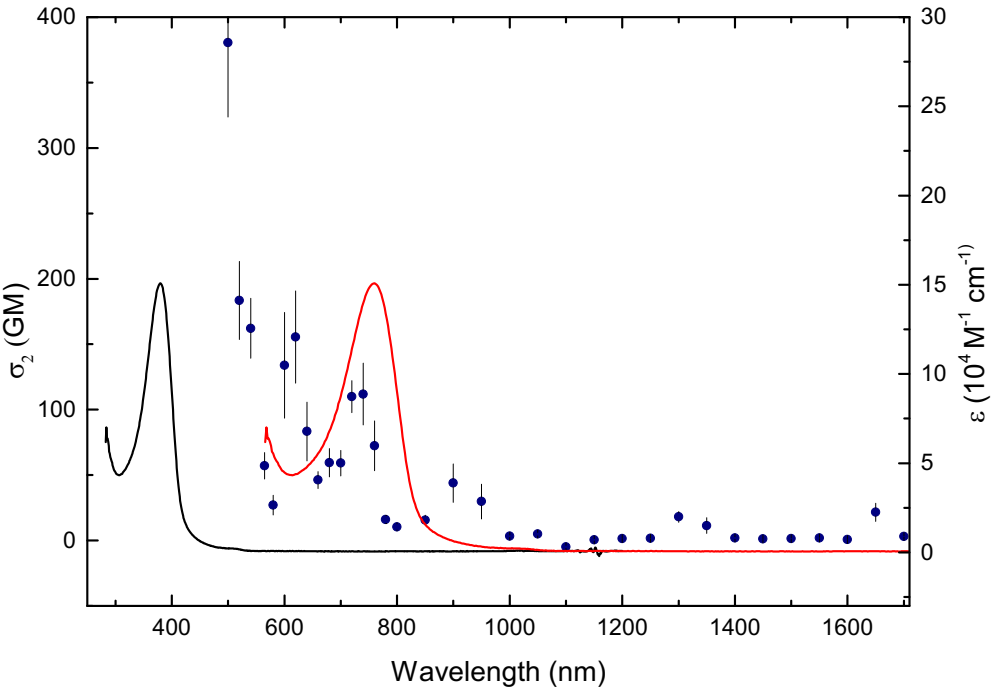

Figure B23 TPA cross-section plot of **4.12** overlaid on the UV-Vis spectrum (black) and at twice (red) the wavelength.

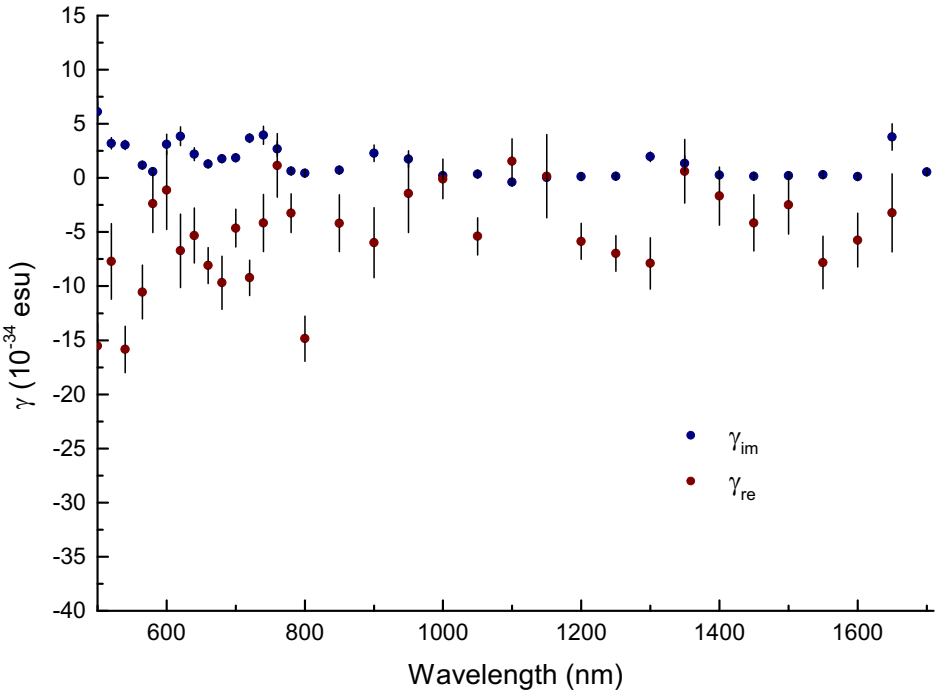

Figure B24 Cubic nonlinear hyperpolarisability γ_{real} (red) and γ_{imag} (blue) traces of **4.12**.

Spectral dependent Z-scan data for **4.13**.

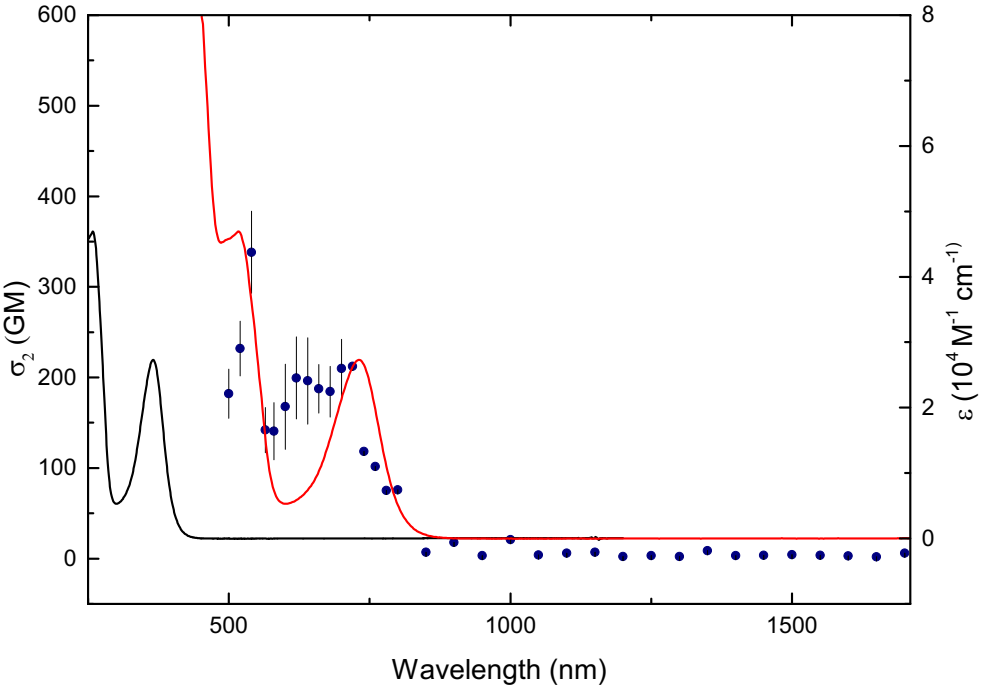

Figure B25 TPA cross-section plot of **4.13** overlaid on the UV-Vis spectrum (black) and at twice (red) the wavelength.

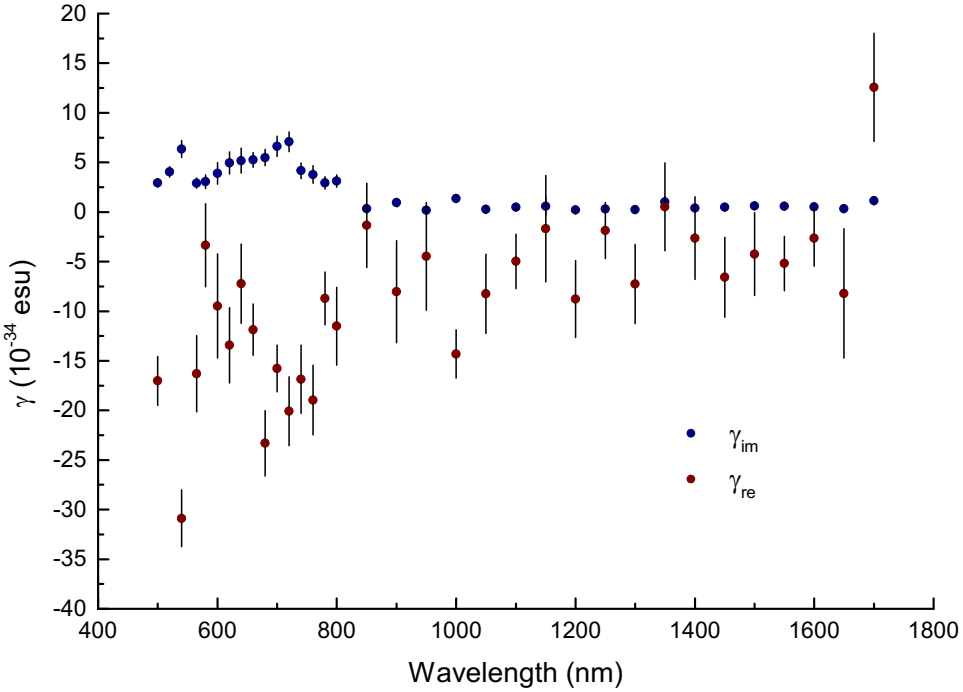

Figure B26 Cubic nonlinear hyperpolarisability γ_{real} (red) and γ_{imag} (blue) traces of **4.13**.

Spectral dependent Z-scan data for **4.14**.

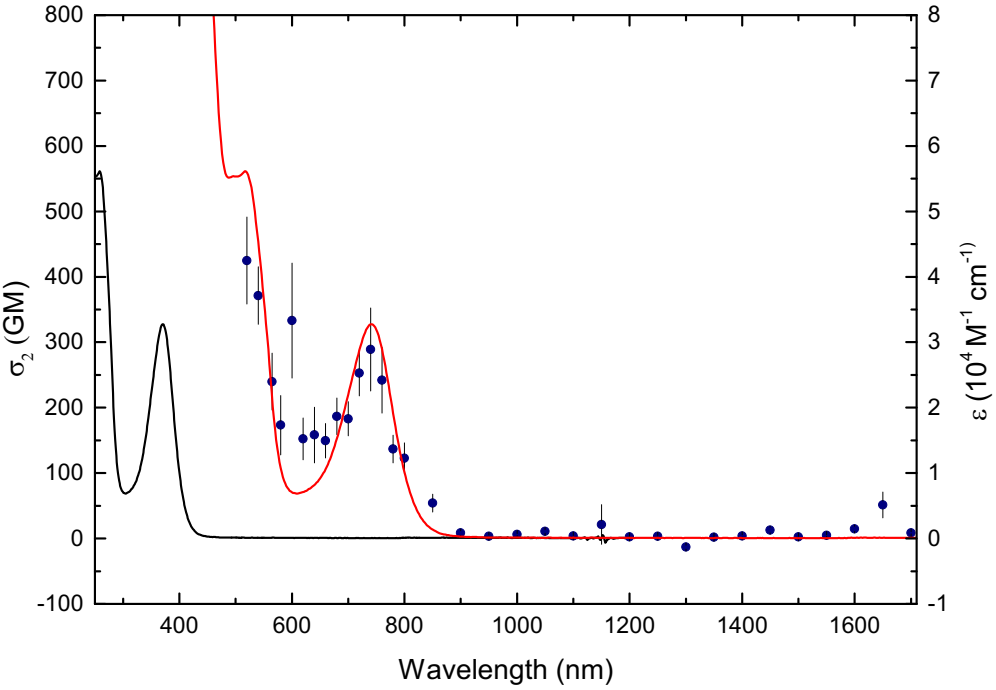

Figure B27 TPA cross-section plot of **4.14** overlaid on the UV-Vis spectrum (black) and at twice (red) the wavelength.

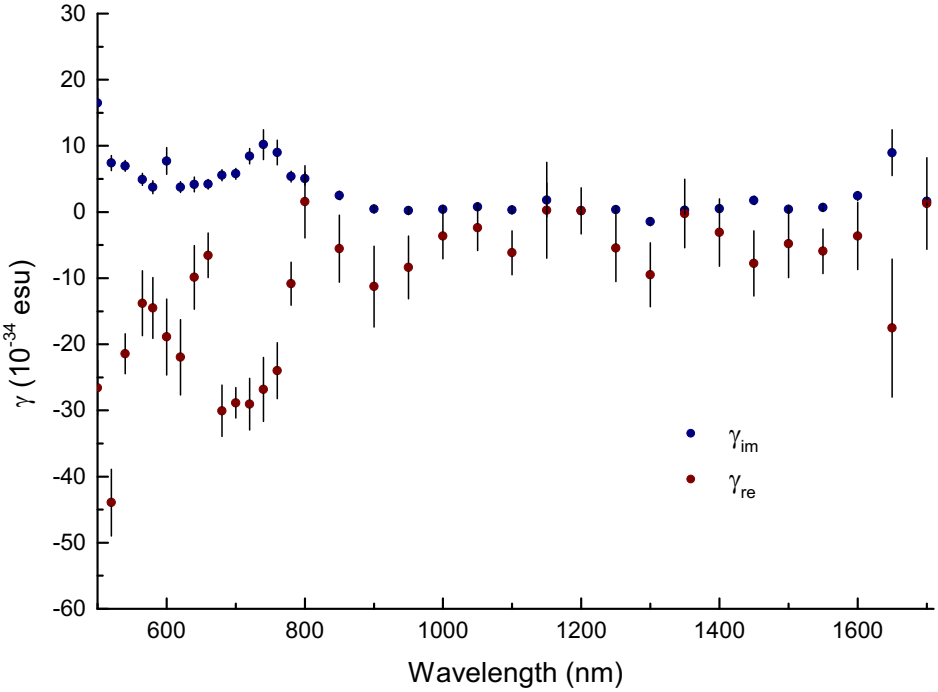

Figure B28 Cubic nonlinear hyperpolarisability γ_{real} (red) and γ_{imag} (blue) traces of **4.14**.

Spectral dependent Z-scan data for **4.15**.

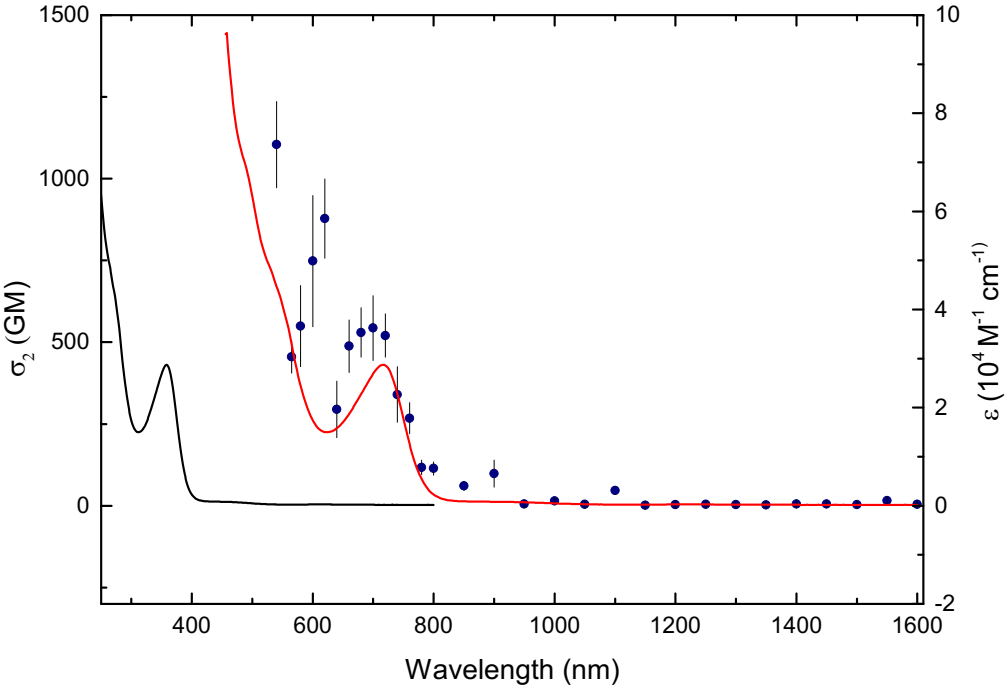

Figure B29 TPA cross-section plot of **4.15** overlaid on the UV-Vis spectrum (black) and at twice (red) the wavelength.

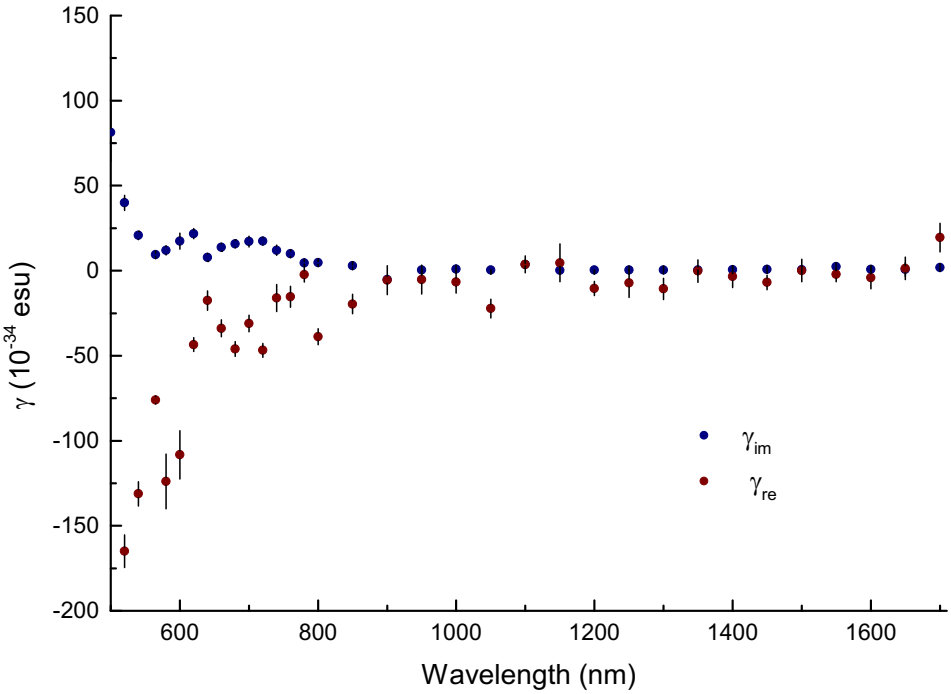

Figure B30 Cubic nonlinear hyperpolarisability γ_{real} (red) and γ_{imag} (blue) traces of **4.15**.

Spectral dependent Z-scan data for **4.16**.

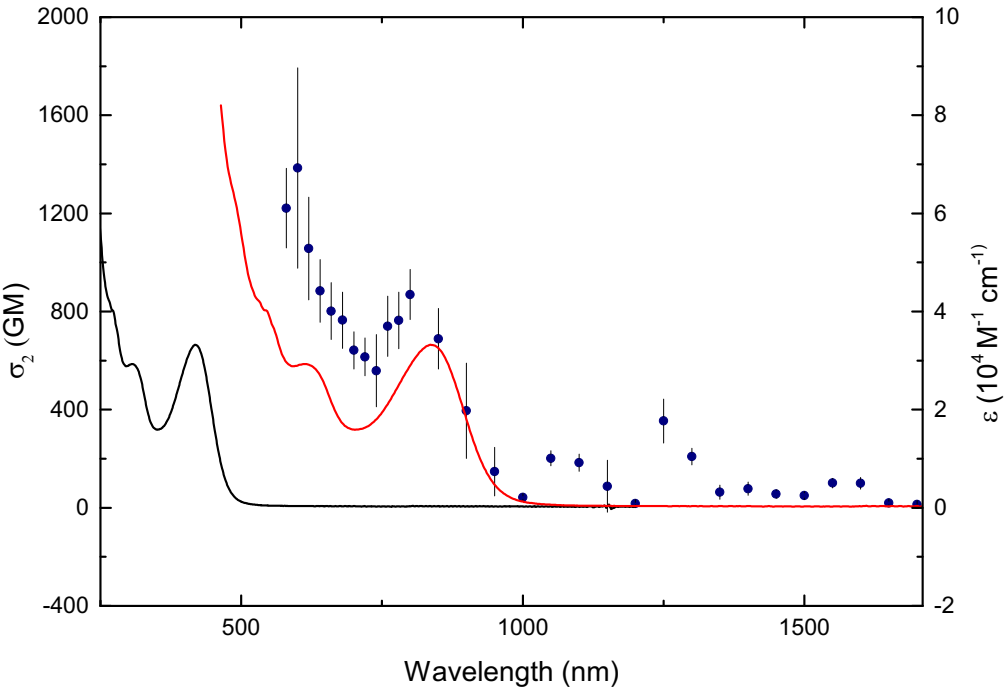

Figure B31 TPA cross-section plot of **4.16** overlaid on the UV-Vis spectrum (black) and at twice (red) the wavelength.

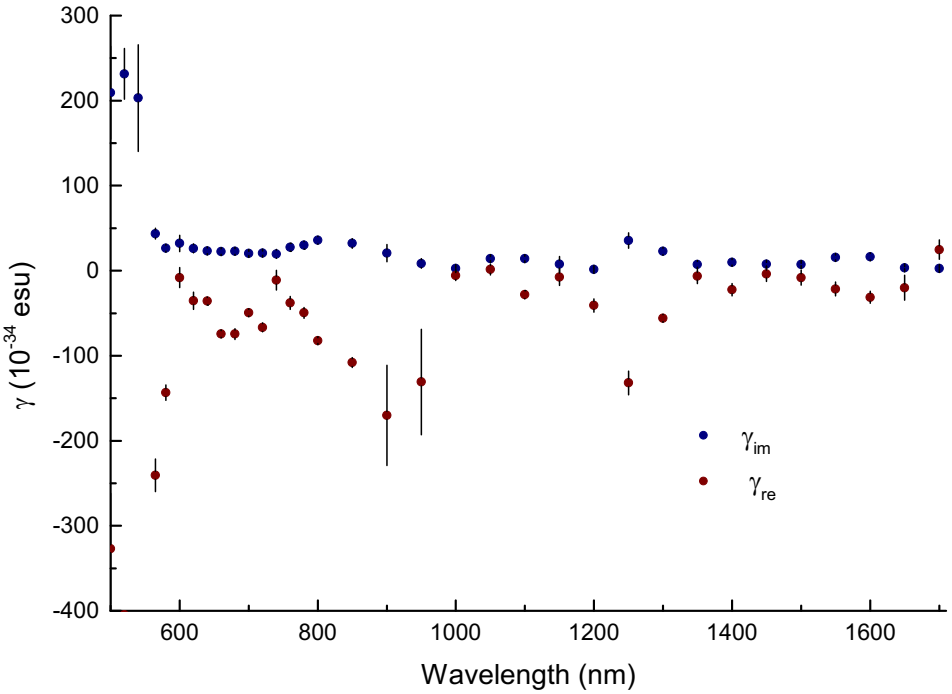

Figure B32 Cubic nonlinear hyperpolarisability γ_{real} (red) and γ_{imag} (blue) traces of **4.16**.

Spectral dependent Z-scan data for **4.17**.

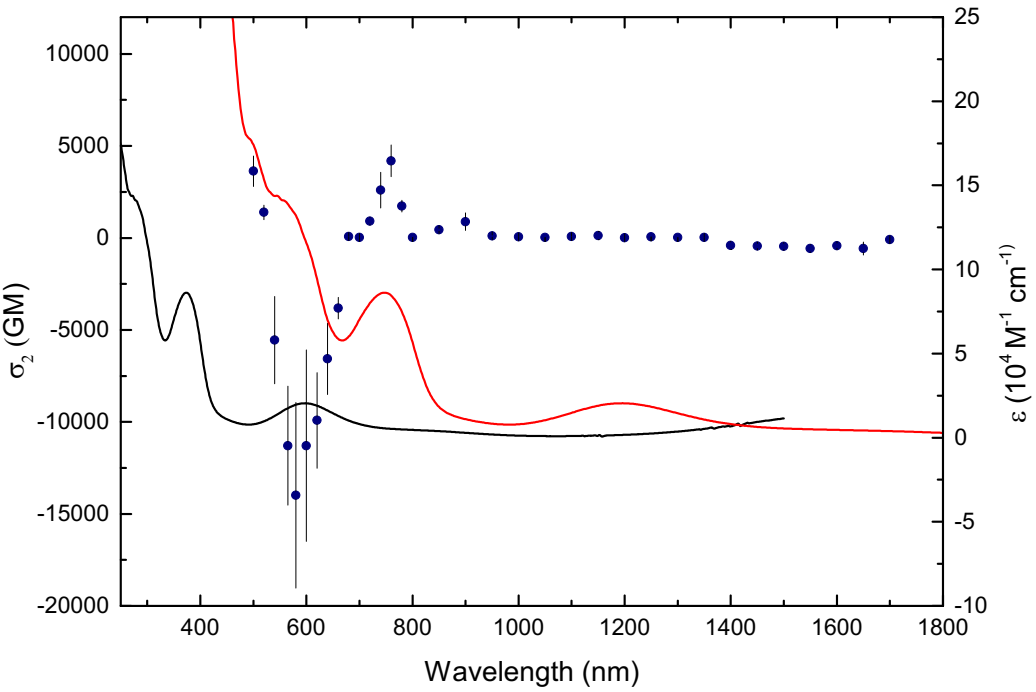

Figure B33 TPA cross-section plot of **4.17** overlaid on the UV-Vis spectrum (black) and at twice (red) the wavelength.

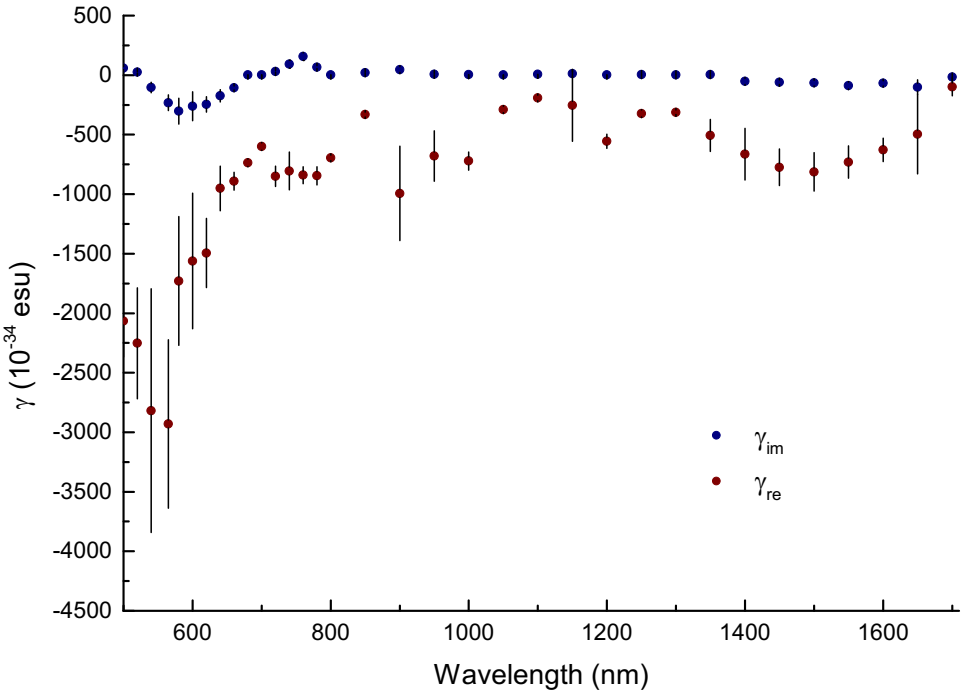

Figure B34 Cubic nonlinear hyperpolarisability γ_{real} (red) and γ_{imag} (blue) traces of **4.17**.

Spectral dependent Z-scan data for **4.18**.

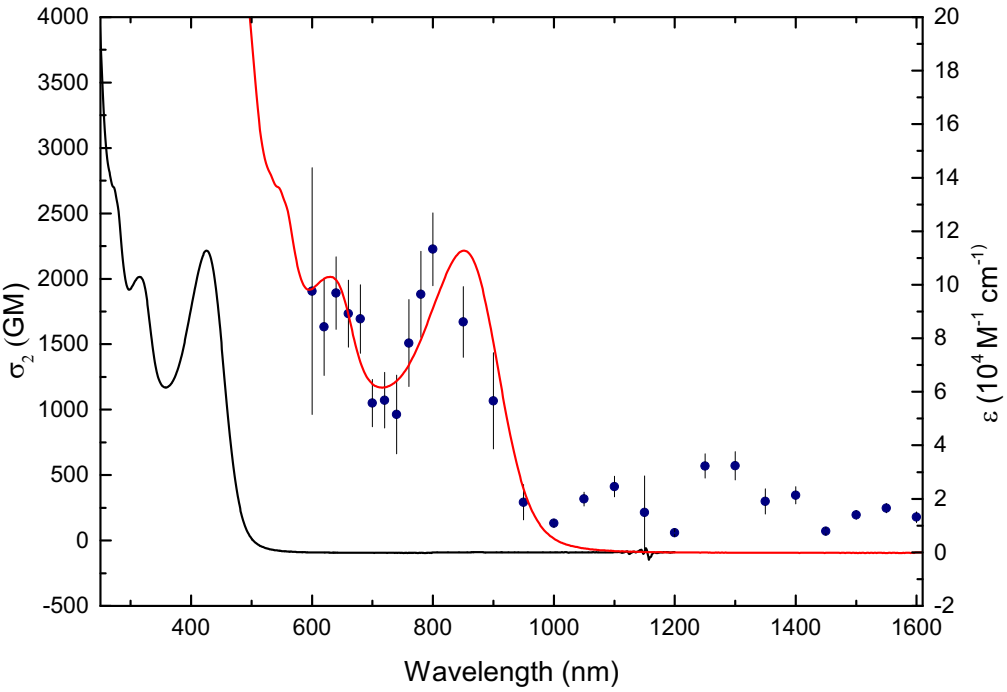

Figure B35 TPA cross-section plot of **4.18** overlaid on UV-Vis spectrum (black) and at twice (red) the wavelength.

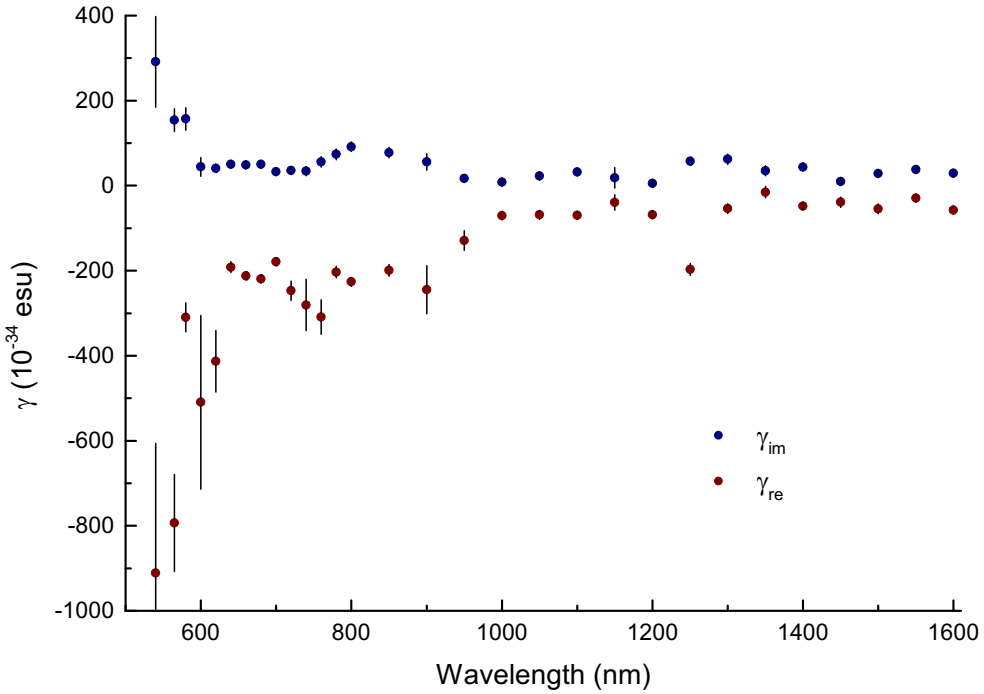

Figure B36 Cubic nonlinear hyperpolarisability γ_{real} (red) and γ_{imag} (blue) traces of **4.18**.

Spectral dependent Z-scan data for **4.19**.

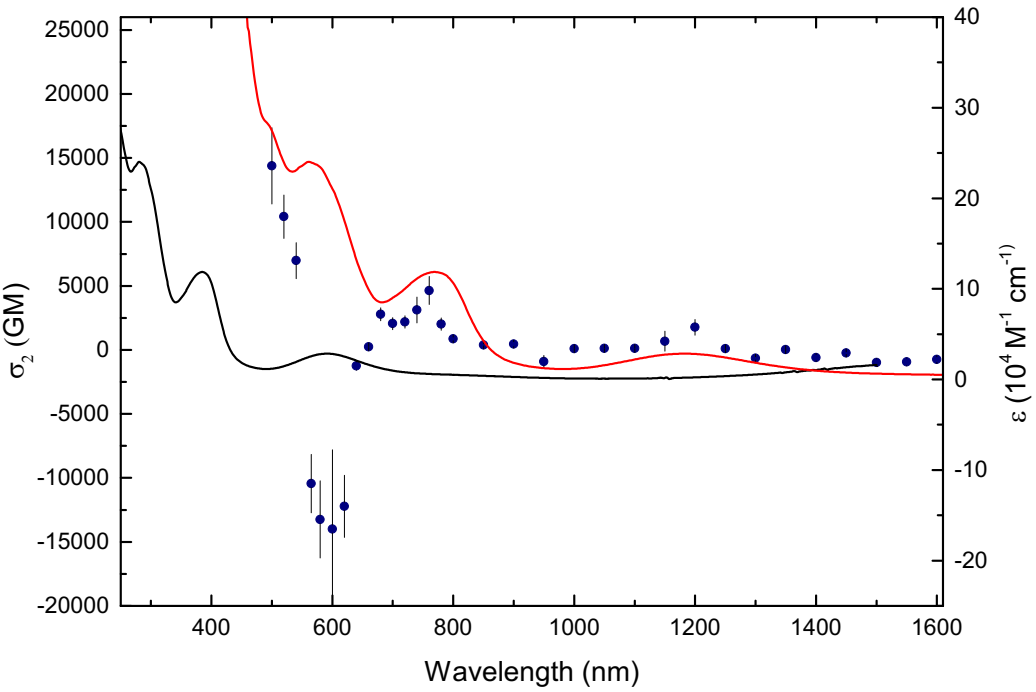

Figure B37 TPA cross-section plot of **4.19** overlaid on the UV-Vis spectrum (black) and at twice (red) the wavelength.

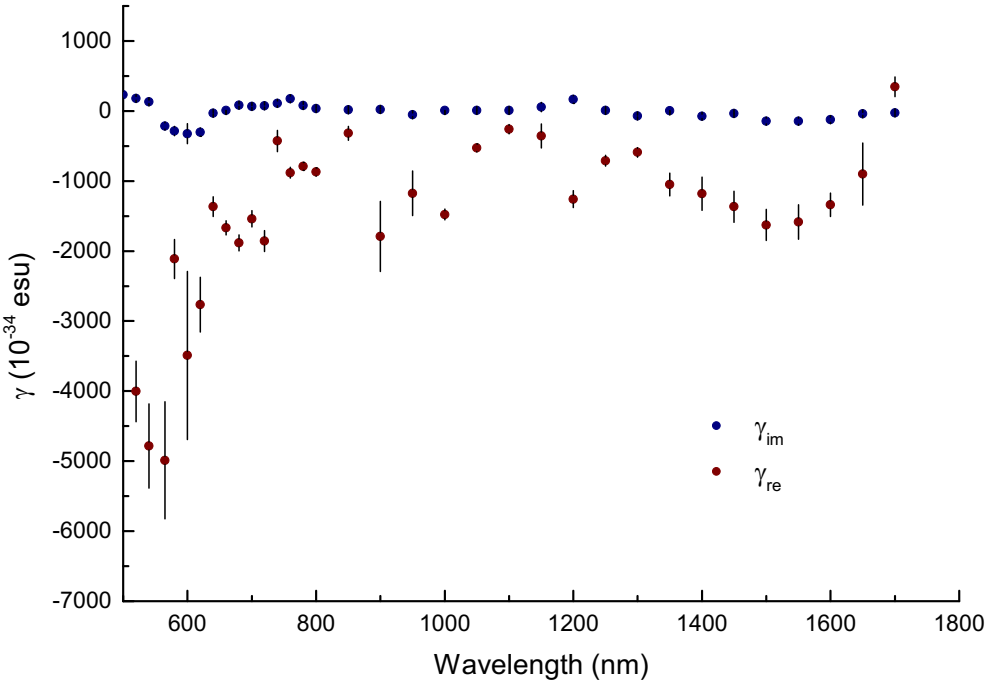

Figure B38 Cubic nonlinear hyperpolarisability γ_{real} (red) and γ_{imag} (blue) traces of **4.19**.

Spectral dependent Z-scan data for **4.20**.

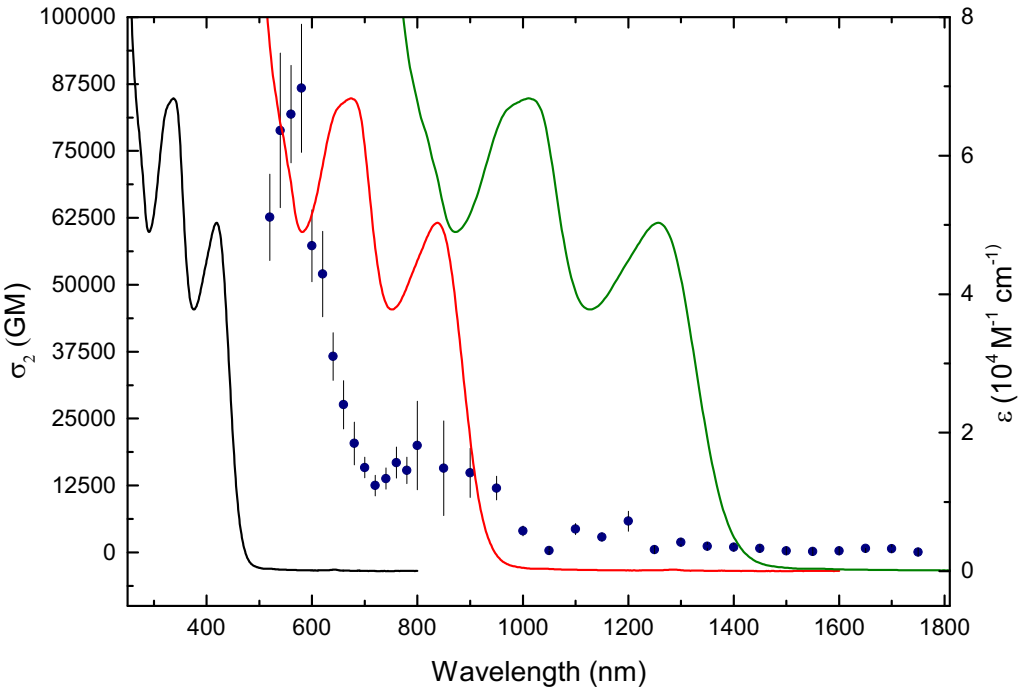

Figure B39 TPA cross-section plot of **4.20** overlaid on the UV-Vis spectrum (black), at twice (red) and three times (green) the wavelengths.

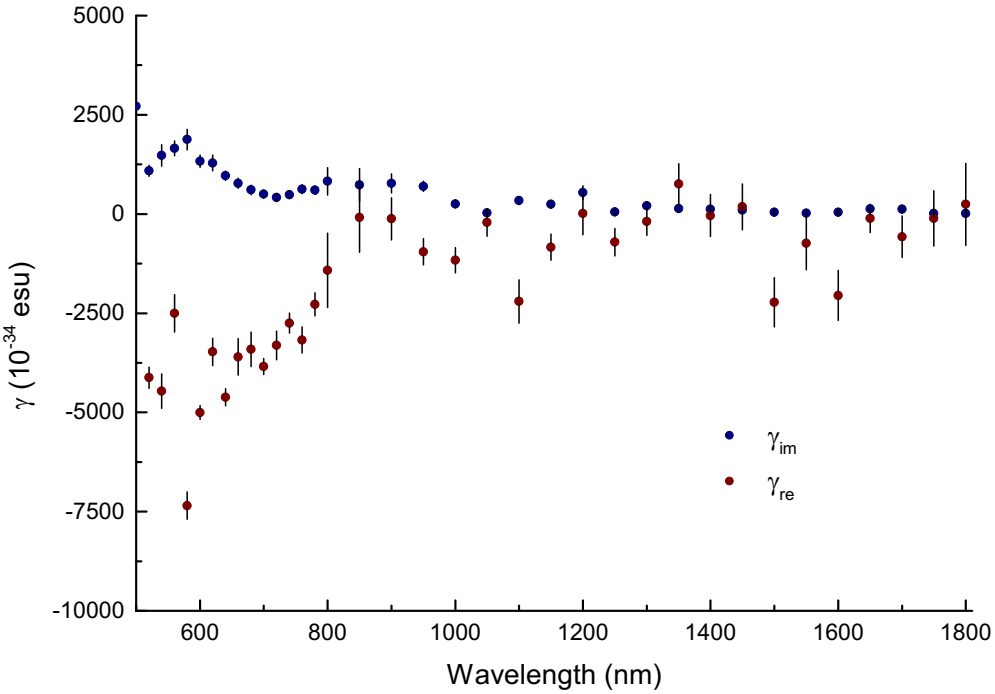

Figure B40 Cubic nonlinear hyperpolarisability γ_{real} (red) and γ_{imag} (blue) traces of **4.20**.

Spectral dependent Z-scan data for **4.21**.

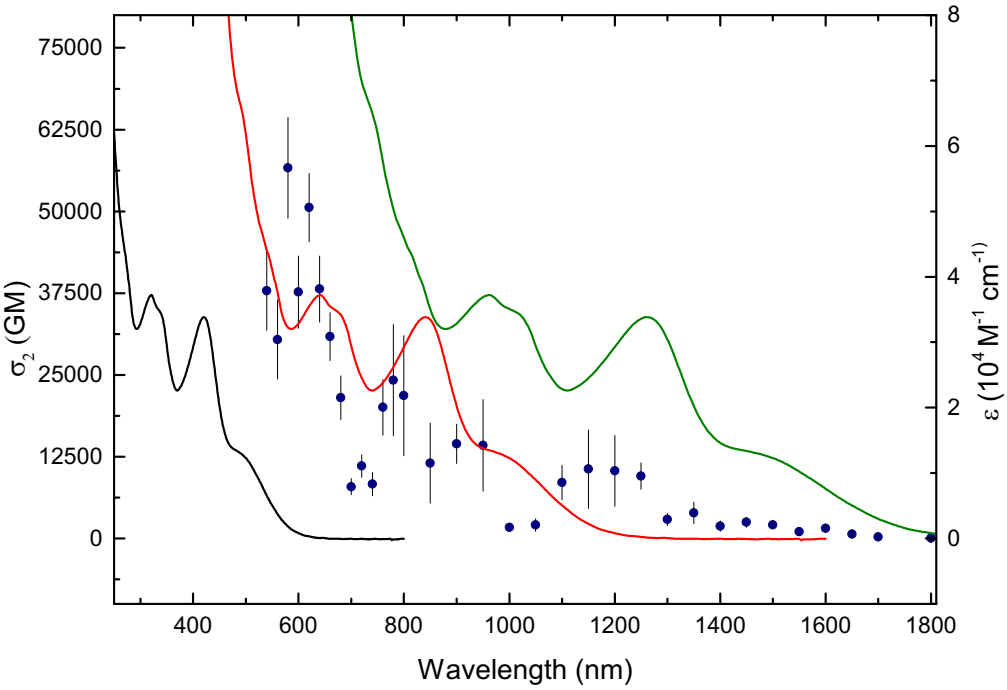

Figure B41 TPA cross-section plot of **4.21** overlaid on the UV-Vis spectrum (black), at twice (red) and three times (green) the wavelengths.

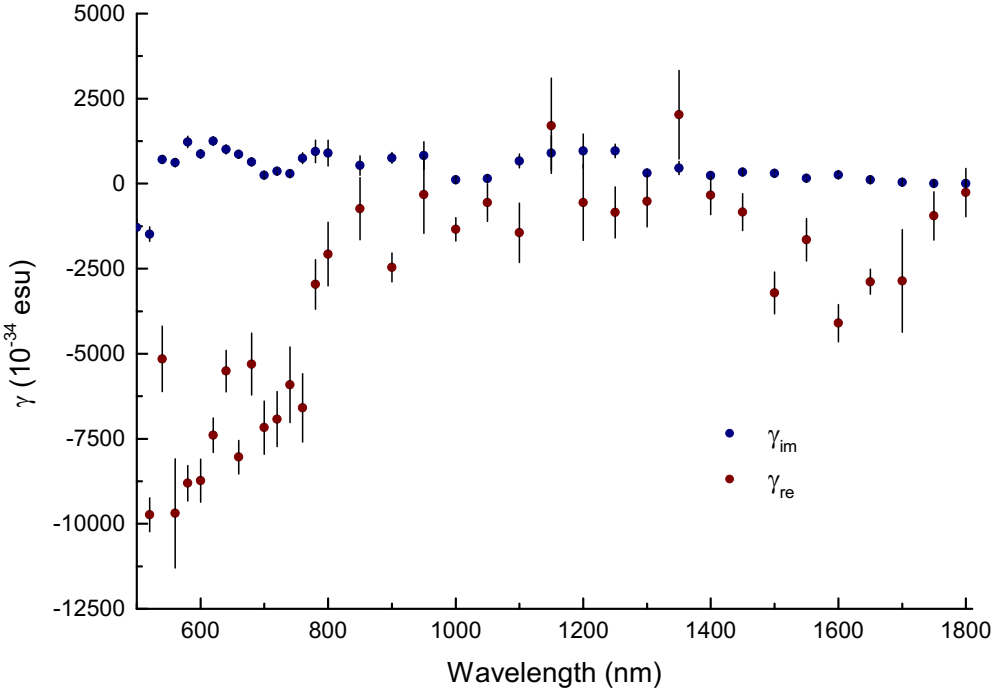

Figure B42 Cubic nonlinear hyperpolarisability γ_{real} (red) and γ_{imag} (blue) traces of **4.21**.

Spectral dependent Z-scan data for **4.22**.

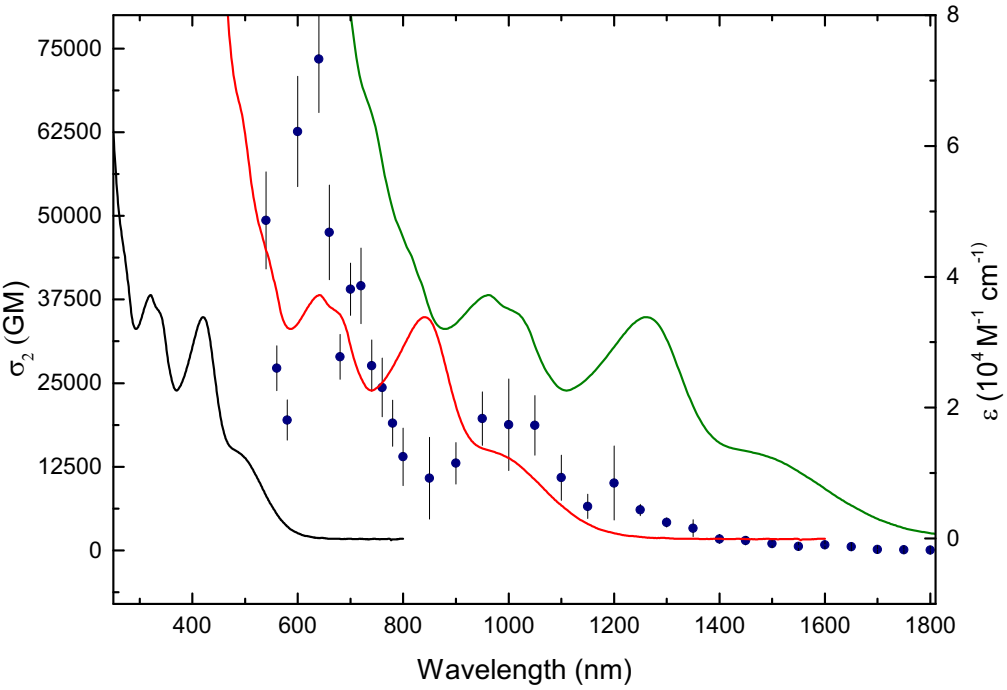

Figure B43 TPA cross-section plot of **4.22** overlaid on the UV-Vis spectrum (black), at twice (red) and three times (green) the wavelengths.

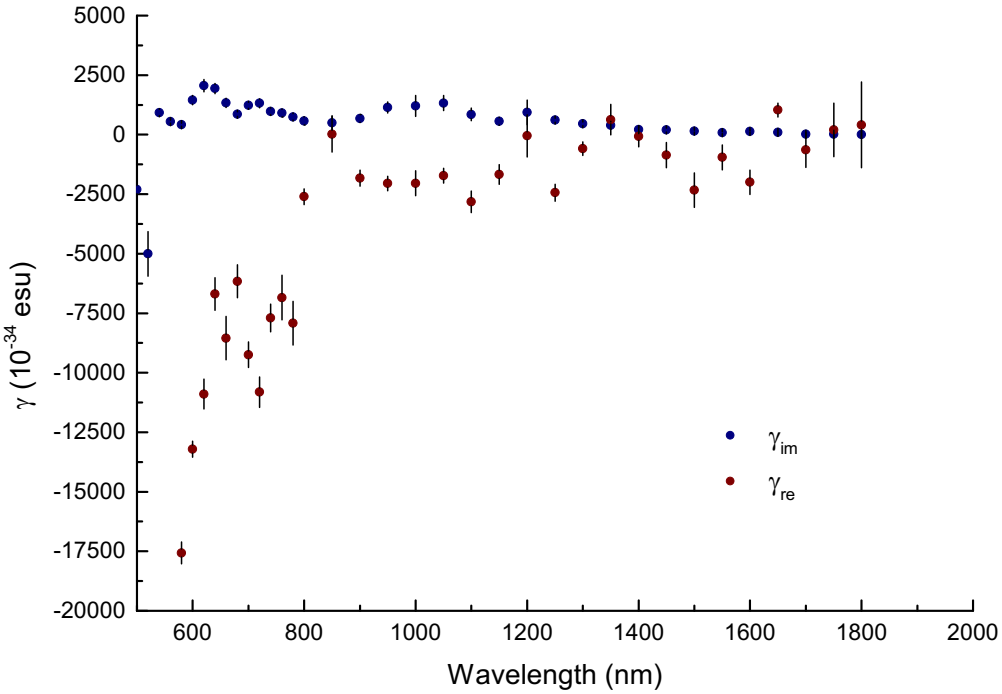

Figure B44 Cubic nonlinear hyperpolarisability γ_{real} (red) and γ_{imag} (blue) traces of **4.22**.

Spectral dependent Z-scan data for **4.23**.

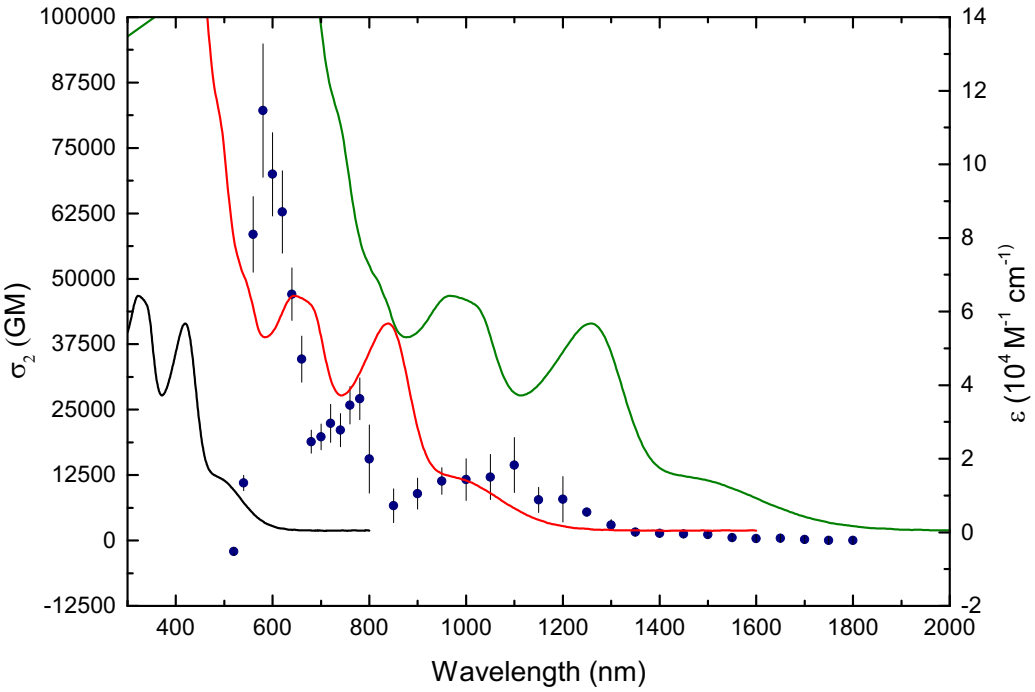

Figure B45 TPA cross-section plot of **4.23** overlaid on the UV-Vis spectrum (black), at twice (red) and three times (green) the wavelengths.

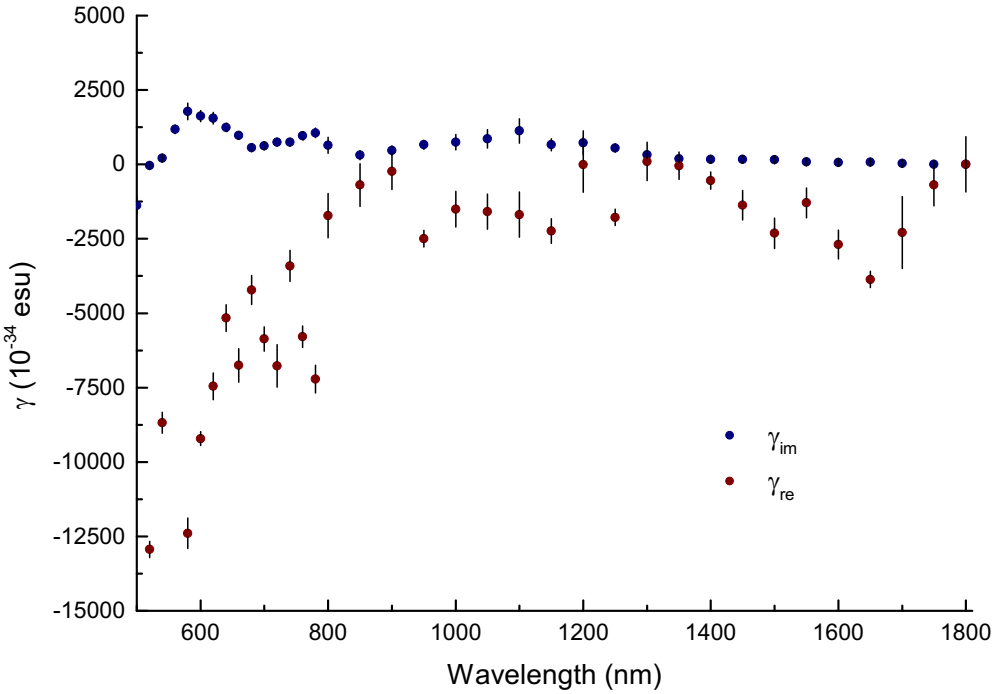

Figure B46 Cubic nonlinear hyperpolarisability γ_{real} (red) and γ_{imag} (blue) traces of **4.23**.

Spectral dependent Z-scan data for **4.24**.

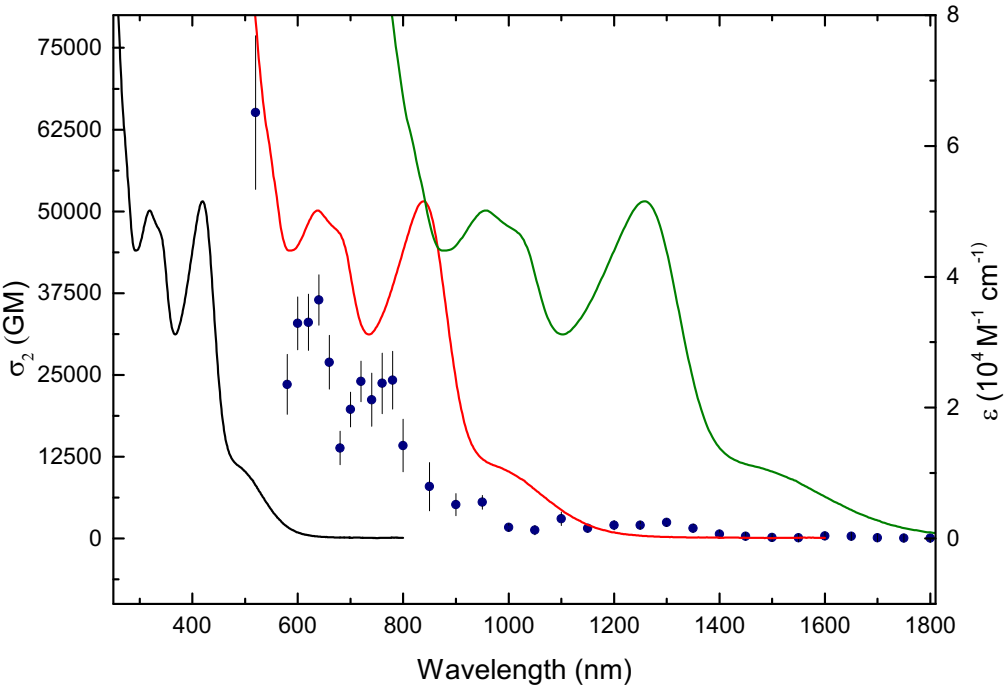

Figure B47 TPA cross-section plot of **4.24** overlaid on the UV-Vis spectrum (black), at twice (red) and three times (green) the wavelengths.

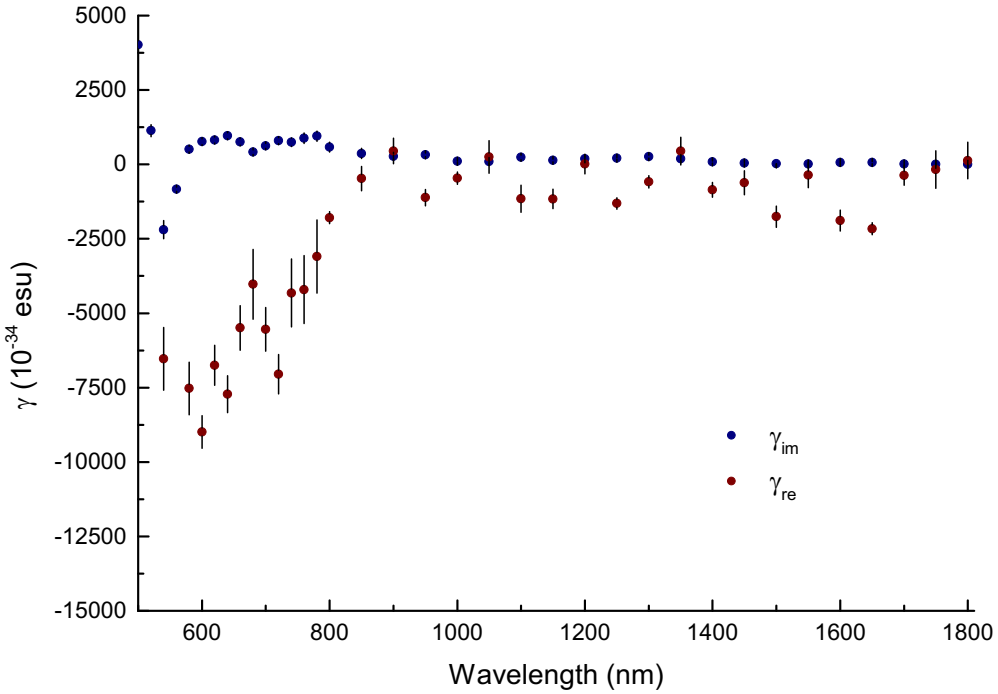

Figure B48 Cubic nonlinear hyperpolarisability γ_{real} (red) and γ_{imag} (blue) traces of **4.24**.

C. Crystal Data in Chapter 2 & 3

Table C01 Crystal data and refinement for compounds **2.1a** and **2.1b**.

	2.1a	**2.1b**
Identification code	GM058	GM090
Empirical formula	$C_{52}H_{52}Cl_2FeN_2P_2Ru$	$C_{44}H_{48}Cl_2N_2P_2Ru$
Formula weight	994.75	838.79
Temperature/K	150(10)	150(10)
Crystal system	monoclinic	monoclinic
Space group	$P2_{1/n}$	Cc
a/Å	14.391(3)	14.390(3)
b/Å	23.473(5)	23.206(5)
c/Å	20.388(4)	15.080(3)
α/°	90	90
β/°	105.13(3)	106.44(3)
γ/°	90	90
Volume/Å^3	6648(2)	4829.6(18)
Z	4	4
ρ_{calc}g/cm^3	1.5703	1.3843
μ/mm^{-1}	1.195	0.756
F(000)	3173.8	2063.9
Radiation	MoKα (λ=0.71073)	MoKα (λ=0.71073)
2Θ range for data collection/°	5.2 to 55.92	5.78 to 57.12
Index ranges	-18≤h≤17, -30≤k≤30, -26≤l≤26	-19≤h≤19, -31≤k≤31, -20≤l≤20
Reflections collected	59444	47524
Independent reflections	13638 [R_{int}=0.0990, R_{sigma}=0.1042]	12065 [R_{int}=0.0450, R_{sigma}=0.0314]
Data/restraints/parameters	13638/0/718	12065/0/507
Goodness-of-fit on F^2	1.064	1.025
Final R indexes [I>=2σ(I)]	R_1=0.0973	R_1=0.0462
Final R indexes [all data]	R_1=0.1653, wR_2=0.2927	R_1=0.0510, wR_2=0.1357
Largest diff. peak/hole/e Å^{-3}	2.50/-1.99	1.54/-1.11

Table C02 Crystal data and refinement for compound **2.1c** and **2.2a**.

	2.1c	**2.2a**
Identification code	GM003	GM036
Empirical formula	$C_{48}H_{48}Cl_2N_2P_2Ru$	$C_{60}H_{56}ClFeN_3O_2P_2Ru$
Formula weight	886.83	1105.42
Temperature/K	150(10)	150(10)
Crystal system	monoclinic	monoclinic
Space group	$P2_{1/c}$	C2/c
a/Å	15.169(3)	27.885(6)
b/Å	17.186(3)	12.263(3)
c/Å	20.451(3)	33.888(7)
α/°	90	90
β/°	102.05(3)	111.29(3)
γ/°	90	90
Volume/Å^3	5213.8(19)	10798(4)
Z	4	4
ρ_{calc}g/cm^3	1.2216	1.3496
μ/mm^{-1}	0.500	0.703
F(000)	1989.7	4301.3
Radiation	MoKα (λ=0.71073)	MoKα (λ=0.71073)
2Θ range for data collection/°	2.04 to 55.84	5.86 to 55.78
Index ranges	-19≤h≤19, -22≤k≤22, -26≤l≤26	-30≤h≤36, -10≤k≤14, -44≤l≤24
Reflections collected	106725	11294
Independent reflections	11986 [R_{int}=0.1112, R_{sigma}=0.0825]	8204 [R_{int}=0.0371, R_{sigma}=0.0952]
Data/restraints/parameters	11986/0/550	8204/0/666
Goodness-of-fit on F^2	1.047	1.042
Final R indexes [I>=2σ(I)]	R_1=0.0663	R_1=0.0965
Final R indexes [all data]	R_1=0.1202, wR_2=0.2563	R_1=0.1661, wR_2=0.3282
Largest diff. peak/hole/e Å^{-3}	2.93/-1.32	3.04/-1.68

Table C03 Crystal data and refinement for compound **2.2b** and **2.2c**.

	2.2b	**2.2c**
Identification code	GM024	GM027
Empirical formula	$C_{60}H_{57}ClFeN_2P_2Ru$	$C_{52}H_{52}ClN_3O_2P_2Ru$
Formula weight	1060.42	949.46
Temperature/K	150(10)	150(10)
Crystal system	triclinic	orthorhombic
Space group	P-1	$Pna2_1$
a/Å	13.597(3)	16.551(3)
b/Å	20.976(4)	25.154(5)
c/Å	21.755(4)	11.891(2)
α/°	84.84(3)	90
β/°	80.07(3)	90
γ/°	88.02(3)	90
Volume/Å^3	6086(2)	4950.7(17)
Z	6	4
ρ_{calc}g/cm^3	1.1916	1.388
μ/mm^{-1}	0.705	0.587
F(000)	2135.7	2136.0
Radiation	MoKα (λ=0.71073)	MoKα (λ=0.71073)
2Θ range for data collection/°	5.22 to 55.88	5.182 to 55.776
Index ranges	-17≤h≤17, -26≤k≤27, -28≤l≤28	-21≤h≤21, -32≤k≤33, -15≤l≤13
Reflections collected	111418	57276
Independent reflections	28688 [R_{int}=0.0959, R_{sigma}=0.1229]	11141 [R_{int}=0.0825, R_{sigma}=0.0848]
Data/restraints/parameters	28688/0/1249	11141/1/583
Goodness-of-fit on F^2	1.921	1.060
Final R indexes [I>=2σ(I)]	R_1=0.1095	R_1=0.0620, wR_2=0.1241
Final R indexes [all data]	R_1=0.1976, wR_2=0.3493	R_1=0.1098, wR_2=0.1433
Largest diff. peak/hole/e Å^{-3}	4.87/-1.84	0.74/-0.42

Table C04 Crystal data and refinement for compound **2.2d*** and **2.2e**.

	2.2d*	**2.2e**
Identification code	GM284	GM039
Empirical formula	$C_{52}H_{53}IN_2P_2Ru$	$C_{56}H_{52}ClN_3O_2P_2Ru$
Formula weight	995.91	997.50
Temperature/K	150(10)	150(10)
Crystal system	monoclinic	orthorhombic
Space group	$P2_1/c$	$Pca2_1$
a/Å	11.8471(4)	26.654(5)
b/Å	29.4344(10)	15.896(3)
c/Å	16.0409(6)	12.420(3)
α/°	90	90
β/°	92.799(4)	90
γ/°	90	90
Volume/Å^3	5587.0(3)	5262.4(18)
Z	4	7
ρ_{calc}g/cm^3	1.468	1.2975
μ/mm^{-1}	1.214	0.553
F(000)	2488.0	2014.4
Radiation	MoKα (λ=0.71073)	MoKα (λ=0.71073)
2Θ range for data collection/°	3.71 to 59.576	5.12 to 55.82
Index ranges	-16≤h≤13, -37≤k≤40, -20≤l≤19	-35≤h≤31, -14≤k≤20, -15≤l≤16
Reflections collected	31463	66001
Independent reflections	13200 [R_{int}=0.0849, R_{sigma}=0.1588]	12285 [R_{int}=0.1053, R_{sigma}=0.1259]
Data/restraints/parameters	13200/12/595	12285/0/612
Goodness-of-fit on F^2	1.048	1.038
Final R indexes [I>=2σ(I)]	R_1=0.1099, wR_2=0.2629	R_1=0.0778
Final R indexes [all data]	R_1=0.1856, wR_2=0.3066	R_1=0.1527, wR_2=0.2259
Largest diff. peak/hole/e Å^{-3}	3.00/-1.68	1.70/-1.16

Table C05 Crystal data and refinement for compound **2.3a**.

	2.3a
Identification code	GM005
Empirical formula	$C_{49}H_{48}ClF_6N_2OP_3Ru$
Formula weight	1024.35
Temperature/K	150(10)
Crystal system	triclinic
Space group	P1
a/Å	10.561(2)
b/Å	11.016(2)
c/Å	12.532(3)
α/°	101.35(3)
β/°	100.37(3)
γ/°	91.10(3)
Volume/Å^3	1403.9(5)
Z	1
ρ_{calc}g/cm^3	1.1543
μ/mm^{-1}	0.462
F(000)	475.5
Radiation	MoKα (λ=0.71073)
2Θ range for data collection/°	3.38 to 55.8
Index ranges	-13≤h≤13, -14≤k≤14, -16≤l≤16
Reflections collected	26934
Independent reflections	12178 [R_{int}=0.0424, R_{sigma}=0.0389]
Data/restraints/parameters	12178/0/542
Goodness-of-fit on F^2	1.723
Final R indexes [I>=2σ(I)]	R_1=0.1258
Final R indexes [all data]	R_1=0.1281, wR_2=0.3458
Largest diff. peak/hole/e Å^{-3}	7.48/-1.07

Table C06 Crystal data and refinement for compound **2.3a-1** and **2.3a-2**.

	2.3a-1	**2.3a-2**
Identification code	GM290	GM294
Empirical formula	$C_{66}H_{63}ClF_6N_2OP_4Ru$	$C_{48}H_{48}Cl_2F_6N_2P_3Ru$
Formula weight	1274.63	1031.79
Temperature/K	150(10)	150(10)
Crystal system	triclinic	monoclinic
Space group	P-1	$P2_1/c$
a/Å	13.5936(4)	16.6903(12)
b/Å	13.6504(4)	15.1120(13)
c/Å	18.7295(5)	19.2706(11)
α/°	71.228(3)	90
β/°	72.190(3)	90.906(6)
γ/°	69.087(2)	90
Volume/Å^3	3001.25(16)	4859.9(6)
Z	2	4
ρ_{calc}g/cm^3	1.428	1.438
μ/mm^{-1}	4.186	4.363
F(000)	1327.6	2148.0
Radiation	CuKα (λ=1.54184)	CuKα (λ=1.54184)
2Θ range for data collection/°	7.13 to 144.562	7.434 to 133.2
Index ranges	-11≤h≤16, -16≤k≤16, -23≤l≤22	-19≤h≤18, -7≤k≤17, -22≤l≤22
Reflections collected	19068	14839
Independent reflections	10073 [R_{int}=0.0363, R_{sigma}=0.0716]	8282 [R_{int}=0.0538, R_{sigma}=0.0851]
Data/restraints/parameters	10073/18/730	8282/0/592
Goodness-of-fit on F^2	1.046	1.086
Final R indexes [I>=2σ(I)]	R_1=0.0898, wR_2=0.2451	R_1=0.1331, wR_2=0.3351
Final R indexes [all data]	R_1=0.1005, wR_2=0.2585	R_1=0.1590, wR_2=0.3599
Largest diff. peak/hole/e Å^{-3}	1.95/-1.28	3.45/-1.73

Table C07 Crystal data and refinement for compound **2.4a** and **2.4b**.

	2.4a	**2.4b**
Identification code	GM200	GM049
Empirical formula	$C_{68}H_{61}F_6FeN_4O_4P_3Ru$	$C_{68}H_{63}F_6FeN_2P_3Ru$
Formula weight	1362.06	1272.07
Temperature/K	150(10)	150(10)
Crystal system	triclinic	orthorhombic
Space group	P-1	$P2_12_12_1$
a/Å	14.417(3)	14.875(3)
b/Å	14.947(3)	17.126(3)
c/Å	22.403(5)	24.082(5)
α/°	105.51(3)	90
β/°	93.86(3)	90
γ/°	114.07(2)	90
Volume/Å^3	4161(2)	6135(2)
Z	7	4
ρ_{calc}g/cm^3	1.3796	1.3772
μ/mm^{-1}	0.746	0.621
F(000)	1689.1	2614.8
Radiation	MoKα (λ=0.71073)	MoKα (λ=0.71073)
2Θ range for data collection/°	5.1 to 57.32	5.48 to 55.74
Index ranges	-19≤h≤19, -20≤k≤19, -30≤l≤30	-16≤h≤19, -22≤k≤22, -29≤l≤31
Reflections collected	86153	84935
Independent reflections	21156 [R_{int}=0.0706, R_{sigma}=0.0547]	14222 [R_{int}=0.0968, R_{sigma}=0.0835]
Data/restraints/parameters	21156/0/417	14222/0/735
Goodness-of-fit on F^2	3.726	1.017
Final R indexes [I>=2σ(I)]	R_1=0.1787	R_1=0.0488
Final R indexes [all data]	R_1=0.2073, wR_2=0.4990	R_1=0.0848, wR_2=0.1010
Largest diff. peak/hole/e Å^{-3}	9.33/-7.93	0.97/-0.84

Table C08 Crystal data and refinement for compound **2.5a** and **2.5b**.

	2.5a	**2.5b**
Identification code	GM050	GM086
Empirical formula	$C_{68}H_{63}ClFeN_2P_2Ru$	$C_{60}H_{57}ClN_4O_4P_2Ru$
Formula weight	1162.55	1096.59
Temperature/K	150(10)	150(10)
Crystal system	triclinic	monoclinic
Space group	P-1	$P2_1/c$
a/Å	12.485(3)	16.814(3)
b/Å	16.145(3)	12.589(3)
c/Å	18.018(4)	32.713(7)
α/°	75.74(3)	90
β/°	74.33(3)	103.39(3)
γ/°	87.69(3)	90
Volume/Å^3	3387.9(14)	6736(2)
Z	2	4
ρ_{calc}g/cm^3	1.2987	1.4162
μ/mm^{-1}	0.723	0.686
F(000)	1298.5	2946.1
Radiation	MoKα (λ=0.71073)	MoKα (λ=0.71073)
2Θ range for data collection/°	5.12 to 55.96	5.12 to 55.94
Index ranges	-16≤h≤16, -21≤k≤21, -23≤l≤23	-21≤h≤18, -16≤k≤15, -42≤l≤42
Reflections collected	66024	37384
Independent reflections	16190 [R_{int}=0.0997, R_{sigma}=0.1103]	12305 [R_{int}=0.0794, R_{sigma}=0.1388]
Data/restraints/parameters	16190/0/749	12305/0/708
Goodness-of-fit on F^2	1.057	1.298
Final R indexes [I>=2σ(I)]	R_1=0.0944	R_1=0.1216
Final R indexes [all data]	R_1=0.1450, wR_2=0.2506	R_1=0.1957, wR_2=0.3859
Largest diff. peak/hole/e Å^{-3}	2.68/-1.55	2.44/-1.82

Table C09 Crystal data and refinement for compound **2.6b** and **2.7a**.

	2.6b	**2.7a**
Identification code	GM154	GM172
Empirical formula	$C_{54}H_{52}ClN_3O_2P_2Ru$	$C_{60}H_{68}ClF_6N_4O_2P_3Ru$
Formula weight	973.48	1220.64
Temperature/K	150(10)	150(10)
Crystal system	monoclinic	monoclinic
Space group	$P2_1/c$	$C2/c$
a/Å	11.956(2)	23.640(5)
b/Å	29.278(6)	22.445(5)
c/Å	15.377(3)	27.540(6)
α/°	90	90
β/°	91.86(3)	113.52(3)
γ/°	90	90
Volume/Å^3	5379.6(19)	13399(6)
Z	4	8
ρ_{calc}g/cm^3	1.4541	1.2101
μ/mm^{-1}	0.694	0.402
F(000)	2416.1	5052.0
Radiation	MoKα (λ=0.71073)	MoKα (λ=0.71073)
2Θ range for data collection/°	5.2 to 56.56	5.22 to 57.32
Index ranges	-15≤h≤14, -39≤k≤37, -20≤l≤20	-31≤h≤31, -30≤k≤30, -36≤l≤37
Reflections collected	78214	152971
Independent reflections	13306 [R_{int}=0.0597, R_{sigma}=0.0406]	17136 [R_{int}=0.0660, R_{sigma}=0.0378]
Data/restraints/parameters	13306/0/639	17136/0/707
Goodness-of-fit on F^2	1.455	1.042
Final R indexes [I>=2σ(I)]	R_1=0.0578	R_1=0.1001
Final R indexes [all data]	R_1=0.0768, wR_2=0.1965	R_1=0.1199, wR_2=0.3275
Largest diff. peak/hole/e Å^{-3}	1.41/-1.39	4.44/-0.98

Table C10 Crystal data and refinement for compound **2.8a** and **2.8b**.

	2.8a	**2.8b**
Identification code	GM074	GM353
Empirical formula	$C_{72}H_{78}Cl_3F_6N_4P_3Ru_2$	$C_{54}H_{54}Cl_3N_2P_2Ru$
Formula weight	1514.82	1000.39
Temperature/K	150(10)	150(10)
Crystal system	monoclinic	monoclinic
Space group	P2/c	$P2_1/c$
a/Å	17.008(3)	17.2448(4)
b/Å	14.528(3)	11.9528(3)
c/Å	18.840(4)	28.4144(6)
α/°	90	90
β/°	107.75(3)	91.8175(18)
γ/°	90	90
Volume/Å^3	4433.6(17)	5853.9(2)
Z	2	4
ρ_{calc}g/cm^3	1.1346	1.354
μ/mm^{-1}	0.533	0.556
F(000)	1549.1	2456.0
Radiation	MoKα (λ=0.71073)	MoKα (λ=0.71073)
2Θ range for data collection/°	5.28 to 55.76	3.66 to 59.68
Index ranges	-21≤h≤22, -19≤k≤19, -24≤l≤24	-22≤h≤21, -13≤k≤16, -31≤l≤38
Reflections collected	96239	50674
Independent reflections	10550 [R_{int}=0.0565, R_{sigma}=0.0266]	14413 [R_{int}=0.0620, R_{sigma}=0.0863]
Data/restraints/parameters	10550/0/562	14413/0/646
Goodness-of-fit on F^2	1.474	1.026
Final R indexes [I>=2σ(I)]	R_1=0.0896	R_1=0.0806, wR_2=0.2006
Final R indexes [all data]	R_1=0.1055, wR_2=0.3338	R_1=0.1254, wR_2=0.2322
Largest diff. peak/hole/e Å^{-3}	3.72/-0.87	2.13/-1.92

Table C11 Crystal data and refinement for compound **2.9a** and **2.9b**.

	2.9a	**2.9b**
Identification code	GM420	GM425
Empirical formula	$C_{36}H_{39}Cl_3N_2PRu$	$C_{54}H_{63}Cl_2N_4PRu$
Formula weight	738.11	971.05
Temperature/K	150(10)	150(10)
Crystal system	monoclinic	triclinic
Space group	$P2_1/n$	P-1
a/Å	13.8363(8)	11.9177(3)
b/Å	14.1360(6)	14.7936(3)
c/Å	20.0447(10)	16.3767(3)
α/°	90	91.7805(15)
β/°	95.351(5)	105.9111(19)
γ/°	90	108.6898(18)
Volume/Å^3	3903.5(3)	2607.76(10)
Z	4	1
ρ_{calc}g/cm^3	1.362	1.237
μ/mm^{-1}	5.771	3.946
F(000)	1656	1016.0
Radiation	CuKα (λ=1.54184)	CuKα (λ=1.54184)
2Θ range for data collection/°	7.664 to 144.432	6.362 to 144.502
Index ranges	-17≤h≤13, -17≤k≤10, -24≤l≤23	-14≤h≤14, -18≤k≤16, -20≤l≤20
Reflections collected	14361	21940
Independent reflections	7530 [R_{int}=0.0533, R_{sigma}=0.0782]	10204 [R_{int}=0.0191, R_{sigma}=0.0294]
Data/restraints/parameters	7530/0/439	10204/0/571
Goodness-of-fit on F^2	1.074	1.122
Final R indexes [I>=2σ(I)]	R_1=0.1041, wR_2=0.2666	R_1=0.0605, wR_2=0.1870
Final R indexes [all data]	R_1=0.1361, wR_2=0.2999	R_1=0.0628, wR_2=0.1899
Largest diff. peak/hole/e Å^{-3}	3.67/-1.90	2.73/-2.31

Table C12 Crystal data and refinement for compound **3.1a** and **3.1a***.

	3.1a	**3.1a***
Identification code	GM215	GM218
Empirical formula	$C_{34}H_{28}Cl_2N_2P_2Ru$	$C_{52}H_{43}Cl_2N_2P_3Ru$
Formula weight	698.53	960.81
Temperature/K	150(10)	150(10)
Crystal system	triclinic	triclinic
Space group	P-1	P-1
a/Å	10.540(2)	11.029(5)
b/Å	14.272(3)	16.365(5)
c/Å	15.501(3)	16.494(5)
α/°	103.65(2)	109.991(5)
β/°	105.63(3)	109.339(5)
γ/°	108.01(3)	93.966(5)
Volume/Å^3	2001.5(11)	2583.3(16)
Z	3	2
ρ_{calc}g/cm^3	1.4462	1.3443
μ/mm^{-1}	0.965	0.639
F(000)	846.2	1067.6
Radiation	MoKα (λ=0.71073)	MoKα (λ=0.71073)
2Θ range for data collection/°	5.58 to 57.4	2.7 to 54.28
Index ranges	-14≤h≤14, -19≤k≤19, -20≤l≤20	-13≤h≤13, -19≤k≤20, -20≤l≤20
Reflections collected	45207	90480
Independent reflections	10192 [R_{int}=0.0463, R_{sigma}=0.0292]	10203 [R_{int}=0.0744, R_{sigma}=0.0343]
Data/restraints/parameters	10192/0/432	10203/0/568
Goodness-of-fit on F^2	2.504	1.053
Final R indexes [I>=2σ(I)]	R_1=0.0809	R_1=0.0671
Final R indexes [all data]	R_1=0.0871, wR_2=0.2907	R_1=0.0791, wR_2=0.1854
Largest diff. peak/hole/e Å^{-3}	4.41/-2.07	2.42/-1.91

Table C13 Crystal data and refinement for compound **3.2a** and **3.2a***.

	3.2a	**3.2a***
Identification code	GM242	GM219
Empirical formula	$C_{68}H_{56}Cl_2F_{12}N_4P_6Ru_2$	$C_{76}H_{62}Cl_2F_{12}N_4P_6Ru_2$
Formula weight	1616.07	1718.22
Temperature/K	150(10)	150(10)
Crystal system	triclinic	triclinic
Space group	P-1	P-1
a/Å	12.7874(8)	15.003(5)
b/Å	13.5514(7)	18.077(5)
c/Å	13.8196(7)	18.188(5)
α/°	113.043(5)	107.344(5)
β/°	91.596(5)	91.991(5)
γ/°	111.718(6)	106.712(5)
Volume/Å^3	2005.1(2)	4470(2)
Z	2	2
ρ_{calc}g/cm^3	1.558	1.5380
μ/mm^{-1}	6.492	0.873
F(000)	944	2008.7
Radiation	CuKα (λ=1.54184)	MoKα (λ=0.71073)
2Θ range for data collection/°	7.1 to 144.22	2.36 to 52.16
Index ranges	-15≤h≤10, -10≤k≤16, -17≤l≤16	-18≤h≤18, -22≤k≤21, -22≤l≤19
Reflections collected	12453	53682
Independent reflections	7631 [R_{int}=0.0359]	17695 [R_{int}=0.0567, R_{sigma}=0.0537]
Data/restraints/parameters	7631/0/478	17695/0/1053
Goodness-of-fit on F^2	1.079	2.483
Final R indexes [I>=2σ(I)]	R_1=0.0791, wR_2=0.2168	R_1=0.1112
Final R indexes [all data]	R_1=0.0903, wR_2=0.2322	R_1=0.1196, wR_2=0.3327
Largest diff. peak/hole/e Å^{-3}	3.43/-1.03	5.15/-2.81

Table C14 Crystal data and refinement for compound **3.1b** and **3.2b**.

	3.1b	**3.2b**
Identification code	GM248	GM252
Empirical formula	$C_{42}H_{32}Cl_2N_2P_2Ru$	$C_{84}H_{64}Cl_2F_{12}N_4P_6Ru_2$
Formula weight	798.64	1816.30
Temperature/K	293(2)	293(2)
Crystal system	orthorhombic	monoclinic
Space group	Pbca	Cc
a/Å	18.41896(16)	14.5449(2)
b/Å	17.38214(16)	24.2257(5)
c/Å	25.2621(2)	25.7756(4)
α/°	90	90
β/°	90	93.3323(14)
γ/°	90	90
Volume/Å^3	8087.95(12)	9066.9(3)
Z	8	4
ρ_{calc}g/cm^3	1.591	1.375
μ/mm^{-1}	7.817	4.417
F(000)	3920.0	3793.0
Radiation	CuKα (λ=1.54184)	CuKα (λ=1.54184)
2Θ range for data collection/°	7 to 144.8	7.1 to 144.36
Index ranges	-19≤h≤22, -19≤k≤21, -30≤l≤30	-17≤h≤17, -16≤k≤29, -30≤l≤31
Reflections collected	31455	26869
Independent reflections	7938 [R_{int}=0.0279]	13710 [R_{int}=0.0455]
Data/restraints/parameters	7938/0/496	13710/2/1025
Goodness-of-fit on F^2	1.032	1.038
Final R indexes [I>=2σ(I)]	R_1=0.0259, wR_2=0.0640	R_1=0.0813, wR_2=0.2240
Final R indexes [all data]	R_1=0.0292, wR_2=0.0662	R_1=0.0910, wR_2=0.2435
Largest diff. peak/hole/e Å^{-3}	0.46/-0.53	2.07/-1.49

D. Systems of units

In the SI system, mechanical properties are measured in mks units (length is measured in metres (m), mass in kilograms (kg), and time in seconds (s)). In the Gaussian system, length is measured in centimetres (cm), mass in grams (g), and time in seconds (s).

In the Gaussian system of units, the polarization $\boldsymbol{P}$ is related to the strength of the field $\boldsymbol{E}$ by Equation 1.3:

$$\boldsymbol{P} = \chi^{(1)}\boldsymbol{E} + \chi^{(2)}\boldsymbol{E}^2 + \chi^{(3)}\boldsymbol{E}^3 + \ldots \qquad \text{(Equation 1.3)}$$

Both $\boldsymbol{P}$ and $\boldsymbol{E}$ have the same units; the units of $\boldsymbol{P}$ and $\boldsymbol{E}$ and the dimensions of the susceptibilities are given as follows:

$$[P] = [E] = \frac{\text{statvolt}}{\text{cm}} = \frac{\text{statcoulomb}}{\text{cm}^2} = \left(\frac{\text{erg}}{\text{cm}^3}\right)^{1/2} \qquad \text{(Equation 1.4)}$$

$\chi^{(1)}$ is dimensionless,

$$\chi^{(2)} = \left[\frac{1}{E}\right] = \frac{\text{cm}}{\text{statvolt}} = \left(\frac{\text{erg}}{\text{cm}^3}\right)^{-1/2} \qquad \text{(Equation 1.5)}$$

$$\chi^{(3)} = \left[\frac{1}{E^2}\right] = \frac{\text{cm}^2}{\text{statvolt}^2} = \left(\frac{\text{erg}}{\text{cm}^3}\right)^{-1} \qquad \text{(Equation 1.6)}$$

For simplicity, the value of the susceptibilities is given in electrostatic units (esu).

In the MKS system of units, the relationship between the polarization $\boldsymbol{P}$ and the strength of the field $\boldsymbol{E}$ is expressed in Equation 1.2.

$$\boldsymbol{P} = \varepsilon_0(\chi^{(1)}\boldsymbol{E} + \chi^{(2)}\boldsymbol{E}^2 + \chi^{(3)}\boldsymbol{E}^3 + \ldots) \qquad \text{(Equation 1.2)}$$

$$\varepsilon_0 = 8.85 \times 10^{-12}\ \text{F/m} \qquad \text{(Equation 1.7)}$$

Since the units of $\boldsymbol{P}$ and $\boldsymbol{E}$, in the MKS system, are as follows:

$$[P] = \frac{\text{C}}{\text{m}^2} \qquad \text{(Equation 1.8)}$$

$$[E] = \frac{\text{V}}{\text{m}} \qquad \text{(Equation 1.9)}$$

and 1 Farad is equal to 1 Coulomb per Volt, the dimensions of the susceptibilities are given as follows.

$\chi^{(1)}$ is dimensionless,

$$\chi^{(2)} = [\frac{1}{E}] = \frac{\mathrm{m}}{\mathrm{V}} \qquad \text{(Equation 1.10)}$$

$$\chi^{(3)} = \left[\frac{1}{E^2}\right] = \frac{\mathrm{m}^2}{\mathrm{V}^2} \qquad \text{(Equation 1.11)}$$

To convert between the two systems of units, the two equations 1.2 and 1.3 are expressed in the following forms:

$$P = \varepsilon_0 \chi^{(1)} E \left[1 + \frac{\chi^{(2)} E}{\chi^{(1)}} + \frac{\chi^{(3)} E^2}{\chi^{(1)}} + \cdots\right] \qquad \text{(Equation 1.2')}$$

$$P = \chi^{(1)} E \left[1 + \frac{\chi^{(2)} E}{\chi^{(1)}} + \frac{\chi^{(3)} E^2}{\chi^{(1)}} + \cdots\right] \qquad \text{(Equation 1.3')}$$

Based on the Equations 1.4 and 1.7 and the fact that 1 statVolt ≈ 300 V, the relationship of E is:

$$\boldsymbol{E}_{\mathrm{MKS}} = 3 \times 10^4 \, \boldsymbol{E}_{\mathrm{cgs}} \qquad \text{(Equation 1.12)}$$

The displacement for a linear medium is given as

$$\boldsymbol{D}_{\mathrm{cgs}} = \boldsymbol{E} + 4\pi\boldsymbol{P} = \boldsymbol{E}(1 + 4\pi\chi^{(1)}) \qquad \text{(Equation 1.13)}$$

$$\boldsymbol{D}_{\mathrm{MKS}} = \varepsilon_0\boldsymbol{E} + \boldsymbol{P} = \varepsilon_0\boldsymbol{E}(1+\chi^{(1)}) \qquad \text{(Equation 1.14)}$$

where $\boldsymbol{D}$ is the electric displacement. Thus, it is found that:

$$\chi^{(1)}_{\mathrm{MKS}} = 4\pi\chi^{(1)}_{\mathrm{cgs}} \qquad \text{(Equation 1.15)}$$

Using Equations 1.12, 1.13 and 1.14 and the power series of Equations 1.2' and 1.3', the nonlinear susceptibilities in the two systems of units are related by

$$\chi^{(2)}_{\mathrm{MKS}} = \frac{4\pi}{3\times10^4}\chi^{(2)}_{\mathrm{cgs}} = 4.189\times10^{-4}\chi^{(2)}_{\mathrm{cgs}} \qquad \text{(Equation 1.16)}$$

$$\chi^{(3)}_{\mathrm{MKS}} = \frac{4\pi}{(3\times10^4)^2}\chi^{(3)}_{\mathrm{cgs}} = 1.40\times10^{-8}\chi^{(3)}_{\mathrm{cgs}} \qquad \text{(Equation 1.17)}$$

It is important to convert correctly between the two systems, and not only to convert correctly, but also to use the corresponding dimensions correctly. Traditionally, the SI system is common for macroscopic usage, while the Gaussian system is used for molecular NLO parameters. Through this work, the Gaussian system of units is adopted to permit systematic comparison with the previously reported data.